INFN/AExxx, LAL-xxx, SLAC-R-xxx

Super$B$ Detector Technical Design Report

Abstract

This report describes the technical design detector for Super$B$.

E. Grauges,
Universitat De Barcelona, *Fac. Fisica. Dept. ECM Barcelona E-08028, Spain*

G. Donvito, B. Santeramo, V. Spinoso
INFN Bari *and* **Università di Bari,** *Dipartimento di Fisica, I-70126 Bari, Italy*

M. Manghisoni, V. Re, G. Traversi
INFN Pavia *and* **Università di Bergamo** *Dipartimento di Ingegneria Industriale, I-24129 Bergamo, Italy*

G. Eigen, D. Fehlker, L. Helleve
University of Bergen, *Institute of Physics, N-5007 Bergen, Norway*

A. Carbone, R. Di Sipio, A. Gabrielli, D. Galli, F. Giorgi, C. Grandi, U. Marconi, S. Perazzini, C. Sbarra, V. Vagnoni, S. Valentinetti, M. Villa, A. Zoccoli
INFN Bologna *and* **Università di Bologna,** *Dipartimento di Fisica, I-40127 Bologna, Italy*

C. Cheng, A. Chivukula, D. Doll, B. Echenard, D. Hitlin, P. Ongmongkolkul, F. Porter, A. Rakitin, M. Thomas, R. Zhu
California Institute of Technology, *Pasadena, California 91125, USA*

G. Tatishvili
Carleton University, *Ottawa, Ontario, Canada K1S 5B6*

R. Andreassen, C. Fabby, B. Meadows, A. Simpson, M. Sokoloff, K. Tomko
University of Cincinnati, *Cincinnati, Ohio 45221, USA*

M. Andreotti, W. Baldini, R. Calabrese, V. Carassiti, G. Cibinetto, A. Cotta Ramusino, A. Gianoli, E. Luppi, E. Luppi, M. Munerato, L. Tomassetti
INFN Ferrara *and* **Università di Ferrara,** *Dipartimento di Fisica, I-44100 Ferrara, Italy*

D. Stoker
University of California, Irvine *Irvine, California 92697, USA*

O. Bezshyyko, G. Dolinska
Taras Shevchenko National University of Kyiv *Kyiv, 01601, Ukraine*

N. Arnaud, C. Beigbeder, F. Bogard, D. Breton, L. Burmistrov, D. Charlet, A. El Berni, J. Maalmi, V. Puill, A. Stocchi, V. Tocut, S. Wallon, G. Wormser
Laboratoire de l'Accélérateur Linéaire, *IN2P3/CNRS, Université Paris-Sud 11, F-91898 Orsay, France*

J.-F. Muraz, J.-S. Real
Laboratoire de Physique Subatomique et Cosmologie, *IN2P3/CNRS, Université Joseph Fourier Grenoble 1 & Institut Polytechnique de Grenoble, 53 rue des Martyrs F-38026 Grenoble Cedex, France*

D. Brown
Lawrence Berkeley National Laboratory, *University of California, Berkeley, California 94720, USA*

A. Calcaterra, R. de Sangro, G. Felici, G. Finocchiaro, P. Patteri, I. Peruzzi, M. Piccolo, M. Rama
Laboratori Nazionali di Frascati dell'INFN, *I-00044 Frascati, Italy*

S. Fantinel, G. Maron
Laboratori Nazionali di Legnaro dell'INFN, *I-35020 Legnaro, Italy*

E. Ben-Haim, G. Calderini, G. Marchiori
Laboratoire de Physique Nucléaire et de Hautes Energies, *IN2P3/CNRS, Université Pierre et Marie Curie-Paris 6, F-75005 Paris, France*

R. Cenci, A. Jawahery, D.A. Roberts
University of Maryland, *College Park, Maryland 20742, USA*

D. Lindemann, P. Patel, S. Robertson, D. Swersky
McGill University, *Montréal, Québec, Canada H3A 2T8*

P. Biassoni, M. Citterio, V. Liberali, F. Palombo, A. Stabile, S. Stracka
INFN Milano *and* **Università di Milano,** *Dipartimento di Fisica, I-20133 Milano, Italy*

A. Aloisio, G. De Nardo, A. Doria, R. Giordano, A. Ordine, S. Pardi, G. Russo, C. Sciacca
INFN Napoli *and* **Università di Napoli Federico II,** *Dipartimento di Scienze Fisiche, I-80126, Napoli, Italy*

A.Y. Barniakov, M.Y. Barniakov, V.E. Blinov, V.P. Druzhinin, V.B.. Golubev, S.A. Kononov, E. Kravchenko, A.P. Onuchin, S.I. Serednyakov, Y.I. Skovpen, E.P. Solodov
Budker Institute of Nuclear Physics, *Novosibirsk 630090, Russia*

M. Bellato, M. Benettoni, M. Corvo, A. Crescente, F. Dal Corso, C. Fanin, E. Feltresi, N. Gagliardi, S. Longo, M. Morandin, M. Posocco, M. Rotondo, G. Simi, R. Stroili
INFN Padova *and* **Università di Padova,** *Dipartimento di Fisica, I-35131 Padova, Italy*

C. Andreoli, L. Gaioni, E. Pozzati, L. Ratti, V. Speziali
INFN Pavia *and* **Università di Pavia,** *Dipartimento di Elettronica, I-27100 Pavia, Italy*

D. Aisa, M. Bizzarri, C. Cecchi, S. Germani, P. Lubrano, E. Manoni, A. Papi, A. Piluso , A. Rossi
INFN Perugia *and* **Università di Perugia,** *Dipartimento di Fisica, I-06123 Perugia, Italy*

M. Lebeau
INFN Perugia, *I-06123 Perugia, Italy, and*
California Institute of Technology, *Pasadena, California 91125, USA*

A. Fella
INFN Pisa *I-56124 Pisa, Italy and* **Laboratoire de l'Accélérateur Linéaire,** *IN2P3/CNRS, Université Paris-Sud 11, F-91898 Orsay, France and* **Università di Ferrara,** *Dipartimento di Fisica, I-44100 Ferrara, Italy*

C. Avanzini, G. Batignani, S. Bettarini, F. Bosi, M. Ceccanti, A. Cervelli, A. Ciampa, F. Crescioli, M. Dell'Orso, D. Fabiani, F. Forti, P. Giannetti, M. Giorgi, S. Gregucci, A. Lusiani, P. Mammini, G. Marchiori, M. Massa, E. Mazzoni, F. Morsani, N. Neri, E. Paoloni, L. Perez Perez, M. Piendibene, A. Profeti, G. Rizzo, L. Sartori, J. Walsh, E. Yurtsev
INFN Pisa, Università di Pisa, *Dipartimento di Fisica, and* **Scuola Normale Superiore,** *I-56127 Pisa, Italy*

D.M. Asner, J. E. Fast, R.T. Kouzes,
Pacific Northwest National Laboratory, *Richland, Washington 99352, USA*

A. Bevan, F. Gannaway, J. Mistry, C. Walker
Queen Mary, *University of London, London E1 4NS, United Kingdom*

C.A.J. Brew, R.E. Coath, J.P. Crooks, R.M. Harper, A. Lintern, A. Nichols, M. Staniztki, R. Turchetta, F.F. Wilson
Rutherford Appleton Laboratory, *Chilton, Didcot, Oxon, OX11 0QX, United Kingdom*

V. Bocci, G. Chiodi, R. Faccini, C. Gargiulo, D. Pinci, L. Recchia, D. Ruggieri
INFN Roma *and* **Università di Roma La Sapienza,** *Dipartimento di Fisica, I-00185 Roma, Italy*

A. Di Simone
INFN Roma Tor Vergata *and* **Università di Roma Tor Vergata,** *Dipartimento di Fisica, I-00133 Roma, Italy*

P. Branchini, A. Passeri, F. Ruggieri, E. Spiriti
INFN Roma Tre *and* **Università di Roma Tre,** *Dipartimento di Fisica, I-00154 Roma, Italy*

D. Aston, M. Convery, G. Dubois-Felsmann, W. Dunwoodie, M. Kelsey, P. Kim, M. Kocian, D. Leith, S. Luitz, D. MacFarlane, B. Ratcliff, M. Sullivan, J. Va'vra, W. Wisniewski, W. Yang
SLAC National Accelerator Laboratory *Stanford, California 94309, USA*

K. Shougaev, A. Soffer
School of Physics and Astronomy, Tel Aviv University *Tel Aviv 69978, Israel*

F. Bianchi, D. Gamba, G. Giraudo, P. Mereu
INFN Torino *and* **Università di Torino,** *Dipartimento di Fisica Sperimentale, I-10125 Torino, Italy*

G. Dalla Betta, G. Fontana, G. Soncini
INFN Padova *and* **Università di Trento,** *ICT Department, I-38050 Trento, Italy*

M. Bomben, L. Bosisio, P. Cristaudo, G. Giacomini, D. Jugovaz, L. Lanceri, I. Rashevskaya, G. Venier, L. Vitale
INFN Trieste*and* **Università di Trieste,** *Dipartimento di Fisica, I-34127 Trieste, Italy*

R. Henderson
TRIUMF *Vancouver, British Columbia, Canada V6T 2A3*

J.-F. Caron, C. Hearty, P. Lu, R. So
University of British Columbia, *Vancouver, British Columbia, Canada V6T 1Z1*

P. Taras
Université de Montreál, *Physique des Particules, Montreál, Québec, Canada H3C 3J7*

A. Agarwal, J. Franta, J.M. Roney
University of Victoria, *Victoria, British Columbia, Canada V8W 3P6*

Contents

1 Introduction

1.1 The Physics Motivation

The Standard Model successfully explains the wide variety of experimental data that has been gathered over several decades with energies ranging from under a GeV up to several hundred GeV. At the start of the millennium, the flavor sector was perhaps less explored than the gauge sector, but the PEP-II and KEK-B asymmetric B Factories, and their associated experiments *BABAR* and Belle, have produced a wealth of important flavor physics highlights during the past decade [1]. The most notable experimental objective, the establishment of the Cabibbo-Kobayashi-Maskawa phase as consistent with experimentally observed CP-violating asymmetries in B meson decay, was cited in the award of the 2008 Nobel Prize to Kobayashi & Maskawa [2].

The B Factories have provided a set of unique, over-constrained tests of the Unitarity Triangle. These have, in the main, been found to be consistent with Standard Model predictions. The B factories have done far more physics than originally envisioned; *BABAR* alone has published more than 480 papers in refereed journals to date. Measurements of all three angles of the Unitarity Triangle – α and γ, in addition to sin 2β; the establishment of $D^0\bar{D}^0$ mixing; the uncovering of intriguing clues for potential New Physics in $B \to K^{(\star)}l^+l^-$, $B \to K\pi$, $B \to D\tau\nu$, and $B \to D^{(\star)}\tau\nu$ decays; and unveiling an entirely unexpected new spectroscopy, are some examples of important experimental results beyond those initially contemplated.

All present measurements confirm the Standard Model, reducing the parameter space for New Physics Models, whose signals remain elusive. With the LHC in full operation, we expect major experimental discoveries during the next few years at the energy frontier, where we would hope not only to complete the Standard Model by confirming that the exciting recent observations by Atlas and CMS around 126 GeV/c^2 indeed come from the Higgs boson, but to find signals of New Physics which are widely expected to lie around the 1 TeV energy scale. If found, the New Physics phenomena will need data from very sensitive heavy flavor experiments if they are to be understood in detail. Determining the flavor structure of the New Physics involved requires the information on rare b, c and τ decays, and on CP violation in b and c quark decays that only a very high luminosity asymmetric B Factory can provide [3]. On the other hand, if such signatures of New Physics are not observed at the LHC, then the excellent sensitivity provided at the luminosity frontier by a next generation super B-factory provides another avenue to observing New Physics at mass scales up to 10 TeV or more through observation of rare processes involving B and D mesons and studies of lepton flavour violation (LFV) in τ decays.

1.2 The SuperB Project Elements

It is generally agreed that the physics being addressed by a next-generation B factory requires a data sample that is some 50—100 times larger than the existing combined sample from *BABAR* and Belle, or at least 50—75 ab^{-1}. Acquiring such an integrated luminosity in a 5 year time frame requires that the collider run at a luminosity of at least $10^{36}\,\mathrm{cm}^{-2}\mathrm{s}^{-1}$.

For a number of years, an Italian led, INFN hosted, collaboration of scientists from Canada, Italy, Israel, France, Norway, Spain, Poland, UK and USA have worked together to design and propose a high luminosity 10^{36} asymmetric B Factory project, called Super$B$, to be built at or near the Frascati laboratory [4].

The Super$B$ project was included in the Italian Ministry National research plan in 2010, with the accelerator site at the University of Tor Vergata in Rome being selected in June 2011. In October 2011, a consortium between INFN and the University of Tor Vergata was formed to manage the construction and operation of the Super$B$ accelerator and related facilities. The consortium is called the Nicola Cabibbo Laboratory.

The accelerator portion of the project employs lessons learned from modern low-emittance synchrotron light sources and ILC/CLIC R&D, and an innovative new idea for the intersection region of the storage rings [5], called crab waist, to reach luminosities over 50 times greater than those obtained by earlier B factories at KEK and SLAC. There is now an attractive, cost-effective accelerator design, including polarized beams, which is being further refined and optimized [6]. It is designed to incorporate many PEP-II components. This facility promises to deliver fundamental discovery-level science at the luminosity frontier.

There is also an active international collaboration working effectively on the design of the detector. The detector team draws heavily on its deep experience with the *BABAR* detector, which has performed in an outstanding manner both in terms of scientific productivity and operational efficiency. *BABAR* serves as the foundation of the design of the Super$B$ detector, although the much higher luminosity and the different physics and machine backgrounds require modifications and enhancements of the detector components in most areas that have required substantial R&D.

The Super$B$ project has been developed over a substantial time frame. In 2010, the design and development of all elements of the project were described in the "Design Progress Reports", a set of several descriptive documents that summarized developments and status of each major division of the project: Physics [7], Accelerator [6], and Detector [8]. These documents present as snapshot of the entire project at an intermediate stage between the Conceptual Deign Report [4], which was written in 2007, and the Technical Design Reports (TDRs) planned for publication during the next one to two years. The Detector TDR presented here is the first of these documents to be published.

1.3 The Detector Technical Design Report

This TDR describes the design and development of the Super$B$ detector, which is based on a major upgrade of *BABAR*. This is one of several major design documents that will be produced as the project proceeds. Each document will present the detailed design and/or motivation for the design choices made for each major elements of the project (Physics, Accelerator, Detector, and Computing). The projected time schedules for these documents are asynchronous, based on the design, project status, and schedule expected for each of the project elements.

This Detector TDR begins with overviews of each of the elements of the project (Accelerator, Detector, and the Physics). In particular, the Detector section summarizes the base detector design, the challenges involved in detector operations at the luminosity frontier, the approach being taken to optimize remaining general design options, and the R&D program that is underway to validate the system and subsystem designs. A chapter detailing the many challenging issues involved in the machine detector interface at this high luminosity machine follows. Each of the detector subsystems and the general detector systems (especially electronics and Data Acquisition) are then described in more detail, followed by a discussion of the computing and software. The detector hall facilities are then described in the context of the integration and assembly of the full detector. Finally, the paper concludes with a discussion project management, detector costs, and a schedule overview. The detailed information in these chapters is expected to continue to develop as as the collaboration grows, and is expected to

lead to a supplementary report on these topics
at a later date.

Bibliography

[1] J. Beringer *et al.* (Particle Data Group),"Review of Particle Physics", Phys. Rev. D **86**, 1 (2012).

[2] http://nobelprize.org/nobel_prizes/physics/laureates/2008/press.html; and http://www-public.slac.stanford.edu/babar/Nobel2008.htm.

[3] D. Hitlin *et al.*, *Proceedings of Super*B *Workshop VI: New Physics at the Super Flavor Factory*, arXiv:0810.1312v2 [hep-ph].

[4] M. Bona *et al.*, *Super*B*: A High-Luminosity Heavy Flavour Factory. Conceptual Design Report*, arXiv:0709.0451v2 [hep-ex], INFN/AE-07/2, SLAC-R-856, LAL 07-15, also available at http://www.pi.infn.it/SuperB/CDR.

[5] P. Raimondi in *2nd LNF Workshop on Super*B, Frascati, Italy, March 16-18 2006 http://www.lnf.infn.it/conference/superb06/; and in *Proceedings of Particle Accelerator Conference (PAC 07)*, Albuquerque, New Mexico, USA, June 25-29, 32 (2007).

[6] *Super*B *Progress Report for the Collider*, arXiv:1009.6178v3 [physics.acc-ph] (2010) http://arxiv.org/abs/1009.6178

[7] *Super*B *Progress Report: Physics*, arXiv:1008.1541v1 [hep-ex] (2010) http://arxiv.org/abs/1008.1541

[8] *Super*B *Progress Report: Detector*, arXiv:1007.4241v1 [physics.ins-det] (2010) http://arxiv.org/abs/1007.4241

2 Accelerator Overview

Biagini + Paoloni Pages ?

3 Detector Overview

FF+BR Pages ?

The Super$B$ detector concept is based on the *BABAR* detector, with those modifications required to operate at a luminosity of 10^{36} or more, and with a reduced center-of-mass boost. Further improvements needed to cope with higher beam-beam and other beam-related backgrounds, as well as to improve detector hermeticity and performance, are also discussed, as is the necessary R&D required to implement this upgrade. Cost estimates and the schedule are described in Section17.

The current *BABAR* detector consists of a tracking system with a five layer double-sided silicon strip vertex tracker (SVT) and a 40 layer drift chamber (DCH) inside a 1.5T magnetic field, a Cherenkov detector with fused silica bar radiators (DIRC), an electromagnetic calorimeter (EMC) consisting of 6580 CsI(Tl) crystals and an instrumented flux-return (IFR) comprised of both limited streamer tube (LST) and resistive plate chamber (RPC) detectors for K_L^0 detection and μ identification.

The Super$B$ detector concept reuses a number of components from *BABAR*: the flux-return steel, the superconducting coil, the barrel of the EMC and the fused silica bars of the DIRC. The flux-return will be augmented with additional absorber to increase the number of interaction lengths for muons to roughly 7λ. The DIRC camera will be replaced by a twelve-fold modular camera using multi-channel plate (MCP) photon detectors in a focusing configuration using fused silica optics to reduce the impact of beam related backgrounds and improve performance. The forward EMC will feature cerium-doped LYSO (lutetium yttrium orthosilicate) crystals, which have a much shorter scintillation time constant, a lower Molière radius and better radiation hardness than the current CsI(Tl) crystals, again for reduced sensitivity to beam backgrounds and better position resolution.

The tracking detectors for Super$B$ will be new. The current SVT cannot operate at $\mathcal{L} = 10^{36}$, and the DCH has reached the end of its design lifetime and must be replaced. To maintain sufficient proper-time difference (Δt) resolution for time-dependent *CP* violation measurements with the Super$B$ boost of $\beta\gamma = 0.24$, the vertex resolution will be improved by reducing the radius of the beam pipe, placing the innermost layer of the SVT at a radius of roughly 1.2 cm. This innermost layer of the SVT will be constructed of either silicon striplets or Monolithic Active Pixel Sensors (MAPS) or other pixelated sensors, depending on the estimated occupancy from beam-related backgrounds. Likewise, the design of the cell size and geometry of the DCH will be driven by occupancy considerations. The hermeticity of the Super$B$ detector, and, thus, its performance for certain physics channels will be improved by including a backwards "veto-quality" EMC detector comprising a lead-scintillator stack. The physics benefit from the inclusion of a forward PID remains under study. The baseline design concept is a fast Cherenkov light based time-of-flight system.

The Super$B$ detector concept is shown in Fig. 3.1., The top portion of this elevation view shows the minimal set of new detector components, with substantial reuse of elements of the current *BABAR* detector; the bottom half shows a configuration with additional new components that would cope with higher beam backgrounds and achieve greater hermeticity.

3.1 Physics Performance

The Super$B$ detector design, as described in the Conceptual Design Report [1], left open a number of issues that have a large impact on the overall detector geometry. These include the

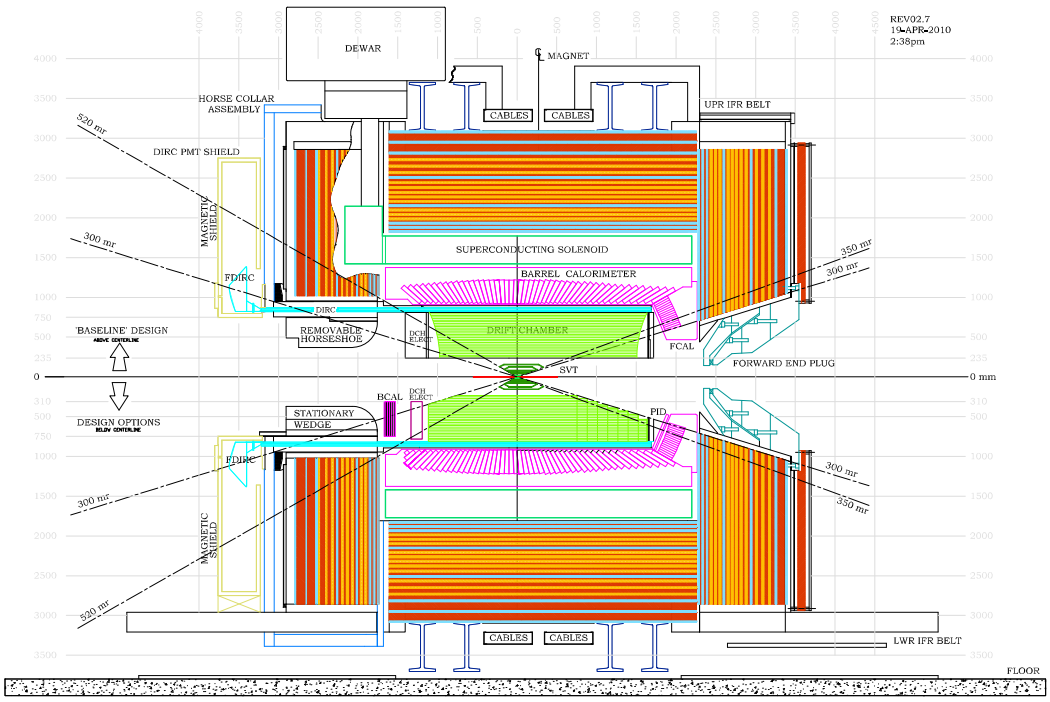

Figure 3.1: Concept for the Super$B$ detector. The upper half shows the baseline concept, and the bottom half adds a number of optional detector configurations.

physics impact of of a PID device in front of the forward EMC; the need for an EMC in the backward region; the position of the innermost layer of the SVT; the SVT internal geometry and the SVT-DCH transition radius; and the amount and distribution of absorber in the IFR.

These issues have been addressed by evaluating the performance of different detector configurations in reconstructing charged and neutral particles as well as the overall sensitivity of each configuration to a set of benchmark decay channels. To accomplish this task, a fast simulation code specifically developed for the Super$B$ detector has been used (see Section14), combined with a complete set of analysis tools inherited, for the most part, from the *BABAR* experiment. Geant4-based code has been used to simulate the primary sources of backgrounds – including both machine-induced and physics processes – in order to estimate the rates and occupancies of various sub-detectors as a function of position. The main results from these ongoing studies are summarized in this section.

Time-dependent measurements are an important part of the Super$B$ physics program. In order to achieve a Δt resolution comparable to that at *BABAR*, the reduced boost at Super$B$ must be compensated by improving the vertex resolution. This requires a thin beam pipe plus SVT Layer0 that is placed as close as possible to the IP. The main factor limiting the minimum radius of Layer0 is the hit rate from $e^+e^- \rightarrow e^+e^-e^+e^-$ background events. Two candidate detector technologies with appropriate characteristics, especially in radiation

length (X_0) and hit resolution, for application in Layer0 are (1) a hybrid pixel detector with 1.08% X_0, and 14 μm hit resolution, and (2) striplets with 0.40% X_0 and 8 μm hit resolution. Simulation studies of $B^0 \to \phi K^0_S$ decays have shown that with a boost of $\beta\gamma = 0.28$ the hybrid pixels (the striplets) reach a $\sin 2\beta_{\rm eff}$ per event error equal to *BABAR* at an inner radius of 1.5 cm (2.0 cm). With $\beta\gamma = 0.24$ the error increases by 7—8%. Similar conclusions also apply to $B^0 \to \pi^+\pi^-$ decays.

The *BABAR* SVT five-layer design was motivated both by the need for standalone tracking for low-p_T tracks as well as the need for redundancy in case several modules failed during operation. The default Super$B$ SVT design, consisting of a *BABAR*-like SVT detector and an additional Layer0, has been compared with two alternative configurations with a total of either five or four layers. These simulation studies, which used the decay $B \to D^*K$ as the benchmark channel, focused on the impact of the detector configuration on track quality as well as on the reconstruction efficiency for low p_T tracks. The studies have shown that, as expected, the low-p_T tracking efficiency is significantly decreased for configurations with reduced numbers of SVT layers, while the track quality is basically unaffected. Given the importance of low momentum tracking efficiency for the Super$B$ physics program, these results support a six-layer layout.

Studies have also shown that the best overall SVT+DCH tracking performance is achieved if the outer radius of the SVT is kept small (14 cm as in *BABAR* or even less) and the inner wall of the DCH is as close to the SVT as possible. However, as some space between the SVT and DCH is needed for the cryostats that contain the super-conducting magnets in the interaction region, the minimum DCH inner radius is expected to be about 20—25 cm.

The impact of a forward PID device is estimated using benchmark modes such as $B \to K^{(*)}\nu\bar{\nu}$, balancing the advantage of having better PID information in the forward region with the drawbacks arising from more material in front of the EMC and a slightly shorter DCH. Three detector configurations have been compared in these simulation studies: *BABAR*, the Super$B$ baseline(no forward PID device), and a configuration that includes a time-of-flight (TOF) detector between the DCH and the forward EMC. The results, presented in terms of $S/\sqrt{S+B}$, for the decay mode $B \to K\nu\bar{\nu}$ with the tag side reconstructed in the semileptonic modes, are shown in Fig. 3.2. In summary, while the default Super$B$ design leads to an improvement of about 7-8% in $S/\sqrt{S+B}$, primarily due the reduced boost in Super$B$ the configuration with the forward TOF provides an additional 5-6% improved sensitivity for this channel. Machine backgrounds have yet to be included in these simulations, but will be considered in our next updates.

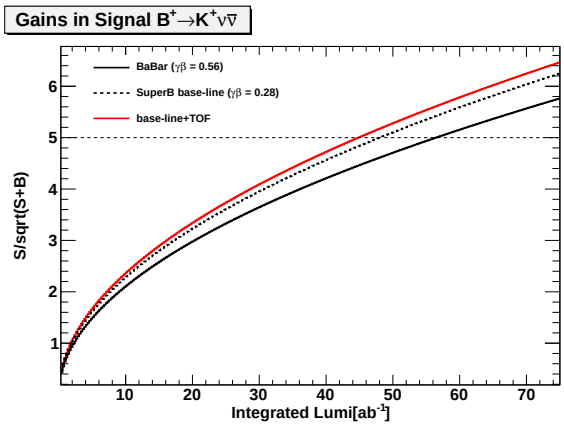

Figure 3.2: $S/\sqrt{S+B}$ of $B \to K\nu\bar{\nu}$ as a function of the integrated luminosity in three different detector configurations.

The backward calorimeter under consideration is designed to be used in veto mode. Its impact on physics can be estimated by studying the sensitivity of rare B decays with one or more neutrinos in the final state, which benefit from having more hermetic detection of neutrals to reduce the background contamination. One of the most important benchmark channels of this kind is $B \to \tau\nu$. Preliminary studies, not including the machine backgrounds, indicate that, when the backward calorimeter is installed, the statistical precision $S/\sqrt{S+B}$ is

enhanced by about 8%. The results are summarized in Fig. 3.3. The top plot shows how $S/\sqrt{S+B}$ changes as a function of the cut on $E_{\rm extra}$ (the total energy of charged and neutral particles that cannot be directly associated with the reconstructed daughters of the signal or tag B) with or without the backward EMC. The signal is peaked at zero. The bottom plot shows the ratio of $S/\sqrt{S+B}$ for detector configurations with and without a backward EMC, again as a function of the $E_{\rm extra}$ cut. This analysis will be repeated soon, including the main sources of machine backgrounds, which could affect the $E_{\rm extra}$ distributions significantly. The possibility of using the backward calorimeter as a PID time-of-flight device is also under study.

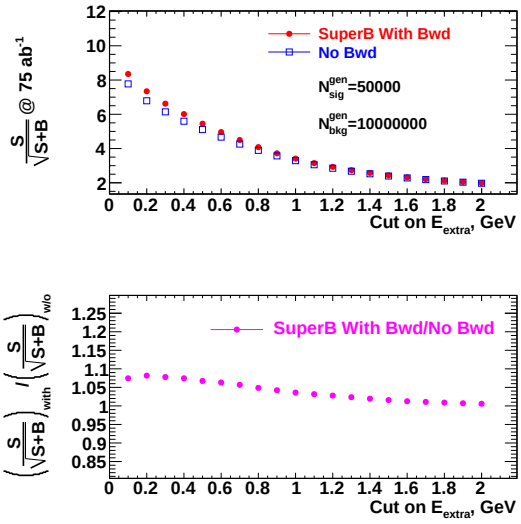

Figure 3.3: Top: $S/\sqrt{S+B}$ as a function of the cut on $E_{\rm extra}$ with (circles) and without (squares) the backward EMC. Bottom: ratio of $S/\sqrt{S+B}$ for detector configurations with or without a backward EMC as a function of the $E_{\rm extra}$ cut.

The presence of a forward PID or backward EMC affects the maximum extension of the DCH and therefore the tracking and dE/dx performance in those regions. The impact of a TOF PID detector is practically negligible because it only takes a few centimeters from the DCH. On the other hand, the effect of a forward RICH device (~ 20 cm DCH length reduction) or the backward EMC (~ 30 cm) is somewhat larger. For example, for tracks with polar angles $< 23°$ and $> 150°$, there is an increase in σ_p/p of 25% and 35%, respectively. Even in this case, however, the overall impact on the physics is generally quite limited because only a small fraction of tracks cross the extreme forward and backward regions.

The IFR system will be upgraded by replacing the *BABAR* RPCs and LSTs with layers of much faster extruded plastic scintillator coupled to WLS fibers read out by APDs operated in Geiger mode. The identification of muons and K_L^0 is optimized with a Geant4 simulation by tuning the amount of iron absorber and the distribution of the active detector layers. The current baseline design has a total iron thickness of 92 cm interspersed with eight layers of scintillator. Preliminary estimates indicate a muon efficiency larger than 90% for $p > 1.5$ GeV/c at a pion misidentification rate of about 2%.

3.2 Challenges on Detector Design

Machine background is one of the leading challenges of the Super$B$ project: each subsystem must be designed so that its performance is minimally degraded because of the occupancy produced by background hits. Moreover, the detectors must be protected against deterioration arising from radiation damage. In effect, what is required is that each detector perform as well or better than *BABAR* with similar operational lifetimes, but for two orders of magnitude higher luminosity.

Background particles produced by beam gas scattering and by the synchrotron radiation near the interaction point (IP) are expected to be manageable since the relevant Super$B$ design parameters (mainly the beam current) are fairly close to those in PEP-II .

Touschek backgrounds are expected to be larger than in *BABAR* because of the extremely

low design emittances of the Super$B$ beams. Preliminary simulation studies indicate that a system of beam collimators upstream of the IP can reduce particle losses to tolerable levels.

The main source of concern arises from the background particles produced at the IP by QED processes whose cross section is $\sim 200\,\mathrm{mb}$ corresponding at the nominal Super$B$ luminosity to a rate of $\sim$ 200 GHz. Of particular concern is the radiative Bhabha reaction (i.e.: $e^+e^- \rightarrow e^+e^-\gamma$), where one of the incoming beam particles loses a significant fraction of its energy by the emission of a photon. Both the photon and the radiating beam particles emerge from the IP traveling almost collinearly with respect to the beam-line. The magnetic elements downstream of the IP over-steer these primary particles into the vacuum chamber walls producing electro-magnetic showers, whose final products are the background particles seen by the subsystems. The particles of these electromagnetic showers can also excite the giant nuclear resonances in the material around the beam line expelling neutrons from the nucleus. Careful optimization of the mechanical apertures of the vacuum chambers and the optical elements is needed to keep a large stay-clear for the off-energy primary particles, hence reducing the background rate.

A preliminary Geant4-based Monte Carlo simulation study of this process at Super$B$ indicates that a shield around the beamline will be required to keep the electrons, positrons, photons and neutrons away from the detector, reducing occupancies and radiation damage to tolerable levels.

The "quasi-elastic Bhabha" process has also been considered. The cross section for producing a primary particle reconstructed by the detector via this process is $\sim 100\,\mathrm{nb}$ corresponding to a rate of about 100 kHz. It is reasonable to assume that this will be the driving term for the level one trigger rate. Single beam contributions to the trigger rate are, in fact, expected to be of the same order as in *BABAR* , given that the nominal beam currents and other relevant design parameter are comparable.

A final luminosity related background effect is the production of electron-positron pairs at the IP by the two photon process $e^+e^- \rightarrow e^+e^-e^+e^-$, whose total cross section evaluated at leading order with the Monte Carlo generator DIAG36 [2] is 7.3 mb corresponding, at nominal luminosity, to a rate of 7.3 GHz. The pairs produced by this process are characterized by very soft transverse momenta particles. The solenoidal magnetic field in the tracking volume confines most of these background particles inside the beam pipe. Those articles having a transverse momentum large enough to reach the beam pipe ($p_T > 2.5\,\mathrm{MeV}/c$) and with a polar angle inside the Layer0 acceptance are produced at a rate of ~ 0.5 GHz. This background will be a driving factor in the design of the segmentation and the read-out architecture for SVT Layer0. The background track surface rate on the SVT Layer0 as a function of its radius is shown in Fig. 3.4.

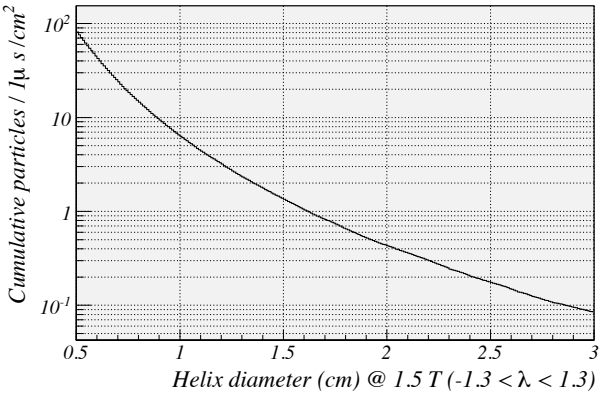

Figure 3.4: Pairs background track rate per unit surface as a function of the SVT Layer0 radius. Multiple track hits have not been taken into account.

An effort to improve the simulation of these background sources with a Geant4 based code is underway at present. A fairly accurate model of the detector and beam-line elements is available to the collaboration. Several configurations have been simulated and studied, providing some guidelines to the detector and machine teams. Further refinements of the interaction region and detector design will require develop-

ment of the Geant4 background simulation tools on the detector response side.

3.3 Open Issues

The basic geometry, structure and physics performance of the Super$B$ detector is mainly predetermined by the retention of the solenoidal magnet, return steel, and the support structure from the *BABAR* detector, and a number of its largest, and most expensive, subsystems. Even though this fixes both the basic geometry, and much of the physics performance, it does not really constrain the expected performance of the Super$B$ detector in any important respect. *BABAR* was already an optimized B-factory detector for physics, and any improvements in performance that could come from changing the overall layout or rebuilding the large subsystems would be modest overall. The primary challenge for Super$B$ is to retain physics performance similar to *BABAR* in the higher background environment described in Section3.2, while operating at much higher ($\sim \times 50$) data taking rates.

Within these constraints, optimization of the geometrical layout and new detector elements for the most important physics channels remains of substantial interest. The primary tools for sorting through the options are: (1) simulation, performed under the auspices of a "Detector Geometry Working Group" (DGWG), that studies basic tracking, PID, and neutrals performance of different detector configurations, including their impact on each other, and studies the physics reach of a number of benchmark channels; and (2) detector R&D, including prototyping, developing new subsystem technologies, and understanding the costs, and robustness of systems, as well as their impacts on each other. The first item, discussed in Section3.1, clearly provides guidance to the second, as discussed in Section3.4 and the subsystem chapters which follow, and vice versa.

At the level of the overall detector, the immediate task is to define the sub-detector envelopes. Optimization can and will continue for some time yet within each sub-detector system. The studies performed to date leave us with the default detector proposal, with only a few open options remaining at the level of the detector geometry envelopes and technology choices. These open issues are: (1) whether there is a forward PID detector, and, if so, at what z location does the DCH end and the EMC begin; and (2) whether there is a backward EMC. These open issues are expected to be resolved by the Technical Board within the next few months following further studies by the DGWG, in collaboration with the relevant system groups.

3.4 Detector R&D

The Super$B$ detector concept rests, for the most part, on well validated basic detector technology. Nonetheless, each of the sub-detectors has may challenges due to the high rates and demanding performance requirements with R&D initiatives ongoing in all detector systems to improve the specific performance, and optimize the overall detector design. These are described in more detail in each subsystem section.

The SVT innermost layer has to provide good space resolution while coping with high background. Although silicon striplets are a viable option at moderate background levels, a pixel system would certainly be more robust against background. However, keeping the material in a pixel system low enough not to deteriorate the vertexing performance is challenging, and there is considerable activity to develop thin hybrid pixels or, even better, monolithic active pixels. These devices may be part of a planned upgrade path and installed as a second generation Layer0. Efforts are directed towards the development of sensors, high rate readout electronics, cooling systems and mechanical support with low material content.

In the DCH, many parameters must be optimized for Super$B$ running, such as the gas mixture and the cell layout. Precision measurements of fundamental gas parameters are ongoing, as well as studies with small cell chamber prototypes and simulation of the properties of

different gas mixtures and cell layouts. An improvement of the performance of the DCH could be obtained by using the innovative "Cluster Counting" method, in which single clusters of charge are resolved time-wise and counted, improving the resolution on the track specific ionization and the space accuracy. This technique requires significant R&D to be proven feasible in the experiment.

Though the Barrel PID system takes over major components from *BABAR*, the new camera and readout concept is a significant departure from the *BABAR* system, requiring extensive R&D. The challenges include the performance of pixelated PMTs for DIRC, the design of the fused silica optical system, the coupling of the fused silica optics to the existing bar boxes, the mechanical design of the camera, and the choice of electronics. Many of the individual components of the new camera are now under active investigations by members of the PID group, and studies are underway with a single bar prototype located in a cosmic ray telescope at SLAC. A full scale (1/12 azimuth) prototype incorporating the complete optical design is planned for cosmic ray tests during the next two years.

Endcap PID concepts are less developed, and whether they match the physics requirements and achieve the expected detector performance remains to be demonstrated. Present R&D is centered on developing a good conceptual understanding of different proposed concepts, on simulating how their performance affects the physics performance of the detector, and on conceptual R&D for components of specific devices to validate concepts and highlight the technical and cost issues.

The EMC barrel is a well understood device at the lower luminosity of *BABAR*. Though there will be some technical issues associated with refurbishing, the main R&D needed at present is to understand the effects of pile-up in simulation, so as to be able to design the appropriate front-end shaping time for the readout.

The forward and backward EMCs are both new devices, using cutting edge technology. Both will require one or more full beam tests, hopefully at the same time, within the next year or two. Prototypes for these tests are being designed and constructed.

Systematic studies of IFR system components have been performed in a variety of bench and cosmic ray tests, leading to the present proposed design. This design will be beam tested in a full scale prototype currently being prepared for a Fermilab beam. This device will demonstrate the muon identification capabilities as a function of different iron configurations, and will also be able to study detector efficiency and spatial resolution.

At present, the Electronics, DAQ, and Trigger (ETD), have been designed for the base luminosity of $1 \times 10^{36}\,\mathrm{cm}^{-2}\,\mathrm{s}^{-1}$, with adequate headroom. Further R&D is needed to understand the requirements at a luminosity up to 4 times greater, and to insure that there is a smooth upgrade path when the present design becomes inadequate. On a broad scale, as discussed in the system chapter, each of the many components of ETD have numerous technical challenges that will require substantial R&D as the design advances.

Bibliography

[1] M. Bona *et al.*, *Super*B*: A High-Luminosity Heavy Flavour Factory. Conceptual Design Report*, arXiv:0709.0451v2 [hep-ex], INFN/AE-07/2, SLAC-R-856, LAL 07-15, also available at http://www.pi.infn.it/SuperB/CDR.

[2] F. A. Berends, P. H. Daverveldt and R. Kleiss, *Monte Carlo Simulation of Two Photon Processes. 2. Complete Lowest Order Calculations for Four Lepton Production Processes in Electron Positron Collisions*, Comput. Phys. Commun. **40**, 285 (1986).

4 Physics with SuperB

4.1 Introduction

The Super$B$ project consists of an e^+e^- collider with a general purpose detector dedicated to the study of precision flavor physics. This will be built at the Cabibbo Laboratory and commence taking data later this decade. Super$B$ is expected to accumulate: $75\,\mathrm{ab}^{-1}$ of data at the $\Upsilon(4S)$, more than 100 times the *BABAR* data sample; $1000\,\mathrm{fb}^{-1}$ at the $\psi(3770)$, 100 times the expected data sample from BES III; and several ab^{-1} at the $\Upsilon(5S)$, 15 times the data sample accumulated by Belle; as well as running at other center of mass energies. Using these data one will be able to search for new physics (NP) and test the standard model (SM) in a multitude of ways.

This document is divided into summaries of the heavy quark flavour physics programme, i.e. $B_{u,d,s}$ and D decays (section 4.2), τ physics (section 4.3), precision electroweak physics (section 4.4), exotic spectroscopy (section 4.5), and direct searches (section 4.6). Finally section 4.7 gives a broad overview of the physics programme and how this fits into the context of furthering our understanding of nature at a fundamental level. More detailed discussions of the Super$B$ project and physics programme can be found in Refs. [**?**, **?**, **?**, **?**, **?**, **?**]. The Super$B$ project submissions to the European Strategy Group on the opportunities offered by detector development and on the computing model can be found in Refs [**?**, **?**].

4.2 B and D decays

4.2.1 Rare B decays

Rare B decays provide an excellent opportunity to search for NP at a flavour factory. Processes highly suppressed in the SM, such as Flavour Changing Neutral Currents (FCNCs), could receive large NP contributions, often resulting in measurable deviations in the branching fractions and other observables.

The Super$B$ detector will be well equipped to study a wide variety of rare B meson decays. Excellent reconstruction of charged and neutral particles, with very good particle identification and virtually fully efficient triggering for $B\overline{B}$ events, allow the study of complex decay chains that involve several charged and neutral particles. In addition, decay modes with missing neutrinos can be studied effectively by employing *hadronic* or *semileptonic tagging* techniques. This approach, which has been used very successfully at the current B Factories, entails fully reconstructing one of the two B meson decays in the event, thus assigning the remaining particles (including missing particles) to the signal decay under study. This powerful technique is used to identify decays with missing neutrinos. We discuss selected rare B decays in the following paragraphs, most of which can only be studied in the e^+e^- environment. These are important parts of the Super$B$ physics programme.

The decay mode $B^+ \to \tau^+\nu_\tau$ is sensitive to NP scenarios that include a charged Higgs boson, such as SUSY and two-Higgs doublet models. Currently, the branching fraction for this decay, measured at *BABAR* and Belle, is approximately 2σ from the SM value, obtained from global fits to CKM quantities [**?**, **?**]. This "tension" will be elucidated by making more precise experimental measurements at future Super Flavour Factories, such as Super$B$. In fact, the technique of hadronic or semileptonic tagging, where the non-signal B meson in the event is fully reconstructed, allows the search on the signal side of a single charged track and missing energy. With this method, Super$B$ will measure $\mathcal{B}(B^+ \to \tau^+\nu_\tau)$ with a precision of approximately 3%. If the central values remain where they are currently, this measurement will

be a clear indication of NP. The related channel $B^+ \to \mu^+\nu_\mu$, which will be measured to about 5% at Super$B$, will increase the overall sensitivity to the presence of charged Higgs bosons. Belle have recently updated their $B^+ \to \tau^+\nu_\tau$ measurement and obtain a result compatible with the SM [**?**], however the corresponding *BABAR* update remains in tension [**?**], prompting the need for further experimental investigation. Figure 4.1 shows the constraint on the charged Higgs mass vs $\tan\beta$ plane that would be obtained from a Super$B$ measurement of $B \to \tau\nu$ and $B \to \mu\nu$ consistent with the SM. A similar constraint would be obtained in the MSSM.

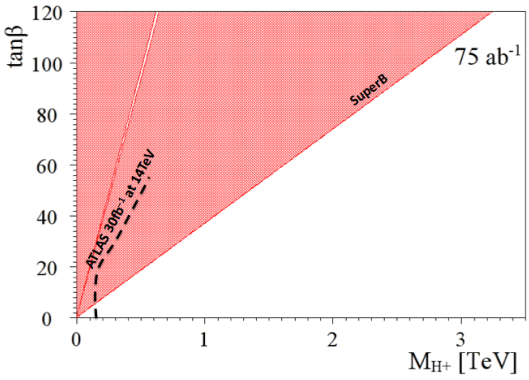

Figure 4.1: The constraint on the mass of a charged Higgs boson as a function of $\tan\beta$ in a 2HDM-II (95% C.L.). The constraint anticipated from the LHC with 30 fb^{-1} of data collected at a centre of mass energy of 14 TeV is also shown for comparison. The Super$B$ constraint is dominated by $B \to \tau\nu$ up to luminosities $\sim 30\,\text{ab}^{-1}$, and the $B \to \mu\nu$ contribution dominates above this. The ATLAS constraint is taken from arXiv:0901.0512.

Semileptonic B decays with a τ lepton in the final state are sensitive to NP effects, in particular those arising from the presence of a charged Higgs boson. The *BABAR* experiment recently reported an excess of $B \to D^{(*)}\tau\nu$ decays with respect to SM expectations, with a combined statistical significance of 3.4σ [**?**]. Interestingly, the results seem to exclude the simplest NP model with a charged Higgs, the Type II Two Higgs Doublet Model. More precise measurements of these channels are needed to determine if the discrepancy is more than a statistical fluctuation. The large data sample of Super$B$ will lead to greatly reduced uncertainties on these branching fractions and will allow the determination of the q^2-dependence of the decay rate, an important measurement for unraveling the nature of possible NP effects.

The decays $B \to K^{(*)}\nu\bar{\nu}$ are interesting probes of NP, since they allow one to study Z penguin and other electroweak penguin effects in the absence of other operators that can dominate in $b \to s\ell^+\ell^-$ decays. Here again hadronic and semileptonic tagging will be used to isolate the non-signal B meson in the event. The signal signature then becomes a single kaon (or K^*) candidate accompanied by a momentum imbalance, and nothing else. Super$B$ will maximize sensitivity to NP by independently measuring the $B \to K\nu\bar{\nu}$ and $B \to K^*\nu\bar{\nu}$ branching fractions, along with F_L, the K^* longitudinal polarization fraction. Furthermore, it may be possible to measure the fully inclusive mode $B \to X_s\nu\bar{\nu}$ at Super$B$, increasing the sensitivity to NP effects in Z penguin processes. The expected constraints on the model-independent NP parameters ε and η introduced in [**?**] are shown in figure 4.2.

One fruitful area to look for NP is in $b \to s\ell^+\ell^-$ transitions, which occur in the SM via electroweak penguin loops and box diagrams. This transition represents a rather broad field of study since it comprises several different exclusive decays of charged and neutral B mesons, along with the fully inclusive channel, usually denoted $B \to X_s\ell^+\ell^-$. Super$B$ will accumulate $10 - 15K$ events in each of the exclusive channels, including final states with an e^+e^- pair. The ratio $R_\mu^{(*)} = B(B \to K^{(*)}\mu^+\mu^-)/B(B \to K^{(*)}e^+e^-)$, an important observable sensitive to neutral Higgs particles in SUSY models, will only be measured precisely at future Super Flavour Factories. The event sample accumulated at Super$B$ will complement the current

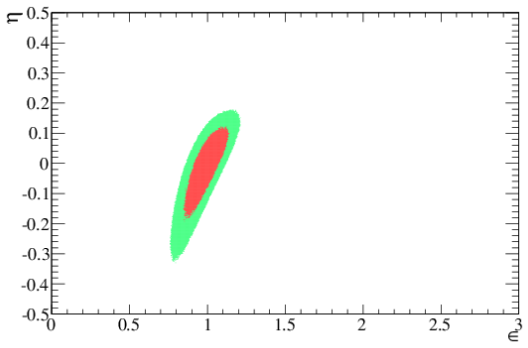

Figure 4.2: Expected constraints on the model-independent parameters ε and η describing NP contributions to $B \to K^{(*)}\nu\bar{\nu}$ [**?**] from Super$B$ measurements.

studies being performed on $B^0 \to K^{*0}\mu^+\mu^-$ at LHC [**?**]. Additionally, Super$B$ will make precise measurements of rates, asymmetries and angular distributions of the inclusive channel $B \to X_s\ell^+\ell^-$, exploiting the possibility of performing hadronic and semileptonic tagging in the e^+e^- environment. The inclusive channel is of interest because theoretical calculations of inclusive observables generally have lower uncertainties compared to the corresponding exclusive channels.

The study of $b \to s\gamma$ transitions has been one of the cornerstones of the B physics programmes at *BABAR* and Belle. The combination of precise measurements of the inclusive branching fraction along with its precise SM calculation, both at the level of about 7%, leads to strong constraints on Flavour Changing Neutral Currents in NP models. Super$B$ will measure this branching fraction to about 3% precision, increasing the constraints imposed by this transition. There is no consensus whether the theoretical uncertainty could match this precision or not. Additionally, the high statistics of the Super$B$ data sample will permit the measurement of the Cabibbo-suppressed $B \to X_d\gamma$ channel to good precision.

4.2.2 Rare D decays

For a long time the HEP community has worked on $K \to \pi\nu\bar{\nu}$ transitions and plans new projects to study this mode in greater detail. Here SM dynamics are greatly suppressed, and one can deal with the impact of long distance (LD) dynamics by using correlations with semileptonic decays. This situation is different for $D \to X_u\nu\bar{\nu}$: short distance dynamics are truly tiny with $\mathrm{BR}_{\mathrm{SD}}(D \to X_u\nu\bar{\nu}) \sim O(10^{-15})$, and LD contributions impact on inclusive final states is negligible in the SM. This rare charm decay mode is a good place to look for signs of NP which could enhance the branching fraction by many orders of magnitude above the SM expectation. For general models of NP like Little Higgs with T parity (LHT) or non-minimal charged Higgs models, one can have enhancements up to 10^4. More exotic models can lead to larger enhancements. This decay can be studied using fully reconstructed hadronically tagged D events at the $\psi(3770)$. Other advantages of studying rare charm decays at Super$B$ include: final states with π, η, η' and 2π can contribute around 10–20% for the inclusive width. This is enough for probing enhancements from NP. One may compare direct and indirect CP violation by comparing $D^\pm \to \pi^\pm\nu\bar{\nu}$ with $D^0/\overline{D}^0 \to \pi^0\nu\bar{\nu}$. At the $\psi(3770)$ one can use quantum correlations between $D\overline{D}$ pairs, e.g. at threshold one can analyze $D_L \to \pi^0/\eta/\eta'\nu\bar{\nu}$ due to correlation with $D \to K^+K^-/\pi^+\pi^-$ to probe direct vs indirect CP violation in the case of large NP manifestations.

Another rare decay D that can be used to obtain an insight into physics beyond the SM is $D \to \gamma\gamma$. This channel is dominated by long distance transitions, however it is possible that NP could enhance the rate well above the SM expectation of a few $\times 10^{-8}$. Super$B$ is expected to be able to achieve a sensitivity that will enable a rudimentary measurement of this mode at the SM rate. If NP is not manifest, then this rate will provide a stringent constraint on the LD contribution to the decay $D \to \mu^+\mu^-$, which itself is a mode very sensitive to NP. The $D \to \mu^+\mu^-$ amplitude is dominated by the LD component, and so in order to interpret if any measured rate is compatible with the SM or

not, one has to have a good understanding of $D \to \gamma\gamma$.

It is also possible to probe NP using the set of decays $D \to h\ell^+\ell^-$, where $h = \pi, \rho$. Even though the total rate is dominated by LD contributions, the shape of the q^2 distribution of the di-lepton pair is sensitive to NP, and in particular one may be able to learn about the underlying dynamics of these final states by comparing resonant to off-resonant features within the di-lepton system.

Finally one can search for light dark matter particles by studying D decays to invisible, or invisible $+\gamma$ final states. Measurements made at the $\psi(3770)$ can complement the corresponding studies of rare $B_{d,s}$ mesons performed at the $\Upsilon(4S)$ and $\Upsilon(5S)$.

4.2.3 CKM matrix and unitarity triangle

Broadly speaking improved determinations of CKM matrix elements will lead to a better understanding of the SM, and in particular more precise tests of unitarity. It should be noted however that some of the rare decay searches that are sensitive probes of NP have significant theoretical uncertainties arising from the lack of precision CKM parameter determinations. Hence not only NP could show up in precision CKM matrix element measurements, but these measurements also play a significant role in the search for NP elsewhere. Super$B$ will be able to improve the determination of four of the CKM matrix elements via measurements of $|V_{ub}|$, $|V_{cb}|$, $|V_{us}|$ and $|V_{cd}|$ as briefly summarized below.

At the end of the B Factory era there is still tension between inclusive and exclusive measurements of $|V_{ub}|$ and $|V_{cb}|$. In anticipation of larger data samples theorists have started working with experimentalists to understand how one can make measurements in the future that are both experimentally and theoretically more robust. Several promising ideas have been made that will require data samples comparable to that achievable at Super$B$. Unitarity tests are just one of the reasons why it is important to improve our understanding of these parameters. Precision measurements of these quantities will be beneficial to the Lattice community and enable a number of rare decay searches for NP.

The measurement of $|V_{us}|$ is currently dominated by the interpretation of semi-leptonic kaon decays. However the limiting factor in those measurements comes from theory and unless significant progress is made on that front there will be essentially no improvement on the precision of $|V_{us}|$ from more precise kaon measurements. If one wishes to make a significant improvement in the measurement of $|V_{us}|$ one has to resort to the use of τ leptons. Super$B$ with about 75 times the existing worlds sample of τ lepton pairs will be able to make a significant improvement on the determination of this parameter.

Data accumulated at the $\psi(3770)$ will enable one to determine $|V_{cd}|$ via the study of semi-leptonic D decays. This CKM factor is currently known to a precision of 4.8%. It is expected that BES III will be able to improve the precision on this quantity before Super$B$ starts to take data, with an expected 100 times the data sample of BES III, Super$B$ should be able to perform a necessary cross check, and improve our understanding of this CKM element.

It should be noted that the ratio of $|V_{td}/V_{ts}|$ can be determined using radiative B decays via $b \to d$ and $b \to s$ transitions. Theoretical uncertainties that would otherwise limit the interpretation of these results cancel in the ratio of rates.

Super$B$ will also improve the measurements of the unitarity triangle angles α, β and γ to expected precisions of 1°, 0.2°, and 1°, respectively. These estimates are for the most sensitive modes and are sufficient to perform a percent level determination of the apex of the unitarity triangle ($\sigma_{\overline{\eta}}/\overline{\eta} \sim 1\%$, $\sigma_{\overline{\rho}}/\overline{\rho} \sim 3\%$) using only angles, and will provide a precision input to global fits. The primary measurements of γ and β are expected to be theoretically clean in the context of the full Super$B$ data sample.

Current theory results in an uncertainty on α of about 1° from SU(2) symmetry breaking. There are four sets of modes that will be used to extract this angle: $B \to \pi\pi$, $B \to \rho\rho$,

$B \to \pi^+\pi^-\pi^0$, and $B \to a_1\pi$, where SU(3) breaking affects the latter measurement. Consistency between modes will allow one to constrain NP entering through loop contributions, as any large difference in the measured central values would not be consistent with the SM.

Current measurements of γ from the B Factories and LHCb highlight the (well known) need for diversity in channels used to measure γ. Dalitz methods can access the weak phase directly, however the most popular methods implemented (ADS and GLW) rely on reconstructing quasi-two-body $D^{(*)}K^{(*)}$ final states whereby the weak phase is measured as a term multiplied by a Cabibbo suppression factor r_B. This number is small (1-2%) and poorly determined, and so the constraint on γ is highly sensitive to the extracted value of this nuisance parameter. For that reason we expect that it will be necessary to continue to average together different sets of constraints on γ in order to obtain a robust measurement for the foreseeable future. With the full data sample from Super$B$ we expect to be able to measure γ to a precision of 1° in a given channel. The GGSZ (Dalitz) method for γ is expected to have significant a systematic uncertainty arising from limited knowledge of the strong phase difference as a function of position in the $D \to K^0_S h^+ h^-$ Dalitz plot. The Super$B$ run at charm threshold is expected to provide 100 times the data available from BES III, which can be used to effectively remove this uncertainty and enable the continued use of this method. The GGSZ method currently dominates our knowledge of γ, so it is important that one retain this powerful approach in the determination of the angles. Also the assumption that *CP* violation in charm decays is negligible in the determination of γ is something that should be revisited in light of recent results from LHCb, CDF and Belle.

4.2.4 *CP* violation in B decays

It is important to compare tree- and loop-level processes which measure the same unitarity triangle angles in the SM. NP, more likely to affect loop-dominated processes, can then be revealed by a difference in the extracted angle.

Typical examples are the loop-dominated $b \to s$ transitions. These are a set of modes that are able to measure β_{eff} in the SM, where $\beta_{eff} \sim \beta$, up to hadronic uncertainties from higher order contributions. By testing the consistency with β from tree dominated charmonium + K^0 modes, one can search for signs of heavy particles with non-trivial quark flavour transitions in loops. The most promising "*golden*" modes are those that are both experimentally precise and theoretically clean. A full list of the golden modes is given in Ref. [**?**], and the highlights are (for $b \to s$ penguin transitions) $B \to \eta' K^0$ ($\sigma_S = 0.007$), $B \to \phi K^0$ ($\sigma_S = 0.02$), and (for $b \to d$ transitions) $B \to J/\psi\pi^0$ ($\sigma_S = 0.02$). The latter mode is used to bound theoretical uncertainties in the tree dominated $B \to J/\psi K^0$ channel.

A set of *CP* violating observables that are central to the B physics programme at Super$B$ are *CP* asymmetries in radiative decays. These include $a_{CP}(B \to X_s\gamma)$ and $a_{CP}(B \to X_{s+d}\gamma)$ which are predicted to be small in the SM. While the former seems theoretically limited, the latter has quite small theoretical uncertainty [**?**]. The experimental error on $a_{CP}(B \to X_{s+d}\gamma)$ at Super$B$ will be about 2%.

Furthermore, a time-dependent analysis of the *CP* asymmetry in the exclusive mode $B^0 \to K^0_s\pi^0\gamma$ will be very sensitive to the presence of right-handed currents arising from NP. For this decay, we estimate an uncertainty of 0.03 on the *CP* violation parameter C.

4.2.5 *CP* violation in D decays

The recent evidence for direct *CP* violation in charm decays using a time-integrated asymmetry ΔA_{CP} is extremely interesting[1]. It is clear from the response of the theoretical community that one needs to perform a detailed analysis of hadronic uncertainty before heralding this result as a sign of NP, since various conclusions have been reached either in favor of NP or of being compatible with the SM. Shortly before this

[1] This is a difference in time-integrated rates of neutral D mesons decaying into K^+K^- and $\pi^+\pi^-$ final states.

result was announced a systematic evaluation of time-dependent CP asymmetries in charm was proposed using data from $\psi(3770)$, $\Upsilon(4S)$ and at hadron machines [**?**]. There are at least thirty five neutral modes that provide interesting tests of the SM, and a number will only be accessible at e^+e^- machines, and will complement the work underway at the LHC. Unlike B decays where golden channels can be readily identified in time-dependent measurements, hadronic effects cloud ones ability to interpret any small (percent level or less) result given the data accessible today. To resolve the issue of hadronic uncertainties one needs to measure a multitude of final states, and once again Super$B$ can contribute to the endeavor. An important step forward would be to perform a time-dependent measurement of a single mode. Currently, in order to control of systematic uncertainties at the LHC, a difference is taken between two modes. One presumes it will soon be possible to extract the TDCP parameters from a single mode at LHCb without resorting to taking a difference. In the case of $D \to \pi^+\pi^-$ (which is more interesting in the context of the SM than the KK final state used for ΔA_{CP} as it can be used to measure an angle of a unitarity triangle) one needs to control penguin contributions, and an Isospin analysis will result in an error of a few degrees. It has been suggested for example that a time-dependent analysis of $D \to \pi^+\pi^-$ and $D \to \pi^0\pi^0$ channels can be used to resolve this problem up to Isospin breaking from electroweak penguins. This residual contribution can be controlled using the direct CP violation measurement from $D \to \pi^+\pi^0$ decays.[2] It should also be noted that if a relatively large non-zero value of ΔA remains, then it is possible that TDCP parameters would be clearly non-SM when measured. Many of these issues can be resolved by Super$B$, and it would be possible to explore this new area in the full range of final states. It is also important to quantify CP violation in charm decays as the methods to measure γ using B decays assume this is negligible, and one must verify this is the case for precision measurements.

It is also possible to measure direct CP violation in charged D decays, however as with B and kaon manifestations of direct CP violation, detailed understanding of hadronic uncertainties and strong phase differences will be required in order to interpret any results in the context of the SM. Four body final states such as $D \to K^+K^-\pi^+\pi^-$ can be used to measure triple product asymmetries related to T odd, CP violating phenomena.

It should be possible for the low energy machine to reach 4.005 GeV, on doing so one could measure the CP asymmetry in $e^+e^- \to DD^* \to D\overline{D}\gamma$.

4.2.6 Other symmetry tests

CPT is conserved in relativistic quantum field theories, and underpins the SM. Super$B$ will be able to test CPT using neutral B and D mesons created in collisions at the $\Upsilon(4S)$ and $\psi(3770)$, respectively. The most recent test of CPT from *BABAR* yields a deviation from the SM expectation of 2.8σ [**?**]. While this is not significant it is important to repeat this measurement to understand if this is an out lier, or if there is some contribution from NP.

If CPT is conserved, then given that CP is violated one can infer that T must also be violated. *BABAR* recently discovered T violation via a time-dependent asymmetry constructed from T conjugated pairs of neutral B meson decays [**?**]. This established the existence of T violation using a self-consistent approach, without invoking CPT to relate CP violation to T violation. This is an significant step forward in the field, and should be studied in greater detail. Super$B$ will be able to significantly improve the precision on this measurement, which can then be compared with complementary tests of CP violation and CPT to test the SM.

4.2.7 Charm mixing

Whatever the outcome of studies of direct and indirect CP violation, an open question remains whether mixing-induced CP violation can also

[2] For this mode in particular, the required precision of parts per mille is probably only possible with data from charm threshold.

be observed. An obvious sign of this phenomenon would be a mode dependence of the mixing parameters x_D or y_D, respectively related to mass and decay widths for the underlying D mass eigenstates. CP violation in mixing itself would show up in $D-\overline{D}$ differences in mixing rates $|q/p|$ and in the phase of this quantity. We anticipate [**?**] that Super$B$ should be sensitive to a value for $|q/p|_D$ differing from 1.0 by a few percent, or to a mixing phase $\arg(q/p)$ differing from zero by $\sim 1°$. Furthermore, we expect that such results can also be obtained in a variety of decay modes. We also anticipate measurements of x_D and y_D with precisions close to $\sim 1\times10^{-4}$, an improvement of an order of magnitude from current world averages. This precision compares well with expectations from LHCb but the comparison will depend on the ultimate LHCb trigger, whose present design limits their yield of decays to the "golden" CP self-conjugate modes (primarily $K^0_S\pi^+\pi^-$ or $K^0_SK^+K^-$). The e^+e^- data should, however, cover a considerably wider range of modes that will complement well the results from LHCb.

The Super$B$ estimates are derived from a robust extrapolation from charm mixing parameters measured by *BABAR* [**?**]. Specifically, we assume that sample sizes at the $\Upsilon(4S)$ will be larger, thereby improving statistical precision by a factor at least ~ 12 [3]. We expect most systematic effects to scale with square root of luminosity, but we do note that the time-dependent Dalitz plot analyses of decays to the golden modes, which are crucial, will be limited in precision by an irreducible systematic uncertainty in the nature of the Dalitz plot decay model. We estimate this limits precision in x_D to 7×10^{-4}, only a factor 4 improvement over *BABAR*. Replacing the Dalitz models with measurements of $D^0\overline{D}^0$ phases obtained from quantum correlations observed in $\psi(3770)$ data from BES III, should improve the precision on $x_D(y_D)$ to $4(2)\times10^{-4}$. This model uncertainty would be virtually eliminated by the use of a 1 ab^{-1} Super$B$ run at charm threshold to reach precisions $\sim 2(1)\times10^{-4}$.

The anticipated integrated luminosity at charm threshold from Super$B$ is expected to be 1 ab^{-1}. Previous estimates of the sensitivity to charm mixing have assumed half of this data sample in order to determine the anticipated precison on x and y. Figure 4.3 shows the corresponding constraint obtained when one uses the full 1 ab^{-1} sample.

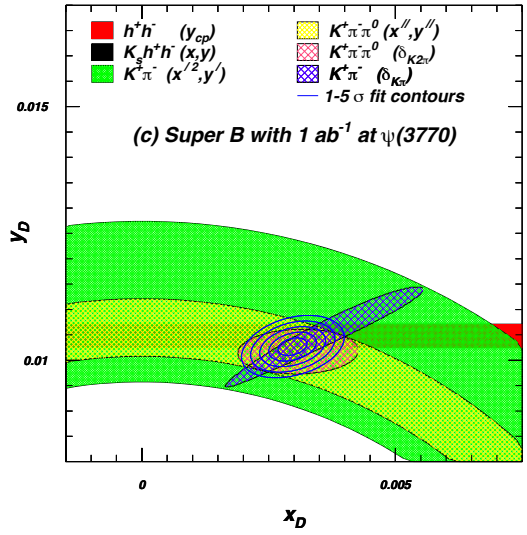

Figure 4.3: The expected constraint from Super$B$ on the charm mixing parameters x and y using the full 75 ab^{-1} sample from the $\Upsilon(4S)$, and 1 ab^{-1} from $\psi(3770)$.

4.2.8 B physics at the $\Upsilon(5S)$

It is expected that Super$B$ will accumulate several ab^{-1} of data at the $\Upsilon(5S)$. The aim of the physics programme at this center of mass energy is to search for physics beyond the SM via rare decays and to perform precision tests of the SM. An example of a decay channel that may be affected by NP is $B_s\to\gamma\gamma$. Various NP scenarios suggest correlations between this B_s decay and $B_d\to X_s\gamma$. Hence, a branching fraction measurement of this decay is an important cross check of searches for NP performed using data collected at the $\Upsilon(4S)$. A number of

[3] Simulation studies indicate that the improved time-resolution in Super$B$ could introduce further gains that we did not include in the estimates.

rare decays with neutral final states or missing energy can be studied in this environment.

The semi-leptonic asymmetry a_{SL} in B_s decays is of interest as this is sensitive to NP and can be correlated with flavor observables measured at the $\Upsilon(4S)$. Super$B$ is expected to be able to measure a_{SL} to a precision of 0.006 with $1\,\mathrm{ab}^{-1}$ of data at the $\Upsilon(5S)$.

It is possible to use tagged neutral B decays at the $\Upsilon(5S)$ to measure time dependent asymmetries of modes that would otherwise be impractical. For example $B^0 \to \pi^0\pi^0$ could be studies by adapting techniques recently used by Belle to measure the golden mode asymmetry using $\Upsilon(5S)$ data.

It will be possible to study B_s decays inclusively using data from the $\Upsilon(5S)$, and one can also search for the $B_s \to \tau^+\tau^-$ channel using kinematics of the final state to suppress background.

Finally, compared to B_d and B_u decays, knowledge of the decay modes of B_s is limited. With a data sample of this size, Super$B$ will be able to contribute to the general level of understanding of absolute branching fractions of B_s decays, which will enable theorists to improve their calculations and may reduce uncertainties on normalization channels for hadronic experiments to use.

4.3 τ physics at SuperB

Measurements on τ leptons at the intensity frontier provide a powerful tool to search for NP effects in a way that is competitive and complementary with respect to LHC and other existing or planned experiments like MEG and Mu2e. Lepton Flavor violation (LFV) in τ decay is a measurable unambiguous signal for many NP models, and the expected sensitivities of the planned Super Flavor Factories is unrivaled. The large and clean dataset of $e^+e^- \to \tau^+\tau^-$ events will also permit additional NP searches based on precision measurements of CPV in τ decays, and of the τ $g-2$ and EDM form factors, with impressive improvements on the present experimental accuracy. Furthermore, Super$B$ offers the unique features of the largest design luminosity and of an 80% polarized electron beam, which provides an extra handle to identify sources of NP in LFV and to improve the experimental precision on the τ $g-2$ and EDM form factors.

In addition to being a powerful probe for NP, a high luminosity τ factory at the $\Upsilon(4S)$ peak represents an ideal facility for most τ physics measurements because the data analysis is facilitated from the fact that events consist in a correlated $\tau^+\tau^-$ pair in a well defined initial state with no superposition of background. And in the Super$B$ project, the information of the initial state is further refined in a useful way using a polarized electron beam. In these conditions, a large number of precision measurements are possible, such as $|V_{us}|$ from τ decays into strange final states, α_s, the $(g-2)_\mu$ hadronic contribution, and leptonic charged weak current couplings.

4.3.1 Lepton flavor violation in τ decay

The SM with neutrino mixing includes Lepton Flavor Violation (LFV) in τ decays, although at rates too small to be detected. On the other hand, measurable LFV rates can naturally arise for a variety of NP models, for instance MSSM [**?**, **?**], MSSM with flavor symmetries [**?**, **?**], Non Universal Higgs Masses (NUHM) SUSY [**?**, **?**, **?**], MSSM with R-parity violation (RPV) [**?**], LHT [**?**], $Z^{'}$ models [**?**]).

In many cases, the most sensitive mode is $\tau^\pm \to \mu^\pm\gamma$, and some important complementary modes are $\tau \to e\gamma$, $\tau \to \ell\ell\ell$, $\tau \to \mu\eta$. The planned Super Flavor Factories, Super$B$ and Belle II, have no significant competition in these NP searches, and Super$B$ has the advantage of a larger design luminosity and electron beam polarization, which can be used to distinguish between left and right handed NP currents.

LFV in muon decay is related to τ LFV in a way that is determined by the specific details of a NP model, on which there are no experimental clues so far. Therefore, LFV searches on $\mu \to e\gamma$ and $\mu \to e$ conversion in material are complementary in nature with the τ ones, and in order to understand NP in the long term one has to understand all three sets of measurements in de-

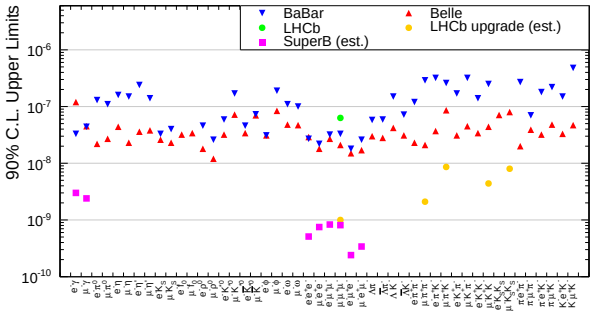

Figure 4.4: Summary of present upper limits on τ LFV compared with expected upper limits from Super$B$ and the LHCb upgrade. The latter estimates are the order-of-magnitude estimates listed in the letter of intent [?]. A naive LHCb-upgrade sensitivity estimate for $\tau \to 3\mu$ based on the 2012 LHCb 90% expected upper limit [?] extrapolated from $1\,\text{fb}^{-1}$ to $50\,\text{fb}^{-1}$ with the square root of the luminosity gives 1.5×10^{-8}, to be compared with 1.0×10^{-9} in the plot. In some cases, the *BABAR* results are hidden by very similar results by Belle, which are superposed in the plot.

tail. While for some specific NP models, with specific choices of parameters, the experimental sensitivity for LFV is larger for muon decays than for τ decays, in general searches for LFV τ decays remain important in understanding the underlying dynamics of NP models.

The Super$B$ design integrated luminosity of $75\,\text{ab}^{-1}$, in combination with moderate improvements in the detector efficiency and resolution, provides a LFV sensitivity 10 times better than the B-factories for background-limited τ decay modes like $\tau^\pm \to \mu^\pm\gamma$ and up to 100 times better for the cleanest $\tau \to \ell\ell\ell$ searches. Figure 4.4 summarizes the expected LFV sensitivities from Super$B$ and the LHCb upgrade [?].

4.3.2 *CP* violation in τ decay

The SM predicts vanishingly small *CP* violation effects in τ decays, for instance, the *CP* asymmetry rate of $\tau^\pm \to K^\pm\pi^0\nu$ is estimated to be of order $\mathcal{O}(10^{-12})$ [?]. For the decay $\tau^\pm \to K_S\pi^\pm\nu$ the SM predicts, with a 2% relative precision, a *CP* asymmetry of 3.3×10^{-3} due to the known *CP*-violating phase of the $K^0\overline{K}^0$ mixing amplitude [?]. Any observed deviation from this clean, and precisely defined, picture would be a clear sign of NP. Specific NP models such as RPV SUSY [?, ?] and non-SUSY multi-Higgs models [?, ?, ?, ?] can accommodate *CP* violation in τ decays up to 10^{-1} or the present experimental limits [?], while satisfying other experimental constraints. Example of decay modes with potentially sizable asymmetries are $\tau \to K\pi\nu_\tau$, $\tau \to K\eta^{(\prime)}\nu_\tau$, and $\tau \to K\pi\pi\nu_\tau$ [?, ?, ?, ?, ?].

The Belle and *BABAR* Collaborations have searched for *CP* violation in τ decay [?, ?] with different analyses on the same decay mode. *BABAR* measured the *CP* asymmetry in the total branching ratio, which is affected by the K_S *CP* violation amplitude and found a 2.8σ discrepancy with respect to the SM. Belle measured an angular dependent *CP* asymmetry where any detectable effect would correspond to NP, with a sensitivity of order 10^{-3}. Super$B$ can conceivably improve by an order of magnitude. As *CP* violation is an interference effect that is linear in the NP amplitude, a 10^{-4} precision on a *CP* asymmetry corresponds very roughly to measuring the $\tau \to \mu\gamma$ branching fraction with 10^{-10} precision [?].

4.3.3 Measurement of the τ $g-2$ and EDM form factors

The anomalous magnetic and the electric dipole moments of the τ are fundamental properties of the heaviest known lepton and are predicted with extreme precision within the SM both at zero and non-zero transferred momentum. They can be measured at transferred momenta of the order of the τ mass from the angular distributions of the τ decay products in $e^+e^- \to \tau^+\tau^-$ events. For this purpose having polarized beams represents a clear advantage [?, ?].

Within the SM, the τ $g-2$ has been computed with very good precision, $\Delta a_\tau = \Delta(g-2)_\tau/2 = 5\times10^{-8}$ [?]; its size is mainly determined by the

first perturbative term which is of order α and is the same for all leptons.

If one assumes that the present muon $g-2$ discrepancy is caused by NP corresponding to the MSSM with $\tan\beta \gtrsim 10$, one expects a much larger NP effect on the τ $g-2$, at the level of 10^{-6}.

There is limited experimental information on the τ $g-2$, the OPAL collaboration obtained a limit on the size of $F_2(q)$ [where $F_2(0) = (g-2)/2$] averaging transferred momenta between approximately the τ and the Z mass at the level of 7% [**?**]. For Super$B$ with $75\,\mathrm{ab}^{-1}$ of data and a 100% polarized electron beam, the real and imaginary part of the $g-2$ form factor F_2 can be measured assuming perfect reconstruction with a resolution in the range $[0.75 - 1.7] \times 10^{-6}$ [**?**]. When the design 80% beam polarization and realistic experimental reconstruction effects are included, the resolution is be estimated at about 2.4×10^{-6}, which is comparable to the size of possible NP MSSM contributions compatible with the muon $g-2$ discrepancy.

The τ EDM is expected to be vanishing small, and the existing upper limit on the electron EDM imposes severe constraints also on contributions from NP to about $d_\tau \lesssim 10^{-22} e\,\mathrm{cm}$. Experimentally, from a Belle analysis on $29.5\,\mathrm{fb}^{-1}$ of data [**?**] (unpolarized beams), we know that the experimental resolution on the real and imaginary parts of the τ EDM is between $0.9 \times 10^{-17}\,e\,\mathrm{cm}$ and $1.7 \times 10^{-17}\,e\,\mathrm{cm}$, including systematic effects.

Recent studies have provided an estimate of the Super$B$ upper limit sensitivity for the real part of the τ EDM $|\mathrm{Re}\{d_\tau^\gamma\}| \leq 7.2 \times 10^{-20}\,e\,\mathrm{cm}$ with $75\,\mathrm{ab}^{-1}$ [**?**]. The result assumes a 100% polarized electron beam colliding with unpolarized positrons at the $\Upsilon(4S)$ resonance. Uncertainty on the polarization is neglected, and a perfect reconstruction of the decay $\tau \to \pi\nu$ is assumed. A refined sensitivity estimate has been obtained assuming an electron beam with a polarization of $80\% \pm 1\%$ and realistic experimental reconstruction efficiency and uncertainties at $\approx 10 \times 10^{-20} e\,\mathrm{cm}$. Such a measurement would constitute a remarkable experimental improvement over current constraints.

4.4 SuperB Neutral Current Electroweak Physics Programme

With its ultra-high luminosity, polarised beam, and the ability to run at both the b-quark and c-quark thresholds, Super$B$ is a unique and versatile facility and no other machine with all of these capabilities is planned. In particular, the polarisation of the electron beam enables Super$B$ to measure the weak neutral current vector coupling constants of the b-quark, c-quark and muon at significantly higher precision than any previous experiment. The precision of the vector coupling to the tau and electron will be measured with a precision comparable to that attained at SLC and LEP. Within the framework of the SM these measurements of g_V^f can be used to determine the weak mixing angle, θ_W, through the relation: $g_V^f = T_3^f - 2Q_f \sin^2\theta_W$, where T_3^f is the 3^{rd} component of weak isospin of fermion f, Q_f is its electric charge in units of electron charge and higher order corrections are ignored here for simplicity. Figure 4.5 shows the determinations of $\sin^2\theta_W$ at present and future experimental facilities including Super$B$.

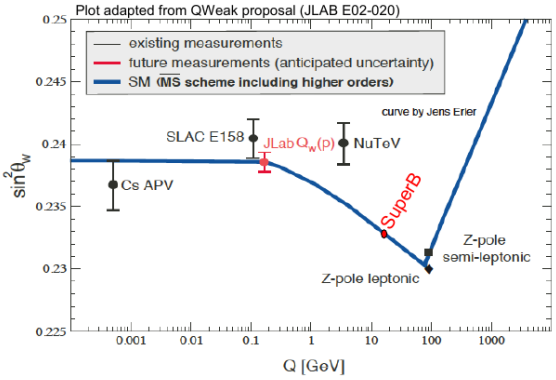

Figure 4.5: Determination of $\sin^2\theta_W$ at present and future experimental facilities.

Super$B$ determines g_V^f by measuring the left-right asymmetry, A_{LR}^f, for each identified final-

state fermion-pair in the process $e^+e^- \to f\bar{f}$.

$$A_{LR}^f = \frac{\sigma_L - \sigma_R}{\sigma_L + \sigma_R} = \frac{sG_F}{\sqrt{2}\pi\alpha Q_f} g_A^e g_V^f \langle Pol \rangle \quad (4.1)$$

where g_A^e is the neutral current axial coupling of the electron, $g_A^e = T_3^e$, G_F is the Fermi coupling constant, s is the square of the center-of-mass energy, and

$$\langle Pol \rangle = 0.5 \left[(N_{asym})_{RPB} - (N_{asym})_{LPB} \right], \quad (4.2)$$

is the average beam polarisation, where N_{asym} is the asymmetry between N_{eR} and N_{eL}, and LPB and RPB indicate left or right polarised beams.

These asymmetries arise from $\gamma - Z$ interference and although the SM asymmetries are small (-3×10^{-4} for the leptons, -3×10^{-3} for charm and -1.3% for the b-quarks), the unprecedented precision is possible because of the high luminosity of Super$B$ together with a 70% beam polarisation measured to $\pm 0.5\%$. To achieve the required precision all detector-related systematic errors are made to cancel by flipping the polarisation from R to L in a random, but known, pattern through a run. $\langle Pol \rangle$ is measured with both a Compton Polarimeter, which has an uncertainty at the interaction point of $< 1\%$ and by measuring the forward-backward polarisation asymmetry of the τ-pairs using the kinematic distributions of the decay products of the τ. The latter can be used to determine $\langle Pol \rangle$ to 0.5% at the interaction point in a manner entirely independent of the Compton Polarimeter.

The 3σ discrepancy between the LEP measurements of the right-handed b-quark couplings to the Z will be experimentally probed with higher precision at Super$B$. Also, measurements with the projected precision will enable Super$B$ to probe parity violation induced by the exchange of heavy particles such as Z-boson or hypothetical TeV-scale Z' boson(s). If such bosons only couple to leptons they will not be produced at the LHC. Moreover, the Super$B$ machine will have a unique possibility to probe parity violation in the lepton sector mediated by light and very weakly coupled particles often referred to as "dark forces" (see section 4.6). Recently, such forces have been entertained as a possible connecting link between normal and dark matter [**?**, **?**]. The enhancement of parity violation in the muon sector has been an automatic consequence of some models [**?**] that aim at explaining the unexpected result for the recent Lamb shift measurement in muonic hydrogen [**?**]. The left-right asymmetry of the $e^-e^+ \to \mu^-\mu^+$ in such models is expected to be enhanced at low-to-intermediate energies, and the Super$B$ facility may provide a conclusive test of such models, as well as impose new constraints on parity-violating dark sector.

4.5 Exotic Spectroscopy in SuperB

Although the SM is well-established, QCD, the fundamental theory of strong interactions, provides a quantitative comprehension only of phenomena at very high energy scales, where perturbation theory is effective due to asymptotic freedom. The description of hadron dynamics below the QCD dimensional transmutation scale is therefore far from being under full theoretical control.

Systems that include heavy quark-antiquark pairs (quarkonia) are a unique and, in fact, ideal laboratories for probing both the high energy regimes of QCD, where an expansion in terms of the coupling constant is possible, and the low energy regimes, where non-perturbative effects dominate. For this reason, quarkonia have been studied for decades in great detail. The detailed level of understanding of the quarkonia mass spectra is such that a particle mimicking quarkonium properties, but not fitting any quarkonium level, is most likely to be considered to be of a different nature.

In particular, in the past few years the B Factories and the Tevatron have provided evidence for a large number of states that do not admit the conventional mesonic interpretation and that instead could be made of a larger number of constituents. While this possibility has been considered since the beginning of the quark model [**?**], the actual identification of such states

would represent a major revolution in our understanding of elementary particles. It would also imply the existence of a large number of additional states that have not yet been observed.

For an overview of the observed states and their interpretation we refer to [**?**], here we will discuss the Super$B$ potential and its interplay with the other planned experiments.

Regardless of the theoretical ansatz in which the observed states are interpreted, the existence of a new fundamental type of state implies the existence of a number of new states that is much larger than the set of states observed so far. For instance, as detailed in Ref. [**?**], under the assumption of the tetraquark nature of the observed new state there are at least 18 states predicted for each J^{PC}; similarly in the molecular model, the number of thresholds close to which a new state could be is extremely large.

The next generation of experiments ought therefore to make the leap from the discovery phase to the systematic investigation of the whole spectroscopy. As an example one should search for a charged state decaying into $J/\psi K$ and produced in B decays in conjunction to a ω. This search was not performed in *BABAR* and Belle both because of lack of a certain theoretical model, but above all because of lack of statistics.

In this process of building the complete picture Super$B$ plays a critical role because of the following characteristics:

- *large statistics.* The largest limitation of the current data sample is the low statistics. As a consequence, signals are still not well established, precision analyses for the determination of the quantum numbers is impossible and several states are likely not to have been observed because of a low branching fraction. In particular all final states with D and D_s mesons will be accessible for the first time at Super$B$.

- *clean environment.* Albeit the high luminosity, that will slightly degrade the detector performances, the experiment is a multipurpose one, like *BABAR*. It will therefore have detection capabilities for all neutral and charged particles. Detection efficiencies are not expected to vary significantly from the *BABAR* ones.

- *center-of-mass scan potential.* The cleanest way to study a particle is to produce it directly, and this is possible, for $J^{PC} = 1^{--}$ states if the machine can adjust its energy to match the mass of the state. This is the case for Super$B$ over a large range of energy, in the vicinity of the charm threshold and for energies above the $\Upsilon(4S)$, thus allowing for direct studies on any $J^{PC} = 1^{--}$ exotic state.

Super$B$ is not the only next generation experiment capable of investigating heavy quark spectroscopy.

The LHCb experiment is starting to investigate its potential in the field. The larger number of mesons produced allows detailed studies of the decay modes with final states made of charged particles. All other modes are best investigated by e^+e^- machines.

The only other next generation experiments at an e^+e^- machine are BES-III and Belle-II. BES-III is a τ-charm factory planning to run below the energies of interest, at the $\psi(3770)$ [**?**], where they expect to collect $5\,\text{fb}^{-1}$ per year. Concerning Belle-II, the Super-KEKB accelerator is not designed to have the scan capabilities of Super$B$ and would not therefore be able to cover the corresponding physics.

A separate mention is deserved by the PANDA experiment at FAIR [**?**], a proton-antiproton collider which could produce the exotic resonances at threshold (i.e. $e^+e^- \to X, Y$). This innovative production mechanism allows for copious production without the hindrance of fragmentation products. The complementarity of the two experiments is guaranteed by the fact that the final states that can be studied by the two experiments are different and that the PANDA experiment can more easily access the narrow states while Super$B$ can study in detail larger states if the production mechanism is favorable. Furthermore, in case the center-of-mass-energy of Super$B$ is changed

to the $Y(4260)$ mass, assuming a factor 10 loss in luminosity with respect to running at the $\Upsilon(4S)$, the number of events produced in a few weeks would be equivalent to the PANDA dataset. Finally, PANDA can only reach center-of-mass energies as high as 5 GeV and therefore has no access to bottomonium spectroscopy.

4.6 Direct searches

Bottomonium decays can also be very sensitive to new particles that might have escaped direct searches at lower luminosity and higher energy facilities because of small couplings with ordinary matter. Among such searches we consider here the quest for dark matter and dark forces.

Two promising reactions for searching **low-mass dark matter** (χ) are the invisible and radiative decays of the $\Upsilon(1S)$ mesons, which can be measured in the mode $\Upsilon(3S) \to \pi^+\pi^- invisible$ [**?**]. The current best sensitivity to this process has been achieved by the *BABAR* experiment [**?**]; however, this result is still an order of magnitude above the SM prediction. The sensitivity is limited by the amount of background that needs to be subtracted, primarily due to undetected leptons from $\Upsilon(1S) \to \ell^+\ell^-$ decays. Achieving a $3-5\sigma$ sensitivity to the SM will require active background tagging down to 5-10 degrees above the beam-line in both the forward and backward directions. Also the searches for bino-like neutralino in radiative $\Upsilon(1S) \to \gamma + invisible$ decays require extended detector coverage in the forward and backward directions to reduce the dominant radiative QED backgrounds.

Concerning the search for **dark forces**, recent cosmic ray measurements of the electron and positron flux [**?**, **?**, **?**] have spectra which are not well described by galactic cosmic ray models and that lead to the introduction of a class of theories containing a new "dark force" and a light, hidden sector. In this model, the observed signals are due to dark matter particles with mass $\sim 400 - 800\,\mathrm{GeV}/c^2$ annihilating into the gauge boson force carrier with mass $\sim 1\,\mathrm{GeV}/c^2$, dubbed the A' (a "dark photon"), which subsequently decays to SM particles. If the A' mass is below twice the proton mass, decays to $p\overline{p}$ are kinematically forbidden allowing only decays to states like e^+e^-, $\mu^+\mu^-$, and $\pi\pi$.

The dark sector couples to the SM through kinetic mixing with the photon with a mixing strength ϵ. Low-energy, high luminosity e^+e^- experiments like the B Factories are in excellent position to probe these theories [**?**, **?**] by searching the A' either in direct production, or in rare B mesons and light mesons decays.

In e^+e^- collision, the simplest reaction to search for dark photon production is $e^+e^- \to \gamma A' \to \gamma l^+l^-$ although it suffers from large irreducible QED backgrounds. Current searches for narrow resonances in $e^+e^- \to \gamma\mu\mu$ and $e^+e^- \to \gamma\tau\tau$ [**?**, **?**] exclude $\epsilon > 5\times10^{-3}$ for $m_{A'}$ between 200 and 700 MeV. With its increased luminosity, Super$B$ should be able to further improve these limits by an order of magnitude.

Other possible search channels are:

- the dark Higgs-strahlung process: the combined production with a dark Higgs (h') (e.g. $e^+e^- \to A'h', h' \to A'A'$) where *BABAR* set a limit on the dark sector coupling constant and the mixing parameter at the level of $10^{-10} - 10^{-8}$ for $0.8 < m_{h'} < 10.0\,\mathrm{GeV}$ and $0.25 < m_{A'} < 3.0\,\mathrm{GeV}$ with the constraint $m_{h'} > 2m_{A'}$ and where Super$B$ could improve these limits by two orders of magnitude;

- very rare decays of the B meson, as resonances in the dilepton spectrum of $B \to Kl^+l^-$, $B^0 \to l^+l^-l^+l^-$ or $B \to Kl^+l^-l^+l^-$, where Super$B$ could probe couplings between a dark pseudoscalar and the top quark at the level of $1000 - 10000\,\mathrm{TeV}$, much larger than the scale accessible at LHC in direct collisions;

- rare meson decays [**?**] where the huge samples of lighter mesons such as π^0, η, K, ϕ, and $J\psi$can be used to search for the channel $\pi^0/\eta \to \gamma A' \to \gamma l^+l^-$.

4.7 Executive Summary

Up to now the SM managed to pass all the experimental challenges unscathed, providing an

overall good description of particle physics up to the energy scales probed in experiments, which is now approaching the TeV scale.

In spite of its phenomenological success, however, the SM is not satisfactory for several theoretical reasons, including the instability of the Fermi scale against radiative corrections, the lack of an explanation for the origin of flavour and *CP* violation and the non-unified description of the fundamental interactions, with gravity totally unaccounted for. In addition, the SM does have phenomenological problems when confronted with astrophysical and cosmological data: it cannot provide a viable dark matter candidate or an amount of *CP* violation large enough to account for the observed matter-antimatter asymmetry in the universe.

For these reasons, the SM is regarded as a low-energy theory bound to fail at some energy scale larger than the Fermi scale, where New Physics (NP) effects become important. The search for these effects is the main goal of particle physics in the next decades, both at present and future experimental facilities.

Flavor physics is the best candidate as a tool for indirect NP searches for several well-known reasons: FCNCs, neutral meson-antimeson mixing and *CP* violation occur at the loop level in the SM and therefore are potentially subject to large virtual corrections from new heavy particles. In addition, flavour violation in the SM is governed by weak interactions and, in the case of quarks, suppressed by small mixing angles. All these features are not necessarily shared by NP which could then produce very large effects.

In spite of its potential, so far flavour physics has not provided a clear NP signal, although deviations with low significance are present here and there. This failure, however, should not be considered discouraging. Broadly speaking, flavour physics probed and excluded so far only the region of small NP scales and/or large NP flavour couplings. On the other hand, we should not forget that flavour physics successfully anticipated the existence and sometimes the mass range of all the heavy quarks which are nowadays part of the SM [**?**, **?**, **?**]. This may well happen again for heavy particles beyond the SM.

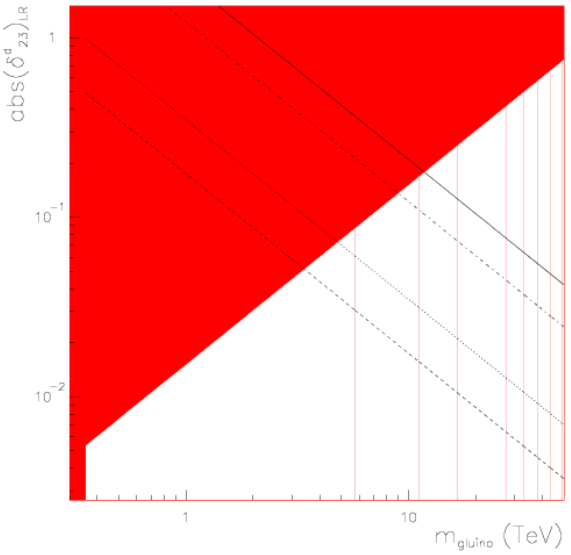

Figure 4.6: Region of the MSSM parameter space where a non-vanishing squark mass insertion parameter $(\delta^d_{23})_{LR}$ can be extracted with at least 3σ significance (in red) using $a_{\rm CP}(B_d \to X_s\gamma)$, $\mathcal{B}(B_d \to X_s\gamma)$ and $\mathcal{B}(B_d \to X_s\ell^+\ell^-)$ as constraints and assuming dominance of gluino-mediated contributions. For $m_{\tilde{g}} \sim 1$ TeV, Super$B$ is sensitive to $(\delta^d_{23})_{LR} \sim 10^{-2}$. For larger values of $(\delta^d_{23})_{LR}$, Super$B$ sensitivity extends to $m_{\tilde{g}} > 10$ TeV.

From a phenomenological point of view, flavour physics can be used in two modes: *i)* in the "NP discovery" mode, deviations from the SM expectation are looked for in each NP-sensitive measurement irrespective of their origin. The name of the game in this case is high precision and a control of the SM contributions which matches it. Depending on the NP at work, measurements in the B and D sectors at Super$B$ can be sensitive to contribution of new particles with masses up to tens or hundreds TeV [**?**, **?**] (see the MSSM example in Figure 4.6). Although in general a precise determination of the NP masses is hindered by the unknown NP flavour couplings, even a

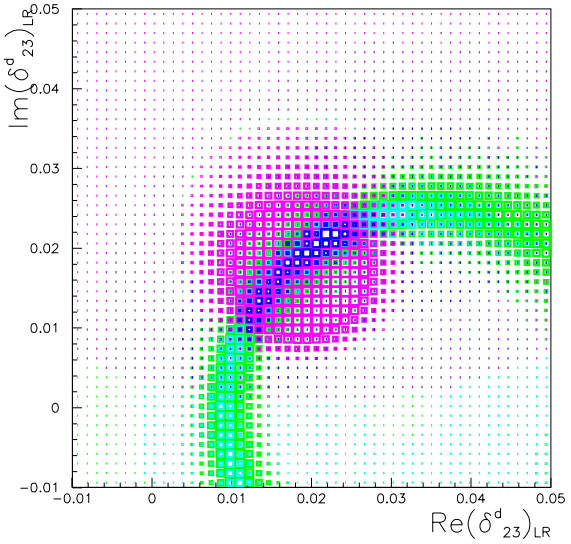

Figure 4.7: Extraction of $(\delta^d_{23})_{LR}$ from the measurements of $a_{\rm CP}(B_d \to X_s\gamma)$ (magenta), $\mathcal{B}(B_d \to X_s\gamma)$ (green) and $\mathcal{B}(B_d \to X_s\ell^+\ell^-)$ (cyan) with the errors expected at Super$B$. Central values are generated using $(\delta^d_{23})_{LR} = 0.028\, e^{i\pi/4}$ and squark and gluino masses at 1 TeV.

broad indication of the NP mass range would be a most valuable information in the unfortunate case direct searches at the LHC will be unsuccessful; *ii)* the "NP characterization" mode entails measuring significant deviations in several observables from different flavour sectors and studying the correlations among them. If some information on the NP mass spectrum is already available, this kind of analysis could provide crucial information to disentangle different NP contributions, elucidate the NP flavour structure and measure the NP flavour couplings [**?**, **?**] (see the MSSM example in Figure 4.7). It is worth reminding that, on top of the intrinsic phenomenological interest, flavour is intimately related to NP symmetry properties in many extensions of the SM. For example, new flavour structures appearing in the MSSM originate from the soft SUSY-breaking sector. By measuring many NP-sensitive observables in different flavour sectors, Super$B$ can give a major contribution to this ambitious program, which needs combining all available flavour information, from kaon fixed-target experiments to hadronic collider results.

The Super$B$ physics programme sketched in this document extends over a large set of rare decays, FCNCs, CP-violation in the B_d/B_u, D and τ sectors, measured at the $\Upsilon(4S)$ and the $\psi(3770)$ resonances [**?**, **?**]. The full set of measurements performed at the B factories can be repeated taking advantage of the much larger data samples which typically allows one to increase experimental precision/sensitivity by a factor 5 to 10. These include the unitarity triangle angles measured with various techniques, inclusive and exclusive semileptonic decays, $B \to X_s\gamma$, $B \to \tau\nu$, $B \to D\tau\nu$, several penguin-dominated $b \to s$ decays, τ flavour-violating decays, D–$\overline{D}$ mixing parameters, and many other processes. Indeed, with very few exceptions, these measurements are not severely limited by systematic or theoretical uncertainties. In addition, several new measurements, which were not feasible before, become possible: these include various observables in the decays $B \to K^{(*)}\nu\bar{\nu}$, $B \to X_s\ell^+\ell^-$, $B \to X_d\gamma$, CP violation in D mixing and decays, τ form factors, including EDM and $(g-2)_\tau$. Some LFV τ decay searches are expected to remain background free at Super$B$, and the corresponding limits are expected to be improved by two orders of magnitude on these modes (e.g. $\tau \to 3\mu$) relative to constraints from the B Factories. Some of these rare decays can be used to probe the nature of the neutral Higgs-like particle recently discovered at CERN, while others can be used to learn about charged and neutral partners of this Higgs predicted by many postulated NP scenarios.

Within its physics programme, Super$B$ will explore to unprecedented precision a number of recent developments in the field of B and D physics that could be a hint of physics beyond the SM. The large $\mathcal{B}(B \to \tau\nu)$ measured at the B factories and the recent evidence for an excess also in $B \to D^{(*)}\tau\nu$ decays reported by *BABAR* is something that needs to be verified and studied to high precision. The same holds true for the CP asymmetry of $\tau \to K_s\pi\nu$ which *BABAR*

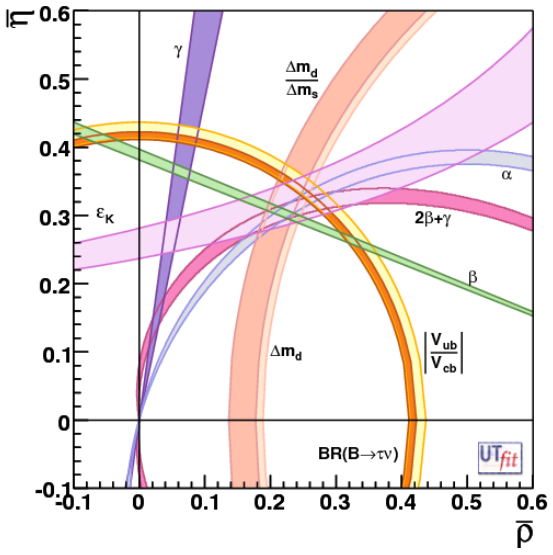

Figure 4.8: Constraints on the $(\bar{\rho}, \bar{\eta})$ plane using measurements from Super$B$. Existing central values are extrapolated to sensitivities expected from Super$B$ with 75 ab^{-1} and one can see that the constraints are not consistent with the CKM scenario. This highlights the importance of performing a precision CKM test with Super$B$.

measured almost 3σ away from the SM and for the direct CP asymmetry in singly Cabibbo-suppressed D decay measured by LHCb. For the latter, an open issue is the actual SM prediction which is hindered by the theoretical inability to compute the relevant D decay amplitudes. Super$B$ will be able to perform time-dependent CP asymmetry studies in neutral D decays at the $\psi(3770)$ and $\Upsilon(4S)$, enabling one to exploit the different statistical data samples using complementary experimental techniques, as well as measuring hadronic modes required to constrain theoretical uncertainties relating to the interpretation of the measured observables.

Given the importance of controlling precisely the SM contributions, it is crucial to improve the determination of the CKM parameters ρ and η in the presence of NP, using fit strategies already applied successfully to B factory data. By combining data taken at the $\psi(3770)$ as well as $\Upsilon(4S)$ one will be able to make competitive measurements of all the angles of the unitarity triangle (α, β, and γ) and the magnitude of several matrix elements (V_{ub}, V_{cb}, V_{us}, and V_{cd}), as well as the ratio $|V_{td}|/|V_{ts}|$. In particular, the crucial information on V_{ub} and V_{cb} coming from semileptonic decays can be improved only at flavour factories, where in addition the large data set can be used to control theoretical uncertainties in inclusive decays. Using this information, one can determine ρ and η with percent precision irrespective of possible NP contributions to $\Delta F = 2$ amplitudes. The reduced uncertainty on the CKM parameters allows one to boost the NP sensitivity of several observables measured at Super$B$ and elsewhere. One should not forget that the CKM fit itself is a test of NP in $\Delta F = 2$ amplitudes which could produce an unmistakable signal at Super$B$, like the one shown in Figure 4.8.

τ physics is another prominent topic of the Super$B$ physics programme. Flavor-violating τ decays would be a clear and clean mark of new physics [**?**, **?**, **?**]. Super$B$ extends sensitivity for $\mathcal{B}(\tau \to \mu\gamma)$ down to the 10^{-9} region, where many NP models produce detectable signals. In addition, this region is complementary to the MEG sensitivity for $\mu \to e\gamma$ (10^{-13}) in some SM extensions, allowing one to probe the mechanism responsible for the LFV. In addition, the excellent performance of Super$B$ in measuring $\mathcal{B}(\tau \to 3\ell)$ not only gives additional chance to detect LFV, but could also allow us to tell apart models where LFV is generated through magnetic dipole operators (such as the MSSM) from those using different mechanisms (for example little Higgs models). Finally, the τ physics programme does not only include LFV: a complete characterization of the τ properties to high precision can be carried out, including CP violation and form factor measurements, such as the EDM and $(g-2)_\tau$. Interestingly enough, assuming that the present deviation of $(g-2)_\mu$ from its SM prediction is a NP effect, then one expects the corresponding deviation in $(g-2)_\tau$

to be measurable at Super$B$ in many SM extensions.

In spite of the superior performance of hadronic colliders in the B_s sector, Super$B$ can still provide few complementary B_s measurements running at the $\Upsilon(5S)$. Examples are $\mathcal{B}(B_s \to \gamma\gamma)$ and the semileptonic asymmetry a_{SL} which can be used, together with $\Delta\Gamma_s$ and Δm_s, to determine the NP-sensitive phase $\phi_s = \arg(-M_{12}/\Gamma_{12})$. In addition, a precise measurement of the branching ratio of reference B_s decay modes would provide a valuable input to the LHCb-upgrade physics programme, allowing for a reduction of systematic uncertainties on high-precision measurements of absolute branching fractions.

Polarisation of the electron beam, a unique feature of Super$B$, makes it possible to measure the e^+e^- LR asymmetry in various channels. The bottom and charm NC vector couplings will be determined with unprecedented precision and $\sin^2\theta_W$ will be measured at the $\Upsilon(4S)$ using leptons with a precision comparable to that at the Z peak [**?**]. These unique measurements provide important EW precision tests which, after the measurement of the Higgs boson mass, become another powerful tool for indirect NP searches. Furthermore, polarisation provides new handles for τ physics studies, in particular FV and form factor measurements.

Finally, Super$B$ can perform direct NP searches as well: elusive light particles like low-mass dark matter or light vector bosons, such as the "dark" photon, can be looked for in bottomonium decays. In addition, a rich spectroscopy programme can be carried out at Super$B$. It is aimed at finding further unconventional states in the quarkonia mass spectra and possibly shedding light on the strong interactions mechanism leading to their formation. In this respect, the Super$B$ scan capabilities offer unique opportunities to study both the charmonium and bottomonium spectra with high statistics.

While there is a subset of Super$B$ measurements which can be interpreted with little or no theoretical input (for example: the CKM angles γ and α, flavour-violating τ decays, many CP violating D transitions), in order to exploit the full phenomenological potential of the Super$B$ program, one needs theoretical uncertainties to match the experimental precision to allow one to reveal and disentangling genuine NP effects. Extrapolation of the present systematics indicates that lattice QCD could reach the required precision on the relevant hadronic parameters in few years [**?**, **?**]. It seems also possible to control theoretical uncertainties at the required level in inclusive semileptonic decays using data-driven methods based on the heavy quark expansion and the huge Super$B$ data set. Inclusive radiative decays, most notably the $B \to X_s\gamma$ rate, could be limited by theory uncertainties, although there is no general consensus on the ultimate theoretical error which could be obtained in the next years. Only for some two-body non-leptonic decays, in particular the penguin-dominated $b \to s$ transitions, theory seems not able, in the absence of a breakthrough, to match the experimental precision. Yet, even in this case, data and flavour symmetries can be sometimes used to bound the theoretical uncertainties and allow for the extraction of the NP signal.

In summary, we have shown that there are a significant number of golden modes for which Super$B$, collecting $75\,\text{ab}^{-1}$ of data, has the best expected sensitivities [**?**]. The physics potential of Super$B$ and Belle II are similar, but Super$B$ provides additional opportunities owing to its charm threshold running capability and beam polarisation. As with *BABAR* and Belle, and ATLAS and CMS, there is a significant benefit in having two super flavour factories, as it will be possible to verify any discoveries made by one of the experiments. The super flavour factories and the LHCb upgrade physics programs are largely complementary and the overlap is confined to $B^0 \to K^{0*}\mu^+\mu$ and the charm mixing parameters, which LHCb upgrade will eventually improve [**?**]. All together, Super$B$, Belle II, LHCb upgrade and experiments measuring ultra-rare K decays and searching for muon flavor violation, will be able to provide full and redundant coverage of all quark and charged

lepton flavour sectors with high-precision measurements of rare decays, FCNCs, flavour and *CP* violating processes. These will be a key tool to characterize NP at the TeV scale or to start probing the multi-TeV region.

5 Machine Detector Interface and Backgrounds

Paoloni Pages ?

5.1 Overview M.Sullivan, M. Boscolo E.Paoloni, - 1 page

Coping with machine-related backgrounds is one of the leading challenges in designing the SuperB detector. Background considerations influence several aspects of the design: readout segmentation, electronics shaping time, data transmission rate, triggering and radiation hardness. With the proposed collider design, the primary sources of background are radiative Bhabha production, Pair (2-photon) production, Touschek scattering and beam scattering with residual gas; photons from synchrotron radiation give smaller, though far from negligible, contributions mainly on the innermost detectors (SVT). These sources give rise to primary particles that can either hit the detector directly, or generate secondary debris that enters the apparatus. In addition, the heat load due to synchrotron radiation photons striking masks and primaries and secondaries particles hitting the super-conducting magnets must be carefully evaluated. We have developed a simulation software called Bruno (See Sec. 14.2.1), a detailed Geant4 detector and beam-line description (from -16 to 16 mts from the IP), which have been used to estimate the impact of the different background sources on the operation of the SuperB detector. The relevant magnetic and physical elements used in the configuration are the two QD0 quadrupoles surrounding the beam-pipe, the QD0H on the outgoing HER line, the two QF1s and the two B0's elements on the downstream lines (see Sec. **??**). Tungsten masks placed around the beam-line protect the detector on both sides of the interaction region (see Sec. 5.3.3). XXX

5.2 Backgrounds sources. M.Sullivan, M.Boscolo, E.Paoloni, - 2 pages

In which the processes producing backgrounds are quickly described and classified in terms of their scaling laws.

5.3 Radiative Bhabha

The process of radiative Bhabha scattering, $e^+e^- \rightarrow e^+e^-\gamma$, is expected to play an important rôle in several physical problems. In the first place, it is the main process by which electrons are lost upon the collisions of $e^\pm$ beams, and so it forms the major ingredient in the finite lifetime. In the second place, given its high cross-section, this process is one of the main sources of background on the SuperB detector. Finally, this kind of events are also intended to be used to monitor luminosity by locating detection devices for low-angle photons/electrons/positrons located downstream the beam lines (beyond 16m from IP). All these reasons set a clear motivation to develop simulation tools for this kind of events.

5.3.1 Simulation tools

The effect on the detector of particles scattered in radiative Bhabha processes is studied with the BBBREM generator [2], a Monte Carlo program which simulates single bremsstrahlung in Bhabha scattering in the very forward direction. Several features of the BBBREM generator are worth mentioning. Since scattering over very small angles completely dominates the process, Bremsstrahlung off the positron and off

the electron are essentially independent, and it is used only the two Feynman diagrams where the electron is seen to radiate the photon. In the BBBREM generator it is used the approach of a full-fledged Monte Carlo (MC) simulation, which gives a good simulation of the angular deflection of the outgoing leptons and radiated photon. The user generates any desired number of events, i.e., sets of momenta of the three produced particles. Their distribution in phase space is matched as closely as possible to the exact distribution. The remaining factor is included in each event's weight. The average of the weights in the sample is the MC estimate of the cross section. This approach is useful as any experimental cut can be imposed by simply setting the weight of events that fall outside the cuts to zero. The surviving particles can then be tracked by other simulation programs, either into a detector or accelerator.

Another feature of the BBBREM generator is that it takes into account a reduction on the cross-section due to the density effect of the colliding beams, i.e. inside each bunch the electromagnetic fields from all electrons/positrons overlap in such a way that each electron has a finite interaction range, in contrast to the usual infinite range. This effect is including by setting up a cutoff on the momentum transfer allowed (Q_0^2). This cutoff depends on the average distance between two electron/positron inside a bunch, which in our case corresponds to around $d = 8\mu$m ($Q_0^2 = \hbar c/2\pi c = 4 \times 10^{-21} GeV^2$). The cutoff is implemented by multiplying the event weight by the factor $(Q/(Q - Q_0))^2$.

The BBBREM generator uses the following input parameters:

- Total center-of-mass energy of the incoming e^+e^- system (including energy dispersion of the electrons/positrons inside the incoming bunches).
- The photon energy cutoff fraction κ_0. This is a minimum value of the energy fraction (in the CM) taken away by the radiated photon ($k = \Delta E/E$). As the total radiative Bhabha cross-section is infinite a sensitive minimum value needs to be set.
- The number of interactions to be simulated ($N_{\rm int}$).

The BBBREM generator is implemented inside the SuperB Geant4-based simulation program. The incoming beams parameters at the IP (see Sec. **??**) are used as input for this program. These parameter includes: beam-energy and energy-dispersion (E and σ_E); beam-sizes and beta-functions ($\sigma(X/Y)$, $\beta(X/Y)$); nominal incoming direction (α_Z); and the number of primary particle inside a bunch ($N_{\rm par}$, which is of the order of 10^{10}). These parameters are used to calculate the beam-luminosity ($\mathcal{L}$), the center-of-mass (CM) e^+e^- energy (including the energy-dispersion), the luminous region and the radiative Bhabha cross-section ($\sigma_{\rm RB}$). The mean number of interactions to be simulated is then $\mathcal{L} \times \sigma_{\rm RB}$, which are then generated with BBBREM with the proper kinematics. In this way the luminous region and parameters are properly taken into account.

It has been checked that the main backgrounds come from radiative Bhabha events with $\kappa > 0.3$ (High-κ Rad-Bhabha). Events with $0.005 < \kappa < 0.3$ (Low-κ Rad-Bhabha) give smaller but non-negligible contribution to the total Rad-Bhabha background rate on the detector and have also been simulated.

5.3.2 Losses at the beam-pipe

Due to the dynamics of the process, the impact of this source of background extends to detector systems other than the tracker. A large fraction of the off-energy electrons and positrons hit the downstream beam-line elements, producing electromagnetic showers. Low energy particles from these showers enter in all detector subsystems. An accurate evaluation requires a careful modeling of the final focus which includes the geometry (beam-pipe, magnets, shields, cryostat, etc.) and the magnetic field. The secondaries produce beside from low-energy electrons/photons, it also includes neutrons with a mean kinetic energy around 1 MeV. Neutrons are produced near by the IP but also from the high energy electrons/positrons that hit the 1st

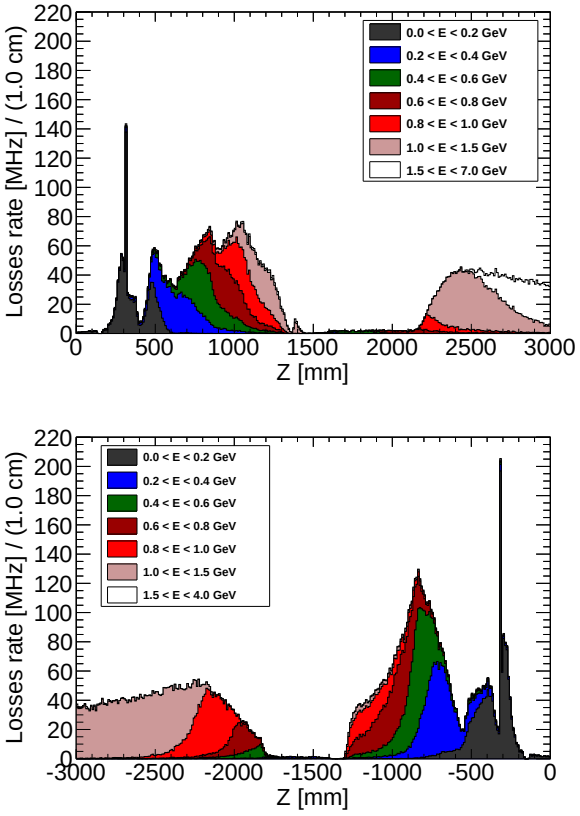

Figure 5.1: Rad-Bhabha loss rate at the beam-pipe due to positrons (top) and due to electrons (bottom) as a function of the Z coordinate.

bending magnets. These neutrons form a neutron cloud that moves around the detector hall for a long time (up to tens of μs) cousing delayed background hits at the EMC and IFR, and also affecting the FEE.

A very useful and low-time-consuming way to understand how the radiative Bhabha background affect the detector is the estimate where and at what rate particles are loss along the beam pipe. This information has been useful to identify the places where to locate protective shields for the detector (see Sec. 5.3.3). The loss rate due to positrons (high-energy-ring or HER) and due to electrons (low-energy-ring or LER) as a function of the Z-coordinate is shown at figure 5.1 in the region $-3\text{m} < Z < 3\text{m}$. The colored histograms are the contributions to the total loss rate for different ranges in energy of the lost particle (see the legends inset on the plots).

Both plots show similar patterns. Only very low-energy (off-energy) particles hit the beam pipe near by the interaction region. The contribution to the losses from higher energy particles increases as going away from the IP. The loss structure is due to two effects: the beam-pipe profile (the beam pipe gets wider for higher $|Z|$); and the location of the magnets along the beamline. Even though the losses occurs inside the SuperB detector, the lost particles are very collimated along the beam-pipe, so the debris generated from them are the ones expected to affect the detector father downstream. Some debris are produced outside the detector ($|Z| > 3\text{m}$) but produce background due to backscattering with the material around the final focus. Even though their efficiency to produce background is small, their large cross-section makes this compotent non-negligigle. This justify the necesity of a model of the final focus up to 16m at both sides of the IP.

Without any shield or mark the SuperB detector would be overwhelm mainly with radiate Bhabha backgrounds. Some shields have cleverly been included to reduce this background source, and will be briefly described in the next section.

5.3.3 Shield System

Several type of shields have been implemented around the problematic regions using all the available space. A Tungsten shield (W-shield) is included inside the detector and surrounding the final focus regions (see Fig. **??**). The aim of this shield is to reduce the amount of secondary electrons and photon coming from the interaction of the primary electrons/positrons with the final focus material around IP. The shield consist of a conical section 3 cm thick which is as close as possible to the IP ($22 < |Z| < 80$ cm) and that does not interferes with the SVT angular acceptance (± 300 mrad). A cylindrical section has the maximum possible thickness (4.5 cm) which is limited by the

maximum allowed weight and the constraints for the detector integration; it extends from $80 < |Z| < 280$ cm ($80 < |Z| < 220$ cm) in the positive (negative) Z-axis direction. This thickness is needed to mainly reduce backgrounds on the EMC/DCH up to acceptable levels, but has the consequence of increasing the DCH internal radius by about 2 cm. In order to shield from secondaries of particles lost outside the detector a couple of lead-plugs in the forward and backward regions (see Fig. **??**) have been included following a similar design to *BABAR*. These shields reduce the radiative Bhabha background by a factor of $2-5$ in most of the subsystems (except SVT). Other shields customized for a given detector are discussed in the corresponding sections below (*e.g.* FDIRC and IFR shields).

5.4 Pairs Production C.Rimbault - 2 pages

In which,

- the pair production process is described
- the simulation tools are presented
- the losses at the beam pipe are reported

5.5 Touscheck bacgkround. M.Boscolo - 2 pages

In which

- the Touschek process is described
- the simulation tools are presented
- the scraping system is sketched
- the losses at the beam pipe are reported

5.6 Beam gas background. M.Boscolo - 2 pages

In which

- the beam gas process is described
- the simulation tools are presented
- the scraping system is sketched
- the losses at the beam pipe are reported

5.7 Synchrotron radiation background. M.Sullivan - 2 pages

In which

- the synchrotron radiation process is described
- the simulation tools are presented
- the shielding system is sketched
- the losses at the beam pipe are reported
- the dosed in the SVT are evaluated

5.8 SVT background overview

The background in the detector environment is affecting the Silicon Vertex Tracker (SVT) in two separate ways. First, a hit rate higher than the design value can deteriorate the general performances of the tracking system. Second, the silicon layers can be progressively damaged when being exposed to a significant rate of particle for a long period of time. In both cases, accurate simulation of the rates is needed to estimate the real performances and the life-span of the SVT itself.

The main tool used to estimate the rate in the SVT is the simulation of the various background sources, described above, using the full simulation described in detail on Sec. 14.2.1. In the full simulation, the silicon layers are implemented as homogeneous volumes of silicon,

and each particle going through those volumes is recorded, together with additional information about the type of particle, the position, the incident energy, the vector momentum, and the deposited energy. The simulation is not aware of the internal structure of the silicon (strips or striplets). This choice, even if it could generate larger amount of data in output, it gives us some flexibility in testing different configurations without running the full simulation multiple times. Therefore, the simulation output need to be further processed to obtain the quantities useful for the tracker design and performance evaluation, e.g. the rate of "fired" strip per cm^2, the radiation dose, and the equivalent fluence of 1 MeV neutrons.

A specific application has been develop to analyze the simulation output and produce the relevant quantities and plots. Due to the similarities with other sub-systems, this application has been also extended using multiple modules that produce the same or similar quantities. Some of the technique detailed below have been applied also for the background analysis in other parts of the detector. The basic information in the simulation output is corresponding to a single interaction (or step) of the particle simulated by GEANT4. A particle crossing a sensitive volume can have multiple interactions, so the information is written separately for each one of those. The first step is to merge the information from successive interactions of the same particle in one crossing of the volume. A crossing of the volume is defined as a particle entering and exiting the volume once, or as a particle entering the volume and destroyed inside, or as a particle created inside the volume and then exiting, or as a particle created and destroyed inside. Each crossing has a well-defined starting and end point, an incident energy, and a deposited energy. Assuming a specific pitch of the strips (or striplets) in each layer, and approximating the trajectory of the particle with a straight line from the starting point to the end point, we can compute the number of strips (or striplets) crossed by the particle in both directions. Counting the number of strips (or striplets) crossed in all the simulated events, and rescaling by the event frequency, we have a measurement of the rate for each silicon module. Useful plots can be produced computing this rate as a function of the coordinate z or ϕ of the module itself, as shown in Fig 5.2, where the different background sources are reported separately and summed together. All the rate

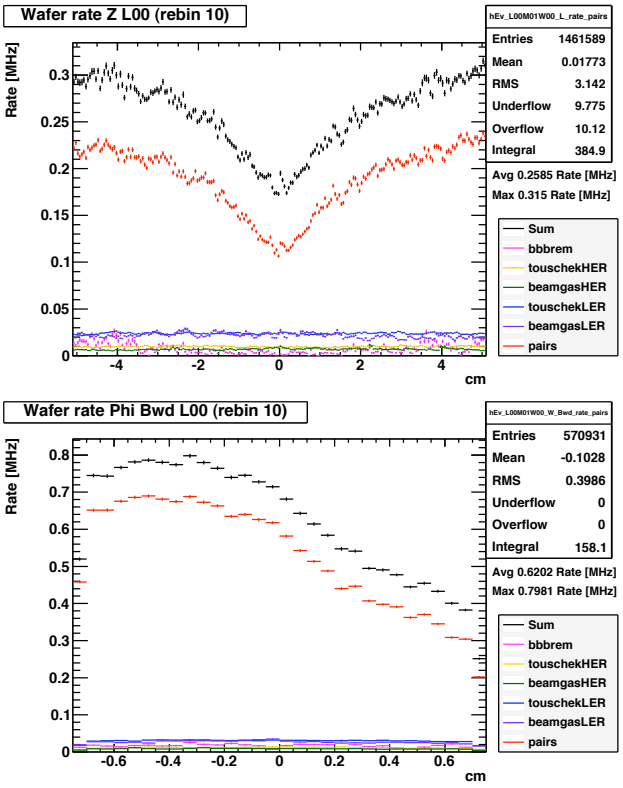

Figure 5.2: Rate of ...

variations observed as a function of the position can be explained with geometrical or topological considerations. For all the layers the largest contribution to the background in the tracker is given by the additional pairs production process, where the particles that hit the silicon are secondaries coming directly from the interaction point. The contribution is going from $\approx 80\%$ of the total for the innermost layer to $\approx 50\%$ for the outermost, and it can be explained considering that secondaries with low transverse momentum are highly favoured for this process, and the solenoidal magnetic field prevents those particles to reach the outer layers. The rate is

pretty high, but it is substantially irreducible, given that this contribution is scaling with the luminosity and no additional shielding can be added in that region.

Together with the strip rate, we can easily compute also the crossing multiplicity and the distribution of deposited energy per strip. All those data are a fundamental input for getting a reliable simulation of the readout electronics, as detailed in Sec. 6.6.4. A similar approach can be used also for the other relevant variables: summing together the deposited energy by all the crossings and dividing by the module mass, we have an estimation of the total ionizing radiation dose; knowing the path length in the volume and the incident energy for each particle, we weight each crossing to get the equivalent damage produced by 1 MeV neutrons [1]. Then, using the appropriate rescaling, we compute the integrated radiation dose, and the fluence by equivalent 1 MeV neutrons after 10 ab^{-1} of collected data. Using previous data or irradiating in a short time a test module with an equivalent amount of particles, we can estimate the deterioration of the tracker performance after a tenth of its designed running period.

Additional details on the impact of the background on the tracker performance can be found in Chap. 6.

5.9 DCH background overview

R.Cenci D.Lindemann - 2 pages

5.10 FTOF background overview

L.Burmistrov - 2 pages

5.11 FDIRC background overview

The FDIRC background is mainly due to low energy electrons and positrons which produce Cherenkov light either in the fused silica bars or in the FBLOCK. Part of these photons reach the MaPMT plane where they are detected and mix up with the hits coming from the high momentum tracks of the physics events. These low momentum particles are the result of complicated interactions between background primaries (both coming from luminosity-driven backgrounds like the radiative Bhabha events and from beam-induced backgrounds: Touscheck and beam-gas losses for instance) and components of the Super$B$ detector or machine elements.

Like for the other Super$B$ systems, the background hits impact the FDIRC in two ways. First, they decrease the performances of the reconstruction algorithm by making more difficult the identification of the Cherenkov cones. More hits mean smaller signal-to-background ratios and more combinatorics; moreover, real signal photons can be masked by background hits close in time in the same pixel. In addition, the background induces ageing on the FDIRC active components: not only the MaPMTs but also the front-end electronics.

Therefore, estimating correctly the FDIRC background rates at the nominal Super$B$ luminosity of $10^{36}\,cm^{-2}s^{-1}$ is crucial, not only to validate the choices made at the hardware level but also to define the requirements on the software algorithms. And the past experience of the *BABAR* DIRC makes this goal even more important. Indeed, less than a year after the beginning of the *BABAR* data taking, the DIRC background was exceeding significantly the predictions. Its dominant component was coming from radiative Bhabha scattering events which were producing electromagnetic showers such as neutrons of a few MeV. The latter particles interacted with the SOB water, generating Compton photons which then scattered, producing electrons and positrons finally giving Cherenkov light. A dedicated shield had to be designed to cover the beam line around the *BABAR* backward endcap. This shield provided a direct reduction of the background by a factor 3 and protected

efficiently the DIRC when the PEP-II luminosity rose over the years.

The simulation of the FDIRC background is based on BRN, the Super$B$ Geant4-based full simulation software. The implementation of the FDIRC hardware components matches the latest design of the detector and has been extensively tested in a dedicated standalone simulation, also based on the `GEANT` framework.The fused silica bars and FBLOCKs have the right optical properties; the MaPMTs (including their quantum efficiency as a function of the wavelength), mirrors (at the forward bar ends and in the FBLOCKs), glue joints, etc. are simulated as well. Hits on the photon detectors are recorded and stored in ROOT format, along with some truth information about the particles which produced the Cherenkov light. The generation, propagation and detection of the optical photons are completely driven by `GEANT`. Offline, during the analysis phase, the locations of the hits are converted into MaPMT and pixel numbers, taking into account dead areas and the space lost between neighbooring photon detectors.

The FDIRC simulation is validated before each major production and dedicated quality checks are run over the simulated events to test their consistency and track unphysical hits due to mis-modeling of detector components or software issues. This monitoring allowed for instance to find that the simulation of the MaPMT photocathode using BK7 glass was responsible for 10-20% excess hits for the dominant (see below) radiative Bhabha background. Changing this material to aluminium made those hits disappear.

5.11.1 Shielding the FDIRC

As explained above, experience based on the *BABAR* DIRC has shown that the FDIRC requires a dedicated shielding to reduce the hit rate. This comes in addition to the design improvements (smaller camera made of quartz instead of water, faster photon detectors and front-end electronics) which aim at mitigating the FDIRC background.

Looking at a side view of the Super$B$ detector, the FDIRC can be split into three main regions:

- $-160\,\text{cm} < z < 220\,\text{cm}$: inside the magnet
- $-280\,\text{cm} < z < -160\,\text{cm}$: within the flux return steel
- $-400\,\text{cm} < z < -280\,\text{cm}$: outside the magnet.

The first region cannot include a dedicated FDIRC shielding for obvious reasons. Therefore, its background protection only relies on the Tungsten shield around the beam pipe. Its current thickness (45 mm) is as big as possible given the maximum weight allowed for this shielding and the constraints coming from the Super$B$ detector integration.

With this W-shielding in, simulations show that the dominant background comes from the third region where there is space for a dedicated shield. As the flux of particles entering this area is dominated by photons with energy below 200 MeV, a detailled optimization procedure has lead to the choice of a steel-lead-steel sandwich shielding (2.5-10-2.5 cm-width respectively) which reduces the background by about one order of magnitude. A side effect of this shielding is to roughly double the number of neutrons in this area. Therefore, it is complemented by a 10 cm layer of Boron-loaded (5%) polyethylene.

Without this shielding, the radiative Bhabha events were dominating by about one order of magnitude the other background components. This is not the case anymore with this new design, as shown in the following section: most background sources give similar contributions to the total rate.

5.11.2 Background rates in the FDIRC

5.11.3 Integrated charges and doses

5.12 EMC background overview.
S.Germani - 2 pages

The main effect of machine background in the EMC is a diffuse energy deposit all over the de-

tector, this is mainly the result of several low energy deposits per crystal which, given the slow crystal decay time ($\tau \simeq 1.2\mu s$ for the CsI(Tl)) compared to the bunch crossing rate, may result in a significant integrated contribution. The angular (θ) dependence and the overall level for the deposited energy varies with the background source as shown in figure 5.3. The Radiative

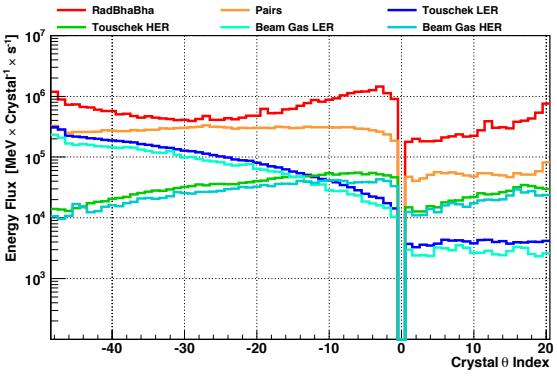

Figure 5.3: Rate of energy deposit per crystal vs polar angle (θ) position. Negative indices are for the CsI(Tl) Barrel crystals, positive indices are for the LYSO crystals in the forward Endcap and the 0 index correspond to the Barrr-Endcap transition. The energy deposit shows no dependence on the azimutal angle.

Bhabha background is the main responsible for the deposit rate and determines the the peaks of the distribution toward the forward and backward directions. The sharp change in average deposited energy for the forward EMC (positvie θ indices), which is shown by all the background sources, is related to the smaller size of the LYSO crystals whose front face is about 1/4-1/5 with respect to the CsI(Tl) ones in the Barrel. Another geometry related feature is the decrease in energy deposit per crystal for the barrel region close to the transition with the forward endcap. This is explained with the fact that the background particles are coming from the beam pipe direction but not directly from the interaction point, so the forward endcap act as a shield protecting the above mentioned barrel section (see figure 9.2 for a cross section of the relative barrel and endcap position). Touschek and Beam Gas backgrounds show a very similar behaviour.

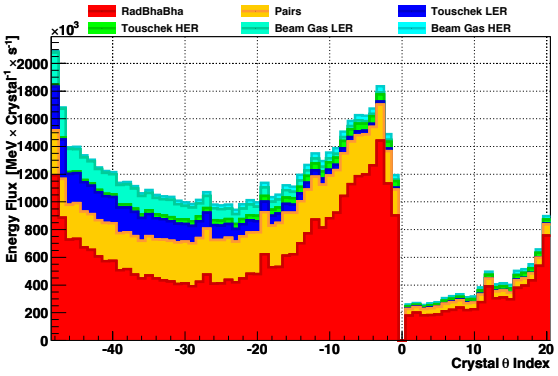

Figure 5.4: Contributions to the total energy deposit rate per crystal vs polar angle (θ) position. Negative indices are for the CsI(Tl) Barrel crystals, positive indices are for the LYSO crystals in the forward Endcap and the 0 index correspond to the Barrr-Endcap transition. The energy deposit show no dependence on the azimutal angle.

As shown in figure 5.4 the sum of all the energy deposit contributions is of the same order of the single Radiative Bhabha one, the maximum difference is the central part of the barrel where lays the maximum of the Pairs contribution and a factor of about 2.5 is reached with respect to the single Radiative Bhaha. The mean energy deposit per crystal keeps the peaked shape in the forward and backward directions but, including all the background sources, the maximum of the deposit is in the backward region of the barrel. This shape change is mainly related to the very asymmetric behaviour shown by the Touschek and Beam Gas backgrounds and to the very different rates between the low energy and the high energy rings. It needs to be stressed about the Touschek and Beam Gas backgrounds that, even if their average energy deposit contribution seems almost negligi-

ble, the incoming particles energy spectrum is much harder compared to both Pairs and Radiative Bhabha so that, considering only the single energy deposits above 10 MeV, Touschek and Beam Gas rates are comparable with the Radiative Bhabha one. This feature is particularly evident in the forward and backward regions of the barrel and becomes more and more conspicuous for higher deposited energy.

Concerning the effect related to machine backgrounds on the EMC performance, the energy deposit from any particle of physical interest will be superimposed with the diffuse contribution from the backgrounds, whose fluctuations may degrade both the angular and energetic resolution. In addition to this effect, machine backgrounds can create clustered energy deposits which in the reconstruction process may be considered as real particle clusters and therefore spoil the event reconstruction. The actual impact on the EMC performance, apart from the overall background level, depends also on the crystal signal processing and on the reconstruction process, more details are given in the dedicated EMC chapter 9.

5.13 IFR background overview
V.Santoro - 2 pages

5.14 ETD background overview
R.Cenci - 2 pages

5.15 SVT radiation monitor.
A.Di Ciaccio- 3 pages

5.16 Quick demounting.
M.Sullivan, F.Bosi, E.Paoloni - 4 pages

Bibliography

[1] A. Vasilescu (INPE Bucharest) and G. Lindstroem (University of Hamburg), *Displacement damage in silicon*, http://sesam.desy.de/members/gunnar/Si-dfuncs.html

[2] R. Kleiss and H. Burkhardt, *Comput. Phys. Commun.* **81**, 372 (1994).

6 Silicon Vertex Tracker

6.1 Overview G.Rizzo - 12 pages

The Silicon Vertex Tracker, as in *BABAR*, together with the drift chamber (DCH) and the solenoidal magnet provide track and vertex reconstruction capability for the Super$B$ detector. Precise vertex information, primarily extracted from precise position measurements near the IP by the SVT, is crucial to the measurement of time-dependent CP asymmetries in B^0 decays, which remains a key element of the Super$B$ physics program. In addition, charged particles with transverse momenta lower than 100 MeV/c will not reach the central tracking chamber, so for these particles the SVT must provide the complete tracking information.

6.1.1 SVT and Layer0

The above goals have been reached in the *BABAR* detector with a five-layer silicon strip detector with a low mass design, shown schematically in Fig. 6.1. The *BABAR* SVT provided excellent performance for the whole life of the experiment, thanks to a robust design that took into account the physics requirements as well as enough safety margin, to cope with the machine background, and redundancy considerations [2].

The Super$B$ SVT design, shown schematically in Fig. 6.2, is based on the *BABAR* vertex detector layout with those modifications needed to operate at a luminosity of 10^{36} or more, and with a reduced center-of-mass boost. In particular the SVT will be equipped with an innermost layer closer to the IP (Layer0) to improve vertex resolution and compensate the reduced boost at the Super$B$ accelerator, thus retaining an adequte Δt resolution for B decays for time-dependent CP asymmetries.

Physics studies and background conditions, as explained in detail in the next sections, set stringent requirements on the Layer0 design: radius of about 1.5 cm; resolution of 10-15 μm in both coordinates; low material budget (about 1% X_0); and adequate radiation resistance.

Several options are under study for the Layer0 technology, with different levels of maturity, expected performance and safety margin against background conditions. These include striplets modules based on high resistivity double-sided silicon detector with short strips (tilted with respect to detector's edge), hybrid pixels and other thin pixel sensors based on CMOS Monolithic Active Pixel Sensor (MAPS).

The current baseline configuration of the SVT Layer0 is based on the striplets technology, which has been shown to provide the better physics performance, as detailed in the next sections. However, options based on pixel sensors, which are more robust in high background conditions, are still being developed with specific R&D programs in order to meet the Layer0 requirements, which include low pitch and material budget, high readout speed and radiation hardness. If successful, this will allow the replacement of the Layer0 striplets modules in a "second phase" of the experiment. For this purpose the Super$B$ interaction region and the SVT mechanics will be designed to ensure a relative rapid access to the detector for a replacement of Layer0.

The external SVT layers (1-5), with a radius between 3 and 15 cm, will be built with the same technology used for the *BABAR* SVT (double sided silicon strip sensor), which is adequate for the machine background conditions expected in the Super$B$ accelerator scheme (*i.e.*with low beam currents). Although SVT module design for layer1 to 5 will be very similar to the *BABAR* one, with a larger coverage, a complete new readout electronics chain need to be developed to cope with the higher background rates expected in Super$B$.

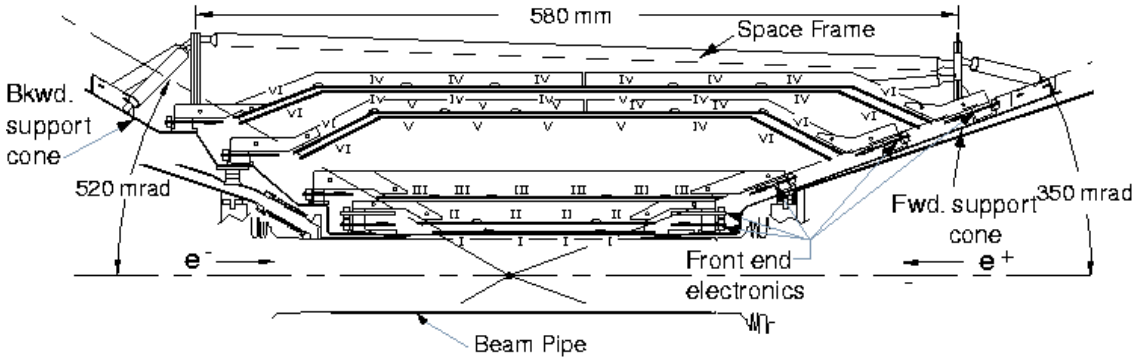

Figure 6.1: Longitudinal section of the *BABAR* SVT

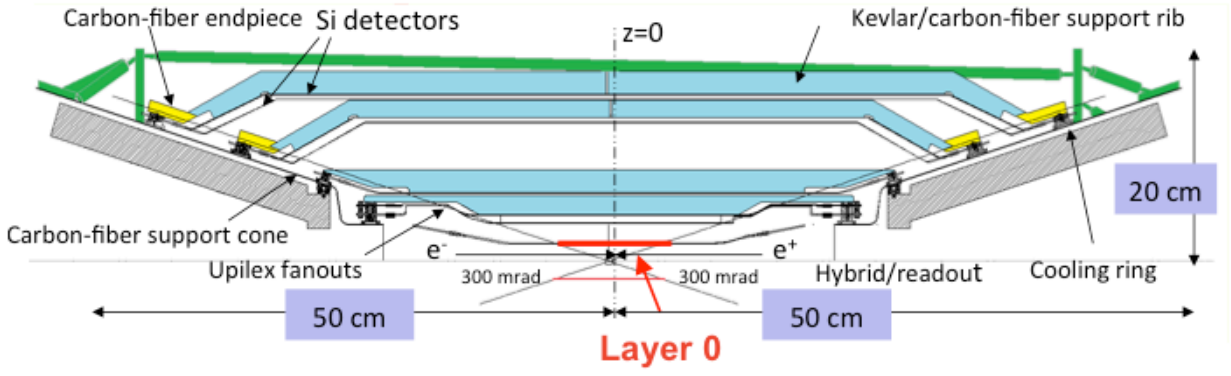

Figure 6.2: Longitudinal section of the Super*B* SVT

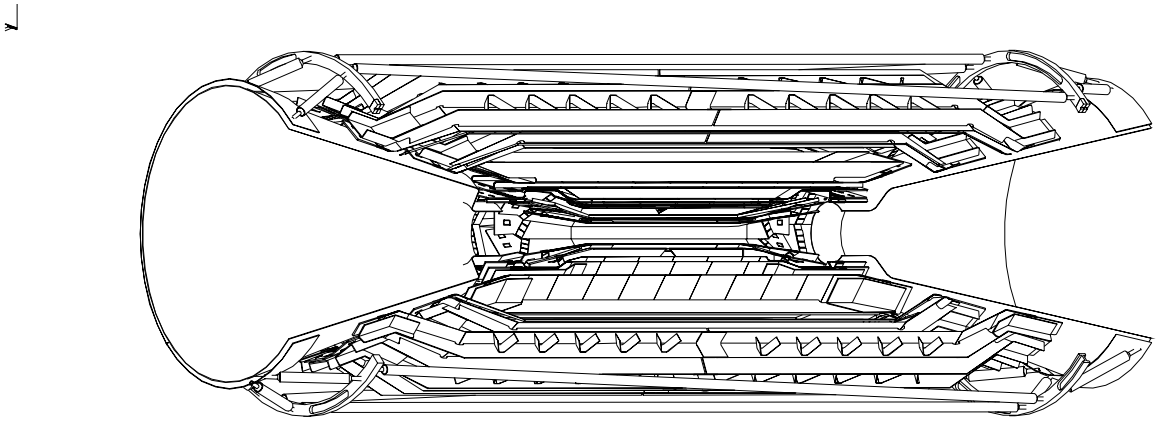

Figure 6.3: Three dimensional cutaway of the SVT.

A review of the main SVT requirements will be given in the next section followed by an overview of the general detector layout. A detailed discussion of all the specific design aspects will be covered in the rest of the chapter.

6.1.2 SVT Requirements

6.1.2.1 Resolution

Without the measurement of the B decay vertex, no useful CP asymmetries can be extracted at the $\Upsilon(4S)$. Therefore one of the main goal of the SVT is the determination of the B decay positions, especially along the beam direction (z). Measurements performed in *BABAR*, where the mean separation between B vertices is $\Delta z \simeq \beta\gamma c\tau_B = 250\,\mu$m, demonstrated that good sensitivity to time dependent measurement can be achieved with typical vertex resolution of 50-80 μm in the z coordinate for exclusively reconstructed modes, and 100-150 μm for inclusively modes (tag side in CPV measurements). The reduced Super$B$ boost ($\beta\gamma = 0.24$) with respect to PEP-II ($\beta\gamma = 0.55$) requires an improved vertex resolution, by about a factor 2, in order to mantain a suitable Δt resolution for time dependent analyses.

The *BABAR* resolution was achieved thanks to an intrinsic detector resolution of about 10-15 μm in the first measured point of the SVT, taken at a radius of about 3 cm, and keeping to the minimum the amount of material between the IP and the first measurement. The multiple scattering has in fact an important effect on impact parameter resolution for low momentum tracks and set a lower limit on the useful intrisic resolution on the various SVT layers, corresponding to a point resolution of about 10-15 μm for measurements made close to the IP and 30-40 μm for the outer layers [1].

The required improved track impact parameter and vertex resolution can be reached in Super$B$ with the same intrisic resolution used in *BABAR*, reducing the radius of the first measured SVT point by a factor of 2 (Layer0 radius at about 1.5 cm) and keeping a very low mass design for the beam pipe and the detector itself.

6.1.2.2 Acceptance

The coverage of the SVT must be as complete as technically feasible, given the constraints of the machine components close to the IP. The SVT angular acceptance, constrained by the Super$B$ interaction region design, will be 300 mrad in both the forward and backward directions, corresponding to a solid angle coverage of 95% in the $\Upsilon(4S)$ center-of-mass frame, thus increasing the acceptance with respect to *BABAR* SVT.

There should be as little material as possible within the active tracking volume. The minimization of the material between the IP and

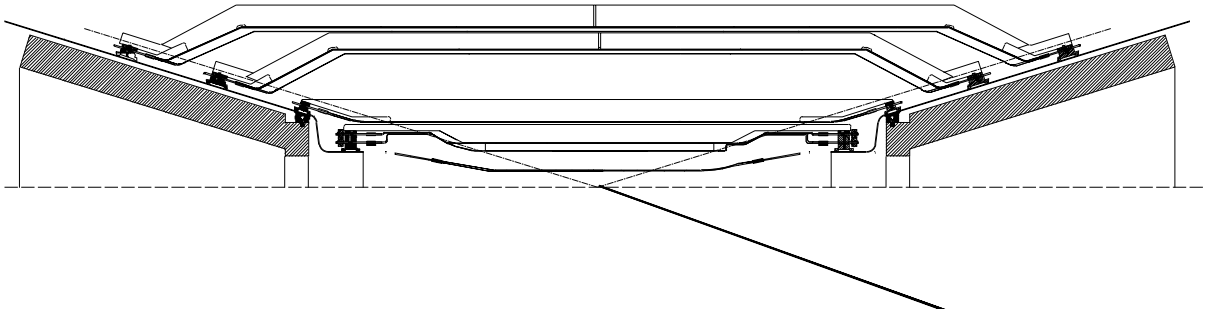

Figure 6.4: Cross section of the SVT in the plane containing the beam axis.

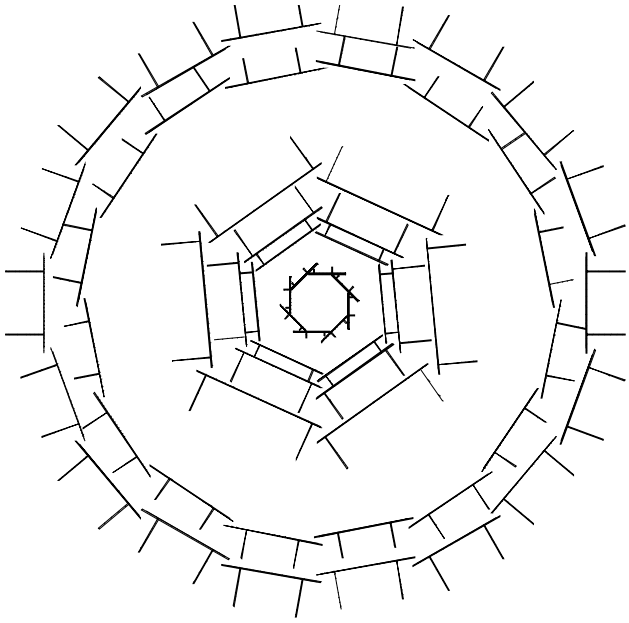

Figure 6.5: Cross section of the SVT in the plane perpendicular to the beam axis. The lines perpendicular to the detectors represent structural support beams.

the first measurement is crucial to reduce the multiple scattering and preserve the impact parameter resolution. The small beam pipe (1 cm radius) in the dector acceptance requires an active cooling with liquid coolant to evacuate the large power dissipated from image beam currents. The total amount of radial material for the actual design of this new beryllium pipe is estimated to be less than 0.5% X_0. Material located beyond the inner layers does not significantly degrade the measurement of track impact parameters, but does affect the performance of the overall tracking system and leads to increased photon conversions in the active region.

6.1.2.3 Efficiency

Our goal is to achieve close-to-perfect track reconstruction efficiency within the active volume of the tracking detectors when information from both the drift chamber and the SVT is used. The pattern recognition capabilities of the combined tracking system must be robust enough to tolerate background levels up to 5 times nominal. *as defined in background section* Low momentum particles that do not traverse many drift chamber planes, such as many of the charged pions from D^* decays, must be reconstructed in the SVT alone. For this category of tracks, with p_T less than 100 MeV/c, we want to achieve reconstruction efficiencies of at least 80–90%. *check these number with fastsim results in high background* The SVT must also be efficient for particles such as K^0_Ss that decay within the active volume.

Together, these requirements determine the number of measurements along a track and the necessary single-hit efficiency. *do we need to quote some numbers here?*. The *BABAR* SVT design with 5 layers was optimized to ensure enough redundancy to keep an high tracking efficiency even in case of failure of some modules and inefficient detectors. The robustness of this choice was demonstrated with the good detector performance over the entire life of the experiment. The Super$B$ SVT design with 6 layers (inserting the Layer0) is inspired to the same philosophy. Specific simulation studies [3] indicated that a reduction in the number of layers, from 6 to 5 or 4, give very modest gain in tracking performance while show a sizeble reduction in the efficiency for low momentum tracks in D* reconstruction, in case of non perfect/real detector, or related to inefficiency in high background conditions.

6.1.2.4 Background & Radiation Tolerance

The expected background influences several aspects of the SVT design (segmentation, shaping time, data transmission rates) and sets the requirements for the radiation resistance of all the SVT components. The design of the system has been optimized to withstand at least 5 times the total expected background rates. Whenever possible, detectors and front-end electronics are specified to be able to survive the entire life of the experiment including a safety factor of 5 on the total dose and equivalent neutron fluence: 7.5×5 yrs at nominal peak luminosity of 10^{36}.

As described in Section 6.2, the effect of background depends steeply on radius, as shown in Tab. 6.1.

With the high strip rates expected, especially in the inner layers (0-3), the front-end electronics should be fast enough to avoid pulse overlap and consequent hit inefficiency (shaping time in the range 25-150 ns). Furthermore a good Time Stamp resolution (30 MHz TS clock) is needed to get a good hit time resolution and reduce the occupancy in the offline time window to acceptable levels for reconstruction. An average 2% offline cluster occupancy is reached in each layer, considering the nominal background x5, with offline time windows of 100-150 ns in layers 0-3, while about 500 ns will be selected in layers 4-5, where the longer shaping time is dominating the hit time resolution. See Sections 6.3.5 and 6.6.2 for more details.

In Layer0 the expected integrated dose is about 3 Mrad/yr and the equivalent neutron fluence is about 5×10^{12} n_{eq}/cm^2/yr in the sensor area. In the other SVT layers radiation levels are at least one order of magnitude lower: in Layer1 TID $\simeq$ 0.3 Mrad/yr and an equivalent neutron fluence of about 8×10^{11} n_{eq}/cm^2/yr are expected.

Table 6.1: Summary of nominal expected background in the sensor area. The design of the SVT has been optimized with ×5 the nominal background. *Elba numbers for rates, New TID-NIEL, syncrotron radiation not included yet.*

Layer	Radius (mm)	Pitch (ϕ–z) (μm)	Total Rate/Area (MHz/cm^2) Track	Cluster	Strip (ϕ–z)	Total Strip Rate (kHz)	TID (Mrad/yr)	NIEL (n/cm^2/yr)
0	15	54–54 (u,v)	1.62	4.10	20–20 (u,v)	187–187	3	5×10^{12}
1	33	50–100	0.217	0.540	2.9–2.4	170–134	0.3	8×10^{11}
2	40	55–100	0.163	0.393	1.9–1.7	134–134	0.2	5×10^{11}
3	59	50-1-00	0.079	0.208	0.54–0.71	116–79	0.1	3×10^{11}
4	120	100–210	0.022	0.037	0.07–0.05	25–13	0.01	2×10^{11}
5	140	100–210	0.014	0.022	0.04–0.03	16–9	0.01	2×10^{11}

With this scenario in Layer1-5 the sensors are proven to be enough radiation hard to survive the entire life of the experiment, with a safety factor of 5 included, with an acceptable degradation of the Signal to Noise performance, as shown in Section 6.6.2. *review this sentence after proper evaluation of S/N.* As an example this requirement translates for Layer1 to a TID $\simeq$ 15 Mrad and an equivalent neutron fluence of about 3×10^{13} n_{eq}/cm^2 (7.5x5 yrs equivalent).

For Layer0, where the radiation is an order of magnitude higher, a quick replacement of the entire layer is foreseen, as frequent as necessary, depending on the actual background and the radiation hardness of the technology chosen.

6.1.2.5 Reliability

Although the SuperB interaction region and the SVT mechanics will be designed to ensure a relative rapid access to the detector for replacement of Layer0, the acces of the SVT is not possible without a major shutdown. The reliability requirements for the SVT are therefore more stringent than usual for such a device, with implications for engineering design at all levels. The detector layout must provide redundant measurements wherever possible; the electronic readout must be very robust; and the functionality of all components must not be compromised by exposure to the expected radiation levels. The detector monitoring and interlock system must serve as a safeguard against catastrophic failure in the event of a component malfunction or a simple human error.

6.1.3 Baseline Detector Concept

6.1.3.1 Technology

The SVT baseline design is based on double-sided silicon microstrip detectors for all layers. The characteristics of this technology that make it attractive for the Super$B$ detector are: high precision for measuring the location of charged particles, tolerance to high background levels, and reduction in mass made possible through double-sided readout. Double-sided silicon detectors have been employed with success already in *BABAR* and in several other large-scale applications and are able to meet the performance standards outlined above.

6.1.3.2 Layout

The SVT will provide six measurements, in two orthogonal directions, of the positions of all charged particles with polar angles in the region $17° < \theta < 167°$. A three-dimensional cutaway view of the SVT is shown in Figure 6.3. The Layer0 has eight detector modules while the rest of the detector keep the same modules numbers as in *BABAR* : layers 1-2-3 have six detector modules, arrayed azimuthally around the beam pipe, while the outer two layers consist of 16 and 18 detector modules, respectively. A

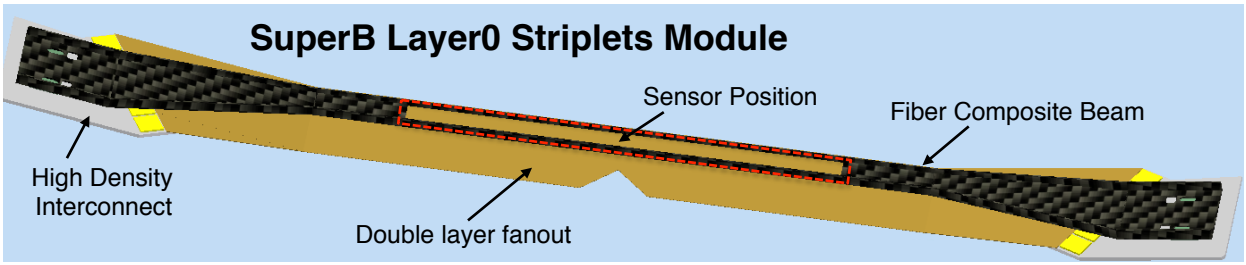

Figure 6.6: Schematic drawing of the Layer0 striplets module

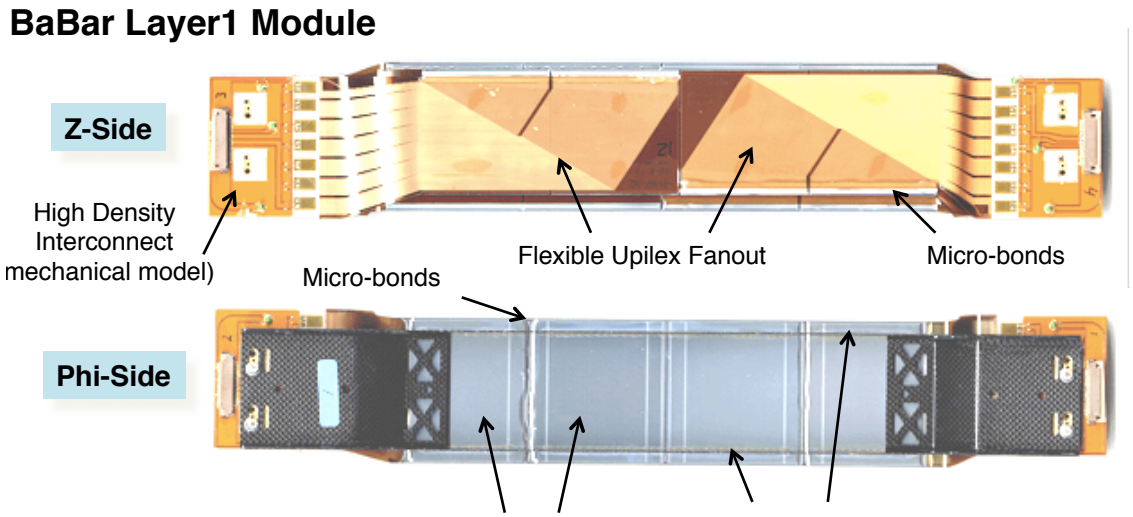

Figure 6.7: Details of the *BABAR* SVT Layer1 module.

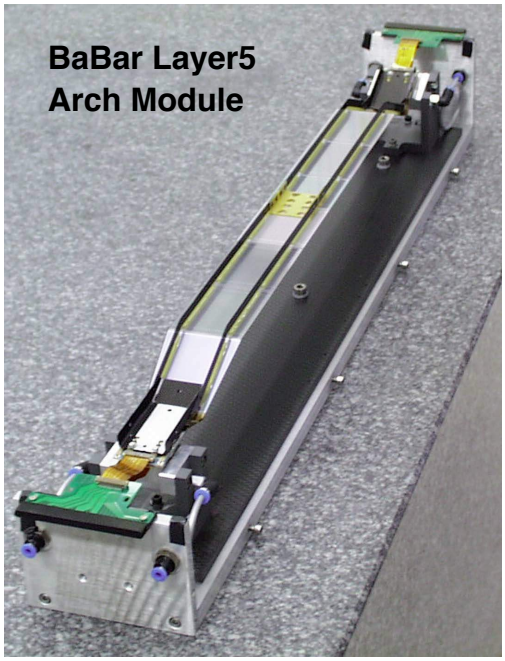

Figure 6.8: Details of the *BABAR* SVT Layer5 arch module.

side view of the detector is shown in Figure 6.4, and an end view is shown in Figure 6.5.

The design of the Layer0 striplets module is completly new, with a quite complex shape, as shown in Fig. 6.6, to fit the very limited space available between the first layer of SVT and the beam pipe. The layout of the other five layers is very similar to the *BABAR* SVT strip modules, shown as a reference in Fig. 6.7 and Fig. 6.8.

The inner detector modules (0-3) are traditional barrel-style structures, while the outer detector modules (4-5) employ an arch structure, in which the detectors are electrically connected across an angle. The bends in the arch modules, proven to be well functional in *BABAR*, minimize the area of silicon required to cover the solid angle and also avoid very large track incident angles.

In order to satisfy the requirement of minimizing material in the detector acceptance region, one of the main features of the SVT design is the mounting of the readout electronics entirely outside the active detector volume. For this reason signals from the silicon strips are carried to the front-end chips by flexible fanout circuits.

There is a 1 cm space between the 300 mrad stay-clear in the forward and backward directions and the first element of the IR region (i.e. the tungsten shield cones) and all of the electronics are mounted here. In both directions, space is very tight, and the electronic and mechanical designs are closely coupled in the narrow region available.

The layout specifications for this six-layer design are given in Table 6.1.3.2 and described in more detail the text.

For Layer0 short strips, oriented at 45 degrees with respect to the detector edges (u, v strips), are adopted on both faces of the sensor in order to reduce the strip length and the related background occupancy to reasonable levels. For layers 1 to 5 the strips on the two sides of the rectangular detectors in the barrel regions are oriented parallel (ϕ strips) or perpendicular (z strips) to the beam line. In the forward and backward regions of the two outer layers, the angle between the strips on the two sides of the trapezoidal detectors is approximately 90°, and the ϕ strips are tapered. Floating strips are used to improve the position resolution for near-perpendicular angles of incidence; the capacitive coupling between the floating strip and the neighboring strips results in increased charge sharing and better interpolation. For larger incident angles with wider readout pitch minimizes the degradation in resolution that occurs because of the limited track path length associated with each strip. These issues are discussed in more detail in section 6.4.2.

The design has a total of 308 silicon detectors of nine different types. The total silicon area in the SVT is about 1.5 m ^{2}, and the number of readout channels is ∼170,000.

6.1.3.3 Electronic Readout

As emphasized above, all readout electronics are located outside the active volume, below 300 mrad in the forward and backward region. To accomplish this, ϕ strips on the forward or backward half of a detector module are electrically connected with wire bonds. This results in

Table 6.2: *need to update the table* Parameters of the SVT layout.
See text for more detail on the meaning of the different quantities. The intrinsic resolution is calculated at 90° track incidence assuming $S/N = 20 : 1$. The z-ganging/pairing numbers represent the percentage of readout channels connected to the specified strip configuration.

Quantity	Layer 0	Layer 1	Layer 2	Layer 3	Layer 4a	Layer 4b	Layer 5a	Layer 5b
Radius (mm)	15	33	40	59	120	124	140	144
Wafers/Module	1	2	4	4	6	6	8	8
Modules/Layer	8	6	6	6	8	8	9	9
Silicon Area (cm^2)	127	554	787	1655	2459	2548	3502	3610
Overlap in ϕ (%)	2.0	2.4	1.8	1.8	4.0	4.0	2.0	2.0
Readout pitch (μm):								
ϕ (u for Layer 0)	54	50	55	100	82–100		82–100	
z (v for Layer 0)	54	100	100	110	210		210	
Floating Strips:								
ϕ (u for Layer 0)	—	—	—	1	1		1	
z (v for Layer 0)	—	1	1	1	1		1	
Intrinsic Resolution (μm):								
ϕ (u for Layer 0)	10	10	10	10	10–12		10–12	
z (v for Layer 0)	12	12	12	12	25		25	
R.O. Section								
ROS/Module	4	4	4	4	4		4	
ICs/ROS (ϕ-z)	6-6	7-7	7-7	6-10	4-5		4-5	
Readout Channels	24576	21504	21504	24576	36864		41472	
Strip Length Half Module (mm):								
ϕ (u for Layer 0)	20	110	130	190	293	303	369	380
z (v for Layer 0)	20	40	48	70	51–103	103–154	103–154	103–154
Fraction of z-side r.o. channels with Pairing/Ganging:								
None		77%	55%	65%	4%			
Pairing ×2		23%	45%	35%				
Ganging ×2					73%	74%	25%	16%
Gang.×2 + Pair.×2					23%	24%	41%	43%
Ganging ×3						2%	34%	41%

total strip lengths associated with a single readout channel of up to ∼19 cm in the inner layers and up to ∼38 cm in the outer two layers.

The signals from striplets for the Layer0 (u and v strips) and the z strips for all the other layers are brought to the readout electronics using fanout circuits consisting of conductive traces on a thin flexible insulator (for example, copper traces on Upilex as in *BABAR*). The traces on fanout are wire-bonded to the ends of the silicon strips.

On the z side of the modules the number of readout strips exceed the number of available electronic channels, constrained by the number of chips that can fit in the limited space available. To reduce the number of readout channels needed, the connection scheme for the z fanout circuits includes "pairing" and "ganging" (described in Section 6.4.2) with two or three strips bonded to a single fanout/readout channel. The length of the z strips is much shorter than ϕ strips, typically 4-7 cm in the inner layers and either 10 or 15 cm in the outer layers, where there is either $\times 2$ or $\times 3$ ganging.

Front-end signal processing is performed by ICs mounted on the High-Density Interconnect (HDI), a thick-film hybrid circuit fabricated on aluminum nitride (AlN) substrate. The HDI provides the physical support, it distributes power and signals, and thermally interfaces the ICs to the cooling system.

New front-end custom-design ICs are currently under developmemnt for the Super$B$ SVT [18] since none of the existing chips is matching all the requirements 6.6.2. The signals from the readout strips, after amplification and shaping, are compared to a preset threshold. The time interval during which they exceed the threshold (time over threshold, or TOT) is an analog variable related to the charge induced on the strip. Unlike the ordinary peak-amplitude measurement at the shaper output, the TOT technique has a nonlinear input-to-output relationship which is approximately logarithmic. This is an advantage since it compresses the dynamic range and allows one to achieve good position resolution and large dynamic range with a minimum number of bits. TOT readout has been successfully employed in the front-end chip of the *BABAR* SVT (i.e. Atom chip [2]) providing sufficient analog resolution for position interpolation, time-walk correction, and background rejection.

For each channel with a signal above threshold, the TOT information together with the hit time stamp will be buffered until a trigger is received; it will be then transferred, with the strip number, to an output interface, where data will be serialized and transmitted off chip on output LVDS lines.

The readout IC is expected to be about 6x4 mm^2 and to dissipate about 4.0 mW per channel. The total power that will be generated by the SVT readout chips is ∼700 watt (*considering 4 mW/chan is correct including the digital power?*).

There are four readout sections per detector module, where the module is divided in half along z, and the ϕ and z strips are grouped together separately. The data from one-half of a detector module will be transmitted from the hybrid on a flexible cable to a transition card located approximately 40 cm away, where the signals are converted and transmitted to optical fibers.

6.1.3.4 Module design and Mechanical Support

review this section The silicon detectors and the associated readout electronics are assembled into mechanical units called detector modules. Each module contains from 1 to 8 silicon detectors, the flex circuits to bring the signal from strip to the front-end chips, and a low-mass beams constructed of carbon and Kevlar fiber-epoxy laminates (i.e. ribs) to stiffen the module structure. The ribs are attached at each end to to the HDI hybrid circuit. A Aluminum Nitride substrate for the HDI provides precise mechanical mounting surfaces and is the heat sink for the electronics.

With this design the module material budget in the active region is very limited, and as in *BABAR* is about 0.45% X_0 per layer. For layers 1 to 5 this is dominated by the 300 μm of the

silicon sensor, a contribution of about 0.1 % X_0 is due to the composite ribs, with about 0.05 % X_0 for the z fanout, the one that sits in the active area. In Layer0 striplets the contribution of the flex circuit is considerably higher: here each face of the sensor need a flex circuit in the active area, since both u and v strips, at 45^0 w.r.t detector edge, need to be connected to the front-end chips. Furthermore the flex on each face of the striplets module is a double layer, since the number of channels to be connected is very high and the pitch is limited to about 50μm. The total material for the two multilayer flex circuits, now uder development, is about 0.15 % X_0, while about 0.1 % X_0 are accounted for the carbon fiber support structure. With sensor thickness of the stripltes of only 200 μm the total material budget is about 0.45% X_0 also for Layer0.

Layer 0 modules are supported on cold flanges, directly coupled with Be beam-pipe *describe Layer0 mounted on beam pipe motivations: minimize radial position and quick demounting of layer 0 without touching the SVT and* The other five SVT layers are mounted on support cones coupled with the conical tungsten shields with kinematic mounts (i.e. the gimbal rings) that will allow relative motions of the forward backward shields without stress on the silicon detectors. The detector modules from Layers 1 and 2 are glued together with rigid beams, forming sextants which are then mounted from the support cones in the forward and backward directions. Each detector module of Layer 3-4-5 is mounted on the support cones independently of the other modules. In layer 4 and 5, there are two different types of modules in each layer, an inner one, labeled a, and an outer one, labeled b, occupying slightly different radial positions. Thus there are eight different types of detector modules.

The support cones are double-layered carbon-fiber structures which are mounted from the tungsten shield cones. Cooling water flows between the two carbon-fiber layers around aluminum mounts which protrude through the outer surface of the cone. Mounting pins in the hybrid structure provide the alignment between the modules and the aluminum mounts in the cone, and thermal contact is made to provide cooling for the front-end electronics located on the hybrid. The support cones are divided to allow the vertex detector to be assembled in two halves and then mounted on t he shielding cones and the beam pipe by clamshelling the pieces together. During the assembly/disassembly procedure the splitting of the support cones with the five SVT layers on, will allows an easy access of the Layer0 without the need to disassemble the entire SVT.

The stiffness of the overall SVT structure is provided by a very low mass space frame, constructed of carbon-fiber tubes, connecting the forward and backward support cones, similar to the one designed for the *BABAR* SVT. It consists of rings at each end held rigid by struts spanning the length of the detector. The rings are connected to the support cones by an additional series of struts at each end. All material is carbon-fiber laminate. The motivation for this space frame stems mainly from the possible relative motion of the two shielding cones during the assembly procedure or earthquake *check this and add gimbal ring description* Cooling water, power, and signal lines are routed along the support cones to points outside the active region where manifolds for the cooling water and drivers for the electronics are located.

6.1.4 Layer0 Pixel Upgrade

6.1.4.1 Motivations

With the machine operated at full luminosity, the layer 0 of SVT may benefit from upgrading to a pixellated detector that have more stable performance in case of high background conditions, thanks to a lower background rate expected. A background rate of about 1 MHz/strip (x5 safety included) is expected with a striplets lenght of about 2 cm and 50μm pitch, while only 2.5 KHz/pixel are expected for pixels with a 50x50 μm pitch.

Possible effects of background hits on performance are: the reduction of the hit reconstruction efficiency (due to pile up), the increase of the effective hit resolution, the reduction of ef-

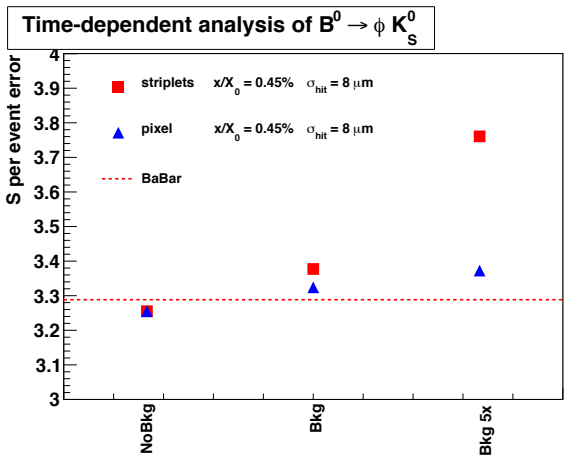

Figure 6.9: Variation of the S per event error in $B^0 \to \phi K^0_S$ time-dependent analysis in presence of background events, for a Layer0 based on striplets or pixel with the same material budget. Efficiency and resolution deterioration are both included in the simulation study.

ficiency of the pattern recognition for charged tracks along with the increase of fake tracks. Most of these effects have been included in specific simulation studies performed to evaluate the SVT performance in the high background scenario, (i.e. full luminosity including x5 safety factor on nominal background). The results, described in more details in Sec.**??**, showed a significant degradation in the striplets performance with high background occupancy, while the pixel solutions explored showed more stable performance against background conditions. The pixel occupancy is reduced at least by a factor 200 w.r.t striplets considering the smaller electrode dimensions and even including a possible worse time resolution of the pixel w.r.t striplets.

An example of these studies is shown here. The impact of machine background on the SVT performance has been studied evaluating the per-event error on the physics parameter S, adding background hits to signal events. S is measured in time-dependent analyses (corresponds to $\sin(2\beta)$ for $B^0 \to J\psi K^0_S$ decays) and the S per-event error is defined as the error on the parameter S normalized to the number of signal events. In Fig.6.9 the impact of background on the physics parameter S is reported for striplets and pixel, for the case of nominal background and with 5 times background rates. For the striplets the reduction to the sensitivity to S w.r.t. BaBar is small with nominal background, only about 3%, but it is up to about 15% with 5 times the nominal background. On the contrary with a pixel option, beeing there the effect of background occupancy negligible, the reduction to the sensitivity to S is only 3%, even in the high background scenario, and it is related to the effect of the background in the rest of the SVT.

It is important to stress that in the study reported here the pixel option has the same material budget used for striplets (about 0.45% X_0), same performance without background included. Of course the use of pixel over striplets in high background is less convenient if the material budget of pixels is significantly higher. On the contrary if one can reach a very low material budget with a thin pixel option, below the striplets target, the upgrade to pixel for Layer0 is well motivated also in nominal background conditions. (see for example Fig.6.19).

While for strip modules most of the material budget is due to the silicon of the sensor itself, in pixel modules there are several other important contributions in the active area. Including the readout electronics, cooling, and the pixel bus for the connection of the front-end chips with the periphery of the module, one one can easily reach a total material budget for pixel above 1% X_0. A discussions on the material for the various pixel options for the Layer0 is presented in the next sections.

6.1.4.2 Technology Options for Layer0 pixel upgrade

Two main technologies are under evaluation for the upgrade of Layer0: hybrid pixel and thinner CMOS Monolithic Active Pixel Sensor (MAPS). Specific R&D programs are ongoing on these

options to meet all Layer0 requirements, such as low pitch and material budget, high readout speed and radiation hardness.

A short summary of the current status of the R&D on the different pixel options is given below, while a more detailed review is presented in Sec.6.8.

Hybrid Pixel technology represents a mature and viable solution but reduction in the front-end pitch and in the total material budget, with respect to pixel systems developed for LHC experiments, is required for application in Layer0.

The spatial resolution constraints of 10-15 μm set a limit to the area of the elementary readout cell and, as a consequence, to the amount of functionalities that can be included in the front-end electronics. For a pixel cell 50×50 μm^2 a planar 130 nm CMOS technology may guarantee the required density to implement in-pixel data sparsification and fast time stamping ($< 1\mu s$), as required for the high target hit rate in Layer0 of 100 MHz/cm^2 in order to keep the module bandwidth to acceptable level (<5 Gbit/s).

Denser CMOS technologies, as the 65 nm technology, can be used to increase the functional density in the readout electronics and include such functions as local threshold adjustment and amplitude measurement and storage. In this case, costs for R&D and production would increase significantly. Vertical integration (or 3D) CMOS technologies may represent a lower cost alternative to sub-100 nm CMOS processes to increase the functional density in the pixel cell [29, 30].

A front-end chip for high resistivity pixel sensors with 50 × 50 μm^2 pitch is under development for the application in Super$B$ A first prototype chip with 4k pixels has been produced with the ST Microelectronics 130 nm process adopting the same readout architecture, with in-pixel sparsification and timestamping, developed within the SLIM5 Collaboration [37] for CMOS Deep NWell MAPS [38, 39]. The chip bump bonded to a high resistivity sensor matrix has been fully characterized, with beams, with good results [25].

In this first prototype only basic functionalities have been implemented. The readout architecture has been recently optimized to sustain efficiently the target Layer0 hit rate of 100 MHz/cm^2 on matrices larger than 50k pixels. The new architecture, that requires a more complex in-pixel logic, implement a data push and a triggered version of the readout [24].

The design of a 3D front-end chip for hybrid pixel with this new readout architecture, and some improved features, is now in progress with the vertical integration CMOS technology offered by the 130 nm Chartered/Tezzaron process.

CMOS MAPS are very appealing for application where the material budget is critical: in this technology the sensor and readout electronics share the same substrate that can be thinned down to several tens of microns. Since a fast readout is another crucial aspect for Layer0 a new Deep NWell MAPS design approach has been developed by the SLIM5 Collaboration[37]) to improve readout speed in CMOS MAPS sensors. This approach allowed for the first time the implementation of thin CMOS sensors with similar functionalities as in hybrid pixels, such as pixel-level sparsification and fast time stamping [38, 24]

Thanks to an intense R&D program the development of DNW CMOS MAPS (with the ST Microelectronics 130 nm process) has reached a good level of maturity. A limiting factor in this design is the presence of competitive N-Wells, inside the pixel cell, that can subtract charge to the main collecting electrode. The last prototype realized, the APSEL4D chip, a 4k pixel matrix with $50 \times 50 \mu$m^2 pitch has been tested with beams [20] reporting a hit efficiency of 92%, related to the pixel cell fill factor (ratio of the DNW area to the total area of N-wells) which is about 90% in the APSEL design. Another critical issue for the application of CMOS MAPS in the Layer0 is their radiation hardness expecially related to bulk damage effect. A significant degradation of the charge collected (about 50%) has been measured after irradiation with neutron up to a fluence of about

$7x10^{12}$ n/cm^2, corresponding to about 1.5 years of operation in the Layer0 [28].

Further MAPS performance improvements are currently under investigation with two different approaches: the use of INMAPS CMOS process, featuring a quadruple well and an high resistivity substrate, and 3D CMOS MAPS, realized with vertical integration technology.

In order to increase the charge collection efficiency the INMAPS 180 nm CMOS process is being explored: a deep P-well implant, deposited beneath the competitive N-Wells, can prevent them from stealing charge to the main collecting electrode. Moreover the use of high resistivity substrate, also available in this process, can further improve charge collection and radiation resistance with respect to standard CMOS devices. First prototype INMAPS matrix, with the improved readout architecture suitable for the application in the SuperB Layer0, are currently under test with promizing results. Radiation hardness of these devices at the level required for a safe operation in Layer0 for at least a couple of years ($> 10^{13}$ n/cm^2) is currently under investigation.

The realization of 3D MAPS, using two CMOS layers interconnected with vertical integration technology, also offer several advantages with respect to standard 2D MAPS. In these devices one CMOS tier is hosting the sensor with the analog front-end and the second tier is dedicated to the in-pixel digital front-end and the peripheral readout logic. With this splitting of functionalities the collection efficiency can be improved, significantly reducing the N-Well competitve area in the sensor layer. Having more room for the in-pixel logic allows the implementation of a more performant readout architecture. Finally in 3D MAPS the cross-talk between analog and digital blocks can be minimized.

The characterization of first 3D MAPS prototypes, realized with the 130 nm Chartered/Tezzaron 3D process is under way and first beamtest results on the MAPS layer implementing the sensor and the analog front end showed a very good hit efficiency (above 98%).

The status of the R&D on the different pixel options under development for the Layer0 upgrade is reviewed in the following documents [17, 25, 28]

6.1.4.3 Pixel Module & Material Budget

The schematic drawing of the full Layer0 made of 8 pixel modules mounted around the beam pipe is shown in Fig. 6.10.

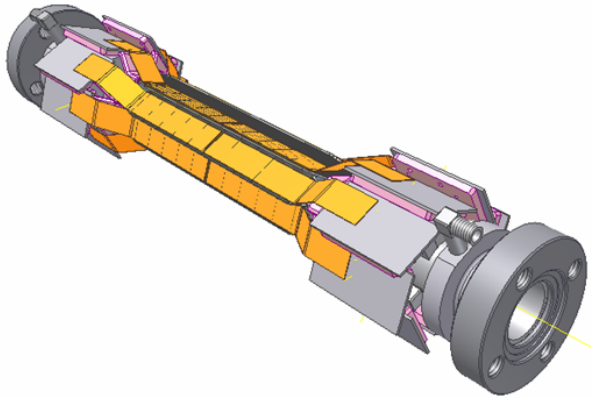

Figure 6.10: Schematic drawing of the full Layer0 made of 8 pixel modules mounted around the beam pipe with a pinwheel arrangement.

In all the pixel options under evaluation, sharing the same multichip module structure, the material budget of all the components must be kept under control to minimize the detrimental effect of multiple scattering.

The main contributions to the material budget for pixel modules with different technologies are discussed in this section and summarized in table 6.3 with a comparison with the striplets option.

In the hybrid pixel solution the contribution of the silicon from the sensor (100-200 μm) and the front-end chip (100-150 μm) can be in the range of 0.25-0.4% X_0. In the CMOS MAPS option the sensor and the front-end electronics are integrated in the same CMOS chip that could be thinned down to 50 μm reducing this contribution down to only 0.05% X_0.

Another important contribution to the material is due to the pixel bus needed for the con-

Layer0 Module Material Budget (X_0)			
	Striplets	Hybrid Pixel	CMOS MAPS
Sensor	0.21%	0.11-0.21%	0.05%
FE-chip+bump bonding		0.14-0.19%	
Multilayer bus or fanout	0.15%	0.15-0.30%	0.15-0.30%
Module Support & ground plane (include cooling for pixels)	0.09%	0.15%	0.15%
Total Material Budget (X_0)	0.45%	0.55-0.85%	0.35-0.50%

Table 6.3: Layer0 module material budget for the different technologies under evaluation.

nection of front-end chips to the periphery of the module. This connection will be realized with an Al/kapton multilayer bus, now under development. With our present requirements on speed (high bandwidth due to a hit rate of 100 MHz/cm2) and power consumption (about 1.5W/cm^2) the estimated material budget for the pixel bus is about 0.15-0.3% X_0, depending on the achievements of present R&D on this item.

The pixel module support structure needs to include a cooling system to evacuate the power dissipated by the front-end electronics, about 1.5W/cm^2, present in the active area. In order to minimize the material budget a light carbon fiber support structure with integrated active cooling, based on microchannel technology [32] and forced liquid convection, has been developed. The support with integrated cooling is build with carbon fiber micro-tubes, with a hydraulic diameter of about 200μm, obtained by a poltrusion process. Measurements on the support prototypes, with a total material budget as low as 0.11% X_0, indicate that such approach is a viable solution to the thermal and structural problem of Layer0 [33] An innovative idea is also under development to integrate into the silicon itself the cooling system based on microchannels made by DRIE technology. The embedded microchannels, with diameters even below 100μm, feature a peculiar geometry, and in the final step a thin oxide layer is deposited to seal the channels, resulting reliable under the operating high-pressure conditions. This technique permits the integration of the cooling system within the detector with obvious advantages on the optimization of thermal bridges and transparency to the incident particles [34].

6.1.5 R&D Main Activities

6.2 Backgrounds R.Cenci - 4 pages

A detailed analysis of background effects is fundamental to have a reliable estimation of performances and expected lifetime of the tracker. As already described in Chap. 5, in addition to well-known background sources as Touschek and beam-gas, we have a significant contribution from physics processes that happens in the interaction point. The very high luminosity of the machine produces an unprecedented rate for additional pairs and radiative Bhabha processes that, in some areas, is similar or larger than other traditional background sources. The effect of those physics processes cannot be mitigated optimizing the machine optics, because they scale with the luminosity and the machine goal is always to get the luminosity as highest as possible. In addition, if the particles produced by those physics processes are within the detector acceptance, they cannot be easily shielded, because particles from the interesting physics processes would be stopped as well.

The different sources of background have been simulated with a detailed Geant4-based

detector model and beamline description (see Sec. 14.2.1). The detailed simulation is needed because not only the detectors themselves, but also the supporting parts (also referred to as "dead material") play an important role in stopping or creating background particles. Then, the raw output of the simulation has to be processed to obtain useful information that can be used for additional specific simulation of the readout electronics and for test with real particle. Simulated background events can also be sampled and added to relevant physics events to estimate the tracking perfomances in real running conditions, as detailed in Sec. 6.3. Background results can have a significant influence on several aspects of the SVT design, like readout segmentation, electronics shaping time, data transmission rate, and radiation hardness (particularly severe for Layer0).

Add a description of the detector model in Bruno ed insert reference to the main Background sections

Crossing multiplicity, deposited energy distruibution, bandwith, crossing with high number of tracks

Describe main feature of each source

6.2.1 Pair production

6.2.2 Radiative Bhabha

6.2.3 Touschek

6.2.4 Beam Gas

6.2.5 Other sources

Include summary tables with rates, doses, equivalent fluences for various layers

6.3 Detector Performance Studies N.Neri - 6 pages

6.3.1 Introduction

The Super$B$ vertex detector can be considered as the evolution of the *BABAR* one. It is capable of maintaining adequate performance for time-dependent measurements in presence of a lower boost of the center-of-mass frame (CM) ($\beta\gamma = 0.24$ compared to $\beta\gamma = 0.55$ of *BABAR*) and much higher background, mainly related to the increased istantaneous luminosity of about a factor 100 higher with respect to *BABAR*.

The beampipe features a reduced radius of about 1.0 cm which allows the positioning of the innermost layer of the SVT (Layer0) at an average radius of about 1.5 cm. The additional Layer0 measurement along with the low radial material budget of the beampipe (0.42% X_0) and of Layer0 (0.45% X_0 with the striplet option), is crucial for improving the decay vertex reconstruction of the B mesons and obtaining adequate proper-time resolution for time-dependent CP violation measurements. In addition, the small size of the luminous region, about $(1 \times 1)\,\mu\text{m}^2$ in the transverse plane, also contributes to the improvement of the decay vertex reconstruction when imposing the constraint that the particles are originated from the interaction point. The baseline solution for the Layer0 is based on short strip technology and an upgrade to pixel is foreseen.

In the following we discuss the baseline layout of the SVT and how the design has been optimized in Section 6.3.2, the impact of the Layer0 on detector performance in Section 6.3.3, and the tracking performance in Section 6.3.4. The impact of the machine background on SVT performance is discussed in Sections 6.3.5, 6.3.6 and the performance with a Layer0 pixel detector is presented in Section 6.3.7. In Section 6.3.8 it is described the performance for particle identification based on ionization $\mathrm{d}E/\mathrm{d}x$ in the SVT sensors.

6.3.2 The SVT layout

The Super$B$ SVT is composed by 6 layers of double-sided silicon strip detectors and has a symmetric coverage in the laboratory frame down to 300 mrad (17.2°) with respect to the forward and backward direction, corresponding to 95% angular coverage in the CM. The inner three layers perform the track impact parameter measurements, while the outer layers are necessary for pattern recognition and low transverse momentum (p_t) tracking.

Table 6.4: Reconstrucion efficiencies for $B^0 \to D^{*-}K^+$ decays for different SVT layout (4, 5 ,6 layers) and running conditions (A, B, C). Case A correspond to ideal running conditions, B represents SVT with a damaged module in Layer3 with z hit efficiency of 70%. Case C introduces additional inefficiency with respect to case B in Layer0: 60% hit efficiency for z and ϕ views.

	A eff. (%)	B eff. (%)	C eff. (%)
6 layers	66.0 ± 0.3	65.0 ± 0.3	64.0 ± 0.3
5 layers	64.0 ± 0.3	62.0 ± 0.3	60.0 ± 0.3
4 layers	60.0 ± 0.3	56.0 ± 0.3	53.0 ± 0.3

The Layer0 strips are short ('striplets') and oriented at $\pm 45°$ with respect to the beam direction. The Layer1 to Layer5 silicon strip detectors are very similar to the *BABAR* ones in terms of radial position and strip pitches. The optimization of the strip z and ϕ pitches for the strip detectors is discussed in Section 6.4.2. A dedicated study to optimize the SVT layout as a function of number of silicon sensors and radial positions was performed [3]. Several figures of merit were studied: the track parameters resolution, the reconstruction efficiency and kinematic variable resolutions of B decays with low momentum tracks as $B^0 \to D^{*-}K^+$. Since low momentum tracks do no reach the DCH, they are reconstructed using only SVT information. The *BABAR* experiment has shown that at least 4 hits in the ϕ view and 3 hits in the z view are necessary for robust track reconstruction [2, 5]. The main result is that the 6-layer design is superior and more robust compared to the alternatives investigated, *i.e.* 4- and 5-layer layout where intermediate layers are removed. Indeed, when accounting for possible inefficiencies in hit reconstruction, due to damaged modules or high background, the 6-layer design insures higher reconstruction efficiencies for low momentum tracks compared to the other solutions where intermediate layers are removed.

In Table 6.4 the reconstruction efficiencies are reported for the decay $B^0 \to D^{*-}K^+$ for the 4-, 5- and 6-layer configuration in different running conditions: ideal conditions (A), with a damaged module in Layer3 (B) and with additional hit inefficiency in Layer0 with respect to case B (C). The outer radius of the SVT was ultimately constrained to about 20 cm by the DCH inner radius. It was demonstrated that there is no real advantage in increasing the outer layer of the SVT with respect to the *BABAR* design (14.4 cm) [6, 7, 9]. Moreover, construction cost and technical difficulties would increase. Radial positions of the Layer1 to Layer4 have very little impact on track resolution when comparing a layout with detectors equally separated and the *BABAR*-like layout.

6.3.3 Impact of Layer0 on detector performance

The additional Layer0 measurement is crucial for maintaining adequate resolution on the B^0 meson proper-time difference $\Delta t \simeq \Delta z/(\beta\gamma c)$ in presence of a relatively low CM boost value $\beta\gamma = 0.24$. The average separation Δz between the decay vertex positions of the two B mesons along the z axis is $\Delta z \simeq \beta\gamma c\tau_B = 110$ μm, where τ_B is the B^0 lifetime of about 1.5 ps. Hence, in order to be able to separate the B mesons in Super$B$, their decay positions have to be determined with a significantly better precision than the average separation Δz. In addition in Super$B$, the B vertex separation in the transverse plane, of about 25 μm, is not completely negligible with respect to the average Δz separation of about 110 μm. It therefore also contributes to the determination of Δt. The reference value for the Δt resolution, $\sigma(\Delta t)$, was determined by the resolution obtained in the *BABAR* experiment according to the Fast Simulation, see Table 6.5. Fig. 6.11 shows the dependence of the per-event error on the physics parameter S as a function of $\sigma(\Delta t)$, with the sensitivity obtained in *BABAR* superimposed. In this simplified model $\sigma(\Delta t)$ corresponds to the width of the core Gaussian of the Δt resolution

function. The S per-event error is defined as the error on the parameter S normalized to the number of signal events. S is measured in time-dependent analyses and corresponds to $\sin(2\beta)$ for $B^0 \to J/\psi K^0_S$ decays. The resolution σ_z on

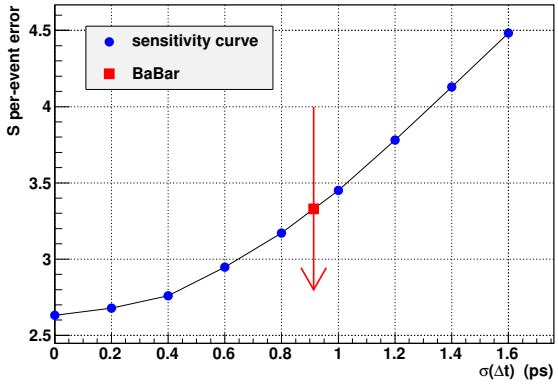

Figure 6.11: The curve represents the dependence of the error on the physics parameter S ($e.g.$ $\sin(2\beta)$) as a function of $\sigma(\Delta t)$. The arrow indicates the $\sigma(\Delta t)$ value obtained in *BABAR* according to the Fast Simulation and the square point is the relative value on the sensitivity curve.

the z coordinate of the track depends on the geometry of the vertex detector and the hit resolution. In a simplified model with two hits measured at radii r_0 and r_1 ($r_1 > r_0$) with z hit resolution σ_0 and σ_1 respectively, σ_z can be approximated as:

$$\sigma_z = \frac{\sigma_0^2 + (\sigma_1 r_0/r_1)^2}{1-(r_0/r_1)^2}. \qquad (6.1)$$

In addition, the tracks are deflected due to multiple scattering interactions with the material in the tracking volume. The scattering angle distribution can be approximated by a Gaussian with a width given by [35]:

$$\theta_{\mathrm{m.s.}} = \frac{13.6\,\mathrm{MeV}/c}{p_t \beta}\sqrt{\frac{x}{X_0}}\left[1 + 0.0038 \ln\left(\frac{x}{X_0}\right)\right] \qquad (6.2)$$

where p_t is the transverse momentum, x is the thickness of the material and X_0 is the interaction length. In order to minimize the uncertainty on σ_z it is important to measure the first hit at r_0 as small as possible with a good hit resolution σ_0. Minimizing the material close to the interaction, $e.g.$ the beampipe and Layer0 material budget is also important.

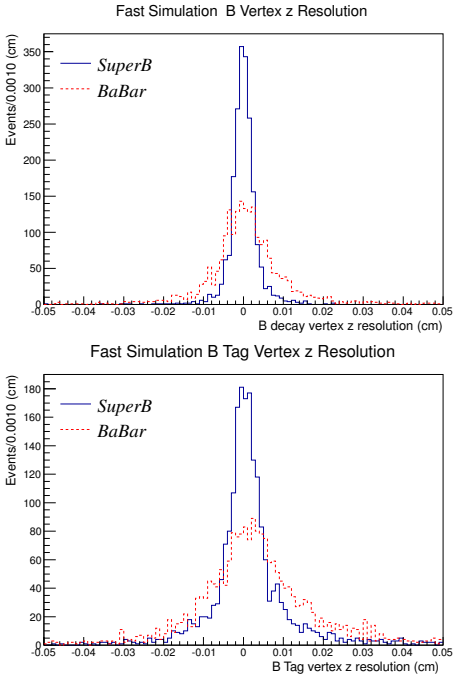

Figure 6.12: B decay vertex z position (top) and B tag z position (bottom) residual distributions in Super$B$ with Layer0 striplets (continuous line) compared with *BABAR* (dashed line) according to Fast Simulation studies.

Fig. 6.12 shows the residual distributions of B decay vertex z positions for exclusively (top) and inclusively (bottom) reconstructed B decays. Fig. 6.13 shows the Δz (top) and Δt (bottom) residual distributions. One B is exclusively reconstructed in the $B^0 \to \phi K^0_S$ mode (B_{reco}), while the other B is inclusively reconstructed using the remaining tracks of the event and is used also for flavor tagging (B_{tag}). The Fast Simulation results for Super$B$ with Layer0 striplets are compared with the *BABAR* ones and

Table 6.5: RMS of the residual distributions for decay vertex z position for exclusively reconstructed $B^0 \to \phi K^0_S$ decays ($B_{\rm reco}$), inclusively reconstructed B decays ($B_{\rm tag}$), Δz and Δt at Super$B$ and compared with *BABAR* results, according to Fast Simulation studies.

	Super$B$	*BABAR*
$B_{\rm reco}$ (μm)	40 ± 1	105 ± 1
$B_{\rm tag}$ (μm)	100 ± 2	145 ± 2
Δz (μm)	105 ± 2	165 ± 2
Δt (ps)	1.40 ± 0.02	1.45 ± 0.02

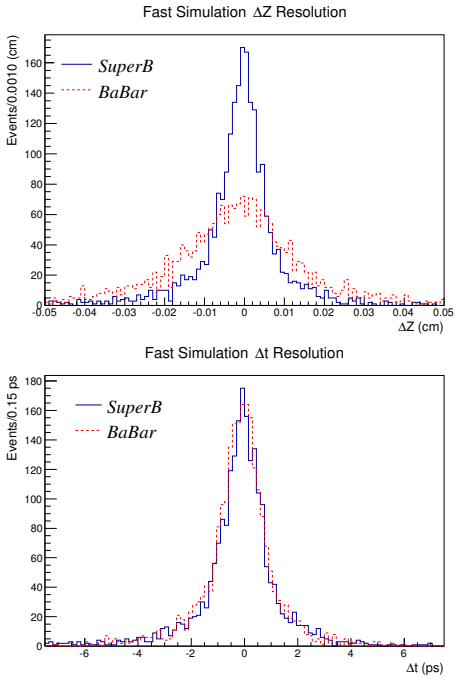

Figure 6.13: Δz (top) and Δt (bottom) residual distributions in Super$B$ with Layer0 striplets (continuous line) compared with *BABAR* (dashed line) according to Fast Simulation studies.

summarized in Table 6.5. In Super$B$ we assume $\sigma_0 = 8\,\mu$m for both u and v hits, as measured on striplets module prototype in a recent beamtest.

The Layer0 has a pinwheel configuration with radius in the range $1.53 - 1.71$ cm and it is modeled in FastSim as a cilinder with average radius of about $r_0 = 1.6$ cm. The total material budget forthe beampipe and the Layer0 striplets is about $x/X_0 \simeq 0.9\%$. For striplets detectors, u and v coordinates are oriented at $\pm 45^\circ$ with respect to the z axis and are perpendicular to each other. In *BABAR* we have $\sigma_0 = 14\,\mu$m for the z hits and $10\,\mu$m resolution for the ϕ hits, with $r_0 = 3.32$ cm and $x/X_0 \simeq 1.6\%$. In Super$B$, the improved Δz resolution is compensated by the reduced boost value, yielding a Δt resolution very similar to *BABAR*. In Fig. 6.14 is shown the Δt resolution obtainable with different Layer0 radii (r_0= 1.4 and 1.6 cm) and material budgets (x/X_0 ranging from 0.1 to 1.0%). The dashed line represents the reference value of *BABAR*.

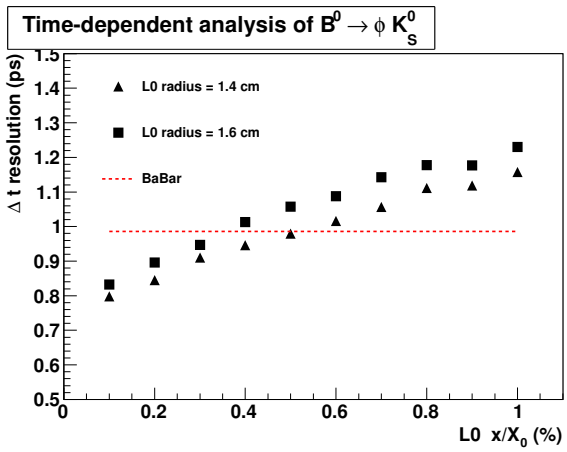

Figure 6.14: Resolution on Δt for different Layer0 configurations in terms of radius (r_0 = 1.4 and 1.6 cm) and material budget (x/X_0 = 0.1 – 1.0%) compared with the reference value of *BABAR* (dashed line).

The impact of the hit resolution on the decay vertex reconstruction has also been studied. With $8\,\mu$m hit resolution in both views of Layer0, the error on the vertex position due to multiple scattering interactions with the material dominates the overall vertex uncertainty.

Even for high momentum tracks from $B^0 \to \pi^+\pi^-$ decays. Hence, without further reduction of the material budget, there is no real advantage in improving the hit resolution with respect to this value. The hit resolution from Layer1 to Layer5 has been chosen according to the *BABAR* SVT design which was optimized for low momentum track reconstruction. The intrinsic detector hit resolution and hit efficiency values used in the Fast Simulation are reported in Table 6.6 for the different SVT layers. The efficiencies have been estimated from simulations taking into account possible hit losses due to the overlap of pulses in the analog section of the FEE with nominal background conditions.

Table 6.6: Intrinsic detector hit resolution and hit efficiency for the ϕ and z sides (Layer0 u and v sides) for the different layers.

	res. u (μm)	res. v (μm)	eff. u (%)	eff. v (%)
Layer0	8	8	99	99
	res. z (μm)	res. ϕ (μm)	eff. z (%)	eff. ϕ (%)
Layer1	14	10	98	98
Layer2	14	10	98	98
Layer3	14	15	98	96
Layer4	25	15	99	98
Layer5	25	15	99	98

6.3.4 Tracking performance

The tracking performance at Super$B$ has been studied considering alternative solutions for the SVT and DCH layout [3, 6, 7]. In particular we have studied alternative SVT configurations: with different values of the SVT outer radius (from about 14 to 22 cm), without Layer2 detector, different radial positions of the layers (*e.g.* uniform distance between layers), different hit resolutions accounting for variations of about 50% with respect to the nominal ones reported in Table 6.6. The main result was that the *BABAR*-like layout for Layer1-Layer5 was very close to be the optimal choice in terms of resolution for track parameters. Small improvements in track parameter resolution would have been possible by removing Layer2. On the other hand, the 6-layer layout has been proved to be more robust against possible problems that might cause loss of efficiency in some layers of the detector [3] and was preferred for this reason. Optimization of the strip pitches for the z and ϕ sides of the different layers are discussed in Section 6.4.2. Fig. 6.15 shows the resolution on the impact parameter d_0, as a function of p_t with the *BABAR* and Super$B$ detectors. The d_0 is defined as the distances of the point of closest approach of the track to the z-axis from the origin of the coordinate system in the xy plane. Results for alternative configurations of the SVT layout, with extended outer radius, with DCH lower radius, and without Layer2, are also shown. A significant improvement in the d_0 resolution of about a factor 2 is achieved with the Super$B$ detector with respect to the *BABAR* one. The alternative SVT layout options investigated give consistent results with the nominal Super$B$ solution.

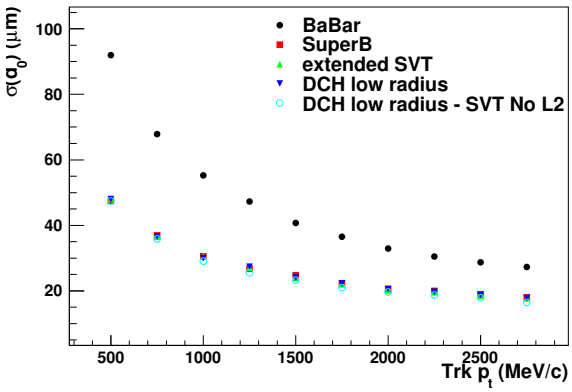

Figure 6.15: Resolution $\sigma(d_0)$ on the impact parameter d_0 as a function of p_t in *BABAR* and for various Super$B$ tracking detector configurations.

6.3.5 Impact of machine background on tracking performance

The background conditions will be more severe in Super$B$ than in *BABAR*, as described in Sec-

tion 6.2. The fast front-end electronics of the SVT provides very good resolution on the time of passage of the particle or time of arrival of the hit. The Time over Threshold (ToT) of the shaper output is used to correct for the time between the time of arrival of the hit and the time the shaper exceeds threshold. The latter is referred in the following as time stamp (TS) of the hit, and registred with a TS clock. The resolution on the time of arrival of the hit depends on the SVT layer due to the different shaper peaking times of the front-end electronics, and has been estimated using 'ad hoc' simulations [8]. Several peaking times will be available on the strip readout chips, as summarized in Table 6.13. The resolution for all layers and sides is reported in Table 6.7 for the nominal peaking-time configuration and for the shortest peaking times in Layer4 and Layer5. It ranges from about 10 ns for Layer0 up to 50 ns for Layer5. In our studies, hits outside a $\pm 5\sigma$ acceptance time window from the event time (determined by the DCH) are discarded. A similar procedure was used in the reconstruction program of the *BABAR* experiment.

Table 6.7: Resolutions on the time of arrival of the hit for the z and ϕ sides (Layer0 u and v sides) for the different layers with selected peaking times. The "old" detector correspongs to the same detector after 7.5 years of running and includes a safety factor of 5 times the level of radiation with respect to the nominal one.

	shaper peak. time (ns)	time res. "fresh" det. (ns, ns)	time res. "old" det. (ns, ns)
Layer0	25	(9.7, 9.7)	(9.7, 9.7)
Layer1	75	(10.7,10.2)	(11.0,10.8)
Layer2	100	(11.4,12.4)	(12.0,11.5)
Layer3	150	(12.4,11.7)	(15.1,14.1)
Layer4	500	(28.8,24.2)	(41.6,49.4)
Layer5	750	(42.6,34.3)	(54.6,46.7)
Layer4	250	(17.8,15.9)	(21.1,19.3)
Layer5	375	(24.9,20.5)	(27.6,23.8)

The Fast Simulation tool does not apply any pattern recognition algorithm. Tracking performance is based on parameterizations tuned on *BABAR* measured performance. Hits from neighboring tracks may be merged or associated to wrong tracks, but all generated tracks are reconstructed and no fake tracks are added. This fast simulation tool allows to study track parameter resolution, but not the tracking efficiency. The impact of the background on the resolution of the track impact parameters is shown in Fig. 6.16. In order to address the issue of

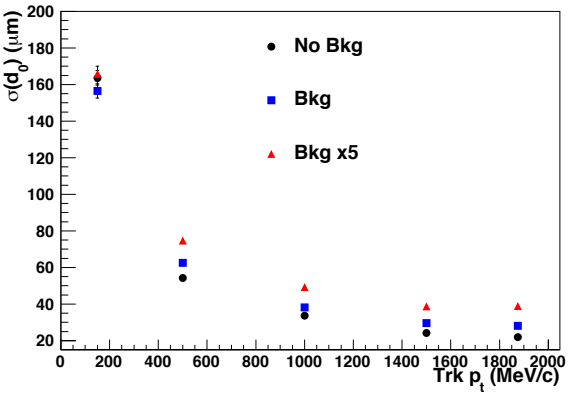

Figure 6.16: Resolution on the impact parameter of the track d_0 as a function of p_t for the Super$B$ detector with Layer0 striplets. The results shown assume no background (points), nominal background (squares) and 5 times the nominal background (triangles).

the pattern recognition capability to reconstruct tracks in the high background environment of Super$B$, SVT detector occupancies estimated in Super$B$ have been compared to those observed in *BABAR*. In particular we compared the cluster occupancy, defined as the detector strip occupancy after applying the time window cut, divided by the hit multiplicity in a cluster. The average cluster occupancy over all layers and sides is estimated to be about 0.4% with nominal background in Super$B$. This cluster occupancy in Super$B$ is smaller than the maximal

value of about 0.7% reached at high luminosity in *BABAR*, thanks to the improved hit time resolution. When considering a scenario with an additional ×5 safety factor on background predictions for Super$B$, the estimated average cluster occupancy is about 2% with nominal peaking-time configuration and about 1.5% with the shortest peaking times in Layer4 and Layer5. *BABAR* studies [11] of SVT performance in high background conditions have been used to estimate the efficiency to assign a hit to a track as a function of the cluster occupancy, that was found to be greater than 95% up to a 3% occupancy [12]. These studies indicate that the pattern recognition should be able to work without major problems also in presence of 5 times the nominal background. Moreover, for low momentum tracks not reaching the DCH, the additional Layer0 measurements should help the pattern recognition when using SVT hits only. Improvements in the pattern recognition algorithm may also be foreseen with respect to what has been used in *BABAR*.

6.3.6 Sensitivity studies for time-dependent analyses

The sensitivity to the physics parameter S has been considered as figure of merit for time-dependent analyses of B^0 decays. Several decay modes have been studied: $B^0 \to \phi K^0_S$, $B^0 \to \pi^+\pi^-$, $B^0 \to J/\psi K^0_S$, $B^0 \to D^+D^-$, but also decay modes such as $B^0 \to K^0_S K^0_S$, $B^0 \to K^0_S \pi^0$ where the impact of the additional Layer0 measurement is less effective due to the presence of neutral and long-lived particles in the final state. The per-event error on the S parameter estimated in Super$B$ with the Fast Simulation is consistent with what is observed with the *BABAR* detector for all decay modes but for $B^0 \to K^0_S K^0_S$ and $B^0 \to K^0_S \pi^0$ decays, where a reduction in sensitivity of about 15% is observed [6, 9]. Only the impact of the Δt resolution on the measurements has been included in the Fast Simulation studies. In particular, possible improvements on the reconstruction efficiency, 95% angular coverage in the CM frame with respect to 91% in *BABAR*, and better flavor tagging performance due to improved particle identification, have not been considered in these studies.

In the case of time-dependent analyses for mixing and CP violation in the neutral D meson system, the determination of the proper time t relies on the measurement of the 3-dimensional flight length ($\vec{L}$) and the momentum $\vec{p}$ of the D^0 according to $t = \frac{\vec{L}\cdot\hat{p}\ M}{|\vec{p}|}$ where M is the D^0 nominal mass. D^0 mesons produced in $e^+e^- \to c\bar{c}$ events gain a natural boost in the reaction. Even though the CM boost is reduced with respect to *BABAR*, the resolution on the D^0 proper time in Super$B$ is about 2 times better [10]. In Fig. 6.17 is reported the distribution of the D^0 proper-time error in Super$B$ and compared with *BABAR*. The average proper-time error is about 0.16 ps in Super$B$ and 0.30 ps in *BABAR* for $D^0 \to K^0_S\pi^+\pi^-$ decays, to be compared with the D^0 lifetime of about 0.41 ps.

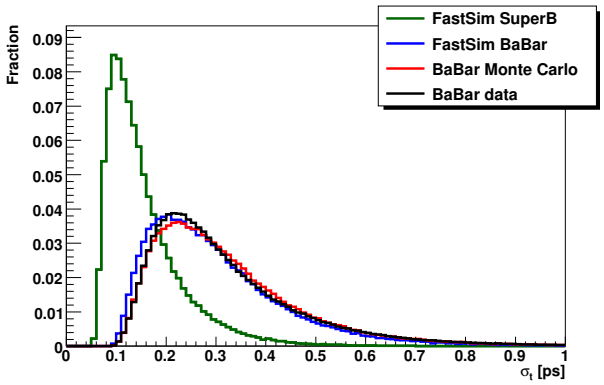

Figure 6.17: D^0 proper-time error distributions obtained with the Super$B$ (green line) and the *BABAR* (blue line) detectors according to Fast Simulation studies. Distributions from *BABAR* Monte Carlo (red line) and data (black line) are also reported in the plot.

The impact of machine background events on the SVT performance has been studied by adding background hits to signal events according to the rates estimated using Full Simulation. Details on the estimates of the machine

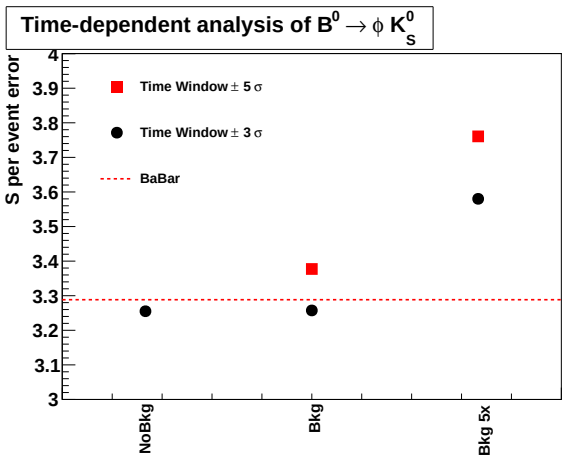

Figure 6.18: Variation of the S per-event error in $B^0 \to \phi K^0_S$ time-dependent analysis in presence of nominal background events and with 5 times the nominal background. A cut on the time of arrival of the hits has been applied at $\pm 3\sigma$ and $\pm 5\sigma$ with respect to the time of the event.

background events can be found in Section 6.2. Background hits may reduce the hit reconstruction efficiency, increase the effective hit resolution, and reduce the efficiency of pattern recognition for charged tracks, along with the increase of fake tracks. Most of the above effects have been included in our Fast Simulation assuming that the charged track pattern recognition algorithm will work with similar performance to the *BABAR* one, but fake tracks are not simulated. Hit efficiency of the readout chips used in the Fast Simulation studies can be found in Table 6.13 for the case of nominal background and with 5 times the nominal background. In Fig. 6.18 is reported the impact of the machine background events on the physics parameter S for the case of nominal background and with 5 times the nominal background rates. Background hits are rejected if they are not within a time window of $\pm 3\sigma$ ($\pm 5\sigma$) with respect to the time of the event. The values of the hit time resolution (σ) are reported in Table 6.7. The reduction of the sensitivity to S is quite limited with nominal background ($< 3\%$) and is about 9% (14%) with 5 times the nominal background conditions when applying a $\pm 3\sigma$ ($\pm 5\sigma$) time window cut.

6.3.7 Performance with Layer0 pixel detectors

A Layer0 technology based on a high granularity silicon pixel sensor, *e.g.* with 50×50 μm^2 cell, is considered for an upgrade of the baseline striplets solution. The different Layer0 technology options are described in Sec. 6.8 and are based on hybrid pixels or thin CMOS MAPS. All these solutions adopt a digital sparsified readout with the area of the pixel cell of about $2500 - 3000\,\mu$m^2. The shape of the pixel can be optimized in such a way to reduce the sensor pitch in the z direction and to improve the relative hit resolution while keeping the pixel area constant.

As already discussed in Sec. 6.3.3, the determination of the decay vertex position is driven by the performance of Layer0. The advantage of the Layer0 pixel solution is to guarantee good detector performance also in presence of relatively high background. The detector occupancy, defined as the probability of having a noise hit in the sensitive time window, is about two orders of magnitude lower with respect to the striplets case, taking into account the different detector granularity and resolution on the time of arrival of the hits. Occupancies at the level of $10^{-4} - 10^{-3}$ in a Layer0 pixel detector would correspond to occupancies of $10^{-2} - 10^{-1}$ with the striplets solution, which are about the highest achievable values in the Layer0 striplets at Super$B$. Therefore, the impact of the the background hits on the determination of the decay vertex and of the track impact parameters is moderate at Super$B$ with a Layer0 pixel solution.

Fig. 6.19 shows the sensitivity to the S parameter in time-dependent CP violation analysis of $B \to \phi K^0_S$ decays as a function of the Layer0 radius (r_0 =1.4 and 1.6 cm) and of its material budget ($x/X_0 = 0.1 - 1.0\%$), in case of

nominal background and ×5 the nominal background. The dashed line represents the reference value obtained in *BABAR*. Material budget in the range $x/X_0 = 0.35 - 0.50\%$ ($x/X_0 = 0.55 - 0.85\%$) is achievable for a Layer0 pixel solution based on CMOS monolithic active pixel sensors (hybrid pixels) depending on the results of the ongoing R&D activities. The S sensitivity is very similar to the one obtained in *BABAR*. The maximal difference is about 6% (10%) in the worst case considered (including 5 times the nominal background).

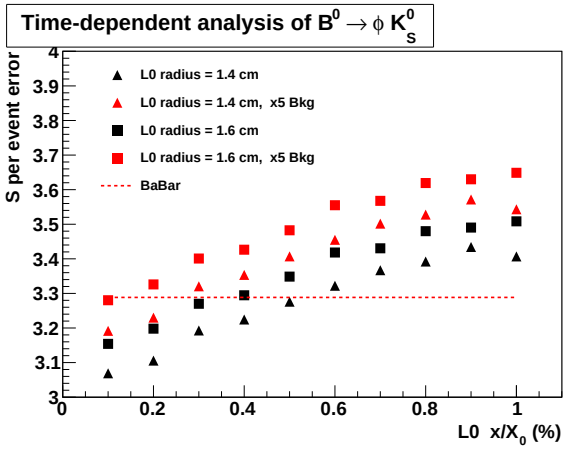

Figure 6.19: S per event error in $B^0 \to \phi K^0_S$ time-dependent analysis for different Layer0 radii ($r_0 = 1.4$ and 1.6 cm) and material budget ($x/X_0 = 0.1 - 1.0\%$) compared with the reference value of *BABAR* (dashed line). Results in presence of 5 times the nominal background are also reported in the plot.

6.3.8 Particle identification with dE/dx

The measurement of the ToT value by the front-end electronics enables one to obtain the pulse height, and hence the ionization dE/dx in the SVT sensors. The dynamic range of the analog readout is about 10-15 times the value corresponding to minimum ionizing particles, which is sufficient to take advantage of the dE/dx capability of the SVT [13].

Each sensor will provide 2 measurements of dE/dx, one for each sensor side, for a total of 12 dE/dx measurements in the SVT. In *BABAR*, where a total of 10 dE/dx measurements (5 layers) were available, for every track with signals from at least four sensors in the SVT, a 60% truncated mean dE/dx was calculated. The cluster with the smallest dE/dx energy was also removed to reduce sensitivity to electronics noise. For MIPs, it was abtained a resolution on the truncated mean dE/dx of approximately 14%.

The intrinsic smearing from the distribution of the energy deposition in the silicon sensors and from the atomic binding effects in the silicon will dominate the uncertainty on the measured dE/dx [13]. The contribution to the dE/dx uncertainty from the electronic noise should be relatively small. Therefore the resolution on dE/dx for MIPs is expected to be similar to the one achieved in *BABAR*. However, the dE/dx precision is inversely proportional to the square root of the number of dE/dx samples used for the truncated dE/dx mean calculation [14]. Two additional measurements in the Layer0 should improve the average resolution of a factor $\sqrt{5/6} = 0.9$, where 5 is the average number of dE/dx samples used in *BABAR* and 6 is the expected average number in Super$B$. The e/π separation is expected to be larger than 3σ for momenta lower than 150 MeV/c and will be very useful for rejecting low momentum electrons from background QED processes.

6.4 Silicon Sensors L. Bosisio - 8 pages

Layers 1 to 5 of the SVT will be based on 300 μm thick double-sided silicon strip detectors, with integrated AC-coupling capacitors and polysilicon bias resistors. These devices are a technically mature and conservative solution to the requirements the SVT must meet to provide precise, highly segmented tracking near the interaction point. For the new Layer0, the baseline

option also foresees double-sided silicon strip detectors, with short strips ('striplets'), 20 mm long, oriented at ±45 degrees from the beam direction, fabricated on 200 μm thick substrates. The detailed requirements which the detectors must meet are discussed below.

6.4.1 Requirements

Material budget. To achieve good vertex resolution, it is especially important to minimize the material up to and including the first measurement. This requirement, and the need to provide precise vertexing in both z and ϕ, leads to the choice of double-sided detectors. Given the increased module length with respect to the *BABAR* SVT, in order to minimize the number of sensors required, the complexity of the assembly and the insensitive area between adjacent sensors – and to ease the alignment task – we foresee to have the sensors fabricated on 150 mm diameter wafers, which is by now an available option from several sensor suppliers. For Layers 1 to 5 we plan to use 300 μm thick silicon wafers, which are a standard choice and present acceptable handling properties. For Layer0, given the very stringent limitations on the amount of material, we will be forced to go to 200 μm thick substrates. Processing double sided sensors on thin, 150 mm diameter wafers is a significant challenge, which very few manufacturers are willing to tackle. Unfortunately, while the other layers could also be assembled from smaller sensors, fabricated on 100 mm wafers, Layer0 sensors do not fit inside 100 mm wafers. This is due to the requirement to have only one sensor per Layer0 module, which in turn is dictated by the need to avoid insensitive regions and mechanical support structures, and also by limitations on the available number of readout channels. These difficulties are mitigated by the very small number of Layer0 sensors required and the fact that five of them can comfortably fit into a single 150 mm wafer. Because of this, a low fabrication and assembly yield can be tolerated for Layer0 sensors.

Efficiency. The silicon detectors must maintain high single-point efficiency in order to achieve the requirements given in Section **??** for high overall track reconstruction efficiency. Loss of efficiency can occur from defective sensor strips, from bad interconnections, or from faulty electronics channels. Sensor related inefficiencies can be due to fabrication defects or handling damage, which can result in strips with high leakage currents, poor insulation or broken AC-coupling capacitor. Our goal is to achieve an overall single-detector strip failure rate of less than 1%. The experience gained from from a large production of double-sided AC-coupled detectors for the ALICE Inner Tracking System indicates that a total rate of defective strips below 1% can be achieved with reasonable yield ($> 70\%$).

Resolution. As described in Section xxx, we have determined from Monte Carlo simulations [xxx] that the intrinsic point resolution should be 15 μm or better in both z and ϕ for the inner layers. These are the point resolutions for tracks at near-normal incidence. As the angle between the track and the plane normal to the strip increases, the resolution degrades. We require the resolution to degrade by no more than a factor of approximately 3 for angles up to 75° ($\lambda \sim 1.3$) from normal.

Radiation hardness. A further requirement is that the sensor values hold up to an integrated dose of ∼2 Mrad of ionizing radiation (electromagnetic in origin). This requirement leads to the use of AC-coupled detectors in order to avoid the problems associated with direct coupling of the large leakage currents which can occur at such large doses. It also has implications in the choice of the strip biasing scheme and on .

6.4.2 Sensor design and technology

From the above requirements and from the discussion in Sections xxx, we have arrived at the detector specifications and design parameters which are described in this section.

Substrate and implant type. The wafers will be n-type, with a resistivity in the range 4–8 kΩ cm, corresponding to a depletion voltage of 40 to 80 V. These values seem to be a reason-

Table 6.8: Physical dimensions, number of strips and pitches for the nine different sensor models. Model VI has a trapezoidal shape.

Sensor Type	0	I	II	III	IVa	IVb	Va	Vb	VI
Dimensions (mm)									
z Length (L)	105.2	111.7	66.4	96.4	114.6	119.8	102.2	106.0	68.0
ϕ Width (W)	15.1	41.3	49.4	71.5	52.8	52.8	52.8	52.8	52.8-43.3
Thickness	0.20	0.30	0.30	0.30	0.30	0.30	0.30	0.30	0.30
PN junction side reads	u	z	z	ϕ	ϕ	ϕ	ϕ	ϕ	ϕ
Strip Pitch (μm)									
z (u for Layer0)	54	50	50	55	105	105	105	105	105
ϕ (v for Layer0)	54	50	55	50	50	50	50	50	$50 \rightarrow 41$
Readout Pitch (μm)									
z (u for Layer0)	54	100	100	110	210	210	210	210	
ϕ (v for Layer0)	54	50	55	100	100	100	100	100	$100 \rightarrow 82$
Number of Readout Strips									
z (u for Layer0)	1536	1104	651	865	540	565	481	499	318
ϕ (v for Layer0)	1536	799	874	701	512	512	512	512	512

able compromise between the need to limit the depletion voltage and the peak electric fields on one hand and on the other hand the desirability of delaying type inversion in the presence of radiation damage.

We will employ p^+ strips on the junction side and n^+ strips on the ohmic side, with p^+-blocking implants in between; see Figure xxx for a cross-sectional view. This choice has proven to be a mature, reliable technology xxx], requiring no R&D.

Coupling to preamplifier. The strips are connected to the preamplifiers through a decoupling capacitor, integrated on the detector by interposing a dielectric layer between the p or n-doped strip and the metal strip. AC coupling prevents the amplifier from integrating the leakage current with the signal; handling high leakage currents due to radiation damage imposes an additional burden on the preamplifier design and has other undesirable operational implications. On each sensor, the value of the decoupling capacitance must be much larger than the total strip capacitance on the same sensor, a requirement which is rather easily met by the fabrication technologies in use.

Bias resistors. We plan to use polysilicon bias resistors, because the alternative biasing method by exploiting the punch-through effect does not offer adequate radiation tolerance. The bias resistors values will range between 4 and 15 MΩ, depending on the layer. The choice of the R_B value is constrained by two requirements. A lower limit is determined by the need to limit the noise contribution, which has a $\sqrt{\tau/R_B}$ dependence, and if several strips are ganged together the effective resistance is correspondingly decreased. The requirement that, for floating strips, the product $R_B \cdot C_{TOT}$ must be much larger than the amplifier peaking time in order to allow for capacitive charge partition is fulfilled with ample margin for any reasonable values of R_B. An upper limit to R_B is dictated by the allowable potential drop due to the strip leakage current, which depends mainly on the irradiation level and decreases going from inner to outer layers. The maximum resistance value is also limited in practice by the need to limit the area occupied on the wafer. Values of 40 kΩ/square for the sheet resistance of polysilicon can be achieved. Thus, it is possible to

Table 6.9: Number of the different sensor types per module, area of the installed sensors, number of installed sensors and number of sensors including spares. Spare sensors include one spare module per module type (two for Layer0), plus additional sensors accounting for possible losses during the whole SVT assembly process.

Sensor Type	0	I	II	III	IVa	IVb	Va	Vb	VI	All
Layer0	1	-	-	-	-	-	-	-	-	1
Layer1	-	2	-	-	-	-	-	-	-	2
Layer2	-	-	4	-	-	-	-	-	-	4
Layer3	-	-	-	4	-	-	-	-		4
Layer4a	-	-	-	-	4	-	-	-	2	6
Layer4b	-	-	-	-	-	4	-	-	2	6
Layer5a	-	-	-	-	-	-	6	-	2	8
Layer5b	-	-	-	-	-	-	-	6	2	8
Silicon Area (m^2)	0.013	0.055	0.079	0.167	0.194	0.203	0.291	0.302	0.222	1.52
Nr. of Sensors	8	12	24	24	32	32	54	54	68	308
Nr. Including Spares	20	20	40	35	44	44	72	72	92	439

fabricate a 10 MΩ resistor with a 6 μm-wide, 1500 μm-long polysilicon resistor. With a suitable shaping of the polysilicon line, the space required by the resistor will be less than 200 μm at 100 μm pitch (corresponding to strips at 50 μm pitch with resistors placed at alternate ends). A final requirement is that the bias resistor be quite stable for the expected radiation doses.

Considering the space needed to accommodate the biasing resistors and to gracefully degrade the electric field close to the edge with a guard ring structure, we specify the active region of the detectors to be 1.4 mm smaller than the physical dimensions, that is, the dead region along each edge has to be no more than 700 μm wide. This is the same specification chosen for the *BABAR* strip detectors and, although stricter than adopted by most silicon sensor designs, has proven to be feasible without difficulty, thanks to the choice of placing the polysilicon resistors in the edge region outside the guard ring. For Layer0 sensors, which have a reduced thickness of 200 μm and smaller value, shorter bias resistors, we specify a 600 μm wide inactive edge region.

Optimization of z and ϕ readout strips. *(This paragraph still needs to be rewritten.)* A major issue is which side of the detector (junction or ohmic) should read which coordinate (z or ϕ). The capacitance, and consequently, the noise is somewhat smaller on the junction side than on the ohmic side, and the strip pitch on the junction side can be 25 μm, while on the ohmic side, it is limited to about 50 μm because of the presence of the p-stop implant. For these reasons and because the z vertex measurement is more important from the point of view of physics, we use the junction side for the z strips on the inner layers. The better performance of the junction side also helps compensate for the additional resistance and capacitance imposed by the longer z fanout circuit.

In order to maintain acceptable signal-to-noise ratios for tracks at large dip angles, we employ a 100 μm readout pitch for these z strips with one floating strip in between every two readout strips. We have considered using a wider readout pitch, for example, 200 μm for the very forward and backward regions in order to increase the signal at large dip angles. However, this would involve yet another detector design, and based on our present estimates of achievable electronic noise, it does not appear to be necessary.

Table 6.10: List of different mask sets for 150 mm wafers, specifying the content of each wafer layout, the minimum value of the distance between the sensors and the wafer edge, the number of wafers required for each design and the total number of wafers. The numbers quoted include the spare sensors, but not the fabrication yield.

Mask Design	Wafer content	Min. Clearance to Wafer Edge (mm)	Number of Wafers
A	5×Mod 0	10.2	5
B	Mod I + Mod VI	8.2	20
C	Mod III	15.0	35
D	Mod IVa	11.9	44
E	Mod IVb	9.5	44
F	Mod Va + Mod VI	9.8	72
G	Mod Vb + Mod II	6.9	72
Total			287

Acceptable resolution can be obtained for the ϕ strips on the inner layers using the ohmic side. Two solutions are possible; either a 50 μm readout pitch without floating strips, since there is no room for them on the ohmic side, or a 100 μm readout pitch with one floating strip. Either solution is feasible, and they should give roughly equivalent position resolution for single tracks. Double-track resolution is better for the first solution, and the noise contribution due to detector leakage currents is doubled in the latter solution. Therefore, preference goes to a 50 μm readout pitch without floating strips. Although this choice has twice as many readout channels, the cost implications are not very important because the electronics cost is dominated by the development effort and consequently the per channel incremental cost is not significant.

The physical dimensions, strip numbers and pitches for the various sensor models are listed in Table 6.8.

6.4.3 Wafer layout and quantities

Table 6.9 reports the sensor composition of the different detector modules, the number of installed sensors of each type, with the corresponding silicon areas, and the total numbers of sensors including spares. Spare sensors account for one spare module of each type (two for Layer0), plus an additional 20% to compensate for possible losses during the assembly process. We see that the current design employs nine different types of sensors, for a total of 308 installed sensors covering 1.52 m^2. Using 150 mm diameter wafers and a dedicated sensor model for each module type allows to cover the $\sim$ 1.5 times larger area with a smaller number of sensors with respect to *BABAR*, at the expense of having nine different models of sensors. However, through optimized usage of the wafer area it is possible to accommodate all nine sensor types in seven different wafer layouts, i.e. seven mask sets, and to fabricate all 439 sensors (spares included) on 287 wafers. This is illustrated in Table 6.10.

6.4.4 Prototyping and tests

(This paragraph still needs to be written.) ... for the electrical parameters one can see Table 6.11

6.4.5 *z*-side strip connection options

On z-side, the readout pitch is set to 100 μm in Layers 1 and 2, 110 μm in Layer3 and 210 μm in Layers 4 and 5, with a 'floating' strip in between, to improve spatial resolution for particle tracks with large incidence angles. Since the number of readout strips exceeds the number of available electronic channels, it is necessary to 'gang' together up to three (depending on the

Table 6.11: Electrical parameters for the different detector models *(Numbers to be updated).*

Detector Model	z (u for model 0) readout Side			ϕ (v for model 0) readout Side		
	C_{strip} (pF/cm)	C_{AC} (pF/cm)	R_{series} (Ω/cm)	C_{strip} (pF/cm)	C_{AC} (pF/cm)	R_{series} (Ω/cm)
0	2.5	40	4	2.5	30	8.5
I	1.7	40	5	2.5	30	9
II	1.7	40	4	2.5	30	7
III	1.7	30	7	1.7	40	4
IVa	1.7	60	3	1.7	40	4
IVb	1.7	60	3	1.7	40	4
Va	1.7	60	3	1.7	40	4
Vb	1.7	60	3	1.7	40	4
VI	1.7	60	3	1.7	30	4.5

SVT layer) strips. This 'ganging' scheme connects two or three far apart strips to the same readout channel (Fig. 6.20), thus preserving the strip pitch at the expense of a higher capacitance and series resistance (resulting in higher noise), plus ambiguities in the hit position. For tracks at small θ angles with respect to the beam direction (that is, large incidence angles on the sensor), the signal-to-noise ratio is further degraded by the fact that a track traverses several z-strips (up to nine in the inner layers) and the signal becomes approximately proportional to the strip readout pitch (only 1/3 the wafer thickness in Layers 1 to 3). This suggest adopting an alternative connection scheme, in which two (or more, at large incidence angles) *adjacent* strips are bonded to a single fanout trace, effectively increasing the strip pitch and the signal into a readout channel, with a less than proportional increase in capacitance, and no increase in series resistance. We call this connection scheme 'pairing'.

At small θ angles, this gives better S/N and, consequently, higher detection efficiency when compared to individually connected strips. The improvement is even more important in comparison to the 'ganging' scheme, where the strip capacitance is proportional to the number of strips ganged together, but the signal remains that of a single strip. Moreover, for paired strips also the fanout capacitance and resistance can be made lower, because of the larger trace pitch.

Due to the lower noise, at small θ angles pairing is also expected to give better spatial resolution with respect to ganging. In order to avoid a significant increase of the input capacitance, pairing will be made between the 'readout' strips (at 100 μm pitch) so that a 'floating' strip is always present *between* two adjacent groups of paired strips. However, we are evaluating the option of connecting also the intermediate (otherwise floating) strips *within* a group of paired strips, as shown by the 'upper' bonds in Fig.xxx.

Strip capacitance measurements performed on test sensors (Ref. xxx) confirm that pairing yields significantly lower capacitance with respect to ganging the same number of strips; the advantage in capacitance of pairing with respect to ganging increases for higher pairing/ganging multiplicity. The additional increase in total capacitance when connecting also the intermediate strips is $4-5\%$ on p-side, $\sim 6\%$ on n-side. In front of this, a better signal collection efficiency is expected.

6.5 Fanout Circuits L.Vitale - M.Prest2+2 pages

The routing of the signals from the silicon sensors to the HDIs is performed by the so-called *fanout circuits*; they consist in flexible circuits that bring the signals to the end of the detector module (where they are wire bonded) to the front-end electronics IC (located a few tens of centimeters from the IP).

The fanouts for the ϕ and z coordinates are designed to minimize the material crossed by the particle within the angular acceptance. However, while the ϕ fanout circuts are just one-to-one connections, the z ones are more complicated since they cover the full length of the detector modules (up to $\sim$40 cm for the outer layers) and have to provide the interconnection (ganging or pairing) where the number of readout strips exceeds the available readout channels.

In the following sections the details about the chosen technology and the geometrical and electrical properties of the fanout circuits are described; the layer 0 fanout will be nalyzed in a dedicated section.

6.5.1 Fanouts for layer0

6.5.1.1 Requirements

6.5.1.2 Technology

6.5.1.3 Design

6.5.1.4 Prototyping and tests

6.5.2 Fanouts for outer layers

6.5.2.1 Requirements

The requirements will be fixed by the detector designs. From the production point of view, the minimum line width is 15 μm with a space between the lines of 15 μm. With the present technology, it is not possible to go below these numbers. No constraints are present on the fanout length given the same machines used for the micropattern gas detector production will be used.

6.5.2.2 Material and production technique

The BaBar fanouts were produced on 50 μm Upilex (by UBE) with a deposit of 150 nm of Cr, 4.5 μm of copper followed by a layer of 150 nm of Cr and 1.5 μm of amorphous gold. The SuperB SVT fanouts will be produced on a similar material by UBE (50 μm of polyamide with 5 μm of copper directly deposited on the base material) which should ensure less defects and thus a better yield. This material will be tested in the prototype phase. The old Upilex is anyway still available if the new material would prove not adequate.

A new technique for the production will be implemented in order to reduce the production times. In the BaBar production line, the photoresist was impressed through a mask after its being deposited on the Upilex requiring to work in a clean room. For SuperB, the idea is to impress the photoresist directly with a laser; this means the photoresist is solid and allows to complete the procedure in a much faster way. This technique has already been tested on the same pitches foreseen for the SVT fanouts.

The increase in the production speed allows to repeat the production of pieces with defects without delaying the SVT assembly. All the pieces will be gold plated with 1.5 μm of amorphous gold for the bonding.

6.5.2.3 Design

The design will follow the same rules of the BaBar fanouts adapting it to the different length of the modules. Differently from the BaBar pieces, no test-tree is foreseen (see next section). To allow the gold plating, all the lines will be shorted. A suitable cutting device will be developed to cut the shorting line after the visual inspection.

Table 6.12 summarizes the geometrical parameters [1] as well as the number of readout strips and channels, the typical pitch and the total number of required circuits per layer and type.

Fig. 6.20 presents a sketch of the ganging principle proposed for the design of layers z 3-4-5.

6.5.2.4 Tests and prototyping

All the fanouts will be automatically optically checked by a dedicated machine which will use

[1] The fanouts dimensions have been taken from the SVT Mechanics talk presented at the 4^{th} SuperB Collaboration Meeting (June 2012, La Biodola - Elba IT).

Table 6.12: Summary of fanout circuit characteristics.

Layer	Fanout Type	Length (mm)		Number of Readout		Typical Pitch at (μm)		Number of Circuits
		Left	Right	Strips	Channels	Input	Output	
1	z	216.76	217.52	1104	896	100	45	12
	ϕ	105.60	105.82	799	896	50	45	12
2	z	209.00	208.80	1302	896	100	45	12
	ϕ	76.20	76.00	874	896	55	45	12
3	z	250.26	246.26	1730	1280	110	45	12
	ϕ	54.76	53.46	701	1280	100	45	12
4a	z	332.91	328.60	1398	640	210	45	16
	ϕ	35.71	31.40	512	640	82	45	16
4b	z	332.15	327.97	1448	640	210	45	16
	ϕ	24.55	20.37	512	640	82	45	16
5a	z	407.13	411.40	1761	640	210	45	18
	ϕ	32.53	36.80	512	640	82	45	18
5b	z	406.63	411.00	1815	640	210	45	18
	ϕ	20.63	25.00	512	640	82	45	18

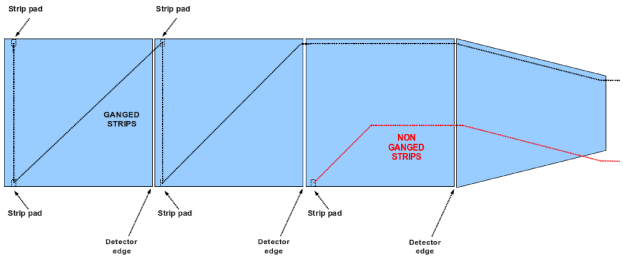

Figure 6.20: Schematic view of two z strips ganged through the fanout circuit.

the gerber files of the fanouts to find shorts or open lines. The machine can work with 25 μm lines. The region with smaller lines (15 μm with a 15 μm space) corresponding to the bonding area (1.5 mm long and around 6 mm wide) will have to be controlled manually.

Given the much shorter time needed for the production, no correction is foreseen for shorts or open lines; the damaged pieces will be produced again. On the other hand, if a short is present in the larger pitch region, the same correction procedure used for BaBar (involving the use of a microprobe) can be implemented.

As far as the tests are concerned, a batch of fanouts will be produced starting from the BaBar design to check the whole production and test chain. These fanouts in principle can be used with working detectors to test also the assembly procedures.

Figure 6.21 shows the design of a z fanout prototype of layer 3. These prototypes were also used to measure the typical capacitance and resistance.

Figures 6.22 and 6.23 show a picture of the prototype of the layer 3 z and a step of the cutting procedure.

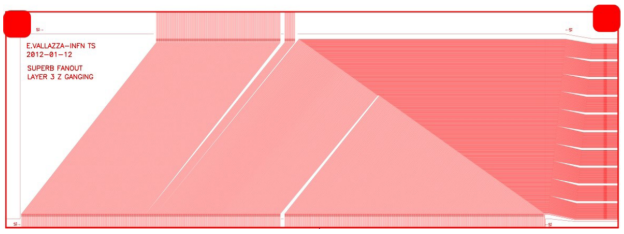

Figure 6.21: Design of a z fanout prototype of layer 3.

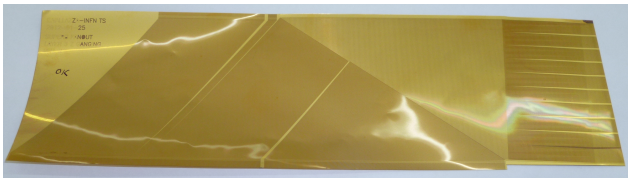

Figure 6.22: Picture of the prototype of the layer 3 z.

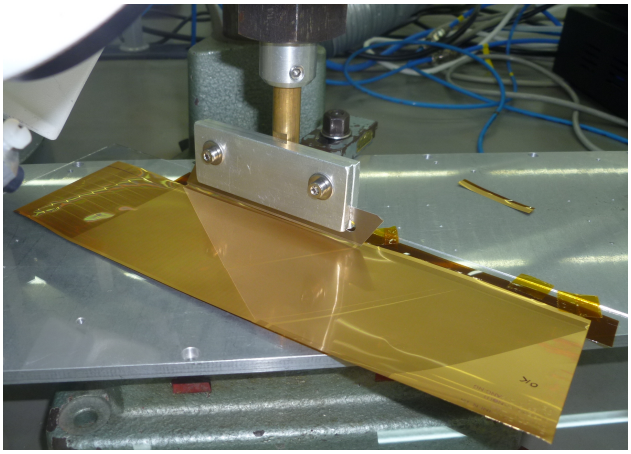

Figure 6.23: Picture of the prototype of the layer 3 z during the cutting procedure.

6.6 Electronics Readout 28 pages

6.6.1 Readout chips V.Re - 10

6.6.1.1 Electronic Readout for Strip and Striplet Detectors

The front-end processing of the signals from the silicon strip detectors will be performed by custom-designed ICs mounted on hybrid circuits that distribute power and signals, and thermally interface the ICs to the cooling system. As discussed below, the very different features of inner (Layer 0-3) and outer layers (4 and 5) of the SVT set divergent requirements to the readout chip, which makes it necessary to include programmable features in the readout ICs, in order to adjust operating parameters over a wide range. This obviously holds also in the case a different technology (pixels) is adopted for Layer 0 instead of short strips (striplets). Generally speaking, the ICs will consist of 128 channels, each connected to a detector strip. The signals from the strips, after amplification and shaping will be compared to a preset threshold. If a signal exceeding the threshold is detected, a 4 bit analog information about the signal amplitude will be provided with the Time Over Threshold technique. The analog information is useful for position interpolation, time walk correction, dE/dx measurements, as well as for calibration and monitoring purpose. The dimensions of the readout IC are expected to be about 6×4 mm^2. As discussed in the SVT HDI subsection of this TDR, the dimensions of the HDI set a 6 mm upper limit on the side of the chip with the bonding pads for the interconnection with the strip sensors. The power dissipation will be below 4 mW/channel including both analog and digital sections. For each channel with a signal above threshold, the strip number, the amplitude information, the chip identification number and the related time stamp will be stored inside the chip waiting for a trigger signal for a time corresponding to the trigger latency (about 6 μs, with 150 kHz trigger rate). When a trigger is received, data will be read out and transmitted off chip, otherwise they will be discarded. The data output from the microstrip detector will be sparsified, i.e. will consist only of those channels generating a hit. The readout integrated circuits must remain functional up to 5 times nominal background.

The option of operating in a data push fashion could be preserved for the external layers, where

this will be allowed by the low strip hit rate. This will give the possibility to feed data from these layers to the trigger system.

6.6.2 Readout chips requirements

The microstrip electronics must ensure that the detector system operates with adequate efficiency, but also must be robust and easy to test, and must facilitate testing and monitoring of the microstrip sensors. AC coupling is assumed between the strips and the readout electronics.

- **Mechanical Requirements:**
  Number of channels per chip: 128
  Chip size: width $\leq$6 mm, length $\leq$4 mm
  Pitch of input bonding pads: $<$45 μm

- **Operational Requirements:** Operating temperature: $<$40 °C
  Radiation tolerance: $>$3 Mrad/year, $>5{\cdot}10^{12}$ n_{eq}/cm^2/year (these are the expected values in Layer 0; in outer layers, radiation levels are at least one order of magnitude lower)
  Power dissipation: $<$4 mW/channel
  Detector and fanout capacitance: 10 pF $\leq C_D \leq$ 70 pF (the chip must be stable when sensor strips are disconnected from the input pads of the analog channels)

- **Dynamic range:** The front-end chips must accept signals from either P and N-side of the strip detectors. A linear response of the analog processing section is required from a minimum input charge corresponding to 0.2 MIP up to a full dynamic range of 10-15 MIP charge for dE/dx measurements.

- **Analog Resolution:** The front-end chips have to provide analog information about the charge collected by the detector, which will be also used for calibrating and monitoring the system. A resolution of 0.2 MIP charge is required for dE/dx measurements. In case of a compression-type ADC, based on the time-over-threshold technique (ToT), this may translate in 4 bits of information.

- **Efficiency:** At design luminosity, the microstrip readout must have a hit efficiency of at least 85% during its entire operational lifetime. This includes any loss of data by readout electronics or readout dead time.

- **Readout bandwidth:** Data coming out of the chip will be substantially reduced by operating in a triggered mode. The chips can use up to 2 output LVDS lines with 180 MHz clock, as it is needed to handle the higher data throughput in inner SVT layers.

- **Radiation Tolerance:** All the components of the microstrip readout system must remain operational over the entire lifetime of the experiment, including a safety factor of 5 on the nominal background expected, this corresponding to 7.5×5 years at nominal peak luminosity of 10^{36}.

  up to 10 years of SuperB running at the nominal luminosity.

- **Peaking Time:** The constraints for the peaking time of the signal at the shaper output are dictated by different needs in inner and outer layers. In Layer 0, the high occupancy due to background and the need to avoid pulse overlap and consequent hit inefficiencies set the required peaking time in the range of t_p=25-50 ns, which also allows for a high time resolution (see below). In the external layers 4 and 5, where background hit frequency is much smaller and where strips are longer and have a larger capacitance, the peaking time will be mostly determined by the need of reducing series noise contributions

and has to be in the range of 0.5-1.0 μs.

- **Signal-to-Noise Ratio:** Concerning the signal, this requirement has to take into account the different thickness of silicon detectors in inner (200 μm) and outer (300 μm) layers, as well the signal spread among various strips that depends on the track angle inside detectors and that, again, may vary in different SVT layers. Noise-related parameters (strip capacitance and distributed resistance) also sizably vary across the SVT. A signal-to noise ratio of 20 has to be ensured across the whole SVT and should not decrease significantly after irradiation. Here are the two extreme cases (where the equivalent noise charge ENC includes the thermal noise contribution from the distributed resistance of the strips):
  - Layer 0 striplets: ENC ≈900 e- at C_D=14.9 pF and at t_p=25 ns
  - Layer 5 strips: ENC ≈1100 e- at C_D=66.2 pF and at t_p=750 ns
- **Threshold and Dispersion:** Each microstrip channel will be read out by comparing its signal to a settable threshold around 0.2 MIP. Threshold dispersion must be low enough that the noise hit rate and the efficiency are degraded to a negligible extent. Typically, this should be 300 rms electrons at most and should be stable during its entire operational lifetime.
- **Comparator Time Resolution:** The comparator must be fast enough to guarantee that the output can be latched in the right time stamp period.
- **Time Stamp:** 30 ns time stamp clock is required for inner layers to get a good hit time resolution in order to reduce the occupancy in the target offline time window (100-150 ns). In the outer layers the time stamp resolution is less critical since the hit time resolution will be dominated by the long pulse shaping time. A single 30 ns time stamp clock in all layers will be used.
- **Chip clock frequency:** Two main clocks will be used inside the readout chip, the time stamp clock (about 30 MHz) and the readout clock (120 MHz or 180 MHz). These clocks will be synchronized with the 60 MHz SuperB system clock. In case the analog-to-digital conversion is based on the Time-Over-Threshold method, a ToT clock has to be generated inside the chip. The ToT clock period should at least match the pulse shaping time to get a good analog resolution. A faster ToT clock could slightly improve the analog resolution but an upper limit (≈3.5) on the ratio between ToT clock frequency and the shaping time frequency is imposed by the required dynamic range needed for low momentum particle dE/dx measurements (≈10-15 MIP) and the number of bits available for ToT. With the experience of the BaBar Atom chip a ToT clock frequency 3 times higher than the pulse shaping frequency could be used.
- **Mask, Kill and Inject:** Each micro-strip channel must be testable by charge injection to the front-end amplifier. By digital control, it shall be possible to turn off any micro-strip element from the readout chain.
- **Maximum data rate:** Simulations show that machine-related backgrounds dominate the overall rates. At nominal background levels (including a safety factor of 5), the maximum hit rate per strip goes from about 1 MHz/strip in Layer 0 to about 50 kHz/strip in Layer 5, z-side.

- **Deadtime limits:** The maximum total deadtime of the system must not exceed 10 % at a 150 kHz trigger rate and background 5 times the nominal expected rate.

- **Trigger specifications:** The trigger has a nominal latency of about 6 μs, a maximum jitter of 0.1 μs, and the minimum time between triggers is 70 ns. The maximum Level 1 Trigger rate is 150 kHz.

- **Cross-talk:** Must be less than 2 %.

- **Control of Analog Circuitry on Power-Up:** Upon power-up, the readout chip shall be operational at default settings.

- **Memory of Downloaded Control of Analog Circuitry:** Changes to default settings shall be downloadable via the readout chip control circuitry, and stored by the readout chip until a new power-up cycle or additional change to default settings.

- **Read-back of Downloadable Information:** All the data that can be downloaded also shall be readable. This includes data that has been modified from the default values and the default values as applied on each chip when not modified.

- **Data Sparsification:** The data output from the microstrip detector shall be only of those channels that are above the settable threshold.

- **Microstrip output data content:** The microstrip hit data must include the time stamp and the microstrip hits (strip number and relevant signal amplitude) for that time stamp. The output data word for each strip hit should contain 16 bits (7 strip address, 4 ToT, 1 type (Hit or Time Stamp) 4 bits to be defined). A 10-bit time stamp information (with 6 additional bits: 1 type, 5 bits to be defined) will be attached to each group of hits associated to a given time stamp (hit readout will be time-ordered).

6.6.3 Readout Chip Implementation

The SuperB SVT readout chips are mixed-signal integrated circuits in a 130 nm CMOS technology and are being designed to comply with the requirements discussed above. Each chip comprises 128 analog channels, each consisting of a charge-sensitive preamplifier, a unipolar semi-Gaussian shaper and a hit discriminator. A polarity selection stage will allow the chip to operate with signals delivered both from n- and p-sides of the SVT double-sided strip detectors. A symmetric baseline restorer may be included to achieve baseline shift suppression. When a hit is detected, a 4 bit analog-to-digital conversion will be performed by means of a Time-Over-Threshold (ToT) detection. The hit information will be buffered until a trigger is received; together with the hit time stamp, it will be then transferred to an output interface, where data will be serialized and transmitted off chip on LVDS output lines. An n-bit data output word will be generated for each hit on a strip. A programming interface accepts commands and data from a serial input bus and programmable registers are used to hold input values for DACs that provide currents and voltages required by the analog section. These registers have other functions, such as controlling data output speed and selecting the pattern for charge injection tests.

Given the very different requirements of inner and outer layers, in terms both of detector parameters and hit frequency, several programmable features will be included in the chips such as the peaking time, the gain and the size of the input device. The block diagram of the analog channel is shown in Fig. 6.24.

The digital readout of the matrix will exploit the architecture that was originally devised for

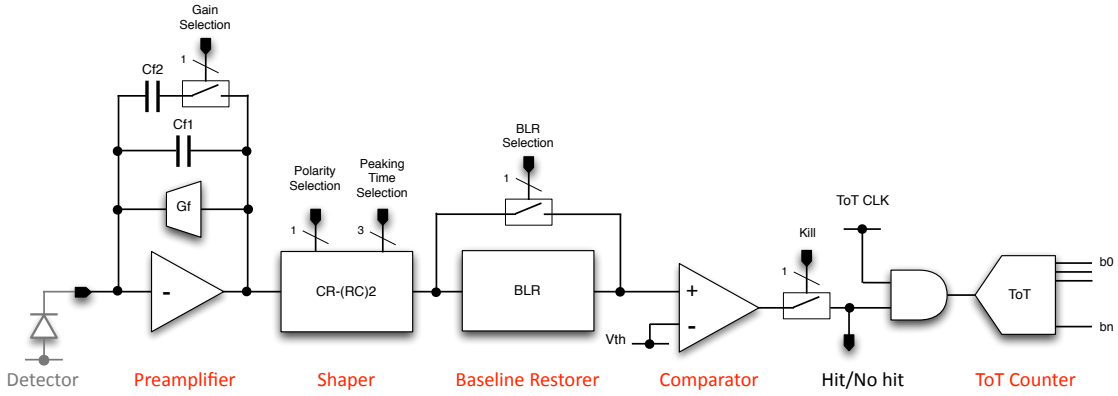

Figure 6.24: Analog channel block diagram.

a high-rate, high-efficiency readout of a large CMOS pixel sensor matrix. Each strip has a dedicated array of pre-trigger buffers, which can be filled by hits with different time stamps. The size of this buffer array is determined by the maximum strip hit rate (inner layers) and by the trigger latency. After arrival of a trigger, only hits with the same time stamp as the one provided by the triggering system send their information to the back-end. The array of 128 strips is divided in four sections, each with a dedicated sparsifier encoding the hits in a single clock cycle. The storage element next to each sparsifier (barrel level-2) acts like a FIFO memory conveying data to a barrel-L1 by a concentrator which merges the flux of data and preserves the time order of the hits. This barrel-L1 will drive the output data bus which will use up to 2 output lines depending on the data throughput and will be synchronous to a 180 MHz clock.

6.6.4 R&D for strip readout chips

The R&D to support the development of the SuperB strip readout chips has begun in 2011. The chosen technology for integration is a 130 nm CMOS process: this has an intrinsically high degree of radiation resistance, which can be enhanced with some proper layout prescriptions such as enclosed NMOS transistors and guard rings. There is a large degree of experience with mixed-signal design in this CMOS node that was gained in the last few years inside the HEP community.

The readout architecture is being tested with realistic data created by Monte Carlo analysis of the interaction region. Verilog simulations demonstrate that the chip will be able to operate with a 99 % digital readout efficiency in the worst case condition, which includes a safety factor of 5 in the background levels.

The analog section of the chip is being optimized from the standpoint of noise, comparator threshold dispersion and sensitivity to variations of process parameters. It will be possible to select the peaking time of the signal at the shaper output (25-200 ns for inner layers, 350-750 μs for outer layers) by changing the value of capacitors in the shaper. In this way the noise performances of the chip can be optimized according to the signal occupancy, preserving the required efficiency. Table 6.13 shows the main parameters of the analog section, according to simulation estimates for realistic values of detector parameters and strip hit rates. The loss in efficiency is determined by the limits in the double pulse resolution of the analog section, which depends on the signal peaking time. An acceptable compromise will be found here with the noise performance. Thought the safety factor of 5 used in noise estimation after 7.5 years represents a really worst case, different strategies will be pursued to mitigate the noise increase after irradiation. In particular S/N may benefit from moving to shorter peaking times after irradiation and from reducing the temperature

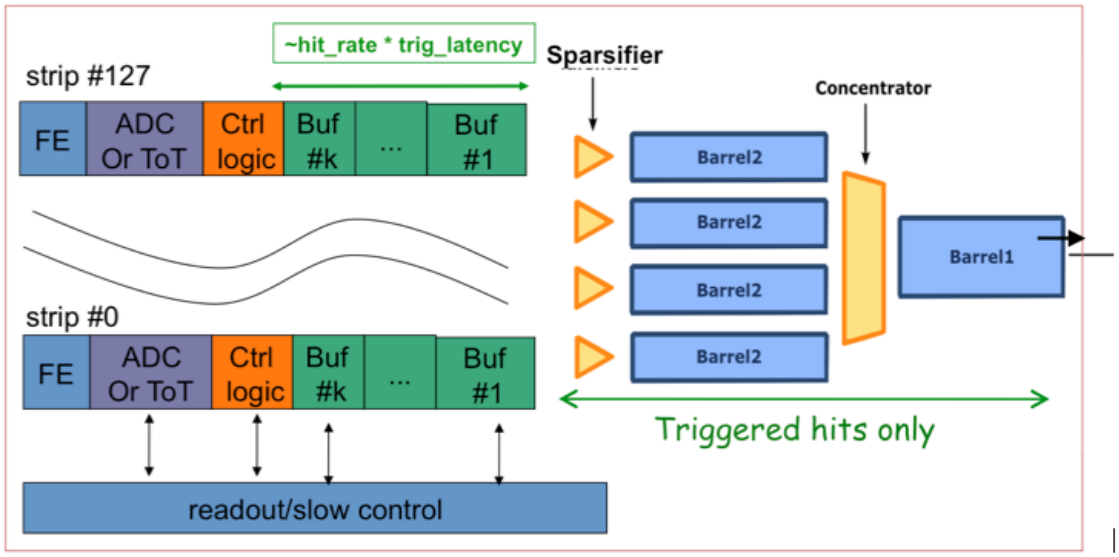

Figure 6.25: Readout architecture of the SVT strip readout chips.

of few degrees w.r.t. ambient temperature. As an outside chance, the replacement of the irradiated detectors with fresh ones can also be considered.

In 2012, the submission of a chip prototype including 64 analog channels and a reduced-scale version of the readout architecture is foreseen.

The submission of the full-scale, 128-channels chip prototypes is then scheduled in late 2013. This version will have the full functionality of the final production chip.

6.6.5 Hybrid Design M.Citterio - 10

6.6.6 Data Transmission M.Citterio - 10

6.6.7 Power Supply - 2

6.7 Mechanical Support and Assembly S.Bettarini/F.Bosi - 14 pages

An overview of the mechanical support and assembly is provided in section 6.1. In this section we provide a more detailed account of the constraints of the mechanical design due to the accelerator components near the IP and describe the details of the detector assembly, installation, survey, and monitoring.

6.7.1 I.R. Constraint

The support structure design and configuration of the SVT is dictated by the configuration and assembly procedure of the machine components near the interaction point, as well as by the SVT geometry. The background condition dictates the need for a pair of Tungsten conical shield located about 25 cm from the IP on either side. There are two further Tungsten shields of cylindrical shape that are located symmetrically with respect to the I.P., starting just at the end of the conical ones and that are fixed at the calorimeter structure.

These conical shields and the final focus permanent magnets occupy most of the region below 17.2 (300 mrad) on both side of the I.P. . In order to minimize the mass inside the active tracking volume , it is desirable to mount all of the electronics below the 300 mrad cone. This requires that in backward and forward directions electronics, cooling, cabling and supports must be confined in a volume of about one centimeter thick around the conical shields. The use of this small space below the 300 mrad must be carefully arranged with the needs of the accelerator.

Table 6.13: Main parameters of the analog section of the SVT strip readout chips.

Layer	C_D [pF] including fanout (with ganging)	t_p [ns] Available	t_p [ns] Selected	Total ENC [e rms]	Total ENC [e rms] after 7.5 years	Total ENC [e rms] after 7.5 years with ×5 safety factor	Hit rate/strip [kHz] nominal	Efficiency 1-N nominal	Efficiency 1-N with ×5 safety factor
0-side u	14.9		25	936	952	1016	187	0.99	095
0-side v	14.9		25	939	956	1019	187	0.99	0.97
1 phi	33.4		75	1122	1197	1457	170	0.98	0.92
1 z	16.2	25-200	75	748	899	1342	134	0.98	0.91
2 phi	37.2		100	1085	1174	1476	134	0.98	0.90
2 z	18.0		100	711	876	1346	134	0.98	0.88
3 phi	35.7		150	897	1125	1763	116	0.96	0.82
3 z	24.6		150	707	935	1540	79	0.98	0.90
4 phi	53.1		500	1121	1709	3090	25	0.98	0.92
4 z	47.2	375, 500	500	836	1555	3041	13.4	0.99	0.95
5 phi	66.2	750	750	1316	2099	3859	16.2	0.98	0.93
5 z	52.2		750	925	1727	3375	8.8	0.99	0.95

The solid angle coverage of the SVT is therefore restricted to a region $17.2° < \theta < 162.8°$. The radial position the SVT fiducial volume is imposed by the inner radius of DCH at about 25 cm.

The Berillium beam-pipe, about 2 cm in diameter and 40 cm long, is positioned symmetrically respect to the I.P. and it supports directly the L0 detector. The eight striplet modules, arranged in a pin wheel geometry, are mounted on the two cooled flanges. The L0 is mechanically decoupled by the other layers of the SVT. They are supported on the backward and forward side on the W conical shields by two gimbal rings, allowing the necessary degree of freedom preventing SVT over-constraints during the mounting operations. The Be beam-pipe is connected at each side through a bellow and a CF flange to the cryostat beam-pipe, splitted in the two arms. The LER and HER pipelines represent the warm internal vessel of the cryostat in the superconducting final focus magnet system. The forward and backward cryostats are symmetrically positioned around the I.P. and as extreme components of the I.R. , with the cryostat beam-pipe terminal CF flanges placed at about 2.2 m far from I.P. The cryostat is rigidly connected to the W conical shield flanges and through the terminal back flange, at a very rigid coaxial external tube, allowing a free space of about 2 cm in radius along its extension, for the SVT-L0 cables way-out. A longitudinal section of the I.R. system showing all the components is reported in Fig. 6.7.1.

Since the SVT and the L0 must be installed with all the components of I.R. system in place, they must be splitted in two halves and them clam-shelled around the beam-pipe. The assembly and alignment of the whole I.R. system, consisting of the Be beam-pipe, the SVT detectors, the forward and backward final focus permanent magnets, the W conical shields and cryostats, will take place in a staging area away from interaction hall. The entire assembly will then transported and installed in the experimental hall during the detector-commissioning phase . From the mechanical point of view, the I.R. system is comparable at two very rigid systems (W

conical shield + cryostat + external tube) joint by a very weak system (the Be beam-pipe, L0 and SVT) that could be damaged during the transportation and mounting in the experiment location. On the other hand no stiffening structure (i.e. a support tube) can be mounted on the L0 and the SVT detectors to connect this two rigid systems. Any further passive material between SVT and DCH in the active region must be avoided. Moreover, there is a strong requirement for a rapid replacement of the L0 detector in the experiment, avoiding a long period of inactivity. Therefore it is necessary to foresee the design of a removable structural support, in the following called temporary cage. It must connect rigidly the backward and forward conical shields and absorb the mechanical stress present at the moment of the first transportation to the experimental hall and during the accesses to demount of the L0. This structure has to be removable at the beginning of the running phase and remounted in the occasion of the shut-down. The operation that allows the access to L0-SVT detector is called quick demounting.

6.7.2 Module Assembly

The SVT is built with detector modules, each mechanically and electrically independent. Each module consists of silicon wafers glued to fiber composite ribs, with an high density interconnect (HDI) electronic hybrid at each end. The HDIs are electrically connected to the silicon strips by means of flexible circuits and are mechanically supported by the fiber composite beam. The entire module assembly is a rigid structure that can be tested and transported in its case. A drawing of a detector module from layer 3 is shown in Fig. 6.7.2.

The assembly of a detector module begins with the preparation of the necessary parts. The silicon detectors must be fully tested, including a long-term (burn-in) test under full bias voltage. The fanout circuits will be optically inspected and single trace tested for spotting short or opens. The readout hybrid must be assembled and tested, starting with the HDI circuit, the front-end chips, additional passive components, and the hybrid support. Finally, the completed rib, which provide mechanical stiffness, must be inspected to ensure they meet specifications. These individual parts will be fabricated by different SVT Institutions from which they can be shipped to the institutions where the module assembly is carried out. The hybrids will be tested again after shipment.

The assembly of the inner barrel-shaped modules and the outer arch-shaped modules is necessarily different. However, there are common steps. Generally the procedure is as follows:

1. each silicon detector is precisely aligned respect to the reference cross and head to head glued to the adjacent to form the module;

2. the z and ϕ fanouts are glued to the detectors and wire-bonded to the strips. The ganging bonds between ϕ strips are then performed;

3. the silicon detectors and the readout hybrid are held on a suitable fixture and aligned. The fanouts are glued to the hybrids and wire bonded to the input channels of the readout ICs. Electrical tests, including an infrared laser strip scan, are performed to assess the quality of the detector-fanout assembly (DFAs). An optical survey is foreseen;

4. the final assembly stage is different for different layers. The module of the layers 1 and 2 are then joined together by gluing the beams on the top of layer 1 to the bottom of layer 2 to give a combined structure called the "sextant". For the layer 3, the DFA is bonded flat to the fiber composite beams. For the modules of layer 4 and 5 , the DFA is held in a suitable fixture and bent on a very precise mask at the corners of the arch and at the connection to the HDI. The fiber composite beams are glued to the module with fixtures assuring alignment between the silicon detectors and the mounting surfaces on the HDI. This procedure has been already successfully adopted

for the external modules of the SVT of the BaBar experiment;

5. once completed, these detector modules are extremely rigid ladders that can be stored and submitted to the final electrical characterization. They are then shipped to the location for the final installation on the detector.

The assembly procedures for the L0 module detector follow in general which we reported for the other SVT layers, although the smaller sensor dimensions and two fanout layers represent a greater difficulty in the handling. Other differences can be outlined. No detector alignment is requested because there is only one detector; the final assembly stage for layer 0 module is more simple respect to the Layer 4 and 5 because there are not bent detectors. But the shape of the L0 module needs a very precise mask able to put the HDI in a in very precise position on to a plane inclined of 10° respect to the detector. The DFA is held in a suitable fixture and bent on a mask at the connection to the HDI. The module is then tested. The fiber composite beams are glued to the module with fixtures assuring alignment between the silicon detectors and the mounting surfaces on the HDI. A drawing of a detector module of the layer 0 is shown in Fig. 6.7.2.

6.7.3 Detector Assembly and Installation

6.7.3.1 SVT Half Detector Assembly

The L1-L5 detector is assembled in halves in order to allow the device to be clam-shelled around the beam pipe. The detector module are supported at each end by cooling/support rings in brass material that are fixed on the support cones realized in laminated carbon-fiber. Cooling water circulates at the internal of the cooling rings and to cool the mounting protrude pieces (buttons) supporting the HDI and in thermal contact with them. The cones are divided along a vertical plane and have alignment pins and latches that allow them to be connected together around the W conical shielding. The two carbon fiber support cones are mechanically connected by a low mass carbon fiber space frame. For a drawing of the cooling cones see Fig. 6.7.3.1.

During the half detector-assembly, the two half-cones will be held in a fixture which holds them in precise relative alignment. The detector modules are then mounted to the half-cones to each end. A fixture holds the detectors module during this operation and allow for well-controlled positioning of the module relative to the half-cones. Pins located in the buttons provide precise positioning of the modules, which are then fixed with screws. Accurate alignment with respect to the silicon wafers is achieved by a pair of mating fixtures . One is a dummy module (Mistress mask) and the other simulate the mating surface of the cone (Master Mask). These fixtures are constructed together and mate perfectly. One is used to verify the right machining of the mounting of the cooling ring on the cones. The other is used to position the mounting point on the HDI during the assembly of the module as mentioned in the module assembly description.
The connection between the module and the cone (called foot) provides for accurate and reproducible alignment of the module and conduction of heat from the HDI heath sink to the water cooled ring.
A detail of the foot region, which contains the readout electronics and the cooling ring with the mounting button pieces is shown in Fig. 6.7.3.1.
After verification of the alignment, the connection between the HDI and the support beam is permanently glued. The glue joint allow for the correction of small errors in the construction of either the cones or the module. After the the beam is glued, the module may be removed and remounted on the cone as necessary. The design of the foot allow this glue joint to be cleaved and remade should major repair of the module be required. After each detector module mounted, it is electrically tested using a laser scan to verify its functionality. As each layer is completed, it is optically surveyed and the data are entered in a database. Finally, the two half cones are con-

nected together with the space frame, resulting in a completed half-detector assembly.

6.7.3.2 Mount L0 on the Be-pipe and L 1-5 on the W Shielding

When the two L1-L5 half-detector assemblies are completed, they are brought to the staging area where both W conical shield and the Final Focus superconductor Magnet Cryostat and L0 have been assembled on the Be beam-pipe . Fixtures are employed to hold the cones as they are brought together and clam-shelled around the L0 and Be beam-pipe. The two half detector assemblies are mated and the latches between them are closed. The cable from HDIs are connected to the transition card, which are mounted in cooling support flanges at the end of W conical shield. The entire detector is then thoroughly tested and an optical survey is performed. After the survey is completed the Temporary Cage Sectors are mounted on the W Conical Shield flanges and rigidly fixed on to the W Conical Shield flanges . At this point the assembly is relatively rigid and can be transported to the interaction hall and installed.
The detector assembly as described above forms a rigid structure as long as the cones and space frame are connected together. This structure is supported on the W conical shields . During transport of the I.R. Assembly to the interaction hall, it is possible to have for the forward side of I.R. Assembly as much as 1mm relative motion respect to the backward side. This motion is reversible, and they will return to their original alignment when installed in normal condition in the accelerator. In addition, differential thermal expansion may affect the relative alignment of the magnets during periods in which the temperature is not controlled, and relative motion of the magnet and the beam-pipe may occur in case of seismic activity.
The support of the detector from the W conical shield must allow for this motion without placing stress on the silicon wafers. In addition, the position relative to the I.R. must be reproducible when installed in the accelerator. These constrains are met by mounting the support cones on a pairs of Gimbal Rings. One gimbal ring connects the forward cone to the W Conical Shield so as to constrain its center in x, y, and z, while allowing rotation about the x and y axes. A second set of Gimbal Ring supports the cone in the backward direction in a similar manner, with an additional sleeve that allows both for motion along z and rotation about the z axis, relative to the W Conical Shields .

6.7.3.3 Installation of Complete Assembly into the SuperB Detector

The clearance between the SVT, the L0 and beam tube are on the order of 1 to 2 mm. During the transportation of the I.R. Assembly, the critical clearances must be monitored in real time to ensure that no accidental damage to the detectors occours. In its final position, the I.R.Assembly will be supported along the External Tube on to the W cylinder Shield. Thus it is necessary that is always supported only on this region during installation. One possible installation scenario employs a crane that handle a long stiff beam that support rigidly the entire I.R. Assembly trough the forward and backward external tube and it is able to lay carefully this system on to that is aligned respect to the W Cylinder Shield and positioned in front of the FCAL region. In a similar way to the Quick Demounting operation procedure, it will be possible to move the I.R. Assembly through the DCH using the translation system existing on the W Cylinder Shield which has been previously aligned with respect to the SuperB detector. Once the I.R. assembly is in the final position the External Mechanical Cradle is removed.

6.7.3.4 Quick Demounting

The quick demounting is the operation required in case the L0 has been damaged and it has to be repaired or replaced with a new detector in a short amount of time. It allows to slide the SVT detector out of the SuperB experiment, leave that just close to the forward door to perform the work and then slide that back inside the whole detector staying always in the experimental hall. It is crucial that the time needed to perform this operation has to be much shorter

with respect to the Babar experiment . Due to the impossibility to operate on the SVT detector at the internal of the experiment, in a forward end plug open conditions, the quick demounting operation plans to move rigidly all the I.R. assembly components along Z axis in the forward direction up to a position that allows the SVT detector to be completely out to of the FCAL wall, at Z=+2650 , where it is possible to operate on the L0 detector around the Be beam-pipe. In this hypothesis it is assumed that W cylindrical backward and forward shields are rigidly fixed onto the calorimeter structure and perfectly aligned along the Z axis direction, having a supporting function in the I.R. translation. The stroke necessary for the SVT demounting position is about 3200 mm. The total weight of the I.R. assembly components is of about 1.65 Tons. A longitudinal section of the I.R. system assembly showing the initial and final positions in the quick demounting operation is reported in Fig. 6.7.3.4. A beam profile infrastructure of about 3x4x3 m^3 volume will be mounted on the FCAL wall and it will be equipped with the appropriate filters and fans to maintain ISO 8 cleanness conditions for a four-person team working to the SVT L0 demounting. From a mechanical point of view the SuperB I.R. is configured such that there are two very rigid systems positioned in both sides respect to the I.P. Each system consists of the Final Focus Superconductive Magnet Cryostat (FFSCM), the Conical shield and the External Tube, joined trough the gimbal ring. The SVT system represents the weak ring of the this mechanical chain. The Be-beam pipe is joined to the Cryostat beam-pipe trough a system of flexible bellow flanges. In a different way from Babar experiment, where the SVT region was stiffened by the C.F. support tube, in the SuperB experiment for physics reasons it is not possible to insert any stiffening structure to overlay with passive material the DCH. Therefore it is necessary to design a temporary and removable structural support. Thus, this temporary cage fixes rigidly the forward and backward W conical shields around the SVT region; it is able to absorb all the mechanical stress that could be present during the quick demounting operations; it can be removable by operating from the FCAL region, once the SVT is in running position, leaving free the space between SVT and DCH.

When the temporary cage is mounted and rigidly connects the two opposite conical shields, we can consider the whole I.R. assembly (forward side + backward sides + SVT) as a rigid body supported by several recirculating spheres embedded in the W cylinder shields, acting on the three rails positioned at 120 ° that are formed on the external tube profile. This translation system is able to guide the entire I.R. assembly and prevent any rotation during the quick demounting movement . The cylinder shields include also a mechanical system (the Radial Blocking Device) able to rigidly block the I.R. assembly at the correct position with respect to the I.P. This blocking is acted by longitudinal bars that push on a mechanical conical device embedded in the W cylinder shield, able to block radially the external tube respect to the W cylinder shield. This blocking system is also useful at the moment of the temporary cage mounting/demounting on the W conical shield flange operations, in order not to transfer any mechanical stress on the SVT detector and the Be beam-pipe.

Due to the translation rails on the external tube the temporary cage is cylindrically shaped in three independent separate sector, confined in a radial space between the external tube and W cylinder shield. The temporary cage sectors are made in a metal sandwich structure with very high flexional resistance. Each temporary cage sector is moved towards the I.P. position supported by two removable beam-rails expressly mounted and embedded in the W cylinder shield for the quick demounting operations. The beam-rails has a length such to arrive and to be fixed on to the opposite W cylinder shields in order to support the temporary cage sector when is located over the SVT region. The temporary cage sector has a special mechanical connection on the front side in order to perform a coupling in a secure conical way on the backward W conical shield flange. Instead on to the

backward side it has special radial bushing device able to be fixed to the forward W conical flange avoiding any mechanical stress to the SVT detector. The temporary cage sector fixing screws are tighten with a long special screw driver by acting at the working area in front of FCAL (forward side) and the Horse Shoes region (backward side) . Once mounted to the Beam Profile Infrastructure and aligned to the beam line it is also needed a Mechanical Support Cradle Facility having the function of rails prolongation and support for the I.R. Assembly when it is in a position out of FCAL . An artistic view of the I.R. System Assembly showing some components of the Quick Demounting operation is represented in Fig. 6.7.3.4. To enable the Quick Demounting operation, the SVT cables are disconnected at the level of the patch-panel. Also for the for the cryogenic service to the Cryostat Final Focus Superconductor Magnet it has to be foreseen an extra-length and flexible pipe connection. Monitoring position devices are planned to be installed on the W Cilinder backward and forward Shields in order to control all the positions of the components during the mounting-demounting operations. Also a strain-gage set is planned to be mounted on the Temporary Cage Sectors to monitor the mechanical stress on the sectors in the different positions of the in /out translation.

6.7.4 Detector Placement and Survey

6.7.4.1 Placement accuracy

6.7.4.2 Survey with tracks

6.7.5 Detector Monitoring

6.7.5.1 Position Monitoring System

6.7.5.2 Radiation Monitoring

6.7.6 R&D Program

6.7.6.1 Cables

6.7.6.2 hybrid

6.7.6.3 Inner layer sextant

6.7.6.4 Arch modules

6.7.6.5 Cones and space frame

6.7.6.6 Full-scale model of IR

6.8 Layer0 Upgrade Options

G.Rizzo/L.Ratti - 10 pages

With the machine operated at full luminosity, the layer 0 of the silicon vertex tracker may benefit from upgrading to a pixellated detector. This solution can actually provide some significant advantages with respect to the baseline striplet option. In particular

- the occupancy per detector element from machine background is expected to fall to a few kHz, with a major impact on the speed specifications for the front-end electronics, mainly set by the background hit rate in the case of the striplet readout chip;
- better accuracy in vertex reconstruction can be achieved with a detector pitch of 50 μm or smaller; the shape of the pixel can be optimized in such a way to reduce the sensor pitch in the z direction while keeping the area in the range of 2500-3000 μm^2, which guarantees enough room for sparse readout functionalities.

A few technology alternatives for pixel detector fabrication are being investigated and R&D activities are in progress to understand advantages and potential issues of the different options.

6.8.1 Technology options

Following is a description of the technology options that are being considered for the upgrade of the SuperB SVT innermost layer.

6.8.1.1 Hybrid pixels

Hybrid pixel technology has reached quite a mature stage of development. Hybrid pixel detectors are currently used in the LHC experiments [42, 43, 44, 45], with pitch in the range from 100 μm to a few hundred μm, and miniaturization is being further pushed forward in view of the upgrade of the same experiments at the High Luminosity LHC (HL-LHC) [64, 47, 48]. Hybrid pixel systems are

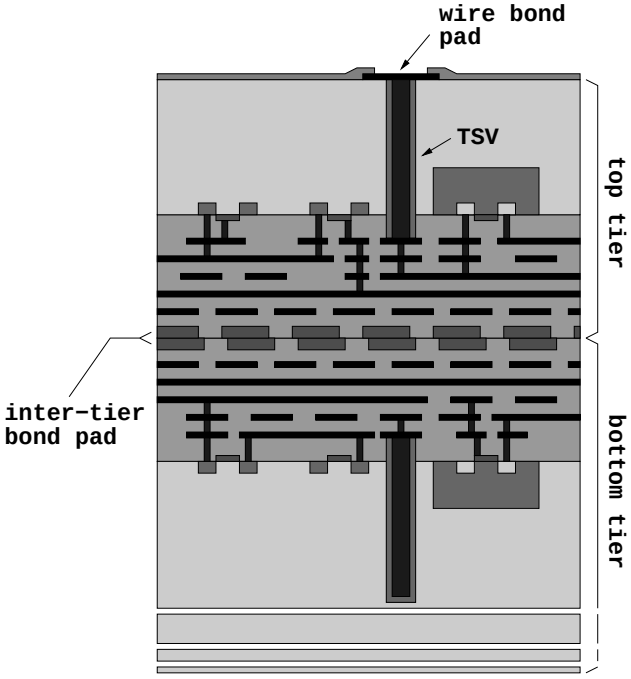

Figure 6.26: cross-sectional view of a double-layer 3D process.

based on the interconnection between a sensor matrix fabricated in a high resistivity substrate and a readout chip. Bump-bonding with indium or indium-tin or tin-lead alloys is the mainstream technology for readout chip-to-sensor interconnection. The design of a hybrid pixel detector for the SVT innermost layer has to meet some challenging specifications in terms of material budget and spatial resolution. Since the readout chip and the sensor are laid one upon the other, hybrid pixels are intrinsically thicker detectors than microstrips. Interconnect material may further degrade the performance, significantly increasing the radiation length equivalent thickness of the detector. As far as the readout and sensor chips are concerned, substrate thinning to 100-150 μm and subsequent interconnection are within present technology reach. Further thinning may pose some issues in terms of mechanical stability and, as the detector thickness is reduced, of signal-to-noise ratio and/or front-end chip power dissipation. Concerning interconnection, the vertical integration processes currently under investigation in the high energy physics community might help reduce the amount of material. Among the commercially available technologies, the ones provided by the Japanese T-Micro (formerly known as ZyCube), based on so called micro-bumps, and by the US based company Ziptronix, denoted as direct bonding technique, seem the most promising [49]. The Fraunhofer EMFT has developed a bonding technique called SLID and based on a very thin eutectic Cu-Sn alloy to interconnect the chips [50]. The spatial resolution constraints set a limit to the area of the elementary readout cell and, as a consequence, to the amount of functionalities that can be included in the front-end electronics. A planar, 130 nm CMOS technology may guarantee the required density for data sparsification and in-pixel time stamping in a 50 μm$\times$50 μm pixel area (as already observed, a different aspect ratio might be preferred to improve the resolution performance in one particular direction). The above mentioned interconnection techniques can fully comply with the detector pitch requirements (in the case of the T-Micro technology, pitches as small as 8 μm can be achieved). A fine pitch (30 μm minimum), more standard bump-bonding technology is also provided by IZM. This technology has actually been successfully used to bond the SuperPIX0 front-end chip (to be described later on in this section) to a 200 μm thick pixel detector.
Denser CMOS technologies (belonging to the 90 or 65 nm technology) can be used to increase the functional density in the readout electronics and include such functions as gain calibration, local threshold adjustment and amplitude measurement and storage. In this case, costs for R&D (and, eventually, production) would increase significantly. Vertical integration (or 3D) CMOS technologies may represent a lower cost alternative to sub-100 nm CMOS processes. The technology cross section shown in Fig. 6.26, in particular, points to the main features of the extremely cost-effective process provided by Tezzaron Semiconductor [51] which was used for the design of the SDR1 chip. The Tezzaron process can be used to vertically integrate two

(or more) layers, specifically fabricated and processed for this purpose by Chartered Semiconductor (now Globalfoundry) in a 130 nm CMOS technology. In the Tezzaron/Chartered process, wafers are face-to-face bonded by means of thermo-compression techniques. Bond pads on each wafer are laid out on the copper top metal layer and provide the electrical contacts between devices integrated in the two layers. The top tier is thinned down to about 12 μm to expose the through silicon vias (TSV), therefore making connection to the buried circuits possible. Among the options available in the Chartered technology, the low power (1.5 V supply voltage) transistor option is considered the most suitable for detector front-end applications. The technology also provides 6 metal layers (including two top, thick metals), dual gate option (3.3 V I/O transistors) and N- and P-channel devices with multiple threshold voltages. The main advantages deriving from a vertical integration approach to the design of a hybrid pixel front-end chip can be summarized as follows:

- since the effective area is twice the area of a planar technology from the same CMOS node, a better trade-off can be found between the amount of integrated functionalities and the detector pitch;
- separating the digital from the analog section of the front-end electronics can effectively prevent digital blocks from interfering with the analog section and from capacitively coupling to the sensor through the bump bond pad.

The design of a 3D front-end chip for pixel detectors is in progress in the framework of the VIPIX experiment funded by INFN.

6.8.1.2 Deep N-well CMOS monolithic sensors

Deep N-well (DNW) CMOS monolithic active pixel sensors (MAPS) are based on an original design approach proposed a few years ago and developed in the framework of the SLIM5 INFN experiment [37]. The DNW MAPS approach takes advantage of the properties of triple well structures to lay out a sensor with relatively large area (as compared to standard three transistor MAPS [52]) read out by a classical processing chain for capacitive detectors. As shown by the technology cross section in Fig. 6.27, the sensor, featuring a buried N-type layer with N-wells (NW) on its contour according to a typical deep N-well scheme, collects the charge released by the impinging particle and diffusing through the substrate, whose active volume is limited to the uppermost 20-30 μm thick layer below the collecting electrode. Therefore, within this extent, substrate thinning is not expected to significantly affect charge collection efficiency, while improving momentum resolution performance in charged particle tracking applications. As mentioned above, DNW MAPS have been proposed chiefly to comply with the intense data rates foreseen for tracking applications at the future high energy physics (HEP) facilities. The area taken by the deep N-well collecting electrode can actually be exploited to integrate the NMOS parts of the analog front-end inside the internal P-well. A small amount of standard N-well area can be used for PMOS devices, instrumental to the design of high performance analog and digital blocks taking full advantage of CMOS technology properties. In this way, both analog functions, such as signal shaping, and digital functions, such as time stamping and data storing, buffering and sparsification, can be included in the pixel operation. Note that the presence of N-wells other than the sensor is instead strongly discouraged in standard MAPS design, where the operation of the tiny collecting electrode would be jeopardized by the presence of any N-type diffusion in the surrounding. Based on the concept of the DNW monolithic sensor, the MAPS detectors of the Apsel series (see Section 6.8.2.2), which are among the first monolithic sensors with pixel-level data sparsification [53, 54], have been developed in a planar, 130 nm CMOS technology. In 2008, the Apsel4D, a DNW MAPS with 128×32 elements has been successfully tested at the Proton Synchrotron facility at CERN [57]. More recently,

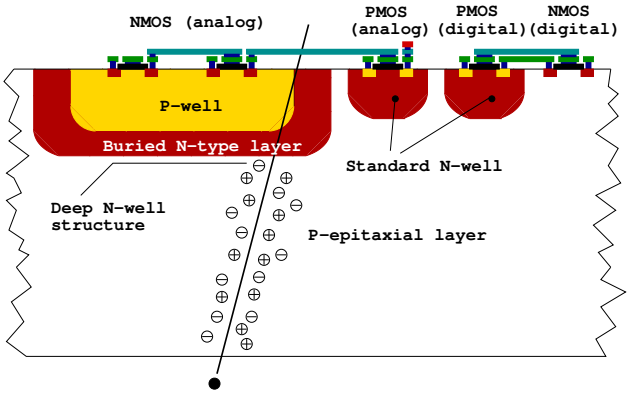

Figure 6.27: simplified cross-sectional view of a DNW MAPS. NMOS devices belonging to the analog section may be built inside the sensor, while the other transistors cover the remaining area of the elementary cell, with PMOSFETs integrated inside standard N-wells.

vertical integration technologies, like the ones discussed in the previous section for hybrid pixels, have been considered for the design of 3D DNW monolithic sensors. Some specific advantages can derive from the vertical integration approach to DNW MAPS. In particular, all the PMOS devices used in digital blocks can be integrated in a different substrate from the sensor, therefore significantly reducing the amount of N-well area (with its parasitic charge collection effects) in the surroundings of the collecting electrode and improving the detector charge collection efficiency (CCE). The first prototypes of 3D DNW MAPS [59, 60] have been submitted in the framework of the 3D-IC collaboration [61]. Characterization has started in the last quarter of 2011.

6.8.1.3 Monolithic pixels in CMOS quadruple well technology

In DNW MAPS, charge collection efficiency can be negatively affected, although to a limited extent, by the presence of competitive N-wells including the PMOS transistors of the pixel readout chain, which may subtract charge from the collecting electrode. Inefficiency is related to the relative weight of N-well area with respect to the DNW collecting electrode area. A novel approach for isolating PMOS N-wells has been made available with a planar 180 nm CMOS process called INMAPS, featuring a quadruple well structure [54]. Fig. 6.28 shows a simplified cross section of a pixel fabricated with the INMAPS process. By means of an additional processing step, a high energy deep P-well implant is deposited beneath the PMOS N-well (and not under the N-well diode acting as collecting electrode). This implant creates a barrier to charge diffusing in the epitaxial layer, preventing it from being collected by the positively biased N-wells of in-pixel circuits and enabling a theoretical charge collection efficiency of 100%. The NMOS transistors are designed in heavily doped P-wells located in a P-doped epitaxial layer which has been grown upon the low resistivity substrate. Epitaxial layers with different thickness (5, 12 or 18 μm) and resistivity (standard, about 50 Ω·cm, and high resistivity, 1 kΩ·cm) are available. The epitaxial layer is obviously expected to play an important role in improving charge collection performance. Actually, carriers released in the epitaxial layer are kept there by the potential barriers at the P-well/epi-layer and epi-layer/substrate junctions. A test chip, including several different test structures to characterize both the

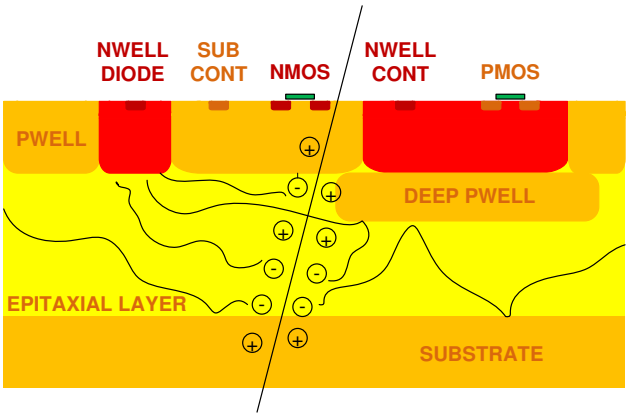

Figure 6.28: cross-sectional view of the INMAPS CMOS technology; emphasis is put on the deep P-well layer.

readout electronics and the collecting electrode performance has been submitted in the third quarter of 2011. Results from the preliminary characterization of the prototypes are discussed in Section 6.8.2.3.

6.8.2 Overview of the R&D activity

6.8.2.1 Front-end electronics for hybrid pixels in planar and 3D CMOS technology

A prototype hybrid pixel detector named SuperPIX0 has been designed as a first iteration step aimed at the development of a device to be used for the layer0 upgrade. The main novelties of this approach are the sensor pitch size ($50\times50\mu$m) and thickness (200μm) as well as the custom front-end chip architecture providing a sparsified and data-driven readout. The SuperPIX0 pixel sensor is made of n-type, Float Zone, high-resistivity silicon wafers, with a nominal resistivity larger than 10 kΩ. The SuperPIX0 chip, fabricated in the STMicroelectronics 130nm CMOS technology, is composed of 4096 channels (50x50 μm^2) arranged into 128 columns by 32 rows. Each cell contains an analog charge processor (shown in Fig. 6.29) where the sensor charge signal is amplified and compared to a chip-wide preset threshold by a discriminator. The in-pixel digital logic, which follows the comparator, stores the hit in an edge-triggered set reset flip-flop and notifies the periphery of the hit. The charge sensitive amplifier uses a single-ended folded cascode topology, which is a common choice for low-voltage, high gain amplifiers. The 20 fF MOS feedback capacitor is discharged by a constant current which can be externally adjusted, giving an output pulse shape that is dependent upon the input charge. The peaking time increases with the collected charge and is in the order of 100 ns for 16000 electrons injected. The charge collected in the detector pixel reaches the preamplifier input via the bump bond connection. Alternatively, a calibration charge can be injected at the preamplifier input through a 10 fF internal injection capacitance so that threshold, noise and crosstalk measurements can be performed. The calibration voltage step is provided externally by a dedicated line. Channel selection is performed by means of a control section implemented in each pixel. This control block, which is a cell of a shift register, enables the injection of the charge though the calibration capacitance. Each pixel features a digital mask used to isolate single noisy channel. This mask is implemented in the readout logic. The input device (whose dimensions were chosen based on [55]) featuring an aspect ratio W/L=18/0.3 and a drain current of about 0.5 μA, is biased in the weak inversion region. A non-minimum length has been chosen to avoid short channel effects. The PMOS current source in the input branch has been sized to have a smaller transconductance than the input transistor. The analog front-end cell uses two power supplies. The analog supply (AVDD) is referenced to AGND, while the digital supply is referenced to DGND. Both supplies have a nominal operating value of 1.2 V. Since single-ended amplifiers are sensitive to voltage fluctuations on the supply lines, the charge preamplifier is connected to the AVDD. The threshold discriminator and voltage references are connected to the AVDD and AGND as well. The in-pixel digital logic is connected to the digital supply. The substrate of the transistors is connected to a separate net and merged to the analog ground at the border of the matrix. The SuperPIX0 chip has been fabricated in a six metal level technology. Special attention has been paid to layout the channel with a proper shielding scheme. Two levels of metal have been used to route the analog signals, two for the digital ones and two for distributing the analog and digital supplies. The supply lines, at the same time, shield the analog signals from the digital activity.

For nominal bias conditions the power consumption is about 1.5 μW per channel. More details on the design of the analog front-end can be found in the literature [56]. The measured threshold dispersion in the chip is around 490 e- with an average pixel noise of about 60 e- (without the sensor connected). Since the threshold dispersion is a crucial characteristic to be considered in order to meet the required specifica-

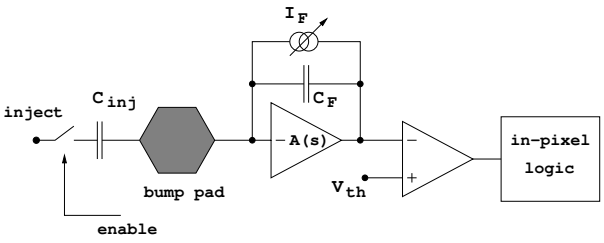

Figure 6.29: block diagram of the analog front-end electronics for the elementary cell of the SuperPIX0 readout chip.

tions in terms of noise occupancy and efficiency, circuits for threshold fine-adjusting have to be implemented in the next version of the chip. These results have been extracted using the gain measured with an internal calibration circuit, implemented in the pixel, injecting a charge from 0 to 12 fC in each channel preamplifier. An average gain of about 40 mV/fC with a dispersion at the level of 5% has been obtained. The front-end chip has been connected by bump-

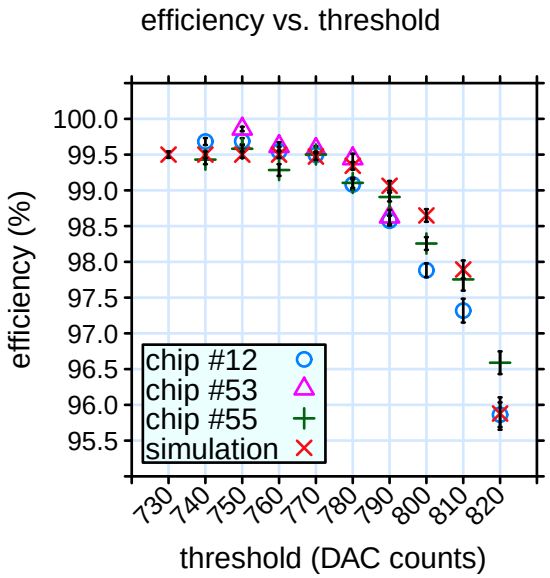

Figure 6.30: Superpix0 efficiency as a function of the voltage discriminator threshold in the case of normal incidence angle.

bonding to a high resistivity pixel sensor matrix of 200 μm thickness. The bump-bonding process has been performed by the Fraunhofer IZM with electroplating of SnAg solder bumps. Measurements on the bump-bonded chip show a working sensor and a good quality of the interconnection at 50 μm pitch. The measured gain and threshold dispersion are compatible with the ones extracted from the front-end chip only. We observe an increase of the noise of around 20%, up to about 76 e-, due to the added capacitive load of the sensor connected. The Superpix0 chip, bump bonded to a high resistivity silicon pixel detector, was also tested on the beam of the Proton Synchrotron (PS) at CERN. The measured efficiency is shown in Fig. 6.30 as a function of the voltage threshold in the discriminator. Efficiencies larger than 99% were obtained for thresholds up to 1/4 of a MIP, corresponding to more than 10 times the pixel noise.

6.8.2.2 The Apsel DNW MAPS series

DNW MAPS in planar CMOS technology

Deep N-well MAPS were proposed a few years ago as possible candidates for charged particle tracking applications. The Apsel4D chip is a 4096 element prototype MAPS detector with data-driven readout architecture, implementing twofold sparsification at the pixel level and at the chip periphery. In each elementary cell of the MAPS matrix integrated in the Apsel4D chip, a mixed signal circuit is used to read out and process the charge coming from a deep N-well (DNW) detector. This design approach, relying upon the properties of the triple well structures included in modern CMOS processes, has been described in Section 6.8.1.2. In the so called DNW MAPS is integrated with a relatively large (as compared to standard three transistor MAPS) collecting electrode, featuring a buried N-type layer, with a classical readout chain for time invariant charge amplification and shaping. In the Apsel4D prototype, the elementary MAPS cells feature a 50 μm pitch and a power dissipation of about 30 μW/channel. The block diagram of the pixel analog front-end electronics is shown in Fig. 6.31. The first block of the processing chain, a charge preamplifier, uses a complementary cascode scheme

as its forward gain stage, and is responsible for most of the power consumption in the analog section. The feedback capacitor C_F is continuously reset by an NMOS transistor, biased in the deep subthreshold region through the gate voltage V_f. The preamplifier input device, featuring an aspect ratio $W/L = 14\ \mu m/0.25\mu m$ and a drain current of 20 μA, was optimized for a DNW detector about 900 μm^2 in area and with a capacitance C_D of about 300 fF. The charge preamplifier is followed by a CR-RC, bandpass filtering stage, with open loop gain $T(s)$, featuring a programmable peaking time which can be set to 200 or 400 ns. C_1 is a differentiating capacitor at the CR-RC shaper input, while G_m and C_2 are the transconductance and the capacitance in its feedback network. A discriminator is used to compare the processed signal to a global voltage reference V_t, thereby providing hit/no-hit information to the cell digital section. More details on the design of the analog front-end can be found in the literature [58]. A dedicated readout architecture to perform on-chip data sparsification has been implemented in the Apsel4D prototype. The readout logic provides the timestamp information for the hits. The timestamp, which is necessary to identify the event to which the hit belongs, is generated by the bunch-crossing signal. The key requirements in this development are 1) to minimize logical blocks with PMOS inside the active area, thus preserving the collection efficiency, 2) to reduce to a minimum the number of digital lines crossing the sensor area, in particular its dependence on detector

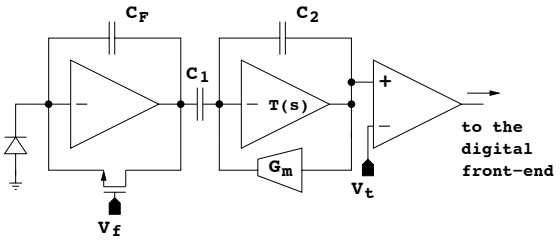

Figure 6.31: block diagram of the analog front-end electronics for the elementary cell of the Apsel4D prototype.

size to allow the readout scalability to larger matrices and to reduce the residual crosstalk effects, and 3) to minimize the pixel dead time by reading hit pixels out of the matrix as soon as possible. With these criteria a readout logic in the periphery of the matrix has been developed, as schematically shown in Fig 6.32. To minimize the number of digital lines crossing the active area the matrix is organized in MacroPixels (MP) with 4x4 pixels. Each MP has only two private lines for point-to-point connection to the peripheral logic: one line is used to comunicate that the MP has got hits, while the second private line is used to freeze the MP until it has been read out. When the matrix has some hits, the columns containing fired MPs are enabled, one at a time, by vertical lines. Common horizontal lines are shared among pixels in the same row to bring data from the pixels to the periphery, where the association with the proper timestamp is performed before sending the formatted data word to the output bus. The chip has been designed with a mixed mode design approach. While the pixel matrix has a full custom design and layout, the periphery readout architecture has been synthesized in standard cell starting from a VHDL model; automatic place-and-route tools have been used for the layout of the readout logic [53]. The chip has been designed to run with a readout clock up to 100 MHz (20 MHz in test beam), a maxi-

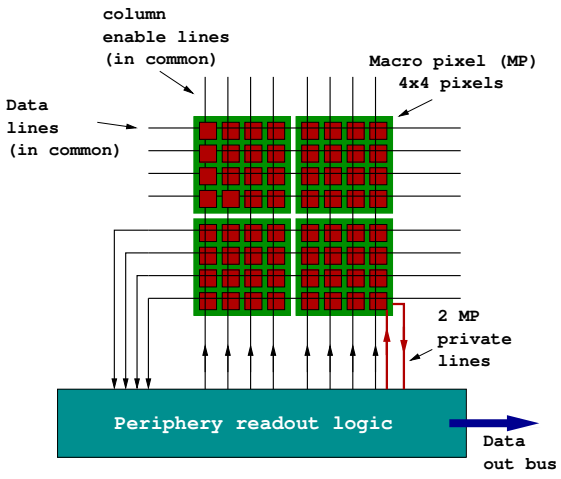

Figure 6.32: schematic concept of the architecture for MAPS matrix readout.

mum matrix readout rate of 32 hit pixels/clock cycle and a local buffer of maximum 160 hits to minimize the matrix sweep time. Apsel4D has been successfully tested with 12 GeV/c protons at the PS-T9 beam line at CERN [57]. The efficiency of the DNW MAPS as a function of threshold for two devices with different silicon thickness (Chip 22 is 300 μm thick, while Chip 23 is 100 μm thick) has been measured. Figure 6.33 shows the measured hit efficiency, determined as described in a published work [57]. At the lowest thresholds a maximum efficiency

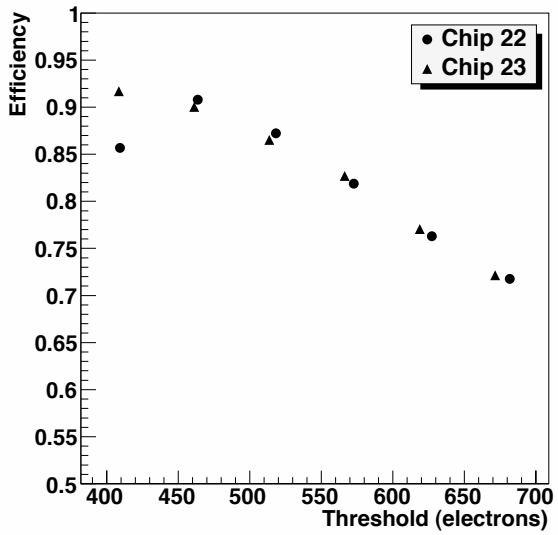

Figure 6.33: efficiency results for two MAPS detectors (the statistical uncertainty on each point is smaller than the size of the plotting symbol).

of approximately 92% and the expected general behavior of decreasing efficiency with increasing threshold can be observed. The noise occupancy for this range of thresholds was found to vary from 2.5×10^{-3} to 1×10^{-6}. The low efficiency observed for Chip 22 at the lowest threshold appears to have been caused by a readout malfunction. Investigations have shown that a small localized area on the detector had very low efficiency, while the rest of the detector behaved normally with good efficiency. Additionally, the efficiency for detecting hits as a function of the track extrapolation point *within a pixel* has been studied. Since the pixel has internal structure, with some areas less sensitive than others, we expect the efficiency to vary as a function of position within the cell. The uncertainty on the track position, including multiple scattering effects is roughly 10 microns, to be compared to the 50 μm pixel dimension. The pixel has been divided into nine square sub-cells of equal area and the hit efficiency within each sub-cell has been measured. The efficiencies thus obtained are "polluted" in some sense due to the migration of tracks among cells. We obtain the true sub-cell efficiencies by unfolding the raw results, taking into account this migration, which we characterize using a simple simulation. The result can be seen in Figure 6.34, where the efficiency measured in each sub-cell is shown. A significant variation in sensitivity within the pixel area can be observed, as expected. In particular, the central region is seen to be virtually 100% efficient, while the upper part of the pixel, especially the upper right-hand sub-cell, shows lower efficiency due to the presence of competitive n-wells. The position of this pixel map relative to the physical pixel is not fixed. This is a consequence of the alignment, which determines the absolute detector position by minimizing track-hit residuals, as described above. If the pixel area is not uniformly efficient, the pixel center as determined by the alignment will correspond to the barycenter of the pixel efficiency map. Thus, it is not possible to overlay Figure 6.34 on a drawing of the pixel layout, without adding additional information, for example a simulation of internal pixel efficiency. The efficiency as a function of position on the MAPS matrix has also been investigated, since disuniformity could indicate inefficiencies caused by the readout. Generally, a uniform efficiency across the area of the MAPS matrix was observed. The intrinsic resolution σ_{hit} for the MAPS devices was measured as already described in a published paper [57]. The expected resolution for cases where the hit consists of a single pixel is given by $50/\sqrt{12} = 14.4$ μm, where 50 microns is the pixel dimension.

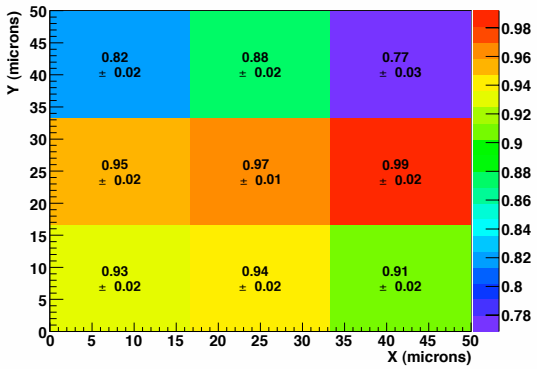

Figure 6.34: hit effiencies measured as a function of position within the pixel (the picture, which is not to scale, represents a single pixel divided into nine sub-cells).

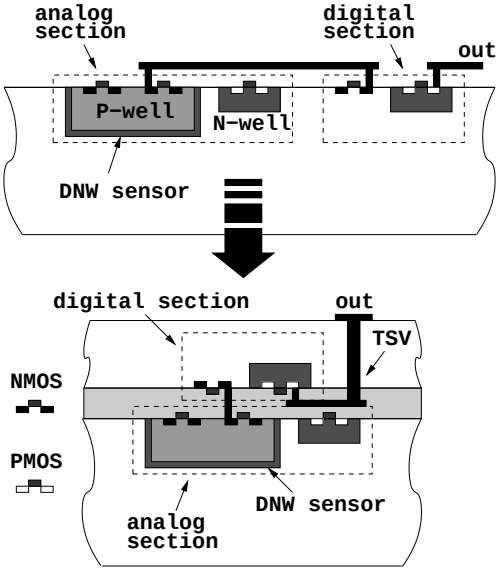

Figure 6.35: cross-sectional view of a DNW CMOS MAPS: from a planar CMOS technology to a 3D process

DNW MAPS in 3D CMOS technology As already mentioned in Section 6.8.1.2, the DNW monolithic sensors have been designed and fabricated also in the Tezzaron/Globalfoundry technology, based on the vertical integration of two 130 nm CMOS layers. The conceptual step from the DNW MAPS in a planar CMOS technology to its vertically integrated version is illustrated in Fig 6.35, showing a cross-sectional view of a 2D MAPS and of its 3D translation. The prototype include two small 3×3 matrices for analog readout and charge collection characterization and a larger one, 8×32 in size, equipped with a digital readout circuit with data sparsification and time stamping features. The pixel pitch is 40 μm. A number of different problems were encountered during fabrication of the first device batch. Among them, the misalignment between the two tiers prevented the analog and digital sections in each pixel cell to communicate to each other [62]. At the time of the TDR writing, other 3D wafers are being processed and devices from the first run are under characterization.

Fig. 6.36 shows the analog front-end channel of the 3D DNW MAPS (quite similar to the analog processor of the SuperPIX0 chip, see Fig. 6.29), simply consisting of a charge preamplifier, whose bandwidth was purposely limited to improve the signal-to-noise ratio (so called shaperless configuration). Equivalent noise charge of between 30 and 40 electrons (in good agreement with circuit simulations) and a charge sensitivity of about 300 mV/fC (a factor of 2 smaller than in simulations) were obtained from prototype characterization. Fig. 6.37 shows the ^{90}Sr spectrum detected by the cluster of 3×3 pixels in a small matrix.

The most probable value of the collected charge is about 100 electrons. Pseudo-3D DNW MAPS (here, the term pseudo-3D refers to de-

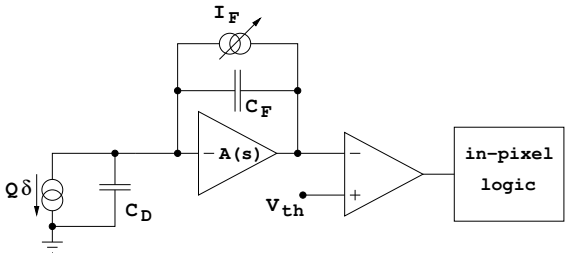

Figure 6.36: block diagram of the analog front-end electronics for the elementary cell of the 3D DNW MAPS of the apsel family.

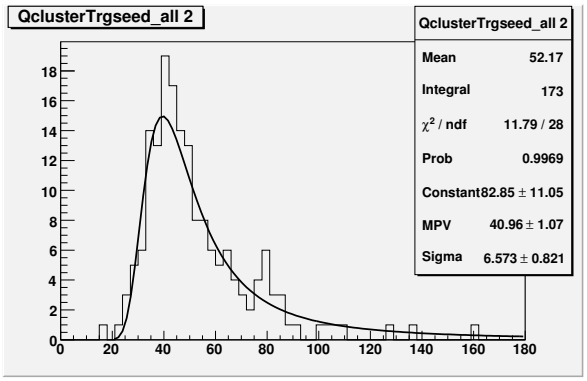

Figure 6.37: spectrum of a ^{90}Sr source detected by a 3×3 matrix of 3D DNW MAPS.

vices consisting of just one tier but suitable for 3D integration) have been tested on the PS beam at CERN. Very promising results were obtained in terms of detection efficiency, as displayed in Fig. 6.38.

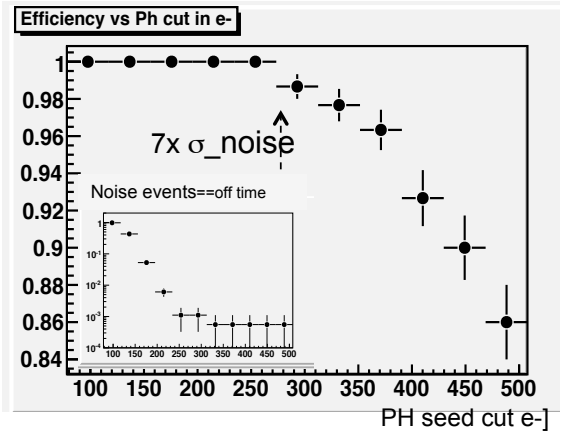

Figure 6.38: Detection efficiency of a pseudo-3D DNW MAPS as a function of the cut on the pulse height of the detected events. The efficiency is 1 up to threshold values of 7 times the pixel noise.

6.8.2.3 The Apsel4well quadruple well monolithic sensor

As already mentioned in section 6.8.1.3, a test chip in the INMAPS, 180 nm CMOS technology, called Apsel4well, has been submitted in August 2011. The chip includes four 3×3 matrices with different number (2 or 4) of the collecting electrodes (each consisting of a 1.5 μm×1.5 μm N-well diffusion), with or without the shielding deep P-well implant, with or without enclosed layout transistors as the input device of the charge preamplifier. The prototype also contains a 32×32 matrix with sparsified digital readout. The test of the first version of the chip, featuring a 5.5 μm thick epitaxial layer with standard resistivity, about 50 Ω·cm) was in progress during the writing of this TDR. Monolithic sensors with a thicker (12 μm) and more resistive (about 1 kΩ·cm) are expected to be out of the foundry by June 2012. Fig. 6.39 shows the analog readout channel of the Apsel4well

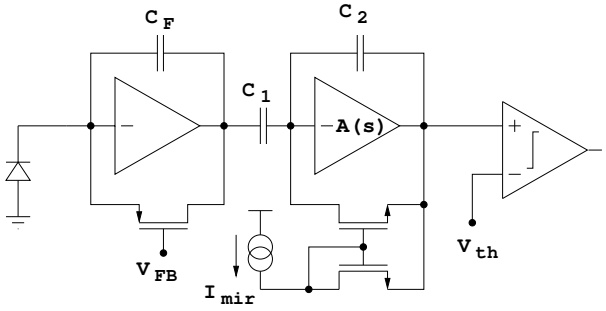

Figure 6.39: block diagram of the analog front-end electronics for the elementary cell of Apsel4well monolithic sensor.

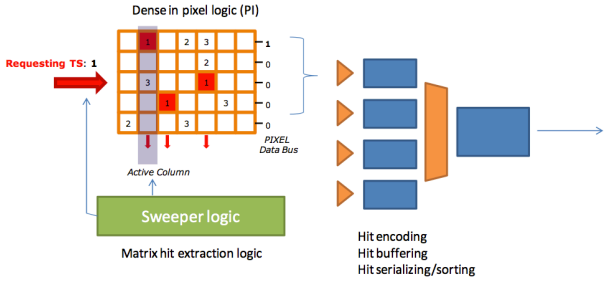

Figure 6.40: conceptual view of the digital readout architecture of the Apsel4well chip operated in the triggered mode.

MAPS. It includes a charge preamplifier, a shaping stage with a current mirror in the feedback network and a two-stage threshold discriminator. Several digital blocks are also integrated in each individual pixel element for data sparsification and time stamping purposes. Time from a peripheral Gray counter is distributed to each pixel in the matrix and is latched to a time stamp register upon arrival of a hit. When a timestamp request is sent to the matrix, a pixel FastOR signal activates if the latched timestamp is the same as the requestd one. The columns with an active FastOR signal are enabled and read out in a sequence; 1 clock cycle per column is needed. A conceptual view of the digital readout architecture is shown in Fig. 6.40. Readout circuits can be operated either in triggered or in data-push mode. They take care of encoding, buffering and serializing/sorting the hits retrieved from the sensor matrix. In order to achieve the remarkably high readout frequency set by the SuperB experiment, the architecture can be subdivided in a number of modules, each serving a submatrix. This choice improves the scalability features of the readout section and makes it suitable for experiment scale detectors. Efficiency well in excess of 99% have been obtained in Monte Carlo simulations with hit rates of 100 MHz/cm^2. Fig. 6.41 shows the signal at the shaper output as a response to an input charge signal with varying amplitude. Figures provided by the preliminary experimental characterization of the analog section are very close to simulation data, with a gain of about 960 mV/fC and an equivalent noise charge of about 30 electrons. The plot in Fig. 6.42 represents the collected charge in a Apsel4well pixel (5 μm epitaxial layer thickness, standard resistivity) illuminated with an infrared laser source. The position of the collecting electrodes is easily detectable.

6.8.3 Radiation tolerance

Hybrid pixels. The high degree of radiation tolerance of modern CMOS technologies, coming as a byproduct of the aggressive scaling down of device minimum feature size, is having a beneficial impact in high energy physics (HEP) applications. Beginning with the 130 nm CMOS processes, which entered the sub-3 nm gate oxide thickness regime, direct tunneling contribution to the gate current has assumed a significant role as compared to trap assisted mechanisms [63]. This may account for the very high degree of radiation hardness featured by devices belonging to the most recent technology nodes, which might benefit from relatively fast annealing of holes trapped in the ultrathin gate oxides. Tolerance to a few hundred of Mrad(SiO_2) has been recently proven in front-end circuits for hybrid pixel detectors [64]. Charge trapping in the thicker shallow trench isolation (STI) oxides is considered as the main residual damage mechanism in 130 nm N-channel MOSFETs exposed to ionizing radiation [65, 66], especially in narrow channel transistors [67]. Ionizing radiation was found to affect also the 90 nm and 65 nm CMOS nodes, although to an ever slighter extent, likely due to a decrease in the substrate doping concentration and/or in the STI thickness. As far a as analog front-end design is concerned, ionizing radiation damage mainly results in an increase in low frequency noise, which is more significant in multifinger devices operated at a small cur-

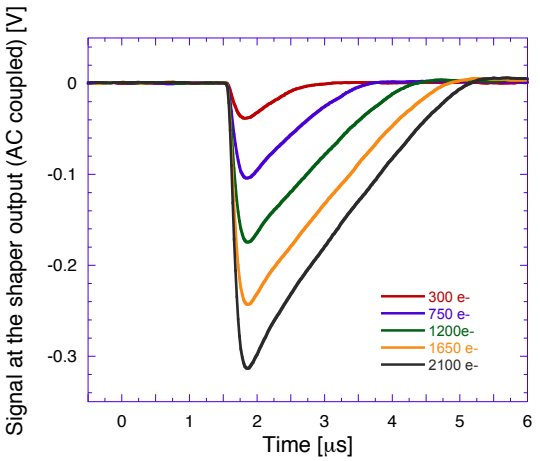

Figure 6.41: signal at the shaper output as a response to an input charge signal with varying amplitude in an Apsel4well sensor.

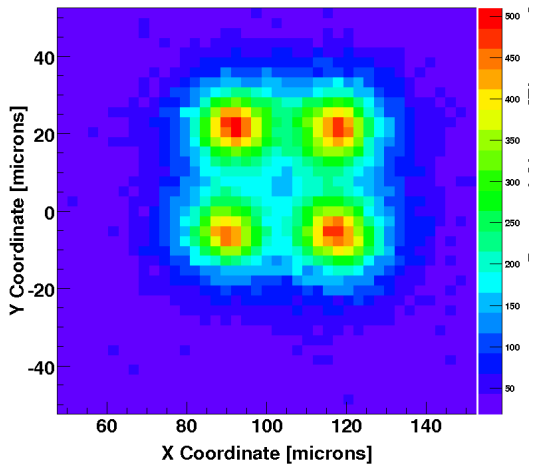

Figure 6.42: collected charge in a Apsel4well pixel illuminated with an infrared laser source.

rent density. This might be a concern in the case of the front-end electronics for hybrid pixel detectors, where the input device of the charge preamplifier is operated at drain currents in the few μA range owing to low power constraints. However, at short peaking times, typically below 100 ns, the effects of the increase in low frequency noise on the readout channel performance is negligible. Also, use of enclosed lay-

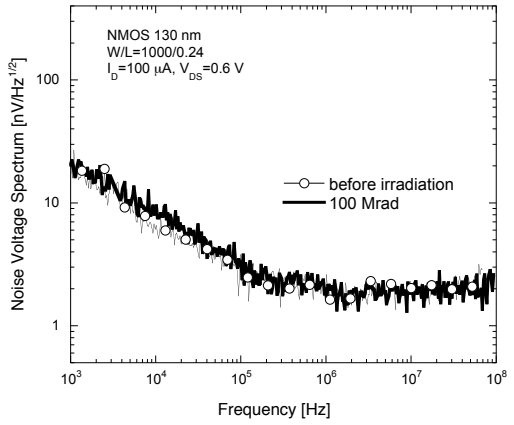

Figure 6.43: noise voltage spectrum for a 130 nm NMOS device with enclosed layout.

out techniques for the design of the preamplifier input transistor (and of devices in other critical parts of the front-end) minimizes the device sensitivity to radiation [68]. For this purpose, Fig. 6.43 shows the noise voltage spectrum for a 130 nm NMOS transistor with enclosed layout, featuring no significant changes after irradiation with a 100 Mrad(SiO_2) total ionizing dose. On the other hand, CMOS technologies are virtually insensitive to bulk damage, since MOSFET transistor operation is based on the drift of majority carriers in a surface channel.

DNW CMOS MAPS DNW MAPS have been thoroughly characterized from the standpoint of radiation hardness to evaluate their limitations in harsh radiation environments. In particular, the effects of ionizing radiation, with total doses of about 10 Mrad(SiO_2), have been investigated by exposing DNW MAPS sensors to a ^{60}Co source [69]. In that case, some performance degradation was detected in the noise and gain of the front-end electronics and in the sensor leakage current, while no significant change was observed as far as the charge collection properties are concerned. Fig. 6.44 shows the equivalent noise charge as a function of the absorbed dose and after the annealing cycle for a DNW monolithic sensor. The significant change can be ascribed to the increase in the flicker noise of the preamplifier input device as a consequence of parasitic lateral transistors being turned on by positive charge buildup in the shallow trench isolation oxides and contributing to the overall noise. Use of an enclosed layout approach is expected to significantly reduce the effect of ionizing radiation. Fig. 6.45 shows event count rate for a DNW monolithic sensor exposed to a ^{55}Fe source before irradiation, after exposure to γ-rays and after the annealing cycle. As the absorbed dose increases, the 5.9 keV peak gets broader as a consequence of the noise increase (in fair agreement with data in Fig. 6.44. At the same time, the peak is shifted towards lower amplitude values, as a result of a decrease in the front-end charge sensitivity also due to charge build up in the STI of some critical devices. DNW MAPS of the same kind have also been irradiated with neutrons from a Triga

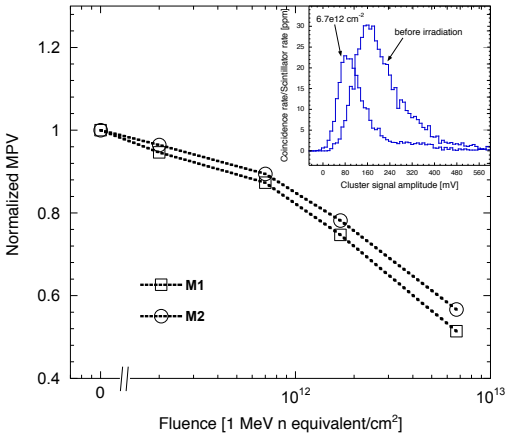

Figure 6.46: most probable value (MPV) of the ^{90}Sr spectra (shown in the inset for one of the tested chips before irradiation and after exposure to a 6.7×10^{12} cm^{-2} neutron fluence) normalized to the pre-irradiation value as a function of the fluence for DNW MAPS with different sensor layout.

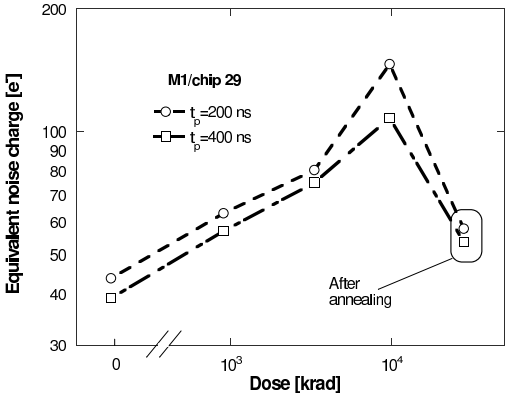

Figure 6.44: equivalent noise charge as a function of the absorbed dose and after the annealing cycle for DNW monolithic sensor. ENC is plotted for the two available peaking times.

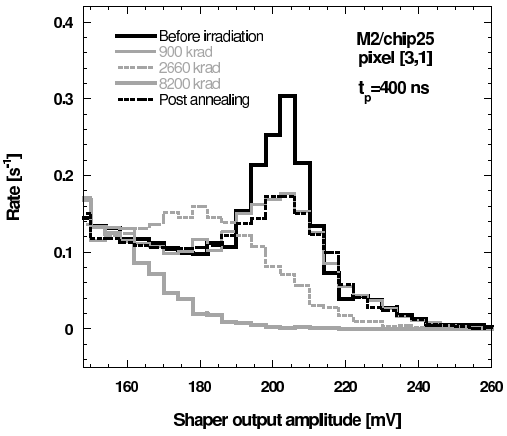

Figure 6.45: event count rate for a DNW monolithic sensor exposed to a ^{55}Fe source before irradiation, after exposure to γ-rays and after the annealing cycle.

MARK II nuclear reactor to test bulk damage effects [70]. The final fluence, 6.7×10^{12} 1 MeV neutron equivalent/cm^2, was reached after a few, intermediate steps. The devices under test (DUT) were characterized by means of several different techniques, including charge injection at the front-end input through an external pulser, sensor stimulation with an infrared laser and spectral measurements with ^{55}Fe and ^{90}Sr radioactive sources. Neutron irradiation was found to have no sizable effects on the front-end electronics performance. This can be reasonably expected from CMOS devices, whose operation is based on the drift of majority carriers in a surface channel, resulting in a high degree of tolerance to bulk damage. Exposure to neutrons was instead found to affect mainly the charge collection properties of the sensors with a reduction in the order of 50% at the maximum integrated fluence. Fig. 6.46 shows the most probable value (MPV) of the ^{90}Sr spectra normalized to the pre-irradiation value as a function of the fluence for DNW MAPS with different sensor layout. A substantial decrease can be observed, to be ascribed to a degradation in the minority carrier lifetime. A higher degree of tolerance was instead demonstrated in monolithic sensors with high resisitivity (1 kΩ cm) epitaxial layer [72]. Actually, doping concentration plays a role in determining the equilibrium Fermi level, which in turn influences the

effectiveness of neutron-induced defects as recombination centers [71].

6.9 Services, Utilities and E.S. & H issues - 4 pages

6.9.1 Service and Utilities

- Data and control lines
- Power
- Cooling water
- Dry air or nitrogen

6.9.2 ES&H Issue

Bibliography

[1] BABAR Collaboration (D. Boutigny et al.), *BaBar technical design report*. SLAC-R-0457.

[2] C. Bozzi *et al.* [BABAR Collaboration], "The design and construction of the BaBar silicon vertex tracker," Nucl. Instrum. Meth. A **447** (2000) 15.

[3] J. Walsh, *Performance with different SVT configurations*, http://agenda.infn.it/getFile.py/access?contribId=132&sessionId=19&resId=0&materialId=slides&confId=1165.

[4] B. Aubert *et al.* [BABAR Collaboration], "The BaBar detector," Nucl. Instrum. Meth. A **479**, 1 (2002).

[5] O. Long, BaBar Note #499,*An alternative algorithm for stand-alone SVT pattern recognition*, July 8, 1999

[6] N. Neri, *Tracking Performance with the SVT baseline configuration*, http://agenda.infn.it/getFile.py/access?contribId=162&sessionId=25&resId=0&materialId=slides&confId=1161.

[7] M. Rama, *Performance studies with different SVT and DCH configurations*, http://agenda.infn.it/getFile.py/access?contribId=161&sessionId=25&resId=2&materialId=slides&confId=1161.

[8] L. Ratti, *Update on time resolution studies*, http://agenda.infn.it/getFile.py/access?contribId=0&resId=0&materialId=slides&confId=5315.

[9] G. Simi, $B^0 \to K^0_S\pi^0$ *vs. SVT radius*, http://agenda.infn.it/getFile.py/access?contribId=164&sessionId=25&resId=3&materialId=slides&confId=1161.

[10] R. Andreassen, *Progress with charm mixing measurements at the 4S*, http://agenda.infn.it/materialDisplay.py?contribId=301&sessionId=34&materialId=slides&confId=1742.

[11] BaBar Analysis Document #707, *Final Report of the SVT Long Term Task Force*. February 24, 2004.

[12] I. Ripp-Baudot, *Update on activities in Strasbourg & tracking in high occupancy*, http://agenda.infn.it/getFile.py/access?contribId=63&sessionId=2&resId=2&materialId=slides&confId=4880.

[13] B. Schumm, BaBar Note #126, dE/dx *identification with a five layer silicon tracker*. February 15, 1994.

[14] Alexandre V. Telnov, BaBar Analysis Document #1500, *Detailed Track-Level* dE/dx *Calibration for the BABAR Drift Chamber and Silicon Vertex Tracker*. July 30, 2007.

[15] *FastSim* program, available online at: http://www.pi.infn.it/SuperB.

[16] M. Bona *et al.*, *Super*B*: A High-Luminosity Heavy Flavour Factory. Conceptual Design Report*, arXiv:0709.0451v2 [hep-ex], INFN/AE-07/2, SLAC-R-856, LAL 07-15, also available at http://www.pi.infn.it/SuperB/CDR.

[17] G. Rizzo et al., "Recent Development on CMOS MAPS for the SuperB Silicon Vertex Tracker", *Proceedings of the 12th Pisa Meeting on Advanced Detectors, La Biodola, Isola dElba, Italy 20-26 May 2012 to be published in Nucl. Instrum. Meth.*

[18] F. Giorgi et al., "The front-end chip of the SuperB SVT detector", *Proceedings of the 12th Pisa Meeting on Advanced Detectors, La Biodola, Isola dElba, Italy 20-26 May 2012 to be published in Nucl. Instrum. Meth.*

[19] I. Rashevkaya et al., "Characterization of strip detector parameters for the SuperB Silicon Vertex Tracker", *Proceedings of the 12th Pisa Meeting on Advanced Detectors, La Biodola, Isola dElba, Italy 20-26 May 2012 to be published in Nucl. Instrum. Meth.*

[20] S. Bettarini et al., "The SLIM5 low mass silicon tracker demonstrator" *Nucl. Instrum. Meth. A* **623** *(2010) 942.*

[21] SLIM5 Collaboration - Silicon detectors with Low Interaction with Material, http://www.pi.infn.it/slim5/

[22] G. Rizzo for the SLIM5 Collaboration., "Development of Deep N-Well MAPS in a 130 nm CMOS Technology and Beam Test Results on a 4k-Pixel Matrix with Digital Sparsified Readout"', *2008 IEEE Nuclear Science Symposium, Dresden, Germany, 19-25 October, 2008*

[23] A. Gabrielli for the SLIM5 Collaboration, "Development of a triple well CMOS MAPS device with in-pixel signal processing and sparsified readout capability" *Nucl. Instrum. Meth. A* **581** *(2007) 303.*

[24] A. Gabrielli et al., "High efficiency readout circuits for large matrices of pixels" *Nucl. Instrum. Meth. A* **658** *(2011) 141.*

[25] F. Giorgi et al., "2D and 3D Thin Pixel Technologies for the Layer0 of the SuperB Silicon Vertex Tracker" *2011 IEEE Nuclear Science Symposium, Valencia, Spain 23-29 October, 2011*

[26] E. Paoloni et al., "Beam test results of different configurations of deep N-well MAPS matrices featuring in pixel full signal processing" *Nucl. Instrum. Meth. A (2010),doi:10.1016/j.nima.2010.06.325*

[27] L. Ratti et al. "Front-End Performance and Charge Collection Properties of Heavily Irradiated DNW MAPS" *IEEE Trans. Nucl. Sci. NS-57 (4) (2010) 1781*

[28] S. Zucca et al. "Characterization of bulk damage in CMOS MAPS with deep N-well collecting electrode" *IEEE Trans. Nucl. Sci. NS-PP (99) (2012) 1*

[29] Ray Yarema, et. al., 3D IC Pixel Electronics-the Next Challenge *TWEPP-08, CERN-2008-008, pp. 183-187, December 10, 2008*

[30] VIPIX Collaboration - Vertically Integrated PIXels, http://eil.unipv.it/vipix/

[31] G. Rizzo et al., "Thin Pixel Development for the SuperB Silicon Vertex Tracker" *Nucl. Instrum. Meth. A* **650** *(2011) 169.*

[32] F. Bosi et al., "Light prototype support using micro-channel technology as high efficiency system for silicon pixel detector cooling" *Nucl. Instrum. Meth. A* **650** *(2011) 213.*

[33] F. Bosi et al., "The micro-cooled light support of the pixel modules for the Super-B experiment", *Proceedings of the 12th Pisa Meeting on Advanced Detectors, La Biodola, Isola dElba, Italy 2026 May 2012, to be published in Nucl. Instrum. Meth.*

[34] M Boscardin et al., "Silicon buried channels for Pixel Detector Cooling", *Proceedings of the 12th Pisa Meeting on Advanced Detectors, La Biodola, Isola dElba, Italy 2026 May 2012, to be published in Nucl. Instrum. Meth.*

[35] K. Nakamura *et al.* [Particle Data Group Collaboration], J. Phys. G G **37**, 075021 (2010).

[36] V. Re *et al.*, IEEE Trans. Nucl. Sci. **53**, 2470 (2006).

[37] SLIM5 Collaboration, *Silicon detectors with Low Interaction with Material*, http://www.pi.infn.it/slim5/.

[38] G. Rizzo for the SLIM5 Collaboration, *Development of Deep N-Well MAPS in a 130* nm *CMOS Technology and Beam Test Results on a 4k-Pixel Matrix with Digital Sparsified Readout*, 2008 IEEE Nuclear Science Symposium Conference Record, Dresden, Germany, 19-25 October, 2008.

[39] A. Gabrielli for the SLIM5 Collaboration, *Development of a triple well CMOS MAPS device with in-pixel signal processing and sparsified readout capability*,Nucl. Instrum. Methods Phys. Res., Sect. A **581**, 303 (2007).

[40] M. Villa for the SLIM5 Collaboration, *Beam-Test Results of 4k pixel CMOS MAPS and High Resistivity Striplet Detectors equipped with digital sparsified readout in the Slim5 Low Mass Silicon Demonstrator*, Nucl. Instrum. Methods Phys. Res., Sect. A (2010) doi:10.1016/j.nima.2009.10.035

[41] E.Paoloni for the VIPIX collaboration, *Beam Test Results of Different Configurations of Deep N-well MAPS Matrices Featuring in Pixel Full Signal Processing*, Proceedings of the XII Conference on Instrumentation, Vienna 2010. To be published in Nucl. Instrum. Methods Phys. Res., Sect. A.

[42] I. PericĹ. Blanquart, G. Comes, P. Denes, K. Einsweiler, P. Fischer et al., *The FEI3 readout chip for the ATLAS pixel detector*, Nucl. Instrum. and Meth., vol. A565, pp. 178-187, 2006.

[43] P. Reiner, *The ATLAS pixel detector*, Nucl. Instrum. and Meth., vol. A579, pp. 664-668, 2007.

[44] D. Bortoletto, *The CMS pixel system*, Nucl. Instrum. and Meth., vol. A636, pp. 559-674, 2007.

[45] A. Kluge, G. Anelli, F. Antinori, A. Badala, A. Boccardi, G. E. Bruno et al., *The ALICE Silicon Pixel Detector: Electronics System Integration*, 2005 IEEE Nuclear Science Symposium Conference Record, pp. 761-764.

[46] M. Garcia-Sciveres, D. Arutinov, M. Barbero, R. Beccherle, S. Dube, D. Elledge et al., *The FE-I4 pixel readout integrated circuit*, Nucl. Instrum. and Meth., vol. A636, pp. S155-S159, 2011.

[47] F. Hügging, *The ATLAS Pixel Insertable B-layer (IBL)*, Nucl. Instrum. and Meth., vol. A650, pp. 45-49, 2011.

[48] C. Favaro, *A new CMS pixel detector for the LHC luminosity upgrade* Nucl. Instrum. and Meth., vol. A658, pp. 41-45, 2011.

[49] *Handbook of 3D Integration: Technology and Applications of 3D Integrated Circuits*. Edited by P. Garrou, C. Bower and P. Ramm. Wiley-VCH, Weinheim, 2008.

[50] A. Klumpp, R. Merkel, P. Ramm, J. Weber, R. Wieland, *Vertical System Integration by Using Inter-Chip Vias and Solid-Liquid Interdiffusion Bonding*, Jpn. J. Appl. Phys. vol. 43, pp. L829-L830, 2004.

[51] R.S. Patti, *Three-Dimensional Integrated Circuits and the Future of System-on-Chip Designs*, Proc. IEEE, vol. 94, no. 6, pp. 1214-1224, Jun. 2006.

[52] Y. Degerli, M. Besanon, A. Besson, G. Claus, G. Deptuch, W. Dulinski, et al., *Performance of a Fast Binary Readout CMOS Active Pixel Sensor Chip Designed for Charged Particle Detection*, IEEE Trans. Nucl. Sci., vol. 53, no. 6, pp. 3949-3955, Dec. 2006.

[53] A. Gabrielli, G. Batignani, S. Bettarini, F. Bosi, G. Calderini, R. Cenci et al., *Proposal of a Data Sparsification Unit for a Mixed-Mode MAPS Detector*, 2007 IEEE Nuclear Science Symposium Conference Record, vol. 2, pp. 1471-1473, Oct. 26 2007-Nov. 3 2007.

[54] M. Stanitzki, J.A. Ballin, J.P. Crooks, P.D. Dauncey, A.M.M. Magnan, Y. Mikami et al., *A tera-pixel calorimeter for the ILC*, 2007 IEEE Nuclear Science Symposium Conference Record, vol. 1, pp. 254-258.

[55] L. Ratti et al., "Design of Time Invariant Analog Front-End Circuits for Deep N-Well CMOS MAPS", *IEEE Trans. Nucl. Sci.*, vol. 56, no. 4, pp. 2360-2373, Aug. 2009.

[56] G. Traversi, "Charge Signal Processors in a 130 nm CMOS Technology for the Sparse Readout of Small Pitch Monolithic and Hybrid Pixel Sensors", *IEEE Trans. Nucl. Sci.*, vol. 58, no. 5, pp.2391-2400, Oct. 2011.

[57] S. Bettarini, L. Ratti, G. Rizzo, M. Villa, L. Vitale, J. Walsh et al., *The SLIM5 low mass silicon tracker demonstrator*, Nucl. Instrum. and Meth., vol. A623, pp. 942-953, 2010.

[58] L. Ratti, *Continuous Time-Charge Amplification and Shaping in CMOS Monolithic Sensors for Particle Tracking*, *IEEE Trans. Nucl. Sci.*, vol. 53, no. 6, pp. 3918-3928, Dec. 2006.

[59] G.Casarosa, C. Avanzini, G. Batignani, S. Bettarini, F. Bosi, M. Ceccanti et al., *Thin Pixel Development for the Layer0 of the SuperB Silicon Vertex Tracker*, 2010 IEEE Nuclear Science Symposium Conference Record, pp. 1901-1905.

[60] L. Ratti, L. Gaioni, M. Manghisoni, V. Re, G. Traversi, *Vertically integrated deep N-well CMOS MAPS with sparsification and time stamping capabilities for thin charged particle trackers*, Nucl. Instrum. and Meth., vol. A624, pp. 379-386, 2010.

[61] http://3dic.fnal.gov.

[62] L. Ratti, L. Gaioni, A. Manazza, M. Manghisoni, V. Re, G. Traversi, *First results from the characterization of a three-dimensional deep N-well MAPS prototype for vertexing applications*, Nucl. Instrum. and Meth., DOI: 10.1016/j.nima.2012.03.021.

[63] A. Ghetti, E. Sangiorgi, J. Bude, T.W. Sorsch, G. Weber, *Tunneling into Interface States as Reliability Monitor for Ultrathin Oxides*, IEEE Trans. El. Dev., vol. 47, no. 12, pp. 2358-2365, Dec. 2000.

[64] M. Garcia-Sciveres, D. Arutinov, M. Barbero, R. Beccherle, S. Dube, D. Elledge et al., *The FE-I4 pixel readout integrated circuit*, Nucl. Instrum. and Meth., vol. A636, pp. S155-S159, 2011.

[65] V. Re, M. Manghisoni, L. Ratti, V. Speziali, G. Traversi, *Total Ionizing Dose Effects on the Noise Performances of a 0.13 μm CMOS Technology*, IEEE Trans. Nucl. Sci., vol. 53, no. 3, pp. 1599-1606, Jun. 2006.

[66] L. Ratti, L. Gaioni, M. Manghisoni, G. Traversi, D. Pantano, *Investigating Degradation Mechanisms in 130 nm and 90 nm Commercial CMOS Technologies Under Extreme Radiation Conditions*, IEEE Trans. Nucl. Sci., vol. 56, no. 4, pp. 1992-2000, Aug. 2008.

[67] F. Faccio, G. Cervelli, *Radiation-Induced Edge Effects in Deep Submicron CMOS Transistors*, IEEE Trans. Nucl. Sci., vol. 52, no. 6, pp. 2413-2420, Dec. 2005.

[68] W.J. Snoeys, T.A.P. Gutierrez, G. Anelli, *A new NMOS layout structure for radiation tolerance*, IEEE Trans. Nucl. Sci., vol. 49, no. 4, pp. 1829-1833, Aug. 2002.

[69] L. Ratti, M. Manghisoni, V. Re, G. Traversi, S. Zucca, S. Bettarini, F. Morsani, G. Rizzo, *Front-End Performance and Charge Collection Properties of Heavily Irradiated DNW MAPS*, IEEE Trans. Nucl. Sci., vol. 57, no. 4, pp. 1781-1789, Aug. 2010.

[70] S. Zucca, L. Ratti, G. Traversi, S. Bettarini, F. Morsani, G. Rizzo, L. Bosisio, I. Rashevskaya, V. Cindro, *Characterization of bulk damage in CMOS MAPS with deep N-well collecting electrode*, Proceedings of the 12th European Conference on Radiation and Its Effects on Components and Systems (RADECS), 2011, pp. 297-304.

[71] G.C. Messenger, *A summary review of displacement damage from high energy radiation in silicon semiconductors and semiconductor devices*, IEEE Trans. Nucl. Sci., vol. 39, no. 3, pp. 468-473, Jun. 1992.

[72] M. Deveaux, J. Baudot, N. Chon-Sen, G. Claus, C. Colledani, R. De Masi et al., *Radiation tolerance of a column parallel CMOS sensor with high resistivity epitaxial layer*, 2011 JINST 6 C02004, DOI: 10.1088/1748-022/6/02/C02004.

[73] R. Yarema, *3D circuit integration for vertex and other detectors*, Proceedings 16th International Workshop on Vertex Detectors (VERTEX2007), Lake Placid (NY, USA), September 23 - 28, 2007, Proceedings of Science PoS(Vertex 2007)017.

[74] F.Bosi and M. Massa, *Development and Experimental Characterization of Prototypes for Low Material Budget Support Structure and Cooling of Silicon Pixel Detectors, Based on Microchannel Technology*, Nucl. Instrum. Methods Phys. Res., Sect. A (2010) doi:10.1016/j.nima.2009.10.138

[75] J. A. Ballin *et al.*, *Monolithic Active Pixel Sensors (MAPS) in a quadruple well technology for nearly 100% fill factor and full CMOS pixels*, Sensors **8**, 5336 (2008).

[76] N. K. Watson *et al.*, *A MAPS-based readout of an electromagnetic calorimeter for the ILC*, J. Phys. Conf. Ser. **110**, 092035 (2008).

[77] J. P. Crooks *et al.*, *A monolithic active pixel sensor for a tera-pixel ECAL at the ILC*, CERN-2008-008.

7 Drift Chamber

7.1 Overview - Finocchiaro, Roney 10 pages

7.1.1 Physics Requirements - 3 pages

7.1.2 Geometrical Constraints

The Drift Chamber inner radius is constrained by the final focus cooling system and by the Tungsten shield surrounding it to $R_{inner}^{DCH} = 265\,mm$, the outer radius is constrained to $R_{outer}^{DCH} = 809\,mm$ by the DIRC quartz bars. The total length available for the Drift Chamber is of $L^{DCH} = 2700\,\mathrm{mm}$. As the rest of the detector, the drift chamber is shifted by the nominal *BABAR* offset (367 mm) with respect to the interaction point.

Simulation studies performed on several signal samples with both high ($e.g.\, B \to \pi^+\pi^-$), and medium-low ($e.g.\, B \to D^*K$) momentum tracks indicate that:

a) as expected, momentum resolution improves as the minimum drift chamber radius R_{min} decreases, see Fig. 7.1; R_{min} is actually limited by mechanical integration constraints with the cryostats and the radiation shields.

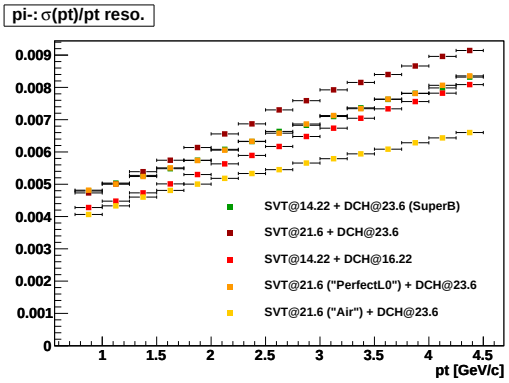

Figure 7.1: Track momentum resolution for different values of the drift chamber inner radius.

b) The momentum and especially the $\mathrm{d}E/\mathrm{d}x$ resolution for tracks going in the forward or backward directions are clearly affected by the change in number of measuring samples when the chamber length is varied by $10 - 30\,\mathrm{cm}$. However the fraction of such tracks is so small that the overall effect is also not large (*to be better quantified with updated FastSim studies*).

7.1.3 Machine Background Considerations - Cenci 3 pages

7.1.4 DCH Design Overview - 2 pages

7.1.5 Expected Performance - 2 pages

7.2 Design Optimization - Finocchiaro, Hearty, Piccolo, Roney 9 pages

The *BABAR* drift chamber operational record has been quite good, both for what performances and reliability is concerned; however there are possible paths of improvements that we have explored to try and design a drift chamber with performances yet better that the *BABAR* one.

7.2.1 Cluster Counting

A possibility being considered to improve the performances of the gas tracker is the use of the *cluster counting* method. Signals in drift chambers are usually split to an analog chain which integrates the charge, and to a digital chain recording the arrival time of the first electron, discriminated with a given threshold. The *cluster counting* technique consists instead in digitizing the full waveform to count and measure the time of all individual peaks. On the assumption that these peaks can be associated to the primary ionization acts along the track, the energy loss and to some extent the spatial coordinate measurements can be substantially improved. In counting the individual cluster, one indeed removes the sensitivity of the specific energy loss measurement to fluctuations in the amplification gain and in the number of electrons produced in each cluster, fluctuations which significantly limit the intrinsic resolution of conventional $\mathrm{d}E/\mathrm{d}x$ measurements.

The ability to count the individual ionization clusters and measure their drift times strongly depends on the average time separation between them, which is, in general, relatively large in He-based gas mixtures thanks to their low primary yield and slow drift velocity. Other requirements for efficient cluster conting include good signal-to noise ratio but no or limited gas-gain saturation, high preamplifier bandwidth, and digitization of the signal with a sampling speed of the order of 1Gs/sec. Finally, it is necessary to extract online the relevant signal features (*i.e.*the cluster times), because the DAQ system of the experiment would hardly be able to manage the enormous amount of data from the digitized waveforms of the about 10 000 drift chamber channels.

7.2.2 Cell Design and Layer Arrangement

The drift chamber cell design must optimise the homogeneity of the electric field inside the cell; this is particularly relevant with the non-saturated mixture we intend to use. Another critical parameter is the overall wire material, and an optimal use of the drift chamber volume for accommodating as many sense wires as possible.

The design for the Super*B* drift chamber employs small rectangular cells arranged in concentric layers about the axis of the chamber. The z coordinate of the track hits is measured by orienting a subset of the wire layers at a small positive or negative stereo angle, ε, relative to the chamber axis. Such a measurement is performed with precision $\sigma_z \simeq \sigma_{R\phi}/\tan\varepsilon$. As in *BABAR*, four consecutive cell layers are grouped radially into a superlayer (SL). This will allow to keep the same *BABAR* algorithms for track-segment finding, both in the track reconstruction and in the formation of the drift chamber trigger.

The rectangular cell layout ensures the most efficient filling of the drift chamber volume, because the transition between superlayers of opposite stereo angles does not require to leave free radial space, nor layers of field-shaping guard wires. Indeed, the latter are only used at a radius inside the innermost SL and at a radius outside the outermost SL. Such guard wires also serve the purpose to electrostatically contain very low momentum electrons produced from background particles showering in the DCH inner cylinder and in the SVT, or background-related backsplash from detector material just beyond the outer SL.

Simulations[1] have shown that a field:sense wire ratio of 3:1 ensures good homogeneity of the electric field inside the cells. In this config-

Table 7.1: A possible drift chamber SL structure, specifying the number of cells per layer, the radius at the center of the chamber of the innermost sense wire layer in the SL, the cell widths, and wire stereo angles, which vary over the four layers in a SL as indicated.

SL	N_{cells}	R [mm]	width [mm]	Angle [mrad]
1	176	286.0	10.2 – 11.3	0
2	192	326.0	10.7 – 11.7	0
3	144	369.0	16.1 – 17.8	+(63 – 66)
4	160	421.0	16.5 – 18.1	−(67 – 69)
5	176	473.0	16.9 – 18.3	+(70 – 72)
6	192	525.0	17.2 – 18.5	−(73 – 75)
7	208	577.0	17.4 – 18.6	+(76 – 77)
8	224	629.0	17.6 – 18.7	−(78 – 79)
9	240	689.0	18.0 – 19.1	0
10	256	741.0	18.2 – 19.1	0

uration each sense wire is surrounded by 8 field wires.

The radial positions of the stereo wires in the j-th layer vary with the z coordinate, being larger at the endplates than at the center of the chamber by the "stereo drop" $\delta_j \equiv R_j^{\rm EP} - R_j$. The cell shapes are most uniform when $\delta_j = \delta$ is a constant for all layers: this is obtained by changing the stereo angle with the radius, by the relation $\tan\varepsilon_j = 2\delta/L_j\sqrt{2R_j^{\rm EP}/\delta - 1}$ (L_j is the chamber length at layer j).

Additional constraints used to determine the cell layout include:

a) the number of cells of width w_j on the j-th sense wire layer, $N_j = 2\pi R_j/w_j$, must be an integer number;

b) to keep a fixed periodicity in signal and high voltage distribution, it is convenient that the number of cells per layer is incremented of a fixed quantity ΔN when passing from a SL to the next one.

c) since the density of both physical tracks and background hits is higher at smaller radii, we choose to have smaller cells in the innermost layers of the drift chamber.

A possible choice for the drift chamber layout, obtained for $k = 4$, $\delta = 8\,$mm $\Delta N = 16$ is shown in Table 7.1. In this arrangement the two innermost SL's contain 1472 cells with height $h = 10\,$mm and widths $w = (10.2 \div 11.7)\,$mm. The cells in the remaining superlayers have $h = 13\,$mm and $w = (16.1 \div 19.1)\,$mm. There are a total of 7872 cells in the drift chamber. The first two superlayers have an axial orientation; this minimizes the occupancy from background hits due to low-momentum spiraling electrons which traverse the drift chamber along its axis (see Sec.7.1.3). The two external super layers are also axial. The fact that the innermost and outermost super layers do not exhibit the stereo drop deformation δ matches the axial simmetry of the inner and outer drift chamber cylinders. The six internal SL's have a stereo arrangement, with angles as shown in the Table.

The corresponding wire map in the region with angle $|\varphi| < 10^\circ$ is shown in Fig. 7.2 at the center of the chamber (a) and at the endplates (b).

It is seen that the axial-stereo transition between SL 2 and SL 3 creates some additional radial space close to the endplates, which disappears at the DCH center. The opposite happens at the stereo-axial transition between SL 8 and SL 9. It is clear that the electric field should be as uniform as possible across layers to ease the drift chamber calibration; however, simulation studies have shown that the field distortion at the two transition radii is moderate and does not require to be compensated by layers of guard wires, which would add material and reduce the sensitive volume.

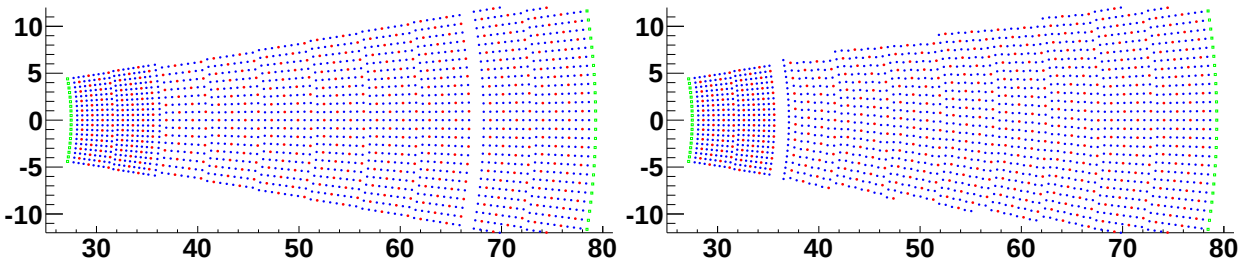

(a) Cell layout at the drift chamber center.

(b) Cell layout at the drift chamber endplates.

Figure 7.2: A possible cell layout of the Super$B$ drift chamber with $h_{\rm in} = 10\,{\rm mm}$, $h_{\rm out} = 13\,{\rm mm}$. Open green squares: guard wires; open blue circles: field wires; full red circles: sense wires. Note how the boundary regions after the first 8 layers of axially strung wires in the inner part of the chamber and after the following 24 layers of stereo layers map differently at the drift chamber center and at the endplates.

Table 7.2: A possible drift chamber layer structure, specifying the number of cells per layer, the wire layer radius at the center of the chamber, the cell width and the wire stereo angle.

layer	$N_{\rm cells}$	R [mm]	width [mm]	Angle [mrad]
1	176	286.0	10.2	0.0
2	176	296.0	10.6	0.0
3	176	306.0	10.9	0.0
4	176	316.0	11.3	0.0
5	192	326.0	10.7	0.0
6	192	336.0	11.0	0.0
7	192	346.0	11.3	0.0
8	192	356.0	11.7	0.0
9	144	369.0	16.1	62.9
10	144	382.0	16.7	63.9
11	144	395.0	17.2	64.8
12	144	408.0	17.8	65.7
13	160	421.0	16.5	−66.6
14	160	434.0	17.0	−67.5
15	160	447.0	17.6	−68.3
16	160	460.0	18.1	−69.1
17	176	473.0	16.9	69.9
18	176	486.0	17.4	70.7
19	176	499.0	17.8	71.4
20	176	512.0	18.3	72.2
21	192	525.0	17.2	−72.9
22	192	538.0	17.6	−73.5
23	192	551.0	18.0	−74.2
24	192	564.0	18.5	−74.9
25	208	577.0	17.4	75.5
26	208	590.0	17.8	76.1
27	208	603.0	18.2	76.7
28	208	616.0	18.6	77.3
29	224	629.0	17.6	−77.8

7.2.3 Gas Mixture

The gas mixture for the Super$B$ drift chamber is chosen to allow optimal resolution in the measurement of both momentum and energy loss. It must also be operationally stable (*e.g.*, have a wide high voltage plateau), and be little sensitive to photons with $E \leq 10\,{\rm keV}$ to help controlling the rate of background hits (see Sec. 7.1.3). Finally, aging in the chamber should be slow enough to match the projected lifetime of a typical High Energy Physics experiment

(about 15 years). These requirements already concurred to the definition of the *BABAR* drift chamber gas mixture, (80%He-20%iC_4H_{10}). Indeed, a high Helium content reduces the gas density and thus the multiple scattering contribution to the momentum resolution. Good spatial resolution calls for high single electron efficiency and for small diffusion coefficient. The effective drift velocity in Helium-based gas mixtures is typically non saturated, therefore it depends on the local electric field, and on the Lorentz angle. This dependences can be taken into account by a proper calibration of the space-time relations and in principle do not pose limits to attaining the required spatial resolution. In practice, a careful choice of the cell shape (see the dicussion in Sec. 7.2.2), and a small value of the Lorentz angle are an advantage.

To match the more stringent requirements on occupancy rates of Super$B$, it could be useful to select a gas mixture with a larger drift velocity in order to reduce ion collection times and so the probability of hits overlapping from unrelated events. The *cluster counting* option would instead call for a gas with low drift velocity and primary ionization. As detailed in Section7.2.4, R&D work is ongoing to optimize the gas mixture.

7.2.4 R&D and Prototype Studies

In order to optimize the gas mixture for the Super$B$ environment, and to asses both the feasibility and the operational improvements for the *cluster counting* technique a complete R&D program has been proposed. The program includes both beam tests and cosmic ray stands to monitor performancs of *ad hoc* built prototypes. While the dE/dx resolution gain of the cluster counting method is in principle quite sizeable compared to the traditional total charge collection, the actual capability of the measured number of cluster might not retain the same analyzing power, due to a pletora of experimental effects that should be studied in detail so that the energy loss measurement derating should be assessed and, if possible, cured.

A few prototypes were built and operated to answer the above mentioned questions.

7.2.4.1 Prototype 1

The first one is a small aluminum chamber, 40 cm long, with a geometry resembling the the original *BABAR* drift chamber. It consists of 24 hexagonal cells organized in six layers with four cells each. A frame of guard wires with appropriate high voltage settings surrounds around the cell array to ensure uniformity of the electric field among the cells. The device was operated in a cosmic ray test stand in conjunction with an external telescope, used to extapolate the track trajectories with a precision of 80 μm or better . Different gas mixtures have been tried in the prototype: starting with the original *BABAR* mixture (80%He-20%iC_4H_{10}) used as a calibration point, both different quencher proportions and different quenchers have been tested in order to assess the viability of lighter and possibly faster operating gases.

As an example, the correlation between the extrapolated drift distance and the measured drift time is shown in Fig. 7.3 for a 75%He-25%C_2H_6 gas mixture. The result of a fit to a 5^{th}-order Chebychev polynomial is superimposed to the experimental points. Track-fit residuals and spatial resolution as a function of the drift distance for the same gas mixture are show in Fig. 7.4.

7.2.4.2 Prototype 2

A full-length drift chamber prototype was designed, built and commissioned to study *cluster counting* in a realistic environment, including signal distortion and attenuation along 2.5 meter long wires. The prototype, which is also meant to serve as a test bench for the final Front-End electronics and for the drift chamber trigger, is composed by 28 square cells with 1.4 cm side, arranged in eight layers and – as in the final Super$B$ drift chamber – with a field-to-sense wire ratio of 3:1. The eight layers have either 3 or 4 cells each, and are staggered by half a cell side to help reduce the left-right ambiguity. Tracks with angle $|\vartheta| \leq \pm 20^\circ$ cross all the eight layers of the chamber. A set of guard

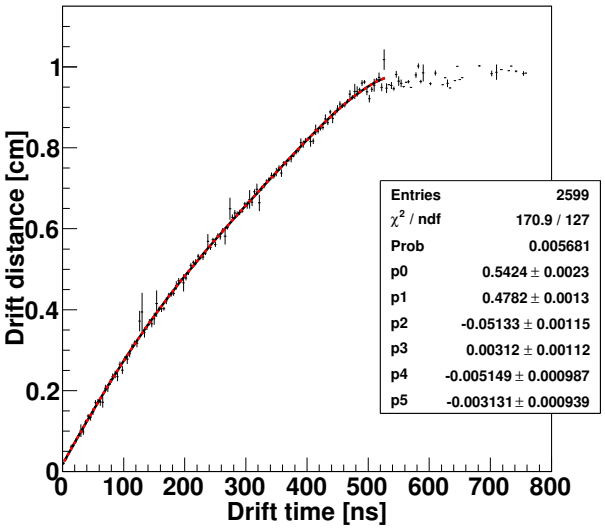

Figure 7.3: Track distance vs. drift time in a cell of the prototype. The line is the result of a fit with a 5^{th}-order Chebychev polynomial.

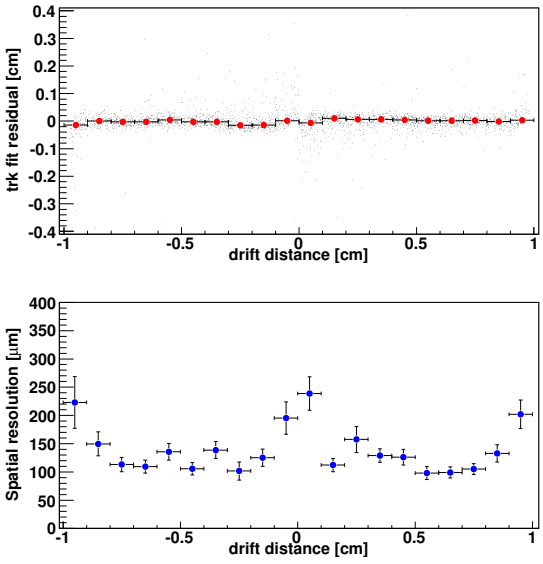

Figure 7.4: Track fit residuals (top) and spatial resolution (bottom) as a function of the drift distance.

wires surrounds the matrix of 28 cells to obtain a well-behaved field distribution at the boundary of the active detector volume. Most of the cells

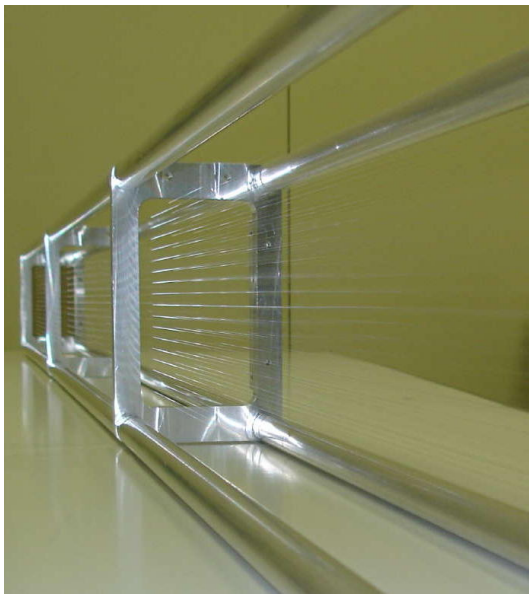

Figure 7.5: Prototype 2: detail of the strung wires.

feature a 25 μm Gold-plated Molybdenum sense wire, while for reference seven cells in two adjacent layers are strung with a 25 μm Gold-plated Tungsten wire, traditionally used in drift chambers. The reason for using the Molybdenum wire is its lower resistivity, therefore smaller dispersion for pulses travelling along the wires. A picture of the chamber after stringing completion is shown in Fig. 7.5. The entire wire structure is enclosed in an Aluminum container 3 mm thick; three pairs of thin windows have been carved in the middle and at the extremities in order to have smaller amount of material in the path of low energy particles measured by the device. Four preamplifier boards are used to extract the cell signals. Each board serves seven channels, each with a transimpedence preamplifier (rise time of about 2.4ns), at a nominal gain of 8mV/fC and a noise of 2200 e rms. Each boards also has a test input, both unipolar and differential outputs (50 Ω– 110 Ω); the latter are used for a test implementation of the Drift Chamber first level trigger. A detail of the Faraday cage housing the FEE boards and of the signal and trigger cables is shown in Fig. 7.6.

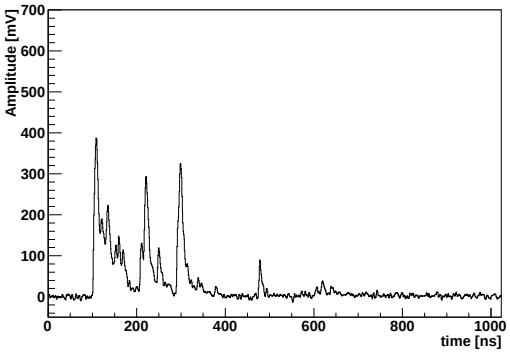

(a) Sample waveform n.1

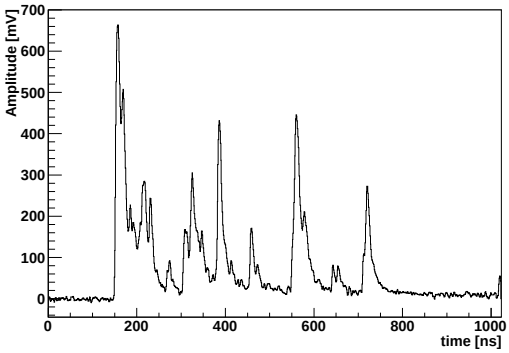

(b) Sample waveform n.2

Figure 7.7: Sample waveforms from two cells of the full-length drift chamber prototype.

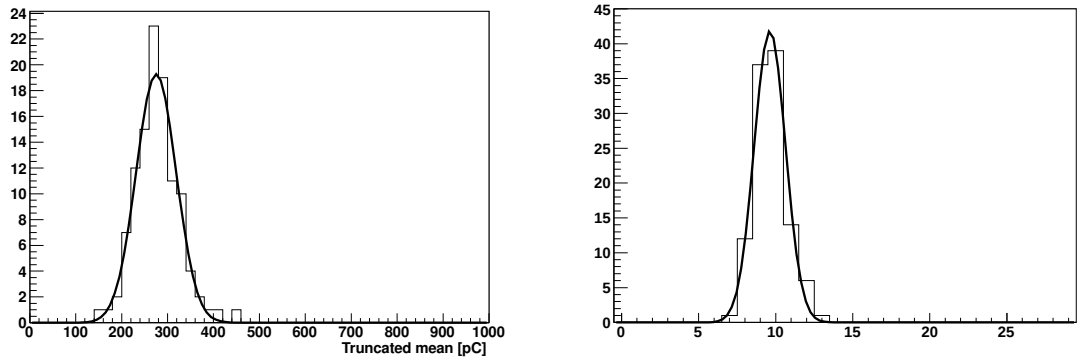

(a) Average dE/dx distribution

(b) Average n. of clusters

Figure 7.8: Average dE/dx and number of clusters from 10 samples of a single cell belonging to a track reconstructed in the prototype.

The data collected with this prototype are fed into a switch capacitor array digitizer[1], which samples the wire signals at 1 GS/sec with and input BW$\geq$ 500 MHz. The challenge of detecting the ionization clusters in signals with a wide dynamic range and non-zero noise levels is apparent from the two sample waveforms shown in Figg. 7.7, recorded in the cosmic-ray setup. Hits associated to cosmic ray tracks reconstructed in the drift chamber prototype are used to compare the performances in the energy loss measurement of the traditional truncated mean algorithm and of the *cluster counting* method. Preliminary results when 10 samples from a single prototype cell are used to form a 70% truncated mean or to count the average number of clusters are shown in Fig. 7.8. In the experimental conditions of our test, *cluster counting* yields a 40-50% better relative resolution than the truncated mean method. Additional R&D efforts are ongoing to extend this encouraging result to different momentum regions, and study how the $K-\pi$ resolving power in the range of interest of Super$B$ ($|p| \leq 5\,\mathrm{GeV}/c$) improves with the *cluster counting* technique.

[1] CAEN V1742: http://www.caen.it/csite/CaenProfList.jsp?parent=13&Type=WOCateg

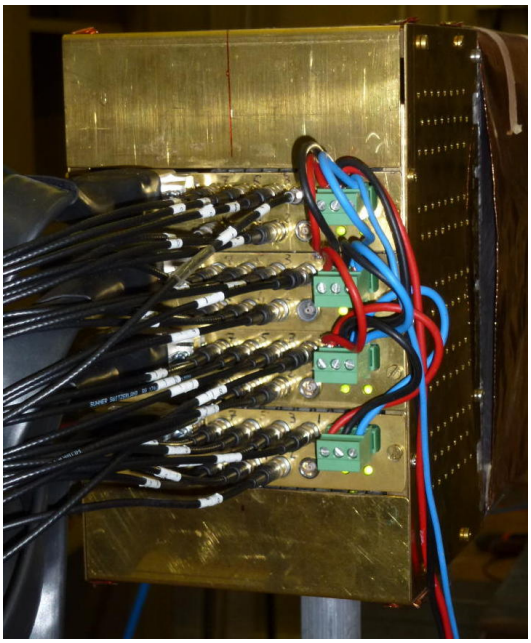

Figure 7.6: Prototype 2: FEE Faraday cage with signal and trigger cables.

7.2.4.3 Single Cell Prototype(s)

A single cell prototype, SW1, 2.7 m long has also been built. Both Proto 2 and SW1 are at the moment operational and collecting data on cosimc ray stands; both devices have been exposed to test beams, a 500 MeV/c electron beam Proto 2, a variety of pion and/or Kaon beams at various momenta SW1.

7.2.4.4 Aging studies: fields, gas gain

7.2.5 R&D Future Developments

- test beam with different particle species
- on-board feature extraction
- AOB

7.3 Mechanical Design

The drift chamber mechanical structure must sustain the wire load with small deformations, while at the same time minimizing material for the surrounding detectors. The structure is also required to ensure tightness for the gas filling the drift volume. We opted for a structure entirely in Carbon Fiber (CF) composite, with an approximately cylindrical geometry. A side view of the chamber is shown in Fig. 7.9.

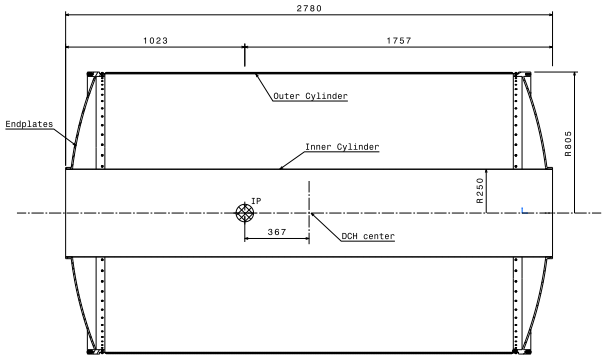

Figure 7.9: Longitudinal section of the DCH with principal dimensions.

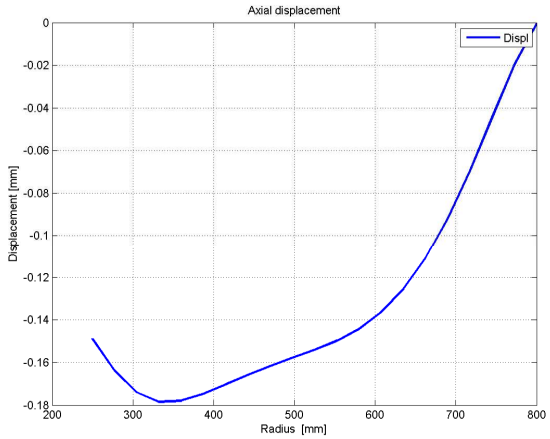

Figure 7.10: Displacement of each endplate due to the wire load.

7.3.1 Endplates

The wires defining the cell layout are strung between the two endplates, which are required to:

a) sustain the total wire load of XXXX tons (or N) (see sec. **??**) with minimal deformations;

b) be as transparent as possible to avoid degrading the performances of the forward calorimeter.

c) have XXXXX precisely machined holes to allow positioning the crimp feed-throughs with tolerances better than XXXX μm;

The endplates are two identical pieces of 8 mm thick CF composite with inner radius of 250 mm and outer radius of 805 mm. Deformations under load can be minimized using for the endplates a shaped profile. An optimization taking into account different constraints resulted in spherical convex ednplate, with a radius of curvature of 2100 mm. Two CF stiffening rings on the inner and outer rims help preventing radial (axial) deformations. An intermediate modulus carbon fiber (as T300 (XXXX), with a Young modulus of XXXXX) will be used. It is expected that the average material characteristics will be degraded by about 30 % or less after drilling the XXXX holes on the endplates. Detailed studies on this aspect will be performed on custom samples. The maximum displacements on the endplates is calculated to be less than 300 μm (Figure **??**).

7.3.2 Inner cylinder

The drift chamber inner cylinder should be as transparent as possible to minimize the multiple scattering degradation to the p_T measurement. For this reason it was designed as a non load-bearing structure: it must only guarantee gas tightness, and sustain possible differential pressures of the order o 10 mbar between the inside and outside of the chamber. It is a thin (200 μm) CF cylinder of 250 mm radius, with a 25 μm aluminum foil glued on it as RF shield. During the stringing phase the inner cylinder will be free to move longitudinally being fixed only to one endplate. Only after stringing, when all endplate deformations are settled, it will be glued to the other endplate.

7.3.3 Outer Cylinder

In addition to guaranteeing gas tightness and withstanding a differential pressure as the inner cylinder, the outer cylinder will also carry the wire load. It will be installed after completion of the wire stringing. To ease the construction and the mounting procedures, the cylinder is longitudinally divided in two half shells. Each shell consists of two 1 mm-thick CF skins laminated on a 6 mm-thick honeycomb core. Two thin alluminium foils, 100 μm on inside surface and 25 μm on outside surface, are glued to the shells to ensure the rf shield. The sandwich structure guarantees a high bendig stiffness and a high safety factor for global buckling.

7.4 Electronics - Felici, Martin 1 page

7.4.1 Design Goals

The Super$B$ Drift Chamber (DCH) front-end electronics is designed to extract and process the about 8000 sense wire signals to:

- measure the electrons drift times for tracking purpose (momentum of charged particles)
- measure the energy loss of particles per unit of length, dE/dx (particle identification)
- provide hits information to the trigger system (trigger primitives)

Concerning the energy loss measurement two options will be considered. The first one foresees the measurement of the sense wires integrated charge, discarding the highest values to remove the Landau tails (Standard Readout), while the second one is based on primary electron clusters counting (Sampled Waveforms). Because the front-end requirements for the two options are quite different each option will be discussed in a dedicated section.

7.4.2 Standard Readout - charge measurements specifications

The method is based on integrated charge measurements thus allowing the use of (relatively) low bandwidth preamplifiers. This makes the front-end chain less sensitive to noise pickup and instabilities, a suitable condition in a system with a large number of channels.
The three main specification for charge measurement are: resolution, dynamic range and linearity.

7.4.2.1 Resolution

Charge measurements for particle identification aim to measure, with a precision of the order of 7.5%, the particle most probable energy loss, despite the large fluctuations involved in single measurement.
The goal can be achieved by sampling many times the collected charge and applying the "truncated mean" method to resolve the distribution peak value to several percent.
Because the Super$B$ DCH design parameters and foreseen working conditions aim to an overall single cell resolution (σ_E) of about 35% and σ_E is mainly driven by the detector contribution, we can set a limit of 15% for the front-end electronics contribution (i.e. $\sigma_{EL} \sim 5\%$) then making it negligible ($\sqrt{\sigma_E^2 + \sigma_{EL}^2} \sim \sigma_E$).
Finally, if we assume that the charge collection due to a m.i.p. crossing orthogonally the cell is about 50 fC ($\sim 2fC/e$ @ 10^5 nominal gas gain) we can infer a limit of the Equivalent Noise Charge (ENC) for the single front-end channel of about $50\ fC \cdot 0.05 \simeq 2.5\ fC$.

7.4.2.2 Dynamic range

With 8 bits ADCs the dynamic is $2.5 - 500\ fC$, actually even more then system requirements.

7.4.2.3 Linearity

As stated above, the single cell energy resolution is about 35%, therfore a linearity of the order of 2% largely satisfies the system requirements.

7.4.3 Standard Readout - time measurements specifications

As for charge measurements we have three main specifications: resolution, dynamic range and linearity.

7.4.3.1 Resolution

One of the Super$B$ DCH requirements is the charged particle tracks reconstruction. The measure is carried out by acquiring the first ionized electron arrival time to the sense wire with a negligible error with respect to the quoted value of σ_S ($\sim 110\mu m$).
Limits to spatial resolution are due to primary ionization statistics, electrons diffusion and time measurement accuracy.
Assuming an intrinsic chamber resolution (σ_{SC}) of about 100 μm **(ref DCH)** the upper limit for electronic contribution can be quoted to be $\sigma_{EL} \leq \sqrt{\sigma_S^2 - \sigma_{SC}^2} \simeq 50\ \mu m$. As helium based gas mixtures are characterized by a non saturated drift velocity up to high fields, [**?**] electrons drift velocity rapidly increase approaching sense wire, thus a 2.5 $cm/\mu s$ (25 $\mu m/ns$) [**?**] has been used to evaluate the maximum acceptable error in time measurement, that is $\sigma_t \leq 50[\mu m]/25[\mu m/ns] \simeq 2$ ns.
Discarding the bunch length contribution (tenths of ps) there are two main error sources in time measurements: the discriminator jitter (different signals cross a fixed threshold at different times) and the TDC resolution (digitization noise). Signal jitter, in turn, has two main contribution: signal noise and time-walk.
Signal noise contribution is generally small and can be evaluated according to $\Delta t = \sigma_{noise}/(dV/dt) \simeq \sigma_{noise} \cdot \tau/V_{max}$ where τ is the preamplifier-shaper peaking time.
Assuming that a single electron cluster generates a signal of $\sim 20\ mV$, and that noise and peaking time associated to the signal are, respectively, $\sigma_{noise} \sim 3\ mV(rms)$ and $\tau \sim 5\ ns$ we get a noise contribution to time resolution of about *0.8 ns*.
The time-walk effect is caused by signal amplitude variation. With a peaking time around 5 ns, a time-walk contribution for a low-threshold leading-edge discriminator of about $1.5ns$ can be estimated.
Finally, the digitization noise is a function of the digitization unit according to $\sigma = \Delta/\sqrt{(12)}$ where Δ is the quantization unit, using $\Delta \simeq 1.5\ ns$ a digitizing noise of about 0.45 ns is obtained.
Summarizing, without corrections, the time resolution is dominated by the signal time walk and can be estimated to be about 1.8 ns (including all contributions). Nevertheless corrections can be applied using digitized signals to minimize time-slewing effects then reducing the time walk contribution (see Front End Boards - Digitization Section).

7.4.3.2 Dynamic Range

The TDC range depends on the drift velocity and on the cell size. A maximum drift time of about 600 ns has been estimated for Super$B$ DCH cells. Providing some safety factor, a TDC range of about 1 μs is enough to include any jitter in trigger generation and distribution.

7.4.3.3 Linearity

A linearity of the order of 1% fully satisfies time measurement requirements.

7.4.4 Standard Readout - DCH Front-end system (block diagram)

The DCH FE chain (see Subdetector Electronics and Infrastructure chapter) is split in two blocks: ON DETECTOR and OFF DETECTOR electronics.
In the following paragraphs we will give a description of the ON DETECTOR electronics and we will refer to the preamplifier boards as Very Front End Boards (VFEB) to distinguish them from Front End Boards (FEB) containing the digitization and buffer sections located far from the detector (OFF DETECTOR electronics).

7.4.5 Standard Readout - ON-DETECTOR electronics

7.4.5.1 Very Front End Boards

Very Front End Boards will contain HV blocking capacitors, protection networks, preamplifiers and (eventually) shapers-amplifiers. Because of the small cell dimensions more cells can be grouped in a single, multi-channel preamplifier-shaper board. Signals and power supply cables will be connected to the boards by means of suitable connectors.

Besides the requirements on SNR, preamplifier should be characterized by enough bandwidth to preserve signal time information and low power requirement, not more than 20-30 mW per channel, to limit the total power dissipation on the backward end-plate to $160 \div 240\ W$ then allowing the use of simpler and safer forced air based cooling system (no risk of leak).

Concerning the circuit implementation, since the channel density is quite low and simple circuit topology can be used, an approach based on SMT technology can be adopted then avoiding dedicated (and expensive) development (ASIC).

Table 7.3: Preamplifier main specifications

Linearity	$< 2\%(1 - 100fC)$
Output Signal Umbalance	$< 2\%(1 - 100fC)$
Gain (Differential)	~ 5.2 mV/fC
Z_{IN}	110 Ω
Z_{OUT}	50 Ω
Rise time	~ 2 ns ($C_D = 24pF$)
Fall time	~ 13 ns ($C_D = 24pF$)
Noise	1350 erms ($C_D = 24pF$)
V_{SUPPLY}	4V
P_D	$\sim$ 30mW

As an example, a simulation of a three stages transimpedance preamplifier based on SiGe transistors has been carried out. The first stage dominant pole is around 26 MHz while other stages have been designed with wider bandwidth then obtaining a good separation in terms of cutoff frequencies.

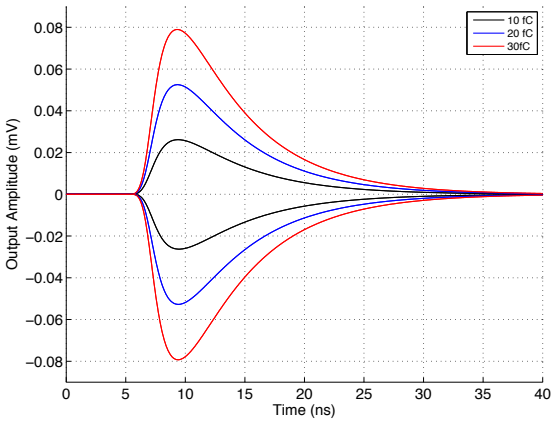

Figure 7.11: Preamplifier output for 10, 20 and 30 fC test pulse ($C_{DET} = 24pF$)

Simulation results are shown in table 7.3 while Fig. 7.11 shows the (simulated) output waveforms for 3 different input charges (10, 20 and 30 fC) injected through the test input.

7.4.6 Sampled Waveforms - specifications

Cluster Counting technique is very powerful as it improves particles identification. The method is based on primary ionization measurement and, to fully exploit the technique, individual clusters must be identified.

On the other hand the front-end requirement are quite onerous as, despite the use of slow drift velocity gas mixtures ($\sim$1 $\mu s/cm$), high sampling frequency digitizers (at least 1 GSPS) and fast processing (data throughput must sustain the Super$B$ expected 150 kHz average trigger rate) are required. These requirements, at the state of art of technology, result in a huge power requirement and, as a consequence in a low FEB modularity.

Also on the VFEB side fast amplifiers must be used, then power requirements will be higher than in the "Standard Readout" scenario thus envisaging the use of a local liquid cooling system. Moreover the wide bandwidth requirement has also an impact on the type of cable used to interconnect on-detector and off-detector electronics and on the full system noise pick-up sensitivity.

Finally, to apply the cluster counting technique correctly, signal reflection on the sense wires must be avoided by means of termination resistors then setting a lower limit on the system intrinsic noise.

Concerning the tracking requirements, if we assume that full efficiency in single electron cluster detection is achieved, Cluster Counting dE/dx measurement already includes information for tracking purpose (it is just required to store clusters arrival time instead of simply counting them).

Specifications for the Sampled Waveforms measurement are the same we defined for the Stan-

dard Readout that is: resolution, dynamic range and linearity.

7.4.6.1 Resolution

Digitizers resolution is a function of both the lowest signal amplitude to be sampled and the system baseline noise. Assuming an average delivered signal of $\sim 6fC/e$ @ $3 \cdot 10^5$ gas gain, a preamplifier-shaper gain of $10mV/fC$ and a safety factor of 2 for gas gain fluctuations the average cluster signal for single electron is about 30 mV.
Preamplifier ENC estimation can be carried out evaluating the contribution of the dominant noise source, that is the termination resistor. Assuming a CR-RC shaping circuit and a 3 ns peaking time we get an ENC of about 0.2 fC, that is about 2 mV rms for a preamplifier gain of 10 mV/fC.
Thus a LSB of about 2 mV allows a good control of system noise and cluster signals reconstruction.

7.4.6.2 Dynamic range

Cluster Counting method requires to find the peaks (corresponding to the clusters) contained in the digitized signals. The expected dynamic range (discarding gas fluctuation) is driven by the cluster size (i.e. the number of primary ionization electrons contained in a single cluster). Signal dynamic range can be, then, defined (as an upper limit) by the expected total ionization. Because helium based gas mixture have already been well characterized [**?**], assuming a 1.2 *cm* square cell and a 90/10 He/Iso gas mixture a m.i.p. crossing orthogonally the cell generates about 26 electrons, thus an 8 bits ADC dynamic range is fully adequate for Cluster Counting measurement.

7.4.6.3 Linearity

As we are interested on finding (and tagging) signal peaks, a resolution of 2% fully satisfies the requirements.

7.4.7 Sampled Waveforms - DCH front-end system (block diagram)

The Sampled Waveforms DCH front-end chain structure is similar to the Standard Readout one. Also in this scenario we will have ON-DETECTOR and OFF-DETECTOR electronics connected by means of mini coaxial cables, but, because of the lower board modularity both the number of crates and boards will increases significantly (see Subdetector Electronics and Infrastructure chapter).

7.4.8 Sampled Waveforms - ON DETECTOR electronics

7.4.8.1 Very Front End Boards

Because Very Front End Boards will host high bandwidth ($\sim$ 350 MHz) preamplifiers both layout and assembly are more difficult with respect to the Standard Readout scenario. Particularly, special attention must be addressed to avoid ground loops in such a way to minimize both instabilities and external noise pickup.

.
.
Something about preamplifier .....
.
.

7.5 High Voltage system - Martin 1 page

7.5.1 HV distribution boards - Standard ReadOut

The high voltage distribution network (Fig. 7.12) will be located on the forward end-plate. The distribution board modularity will match the preamplifier modularity while the number of distribution boards connected to a single HV channel will depend on the layer (example: inner layers = 2 boards, outer layers = 5 boards).

7.5.2 HV distribution boards - Sampled Waveforms

Most of the remarks shown before also apply for Sampled Waveforms scenario. Anyway, because sense wires require termination resistors the boards layout will be slightly different and,

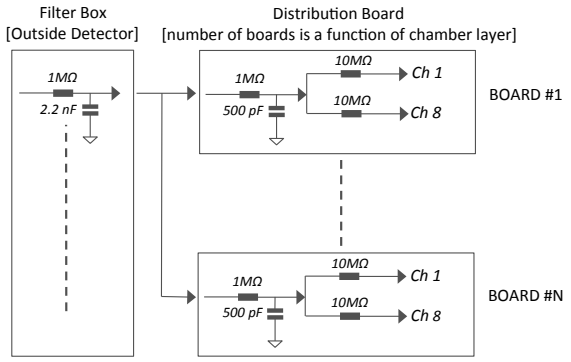

Figure 7.12: Standard Readout High Voltage distribution network

moreover, high frequency layout is required for ground connections. HV distribution network is shown in fig. 7.13.

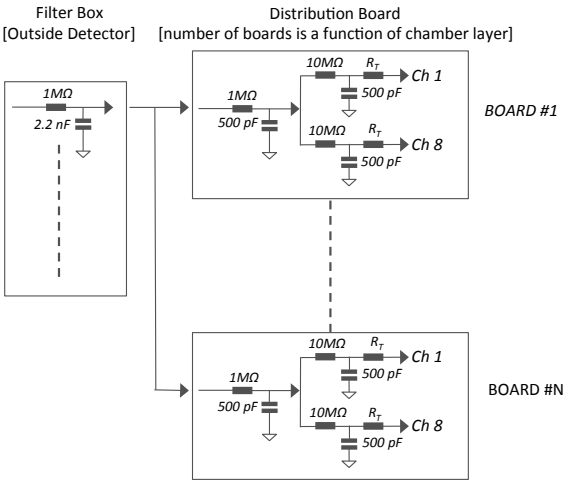

Figure 7.13: Sampled Waveforms High Voltage distribution network

7.6 Gas system - Roney 2 pages

7.7 Calibration and monitoring - Roney 3 pages

7.7.0.1 Slow control systems

7.7.0.2 Calibration

7.7.0.3 Gas monitoring system

7.7.0.4 On-line monitor

7.8 Integration - Hearty, Lauciani 6 pages

7.8.1 Overall geometry and mechanical support

7.8.2 Cable supports and routing

7.8.3 Access

7.8.4 Gas system

7.8.5 Off-detector electronics crates

7.8.6 High voltage crates

7.8.7 Installation and alignment

Bibliography

[1] R. Veenhof, *Garfield - simulation of gaseous detectors* CERN-W5050, Version 9.

[2] CLEO reference.

[3] M. Adinolfi *et al.* (KLOE Collaboration), *The tracking detector of the KLOE experiment*, Nucl. Instrum. Methods Phys. Res., Sect. A **488**, 51 (2002).

8 Particle Identification

Chapter editors: Nicolas Arnaud & Jerry Va'vra

The current version of the plan for the PID TDR chapter can be found at http://mailman.fe.infn.it/superbwiki/images/8/8c/PID_TDR_plan.pdf

The latest version of the PID TDR chapter (updated daily) is available at http://www.slac.stanford.edu/~narnaud/SuperB/DTDR/dtdr-PID.pdf

8.1 Summary of Physics Requirements and Detector Performance goals

8.1.1 Physics requirements

The Standard Model successfully explains the wide variety of experimental data that has been gathered over several decades with energies ranging from under a GeV up to several hundred GeV. At the start of the millennium, the flavor sector was perhaps less explored than the gauge sector, but the PEP-II and KEK-B asymmetric B Factories, and their associated experiments *BABAR* and Belle, have produced a wealth of important flavor physics highlights during the past decade [1]. The most notable experimental objective, the establishment of the Cabibbo-Kobayashi-Maskawa phase as consistent with experimentally observed CP-violating asymmetries in B meson decay, was cited in the award of the 2008 Nobel Prize to Kobayashi & Maskawa [2].

The B Factories have provided a set of unique, over-constrained tests of the Unitarity Triangle. These have, in the main, been found to be consistent with Standard Model predictions. The B factories have done far more physics than originally envisioned; *BABAR* alone has published more than 400 papers in refereed journals to date. Measurements of all three angles of the Unitarity Triangle; the establishment of D^0 mixing; the uncovering of intriguing clues for potential New Physics in B decays; and unveiling an entirely unexpected new spectroscopy, are some examples of important experimental results beyond those initially contemplated.

8.1.2 Detector concept

The DIRC (Detector of Internally Reflected Cherenkov light [3] is an example of innovative detector technology that has been crucial to the performance of the *BABAR* science program. The DIRC main performance parameters are the following: (a) a measured time resolution ∼1.7 ns per photon, the photomultiplier (PMT) transit time spread (TTS) of 1.5 ns, (b) a single photon Cherenkov angle resolution of 9.6 mrad for tracks from di-muon events, (c) a Cherenkov angle resolution 2.5 mrad per track in di-muon events, and (d) a π/K separation greater than 2.5σ over the entire track momentum range, from the pion Cherenkov threshold up to 4.2 GeV/c. The *BABAR* DIRC performed reliably and efficiently over the whole *BABAR* data taking period (1999-2008). Its physics performance remained consistent throughout the whole period, although some upgrades, such as the addition of shielding and replacement of electronics, were necessary to cope with evolving machine conditions.

An excellent DIRC S/N performance did not come without some effort, and this experience is useful for knowing how we want to design the 'Focusing Detector of Internally Reflected light' (FDIRC) at Super$B$. To obtain the final background performance it was necessary to: (a) apply a tight timing cut of ±8 ns around each

event, (b) add a substantial shielding around the beam pipe under the DIRC, which reduced the PMT background by at lest a factor of 6, (c) install many background detectors (here we found, for example, that the rate in neutron detectors correlates with the DIRC background very well, indicating a common origin), and (d) improve operation of the machine. After ∼10 years of operation, the PMT gain was reduced by ∼30%. The electronics dead time was limited to ∼5% at a rate of ∼250 kHz/PMT.

Excellent flavor tagging will continue to be essential for the program of physics anticipated at Super$B$, and the gold standard of particle identification in this energy region is that provided by internally reflecting ring-imaging devices (the DIRC class of ring imaging detectors). The challenge for Super$B$ is to retain (or even improve) the outstanding performance attained by the *BABAR* DIRC [4], while also gaining an essential factor of 100 in background rejection to deal with the much higher luminosity.

A new Cherenkov ring imaging detector is being planned for the Super$B$ barrel, called the Focusing DIRC, or FDIRC. It will reuse the existing *BABAR* bar boxes and mechanical support structure. This structure will be attached to a new photon "camera", which will be optically coupled to the bar box exit window. The new camera design combines a small modular focusing structure that images the photons onto a focal plane instrumented with very fast, highly pixelated, PMTs [5].

To cope with higher luminosity, the FDIRC photon camera will provide an overall safety factor of 250 compared to the *BABAR* DIRC. Indeed,

- it is 25× smaller in total than the DIRC water-based camera;
- its new highly pixilated photon detectors will be about 10× faster;
- the photon camera is built using radiation-resistant Fused silica material – instead of water or oil which would be more sensitive to neutron background.

Furthermore, (a) the entire system will have ∼18,000 pixels (each photon detector has 32 pixels as two H-8500 pixels are shorted together, there are 48 detectors per each photon camera and altogether 12 bar boxes), (b) will reconstruct photons in 3D (x, y, and time), (c) the Cherenkov angle could be reconstructed based on pixels alone, however, time is included in the final PID likelihood hypothesis, (d) time also plays the important role in FDIRC to reduce the background, and (e) the expected timing resolution of σ∼200 ps will also make it possible to reduce the chromatic broadening of Cherenkov angle resolution by 0.5-1 mrad, depending on the photon propagation path length.

Several options were under consideration for a possible PID detector in the forward direction: (a) "DIRC-like TOF" time-of-flight (FTOF) [6], (b) pixelated TOF [7] and (c) Aerogel RICH [8]. The chosen technology, based on time-of-flight technique, has been selected by the Super$B$ collaboration in May 2011 and room has been reserved in the Super$B$ design to accommodate this new detector on the forward side. Tests of a full-scale prototype of one sector of the FTOF detector are foreseen in near future; if they are successful, the FTOF will be included in the Super$B$ baseline. See section 8.5 for more information on this topic.

8.1.3 Charged Particle Identification

The charged particle identification at Super$B$ relies on the same framework as the *BABAR* experiment. Electrons and muons are identified by the EMC and the IFR respectively, aided by $\mathrm{d}E/\mathrm{d}x$ measurements in the inner trackers (SVT and DCH). Separation for low-momentum hadrons is primarily provided by $\mathrm{d}E/\mathrm{d}x$. At higher momenta (above 0.7 GeV/c for pions and kaons, above 1.3 GeV/c for protons), a dedicated system, the FDIRC – inspired by the successful *BABAR* DIRC – will perform the π/K separation.

8.2 Particle Identification Overview

8.2.1 Experience of BABAR DIRC

The *BABAR* DIRC – see Fig. 8.1 – is a novel ring-imaging Cherenkov detector. The Cherenkov light angular information, produced in ultra-pure synthetic fused silica bars, is preserved while propagating along the bar via internal reflections to the camera (the SOB) where an image is produced and detected.

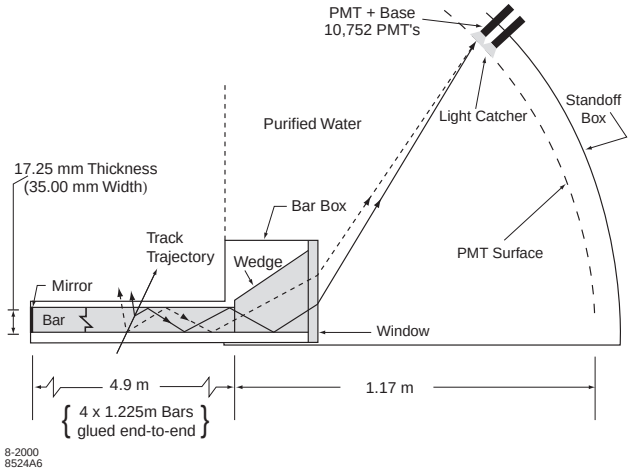

Figure 8.1: Schematic of the *BABAR* DIRC.

The entire DIRC has 144 quartz bars, each 4.9 m long, which are set along the beam line and cover the whole azimuthal range. Thanks to an internal reflection coefficient of ∼0.9997 and orthogonal bar faces, Cherenkov photons are transported to the back end of the bars with the magnitude of their angles conserved and only a modest loss of photons. They exit into a pinhole camera consisting of a large volume of purified water (a medium chosen because it is inexpensive, transparent, and easy to clean, with average index of refraction and relative chromatic dispersion sufficiently close to those of the fused silica). The photon detector PMTs are located at the rear of the SOB, about 1.2 m away from the quartz bar exit window.

The reconstruction of the Cherenkov angle uses information from the tracking system together with the positions of the PMT hits in the DIRC. In addition, information on the time of arrival of hits is used in rejecting background hits, and resolving ambiguities due to the unknown path of a given photon in the quartz.

8.2.2 Barrel PID: Focusing DIRC (FDIRC)

As discussed above, the PID system in Super*B* must cope with much higher luminosity-related background rates than in *BABAR* – current estimates are on the order of 100 times higher. The basic strategy is to make the camera much smaller and faster. A new photon camera imaging concept, based on focusing optics, is therefore envisioned. The focusing blocks (FBLOCK), responsible for imaging the Cherenkov photons onto the PMT cathode surfaces, will be machined from radiation-hard pieces of fused silica. The major design constraints for the new camera are the following: (a) it must be consistent with the existing *BABAR* bar box design, as these elements will be reused in Super*B*; (b) it must coexist with the *BABAR* mechanical support and magnetic field constraints; (c) it requires very fine photon detector pixelation and fast photon detectors.

Imaging is provided by a mirror structure focusing onto an image plane containing highly pixelated PMTs. The reduced volume of the new camera and the use of fused silica for coupling to the bar boxes (in place of water as it was in *BABAR* SOB), is expected to reduce the sensitivity to background by about a factor of ∼ 25 compared to *BABAR* DIRC. The very fast timing of the new PMTs is expected to provide many additional advantages: (a) an improvement of the Cherenkov resolution; (b) a measure of the chromatic dispersion term in the radiator [9, 10, 11]; (c) separation of ambiguous solutions in the folded optical system; and (d), another order of magnitude improvement in background rejection.

Figure 8.2 shows the new FDIRC photon camera design (see Ref. [5, 12] for more details). It consists of two parts: (a) a focusing block (FBLOCK) with cylindrical and flat mirror surfaces, and (b) a new wedge. The wedge at the end of the bar rotates rays with large transverse angles in the focusing plane before they emerge into the focusing structure. The old wedge is too short so that an additional

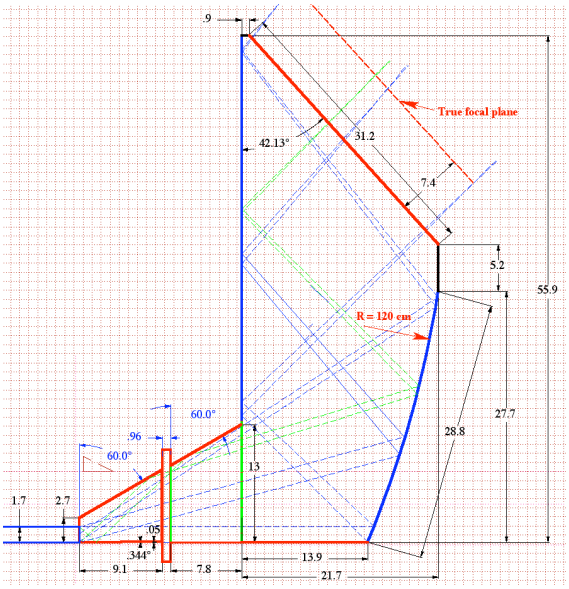

(a) FDIRC optical design (dimensions in cm).

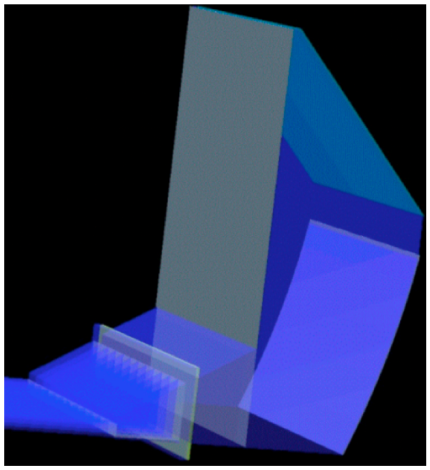

(b) Its equivalent in the Geant4 MC model.

Figure 8.2: Barrel FDIRC Design.

wedge element must be added to insure that all rays strike the cylindrical mirror. The cylindrical mirror is rotated appropriately to make sure that all rays reflect onto the FBLOCK flat mirror, preventing reflections back into the bar box itself; the flat mirror then reflects rays onto the detector focal plane with an incidence angle of almost 90°, thus avoiding reflections. The focal plane is located in a slightly under-focused position to reduce the FBLOCK size and therefore its weight. Precise focusing is unnecessary, as the finite pixel size would not take advantage of it. The total weight of bare solid fused silica FBLOCK is about 80 kg. This significant weight requires good mechanical support.

There are several important advantages gained in moving from the *BABAR* pinhole focused design with water coupling to a focused optical design made of solid fused silica: (a) the design is modular; (b) sensitivity to background, especially to neutrons, is significantly reduced; (c) the pinhole-size component of the angular resolution in the focusing plane can be removed by focusing with cylindrical mirror, and timing can be used to measure the chromatic dispersion, thus improving performance; (d) the total number of photomultipliers is reduced by about one half compared to a non-focusing design with equivalent performance; (e) there is no risk of water leaks into the Super*B* detector, and no time-consuming maintenance of a water system, as was required to operate *BABAR* safely.

Figure 8.3 shows the FDIRC coordinate system as used in the analysis.

Each new camera will be attached to its *BABAR* bar box with an optical RTV glue, which will be injected in a liquid form between the bar box window and the new camera and cured in place. As Fig. 8.2 shows, the cylindrical mirror focuses in the radial y-direction, while pinhole focusing is used in the direction out of the plane of the schematic (the x-direction). Photons that enter the FBLOCK at large x-angles reflect from the parallel sides, leading to an additional ambiguity. However, the folded design makes the optical piece small, and places the photon detectors in an accessible location, improving both the mechanics and the background sensitivity. Since the optical mapping is 1 to 1

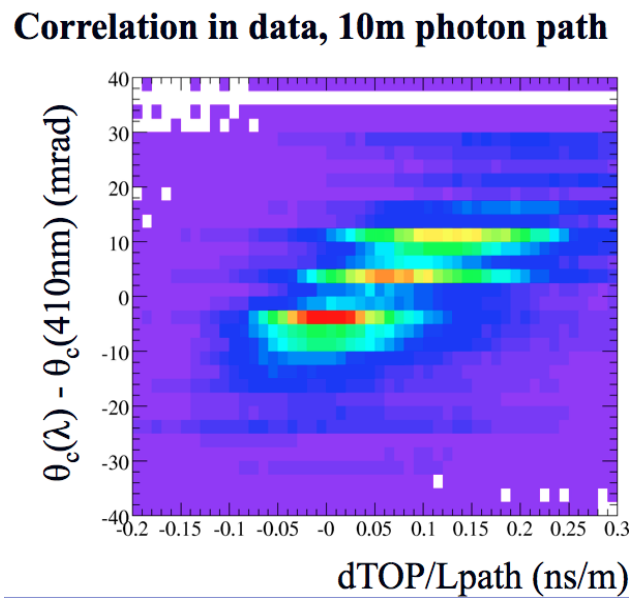

Figure 8.5: The same correlation between the change of the Cherenkov angle and the change in TOP for photons propagating 10 meters in the bar, as seen in the beam test data in the first FDIRC prototype [9, 11].

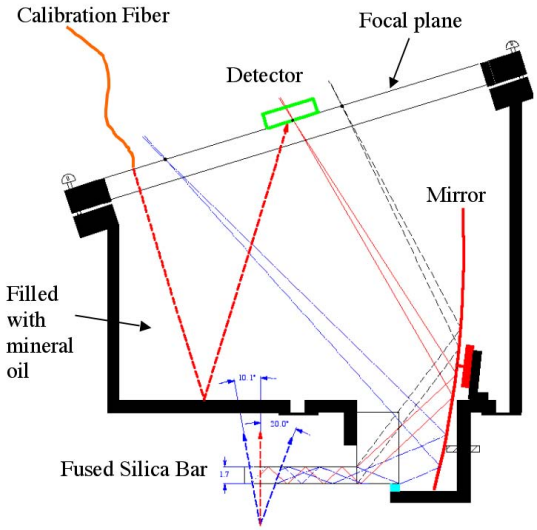

Figure 8.6: The first FDIRC single-bar prototype employing a spherical mirror, oil-filled photon camera, and highly-pixilated photon detectors [9], [10], [11].

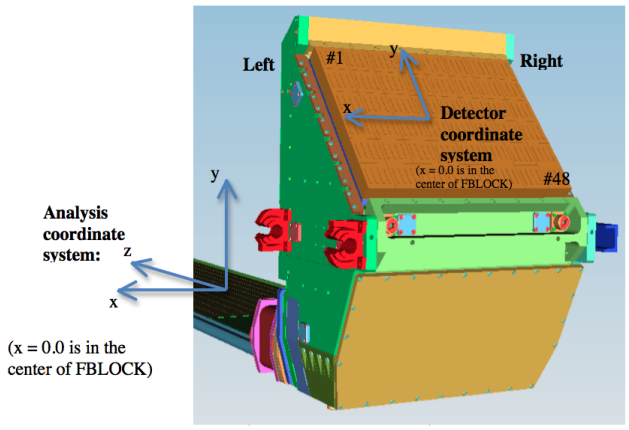

Figure 8.3: FDIRC coordinate system used in the analysis.

in the y-direction, this "folding" reflection does not create an additional ambiguity. Since a given photon bounces inside the FBLOCK only 2-4 times, the requirements on surface quality and polishing for these optical pieces are much less stringent than that required for the DIRC bar box radiator bars.

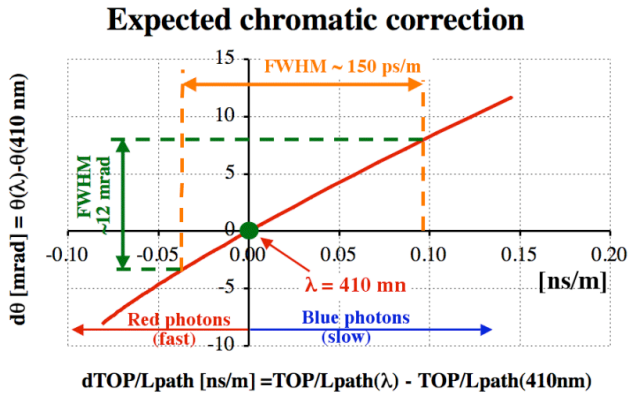

Figure 8.4: Analytical correlation between the variation of the Cherenkov angle and the change in TOP, relative to the mean wavelength of 410 nm [9, 11].

As an intermediate step towards an upgrade of DIRC for the Super$B$ detector, we have built and tested the first FDIRC prototype (see Fig. 8.6), in order to learn how to design a smaller FDIRC with new highly-pixilated fast PMTs [9, 11]. This prototype demonstrated for the first time that a chromatic correction could

be done with timing. The principle is displayed in Fig. 8.4 showing the analytical correlation between the change of the Cherenkov angle and the change in time-of-propagation (TOP), relative to the mean wavelength of 410 nm. Figure 8.5 shows the same plot, this time with real data from photons propagating 10 meters in the bar. Figure 8.7 shows the final result of the chromatic correction in the beam test data. One can see that the chromatic correction improves the Cherenkov angle resolution by 0.5-1 mrad depending on photon propagation path length. To achieve this, a single photoelectron timing resolution of ∼200 ps is required. This can be achieved with H-8500 or H-9500 MaPMTs.

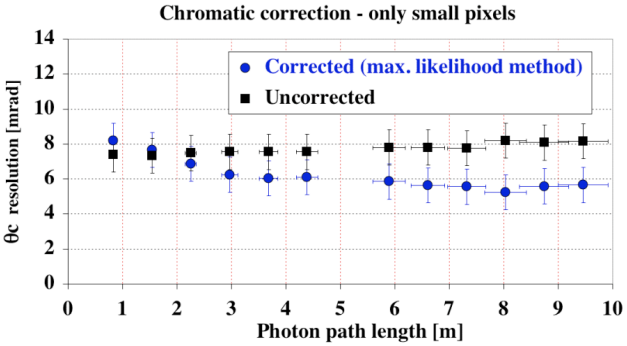

Figure 8.7: Beam test data showing the effect of the chromatic correction for 3 mm × 12 mm pixels obtained with H-9500 MaPMT in the first FDIRC prototype. Note that the Super*B* active region starts 1-2 meters away from the detector camera end. Results with the H-8500 MaPMT are similar, but with slightly worse resolution [9, 11].

We have also learned from the first prototype that the Cherenkov ring has worse resolution on the wings than on the center, due to the optical aberration caused by the bar, which is amplified by a mirror. Figures 8.8 and 8.9 show that this error contribution goes from 0 mrad (at ring center) to ∼9 mrad (near the ring wings) and it is z-dependent. This aberration is present in the non-focusing *BABAR* DIRC as well, but it is smaller, i.e., the mirror amplifies this effect. The effect is similar for spherical, parabolic and spherical mirrors. For more details see Ref. [12].

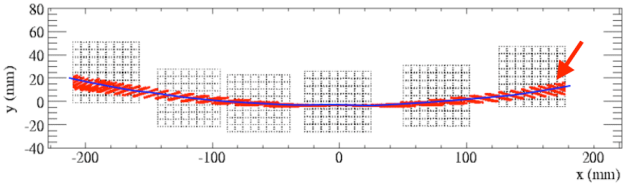

Figure 8.8: Optical ring aberration near the ring wings for the first FDIRC prototype with overlaid detectors and their pixels to show that it is a substantial effect. Calculated for a position in the middle of a bar [9].

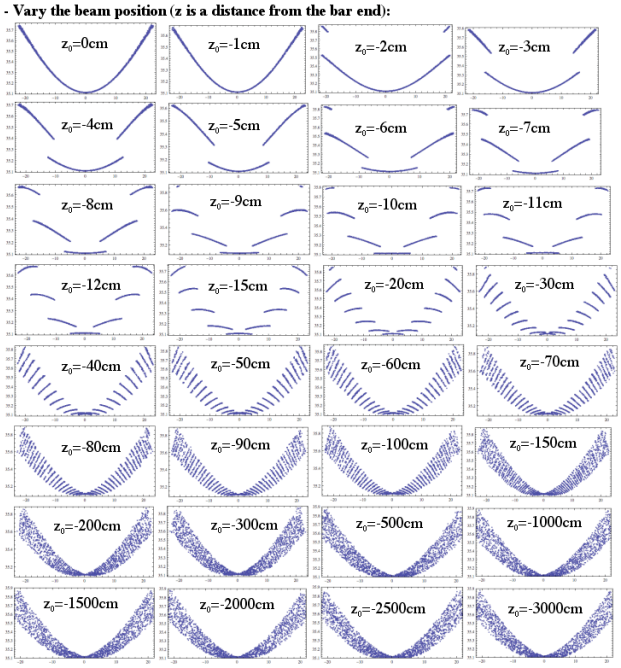

Figure 8.9: Optical ring aberration near the ring wings for the first FDIRC prototype as a function of z-position along the bar [12].

Each DIRC wedge inside an existing bar box has a 6 mrad angle at the bottom. This was done intentionally in *BABAR* to provide simple step-wise "focusing" of rays leaving the bar towards negative y to reduce the effect of bar thickness. However, in the new optical system, having this angle on the inner wedge somewhat

worsens the design FDIRC optics resolution. Figure 8.10 shows the result of a simulation with Mathematica [12]. One can see that the micro-wedge splits the image. There are two choices: (a) either leave it as it is, or (b) glue a micro-wedge at the bottom of the old wedge, inside the bar box, to correct for this angle. Though (b) is possible in principle, it is far from trivial, as the bar box must be opened. Because of this difficulty we have decided for the option (a).

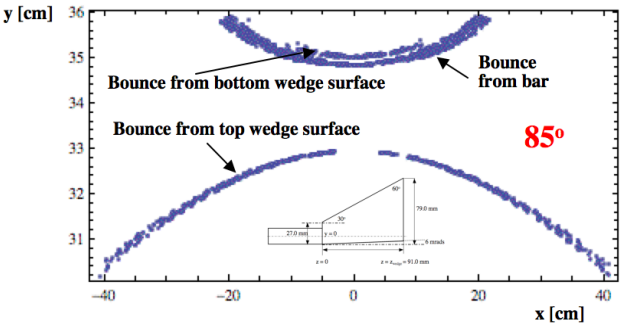

Figure 8.10: Split of Cherenkov ring caused by inclined bottom surface of the old wedge [12].

Figure 8.11 shows a Cherenkov ring image for one of the central bars in the new FDIRC. The ring image is more complicated than those from *BABAR* DIRC or from the first FDIRC prototype. This is due to reflections from the sides of the FBLOCK, and the pattern is different for each bar. The ring radius is not used in the analysis; instead, we use a dictionary of MC assignments for each pixel. These assignments are generated by placing a random photon source in a given bar and checking which pixel was hit. In this way we create pixel assignments of $k_{pixel} = (k_x, k_y, k_z)$. One can also generate time-of-propagation for direct and indirect photons TOP_{direct} and $TOP_{indirect}$ for tracks with $\theta_{dip} = 90°$ and $z = z_{middle}$ for each bar. For any other track direction one can then calculate the Cherenkov angle simply as a dot product of two vectors: $\cos\theta_C = k_{track} \cdot k_{pixel}$. This procedure has been used successfully with the first FDIRC prototype in the cosmic ray telescope with 3D tracking [32]. In the final physics analysis, the measured photons for each track will be tested against probability distribution functions (PDFs) for each particle hypothesis.

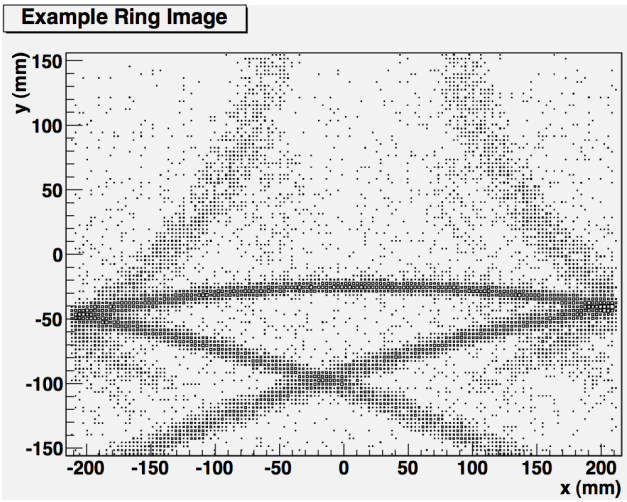

Figure 8.11: Cherenkov ring image from GEANT4 for tracks with $\theta_{dip} = 90°$ in the central bar at 4 GeV/c [13].

8.3 Projected Performance of FDIRC 2-3 pages

8.3.1 Reconstruction Arnaud, Roberts

8.3.2 MC Simulation

Fast simulation Arnaud

Full simulation Roberts

8.3.3 Effect of Background on performance Roberts

8.4 The Barrel FDIRC Detector Overview

8.4.1 Impact on other systems Benettoni, Simi, Vavra

8.4.2 Photodetectors

Photon Detector choice There are three photon detectors under consideration, the H-8500

FDIRC Design	Option	θ_C resolution [mrad]
1	3 mm×12 mm pixels with a micro-wedge	8.1
2	3 mm×12 mm pixels and no micro-wedge	8.8
3	6 mm×12 mm pixels with a micro-wedge	9.0
4	6 mm×12 mm pixels and no micro-wedge	9.6

Table 8.1: FDIRC performance simulation by Geant4 MC [13].

(64 pixels) and the H-9500 (256 pixels), and very recently R-11265-00-M64 (64 pixels) multi-anode PMTs (MaPMT) by Hamamatsu. At present, we have selected the 12-dynode H-8500 tube from several reasons: it is the tube preferred by the medical community and is therefore produced in a larger quantity, it has much smaller price than the H-9500 MaPMT, it has a smaller single electron timing spread (σ_{TTS} ~140 ps vs. σ_{TTS}~220 ps), it can be obtained with somewhat enhanced QE (~24% vs. ~20%), it has more uniform gain response across its face (1:2 vs. 1:5), and Hamamatsu strongly recommends (at the time of writing this document) not to consider this tube to keep a reasonable delivery schedule of large quantities. On the other hand, H-9500 MaPMT can provide finer sampling in the y-direction and thus provides significantly better Cherenkov angle resolution. We should keep it on the list of possible tubes.

Very recently another Hamamatsu tube, R-11265-00-M64, came up for a consideration [14]. Its main attractions are (a) Super-bialkali QE of 36%, (b) small 2.8 mm pixels, which would allow small binning in y-direction, and therefore better Cherenkov angle resolution, and (c) small dead space around tube boundaries. We would combine 8 small pixels horizontally to create wide pixels in the x-direction, where we do not have focusing; at the same time we would keep the same total number of electronics channels in the system. We will test this tube and decide later. It would require 2304 tubes of this type in the FDIRC system. One should add that Hamamatsu also sells R-11265-00-M16 tube, which has the same pixel size as H-8500 tube. It would be still useful to consider this tube as it has a Super Bialkali QE, and we would benefit from using it. But we would prefer smaller pixel size tube.

The performance of the new FDIRC is simulated with a Geant4 based program [13]. Preliminary results for the expected Cherenkov angle resolution are shown in Table 8.1 for different layouts [5]. Design #1 (a 3 mm × 12 mm pixel size with the micro-wedge glued in) gives a resolution of σ~8.1 mrad per photon for 4 GeV/c pions at 90° dip angle. The micro-wedge option was supposed to remove a ~6 mrad inclined surface on the old wedge, but adding it would require to open the bar box, and this was judged as too difficult to implement in practice and was discarded. Presently preferred option is #4, which would give σ~9.6 mrad per photon. This would be a performance about the same as in *BABAR* DIRC [4]. However, if the chromatic correction would be implemented successfully, one could reduce the error by 0.5-1 mrad depending on the photon path length [11].

During the prototyping stage we used H-8500C tube with resistor chain and a HV cable with the SHV connector. In the final application we would still prefer to use the H-8500C tube, as it gives a HV control of each tube - see more discussion in the HV section. This tube comes with a 1.5 mm-thick Borosilicate glass window with a spectral sensitivity between 300 and 650 nm. We would require a minimum QE of ~24%, which corresponds to a blue sensitivity index of 9.5. The dark anode current of this tube is very low (0.1 nA per pixel and 6 nA total), and the after-pulse rate is also almost negligible. Given the design of the dyn-

ode structure preventing direct ion backflow to the photocathode, we expect a nominal cathode PMT aging behavior.

Figures 8.12 show (a) a single photoelectron pulse from H-8500 before the amplification at ∼1.0 kV, (b) a single electron pulse height spectrum. As one can see from the Hamamatsu spreadsheet shown in Fig. 8.12, the rise time of H-8500 tube is about 0.7 ns. With SLAC amplifier, based on the Analog devices chip AD8000, the amplified rise time was about 1.5 ns, which is sufficient for our purpose. We believe that the tube needs an amplifier with an effective gain of ∼40× if one is using a LeCroy 4413 discriminator with a threshold of ∼25 mV. Hamamatsu also points out that the pulse height spectra are not uniform across all pixels in a H-8500 tube. How this effect translates into the detection efficiency depends on the type of electronics, noise level and threshold; it will be studied in detail in the FDIRC prototype first using the SLAC amplifier with the IRS-2 waveform digitizing electronics [15], and then be compared to the Super$B$ CFD electronics [16] (see section 8.4.6.).

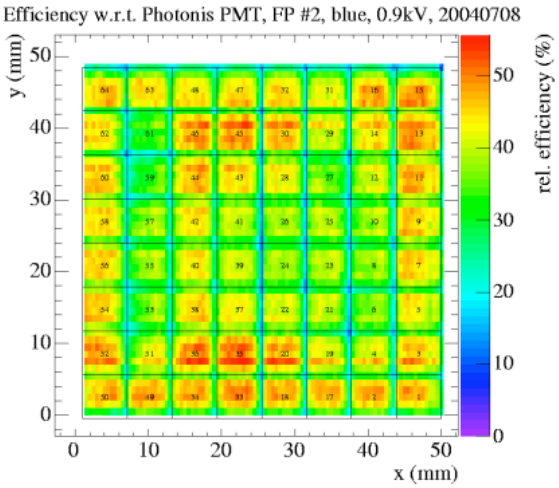

Figure 8.13: Single photoelectron efficiency of a H-8500 tube, normalized to Photonis Quantacon XP2262/B PMT [17].

Figure 8.13 shows the single photoelectron efficiency of a H-8500 tube, normalized to a Photonis Quantacon XP2262/B PMT [17]. This plot was obtained with a SLAC amplifier with Elantek 2075 chip, LeCroy 4413 discriminators with 100mV threshold, LeCroy 3377 TDCs with 0.5 ns/count, and a 407 nm laser. We plan to short two neighboring pixels in the x-direction, as there is only pinhole focusing available, and thus create 3 mm × 12 mm pixels (H-8500), providing 32 readout channels per tube. Each photon camera would have 48 H-8500 MaPMT detectors, which corresponds to a total of 576 tubes for the entire Super$B$ FDIRC, resulting in 18432 pixels total. The H-8500 tube has a pixel size 5.8 mm×5.8 mm, with a pitch between pixels equal to 6.08 mm, the effective detection area of 49 mm × 49 mm, and the H-8500 tube total area of 52 mm × 52 mm.

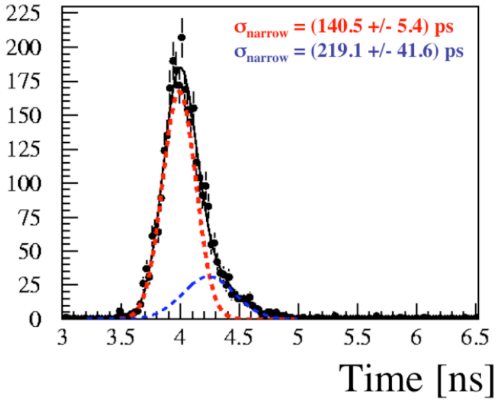

Figure 8.14: The H-8500 single photoelectron transit time resolution is σ_{TTS}∼140 ps [17].

Figure 8.14 shows H-8500C tube TTS timing resolution with single photoelectrons, indicating σ_{TTS}∼140 ps [17], obtained with a laser pointing to the center of a pixel, and using SLAC amplifier with Elantek-2075 chip, Philips 715 CFD and LeCroy 2228A TDC. Hamamatsu data sheets for H-8500 tube indicates a value of FWHM ∼400 ps, which gives σ_{TTS}∼170 ps. Another measurement comes from R. Montgomery showing an average H-8500 tube TTS resolution of σ_{TTS}∼154 ps [19]. This timing performance, coupled to the electronics timing resolution contribution of $\sigma_{Electronics}$∼100 ps, allows corrections of the chromatic error for photon path length of more than 2 meters, as long as

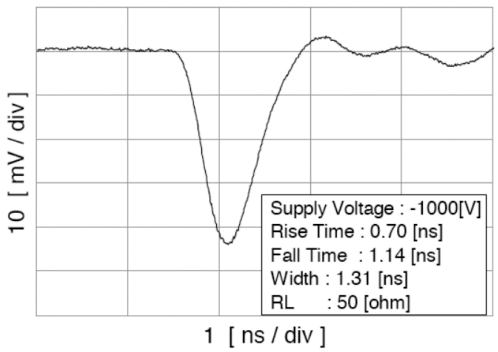

(a) H-8500 MaPMT single electron pulse without an amplifier (response to a 30 ps laser pulse at 407 nm).

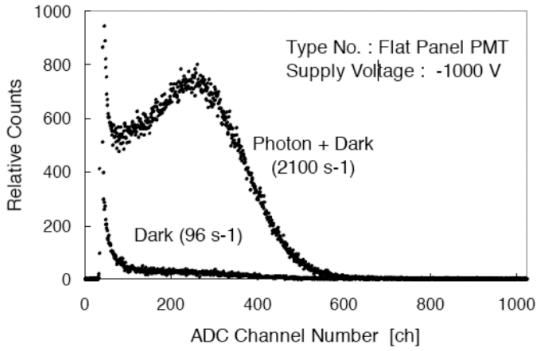

(b) H-8500 MaPMT single electron pulse height spectrum.

Figure 8.12: H-8500 MaPMT single electron pulse, noise and single electron pulse height distribution, Hamamatsu data [18].

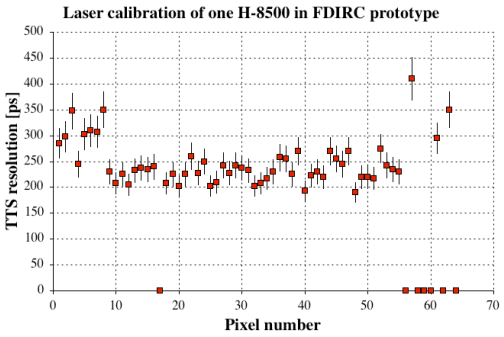

Figure 8.15: The H-8500 single photoelectron transit time resolution across all pixels [17].

the total timing resolution per single photon is $\sigma \sim 200 - 250$ ps [11].

There is also a new measurement showing that the TTS resolution depends on the position within a given pixel, which is driven by the PMT's electrode structure [20]. The electrode structure, PMT edge effects and gain variation generally degrade the overall TTS resolution, so one should probably assume that the single photoelectron timing resolution is more like 200-250 ps. This agrees with Fig. 8.15 where we plot TTS timing resolution in the first FDIRC prototype [17], where laser photons populate the entire H-8500 face, i.e., pixels were hit uniformly, including their edges. Figure 8.6 shows how the laser calibration was done in the first FDIRC prototype. This plot probably represents what will be a real TTS performance in practice. Notice also that edge pixels tend to have worse resolution.

There are two effects to take into account when considering interaction between two neighboring pixels: the pixel-to-pixel cross-talk, and the charge sharing avalanche between two pixels. The neighbor pixel-to-pixel single electron cross-talk was measured to be ∼3%, when a laser light was placed on the center of a pixel while looking at its neighbor – see Fig. 8.16 (this test used a newer SLAC amplifier with AD8000 chip). However, the pixel-to-pixel cross-talk is even more complicated in all multi-anode tubes [19]. Figure 8.17 shows that the cross-talk depends on the position within a pixel. This will clearly require more study with the FDIRC final electronics. We hoped to utilize the charge sharing, which is related to the avalanche size, to reduce the size of pixels in the y-direction by charge interpolation. However, the attempt to utilize the charge sharing was not successful in this particular tube as it has entrance focusing electrodes defining pixel boundaries, which sweep electrons away from pixel boundaries, *i.e.* Hamamatsu has designed

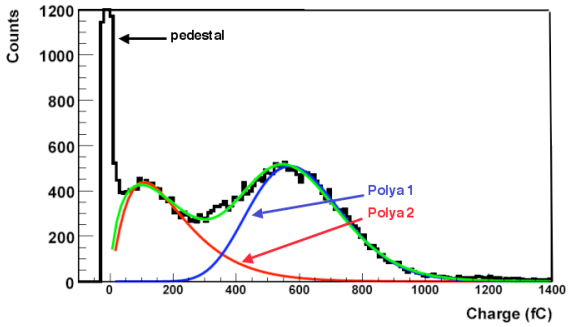

(a) Double-Polya fit to single electron distribution as observed in R7600-03-M16 MaPMT. The lower peak originates from photoelectrons which are missing one amplification stage in the MaPMT [24].

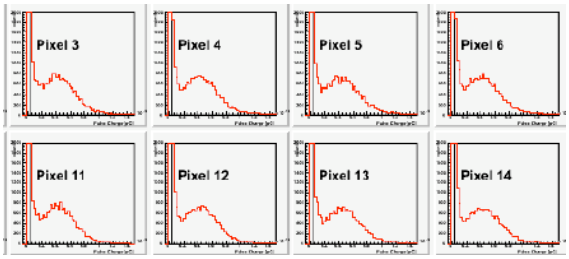

(b) Single electron distributions in H-8500 MaPMT. The lower peak shows up only as a shoulder [23].

Figure 8.18: Single electron pulse height distribution in MaPMTs.

the MaPMT electrode structure in such a way to suppress the charge sharing in these tubes. Both H-8500 and H-9500 have this charge sharing-suppressing feature. Such feature does not exist in MCP-PMT detectors.

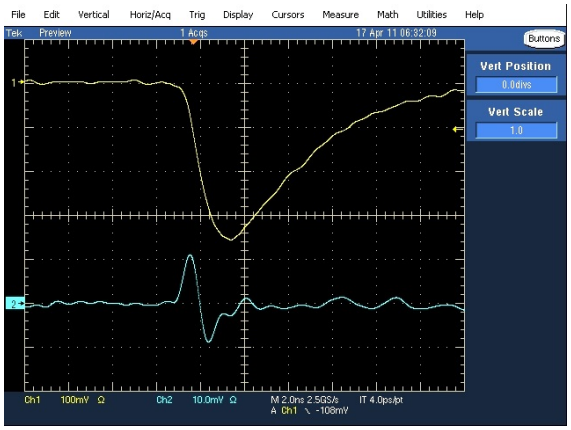

Figure 8.16: The H-8500 tube pixel-to-pixel single electron cross-talk was measured to be ∼3%, when the laser light was placed on the center of a pixel while looking at its neighbor [21].

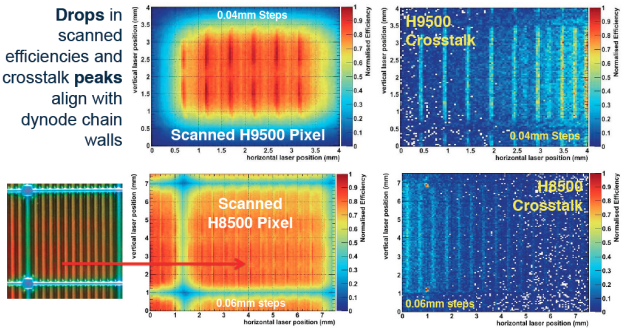

Figure 8.17: Observed periodicities in single electron efficiencies and cross-talk are aligned with the dynode electrode structure [19].

Another special feature of all MaPMT detectors is a double Polya distribution, one corresponding to a photoelectron produced at the cathode and the amplification utilizing all 12 dynodes (this is a nominal distribution), and another one corresponding to a case that a photon produces a photoelectron striking the very first dynode rather than at the photocathode, and the amplification is utilizing only 11 dynodes instead of 12. Missing one amplification stage produces a gain 2-3 smaller than the nominal amplification process, pulses arrive 2-2.5 ns earlier (see Fig. 8.19 [21]). Figure 8.20 shows a time spectrum of normal photoelectrons produced at the cathode, pre-pulse spectrum produced at the first dynode arriving ∼2.5 ns earlier, and backscattered photoelectrons arriving ∼6 ns later [22]. Figures 8.18 show the resulting single electron pulse height spectra either a small shoulder near the pedestal at lower gain [23], or a clear double-Polya distribution at higher gain [24]. Although the pre-pulses are a nuisance, they can be used as normal photoelectrons in the Cherenkov ring analysis and their time can be calibrated out. Their time shift will

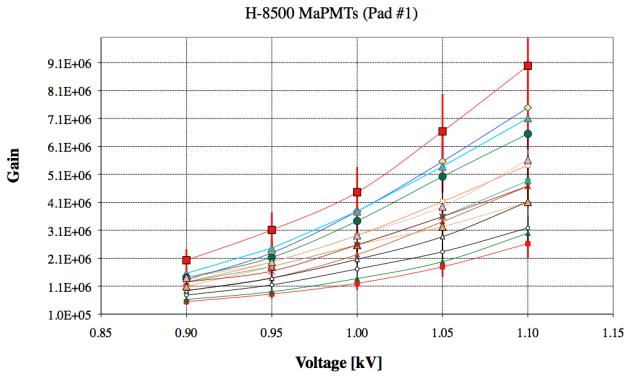

Figure 8.21: The H-8500 tube gain range and dependence on voltage for 14 tubes using pixel 1 in each tube [21].

not affect the chromatic correction, which has a range of only ∼1 ns.

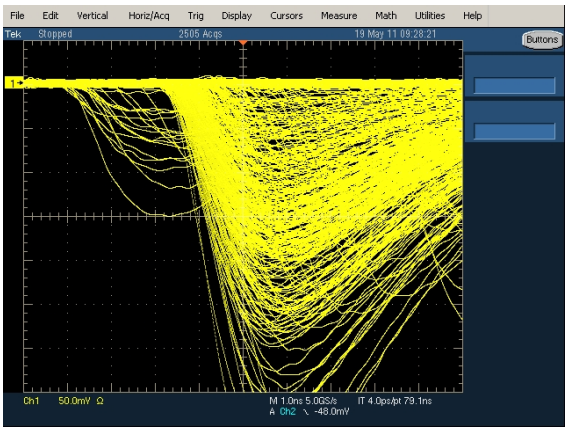

Figure 8.19: The H-8500 single electron pre-pulses corresponding to a case when a photon produces a photoelectron at the very first dynode rather than at the photocathode, and the amplification is utilizing only 11 dynodes instead of 12 [21].

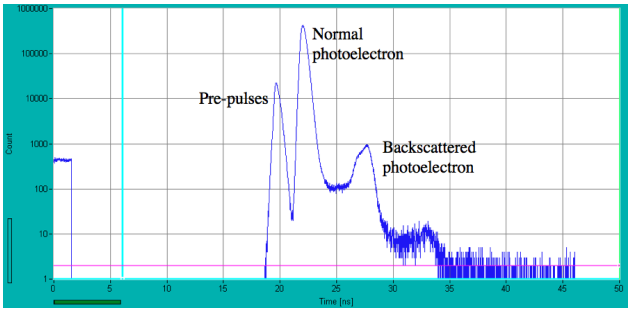

Figure 8.20: The H-8500 single electron time spectrum showing normal photoelectrons, pre-pulses and the backscattered photoelectrons [22].

Figure 8.21 shows that the H-8500 tube gain range is $1 - 3 \times 10^6$ for nominal operating voltage of -1.0 kV [21]. There is a variation of gain from pixel-to-pixel due to non-uniformities in the multi-anode structure. As a result there is a variation in detection efficiency.

Figure 8.22 shows scans of 15 tubes [21], operating at -1.0 kV and -1.1 kV, amplifier gain of ∼40×, a threshold electronics of -25 mV, and indicates that typically the best-to-worst single electron detection efficiency might vary as much as 1:2 across the H-8500 PMT face. This is compared to the anode current response across all pixels to a fixed high photon flux (Hamamatsu data). This figure also shows the efficiency maps of 15 tubes [21], all operating at -1.0 kV, with an amplifier gain of 40×, with a simple threshold electronics, and normalized to the Photonis Quantacon XP2262/B PMT. It indicates that the best-to-worst detection efficiency variation is as much as 1:2 across the H-8500 PMT face. One should stress that the detection efficiency relative to the Quantacon XP2262/B PMT is typically at a level of 40-50% for the worst pixels, and 80-100% for the best pixels.

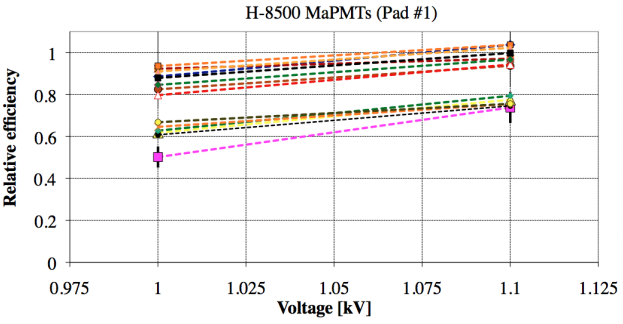

Figure 8.23: The H-8500 single electron detection efficiency dependence on voltage [21].

Figure 8.23 shows how the H-8500 tube single electron detection efficiency depends on volt-

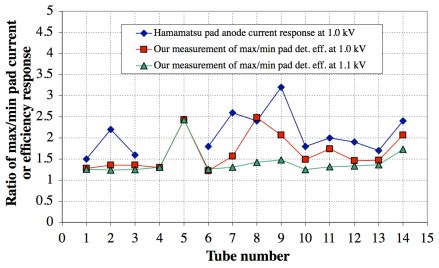

(a) Min-max efficiency uniformity of 64 pixels. This is compared to anode current min-max response across 64 pixels to a fixed photon flux.

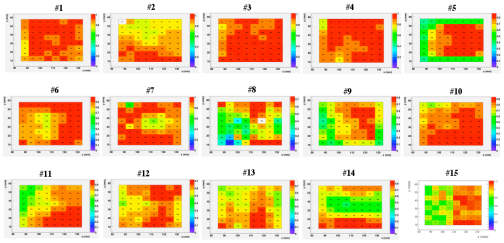

(b) Relative efficiency scan of 15 H-8500 tubes operating at -1.0 kV, normalized to XP2262/B PMT).

Figure 8.22: 2D single electron detection efficiency across pixels of 15 H-8500 tubes [21].

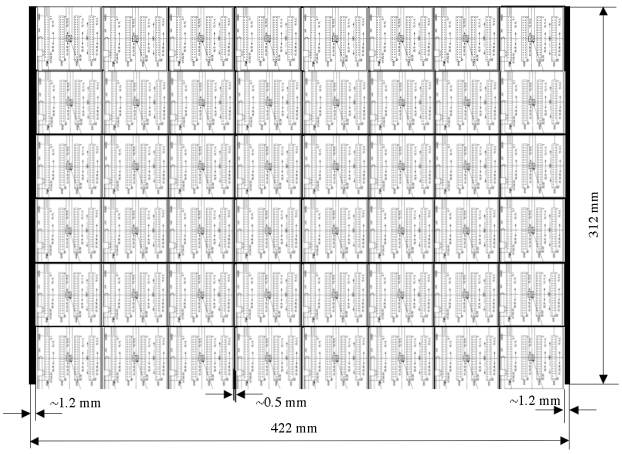

Figure 8.24: Detector matrix on one FDIRC detector camera with 48 H-8500 MaPMTs. The entire FDIRC system needs 576 tubes and 18,432 pixels [5].

age [21]. One can see that one can improve the detection efficiency by 10-20% per 100V increase.

There are three possible ways to deal with the pixel-based gain non-uniformity: (a) process each tube, equipped with the final electronics, in a scanning setup; record the individual relative efficiency values and store them into an analysis database, or (b) adjust a discriminator threshold on each pixel, or (c) adjust an amplifier gain on each pixel. This concept has yet to be worked out in detail as this effect depends on details of final electronics. One should remember, when doing the overall gain adjustment, that the absolute maximum voltage on H-8500 is -1.1 kV. We want to stay below about -1.05 kV for the initial setting to have enough headroom for later period when the detector will loose gain due to aging.

Modularity: photodetector mechanical packing fraction There are two factors to consider when determining the photon coverage: (a) detection coverage in the focal plane of the photon camera, and (b) coverage within each tube (we will consider detection losses within the dynode structure later and loss factors later). Figure 8.24 shows the H-8500 matrix of 48 tubes in one photon camera. The size of each H-8500 tube is 52.0 ± 0.3 mm, and a gap between each tube is ~0.5 mm; this gives a contribution to the packing fraction of ~98.6%. The photon packing density (effective area/external size) within each tube is ~89%. These factors give the overall photon packing efficiency of ~88% for the photon camera based on 48 H-8500 tubes.

Photon detector mechanical support Photon detectors will be supported by the electronics motherboard. The original scheme to have one large motherboard for all 48 detectors was considered as too difficult to implement in practice. Instead, we will use smaller motherboards supporting groups of 6 detectors running in vertical direction. **[yet to be written]**

Optical coupling of detectors to FBLOCK The MC simulation shows (see Fig. 8.25) that we loose 8-25% of photons if we do not optically couple PMTs to the FBLOCK [13]. The event Cherenkov angle resolution (σ∼2.94 mrad) improves by ∼10% with optical coupling [13]. On the other hand, an access to a single failed detector will become complicated, and we may have to abandon a concept of one large single motherboard. If we use the optical coupling, we are considering eight vertical segments, each handling six detectors; each segment could be removable by sliding it vertically off the FBLOCK. In addition, we have not yet selected the optical coupling grease. One should realize that any leak of the grease on the FBLOCK side optical surfaces, would result in a serious loss of photoelectrons. The optical coupling concept has yet to be tested to investigate its practicality, reliability and radiation hardness, and therefore it remains an open issue.

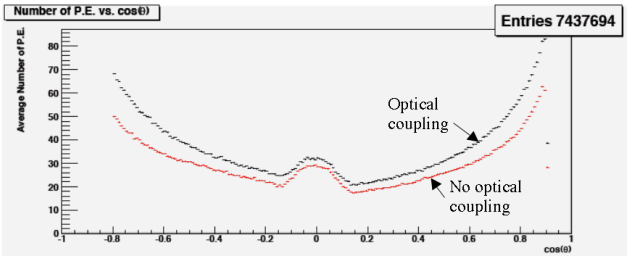

Figure 8.25: Simulated (Geant4 MC) number of detected photoelectrons as a function of the polar angle for two cases: with and without optical coupling between detector face and the FBLOCK [13].

Temperature requirements in Fbox enclosure There are two major sources of heat in the detector enclosure: (a) HV resistor dividers, and (b) electronics. Each tube has a HV divider. All dividers together draw ∼9 W per 48 tubes, which is a trivial amount of heat. Assuming for now that the electronics will dissipate ∼10 W per package, one gets a total amount of heat of ∼500 W per 48 detectors. We will need a water-cooled heat exchanger.

Another worry is what happens if we loose cooling. Based on tests with the FDIRC prototype detector enclosure, the temperature would rapidly climb beyond ∼80°C. That would be dangerous for tubes, optical grease coupling, glues and that could also create mechanical stresses. Therefore we need an automatic power shutoff system.

Rates and aging issues in H-8500 PMTs One strong point of our design is that we share a total photon background load from a single bar box among 48 H-8500 detectors, and this results in acceptable rate even at the highest luminosity, and an acceptable total charge load after 10 years of operation.

We use two methods to estimate FDIRC rates: (a) empirical scaling (ES) from Belle-I Aerogel counter rates and assuming that the background rate scales as the luminosity (we use Belle-I rates rather than *BABAR* rates because that machine is believed to be closer to the Super*B* for the background scaling). (b) We then use the MC simulation, which simulates all physics background processes involved in the background production and includes the precise modeling of beam line magnet components all the way up to 16 meters from IP in either direction, and uses correct FDIRC geometry with a proper handling of optical photons. The MC simulation shows that the rate is dominated by the radiative Bhabha scattering (thus, our assumption above that the background scales as the luminosity is justified). The ES method is rather close to the MC prediction (MC) for the contribution from the active detector volume without shielding: 75 kHz (ES) vs. 120 kHz (MC) per double-pixel, or 2.4 MHz (ES) vs. 3.8 MHz (MC) per tube, which would correspond to the total accumulated charge of 1.2 C/cm^2 (ES) vs. 2.3 C/cm^2 (MC) for a total integrated luminosity of L_{int} ∼75 ab^{-1}. However, the contribution from the photon camera, which is outside of the magnet, would be much higher without a shielding: 120 kHz (ES) vs. 550 kHz (MC) per double-pixel. The dominating background is due to the Bhabha scattering, the Touschek effect's contribution is less than 10%.

Given the design of the H-8500 dynode structure, which prevents the direct ion backflow to the photocathode, we expect the MaPMT tube cathode-aging rate to be similar to an usual PMT aging behavior, which means that the above numbers appear to be safe. For example, *BABAR* DIRC PMTs accumulated at least ∼150 C per tube during ∼10 years of *BABAR* operation and tubes have lost some efficiency (∼30%), but operated well until the end with a few voltage adjustments to correct the gain loss. This tells us that our nominal starting voltage should not exceed ∼1.05 kV to allow possible later gain adjustments. One should, however point out that aging tests are yet to be done for the H-8500 tube. One should also worry about unusual background conditions caused by the machine misbehavior, changes in tune, beam losses, etc., especially in the early periods before reaching the full luminosity. Hamamatsu recommends that the absolute maximum current be ∼100μA per tube or ∼2μA per pixel. Another constraint is the capability of the electronics to cope with high rates. Super*B* FDIRC electronics can handle rates up to ∼20 MHz per pixel, if one pixel is firing, and up to ∼2.5 MHz per tube if all pixels are firing. [**We still need to add a total number of neutrons per cm^2 per year, rate of slow protons from np collisions, rate of ions, and expected dose obtained by electronics. All this after the background shielding and magnetic shielding are added correctly**]

Figure 8.27 shows the Hamamatsu aging data for R8400-00-M64 MaPMT running at 100μA for 10,000 hours. There is no obvious large effect which could not be corrected by a voltage adjustment. Translating this to our expected conditions, and assuming that H-8500 behaves the same way as R-8400 tube, the maximum expected anode current is approximately 500 kHz/double-pixel × 32 channels/pmt × gain × electron charge = $500\times10^3\times32\times2\times10^6\times 1.6\,10^{-19}$∼5$\mu$A, which is only ∼2× smaller than Hamamatsu's safe limit from their aging test, if one runs with this rate for 10 years.

Therefore we do need to shield the FBLOCK's contribution to the overall rate, and keep only a contribution from the active region of bar boxes. The present MC background simulation estimate is (a) ∼50 kHz/double-pixel as contribution from bar boxes in active region with shielding and ∼120 kHz/double-pixel without shielding, and (b) ∼60 kHz/double-pixel from FBLOCK with shielding and ∼550 kHz/double-pixel without shielding. Table 8.26 summarizes rates under various conditions. Figure 8.53 shows the FDIRC shielding design.

1) Contribution from active volume (with & without shielding):

	Lumi	H-8500 MaPMT rate	One single Double-pixel rate	Total dose (after 50 ab^{-1}) (~ 10 years)	Expected anode current at a gain of ~2 x 10^6	Maximum allowed current for 10 years of operation
without	10^{36}	~ 3.84 MHz	~ 120 kHz	~ 1.3 C/cm^2/50 ab^{-1}	~ 1.2 μA /PMT	~ 10 μA /PMT
with	10^{36}	~ 1.5 MHz	~ 50 kHz	~ 0.5 C/cm^2/50 ab^{-1}	~ 0.5 μA /PMT	~ 10 μA /PMT

2) Contribution from FDIRC photon camera (with & without shielding):

	Lumi	H-8500 MaPMT rate	One single Double-pixel rate	Total dose (after 50 ab^{-1}) (~ 10 years)	Expected anode current at a gain of ~2 x 10^6	Maximum allowed current for 10 years of operation
without	10^{36}	~ 17.6 MHz	~ 550 kHz	~ 5.9 C/cm^2/50 ab^{-1}	~ 5.6 μA /PMT	~ 10 μA /PMT
with	10^{36}	~ 1.92 kHz	~ 60 kHz	~ 0.6 C/cm^2/50 ab^{-1}	~ 0.6 μA /PMT	~ 10 μA /PMT

Figure 8.26: FDIRC pixel rates with and without shielding.

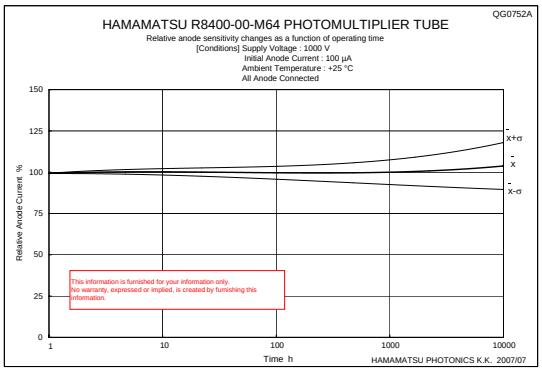

Figure 8.27: Hamamatsu data for R8400-00-M64 MaPMT showing that there is no large drop in photo-current when running 100μA for 10,000 hours (∼400 days).

Magnetic shield of H-8500 PMTs For *BABAR* DIRC PMTs, which have a classical

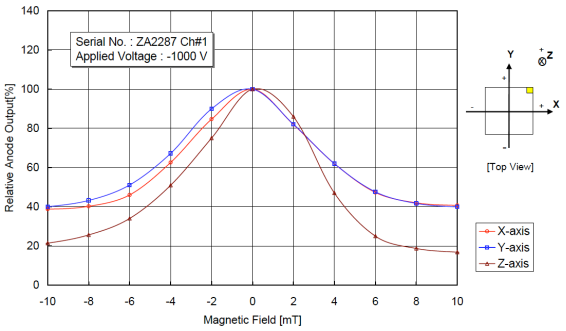

(a) The effect on boundary pixels.

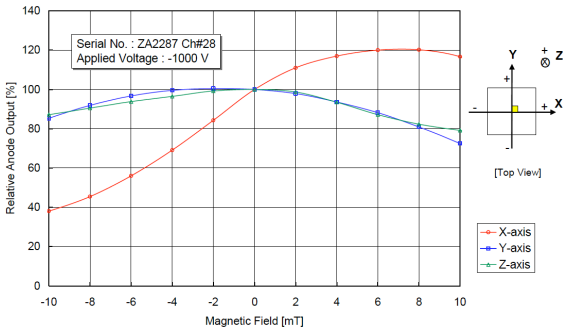

(b) The effect on pixels near center.

Figure 8.28: Magnetic field effect on the H-8500 MaPMT's pulse height (Hamamatsu data).

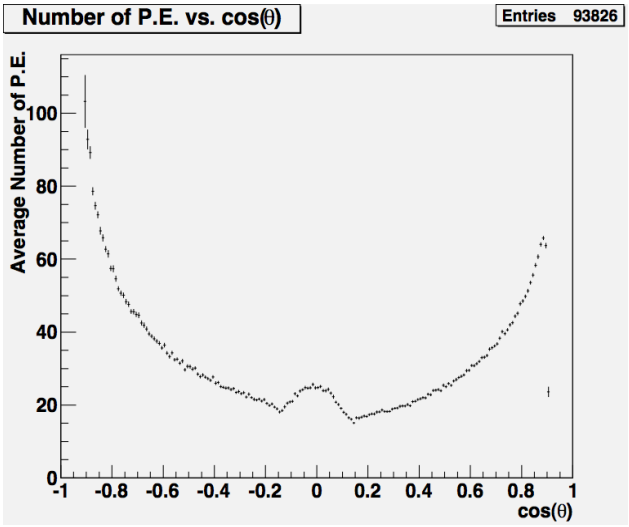

Figure 8.30: MC simulation of number of photoelectrons in FDIRC [13].

PMT dynode design, it was necessary to keep the magnetic field below ∼1 Gauss in the SOB to prevent a serious degradation of pulse height spectra [4]. To do that, it was necessary to enclose the entire photon camera into a large magnetic shield. Figure 8.28 shows the effect of the magnetic field on the H-8500 tube pulse height. One can notice that the effect is different near the tube boundary compared to its central region. We conclude that we can tolerate a residual magnetic field up to a level of a few Gauss with no effect on the pulse height. We plan to use a magnetic shield similar to that of *BABAR*.

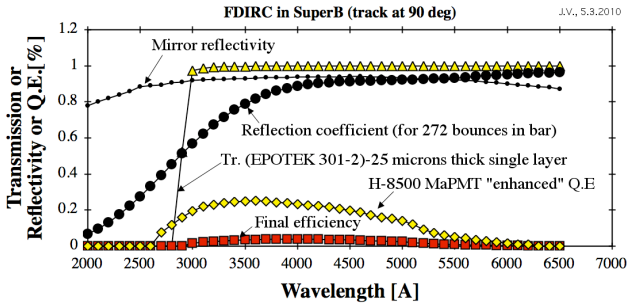

Figure 8.29: FDIRC wavelength response is limited on low wavelength side by EPOTEK 301-2 glue used to glue bars together [5].

Prediction of number of photoelectrons per ring Figure 8.29 shows FDIRC's wavelength bandwidth [5]. One can see that we operate in the visible wavelength region and that the effective filter is the Epotek 301-2 epoxy. Assuming a peak QE of 24%, and no optical grease coupling between PMTs and the FBLOCK, one obtains ∼32 photoelectrons for tracks with $\theta_{dip} = 90°$ using a simple spreadsheet calculation. Figure 8.30 shows the MC simulation of number of photoelectrons as a function of the dip angle [13]. At $\theta_{dip} = 90°$ it predicts ∼27 photoelectrons. We find the FDIRC performance slightly better than the DIRC performance in *BABAR* [4]. **[numbers are still being checked]**

Radiation damage of optical components We used the ^{60}Co source for the irradiation of

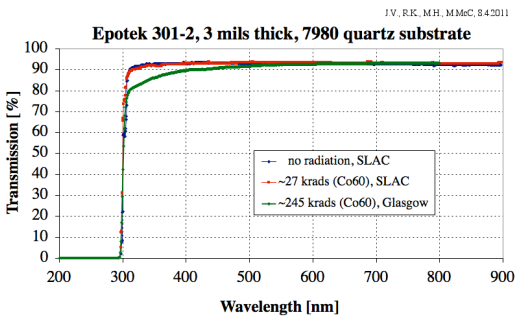

(a) Transmission of Epotek 301-2 epoxy (50-75 microns thick).

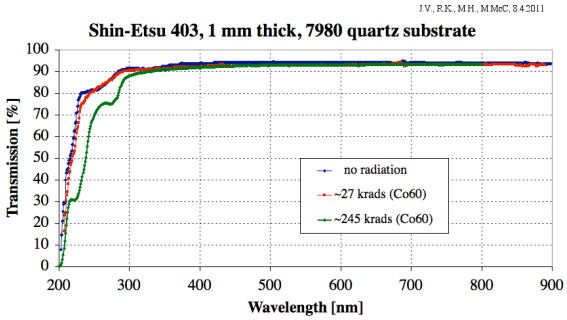

(b) Transmission of Shin-Etsu 403 RTV (1 mm thick).

Figure 8.31: Radiation damage by the ^{60}Co source of glues used in the construction of the photon camera [25].

the glue samples. First, we have investigated the radiation damage of Corning 7980 Fused Silica 3 mm-thick coupons used for support of glue samples and, as expected, found no loss of transmission up to 250 krad. Figure 8.31 shows the irradiation of the Epotek 301-2 epoxy, used for coupling of the new Wedge to the bar box window, and the Shin-Etsu 403 RTV, used for coupling of the FBLOCK and the new Wedge. We show that these glues are acceptable for the Super*B* conditions, although the Epotek 301-2 does see some small loss of transmission [25].

8.4.3 Laser calibration system

Optics of calibration The aim of this calibration is twofold: (a) check the operation of tubes and electronics, (b) provide pixel offset constants for FDIRC timing calibration, which was found to be useful in the first FDIRC prototype doing the chromatic corrections [21]. Figure 8.32 shows the laser entry into the FBLOCK as implemented in the final FDIRC prototype. The fiber plugs into a connector with a lens (F230FC-A), which makes a parallel laser beam, which then strikes a 5 mm diameter Opal diffuser, which was selected out of several choices for it uniform light diffusing effect. The small diameter diffuser is necessary to limit losses of real Cherenkov photons. We found experimentally that the best arrangement is if the diffuser is pressing against the bottom surface of the FBLOCK with the help of a spring (no gluing as it affects a uniformity of the scattered light). There is one fiber entry per photon camera serving one bar box. Figure 8.33 shows a MC simulation indicating that the total time spread across the focal plane is about 2 ns, which will have to be corrected out to get a single t_0. It also shows an example of MC simulation of the photon time of arrival in a single pixel. It shows multiple peaks corresponding to direct light and various FBLOCK side reflections. We believe that we will be able to determine timing offsets with enough precision using selected significant peaks. This calibration scheme is going to be tested in the final FDIRC prototype.

Laser and fiber optics choice We will use the Pilas laser diode providing a light with 407 nm. We would like to split the light from one Pilas source into 6 branches, but the fiber splitter has yet to be tested to check that splitting is equal. If this works we will need two Pilas control units serving the entire system. The Pilas control unit can be triggered externally so we can control both the timing and when the calibration should happen.

8.4.4 FDIRC Mechanical Design

Description of BABAR bars, bar boxes We will reuse bar boxes from the *BABAR* DIRC. Bar boxes will not be modified as it is considered too difficult to do. This has some disadvantages, for

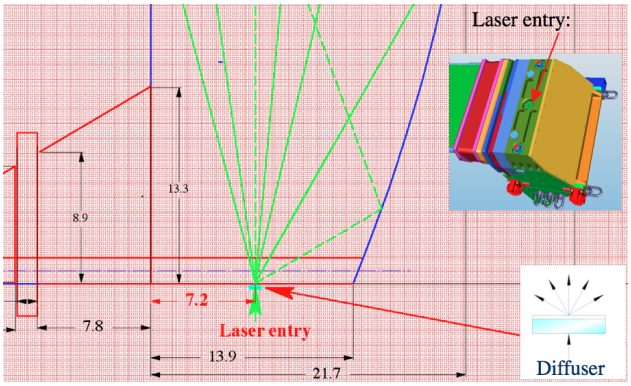

(a) Optical details of laser entry [21].

(b) OPAL diffuser used to spray laser photons into the FBLOCK.

Figure 8.32: Laser entry into the FBLOCK.

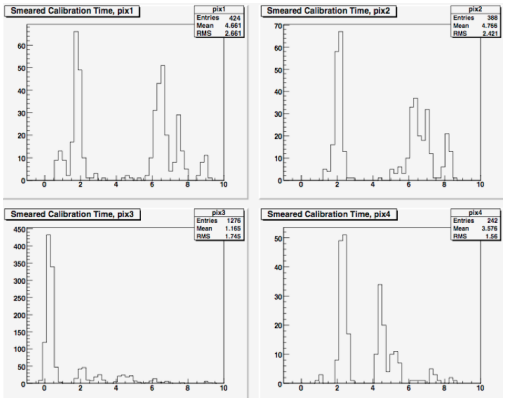

(a) Time peaks from the laser calibration as it appears in several pixels [13].

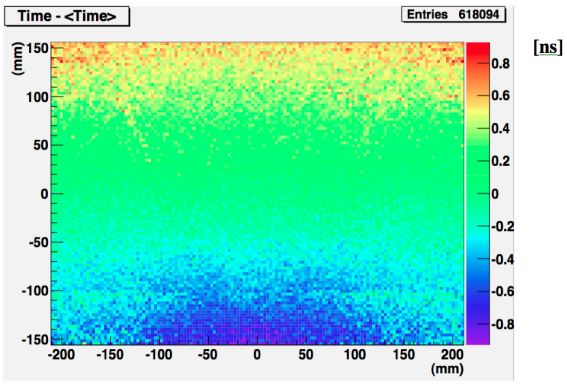

(b) Laser time spread is a few ns across the focal plane [13].

Figure 8.33: Laser calibration timing.

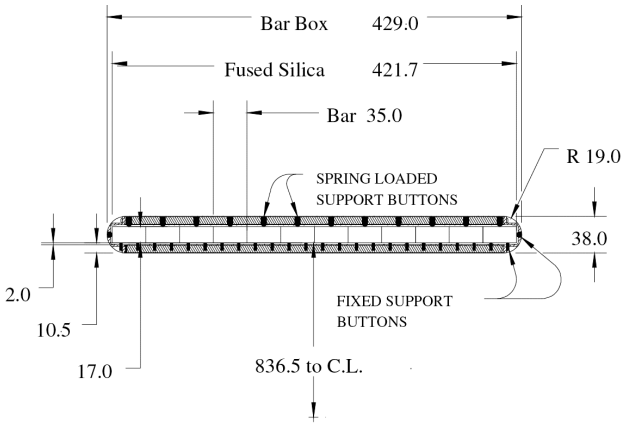

Figure 8.36: A cross-section of bar box with 12 bars [4].

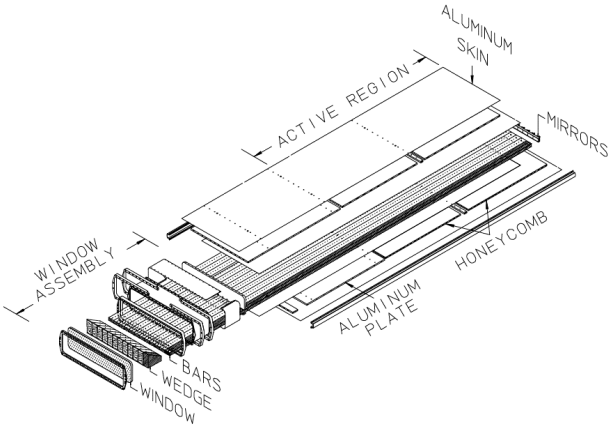

Figure 8.34: *BABAR* DIRC bar box [4].

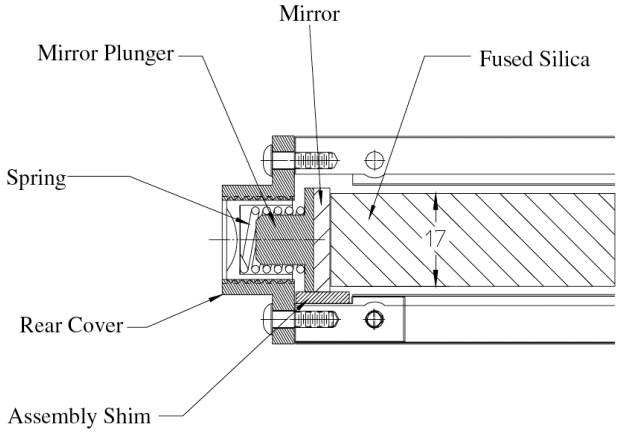

Figure 8.37: Bar end with a mirror [4].

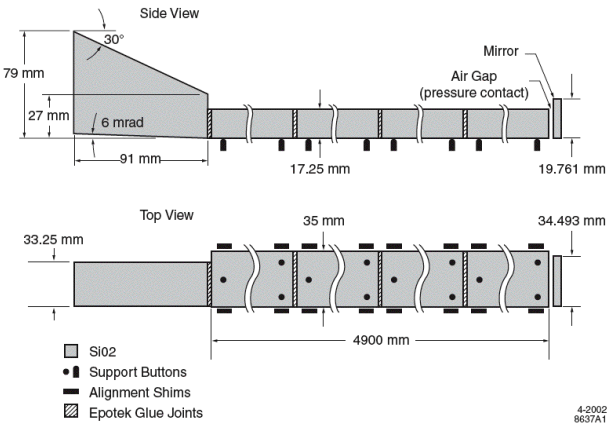

Figure 8.35: One bar segment with nominal dimensions [4].

example, the old wedge, with its 6 mrad angle at the bottom surface, somewhat worsens the new camera optics by adding ∼0.5 mrad to the Cherenkov angle resolution. Another potential problem is that the glue has sees ∼10 years of radiation during the *BABAR* experiment. Extensive studies were performed with the *BABAR* dimuon data and no detrimental effect was found on the glue transmission [26]. However, we do need to be extra careful when transporting bar boxes, as it is not known if the Epotek 301-2 glue strength was not affected, and some tests will be required.

Figure 8.34 shows the *BABAR* DIRC bar box with its 12 Fused silica bars, each glued out of 4 bar segments 122 cm long [4]. Figure 8.35 shows the nominal dimensions of each bar including the wedge. In reality it is somewhat more complicated, as bar dimensions vary and each bar box is slightly different. This has been recorded in spreadsheets [27]. Figure 8.36 shows the cross-section of a bar box containing 12 fused silica bars. Figure 8.37 shows the bar end with a mirror. There are altogether 12 bar boxes and 144 full-length bars in the entire system.

Fused silica optics: New Wedge and FBLOCK The new Wedge and the FBLOCK are made of radiation hard Fused silica Corning 7980. Corning Co. makes fused silica 7980 material in a form of boules of up to 60" diameter – see Fig. 8.38. The striae are running

Figure 8.38: An example of the fused silica 7980 material in the form of a 60 inch dia. boule made by Corning.

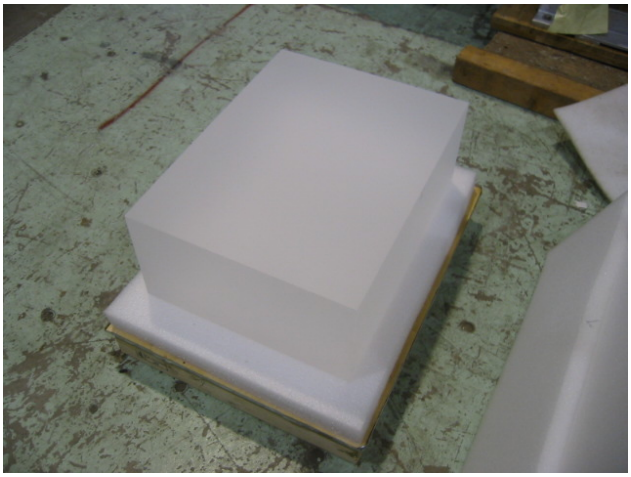

Figure 8.39: The fused silica 7980 material in a form of block ready for machining.

typically perpendicular to axis of a 60 inch dia. boule. The best homogeneity of the refraction index dn/n is along the axis of the boule. There are two types of 7980 material: (a) standard (characterized much less and therefore should be checked more), and (b) so called KrF (very characterized material; Corning qualifies striae with an optical interferometer; to get this data we will have to sign a non-disclosure agreement). We chose the "standard" material, as the cost of the KrF material is about 2-3 times higher. For the standard fused silica material these are typical specifications: (a) dn/n is less than 1 ppm over the scale of a mm. (b) The bottom-to-top of the boule along the axis: dn/n less than 5 ppm at 200 nm and better at longer wavelengths. c) dn/n is about 5-7 ppm in the direction perpendicular to the bull axis. Part-to-part variation is expected at a level of dn/n ∼20 ppm in the visible wavelength range. One should avoid the very bottom and top of the boule as there could be larger stria. To avoid it one should buy thicker boule, and this issue should be remembered for the final production. We visited the company and tested the material for stria with a laser. None was detected. Out of one boule one expects to make three blocks such as shown in Fig. 8.39. One has to pay attention to orientation of the FBLOCK within the raw block. The back side of the FBLOCK needs to be at the bottom of the boule as there is more possible contamination from sand used as a seed of fused silica material deposition.

The manufacturing was then split into three steps done in three different companies: (a) grinding final shapes about 1-2 mm oversized, (b) polishing to final size and surface polish of better than 30 Å rms, (c) coating two FBLOCK's reflecting surfaces with aluminum with SiO_2 overcoat to protect it, and (d) the final QC of finished pieces. Figure 8.40 shows the finished new Wedge and FBLOCK (before the two mirror plating step). These optical pieces were successfully produced, which demonstrates that the new camera optics is doable. However, there is a number of critical steps where error can be made, for example: (a) damages when handling, (b) surface pollution either before plating or in a final assembly, c) stria problem needs to be checked, (d) accidental swaps of correct and wrong materials, etc.

FBLOCK mirror surfaces It is absolute mandatory to have a very good surface cleanliness before the aluminum plating is attempted. Any contamination will result in peeling problems. FBLOCK's two aluminum plated mirror surfaces are protected by a SiO_2 layer. Even though there is the protection layer, mirror sur-

(a) FBLOCK after polishing but before plating.

¡¡¡¡¡¡¡ .mine

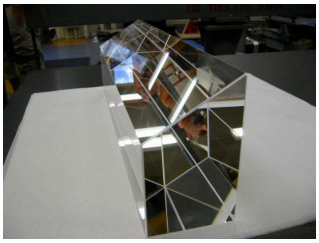

(b) New Wedge after polishing.

=======

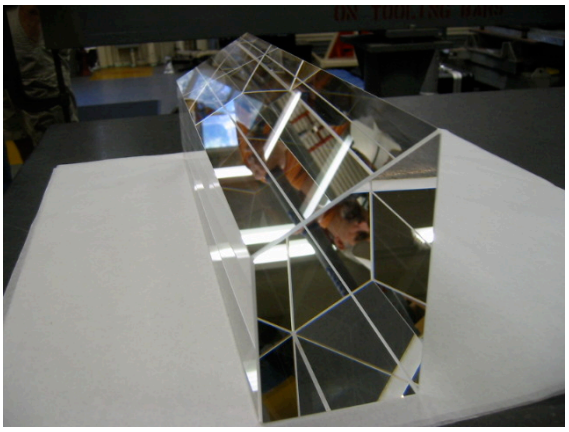

¿¿¿¿¿¿¿ .r2284

(c) New Wedge after polishing.

Figure 8.40: New photon camera parts: New Wedge and FBLOCK.

face are still fragile, especially if the surface is polluted during handling.

Another complicated issue is the FBLOCK shipping from the polishing company to the laboratory where it will be used. The FBLOCK is very heavy and its polished surfaces and two mirrored sides can be easily damaged by a rubbing motion created by shipping. Surfaces have to be protected by a plastic film during the shipment, but the film must not stick to mirror surface to cause peeling problems. Based on our tests, we have decided to use the Grafix plastic vinyl film in future, which adheres to surfaces via electrostatic forces, does not remove plated layer and does not leave a surface pollution, which would be difficult to clean.

Gluing the new Wedge to the Bar Box Window This optical coupling of Wedge to bar box window is done in the clean room. Figure 8.41 shows a detail of coupling of the new Wedge to the bar box. The coupling is done with the Epotek 301-2 optical epoxy of 25-50 micron thickness. The bottom of the new Wedge is aligned to the bottom bar surface, i.e., not to the old wedge as it has a ∼6 mrad angle. The new Wedge is centered left-right in the bar box window. This coupling is not possible to remove in the future as one would risk damaging the bar box.

Gluing FBLOCK to Wedge The optical coupling between the new Wedge and the FBLOCK is done in situ, and, in principle, it is removable. We set the gap between the new Wedge and the FBLOCK to 1 mm, and fill it with Shin-Etsu 403 RTV. In case of some problem with Fbox, one can first separate the two pieces using a thin razor wire, then clean the surfaces and finally couple again the two surfaces. The penalty for this option is that an RTV joint is not as strong as an epoxy joint. The breaking force of this RTV coupling was measured to be ∼520 kg using glass windows of the correct size (we have not done with a quartz material); it was found that this value depends strongly on the glass cleaning procedure. See Figure 8.48 and chapter "Support of Fbox in the Super$B$ magnet" for more details on the installation procedure.

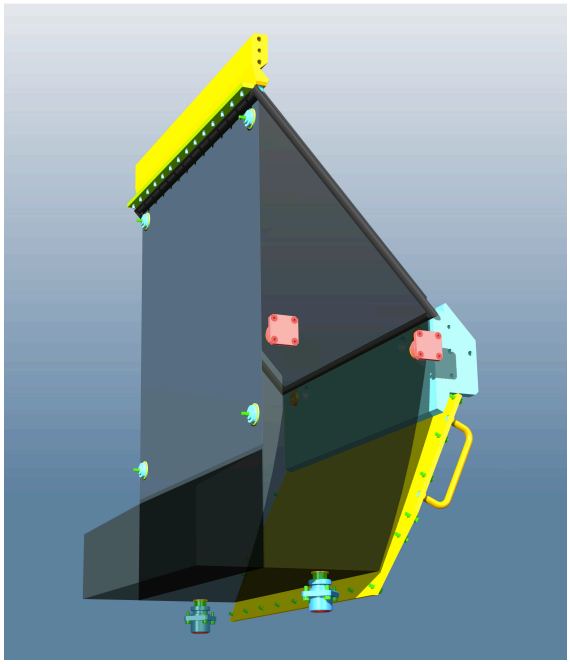

Figure 8.44: FBLOCK support buttons (small buttons are fixed, larger ones, two from the bottom and two from one side, are adjustable to keep FBLOCK stable even if Fbox, made of aluminum, expands due to thermal effects).

Fbox: Mechanical support of FBLOCK Figure 8.42 shows Fbox enclosure of the optics. Figures 8.43 and 8.44 show details of how FBLOCK is supported by plastic buttons. Plastic buttons, made of PET (polyethylene terephthalate) plastic, prevent FBLOCK optical surfaces from touching the aluminum surface of Fbox. Some buttons are fixed and some are spring-loaded. The spring loading is made using a stack of 8 belleville washers, which is the most compact way to produce predictable force. They are set to offset the total weight of FBLOCK and to take into account thermal effects. Placing the FBLOCK into the Fbox requires a very careful procedure as it is very heavy (∼80 kg) and easy to be damaged. It was very useful to work out a step-by-step procedure [28] with a dummy plastic FBLOCK [29]. At the time of TDR writing, however, we al-

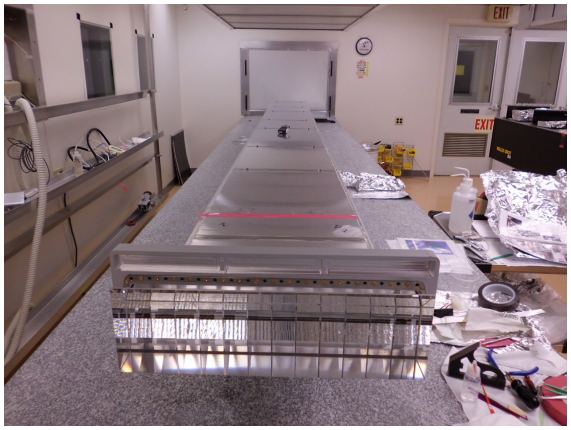

(a) The bar box with the new Wedge in the clean room.

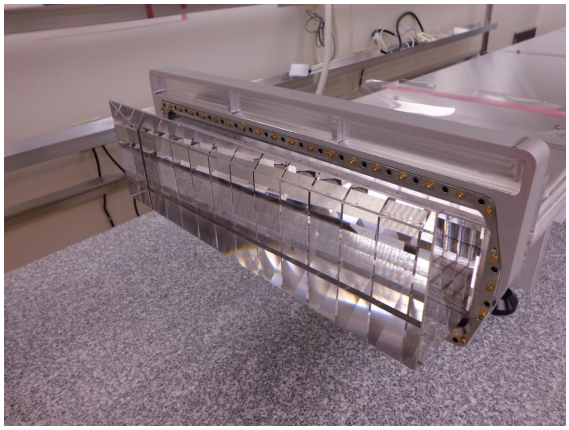

(b) Detailed view of the new Wedge and the bar box window.

Figure 8.41: Coupling of the new Wedge to the bar box.

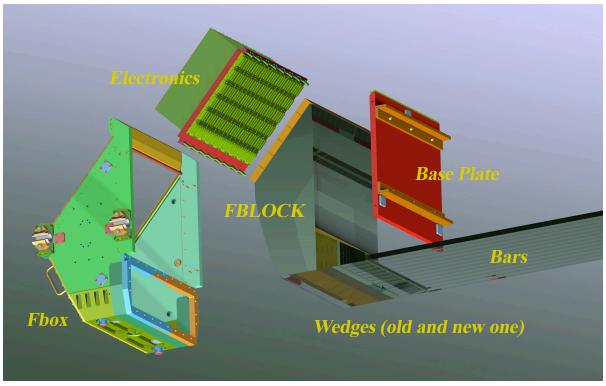

(a) Various components for the optics enclosure.

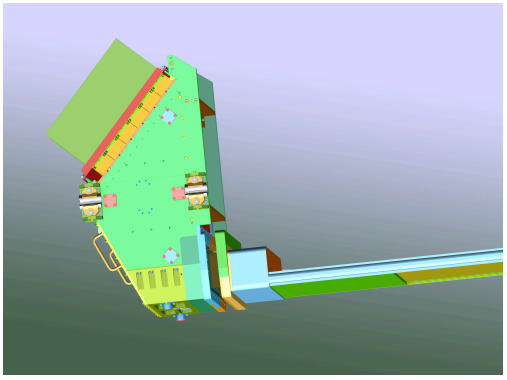

(b) Complete Fbox enclosure, including bar box.

Figure 8.42: Fbox enclosure of FBLOCK optics, including wedges, bars, detectors and electronics.

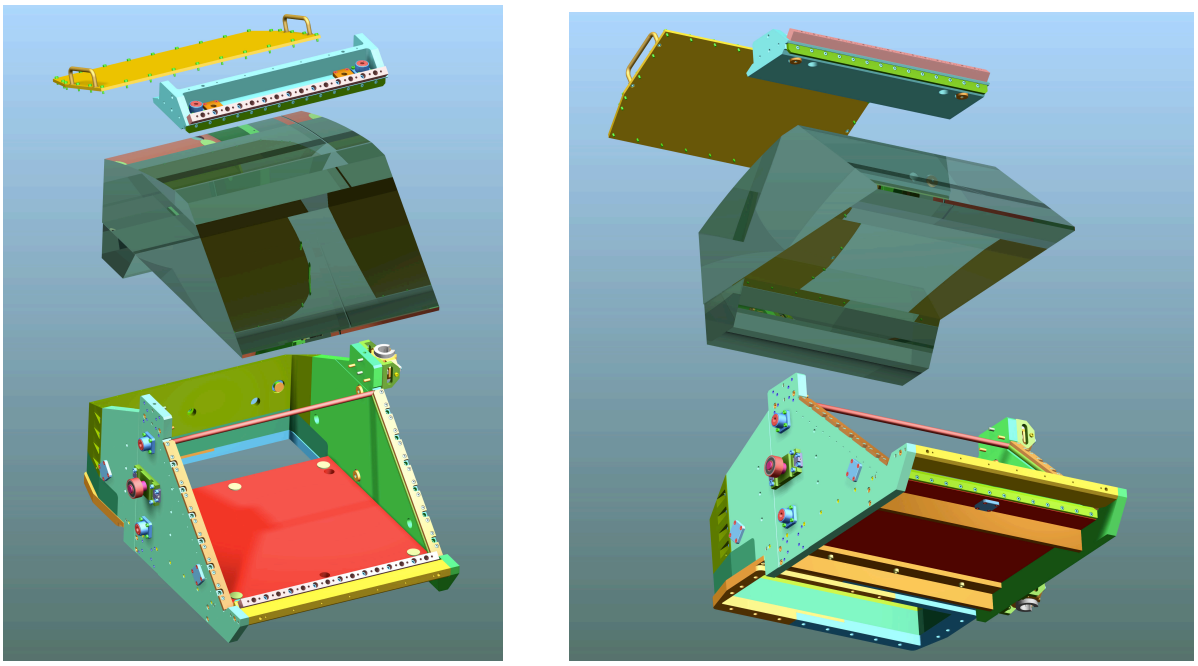

(a) Top view.

(b) Bottoms view.

Figure 8.43: Button support of FBLOCK optics in Fbox.

ready have the experience of putting together the real photon camera with the Fused Silica FBLOCK. Figure 8.45(a) shows the first step of Fbox assembly where we placed the FBLOCK on four plastic support buttons. We have chosen a four-point support rather than a three-point one because it was judged to be easier to place the FBLOCK on the Fbox base plate, which is actually a very tricky operation. The front mirror surface is protected by four quartz coupons about 1.5 mm-thick, glued to the flat mirror surface by Epotek 301-2 epoxy. These four coupons are then touching plastic buttons located in the Fbox. The idea is that a rubbing motion due to thermal effects will be better dealt with if plastic buttons slide on quartz coupons rather than on the mirror plating directly. Figure 8.45(b) shows a fully assembled Fbox with the real Fused Silica FBLOCK.

The Fbox and bar box have to be optically coupled. Figure 8.46 shows an example how this is done in the CRT setup.

Protection of optical surfaces As one deals with internal reflections, all optical surfaces have to be very clean, and therefore every part of the Fbox was very carefully cleaned before a final assembly to prevent outgassing. In addition, optical surfaces are protected against the environmental pollution and the moisture condensation by flowing a boil-off N_2 through the sealed Fbox. Fbox is sealed with a combination of Viton flat gaskets, Viton O-ring and the Gore gasket tape (near the detector area), and in some difficult sections simply with DP-190 glue. Based on experience in *BABAR* each bar box requires a flow of about 100 cc/min.

Bar box storage at SLAC Figure 8.47 shows present storage of 12 bar boxes. They are supported on pre-aligned shelves to prevent mechanical stresses due to support distortions. They are under a constant flow of the boil-off N_2 and thermally insulated. The storage box is kept at a nominal temperature of 18°C. In addition, there is no light to prevent yellowing of the Epotek 301-2 glue, an important issue to consider in future.

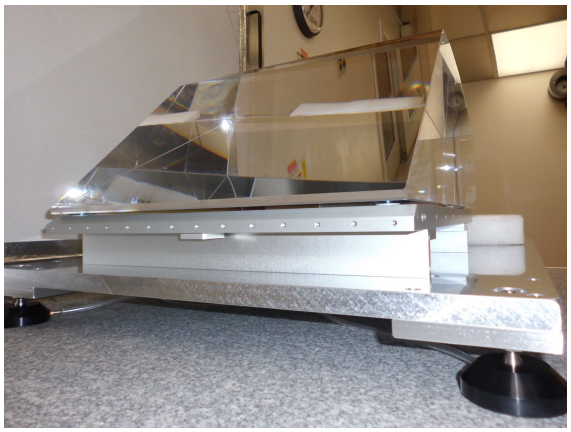

(a) FBLOCK placed on the base plate of Fbox.

(b) Assembled Fbox in front of bar box.

Figure 8.45: Fbox assembly around the real Fused Silica FBLOCK.

(a) Fbox and bar box in the CRT setup.

(b) Details of coupling of new Wedge to FBLOCK.

Figure 8.46: Fbox coupling to bar box in the CRT setup.

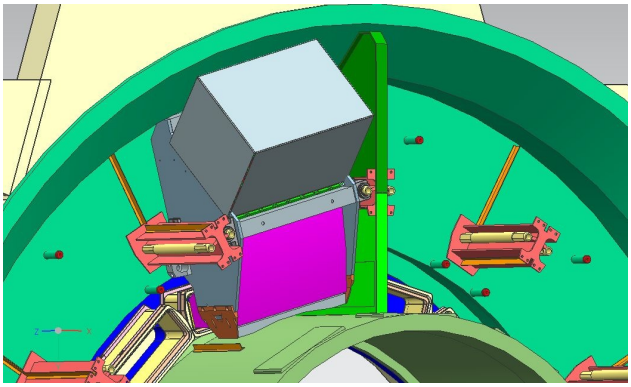

Figure 8.49: Finished installation of the camera.

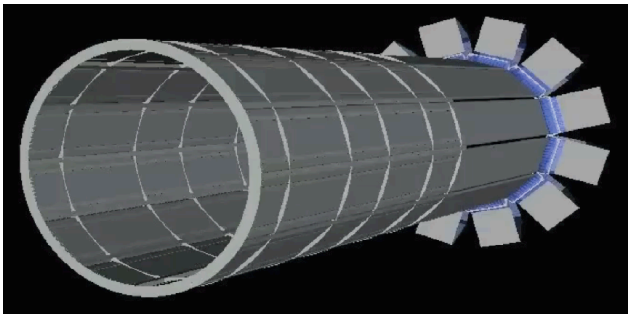

Figure 8.50: Overall view of the FDIRC layout with 12 bar boxes and 12 photon cameras.

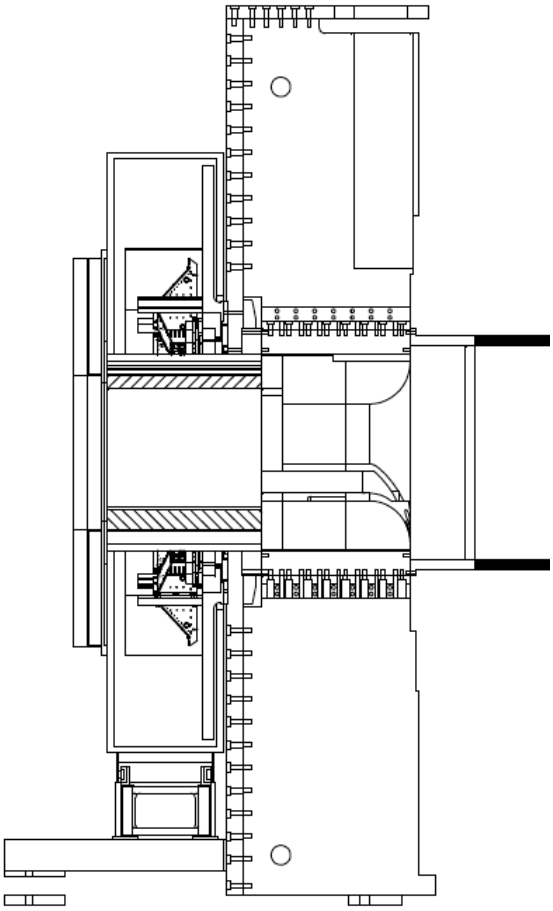

Figure 8.52: Side view of the FDIRC showing magnetic and background shields, and rails on which they move.

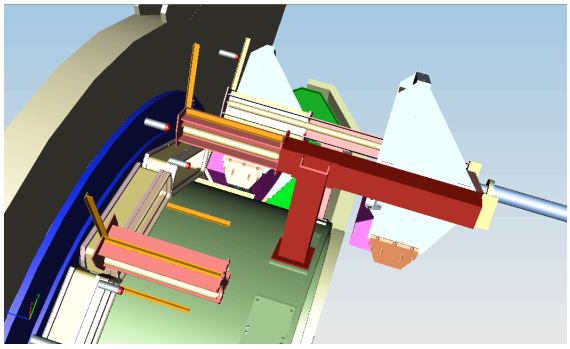

(a) Fbox installation fixture for position pointing up.

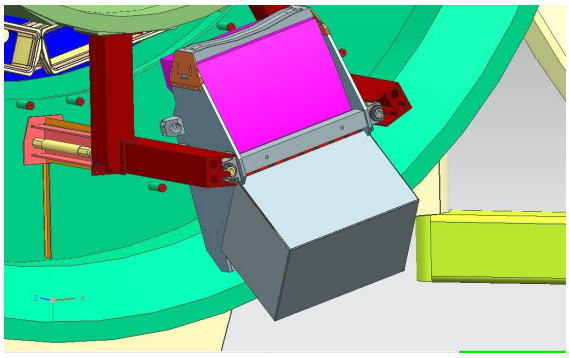

(b) Fbox installation fixture for position pointing down.

Figure 8.48: Fbox installation in the Super$B$ magnet.

Figure 8.47: Bar box storage at SLAC.

Support of Fbox in the SuperB magnet The plan is to install bar boxes with Wedge already glued to the bar box windows. The Fbox will be installed in situ. Figure 8.48 shows the procedure. The bar box has to be moved beyond the neighboring already installed Fbox, so one has enough room for gluing. With a temporary rail support it is possible to bring the Fbox close to the bar box so that the Wedge and the FBLOCK surfaces are parallel and the gap is set to 1 mm, bottom surfaces of FBLOCK and the new Wedge are aligned, and both are centered left-right. The gap between FBLOCK and the new Wedge is then filled with the Shin-Etsu 403 RTV. Once the RTV is cured, the gas sealing is made, the Fbox is pushed on the rail to its final position, and the earthquake bracing is installed. The temporary rail support is then removed. Figure 8.49 shows the finished installation.

Figure 8.50 shows the overall FDIRC detector schematic layout with its 12 bar boxes, and the 12 corresponding photon cameras. Figures 8.51 and 8.52 show overall mechanical views of the FDIRC in the Super$B$ experiment.

Background shielding to protect electronics & detectors We need background shielding to (a) reduce the contribution to the rate from the FBLOCK, which is located outside of the magnet, and (b) to reduce effect of radiation to detectors and electronics. Based on simulations, the dominant background in FDIRC is due to Radiative Bhabha scattering. The resulting background is mainly gammas, electrons, positrons and neutrons. The background estimate of the photoelectron rate without shielding is 120 kHz/double-pixel coming from the active region of bar boxes within the magnet, and 550 kHz/double-pixel coming from the FBLOCK section located outside the magnet. To reduce this rate, it is essential to provide a shield of the FBLOCK outside of the magnet. To design the shielding, two main constraints have to be taken into account: first, to allow an easy access to detectors and electronics, and then to minimize the overall weight

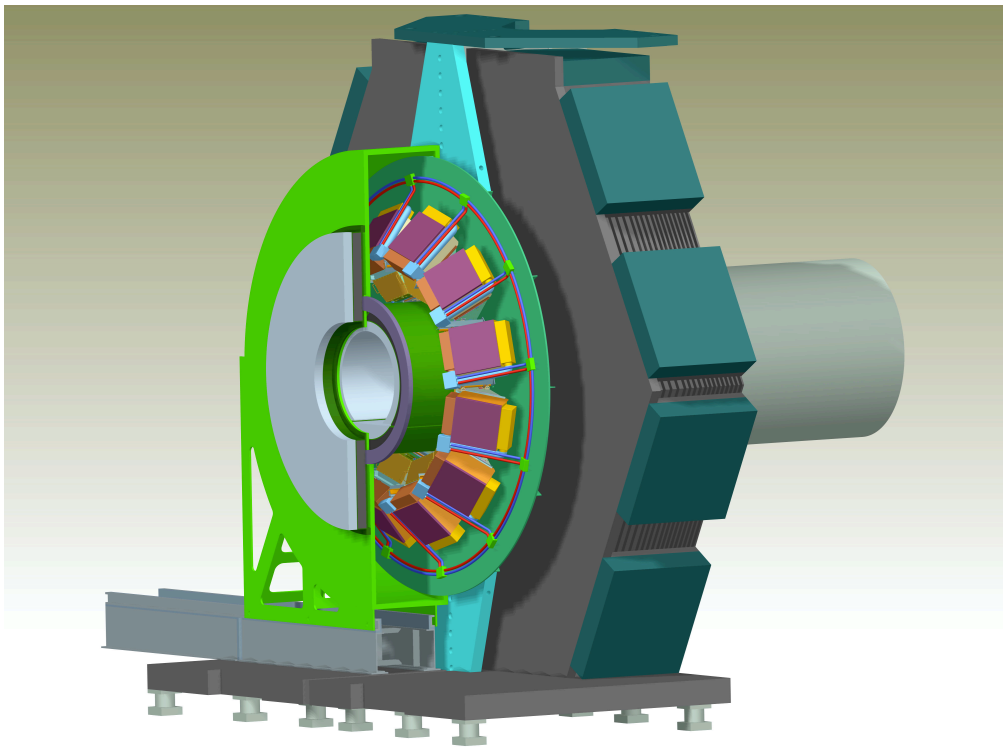

(a) A 3D view showing the new magnetic shield and background shields, and Fboxes.

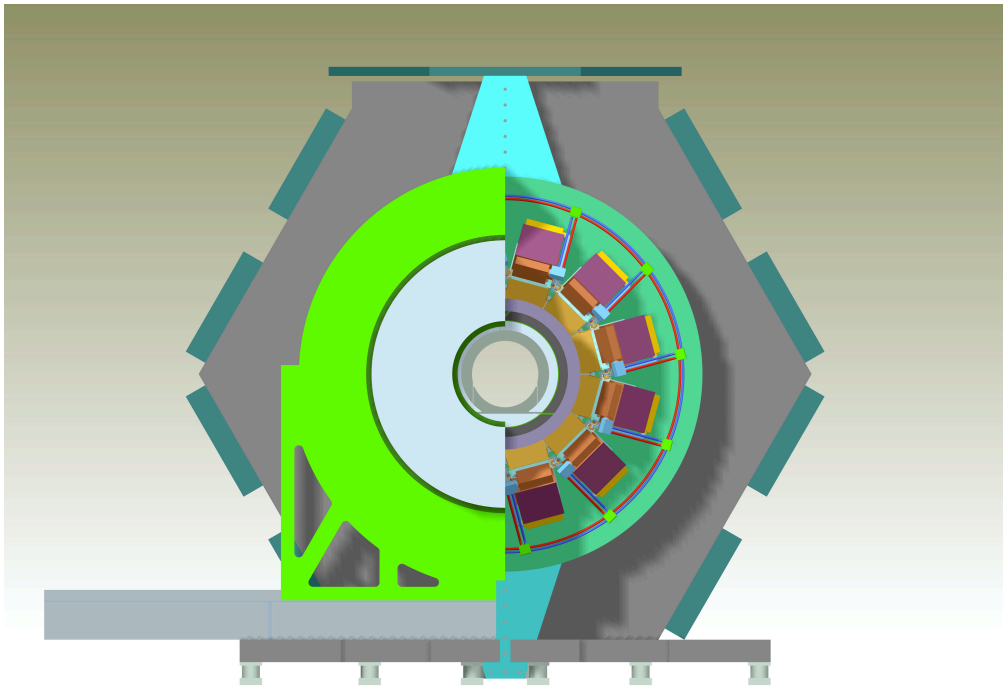

(b) Front view showing six Fboxes, the rest is hidden behind magnetic and background shields.

Figure 8.51: FDIRC in the magnet.

of the shielding. Figure 8.53 shows the present concept of the FBLOCK shielding. It consists of 10 cm of Boron-loaded polyethylene layer sitting on 10-15 cm lead-steel sandwich, both located on inner radius and front side of the FBLOCK with its detectors and electronics. The front section of the shielding is moving on the magnetic door allowing a quick access to electronics and detectors – see Figure 8.53. In addition, the beam pipe tungsten shielding was strengthened. After this shield was added into the MC simulation, the FBLOCK contribution was reduced to ∼60 kHz/double-pixel, thus making a total rate of ∼110 kHz/double-pixel, and total dose of neutrons in the electronics region was reduced to ??? n/cm^2/year.

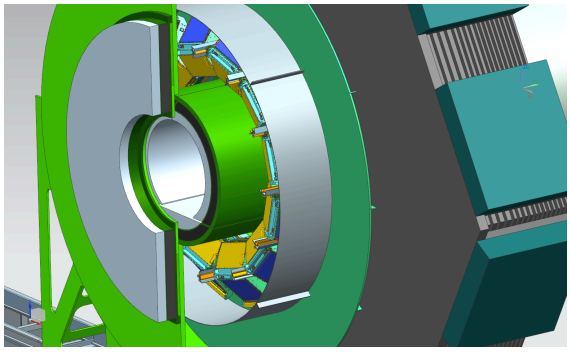

Figure 8.53: Details of local shielding around the FDIRC photon camera (a layer of 10 cm of Boron loaded polyethylene followed by 10-15 cm of lead-steel sandwich, located both on inner and front sides of the FBLOCK with its detectors and electronics).

Bar box shipment to Italy There are several issues to consider: (a) vibration and mechanical shocks, (b) thermal effects, (c) pressure changes, and (d) light exposure. Each bar box will have a container providing mechanical support and constant thermal environment. The vibrations and mechanical shocks will be mitigated by placing bar boxes on a precisely leveled support with a foam on top of it. The support structure will need telescopic mount to suppress large shocks. They will be thermally isolated and equipped with active thermal blankets to keep temperature constant. We will also provide a N_2 boil-off gas flow. Another important issue is pressure changes if air transport is used. The Hexel panels, used to construct bar boxes, do not have perforated walls, and therefore some stresses will be created. This has to be tested and carefully evaluated. Finally, bar boxes must not be left exposed to a strong light as one could yellow the Epotek 301-2 epoxy. [**To be finished or modified after we conclude all discussions**]

8.4.5 Electronics readout, High and Low voltage

The electronics for the FDIRC can be seen as an upgrade of the electronics of the *BABAR* DIRC. The new requirements of the experiment (trigger rate, background, radiation environment) and FDIRC specific requirements (resolution, number of channels and topology) have led to a similar but new design of the electronics chain.

The FDIRC electronics will handle 18,432 channels in total. The electronics chain is based on a high resolution and high count rate TDC, a time-associated charge measurement with 12 bit resolution, and an event data packing, sending data frames to the data acquisition system (DAQ). The target timing performance of the overall electronics chain is a time resolution of 100 ps rms. It has to deal with hit rate of 100 kHz per channel, a trigger rate up to 150 kHz, and a minimum spacing between triggers of about 50 ns.

The radiation level is expected to be less than 100 rads per year. The use of radiation tolerant components or off-the-shelve radiation-qualified components is mandatory. However, the expected energy of the particles may make the latch-up effect almost impossible. Thus, the design has only to take into account Single-Event-Upsets (SEUs). We selected the Actel family FPGA components for their non-volatile flash technology configuration memories, which are well-adapted to radiation environment.

Several architectures have been considered: (a) all electronics directly mounted on the FBLOCK, (b) all electronics mounted next to the detector and linked to PMTs by cables, and

(c) a part of it on the detector (the Front-end boards) and the other part, called crate concentrator , situated close to the detector (this board is in charge of interfacing with the Front-end, reading out event data, packing and sending it to the DAQ).

The first solution has been chosen as baseline for the TDR for two main reasons: (a) The cost of cables (PMT to Front-end boards) is estimated to be close to 200 kEuros (1/3 of the price of the overall electronics cost), making this solution too expensive. Moreover, the possible option to have pre-amps on the PMT bases does not prevent from having electronics and power supplies on the detector. (b) The large amount of data per channel leads to have the L0 derandomizer and buffer on the Front-end boards. The FCTS receiver could be individually located on each Front end board but the number of cables needed pushes to distribute all the control signals on a backplane. Consequently the board dedicated to receiving and transmitting FCTS signals on the backplane naturally tends to also become the event data concentrator and the link to the DAQ. The baseline design assumes a 16-channel TDC ASIC, offering the required precision of 70 ps rms, embedding an analog pipeline in order to provide an amplitude measurement transmitted with the hit time. Thanks to a 12-bit ADC, the charge measurement will be used for electronics calibration, monitoring and survey purposes. The Front-end board FPGA synchronizes the process, associates the time and charge information and finally packs them into a data frame which is sent via the backplane to the FBLOCK control board (FBC). The FBC is in charge of distributing signals coming from the FCTS and the ECS, packing the data received from the FE boards to a n-event frame including control bits and transferring it to the DAQ.

The FDIRC electronics (Amp/TDC/ADC) An earlier version of the TDC chip, offering a similar resolution, has already been designed for the SuperNemo experiment. It provides a time measurement with both a high resolution (70 ps RMS) and a large dynamic range (53 bits). The architecture of this chip is based on the association of Delay Locked Loops (DLLs) with a digital counter, all of these components being synchronized to a 160 MHz external clock.

The Super*B* chip, called the SCATS, will keep the same philosophy but the high input rate requirement lead to a complete re-design of the readout part, in order to minimize the dead time per channel by increasing the data output speed. Instead of registers and multiplexer, which are the bottlenecks of the SuperNemo chip readout, it makes use of an individual FIFO memory per channel in order to derandomize the high frequency bursts of input data. With this architecture, data from the DLLs and the coarse counters are transferred into the FIFO memory within two 80 MHz clock cycles. When the transfer is complete, the channel is automatically reset and ready for the next hit. Simulations of the readout state machine showed an output FIFO data rate capability of 80 MHz. Time ranges for the DLLs and the coarse counter can be easily customized by adjusting the output data format (16, 32, 48 or 64 bits). Therefore, this chip is suitable for various applications with either high count rate and short integration time, or low count rate and long integration time. Figure 8.54 shows the block diagram of the Super*B* FDIRC TDC chip (SCATS).

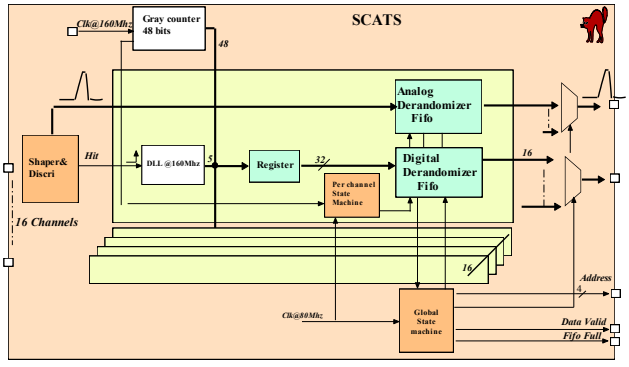

Figure 8.54: Super*B* FDIRC TDC chip (SCATS) block diagram.

A FIFO depth of 8 words (16 bits each) has been selected after simulation with a exponential distribution model of delta time between

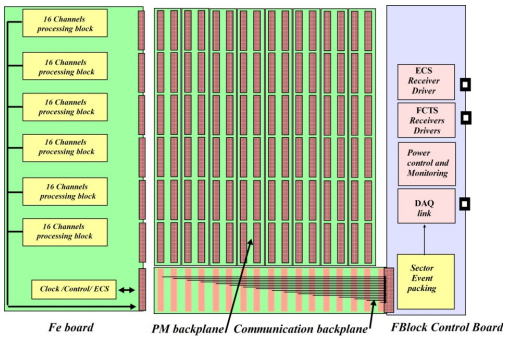

Figure 8.55: Front-end crate: PMT backplane, Communication backplane, FE-board, FBLOCK controller (FBC).

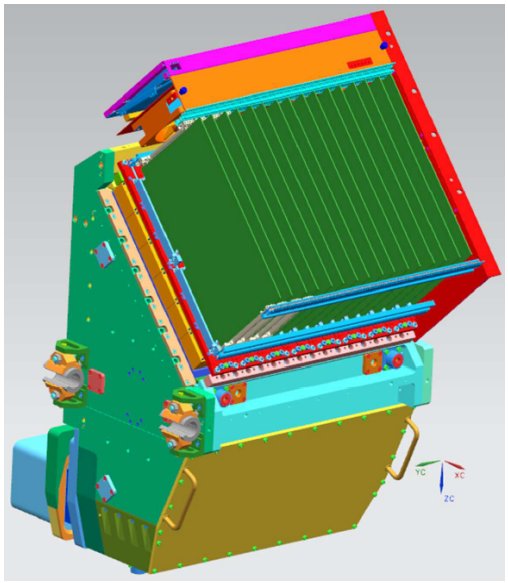

Figure 8.56: Fbox equipped with electronics and its cooling.

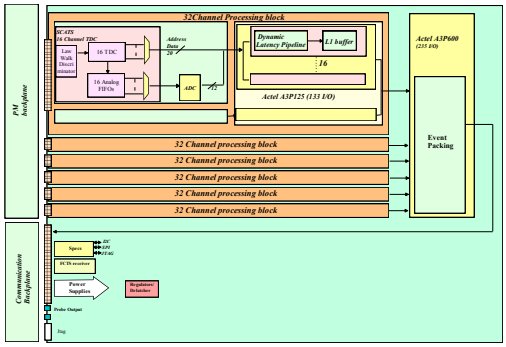

Figure 8.57: Front-end board connected to backplanes.

hits (mean rate ∼1 MHz) applied to inputs. To design this FIFO a full custom RAM has been developed. It permits reducing the size of the chip and consequently its cost. The chip is designed using known and proved mitigation techniques to face SEU issues due to the low-level radiation environment. The first version of the chip without the analog FIFO and the discriminator has been submitted in November 2011. We plan to submit by end 2012 one chip dedicated to the currently missing parts: (a) A low walk discriminator receiving the PM outputs and sending logic signal to the TDC part of the chip, and (b) a peak detector. After testing and validation, a final version of the SCATS chip will then be assembled and submitted by end 2013.

The Front-end Crate: The board input will fit the topological distribution of the PMT on the FBLOCK – see Fig. 8.55. In each sector, the PMTs are arranged as a matrix of 6 in vertical direction by 8 in horizontal direction. Each column of 6 PMTs will fit to two FE boards. One vertical motherboard will couple to one column of 6 PMTs. There will be altogether 8 motherboards. The motherboard will convert 4 H-8500 PMT connectors to two connectors, one per FE board. Figure 8.56 shows the Fbox with the front-end electronics.

The motherboard will also distribute High Voltage to the PMT if we use H-8500D. However, in case that we choose the H-8500C PMT, each PMT will have its own HV cable and HV distribution will be separate. In addition to the 8 motherboards, the backplanes receives one communication board for distributing control signals and data between FE boards and the FBLOCK control board. The FB-crate will use many features of commercial crates, such as board guides, rails, etc.

The Communication Backplane: Distributes the ECS and FCTS signals from the FBC to the 16 FE boards thanks to point to point LVDS links. Connects each FE board to the FBC for data transfer. A serial protocol will be used between FE board and the FBC in order to reduce the number of wires and consequently

ameliorate the reliability. It will also distribute JTAG signals for FPGA board reprogramming, and also distribute all signals for monitoring and control of the crate.

PMT Backplane: It is an assembly of 8 motherboards each one corresponding to column of 6 PMTs. One motherboard receives 2 FE boards. The 64 channels from 4 connectors per each PMT are merged on the motherboard into two connectors to get into the Front end board to get 16 channels per half PMT, i.e., 6 PMTs correspond to 96 channels per FE board. It also insures the ground continuity between the FE boards, the FE crate and the FBLOCK.

The Front-end Board (FE board): One FE board is constituted of 6 channel-processing blocks handling the 96 channels. The ¡¡¡¡¡¡¡ .mine channel-processing block is constituted by one SCATS chips, one ADCs, one small Actel FPGA and glue logics. The FPGA receives event data from the TDC and the converted associated charge from the ADC. From one 16 bit bus of the 16 channels coming from the TDC, it de-serializes to 16 data path where events are keeping in a buffer until they are thrown away if there are too old (relatively to the trigger) or sent upon its reception. The PGA master receives event data from the 6 channel processing blocks and packs the event. The FE board transfers the event frame in differential LVDS to the FBC via the communication backplane. ======= channel-processing block is constituted by one SCATS chip, one ADC, one small Actel FPGA and glue logics. The FPGA receives event data from the TDC and the converted associated charge from the ADC. From one 16 bit bus of the 16 channels coming from the TDC, it de-serializes to 16 data paths where events are kept in a buffer until they are thrown away if there are too old (relatively to the trigger) or sent upon its reception. The PGA master receives event data from the 6 channel processing blocks and packs the event. The FE board transfers the event frame in differential LVDS to the FBC via the communication backplane. ¿¿¿¿¿¿¿ .r2284 Figure 8.57 shows the architecture of the FE-board connected to the backplanes.

The crate controller board (FBC): The FBC board gathers the front-end data and sends them via optical fibers to the DAQ system. There will be one PBC board per crate. The board is separated in several functionalities: (a) acquisition from the front-end boards and DAQ interface, (b) spy data building, c) ECS (SPECS or...) interface, (d) de-serialize clock and control signal from FCTS, and (e) monitor the crate temperature, power supplies, fans, etc.

Cooling and Power Supply: The electronics is located on the detector in a place enclosed by the doors. There are 2 major consequences: one is the problem of the cooling which must be carefully studied in terms of reliability and capability, and the second is that the location is naturally shielded against magnetic field. Consequently the use of magnetic sensitive components as coils or fan trays is possible. An estimate of the overall electronics consumption lead to ∼6.1 kW, not including the external power supplies. This can be broken down to individual contributions as follows: (a) electronics: 0.325 W/channel, 500 W/sector, and 6 kW/system; (b) HV resistor chain: 0.19 W/tube, 9.1 W/sector, and 109 W/system. The cooling system must be designed in order to maintain the electronics located inside at a constant temperature close to the optimum of 30 degrees. The air inside the volume must be extracted while the dry, clean temperature controlled air will be flowing inside. Each FB crate will have its own fan tray like in a commercial crate. Targeting a difference of 10 degrees between inside and outside temperature drives to a rough estimate value of 300 m^3 per hour per crate. 4000 m^3 per hour can be considered as the baseline value for the whole detector.

H-8500 PMT has a AC-connection to the last dynode, and this can be used either for triggering or calibration purposes. One can do the calibration with HV off by injecting a pulse and looking at response of all anodes. Figure 8.58 shows a relative pulse height response of 64 anodes to such pulse injection [22]. It is not uniform, but it could be useful to identify possible electronics problems.

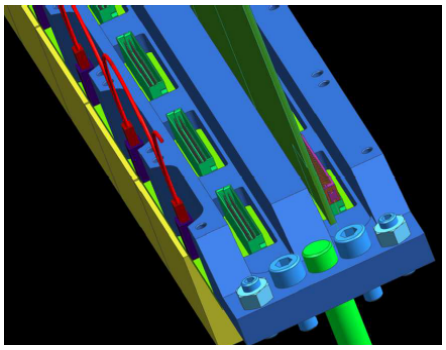

Figure 8.59: A motherboard for six H-8500D tubes, which uses ERNI SMC-Q64004 press fit connectors to couple to FE boards. The total insertion force is 160N/FE board.

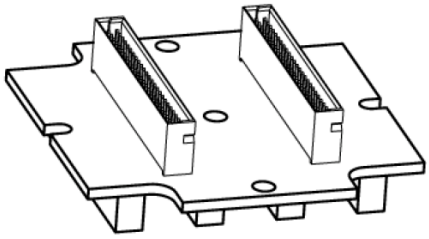

Figure 8.60: A single motherboard for each H-8500C.

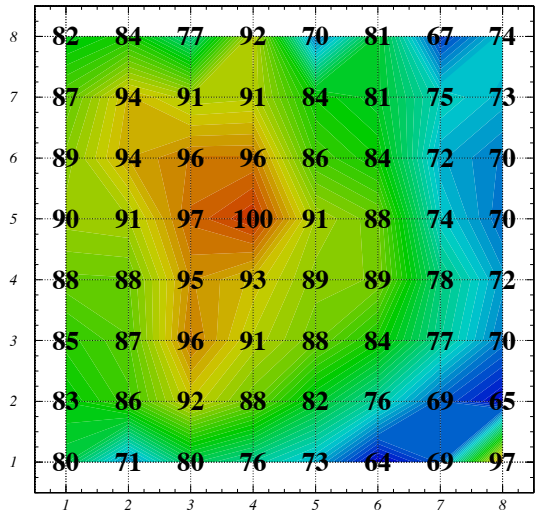

Figure 8.58: A relative pulse height response of H-8500 anodes to a pulse coupled to the last dynode [22].

Motherboard We presently consider two choices for motherboard geometry: (a) a PC-board combining a group of 6 PMTs (see Fig. 8.59), i.e., we need altogether 8 such motherboard per photon camera, or (b) a single PMT PC-board (see Fig. 8.60). The nominal choice is the 6-PMT motherboard. The total insertion force is 160N/FE board with ERNI connectors and this will have to be tested. To make sure that we do not bend pins in connectors, we will need guiding pins. We were considering also zero-insertion connectors (ZIF connectors), however, they are being discontinued and we were advised by TYCO co. not to use them. There will be 16 FE boards per one single FBLOCK. These boards will either be inserted or extracted with a help of tools and rails, a similar procedure as in some commercial crates. Figure 8.61 shows the complete photon camera with the electronics for 48 H-8500 PMTs and 1536 double-pixels.

HV distribution and HV power supplies In case that we choose H-8500C tube, HV cables will be routed under the motherboard as shown on Fig. 8.62. Drawback of this solution is that we will have 48 HV cables in a relatively small volume, and tubes will have to be rotated to fit HV cables in an efficient way.

Resistor chain of each H-8500 tube draws $\sim$150μA at -1.0 kV. The HV power supply will be CAEN, Model A1835, or equivalent. It has 12 independent channels per module, each channel capable of providing up to 1.5 kV and either 7 mA or 0.2 mA (selectable by a jumper). The current monitor has 20 nA resolution. The entire FDIRC HV system would need 48 such HV power supplies, i.e., four per each photon camera. They will be located behind the background shield in the non-radiation area.

In case that we choose H-8500D tube, HV distribution will be distributed on the board as shown on Fig. 8.63. Drawback of this solution is that we would be grouping six PMTs on one HV power supply, which would have to supply 1 A.

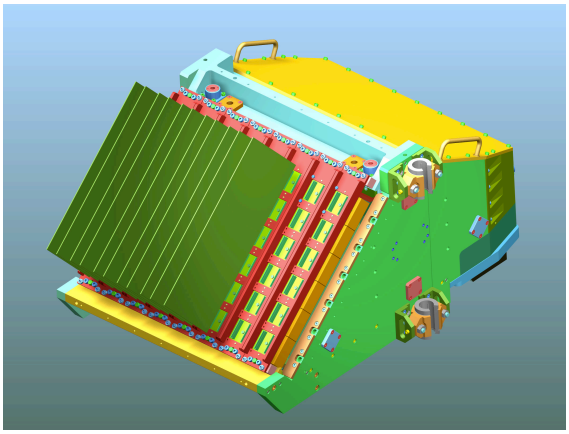

(a) Photon camera with its electronics.

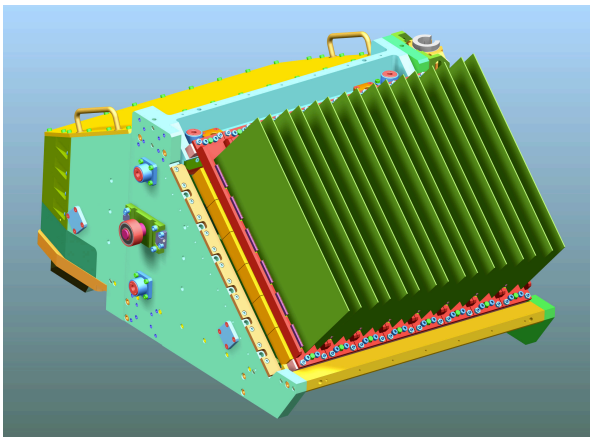

(b) Photon camera with its electronics.

Figure 8.61: Photon camera with a high density electronics for 48 H-8500 PMTs.

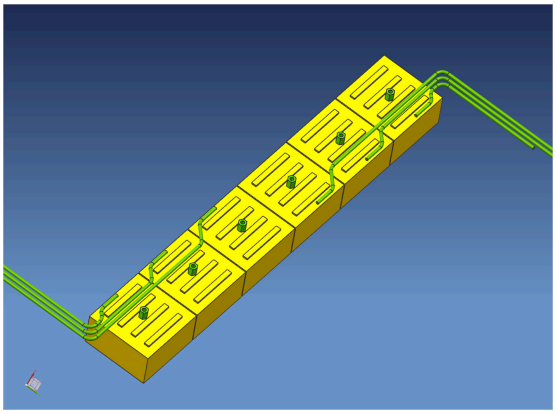

Figure 8.62: HV distribution to H-8500C tubes along the vertical column. Half of tubes are rotated to pack cables efficiently.

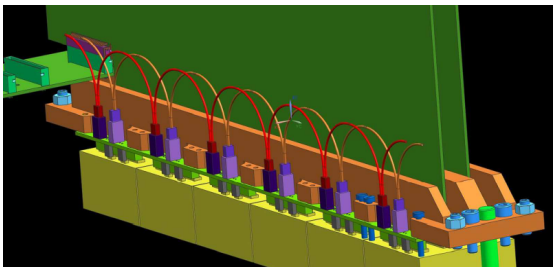

Figure 8.63: HV distribution to H-8500D tubes along the vertical column.

Support services FDIRC detector will need these services:

- A boil-off N_2 flow in each bar box up to 100 cc/min per bar box. The N_2 gas has to be distributed in stainless steel electropolished tubing.
- Total power dissipation in the entire system is about 15kW. The cooling is with water-based heat exchanger and forced air.
- Etc.

8.4.6 Integration issues

Background shield and access to detector maintenance Because the front part of the FBLOCK background shield is mounted on the magnetic door, which is on rails, it will be easy to move it sideways to allow a quick access to the detectors and electronics – see Figure 8.53.

Earthquake analysis of FBLOCK & bar box structure Bar box axial and radial constraints will be equivalent to *BABAR* DIRC setup. The Fbox system itself is not critical, being compact, rigid, and with very limited lever arms. Of course the support disk and the support rails structures of the Fbox must be adequately stiff to avoid resonance in the typical quake range. Axially, the Fbox must be constrained as bar box. The increased risk relative to *BABAR* DIRC consists in the coupling of Fbox and bar box. However, the presence of a RTV gluing layer instead of a rigid coupling and an adequately stiff support of the Fbox should prevent risks due to this coupling. Calculations are in progress.

PMT protection (helium, large backgrounds) It is well known that the PMT operation can be affected by a helium contamination, which can penetrate the PMT glass. These atoms convert to ions in the avalanche process, which can drift back to the photocathode creating secondary photoelectrons, often called 'after pulses'. Therefore, just like in case of the *BABAR* DIRC (which had ∼11,000 PMTs) we assume that any helium leak checking close to the Super*B* detector by accelerator people must not be allowed. Even if it is done far away in the tunnel, air draft could bring it to the detector. We will need a helium detector to monitor this.

Reference [30] summarizes the effect of helium contamination on a PMT. We should stress, however, that we did not do any experimental study with the H-8500 tube up to this point, i.e., we assume that it behaves the same way as any other PMT from this point of view, i.e., that its 64 feedthroughs do not affect it.

The ion contamination in a PMT can be estimated by measuring the after pulsing rate. Figure 8.64 shows how the H^+, H_2^+ and He^+ ion contamination [22] affects a time spectrum of afterpulses in a H-8500 tube. The total measured rate of after pulses was less than ∼1% rate for this tube. This measurement will have to be part of PMT QC procedure to weed out bad tubes. It will be useful to repeat it periodically on some tubes during the Super*B* data taking.

The H-8500 PMT sensitivity to large background were discussed in the chapter about PMT background rate and aging issues. Here we add only that a PMT protection strategy, for example an automatic HV lowering to 80% value if a certain background level is reached, has yet to be developed.

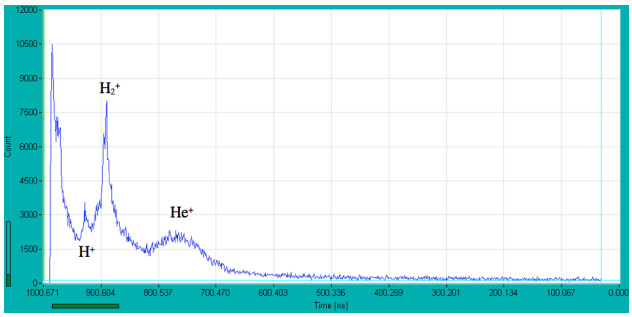

Figure 8.64: A time spectrum of after pulses showing H^+, H_2^+ and He^+ contamination [22].

8.4.7 FDIRC R&D Results until now

Test beam results from the first FDIRC prototype Figure 8.6 shows the prototype. This prototype was tested in a 10 GeV electron test beam at SLAC. This beam entered the bar perpendicularly. It was a very successful R&D program resulting in a number of very useful results [9, 10, 11], which can be summarized as follows:

- Learned how to operate new fast highly pixilated detectors (Hamamatsu H-8500 and H-9500 MaPMTs; Burle MCP-PMTs). The H-9500 MaPMT was arranged to have 3 mm × 12 mm pixel size, while the other two tubes had 6 mm × 6 mm pixels.
- Test achieved ∼10× better single-electron timing resolution than DIRC: σ_{H-8500}∼240 ps, σ_{H-9500}∼235 ps, and $\sigma_{MCP-PMT}$∼170 ps.
- Learned how to design a new optics, which is a combination of pin hole coupled to focusing optics, resulting in ∼25× smaller photon camera that the *BABAR* DIRC SOB.
- This was the very first RICH detector establishing that the chromatic error can be

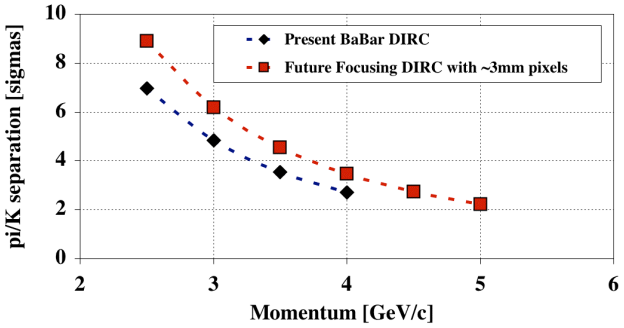

Figure 8.66: Expected $K - \pi$ separation as a function of momentum for a FDIRC detector equipped with H-9500 MaPMTs with 3 mm × 12 mm pixels, compared to the *BABAR* DIRC performance [11].

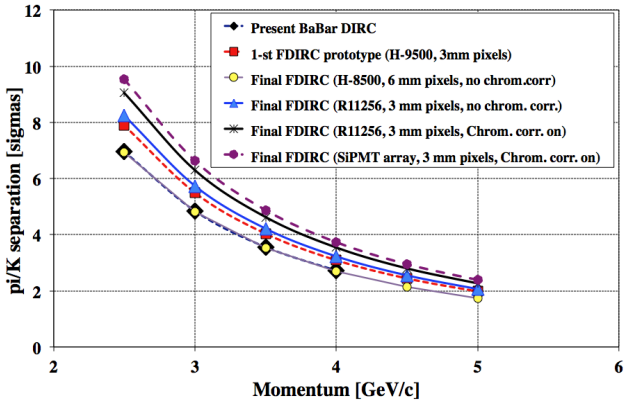

Figure 8.67: Expected $K - \pi$ separation as a function of momentum for various detector schemes, including R11265 pmt and a SiPMT 8 × 8 array (3mm pixel sizes).

corrected by timing – see Fig. 8.7. To be able to do such correction, one needs to achieve a timing resolution at a level of ∼200 ps per single photon, and the photon path length needs to be longer than 2-3 meters. The fact that FDIRC bars are longer due to a penetration of the magnet iron helps to improve this correction.

- With 6 mm size pixels we could reproduce *BABAR* DIRC performance of Cherenkov angle resolution of ∼10 mrad per single photon if we do not perform the chromatic correction. With the chromatic correction one could improve this resolution by 0.5-1 mrad for photon path lengths longer than 2-3 meters – see Fig. 8.5.

- With 3 mm size pixels we could substantially improve on the FDIRC performance – see Figure 8.65. Figure 8.66 shows the expected overall PID performance relative to the *BABAR* DIRC. Clearly, smaller binning in the y-direction would be beneficial to improve the overall performance. However, Hamamatsu has strongly discouraged us to switch to the H-9500 tube as it could not guarantee the deliveries. In addition, the cost of H-9500 tube would be higher. Instead they encourage to use R11256 tube, which would give use 3 mm × 12 mm pad sizes, and possibly QE ∼36%. Figure 8.67 shows the overall PID performance for various detector schemes. The comparison also includes the new Hamamatsu 8 × 8 SiPMT array, where we assumed PDE ∼52% (this is just an example as we do not assume to use it due to its large random noise rate at room temperature and further worsening by a possible neutron damage).

- Discovered a new Cherenkov ring aberration, which worsens the resolution near the Cherenkov wings – see Figures 8.8, 8.9.

CRT test results from the first FDIRC prototype The first prototype was also tested in the cosmic ray telescope (CRT) [31]. The SLAC CRT setup consists of energy absorber made of 4 ft-thick iron, which provides a muon energy lower cut-off of 1.6 GeV. It also provides tracking with 1.5 mrad resolution over angular range of dip angles within 15 degrees. This was also a significant test because it allowed to investigate the Cherenkov angle resolution with 3D tracks [32]. Results can be summarized as follows:

- We learned how to handle 3D tracks in the Cherenkov angle analysis (during

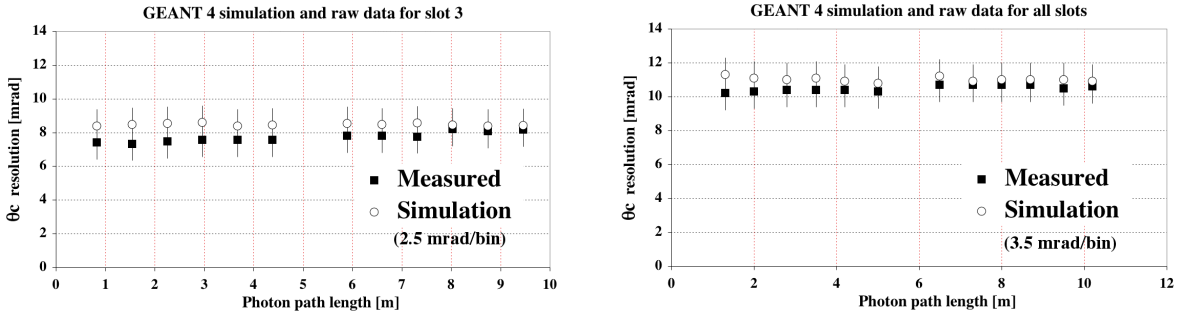

(a) Resolution with 3 mm pixels.

(b) Resolution with 6 mm pixels.

Figure 8.65: Measured and simulated Cherenkov angle resolution without chromatic correction [11]

the beam test tracks entered perpendicularly [9], [10], [11]).

- Tail in the Cherenkov angle distribution is related to the ambiguity treatment and it is more significant for 3D tracks. The first FDIRC prototype had only two ambiguities: we could not tell a sign of photon vector in the x-direction for photons exiting the bar end, and therefore in the analysis we had to consider both signs. In the final FDIRC prototype we will have six ambiguities. This ambiguity effect enhances the tail as one cannot always reject wrong solution, and it is magnified by a presence of background such as delta-rays or showers accompanying CRT muons. The CRT setup is very good to learn how to deal with it. The major conclusion is that one has to use a quantity dTOP = $\text{TOP}_{measured}$ - $\text{TOP}_{expected}$, where TOP = time-of-propagation of photon in the bar. One makes a tight cut on dTOP and this helps to reject the background, however, it does not help the ambiguity problem.

- Running CRT continuously allowed to test various versions of electronics very conveniently, and to produce the Cherenkov angle resolution under real conditions. So far, every electronics used in the CRT setup, was caught to have some problems, which then had to be fixed. Therefore, we consider the CRT test to be very useful. It is interesting to point out that Belle-II TOP people are trying to create a similar CRT setup.

- The CRT trigger was also used to trigger a PiLas laser diode, which provided a single photoelectron monitoring of all pixels all the time while we were running. The laser trigger did not overlap with the CRT data to avoid a confusion. This allowed to study the stability of FDIRC timing.

- This feature has not been studied so far, but we plan to test the Final FDIRC prototype at high rate background in the CRT setup. This will be done by admixing an asynchronous random light source to the laser calibration signal, while taking a normal CRT data. This task will be accomplished with a fiber mixer, which will mix the laser signal with the random light source. In this way we can study the reconstructed Cherenkov resolution as a function of the random background in a controlled way, and see at what point the reconstruction algorithm breaks down. At the same time we will be monitoring the timing resolution deterioration using the laser signal.

Scanning setups to test H-8500 PMTs and Electronics We have several PMT scanning setups located at SLAC, Maryland, Bari, Padova and LAL-Orsay. These setups differ in their

capabilities, designs and electronics. Although these setups did not use yet the final electronics, they were nevertheless already very useful to reveal many H-8500 detector details. So far, the following topics have been studied in some details: (a) efficiency uniformity across PMT for 15 tubes, (b) gain uniformity for 15 tubes, (c) cross-talk, (d) charge charing, (e) after-pulses, (f) pre-pulses (amplification starts on first dynode), (g) anode response to pulses on the last dynode (for calibration purposes), etc. We used many results from these tests throughout this TDR chapter.

In these studies we learned that:

- Based on a study of 15 tubes (960 pixels), the gain uniformity among pixels is typically better than 1:2.5.
- The single photoelectron timing resolution (TTS) has a structure within each pad.
- The charge sharing effect is very small in this particular tube due to its electrode structure, and it is not worthwhile to utilize it to reduce the effective pixel size, which would help to improve the Cherenkov angle resolution.
- Although one can find a good spot in the H-8500 PMT giving a TTS resolution of ∼140 ps (see Fig. 8.14), if one averages over an entire pixel area the TTS resolution is more like $\sim 200 - 250$ ps, with edge pixels being worse (see Fig. 8.15).
- A typical pixel-to-pixel cross-talk in H-8500 tube is about 3%, judging from the scope measurement of pulse amplitudes on neighboring pixels using the SLAC amplifier – see Fig. 8.16.

8.4.8 Ongoing FDIRC R&D

Experience with the final FDIRC prototype in CRT During this stage we learned many things.

- It is possible to build this kind of optics, for affordable cost and within the required tolerances.
- It is possible to handle heavy FBLOCK fragile optics and to assemble Fbox around it.
- We learned how to couple bar box window to the new wedge with Epotek-301 glue.
- We learned how to couple optically the FBLOCK to the new Wedge. It is done with a 1 mm-thick RTV. It is a very large area optical coupling and we learned how to develop a bubble-free coupling. We have demonstrated that this RTV coupling can be cut by a razor wire, surfaces cleaned and glued again.
- The full size FDIRC prototype is now being studied in the cosmic ray telescope.

Detector studies in various scanning setups The study of the H-8500 PMT continues in several scanning setups: SLAC, Maryland, Bari and Padova. So far all tests used various kinds of electronics. It is essential to repeat some of these studies with the final electronics. This, however, cannot be done sooner than in 2013. We also want to make a decision of other tube possible tube choices, namely Hamamatsu H-9500 and R-11256.

Electronics R&D The final electronics is being developed at LAL. The detector motherboard is being designed at LAL, Padova and Bari. Once the first prototype of a small single-PMT motherboard is tested and understood in the Bari scanning setup, 2 complete packages will be available to join the CRT test at SLAC.

8.4.9 System Responsibilities and Management

Management board structure The PID group has a management board, where each institution will have a representative. The role of this management board is to resolve monetary, manpower and other global issues within various institutions as they come during the construction stage. It is assumed that this group will meet with PID conveners during collaboration meetings.

Institutional breakdown by task Table 8.2 shows a breakdown of tasks for various institutions. This should be considered as an expression of interest in a given topic at present. More detailed subdivision into deliverables will be made once the project is in more advanced stage.

8.4.10 Cost, Schedule and Funding Profile

Budget Table 8.3 shows a breakdown of major M&S costs. The cost of FDIRC optics is based on our experience building the FDIRC prototype; it is based on US-based sources. It is interesting to point out that the cost came down by a factor two by the time we finished building it, mainly because we were working directly with companies involved building it. Therefore we have real companies behind each task, and, in principle, we are ready to build it. But one should realize that this is the cost as of the end of 2011.

Schedule and Milestones The FBLOCK production determines the entire production time line, i.e., all other tasks take less time. Figure 8.68 shows the present estimate of FBLOCK production (for clarity we show only 2 FBLOCK production cycles). The manufacturing speed is limited by FBLOCK machining and polishing. The total duration of FBLOCK production, as it stands now, is ∼28 months. The next longest part of the project is the PMT production, which will take about 2 years, including procurement, delivery and testing.

Critical path items Clearly, the most critical path items are: (a) machining and polishing of the FBLOCK optics and (b) delivery of 600 Hamamatsu H-8500 PMTs. The FBLOCK delivery is controlled by the production capacity, which limits deliveries to one FBLOCK every 6-8 weeks. We will try to find a way to speed it up, or find a parallel production possibility, but it is generally difficult to replicate relevant experience with a different company when one deals with a non-standard optics. Hamamatsu company told us that they can deliver 600 H-8500 tubes over a period of 2 years, which is about 25 tubes per month. It is important that we check that delivered tubes have required performance. We may have to split testing into 2 different scanning setups to be able to verify 25 tubes per month.

==========

8.5 A possible PID detector on the SuperB forward side

8.5.1 Physics motivation and detector requirements

The Super$B$ barrel region is covered by a dedicated PID detector: the FDIRC, described in the previous sections of this report. The information from this detector, combined with the energy losses from the DCH, ensures a good π-K separation up to about 4 GeV/c.On the other hand, PID in the Super$B$ endcaps only relies on dE/dx measurements from the tracking system. In the high momentum region, pions and kaons are only separated at the $\sim 2\sigma$ level – however, the use of the cluster counting method in the DCH [**Ref!? Option or baseline?**], still under study, would increase this separation. Moreover, dE/dx distributions exhibit a 'cross-over' π/K ambiguity region around 1 GeV/c, inside which charged hadrons cannot be properly identified as the energy loss curves overlap.

Improving PID in these two regions requires thus new dedicated detectors which should be both powerful and relatively small. The latter characteristic is needed in order to fit in the limited space available in the endcap regions.

In the backward side – where the particle momentum is quite low in average –, the EMC group is proposing to install a veto calorimeter [**Reference!? Sentence to be updated!?**] to improve the Super$B$ energy measurement. Should this device be fast enough, it would allow one to separate pions from kaons using the particle time-of-flight.

Due to the Super$B$ boost, the forward region of the detector corresponds to a fraction of

Item	Task	Institution
1	FBLOCK optics	SLAC, Padova, Bari
2	Wedge optics	SLAC, Padova, Bari
3	Gluing Wedge to bar box	SLAC
4	Fbox	Padova, Bari, SLAC
5	Assembly of optics to Fbox	SLAC, Padova, Bari
6	Fbox mechanical support	Padova, Bari, SLAC
7	Electronics	LAL
8	Motherboard	Padova, LAL, Bari
9	Electronics cooling	LAL, Padova
10	Detector testing	Maryland, LAL, Bari, Padova, SLAC
11	Final FDIRC testing in CRT	SLAC, Maryland, LAL, Bari, Padova
12	High voltage	Padova
13	Low voltage	LAL
14	Fiber calibration	Maryland
15	Fast simulation	LAL
16	Full simulation	Maryland
17	Final installation in Super$B$	SLAC, Padova, Bari
18	Thermal protection	LAL, Padova
19	Background monitoring	SLAC, LAL, Padova
20	Helium protection	Bari, ???
21	Boil-off nitrogen distribution	Cabbibo lab, SLAC, Padova
22	Essential services	Cabbibo lab
23	On-line monitoring	???

Table 8.2: Institutional expression of interest in a given topic at present (SLAC involvement is only tentative at present).

WBS	Task	M&S Cost (Euros)
1.3	FDIRC Barrel (Focusing DIRC)	4.2M total
1.3.1	Radiator Support Structure (new support disc)	18.8k
1.3.2	New magnetic door and inner cylinder	100k
1.3.3	FDIRC photon camera background shielding	125k
1.3.4	Background shield displacement system and rails	31.3k
1.3.5	Bar box transport to Italy	125k
1.3.6	Radiator box/Photon camera assembly	1160k
1.3.6.1	FBLOCK and Wedge material and raw finish (12+2)	761.6k
1.3.6.2	FBLOCK polishing (12+2)	235.2k
1.3.6.3	FBLOCK mirror plating (12+2)	31.25k
1.3.6.4	New Wedge polishing (12+2)	19.04k
1.3.6.5	Gluing Wedge to Bar Boxes	12.5k
1.3.6.6	Clean room (in Italy)	25k
1.3.6.7	Clean room fixtures	25k
1.3.6.8	Shipping charges within US and for shipping to Italy	12.5k
1.3.6.9	QC of optics with digital arm	12.5k
1.3.6.10	Storage cost, services in Italy	25k
1.3.7	Photon Camera mechanical boxes	293.75k
1.3.8	Photodetector assembly	2004.5k
1.3.9	Calibration System	75.6k
1.3.10	Temperature, water, nitrogen, helium leak safety system	10.5k
1.3.11	Alignment services	37.5k
1.3.12	Mechanical Utilities	62.5k
1.3.12	System Integration	125k

Table 8.3: M&S cost breakdown of major PID tasks, except electronics (FDIRC optics cost estimate is based on US-based quotes only and for quantity of 12+2) For currency conversion we used: 1.216 $\times$ Euro = 1 dollar.

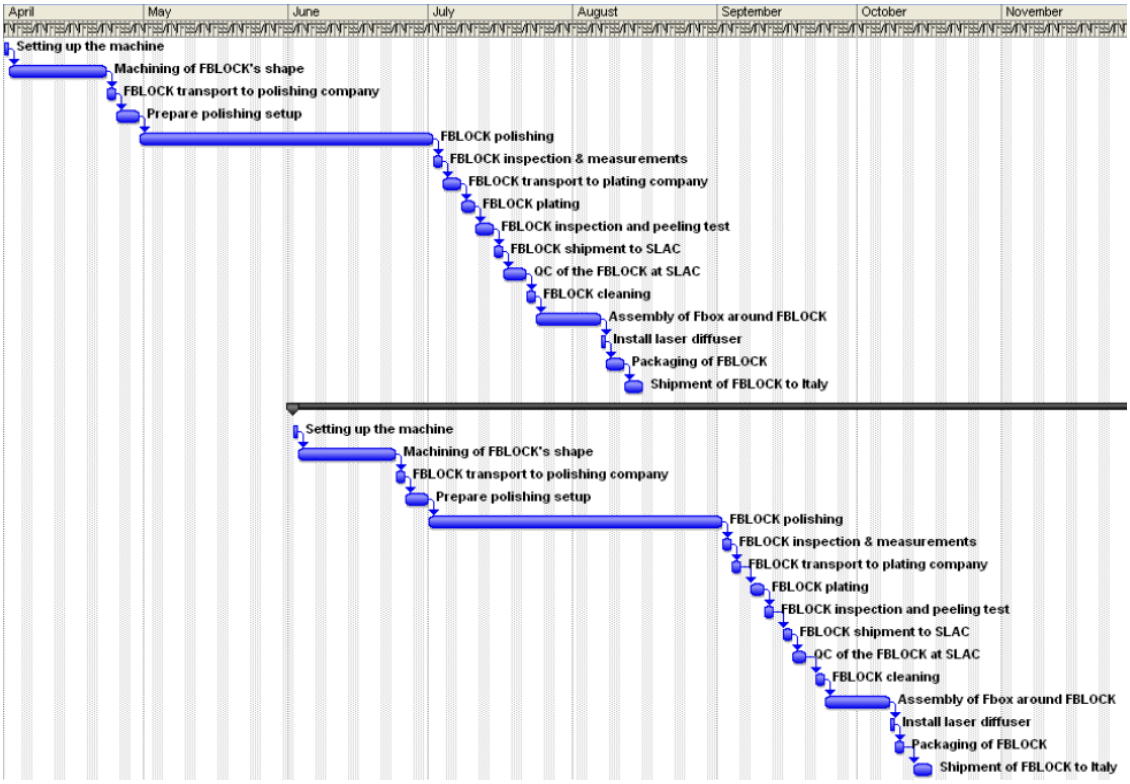

Figure 8.68: FBLOCK production schedule (2 FBLOCK production cycles only).

the geometrical acceptance larger than its angular coverage in the laboratory frame – about $17 - 25°$ – while the particles have higher momentum in average. Therefore, a forward PID detector should be efficient from about 1 GeV/c to 3 GeV/c.

Physics-wise, the Super$B$ performance would benefit from improved PID in many areas:

- larger efficiency in various rare and exclusive B decays;
- reduced background;
- improved exclusive reconstruction of hadronic and semileptonic B channels. This technique is used for recoil physics analysis of rare and hard-to-reconstruct decays. Based on the coherent production of a $B\overline{B}$ pair at the $\Upsilon(4S)$, it first identifies events for which one of the B's, the B_{tag}, is fully reconstructed. Once this is done, the rest of the event automatically corresponds to the (other) signal B: B_{sig}. This constraint provides additional kinematical information on B_{sig} decays which would otherwise be less constrained – e.g. because of undetected neutrinos in the final state. Each of the hundreds of exclusive modes used by this method to reconstruct the B_{tag} is characterized by two numbers: its reconstruction efficiency and the purity of the selected sample. Both numbers increase with an improved PID and the larger the number of particles in the final state, the faster the gain.

Given the integration constraints in the Super$B$ forward region [**update needed!?**], a forward PID detector must be compact. A total thickness around 10 cm would likely put some constraints on the position and dimensions of the DCH and of the forward EMC, but studies [**reference from Matteo!?**] have shown that such changes would only have a limited impact on the performances of these two devices. Yet, the forward PID detector should add the smallest possible X_0 fraction in front of the calorimeter to limit preshowers.

Finally, the cost of the forward PID detector should be moderate in comparison to the one of the FDIRC as it covers a much smaller fraction of the Super$B$ acceptance.

8.5.2 Forward PID R&D activities

From early 2009, several possible designs of forward PID detectors have been studied within the PID group. The proposals were submitted to a task force representative of the whole collaboration. It was charged to review the different designs and to make recommendations to the Super$B$ Technical Board, which would then take the final decisions This step was completed in June 2011 and lead to the choice of a technology, as reported below. In the following paragraphs, the main characteristics of the different proposals such as their advantages/drawbacks are briefly summarized.

Focusing aerogel RICH (FARICH) Ring Imaging Cherenkov detectors are the most powerful instruments used for hadron identification in the momentum region from ∼0.5 to ∼100 GeV/c. The use of multilayer aerogel radiators in proximity focusing RICH detectors (Focusing Aerogel RICH) significantly improves PID performance capabilities of such detectors in comparison with a single layer aerogel RICH. To provide PID at momenta below 0.6 GeV/c we put an additional radiator with the high refractive index.

The FARICH system was suggested for a particle identification in the forward part of the detector. It was known that the main drawbacks of the FARICH in the SuperB detector are space considerations and cost. One of the factors which drives the cost of such detectors is the number of channels. This design was optimized to minimize the number of channels and the total thickness of the system while keeping PID performance on a high level. The concept of the system is presented in Figure 8.69. The main parameters of the system are:

- Expansion gap – 65 mm (total thickness of the system ∼150 mm),
- Photon detectors – the Photonis MCP PMT with 6x6 mm anodes (8x8 matrix),

photoelectron collection efficiency – 70%, geometrical factor – 80%,

- 2-layer 'focusing' aerogel, n_1=1.039, n_2=1.050, the total thickness 30 mm,
- NaF radiator, n=1.33, 5 mm thickness
- Number of PMTs – 312
- Number of channels – 20000
- Amount of the material (X/X_0) – 25% = 2.4%(aerogel) + 4.3%(NaF) + 10%(MCP PMT) + ~8% (support, electronics, cables).

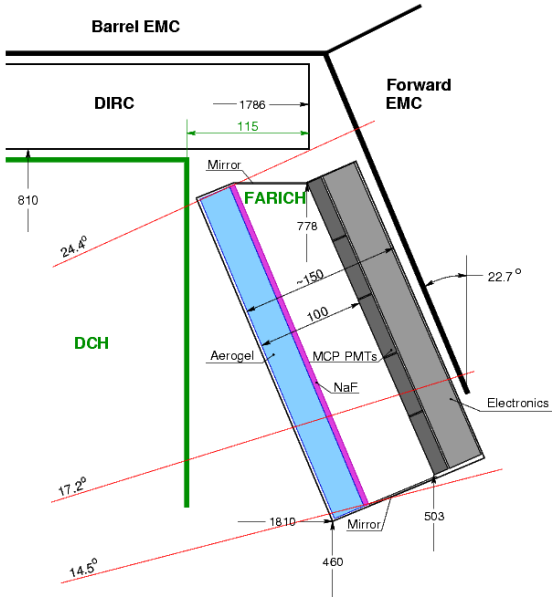

Figure 8.69: Possible FARICH detector layout in the SuperB detector.

The Monte Carlo simulation was done for the proposed configuration. The numbers of detected photons for $\beta = 1$ particle are 16 from the aerogel radiator and 10 from the NaF one. The detector will be able to perform the π/K separation at 3σ level and better from 0.2 to 5 GeV/c, the μ/π separation — from 0.13 to 1 GeV/c, π/p separation — from 1 to 8 GeV/c.

The main goal of the test beam experiment was to demonstrate 'focusing' capabilities of a real multilayer aerogel radiator at short expansion gap and to measure the contribution from aerogel radiator into the resolution on the Cherenkov angle. The measured aerogel tile had 4 layers, maximum index of refraction of the layer was 1.05 and total thickness of 30 mm. The FARICH prototype used 32 MRS-APDs (SiPMs) from the CPTA company (Moscow, Russia) as photon detectors. The APDs active area was 2.1x2.1 mm^2. The custom made discriminator boards and the CAEN V1190B multihit TDC were used for the signal readout. The test beam facility was constructed at VEPP-4M collider at the Budker INP in Novosibirsk for a detector development. The test beam apparatus also comprised the trigger and veto scintillation counters, the coordinate drift chambers and the NaI calorimeter.

During the experiment we have measured simultaneously coordinates of the track of 1 GeV/c electrons and coordinates of the detected Cherenkov photon from multilayer aerogel radiator. Having this information, we determined Cherenkov angle single photon resolution. The expected π/K separation based on measured single photon resolution and producer's data for Photonis MCP PMTs is presented in Figure 8.70.

Our research has shown the ability to build FARICH PID system for SuperB detector. The multilayer 'focusing' aerogel radiators are available. The background conditions are on the low level for this detection technology. The expected life time of the PMTs during experiment is about 10 years or more. After the detail investigations it was concluded that the gain in detection efficiency of the whole detector is not so significant in comparison with the cost of the system and the necessity to cut drift chamber to organize space for FARICH. Finally, the FARICH option for Forward PID is not supported.

Pixelated time-of-flight detector with Cherenkov radiators Figure 8.71 shows a possible concept of a final TOF detector. It uses polished and side-coated fused silica radiator cubes, which are optically isolated from each other. The radiator cubes are coupled to

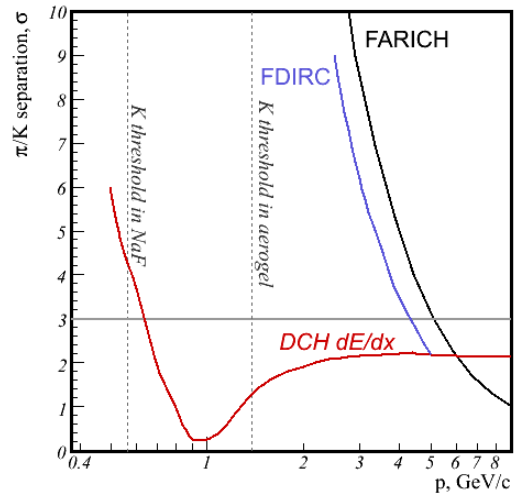

Figure 8.70: The expected FARICH π/K separation based on the test beam data together with expected FDIRC and dE/dX π/K separation.

a MCP-PMT detector with 10 micron holes. This concept is the most simple of all TOF concepts as it avoids complicated 3D data analysis and minimizes the chromatic effects. On the other hand, it requires a large number of MCP-PMT detectors, which increases the cost prohibitively at present. However, if such detectors would become cheap at some point in future, one could revive this concept again.

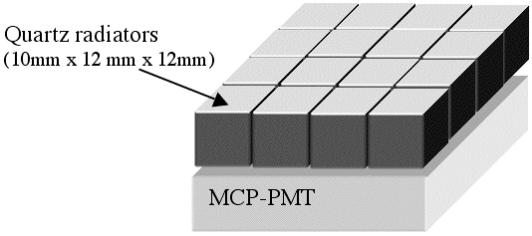

Figure 8.71: A possible geometry of final pixilated TOF detector: polished and side-coated fused silica cubes coupled to the MCP-PMT detector.

Figure 8.72 shows a prototype of the pixilated TOF concept, with a coated fused silica radiator cylinder. The detector had a fiber allowing calibration and laser-based bench-top tests. The radiator was coupled to Photonis MCP-PMT with 10 micron holes. There were two such detectors, operating in tandem, and the quoted resolution is a relative between them. The reference [33] summarizes all work towards this concept.

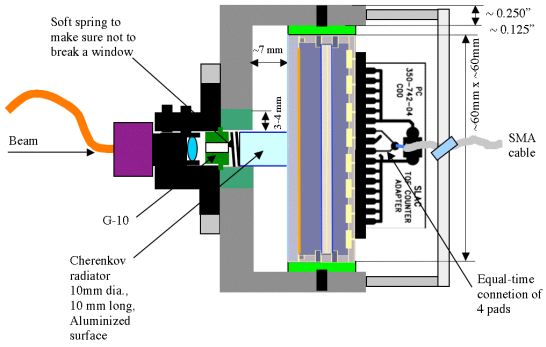

Figure 8.72: A geometry of pixilated TOF prototype detector used in our tests (a pair of such detectors were used in our tests).

Figure 8.73 shows the best resolution obtained with the TOF prototype in the Fermilab beam test. The detector operated at low gain, which means it did not achieve the ultimate resolution. The low gain operation was intentional to avoid aging in the SuperB environment.

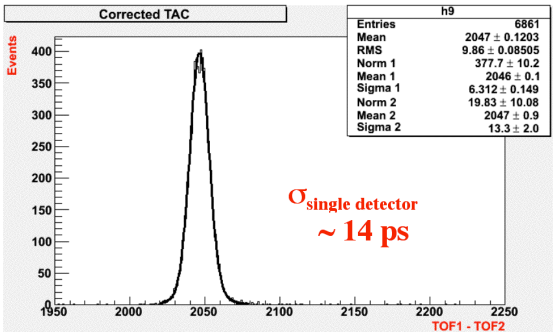

Figure 8.73: The best result obtained in the Fermilab test beam with the Ortec 9327 electronics.

Figure 8.74 shows all our test results both in the test beams and laser-based bench-top experiments. These results were obtained with Ortec

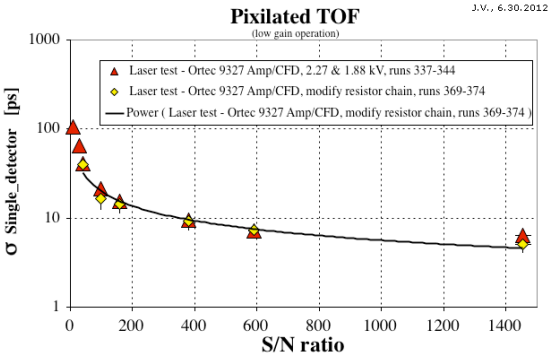

Figure 8.75: A summary of our laser-based results with the pixilated TOF prototype with the Ortec 9327 CFD electronics as a function of signal to noise ratio (S/N).

9327 CFD electronics, WaveCatcher, DRS4 and Target waveform digitizers. One can see that waveform digitizers "almost" reach the resolution of the classical CFD electronics, but not quite.

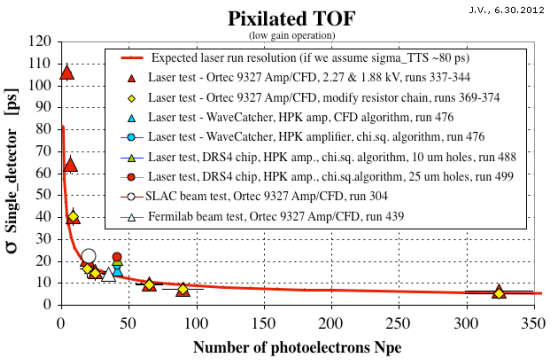

Figure 8.74: A summary of all results with the pixilated TOF prototype, which included beam and laser tests.

Figure 8.75 shows the laser-based test results as a function of the signal-to-noise ratio (S/N). A large value of S/N ratio is essential to achieve a good timing resolution. In these tests we achieved $\sigma(electronics)$~2.42 ps with Ortec 9327 CFD electronics. Therefore the detector contribution to the final ultimate timing resolution was $\sigma(detector)$~3.6 ps for S/N of ~1400. To achieve such a high value of S/N ratio in practice is difficult, as there are many limitations. The most important limitation is due to MCP detector aging, which erquires a low gain operation. One could also have to avoid using an amplifier entirely to improve S/N, as the amplifier is a large contributor to the noise (Ortec 9327 CFD electronics has internal 10x amplifier). It is probably more realistic in practice to reach S/N ~200, i.e., the resolution of 10-12 ps.

Scintillating detector coupled to G-APD arrays [**Jerry**] Because of the prohibitive cost of MCP-PMT detectors for the entire forward pixilated TOF detector design at present, we considered other possible "pixilated" schemes based on scintillators and G-APDs. We used the CRT telescope at SLAC capable of testing various options using 3D muon tracks. The 3D tracks with dip angle up to 20 degrees will somewhat worsen the timing resolution, however, it provides more realistic results compared to test beam. We used various types of scintillators (BC-404, BC-420, small and a full size LYSO) for the radiator. The logic for the full size LYSO radiator was to see if one could "parasite" on end-cap calorimeter by adding a 4x4 G-APD array on its front face. The photon detection in these tests was provided by either MCP-PMT (for a reference run only), or Hamamatsu 4x4 G-APD array (each pixel size is 3 mm x 3 mm), or simply a pair of single 3 mm x 3mm G-APDs (either MEHTI or Hamamatsu MCCP) coupled to side of the small scintillator. The overall goal was to reach ~100 ps only to provide a PID identification in the dE/dx cross-over region. Table 8.4 shows a summary of all results [34]. One can see that we could reach resolutions between 110 and 180 ps for several small scintillators. However, the full size LYSO crystal results were considerably worse. Although one could search for some further improvements in future, it was felt that this type of TOF counter cannot compete with FTOF concept at present.

DIRC-like forward time-of-flight detector (FTOF) As indicated by its name, the FTOF [6] belongs to the family of the DIRC detectors [3]. Charged particles cross a thin layer of fused silica; provided that their momentum is high enough, they emit Cherenkov light along

Radiator	Detector	Measured resolution
Small LYSO (17 x 17 x 17 mm^3)	MCP-PMT	109 & 159 ps
Small LYSO (17 x 17 x 17 mm^3)	4x4 G-APD array (pixel 3 mm^2)	140 ps
Large LYSO (25 x 25 x 200 mm^3)	4x4 G-APD array (pixel 3 mm^2)	220 ps
Scintillator (17 x 17 x 17 mm^3)	4x4 G-APD array (pixel 3 mm^2)	136 ps
BC-404 scintillator (38 x 38 x 25 mm^3)	Two single 3 mm^2 G-APDs	156 ps
BC-420 scintillator (38 x 38 x 10 mm^3)	Two single 3 mm^2 G-APDs	177 ps

Table 8.4: Results with TOF pixilated detector using scintillator radiators using 3D tracks in the cosmic ray telescope (CRT).

their trajectories. Part of these photons are trapped by total internal reflection and propagate inside the quartz until an array of Multi-Channel Plate Photomultipliers (MCP-PMT) where they are detected. Unlike the (F)DIRC, no attempt is made to reconstruct Cherenkov angles: K/π separation is provided by time-of-flight: at given momentum, kaons fly more slowly than pions as they are heavier. Given the short flight distance between the IP and the FTOF (about 2 meters, hence a 90 ps difference for 3 GeV/c particles), the whole detector chain must make measurements accurate at the 30 ps level or better. This is one of the main challenges of this design, the others being the photon yield, the sensitivity to the background (including ageing effects due to the charge integrated over time by the photon detectors) and the event reconstruction. Regarding the latter point, one should emphasize that the FTOF is in fact a two-dimensional device: the PID separation uses both the timing and spatial distributions of the photons detected in the MCP-PMT arrays.

8.5.3 The Forward task force

Charge and activities In July 2010, a taskforce on a possible forward PID system in the Super$B$ detector was formed. Its primary charge was to provide an assessment of

- the physics impact of a PID system in the forward region of the Super$B$ detector, roughly defined by the polar angle range 17° to 25°;
- the feasibility of the proposed detector technologies for the forward PID system.

The taskforce considered a list of questions and criteria for both physics and technology assessments, as discussed below.

- Physics evaluation
  - A list of key benchmark physics channels that are affected by a forward PID system were evaluated for both the gain and any potential negative impact due to the added material before the forward EMC or any required changes to the DCH dimensions.
  - A preliminary performance evaluation was made of some of the proposed technologies, in the presence of background hits.
  - The impact of each proposed forward PID technology on π^0 efficiency, and momentum and dE/dx resolutions in the DCH was performed.
- Detector technology issues
  - Estimates of cost, required manpower, and construction schedule for each of the proposed technologies were performed. These include information on the availability of components on the time scale of the Super$B$ construction schedule.

  - The need for a proof-of-principle was considered for each of the proposed technologies – at least with cosmic rays and if possible with beam tests. Issues common to nearly all devices are: performance in presence of background; the effect of the Super$B$ magnetic field on the photodetectors and on the overall performance of the device; photodetector aging.
  - Integration issues.

The taskforce met with forward PID proponents at all Super$B$ workshops between September 2010 and May 2011 when the committee recommendation was released. There were also phone meetings in between workshops.

Summary and taskforce recommendation The physics gain from a forward PID deviced is around 4-5 % for the benchmark channel $B \to K^{(*)}\nu\bar{\nu}$: roughly 2%/kaon. No physics channel with higher gain has been identified. Results based on simulation and beam test (1 GeV electrons) show no significant degradation of resolution & efficiency for γ and π^0. In addition, the impact on tracking resolution due to shortened DCH has been estimated to be $\sim$1% degradation in momentum resolution/cm cut.

The overall assessments for the proposed detector technologies are the following.

- FARICH. On the whole, this technology is likely to yield the most powerful – and robust – PID performance, extending well above the nominal 4 GeV for B decays. The expected performance is verified by impressive beam test results. However, no physics channel that would significantly gain from the extended performance has been identified. Moreover, the required cut of $\sim$17 cm to DCH length significantly degrades momentum resolution in this angular region. This is an unacceptably large negative impact on the detector performance and a too severe constraint on the tracking system. Hence, the taskforce does not see this technology appropriate for forward PID in the Super$B$ detector
- Pixelated TOF (LYSO plus G-APD array option). This technique, due to its potential minimal disturbance on the rest of the detector and likely modest cost, was deemed very attractive. At the aimed resolution of $\sim$100 ps, it would complement the $\mathrm{d}E/\mathrm{d}x$ measurements for K/π coverage below 2 GeV. However, with the obtained time resolution ($\sim$230 ps) for a full size LYSO crystal in cosmic ray tests, the proponent & taskforce have concluded that this technique will not deliver the required performance.
- FTOF. Simulation studies and cosmic ray tests – see below – have demonstrated that key aspects of this technique can be attained – including the goal of a time resolution of $\sim$90 ps/hit. But there remains significant uncertainties on the expected background level and its impact on PMT lifetime. The taskforce believes this technique could be appropriate for the forward PID system provided that background (and radiation) issues are understood – which may require further studies of the IR design and shielding – and that a full prototype of the system is developed and tested, to verify the expected performance, in particular the pattern recognition in the presence of background hits.

The final recommendation for the forward Super$B$ region is the following: the importance of hermeticity (and redundancy) in PID coverage will increase as we approach the systematics-dominated era in the Super$B$ physics program. Hence, the taskforce members believe – independently of the outcome of the current technology evaluation – that there is physics merit to allowing a gap of $\sim 5-10$ cm in the forward region for a PID device. This would allow for introduction of a system at a later stage of the experiment, in case the detector studies are not completed in time for the initial installation of the Super$B$ detector.

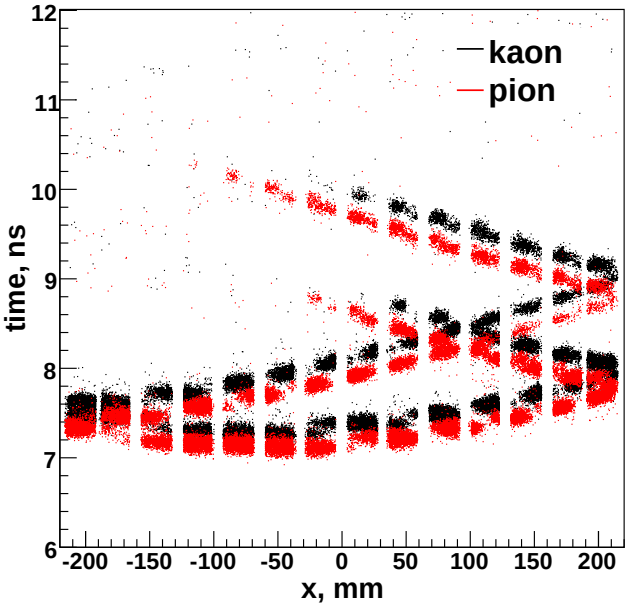

Figure 8.77: The FTOF is a 2D-device: in addition to the photoelectron timing, the distribution of hits in the MCP-PMT channels is also a discriminating variable to separate kaons from pions, as shown on the two plots displayed in this figure. Both show the time versus position of hits generated by 2 GeV/c kaons (black) and pions (red) [**To be updated**]. $t = 0$ corresponds to the particle generation at the IP while x is an axis along the tile width which shows the MCP-PMT position. The 14 photodetectors are clearly visible such as the small gaps between them.

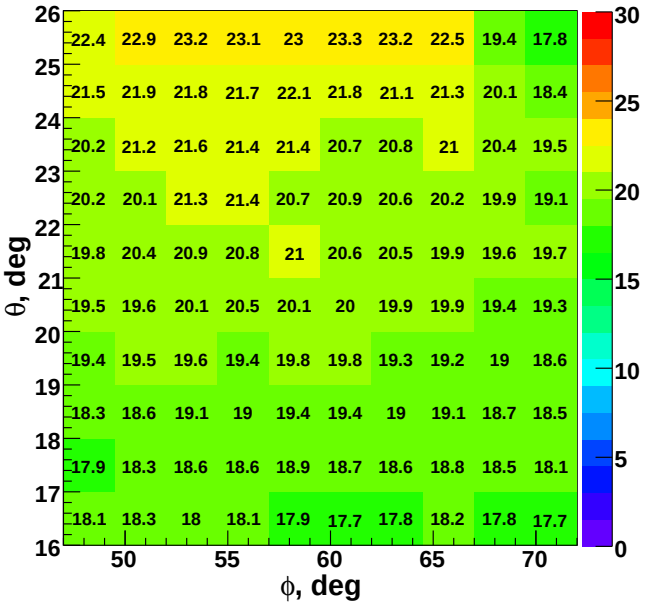

Figure 8.76: Map giving the mean number of detected photoelectrons in a FTOF sector as a function of the polar (θ) and azimuthal (ϕ) angles. This map is drawn for 800 MeV/c kaons shot from the IP in a simplified detector model including the 1.5 testa longitudinal solenoid field.

8.5.4 The DIRC-like forward time-of-flight detector (FTOF)

Design optimization The performances of the FTOF depend on two main parameters which should be optimized simultaneously. One is the photon yield per track, which should be as high as possible; the other is the photon timing jitter, which should be minimized in order to efficiently separate kaons from pions. Both are strongly related to the geometry of the detector.

The number of Cherenkov photons produced by a given track scales linearly with its path length in fused silica. Simulations show that a 1.5 cm thickness for the quartz tile is a good compromise between light yield and detector thickness in term of X_0. This finite size introduces an irreducible component of the photon time jitter (about 50 ps), as Cherenkov photons are emitted uniformly along the track path inside the tile. Their initial directions lie on a cone which opening angle depends on the track velocity (which is a function of the particle measured momentum and of its unknown mass) and on the medium optical index ($n \approx 1.47$ in fused silica). Therefore, the total length of the Cherenkov photon path inside the tile depends on the track direction.

Therefore, it is clear that photons from a given track can follow several different paths

before being detected in a MCP-PMT channel. This is another source of time jitter which has to be taken into account. One way to mitigate it is to select only the 'most-direct' photons which reach the detectors after at most few reflections on the tile front and back faces. This can be done by covering the tile sides by photon absorbers but the loss in photon yield would be too high. In the current design, only the tile inner radius is covered by absorber to stop the 'downward-going' photons which paths are too long and make their timing unusable. Indeed, with tiles perpendicular to the beam axis, photons are mainly 'upward-going': they are travelling towards the tile outer radius first which is why the MCP-PMTs are located in this area.

Given the accuracy of the timing measurements required by the FTOF, chromaticity is another effect which cannot be neglected: the smaller the photon wavelength the larger its speed – 'red' photons are faster than 'blue' ones.

The FTOF photon yield also depends on the tile orientation as only Cherenkov photons trapped inside the quartz by total internal reflection can be detected. Using vertical tiles as reference, simulations show that a 10° tilt in the forward (backward) direction increases (decreases) the yield by about 15% in average. But configurations in which the FTOF is bent forward are impossible in practice, due to integration constraints on the Super$B$ forward side.

Current design The DIRC-like forward time-of-flight detector is made of 12 thin fused silica tiles (1.5 cm thick each, which corresponds to 12% X_0) located perpendicularly to the beam axis and covering 30° in azimuth each. The requirements for the tile dimension accuracy and the fused silica polishing quality are less stringent than for the *BABAR* DIRC bars, as the Cerenkov photons will bounce much less in the quartz. Therefore, building the FTOF tiles should not be an issue given the knowledge accumulated in this area over the past two decades.

Each FTOF tile will be placed into a light aluminium box which will be the equivalent of the DIRC bar boxes for the DIRC quartz bars. To keep the fused silica tiles as clean as possible, the tile box should not contain any other detector component; there will just be an optical contact between the quartz and the MCP-PMTs. Both the tile box and the box enclosing the MCP-PMTs will be light-tight; in addition, the tile box will be leak-tight and N_2 will flow continuously inside it to avoid any moisture.

Figure 8.79: The 16-channel Wavecatcher board.

The prototype FTOF front-end electronics is based on the new 'WaveCatcher' boards commonly developed by LAL Orsay and CEA/Irfu Saclay. They are 12-bit 3.2 GS/s low power and low cost waveform digitizers based on the SAMLONG ultra-fast analog memory. The sampling time precision is as good as 10 ps rms, a value measured at the level of a crate hosting eight 2-channel boards. The photon arrival time is extracted via digital Constant Fraction Discrimination (CFD). A new 16-channel board recently designed has been characterized: it exhibits the same timing performances.

The final electronics will be highly integrated and based on a new principle of TDC, called SAMPIC. The latter, designed in AMS CMOS 0.18 μm technology, will be able to tag the ar-

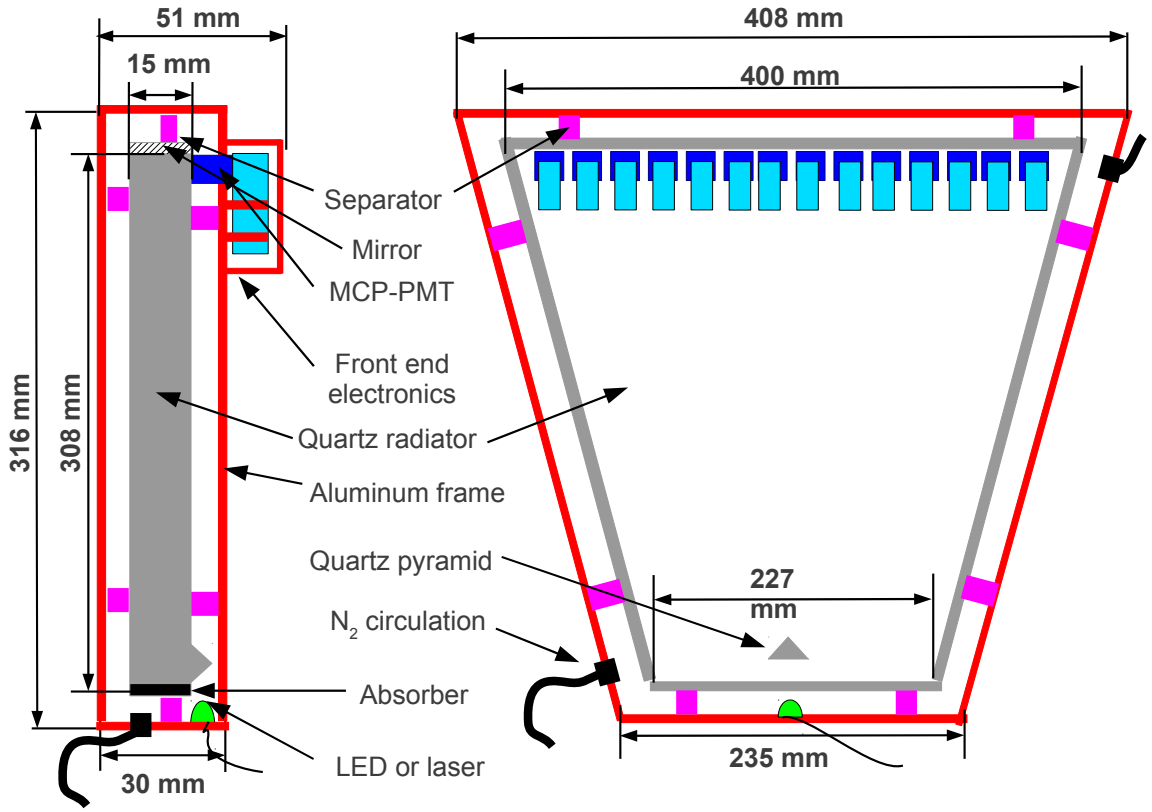

Figure 8.78: Current design of the FTOF tile: front and side views.

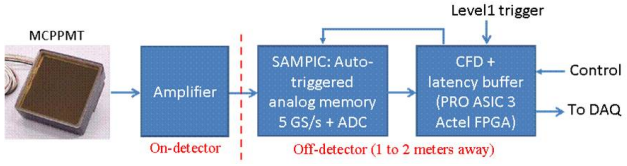

Figure 8.80: Schematics of the FTOF whole electronics chain.

rival time of 16 analog signals with a precision of a few ps thanks to its embedded analog memory (running between 5 and 10 GS/s) and its embedded ADC. This will permit housing at least 64 channels in a final front-end board. In the current FTOF design, there are 56 channels per sector; hence, a single 16-channel Wavecatcher board will be enough to readout a sector (hence 12 boards will be needed in total for the whole FTOF).

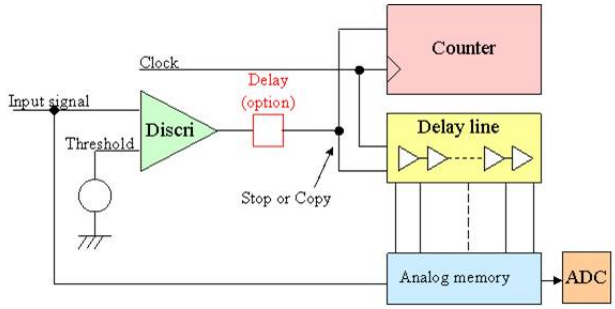

Figure 8.81: Scheme of the new TDC for the FTOF electronics.

The FTOF front-end boards will be located outside the detector, both for protection from background and radiation, and to allow easy access for repair. The analog signal will be amplified right behing the MCP-PMTs and then transfered to the front-end board via signal cables.

As explained above, the whole FTOF measurement & processing chain must be ultra-fast. The time resolution per photon must be at the level of 100 ps or better, which makes the use of MCP-PMTs mandatory. Among the product available on the market, the Hamamatsu SL-10 is currently our baseline. With an advertised time-transit-spread (TTS) of 70 ps (FWHM), an active area of 22×22 mm^2, a quantum efficiency of 17% and a lifetime of $\sim$2 C/cm^2, it offers a good compromise given the FTOF requirements. Two such photon detectors will be characterized at LAL-Orsay in the coming months. In the current design, one needs 14 SL-10 per sector, hence 168 in total; each MCP-PMT will host 4 different channels which will all have their own HV channel. The HV power supplies will be located behind the detector shield wall and could then be accessed 24/7.

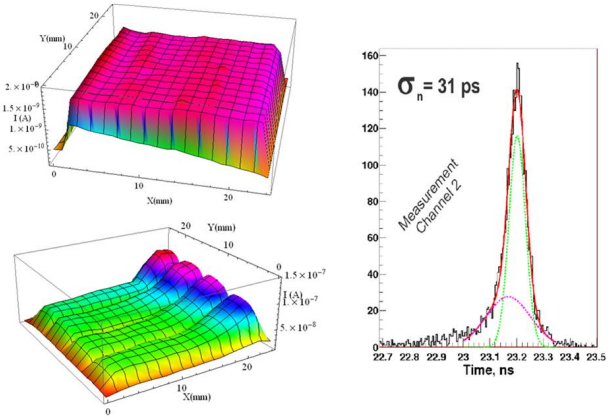

Figure 8.82: Top left plot: SL-10 photocathode response mapping; bottom left plot: 4 anode response mapping; right plot: single photoelectron timing resolution (FWHM).

A fully instrumented FTOF sector is expected to be very light: about 12 kg total.

First test of the detection method A test of the FTOF detection concept was run at SLAC in the Cosmic Ray Telescope (CRT) between Fall 2010 and Spring 2011. The SLAC group provided the hardware (two short rectangular fused silica bars readout by a photonis MCP-PMT) and the test facility while the LAL team brought new 2-channel USBWC boards, which performances were tested for the first time at the level of a whole crate. The test setup is shown in Figure 8.83. Cosmic muons cross the two bars located on top one another. They emit Cherenkov light inside, which partly propagates until the instrumented end of the bars. By shorting and grounding pixels, one defined 16 MPC-PMT vertical pads – 8 for each bar – which were connected to the USBWC electronics.

For technical reasons, the CRT and USBWC DAQ systems were separated. CRT trigger is asserted by a fast Cherenkov counter located under the two bars. When a trigger signal is sent out, the 16 USBWC analog buffers are

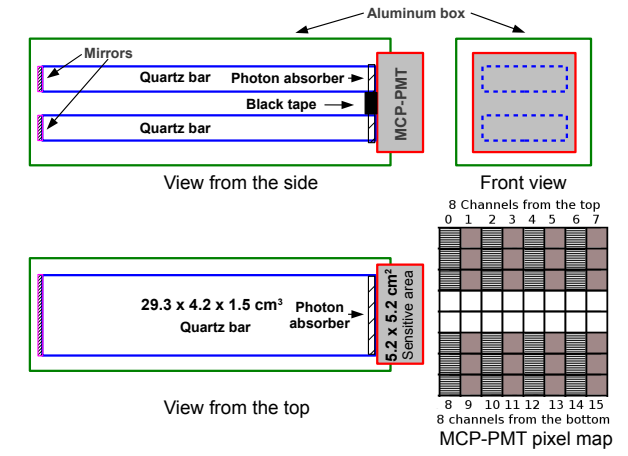

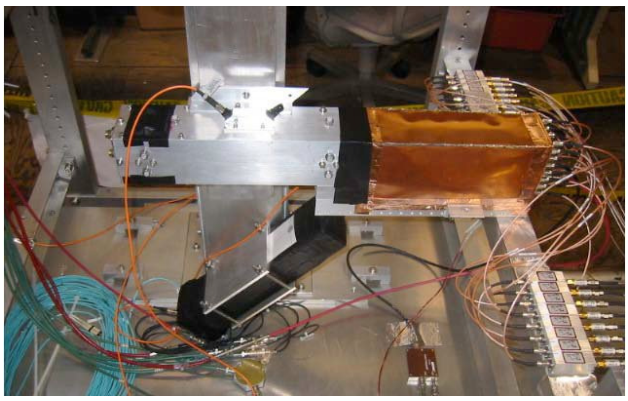

Figure 8.83: Top: side and top views of the 2-bar setup; the 16 channels readout by the USBWC boards are shown on the right-hand side. Bottom: picture of the apparatus in the SLAC CRT: the orange box is a Faraday cage containing the USBWC electronics while the grey box contains the prototype. Under these items, on can see the enclosure of the sloping fast quartz counter which is used to trigger the CRT in coincidence with the hodoscopes.

readout to see if photons have been detected by one or more pads. If this is the case, the USBWC event is written to disk. Coincidence between CRT and USBWC events is done offline by comparing the time of the recorded events in the two streams. After an initial period of commissionning, about 400,000 cosmic muons were collected during two months of nominal running. Absorber sheets had to be placed in front of the MCP-PMT to reduce significantly the number of photons detected by channel. Indeed, as the photon timing is measured by a sophisticated CFD-based algorithm, a second photon too close in time from the first detected one would distort the waveform shape and spoil the timing measurement.

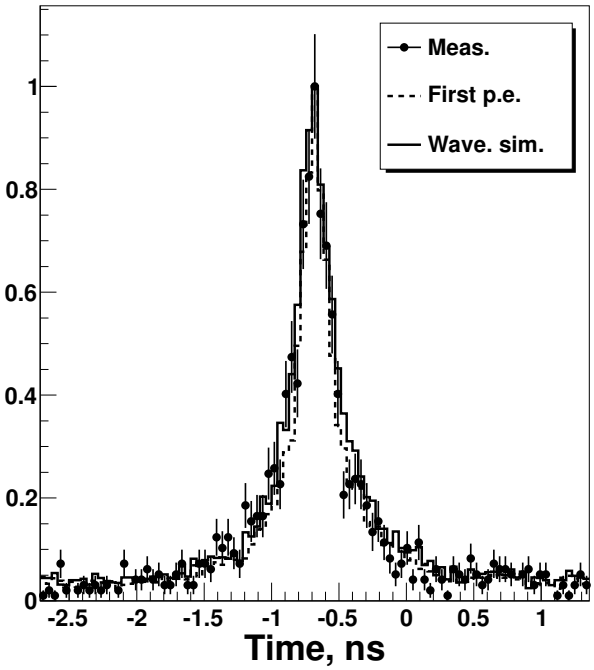

Figure 8.84: Comparison between data (bullets) and simulations (histograms) **[To be updated]** for the time difference between two MCP-PMT channels among the 16 readout by the USBWC boards. All distributions are scaled so that their peak is equal to 1 in arbitrary units. The data-MC agreement is impressive, both for the core and the tails of the distributions. Similar results are achieved for all pairs of channels studied.

As explained above, USBWC events of interest are selected by requiring a time coincidence with a CRT event, plus some additional quality

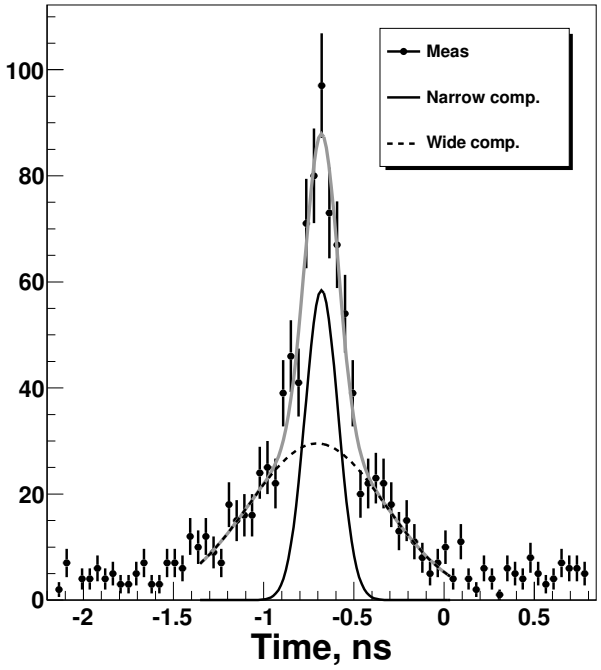

Figure 8.85: Double Gaussian fit to a representative distribution of the time difference between two channels. The width of the narrow component is interpeted as the prototype device while the wide component accounts for multiple photon paths (and hence multiple timings) between pads.

cuts on the CRT data. As no accurate timing reference is available, the current determination of the prototype time resolution is based on time difference between channels. All pairs of channels have been considered but they are studied separately as the resulting timing distributions depend on the photon paths compatible with the particular two MCP-PMT pads. The interpretation of these data is not straightforward as photons emitted by a muon track can follow several different paths to reach a particular pad. Yet, a good data-Monte-Carlo agreement makes us confident that this analysis is valid. The measured single photon timing accuracy is in the range 80-100 ps, dominated by detector effects (spread of the Cherenkov photon emission time due to the finite quartz tile width; multiple photon paths inside the fused silica to the MCP-PMTs; variation of the cosmic muon track parameters, etc.). This preliminary result should be confirmed by a reanalysis of the data based on 3D-tracking and aiming at comparing the photon measured and expected times.

Background and ageing studies The FTOF sensitivity to background can be seen in two ways. First, background hits could shadow real signal hits too close in time and/or add confusion in the pattern reconstruction algorithms used to extract PID information from the FTOF data. Moreover, the background rate will translate into a acculumated charge on the MCP-PMT cathode. The consequence of the latter will be a slow decrease of the MCP-PMT quantum efficiency; at an integrated charge around 1-2 C/ cm^2, the photon detectors will cease working properly. Therefore, it is crucial to estimate the FTOF background accurately and to find ways to decrease it as much as possible. In addition, the MCP-PMT gain should be high enough to keep the TTS low, but not too high as it limits the MCP-PMT rate.

Full Geant4 simulations of the Super$B$ interaction region (detector included) simulating the main backgrounds – radiative Bhabha, Touschek particles, etc. – have shown that the dominant FTOF background is due to off-energy positrons which hit the beampipe about one meter away from the IP on the forward side. This localized background source can be mitigated by increasing the thickness of the tungsten shield which protects the detector. Initial studies have shown that going from 3 cm to 4.5 cm decreases the FTOF rate by a factor 3 to about 115 kHz/ cm^2 The latter value is still a bit high for five years of high gain running at nominal luminosity; therefore, work is ongoing to confirm and improve this promising result.

Ongoing activities and plans As explained above, the FTOF technology has been chosen by the Super$B$ collaboration for the forward PID detector. Therefore, if one such device is to be built, that will be the FTOF. Yet, to be included in the detector baseline, a full-size pro-

totype of a FTOF sector must be built and validated, both in cosmics and test beam.

As a first step, a fused silica tile (Spectrosil 2000 from Heraeus) has been purchased by the LPSC Grenoble group (which joined the FTOF development in 2011). It will be placed in a cosmic ray telescope specifically designed for the FTOF geometry with an active area of 0.23 m^2 and good resolution on position ($\sim 0.3 - 0.6$ cm) and angle ($\sim$0.2 deg). Different absorber thicknesses are used to select 7 momentum ranges of the muons from 300 MeV/c, the thicker absorber giving a lower cut at 1.7 GeV/c. The yield of this telescope is 1 Hz for the full momentum spectra and only 0.2 Hz for the higher energy bin. The main purpose of this setup is to study the photon yield versus the muon impact position and incident angle, using several coatings on edges and faces.

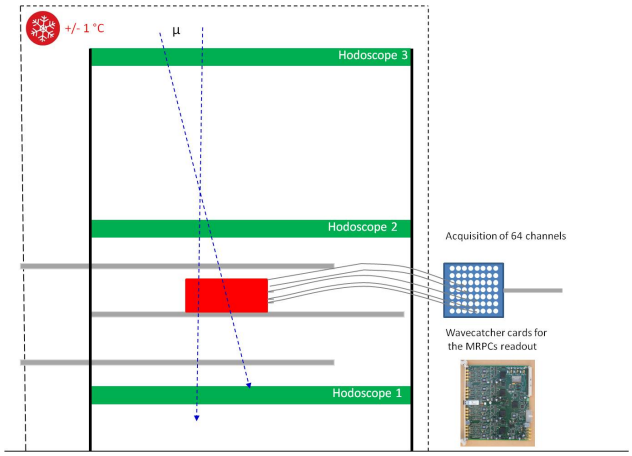

Figure 8.86: The CORTO setup.

These setups will be used to measure the photon collection efficiency and timing in various configurations. These data will allow one to validate the full Geant4-based optical simulations.

In CORTO, the fused silica tile will be tested with different MCP-PMTs: R10754X (SL-10) from Hamamatsu and XP85112 from Photonis. [+ **Russian MCP-PMT!?**]

In the meantime, the FTOF design will go on, benefiting from improved simulations and progress on the geometry of the crowded Super$B$ forward region. Discussions are also ongoing about the best location of the MCP-PMTs: at the outermost radius they are subject to less background but accessing them for repair would be extremely difficult. On the other hand, putting the MCP-PMTs at the innermost radius would require tilting the FTOF significantly (to have a larger fraction of Cherenkov photons downward-oriented), which is likely unfeasible given the integration constraints on the Super$B$ forward side.

Once the FTOF design is frozen, the building of the prototype will start – its cost is strongly dominated by the MCP-PMT price. Assuming that the whole project proceeds smoothly and that the FTOF is accepted by Super$B$, a detailled appendix of the present detector TDR will be published to provide all the needed information to support this innovative detector.

MCP-PMT	Effective area (mm^2)	Quantum efficiency (QE) @ 400 nm	Typical gain	Transit time spread (FWHM)	QE reduction after 2 C/cm^2 accumulated charge
R10754X-01-L4	22×22	17%	10^6	70 ps	20%
XP85112/A1	53×53	22%	10^5	82 ps	Unaffected

Table 8.5: Comparison of two MCP-PMTs candidate for the FTOF.

Bibliography

[1] C. Amsler *et al.*, (Particle Data Group), Phys. Lett. B 667, 1 (2008).

[2] http://nobelprize.org/nobel_prizes/physics/laureates/2008/press.html, and http://www-public.slac.stanford.edu/babar/Nobel2008.html.

[3] B. Ratcliff, SLAC-PUB-5946, 1992; and *Simple considerations for the SOB redesign for Super*B, http://agenda.infn.it/conferenceDisplay.py?confId=458, Super*B* PID meeting, March 18, 2008.

[4] I. Adam *et al.*, Nucl. Instrum. Methods Phys. Res., Sect. A **583**, 281 (2007).

[5] J. Va'vra *et al.*, Nucl. Instrum. Methods Phys. Res., Sect. A **639**, 404 (2011)282-286.

[6] J. Va'vra, Super*B* workshop, Perugia, June 2009, http://agenda.infn.it/conferenceDisplay.py?confId=1161, and Super*B* workshop, October 2009, SLAC, http://agenda.infn.it/conferenceDisplay.py?confId=1742.

[7] J. Va'vra *et al.*, Nucl. Instrum. Methods Phys. Res., Sect. A **606**, 404 (2009)404-410.

[8] E. Kravchenko, Super*B* workshop, June 2009, Perugia, http://agenda.infn.it/conferenceDisplay.py?confId=1161.

[9] J.Benitez *et al.*, SLAC-PUB-12236, October 2006.

[10] J. Va'vra *et al.*, SLAC-PUB-12803, March 2007.

[11] J. Benitez *et al.*, Status of the Fast Focusing DIRC (FDIRC), Nucl. Instrum. Methods Phys. Res., Sect. A **595**, 104 (2008) 104-107.

[12] J. Va'vra, *Simulation of the FDIRC optics with Mathematica*, SLAC-PUB-13464, 2008; and *Focusing DIRC design for Super*B, SLAC-PUB-13763, 2009.

[13] D. Roberts, Super*B* workshop, October 2009, SLAC, *Geant4 model of FDIRC*, http://agenda.infn.it/conferenceDisplay.py?confId=1742.

[14] M. Maino, Charactherisation of Multi-Anode Photomultiplier Tubes in Milano-Bicocca, Super*B* workshop, Frascati, March 2012, http://agenda.infn.it/conferenceDisplay.py?confId=4441.

[15] G. Varner, Deeper Sampling CMOS Transient Waveform Recording ASICs, TIPP conference, June, 2011, Chicago, http://www.phys.hawaii.edu/~varner/TIPP_DeeperWFS_ASICs_10jun2011_varner.pdf.

[16] C. Beigbeder, Status of FDIRC electronics, Super*B* workshop, Elba, May 2011, http://agenda.infn.it/conferenceOtherViews.py?view=standard&confId=3352.

[17] C. Field *et al.*, *Development of Photon Detectors for a Focusing DIRC*, Nucl. Instrum. Methods Phys. Res., Sect. A **553**, 96 (2005) and SLAC-PUB-11107, 2004.

[18] H. Kyushima *et al.*, *The Development of Flat Panel PMT*, Hamamatsu Photonics K.K., Electron Tube Center, Nuclear Science Symposium Conference Record, 2000 IEEE.

[19] R. Montgomery *et al.*, Multianode Photomultiplier Tube Studies for Imaging Applications, presented as NDIP conference poster, Lyon, France, 2011.

[20] F. Gargano, Update on H8500 test in Bari, Super*B* workshop, Frascati, March 2012, http://agenda.infn.it/conferenceDisplay.py?confId=4441.

[21] J. Va'vra, FDIRC status, Super*B* workshop, Elba, May 2011, http://agenda.infn.it/conferenceOtherViews.py?view=standard&confId=3352.

[22] G. Simi, H-8500 studies, Super*B* workshop, Frascati, December 2011, http://agenda.infn.it/conferenceOtherViews.py?view=standard&confId=4107.

[23] C. Pauly, Single photon detection with H-8500 MaPMTs for the CBM RICH detector, DPG Munster, March 2011, http://www.gsi.de/documents/DOC-2011-Mar-233-1.pdf.

[24] P. Abbon *et al.*, Nucl. Instrum. Methods Phys. Res., Sect. A **595**, 204 (2008).

[25] J. Va'vra, FDIRC status, Super*B* workshop, London, September 2011, http://agenda.infn.it/conferenceOtherViews.py?view=standard&confId=3827.

[26] N. Arnaud, Study of the glue transmission with di-muon *BABAR* data, 2009.

[27] J. Va'vra, spreadsheet accompanying each bar box construction, 1999.

[28] M. Benettoni, Fbox assembly procedure, Super*B* workshop, Elba, May 2011, http://agenda.infn.it/conferenceOtherViews.py?view=standard&confId=3352.

[29] N. Mazziota, Activity in Bari, Super*B* workshop, London, September 2011, http://agenda.infn.it/conferenceOtherViews.py?view=standard&confId=3827.

[30] N. Mazziotta, A study of after-pulse effect due to Helium permeation in the H8500 MaPMT, Super*B* workshop, Frascati, December 2011, http://agenda.infn.it/conferenceOtherViews.py?view=standard&confId=4107.

[31] J. Va'vra, *SLAC cosmic ray telescope facility*, SLAC-PUB-13873, Jan. 2010.

[32] K. Nishimura *et al.*, *A detailed study of FDIRC prototype with waveform digitizing electronics in cosmic ray telescope using 3D tracks*, SLAC-PUB-15202, July, 2012.

[33] J. Vavra *et al.*, Development of pixilated TOF concept, Nucl. Instrum. Methods Phys. Res., Sect. A **595**, 270 (2008), Nucl. Instrum. Methods Phys. Res., Sect. A **606**, 404 (2009), Nucl. Instrum. Methods Phys. Res., Sect. A **629**, 123 (2011), and overall summary in DOE OHEP Review of Laboratory Detector R&D, Washington, July 24-26, 2012, available at http://www.slac.stanford.edu/~jjv/activity/fdirc/Vavra_DOE_review_detectorRD_2012.pdf.

[34] J. Va'vra, TOF with LYSO and G-APD, Super*B* workshop, Frascatti, April 2011, http://agenda.infn.it/conferenceDisplay.py?confId=3410, Pixilated TOF options, Sept. 2011, http://agenda.infn.it/conferenceDisplay.py?confId=2303.

[35] D. Breton, E. Delagnes and J. Maalmi, *Picosecond time measurement using ultra fast analog memories*, talk and proceedings at TWEPP-09, Paris, September 2009. **Not used (2012/08/28)**

[36] G. Varner, Nucl. Instrum. Methods Phys. Res., Sect. A **538**, 447 (2005), Nucl. Instr. Methods Phys. Res., Sect. A **538** (2005) 447. **Not used (2012/08/28)**

[37] L. Burmistrov, PhD. thesis, Université Paris Sud (2011), http://tel.archives-ouvertes.fr/tel-00673482. **Not used (2012/08/28)**

9 Electromagnetic Calorimeter

9.1 Overview

The Super$B$ electromagnetic calorimeter (EMC) will play an essential role in the study of the flavor physics, especially in the study of B meson decays involving neutral particles. The calorimeter provides energy and direction measurement of photons and electrons, reconstruction of neutral hadrons such as π^0's and discrimination between electrons and charged hadrons. Channels containing missing energy due to the presence of neutrinos will rely on information from the EMC to discriminate against backgrounds. The same criteria for good energy and position resolution apply for Super$B$ as for the *BABAR* calorimeter.

The electromagnetic calorimeter has three major components: a CsI(Tl) "barrel" calorimeter covering the central region, a "hybrid" CsI(Tl)/LYSO(Ce) "forward" calorimeter covering the small angle region in the direction of the high energy beam, and a lead-scintillator "backward" calorimeter covering the small angle region in the direction of the low energy beam. Table 9.1 shows the solid angle coverage for each of the three parts of the Super$B$ EMC.

The Super$B$ EMC reuses the barrel part of the *BABAR* EMC detector consisting of 5760 CsI(Tl) crystals as shown in Fig. **??**. However the *BABAR* forward calorimeter will need to be partially replaced, due to the higher radiation and higher rates at Super$B$ compared with PEP-II. The innermost Csi(Tl) rings of the forward endcap will be replaced by new LYSO crystals designed to perform well in the Super$B$ environment.

Reuse of the *BABAR* barrel calorimeter still requires a substantial effort. There is an ongoing engineering investigation of whether the barrel structure can be shipped as a unit, or whether it is necessary to disassemble it into its 280 individual modules for safe shipment. In either eventuality, it will be necessary to replace the crystal-mounted premamplifier-shapers with versions having a shorter integration time, due to the substantial increase in background and signal rates at Super$B$ compared to PEP-II.

After an intensive R&D program, the baseline choice for the forward endcap is to replace the inner rings of the *BABAR* forward calorimeter with faster and more radiation resistant LYSO crystals. As will be discussed below, this is the clear favorite in terms of performance and radiation hardness over the alternatives we have considered. The faster response time and shorter Molière radius serve together to address the higher event and background rates at Super$B$. LYSO is a fast scintillator heretorfore largely used in medical applications with crystals of small size. Our R&D program has concentrated on the optimization of performance of large crystals (2cm x 2 cm x 20 cm) with good light yield uniformity and optimized Ce doping in order to have the best possible light output. Thanks to this effort, more than one producer is able to grow LYSO crystals of good quality that can be used in high energy physics applications. Table 9.3 shows the comparison between LYSO and other materials used in electromagnetic calorimeters. The largest disadvantage of LYSO is cost. The present design is a compromise. We have studied other lower cost alternatives as described below.

A lead-scintillator-sandwich backward endcap calorimeter improves the hermeticity of the detector. The main purpose of this component is to detect energy in the backward endcap region, as a veto of events with "extra" energy. This is particularly important for studying

Table 9.1: Solid angle coverage of the electromagnetic calorimeters. Values are obtained assuming the barrel calorimeter is in the same location with respect to the collision point as for *BABAR*. The CM numbers are for massless particles and nominal 4 on 7 GeV beam energies.

Calorimeter	$\cos\theta$ (lab)		$\cos\theta$ (CM)		Ω (CM)(%)
	minimum	maximum	minimum	maximum	
Backward	-0.974	-0.869	-0.985	-0.922	3.1
Barrel	-0.786	0.893	-0.870	0.824	84.7
Forward	0.896	0.965	0.829	0.941	5.6

channels with neutrinos in the final state. Because of the fast time response, the backward EMC may also have a role in particle identification by providing time-of-flight for the relatively slow backward-going charged particles.

9.1.1 Background and radiation issues

One of the major concerns for the electromagnetic calorimeter is its capability to sustain the radiation dose, which is larger than in previous experiments due to the increased luminosity. The dominant contribution to radiation in Super*B* is in fact expected to come from radiative Bhabha events that emit a large number of low energy photons at an extremely high rate. This photon rate can impact the performance of the detector because of two effects: the radiation can reduce the transmittance of the crystals and therefore alter as a function of time the calibration of the detector; the large number of photons can result in pile-up thus introducing a degradation in energy resolution.

To estimate the impact of these effects simulations have been set up as described in Sec. 5.12. The energy deposited by background events in each crystal is simulated at each beam crossing. The resulting rates of energy deposit are shown in Fig. 5.4. The result shows that there is no significant difference in the irradiation between the barrel and the forward endcap. This can be understood because the dimension of the crystals is significantly different: due the different density and consequently Molière radius, the transverse dimensions of LYSO crystals are two times smaller than the CsI crystals (both doped and not) and the overall volume of a LYSO crystal is 6.7 times smaller (120cm^3 vs 800cm^3) than the CsI ones. Since the rates of signals from the machine background scales linearly with volume, the most forward LYSO crystals of the Barrel will suffer a background more than six times larger than the more central crystals of the FWD calorimeter, albeit contiguous.

From the radiation hardness point of view, the dose to which the crystals are sensitive is defined as the total energy deposited in a crystal divided by its mass. The dose expected per year (conventionally considered $10^7 s$ long) was estimated to range between 0.1 and 0.2 krad. Conservatively, assuming a maximum of 10 years of operations, crystals need to be radiation resistant up to at least 3krad. Also the impact on resolution of a $\sim$ 0.03rad/hour dose rate needs to be considered.

9.1.2 Simulation tools

9.1.2.1 Fastsim

A fast simulation (FastSim) tool based on the *BABAR* software framework has been developed to evaluate the detector performance, geometry optimization, and to study physics reach. The detector geometry is modeled by two-dimensional "shells" of basic topologies; cylinders, disks, cones, rectangles, etc. The event generators are identical to those in *BABAR*. Each particle is tracked in the detector volume; when it crosses a detector element, the interaction type and the energy loss are determined based on particle type, detector material and thick-

ness. Secondary particles are created if necessary. Particle showers are represented by a quasi-particle instead of a (large) number of particles.

Charged track hits are fitted with a Kalman filter; EMC clusters are created based on the Moliere radius, interaction type (EM shower, hadron shower or minimum ionizing), detector segmentation, and parametrized shower shape. Geometry and model parameters can be easily set up and modified. The high level data structure of an event is the same as *BABAR*, including tracks, clusters, and particle identification objects, so one can directly apply available *BABAR* analysis tools.

Background cannot be simulated with FastSim because it is highly sensitive to the details of beam line and interaction region geometries, magnetic fields, beam trajectories, and so on. The secondary particles from beam and material interactions must be simulated precisely, which can only be done with a complete GEANT4 simulation. In order for the FastSim to include background effects, periodic "background frame" productions are carried out with GEANT4, including beam lines up to ±5 meters from the interaction point. For each bunch crossing, background particles that cross the boundary between the beam line elements and the detector volume are recorded and stored in a background frame file. In FastSim, for each signal event, background particles of a number of bunch crossings are read in from the background frame file and are appended to the list of signal particles, and then the FastSim proceeds as usual. The number of bunch crossings per signal event is determined by the crossing frequency and an overall sensitive time window. Each sub-detector has its own response timing structure to model the signal pulse.

9.1.2.2 FullSim

The calorimeter full simulation tool (FullSim) is based on GEANT4 and the Bruno tool (see Section 14.2.1) which is used to simulate particle interactions and the energy deposits. The geometry description includes all of the Super*B* subdetectors and in the case of the Calorimeter it contains all the crystals and support structures. Bruno puts out information about the calorimeter is the deposited energy per crystal. Each single source of machine background is simulated separately for the whole SuperB detector and, if needed, they are combined in a second step of the analysis.

At the present stage of development the FullSim does not perform the digitization of signals and the reconstruction of clusters, which are instead obtained with a two step procedure through stand-alone programs. During the digitization stage, on top of the GEANT4 simulation, the electronic signal shape is generated for each crystal an with energy deposit; photostatistics, noise and time resolution effects are added using extrapolations from *BABAR*, or according to measurements when possible. For studying performance, signal particles events are overlapped with machine background events following the time structure of the bunch crossing rate in a time window centered on the signal particle arrival time; this allows the emulation of effects from the background including electronic signals pile-up. The different sources of background are mixed according to their probability and time behaviour.

Starting from the outcome of the digitization step a clustering is performed following the *BABAR* algorithm [1]; when the cluster energy is computed a random intercalibration error is applied at the 1% level (see for example [2]). To be accepted for clustering the signal peak from a crystal should be within a time window centered on the expected signal time.

9.2 Barrel Calorimeter

We propose to reuse the barrel portion of the *BABAR* EMC [2], retaining the fundamental mechanical structures and the 5760 CsI(Tl) crystals and associated pairs of photodiodes mounted on each crystal, along with some modifications required for optimal performance at Super*B*.

Below, we describe first the condition, as of the end of *BABAR* running, of the CsI(Tl) crystals which will be reused in the Super$B$ detector. We then discuss the additional factors present at Super$B$, principally the high pile-up and backgrounds environment, which must be addressed to optimize energy resolution. Next, we describe the mechanical design and calibration systems for the barrel, each of which will be minimally changed from their current configurations, as well as the detector readout. We then discuss the barrel's energy and position resolution, as well as the $\gamma\gamma$ mass resolution, and the effects on these due to long-term exposure to backgrounds at Babar. These trends are extrapolated to decreases in performance which might be expected over the lifetime of Super$B$.

We then describe the current barrel crystal photodiodes, which will not be replaced, and the changes proposed for the on-crystal preamplifier package and the front-end electronics. Lastly, we present the proposed plan for de-integration of the barrel EMC down to its component structures, the packaging and shipping of these, and their local storage and reintegration at a facility to be located at or near Tor Vergata.

9.2.1 Requirements Relevant to the SuperB Environment

9.2.1.1 Crystal Aging at BABAR

Over the span of *BABAR*'s running, the EMC barrel crystals have been damaged to a certain extent by high levels of radiation, which are monitored by 116 radFETs distributed throughout the subdetector. The most common form of damage [3] comes from the development of absorption bands which reduce an affected crystal's light yield. Although crystals in the EMC endcap experienced higher levels of radiation than those in the barrel, all EMC crystals from the furthest backward to those more forward integrated non-negligible doses. The resulting changes in crystal light yields were monitored and corrected for during *BABAR* operation using calibrations performed at either end of the dynamic range of the detector: a low-energy calibration using a 6.13 MeV radioactive photon source, which is discussed below in Sec. 9.2.2.3, and a high-energy calibration with Bhabha events.

The change in light yield for barrel crystals as a function of absorbed radiation dose, based on the low-energy calibration data, is shown categorized by crystal manufacturer in Figure 9.1. Though care was initially taken to produce uniformity between crystals before they were integrated into the detector, there have been varying degrees of degradation in performance as time has progressed. Depending on the manufacturer, the total decrease in light yield can be up to $\sim 10\%$. Much of the decrease in light yield occurred during the initial years of *BABAR* running and, as the integrated dose increases, there is less light loss per unit dose received. However, as can be seen in Fig. 9.1, in the Super$B$ environment, the eventual loss in light yield for the worst-performing barrel crystals, generally those provided by Kharkov and Hilger, may be substantial. The relative poor performance of the crystals provided by these manufacturers was known at the time of the barrel's construction and, to the extent possible, these manufacturers' crystals were placed as far backwards in polar angle as possible. as is shown in Fig. 9.1.

9.2.1.2 Backgrounds

In addition to crystal aging, background can degrade energy resolution due to electronic signal pile-up. The dominate source is expected to be photons and neutrons from radiative Bhabha events interacting with the detector material. This effect is negligible in *BABAR*. But in Super$B$, it could be substantial, especially in the low energy range.

The pile-up effect is a function of signal pulse shape. Since Super$B$ is reusing *BABAR*'s barrel, the long decay time of CsI(Tl) crystal cannot be changed. Nonetheless, readout and electronics can be optimized to minimize the the impact of the pile-up effect. To ensure similar physics sensitivity as *BABAR*, the background pile-up should have a negligible effect in energy resolution of high energy photons (*how high?*)

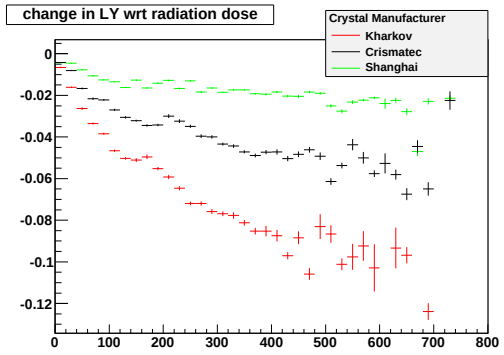

(a) Barrel backward

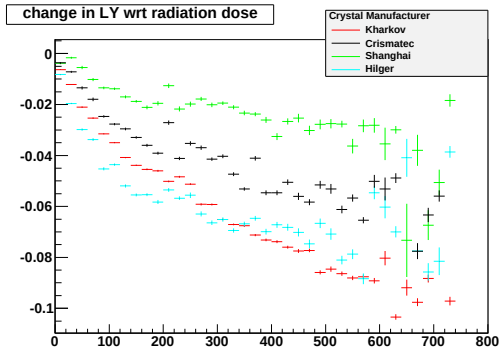

(b) Barrel forward

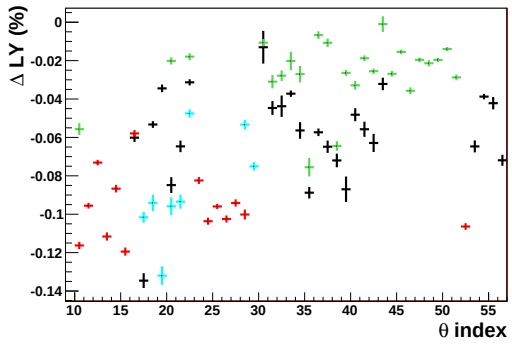

(c) Δ LY vs theta

Figure 9.1: Backward and forward barrel crystal light yield decreases versus absorbed radiation dose, with the different crystal providers indicated. The bottom plot shows the light yield decrease as a function of polar angle index for each manufacturer using the same color legend.

and contribute to no more than $x\%$ to energy resolution of photons at 100 MeV.

9.2.2 Description of BABAR Barrel Calorimeter

9.2.2.1 Mechanical design

The *BABAR* barrel EMC consists of a cylindrical shell with full azimuthal coverage, extending in polar angle from 26.8° to 141.8°. A longitudinal cross-section, including the forward endcap, is shown in Figure 9.2. The barrel EMC contains 5,760 crystals arranged in 48 separate azimuthal rings, with 120 identically dimensioned crystals in each ring. Each crystal has a tapered trapezoidal cross section, with length increasing from 29.6 cm furthest backward to 32.4 cm furthest forward in order to minimize the effects of shower leakage from increasingly higher energy particles. To minimize the probability of preshowers, the crystals are completely supported at the outer radius, with only a thin gas seal at the front. The amount of material in front of the crystal faces is $0.3 - 0.6X_0$.

Figure 9.3 is a schematic of a single crystal, showing the layered crystal wrappings, silicon photodiodes, diode carrier plate, preamplifier, and the aluminum housing enclosing the items at the crystal rear face.

The barrel crystals are inserted into modules that are supported individually from an external cylindrical support structure. At *BABAR*, the barrel support cylinder carries the load of the barrel modules plus the forward endcap to the magnet iron through four flexible supports, which decouple and dampen any acceleration induced by movements of the magnet iron during an earthquake.

The crystal modules are built from tapered, trapezoidal compartments made from carbon-fiber-epoxy composite (CFC) with 300 μm-thick walls. Each compartment loosely holds a single wrapped and instrumented crystal, assuring that the forces on the crystal surfaces never exceed its own weight. Each module is surrounded by an additional layer of 300 μm CFC to provide additional strength. The modules are bonded to an aluminum strong-back that is mounted on the external support structure. Figure 9.4 shows some details of a module and its mounting

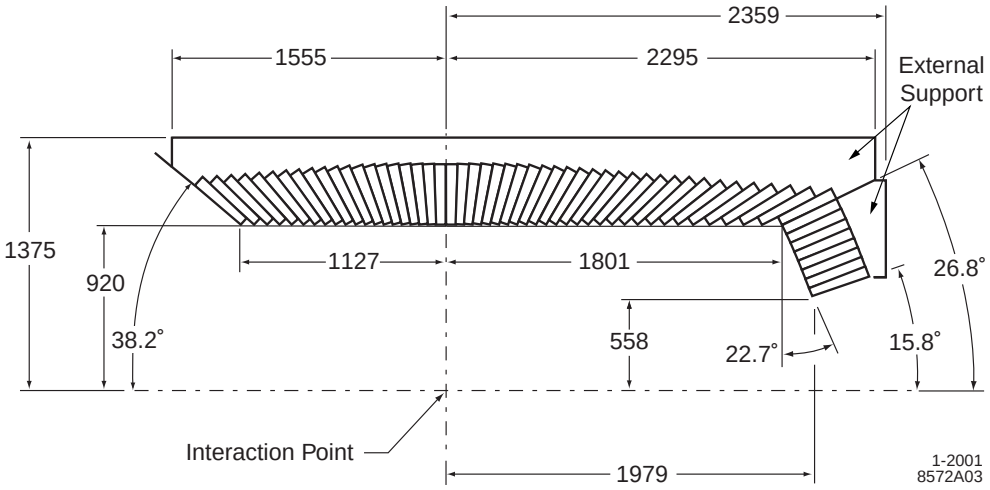

Figure 9.2: Longitudinal EMC cross-section (top half) showing the arrangement of the 48 barrel and 8 endcap crystal rings. The detector is axially symmetric around the z-axis. Dimensions are in mm.

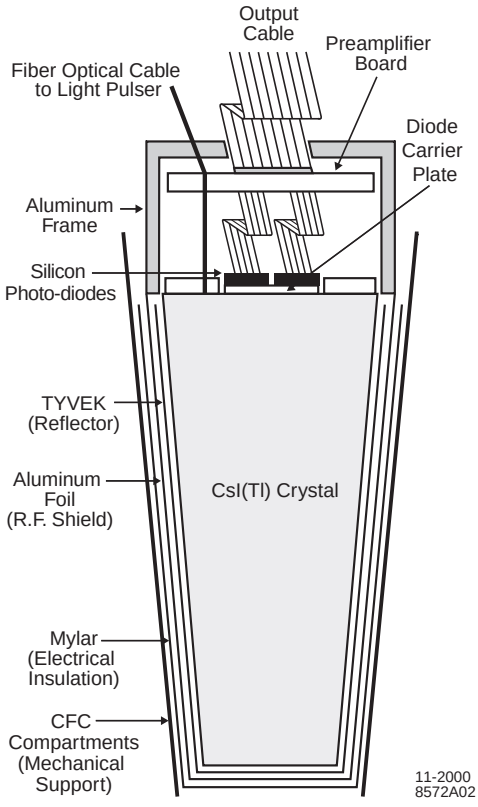

Figure 9.3: A schematic (not to scale) of a wrapped barrel crystal and the front-end readout package mounted on the rear face. Also indicated is the tapered, trapezoidal CFC compartment, which is open at the front.

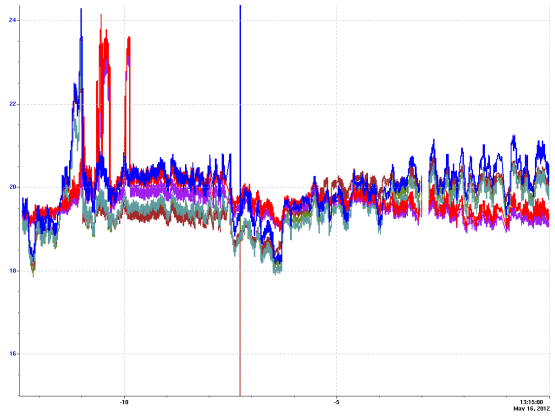

Figure 9.5: Barrel and endcap thermal history for one year. The four barrel quadrants are blue, brown, and dark and light green; the endcap halves are purple and red. The horizontal axis shows months prior to 16 May 2012. The vertical line extending the full range of the plot is an artifact due to a bad database record.

to the support cylinder. This scheme minimizes inter-crystal materials while exerting minimal force on the crystal surfaces, preventing geometric deformations and surface degradation that could compromise performance.

The barrel is divided into 280 separate modules, each holding 21 crystals (7×3 in $\theta \times \phi$), except for the furthest backward modules which are only 6×3. After insertion of the crystals, the aluminum readout frames, which also stiffen the module, are attached with thermally-conducting epoxy to each of the CFC compartments. The entire $\sim$ 100 kg module is then bolted and again thermally epoxied to an aluminum strong-back, which is shown in Figure 9.4. The strong-back contains alignment features as well as channels that couple to the cooling system. Each module is installed into the 2.5 cm-thick, 4 m-long aluminum support cylinder, and subsequently aligned. On each of the thick annular end-flanges, the support cylinder contains access ports for digitizing electronics crates with associated cooling channels, as well as mounting features and alignment dowels for the forward endcap. Figure 9.4 shows details of an electronics mini-crate situated within the support cylinder.

The primary heat sources internal to the calorimeter are the preamplifiers (2×50) mW/crystal and the digitizing electronics (3 kW per end-flange). In the barrel, the preamplifier heat is removed by conduction to the module strong backs which are directly cooled by Fluorinert (polychlorotrifluoroethylene). The digitizing electronics are housed in 80 mini-crates, each in contact with the end-flanges of the cylindrical support structure. These crates are indirectly cooled by chilled water pumped through channels milled into the end-flanges close to the inner and outer radii.

The entire barrel is surrounded by a double Faraday shield composed of two 1 mm-thick aluminum sheets so that the diodes and preamplifiers are further shielded from external noise. This cage also serves as the environmental barrier, allowing the slightly hygroscopic crystals to reside in a dry, temperature-controlled nitrogen atmosphere.

During *BABAR* data-taking, of particular concern is the stability of the photodiode leakage current, which rises exponentially with temperature, and crystal light yield, which is weakly temperature dependent. Currently, the most important issue is that the large number of diode-crystal epoxy joints experience as little stress as possible due to differential thermal expansion. Studies performed prior to the construction of the EMC showed that these joints should be safe when maintained at a temperature of (20 ± 5) C, and both the barrel and endcap are currently maintained in this state, with temperatures monitored in real-time and recorded in the conditions database. Fig. 9.5 shows the temperature history for one year for the four quadrants of the barrel and the two halves of the endcap.

9.2.2.2 Readout

Each CsI(Tl) barrel and endcap crystal is read out using $2 \times 1\,\mathrm{cm}^2$ silicon PIN diodes glued to a transparent 1.2 mm-thick polysterene substrate that, in turn, is glued to the center of the rear face of the crystal by an optical epoxy to max-

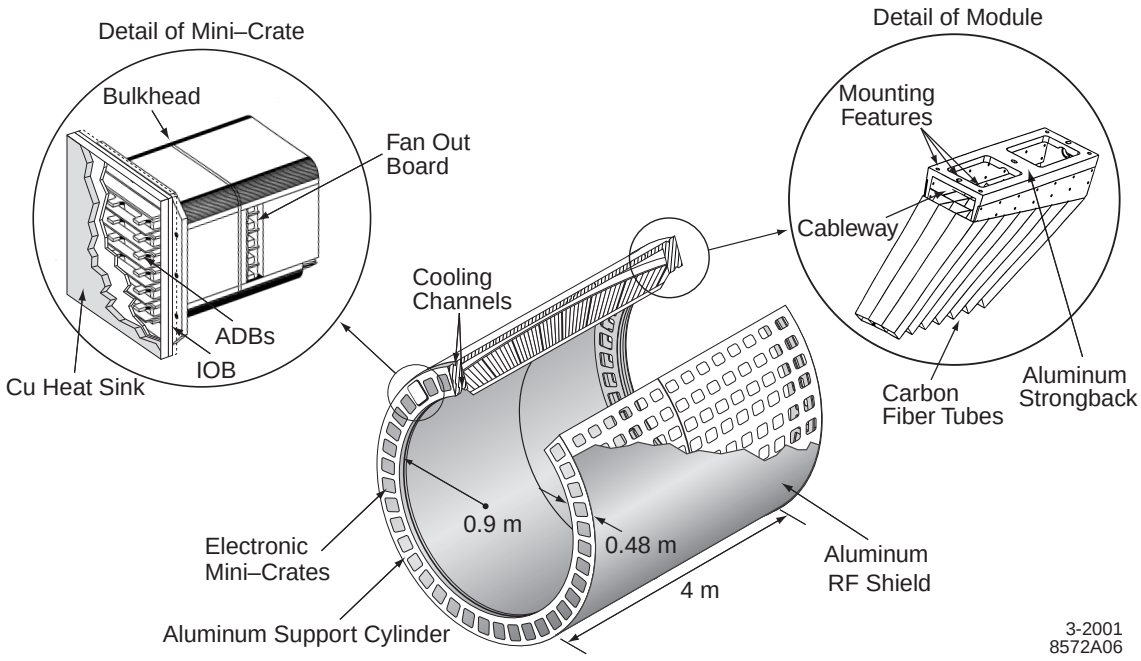

Figure 9.4: The EMC barrel support structure, with details on the modules and electronics crates (not to scale).

imize light transmission. The surrounding area of the crystal back face is covered by a plastic plate coated with white reflective paint, which has has two 3 mm-diameter penetrations for the fibers of the light pulser monitoring system.

The signal from each of the diodes is transmitted to the preamplifier through a cable terminated in a connector that allows detachment of the preamplifier from the photodiodes. Each of the diodes is directly connected to a low-noise preamplifier, whose characteristics are discussed below in Sec. **??**. The entire assembly at the crystal's rear facee is enclosed in an aluminum fixture as shown in Figure 9.3. This fixture is electrically coupled to the aluminum foil wrapped around the crystal and thermally coupled to the support frame in order to dissipate the heat load from the preamplifiers.

9.2.2.3 Low-energy Source Calibration

Calibration and monitoring during data-taking is important for achieving the best possible performance of the EMC. The low-energy calibration system devised for *BABAR* produces a 6.13 MeV photon line from a short-lived ^{16}O transition that can be activated as required. This system was successfully used for routine bi-weekly calibrations of the *BABAR* calorimeter, and is an ideal match to the Super*B* requirements. We therefore propose to refurbish the *BABAR* system for use in Super*B*. The final *BABAR* calibration run was taken on 3 July 2008, and records of this run, as well as a few earlier ones, will be maintained for comparisons with the refurbished EMC.

In this system, fluorine, a component of Fluorinert^{TM} (polychlorotrifluoro-ethylene) coolant liquid, is activated with a neutron source to produce the ^{16}N isotope, which β-decays to an excited state of ^{16}O. This state in turn emits a 6.13 MeV photon as it cascades to its ground state. The source spectrum, as seen with a CsI(Tl) crystal with the PIN diode readout used in *BABAR*, is shown in Figure 9.6. There are three principal contributions to the overall peak, one at 6.13 MeV, another at 5.62 MeV, and the third at 5.11 MeV; the latter two

representing e^+e^- annihilation photon escape peaks. Since all three peaks have well-defined energies, they simultaneously provide an absolute calibration, as well as a measure of the linearity of the system at the low end of the energy scale.

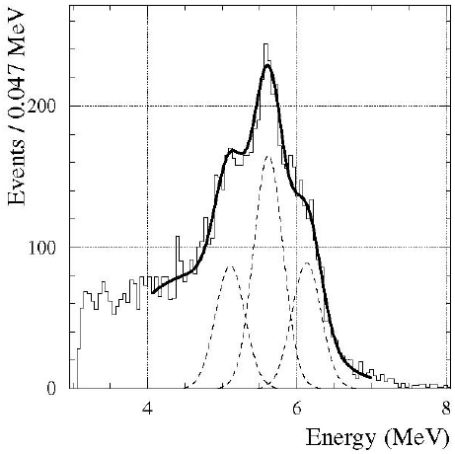

Figure 9.6: Energy spectrum in a single *BABAR* CsI(Tl) crystal irradiated with 6.13 MeV photons from an $^{16}O^*$ source, read out with a PIN diode. The solid curve is a fit to the spectrum, including Gaussian contributions at 6.13 MeV, 5.62 MeV, and 5.11 MeV, indicated by the dashed curves.

The fluorine activation is provided by a commercial deuterium-tritium (DT) generator, which produces 14.2 MeV neutrons by accelerating deuterons onto a tritium target, at typical rates of several times 10^8 neutrons/second. The DT generator is surrounded with a bath of fluorine-containing liquid, which is then circulated in a manifold to the barrel and endcap crystals. There are many suitable fluorine-containing liquids available; "Fluorinert FC77" [9], was used in *BABAR*. The half-life of the activated liquid is 7 s, hence residual radioactivity is not a substantial concern when the DT generator is not operating.

The Fluorinert is stored in a reservoir near the DT generator. When a calibration run is started, the generator and a circulating pump are turned on. Fluid is pumped from the reservoir through the DT bath to be activated, and then to the calorimeter. The system is closed, with fluid returning from the calorimeter to the reservoir. A schematic of the system is shown in Figure 9.7. In *BABAR*, the fluid is pumped at 3.5 l/s, producing a rate of approximately 40 Hz in each of 6500 crystals. This produces a calibration with a statistical uncertainty of 0.35% on peak positions in a single crystal in a 10-minute calibration run [8][10]. The crystals are approximately 12 m from the DT generator. Although Fluorinert FC-77 is no longer manufactured, an adequate supply is on-hand. Should it be necessary to substitute a commercially available coolant liquid (all of which have slightly reduced fractions of fluorine), the pumping rate would have to be adjusted accordingly.

In *BABAR*, the fluid transport manifold consisted of thin-wall (0.5 mm) aluminum tubing (3/8 inch diameter), flattened to meet space constraints. One millimeter of Al presents 1.2% of a radiation length. This material is placed in front of the *BABAR* crystals, as is an additional 2mm of Al in the structural support of the tube assemblies, which are deployed as a set of curved panels. This system can be reused for the barrel in Super$B$, or it could be rebuilt to better integrate into the barrel structure, reducing the amount of material and providing additional radial space.

The DT generator is a small accelerator; radiation safety protocols factor into the mechanical design of the system. For example, operation of the source will be done remotely, in a no-access condition. It will be shielded according to INFN radiation safety regulations. The shielding will be interlocked such that the DT generator cannot be operated if the shielding is not in place. The reservoir is capable of holding the entire volume of Fluorinert fluid. Operation of the system is anticipated to be approximately weekly. In the event of a fluid leak, the maximum exposure for the similar *BABAR* system is calculated to result in an integrated dose of less than 1 mrem. A detailed hazard analysis will be performed in collaboration with INFN radiation safety experts.

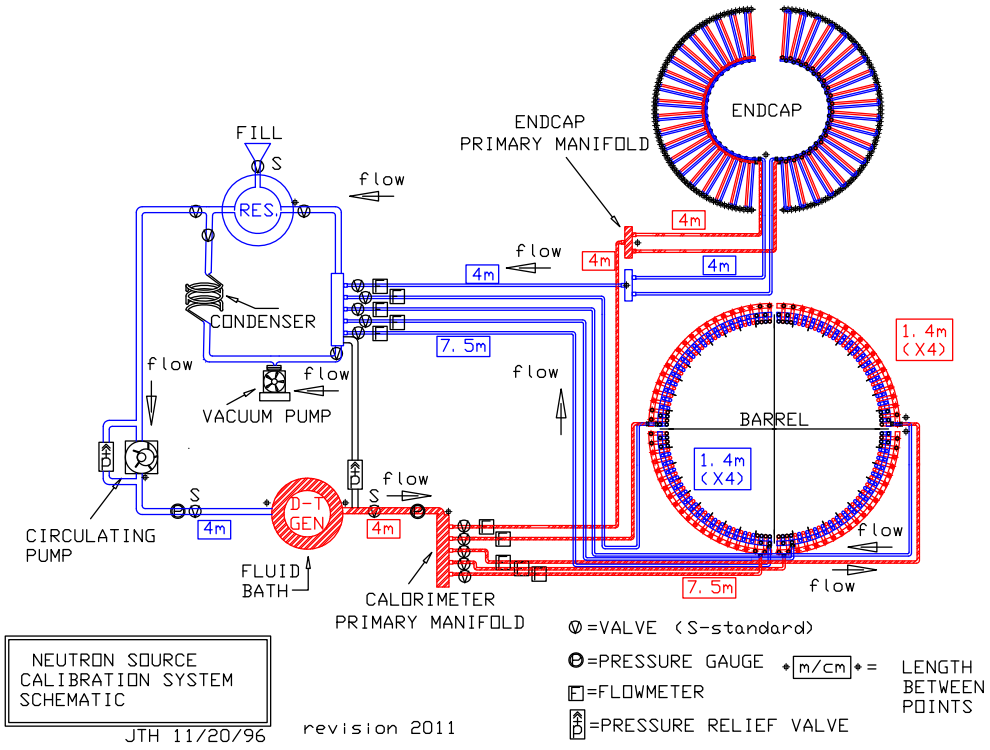

Figure 9.7: Schematic of the *BABAR* calibration system, which produces ^{19}F 6.13 MeV photons from an ^{16}O* source, as updated for Super*B*. The system is used for both the barrel and forward endcap calorimeters.

9.2.2.4 Light Pulser

The light response of the individual crystals during *BABAR* running was measured daily using a light-pulser system, which transmitted spectrally filtered light from a xenon flash lamp through optical fibers to the rear of each crystal, and we propose to refurbish the *BABAR* system for use in Super$B$. The light pulse is similar in spectrum, rise-time and shape to the scintillation light in the CsI(Tl) crystals. The pulses were varied in intensity by neutral-density filters, allowing a precise measurement of the linearity of light collection, conversion to charge, amplification, and digitization. The intensity was monitored pulse-to-pulse by comparison to a reference system with two radioactive sources, ^{241}Am and ^{148}Gd. Each of these was attached to a small CsI(Tl) crystal read out by both a photodiode and a photomultiplier tube, and were stable to 0.15% over a period of one week.

9.2.3 Performance of BABAR barrel

9.2.3.1 Energy and position resolution

The energy resolution of a homogeneous crystal calorimeter is generally given empirically as two terms summed in quadrature:

$$\frac{\sigma_E}{E} = \frac{a}{\sqrt[4]{E(GeV)}} \oplus b, \qquad (9.1)$$

where E and σ_E refer to the energy of a photon and its RMS error in GeV. The energy-dependent term, a, arises from fluctuations in photon statistics, electronics noise, and beam background generated noise. The constant term, b, arises from non-uniformity in light collection, leakage, and absorption in the material between and in front of the crystals, as well as uncertainties in the calibration. The angular resolution is primarily determined by the crystals' transverse dimension. Figure 9.8 shows the energy and angular resolution of the *BABAR* calorimeter derived from various data control samples, as indicated in the plot legends, and from which are derived the fundamental EMC performance characteristics:

$$\frac{\sigma_E}{E} = \frac{(2.30 \pm 0.03 \pm 0.3)\%}{(E(\mathrm{GeV}))^{0.25}} \oplus (1.35 \pm 0.08 \pm 0.2)\% \qquad (9.2)$$

$$\sigma_\theta = \sigma_\phi = \frac{(4.16 \pm 0.04)\mathrm{mrad}}{\sqrt{E(\mathrm{GeV})}} \oplus (0.0 \pm 0.0)\mathrm{mrad} \qquad (9.3)$$

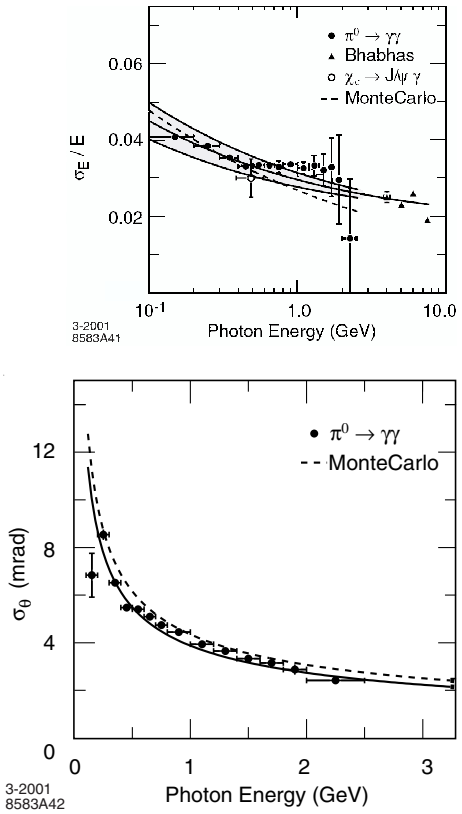

Figure 9.8: Photon energy (top) and angular (bottom) *BABAR* EMC resolutions.

Figure 9.9 shows similar plots from the December 2011 Super$B$ Fastsim using single photon MC at several energies. *[COMPARE-AND-CONTRAST BETWEEN BABAR DATA AND SUPERB MC.]*

9.2.3.2 Gamma-gamma mass resolution

Figure 9.10 shows a two-photon invariant mass distribution in the π^0 and η mass ranges for selected *BABAR* data multi-hadron events from 2001. Photons are required to have $E_\gamma > 30\,\mathrm{MeV}$, with π^0 candidate energy $E_{\pi^0} > 300\,\mathrm{MeV}$ and η candidate energy $E_\eta > 1\,\mathrm{GeV}$. The reconstructed π^0 mass is found to be

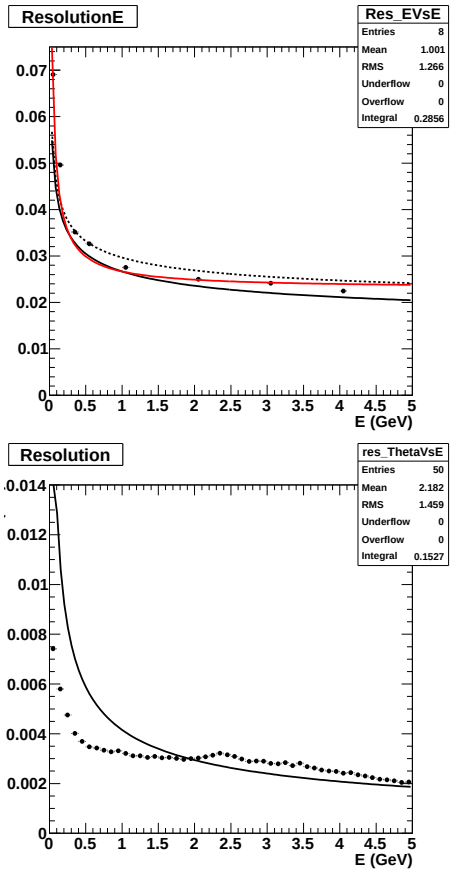

Figure 9.9: Fastsim single photon energy (top) and angular (bottom) resolution.

134.9 MeV/c^2, with a width of 6.5 MeV/c^2; the fitted η mass is 547 MeV/c^2, with a width of 15.5 MeV/c^2. These can be compared to a two-photon invariant mass distribution from the June 2012 Fastsim MC production *ADD FIGURE.*

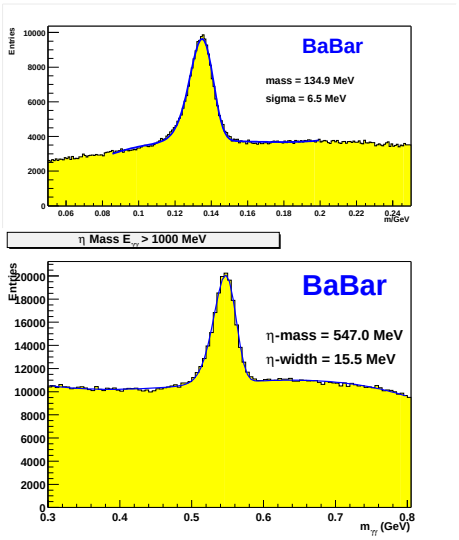

Figure 9.10: Two-photon invariant mass distribution in π^0 (top) and η (bottom) mass ranges.

9.2.3.3 Radiation Damage Effects on Resolution

Beam generated backgrounds are the major cause of reduction in the light yield of the crystals over time. In order to monitor this source of background, 116 Rad FETs are placed in front of the calorimeter barrel and endcap crystals. These RadFETs are real-time integrating dosimeters based on solid-state MOS technology and are integrated into the EPICS monitoring system. As can be seen in Fig 9.11, the integrated dose is largest in the endcap, which is closer the the beam line as well as more forward in polar angle making it more susceptible to beam generated background photons from small angle radiative Bhabha events in which an $e^{\pm}$ strikes a machine element.

Radiation damage impacts CsI(Tl) through the creation of color centers in the crystals, inducing absorption, and resulting in a degradation of response uniformity and light yield. The nominal dose budget for the *BABAR* CsI(Tl) calorimeter is 10 krad over the lifetime of the detector. Pure CsI and L(Y)SO are considerably more radiation hard (see Table **??**). The dominant contribution to the dose arises from luminosity and single-beam background sources, and hence is due to MeV-level photons and (presumably) neutrons; the integrated dose scales approximately linearly with integrated luminosity.

The measured reduction of light yield due to radiation damage is shown as a function of integrated luminosity in Fig. 9.11. To date, a total dose of about 1.2krad has been received in the most heavily irradiated regions, resulting in a loss of about $\sim 15\%$ of the total light yield, but with no measurable impact on physics performance. It is notable that most of the observed light loss occurred relatively early in *BABAR* running, although radiation dose has been accumulating relatively steadily, and that crystals from different manufacturers have responded somewhat differently to irradiation. It is anticipated that the CsI(Tl) barrel will have accumulated approximately 1.5 krad in the most irradiated regions by the end of nominal *BABAR* running in 2008.

In order for the barrel calorimeter to function in the Super*B* environment, beam background rates must be maintained at a level of approximately 1 MeV/μs or less per CsI(Tl) crystal. If this condition is achieved, then radiation dose rates are anticipated to be roughly comparable to current *BABAR* levels. A dose budget of well under 1 krad/year is expected to be achievable. At this a level, the CsI(Tl) barrel would survive for the duration of Super*B* operations. This assumption will, however, need to be verified by detailed simulation.

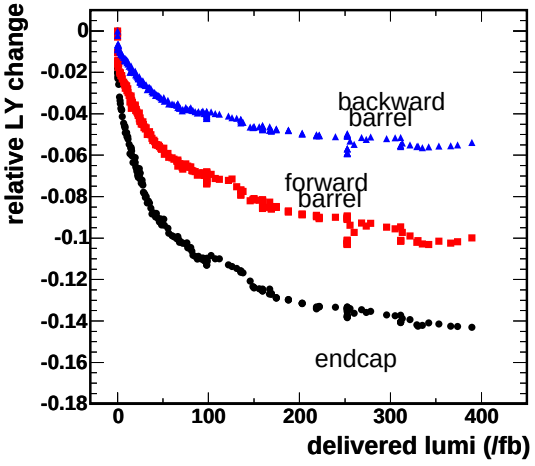

Figure 9.11: The light yield loss in the *BABAR* CsI(Tl) crystals due to radiation damage as a function of luminosity. The total dose received after 300 fb^{-1} is 1.2k rad in the endcap and 750 rad in the barrel.

9.2.3.4 Expected Changes in Performance at SuperB

The CsI(Tl) crystals used in the barrel calorimeters of both *BABAR* and Belle are the most expensive elements of the two detectors. Based on the performance that has been achieved, and the radiation damage that has been observed so far, both collaborations have concluded that the reuse of the barrel crystals is possible at a Super *B* Factory.

The baseline assumption is that the geometry of the crystals is unchanged from that of the current *BABAR* detector. The one change that should be made is to move the position of the interaction point from −5 cm to +5 cm relative to the position of the crystal gap normal to the beam axis. This adjustment retains the current non-pointing geometry, but moves the barrel to a slightly more symmetric position, in view of the reduced energy asymmetry. The effect of the change in boost from $\gamma\beta = 0.56$ to 0.28 and the shift of the IP is to increase the angular coverage of the barrel from 79.5% ($\cos\theta = -0.931$ to $+0.661$) to 84.1% ($\cos\theta = -0.883$ to $+0.798$).

If the crystal geometry is unchanged, it is in principle possible to transport the entire barrel calorimeter as one cylinder. However, the barrel was not designed for long-haul moves, and entertaining this option requires a substantial engineering evaluation. Alternatively it could be disassembled into its 280 individual modules, which would be transported separately and reassembled on arrival. This option carries lower risk and is the baseline, unless further study demonstrates that the barrel can be moved as a unit. The costs of these alternatives are discussed in the chapter on the reuse of existing *BABAR* detector elements.

A possible change to improve the coverage in the backward region would be to add one or two additional rings of crystals to the last module ring in θ, which currently only contains 6 rings of crystals. However, this would lead to major changes in the mechanical support structure and a redesign of the electronics readout, so it will not be undertaken unless there is a significant gain from the extra ring(s). Changes to the rear section of the barrel also interact strongly with the possible addition of a backward endcap calorimeter (Sec. 9.4).

9.2.4 Electronics changes

The BaBar EMC barrel crystals are coupled to two PIN (Hamamatsu S2744-08) diodes glued to the large area of the crystal face. The possibility to change these photo-detectors with new devices was investigated but discarded due to the strong mechanical constraints and the impossibility to unglue the PIN photodiodes without the risk of damage. Each PIN diode is read with a separate electronic chain composed of a charge sensitive preamplifier and a CR-RC-RC shaper, with 800 ns −250 ns −250 ns shaping time. The output of each channel is amplified in two chains respectively with a gain of 1 and 32.

9.2.4.1 Requirements

The increased background radiation in the Super$B$ environment calls for a shorter integration time at the prize of a reduction of the integrated light and correspondingly a worsening for the signal-to-noise ratio. Furthermore, also the shaping time needs to be reduced at the level of few hundreds of nanoseconds and this increases the bandwidth of the shaper and consequently the electronic noise. Finally, the need to have a good time signal to use in the EMC trigger focused the design of the charge preamplifier to a transimpedence amplifier with a low feedback capacitance.

The design of the preamplifier requires special care to obtain a lower noise from the beginning by choosing low noise components. We expect also an increase of the power consumption of the new Front End Boards due to the use of larger bandwidth operational amplifiers and of off-the-shelf components.

The choice among possible solutions will come from a compromise between radiation background and electronic noise. In order to estimate the latter

9.2.4.2 Electronic noise measurements

A test stand has been setup in the Electronics Laboratory (LABE) of the INFN in Rome in order to study the electronic noise of the FEE of the Barrel EMC. The aim of this test is to study the effect of short integration times, of the order of 100 ns, by measuring the noise level for different FEE configurations. To this aim a CsI(Tl) crystal from the BaBar calorimeter, of about $6 \times 6 \times 30$ cm^3, has been equipped with the photosensor under test on one side, and with an EMI9814B PMT on the opposite side to provide the trigger. As photosensors,

standard PIN diodes from BaBar have been used, of 1×2 cm^2 sensitive area (only one of the pair is readout), operated at 60 V. As an alternative option, the Avalanche PhotoDiodes (APD) of the CMS experiment have been considered; they have 0.5×0.5 cm^2 sensitive area, and have been operated at two different voltages, 340 and 380 V.
The scintillation of the crystal has been excited with a ^{60}Co radioactive source characterized by two well defined γ lines of 1.17 and 1.33 MeV. The photosensor has been readout through a Charge Sensitive Preamplifier (CSP) followed by a gaussian shaper. Both the photosensor and the PMT signals have been acquired by a LeCroy 12 bits digital oscilloscope. The waveforms have been recorded at a sampling rate of 20 GSamples/s, and 50000 events have been collected for each configuration studied. In fig.**??** 100 superimposed waveforms for a run with an APD are shown: the signal is hardly visible due to the large noise, but averaging over a large number of waveform the random noise almost disappears, and the signal becomes visible, see fig.**??**. PMT signal and the vertical line indicates the time of the trigger; the bottom curve is the photosensor signal (PIN diode in this example). For each event the maximum amplitude of the photosensor signal after the trigger time is searched for, while the region before the trigger is used to evaluate the baseline.
The chosen CSP is the Hamamatsu H4083 with 100 ns integration time. It has been tested in combination with a gaussian shaper with shaping times ranging from 100 to 500 ns.
A prototype amplifier (LNA02V0) developed at LABE in Rome, has also been tested. This prototype is very similar to the Hamamatsu CSP, but with slower rise time of the output signal, 400 vs 300 ns, and then with narrower bandwith.
As a benchmark, a CSP with very large integration time, 140 μs, similar to the BaBar readout chain, has been used. Finally a test of a PIN diode with the original BaBar FEE has also been performed, to check the performance of our experimental setup.

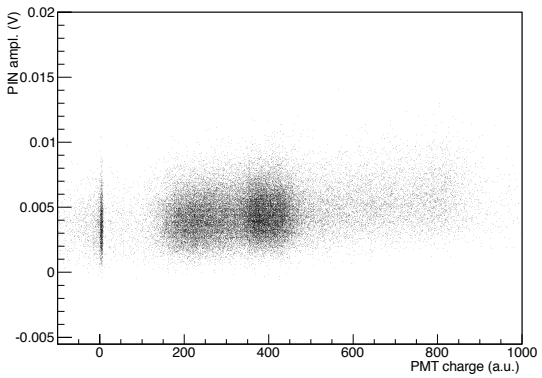

Figure 9.12: PMT vs APD response.

In fig.**??** the charge spectrum of the PMT is shown, with a fit superimposed: the two γ lines of $^{)}$Co are clearly visible as well as the small peak corresponding to the sum of the photon energies, 2.5 MeV. The basic idea is to use the two γ lines and their sum to calibrate the energy response of the photosensor, and to use this calibration to evaluate the equivalent electronic noise (in MeV) starting from the absolute noise (expressed in mV).
In the scatter plot of fig.9.12, an example of APD maximum amplitude as a function of PMT charge is reported. This scatter plot is divided into six regions: the pedestal around $Q_{PMT} = 0$, the crystal background, the two γ lines, the tail of the crystal background and the region of the sum of the two γ's. The calibration of the energy scale is obtained from a linear fit of the peaks of the distributions as function of the photon energy (Fig. 9.13). The dependence of the widths of the same distributions on photon energy is shown in fig.9.13; as an estimate of the electronic noise the average of the first four points is taken, and the equivalent noise is obtained by dividing it by the calibration factor. For the shown example:

$$\frac{1.5\text{mV}}{0.8\text{mV/MeV}} = 1.9\text{MeV} \qquad (9.4)$$

The same analysis has been repeated for all the studied configurations. In Tab. 9.2 the absolute noise is reported. The shortening of the shaping time increases the noise level, then in the study of the PIN only 500 ns is considered.

The energy calibration factors are related to the overall gain of the sensor plus FEE chain, and the shortening of the shaping time corresponds to a decrease of the gain. It has also been noted that the gain of the APD's at 380 V is about three times the gain at 340 V, in spite of the fact that the absolute noise is only slightly higher.

Table 9.2 reports also the equivalent noise. Only one PIN of the two paired together is readout, then it can be extrapolated that if both PINs were acquired, the gain would double, while the electronic noise would increase by a factor of $\sqrt{2}$, then the equivalent noise should decrease by the same factor. In this case the BaBar FEE noise goes from 0.78 to 0.55 MeV and the Hamamatsu from 2.5 to 1.8 MeV, and for the prototype LNA02V0 from 1.9 to 1.3 MeV.

The impact of the reduction in integration and shaping time is significant and therefore the search for further options and the optimization including all effects is still ongoing.

9.2.4.3 Readout design

The readout of each PIN diode is done using two separate channels. This choice is motivated from the necessity to have high redundancy and minimize the possibility to have dead channels in case of a PIN diode break. In order to minimize the noise of the Front End Boards we provide two outputs for each channel, one for the low energy range and the other for the high energy range, with a gain of 1 and 32 as in *BABAR*. The idea to use only one gain in the Front-End was dropped because using shorter integration times give smaller signals than *BABAR*. Consequently we have to improve signal to noise from the beginning, avoiding passing low level signals in long cables. The four signals for each crystal (two channels with two different gains) are combined in the digitizer board; normally the mean signal from two PIN diodes is chosen but in case of breakage of one PIN diode only one signal can be chosen. A dedicated circuit chooses the signal range to use for the digitalization. The digitalization is done using a 12 bit ADC, with a shaping time of 500 ns, a sampling rate of 7.43 MHz (RF/8) plus a range bit. If full granularity data were pushed synchronously to the trigger, about 520 optical links would be necessary. The number of synchronous trigger links can be drastically reduced by performing sums of 4 3 cells on the detector side, so that 6 such energy sums could be continuously transmitted through a single optical serial link. This permits a reduction in the number of trigger links so as to match the topology of the calorimeter electronics boxes, which are split into 40 sectors on both sides of the detector. Therefore, the total number of links would be 80 both for the trigger and the data readout toward the ROMs, including a substantial safety margin ($>$ 1:5).

9.2.5 SLAC De-installation, Transport and Local Storage

9.2.6 Electronics refurbishment

The guiding criterion in the upgrade of the Barrel electronics is to maintain the same hierarchy in the components as in *BABAR*, by using the same mechanical form factor for each board to fit the new system in the old mechanics.

The front end preamplifiers are located on the top of the crystals inside brass cages. The design of the cages is strictly connected to the crystal photodiodes assembly which is very difficult to unglue and disassemble. The brass cages are robust and can be dismounted and reused without the risk of damage.

With the intent to reuse this brass cage we choose the preamplifier form factor to fit inside using also the same form factor connector and cable.

The Barrel electronics in *BABAR* was housed inside 48 small custom-built crates (minicrates) located on the top of the 24 Barrel's for each side. Each minicrate contains a backplane that divides the connection board from the digitizer boards and an optical board on top.

Table 9.2: Absolute noise (mV) / Equivalent noise (MeV) for several electronic solutions

CSP - integration time - shaping time	$V_{APD} = 340$ V	$V_{APD} = 380$ V	PIN diode
Cremat - 140 μs - 500 ns	2.4/1.3	3.3/0.62	1.5/0.56
Hamamatsu - 100 ns - 500 ns	2.9/1.3	4.5/0.85	2.5/2.5
Hamamatsu - 100 ns - 250 ns	5.1/3.4	6.0/1.3	-
Hamamatsu - 100 ns - 100 ns	5.3/4.4	6.0/1.5	-
LNA02V0 - 100 ns - 500 ns	-	3.0/0.57	1.5/1.9
BaBar FEE	-	-	0.7/0.78

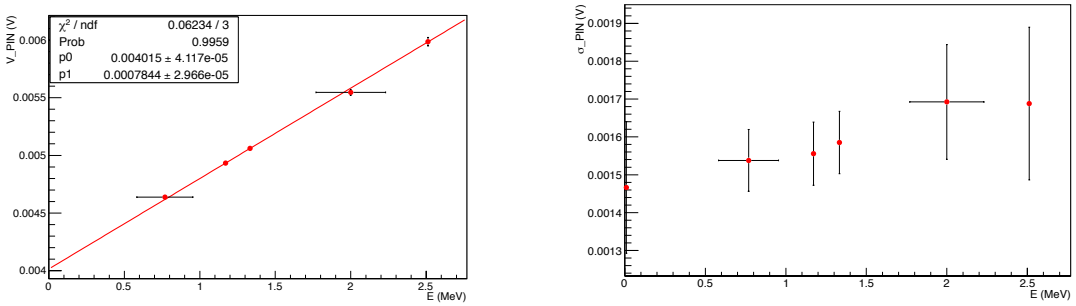

Figure 9.13: Left: calibration plot for the electronic noise measurements. Right: resolution as a function of the deposited energy.

We plan to use the mechanical structure of the minicrates maintaining the same form factors of the four boards (connection boards, backplane, digitizer board, and optical transmission board).

9.2.7 Re-installation at Tor Vergata

9.3 Forward Calorimeter

The Forward Calorimeter is designed to extend the coverage of the electromagnetic calorimeter to low angles, as detailed in Tab. 9.1. To be effective its performance needs therefore to be comparable with the Barrel Calorimeter. Thus, the design considers a calorimeter made of crystals and read-out by compact photodetectors capable of operating in magnetic field.

Taking as benchmark the *BABAR* detector, the relative energy resolution should be at most 4.3% at 100 MeV and 2.7% at 1 GeV. Also, in order to assure appropriate resolution on the π^0 invariant mass and to allow the $\pi^0 \to \gamma\gamma$ reconstruction up to sufficiently high energies, a segmentation at least comparable with the *BABAR* one is needed. Since the transverse crystal size is dictated by the Molière radius of the material, only crystals with a Molière radius at most as large as the CsI(Tl) can be considered. Finally hermeticity is also important, so the requirement on mechanics is that the fraction of particles originating from the interaction point passing through the cracks between the crystals be minimal, comparable with the barrel.

As already described for the Barrel Calorimeter, the most stringent constraints come from the presence of large background due to the extremely high luminosity. As shown in Fig. **??**, the expected dose integrated in a year ranges from $\sim$ 200 rad for the outermost rings to $\sim$ 2500 rad for the innermost ones. Consequently, the dose rate the crystals need to tolerate ranges from $\sim$ 0.1 rad/s to $\sim$ 1.0 rad/s, respectively.

As described in Sec. 9.1.1, the large rate of low energy photons can create radiation damage on the crystal themselves, thus reducing the light yield, and induce a degradation of the energy resolution due to pile-up. Therefore the chosen crystal must show a stable light yield under the expected radiation and the signal shape produced by the readout must be compatible with the expected rates.

We have investigated several combinations of crystals and electronics, as described below. The best option for performance is to use crystals made of LYSO, with readout by Avalance Photo-Diodes (APD). This configuration has been studied in detail. However, budget restrictions force us to adopt as baseline a "hybrid" scheme, making use of LYSO at the smallest radii while keeping the BaBar crystals, made of $CsI(Tl)$, in the outermost endcap layers. This permits a significant reduction in cost, while obtaining the benefits of LYSO where it is needed most, where the rate and radiation issues are most severe. As part of this cost compromise, the structural support of the *BABAR* endcap is reused instead of adopting a lower mass solution.

9.3.1 LYSO Crystals

In the last two decades, cerium doped lutetium oxyorthosilicate (Lu_2SiO_5 or LSO) [4] and cerium doped lutetium yttrium oxyorthosilicate ($Lu_{2(1-x)}Y_{2x}SiO_5$ or LYSO) [5] have been developed for the medical industry with mass production capabilities established. This section addresses the crystal properties, specifications, production and testing.

9.3.1.1 Introduction

Table 9.3 [6] lists basic properties of heavy crystals: NaI(Tl), CsI(Tl), pure CsI, bismuth gemanade ($Bi_4Ge_3O_{12}$ or BGO), lead tungstate ($PbWO_4$ or PWO) and LSO/LYSO. All have either been used in, or are actively being pursued for, high energy and nuclear physics experiments, which are also listed in the table. The experiment names in bold refer to future crystal calorimeters. NaI(Tl), CsI(Tl), BGO, LSO and LYSO crystals are also widely used in the medical industry. Mass production capabilities exist for all these crystals.

Because of their high stopping power, high light yield, fast decay time, small temperature coefficient and excellent radiation hardness, LSO and LYSO crystals have attracted a broad interest in the high energy physics (HEP) community [7, 8, 9, 10], and are chosen for the baseline material for the SuperB forward calorimeter. LSO and LYSO crystals from the following vendors have been tested during the R&D phase of the project: CTI Molecular Imaging (CTI), Crystal Photonics, Inc. (CPI), Saint-Gobain (SG), Sichuan Institute of Piezoelectric and Acousto-optic Technology (SIPAT) and Shanghai Institute of Ceramics (SIC).

9.3.1.2 Optical and Scintillation Properties

Transmittance and Emission

LYSO crystals of 20 cm (18 X_0) length are routinely produced in industry with good transmittance spectra. The left plot of Figure 9.14 shows the longitudinal (green) and transverse (red) transmittance spectra measured for a rectangular LYSO sample with a dimension of 2.5 $\times$ 2.5 $\times$ 20 cm (18 X_0). Significant red shift is observed in the absorption edge of the longitudinal transmittance as compared to the transverse transmittance, caused by internal absorption. The black line at the top is a fit to the theoretical limit of transmittance calculated by using the refractive index assuming multiple bounces between two end surfaces and no internal absorption [11]. It overlaps with the transverse transmittance spectrum at wavelengths longer than 420 nm, indicating excellent optical quality of the crystal. Also shown in this plot is the photo-luminescence spectrum (blue) [12]. The

Table 9.3: Properties of Heavy Crystal with Mass Production Capability

Crystal	NaI(Tl)	CsI(Tl)	CsI	BGO	$PbWO_4$	LSO/LYSO(Ce)
Density (g/cm^3)	3.67	4.51	4.51	7.13	8.3	7.40
Melting Point (°CC)	651	621	621	1050	1123	2050
Radiation Length (cm)	2.59	1.86	1.86	1.12	0.89	1.14
Molière Radius (cm)	4.13	3.57	3.57	2.23	2.00	2.07
Interaction Length (cm)	42.9	39.3	39.3	22.7	20.7	20.9
Refractive Index[a]	1.85	1.79	1.95	2.15	2.20	1.82
Hygroscopicity	Yes	Slight	Slight	No	No	No
Luminescence[b] (nm)	410	560	420	480	425	420
(at Peak)			310		420	
Decay Time[b] (ns)	245	1220	30	300	30	40
			6		10	
Light Yield[b,c]	100	165	3.6	21	0.30	85
			1.1		0.077	
d(LY)/dT[b,d] (%/°CC)	-0.2	0.4	-1.4	-0.9	-2.5	-0.2
Experiment	Crystal	CLEO	kTeV	L3	CMS	**Mu2e**
	Ball	*BaBar*		BELLE	ALICE	**SuperB**
		BELLE			PrimEx	**HL-LHC?**
		BES III			**Panda**	

a At the wavelength of the emission maximum.
b Top line: slow component, bottom line: fast component.
c Relative light yield of samples of 1.5 X_0 and with the PMT quantum efficiency taken out.
d At room temperature.

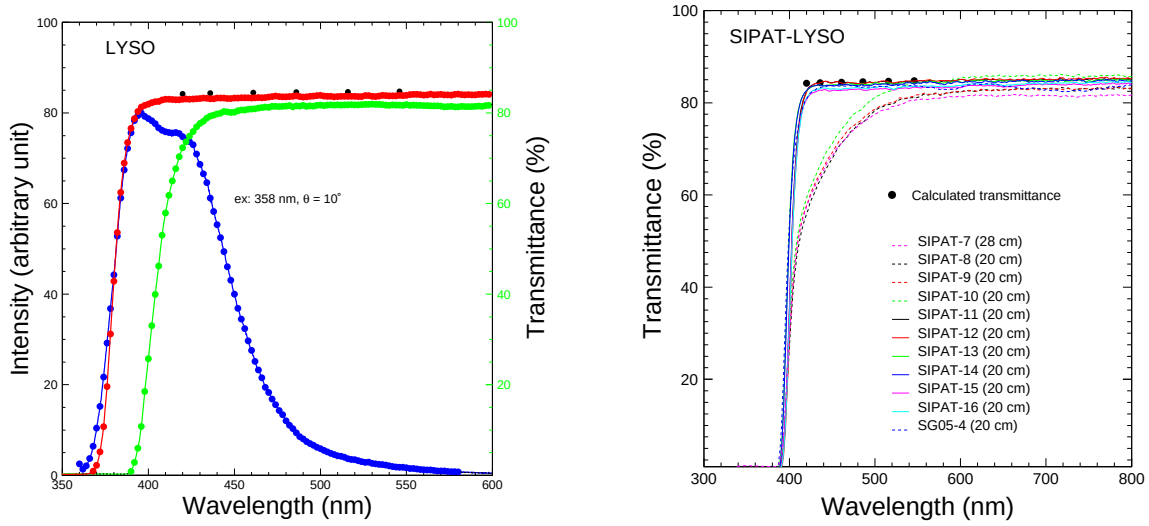

Figure 9.14: Left: The longitudinal (green) and transverse (red) transmittance spectra and the photo-luminescence (blue) spectrum are shown as a function of wavelength for a rectangular LYSO sample with a dimension of 2.5 × 2.5 × 20 cm. Right: Longitudinal transmittance spectra are shown as a function of wavelength for eleven LYSO crystals: ten from SIPAT and one from Saint-Gobain. All except SIPAT-7 are 20 cm long.

fact that a part of the emission spectrum is at the wavelengths shorter than the absorption edge indicates that this part of the scintillation light is absorbed internally in the crystal bulk, usually referred to as self-absorption effect. There is no such self-absorption effect in other scintillation crystals commonly used for HEP calorimeters, such as BGO, CsI(Tl) and PWO [6]. While this self-absorption has little consequence to 6 mm long pixels used in medical instruments, it affects light response uniformity for 20 cm long crystals used in the SuperB calorimeter. This effect will be discussed in section 9.3.1.2.

During the R&D phase for crystal development poor longitudinal transmittance was observed in some samples [13]. The right plot of Figure 9.14 shows that four samples (SIPAT-7 to SIPAT-10) have poor longitudinal transmittance between 380 nm and 500 nm, showing an absorption band. Further investigation shows that this absorption band is located at the seed end and is caused by point defects [12], associated with a bad seed used in their growth. With rigorous quality control, LYSO crystals grown later at SIPAT (SIPAT-11 to SIPAT-16) show no absorption band at the seed end, as shown in the right plot of Figure 9.14. An increase of light output of about 30% was found after this problem was resolved. It thus is important to include in crystal specifications a requirement on the crystal's longitudinal transmittance.

The left plot of Figure 9.15 shows typical quantum efficiencies of a PMT with multi-alkali cathode (Photonis XP2254b) and an APD (Hamamatsu S8664) [14]. Also shown in the figure are the photo luminescence spectra of LSO/LYSO, BGO and CsI(Tl) crystals, where the area under the luminescence spectra is roughly proportional to the corresponding absolute light output. Table 9.4 summarizes the numerical values of the photo luminescence weighted average quantum efficiencies for various readout devices. These numbers can be used to convert the measured photo-electron numbers to the absolute light output in photon numbers.

A significant red component was observed in the γ-ray induced luminescence spectra in the CTI LSO samples, but not in the LYSO samples from other growers [12]. This red compo-

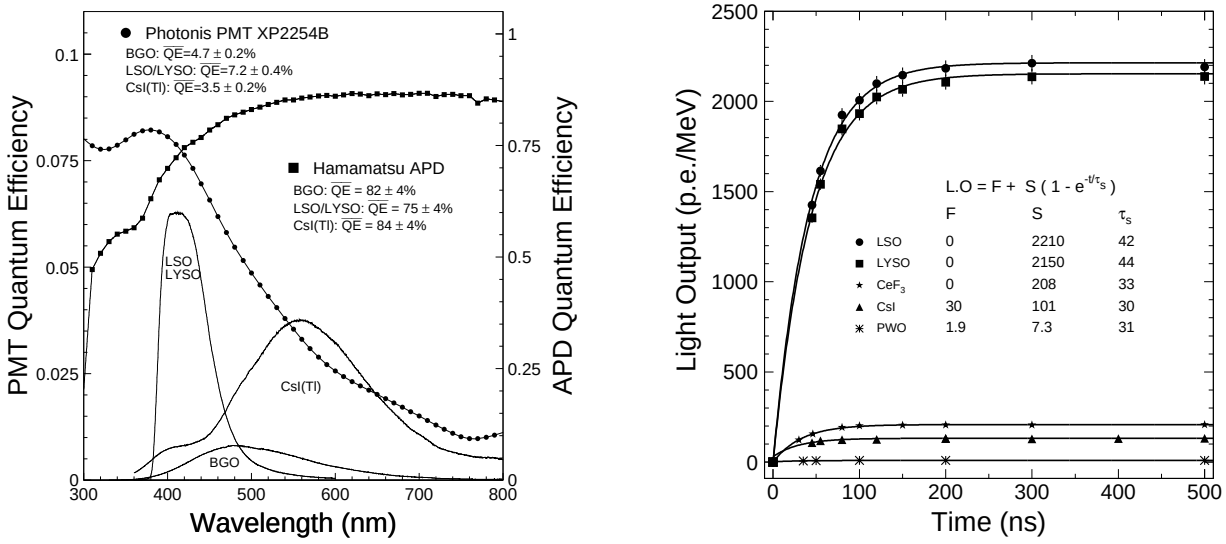

Figure 9.15: Left: The quantum efficiencies of a Hamamatsu R2059 PMT (solid dots) and a Hamamatsu S8664 APD (solid squares)are shown as a function of wavelength together with photo-luminescence spectra of the LSO/LYSO, BGO and CsI(Tl) samples, where the area under the luminescence spectra is roughly propotional to the corresponding absolute light output. Right: Light output measured by using a Photonis XP2254 PMT is shown as a function of integration time for six crystal scintillators.

nent disappeared after a γ-ray irradiation with an accumulated dose of 5×10^3 rad. This is the only significant difference observed between the large size LSO and LYSO samples [12], indicating that LYSO is a preferred choice.

Decay time and Light Output

The right plot of Figures 9.15 shows light output in unit of photo-electron/MeV, measured using a Photonis XP2254 PMT as a function of integration time, for six crystal scintillators [6]. The light output can be fit to the following function to determine the fast and slow components and the decay kinetics:

$$LO(t) = F + S(1 - e^{-t/\tau_s}), \qquad (9.5)$$

where F is the fast component of the scintillation light with a decay time of less than 10 ns, and S represents the slow component with a decay time of τ_s longer than 10 ns. The decay time of both LSO and LYSO crystals is about 40 ns.

As shown in Table 9.3 LSO and LYSO crystals have high light output, about 85% and 50% of NaI(Tl) and CsI(Tl) respectively, and about 18, 4, and more than 200 times of pure CsI, BGO, and PWO, respectively. Figure 9.16 shows 0.511 γ-ray pulse height spectra measured by a Hamamatsu R1306 PMT (left) and two Hamamatsu S8664-55 APDs (right) for four LSO and LYSO samples of $2.5 \times 2.5 \times 20$ cm^3 from CTI, CPI, SG, and SIPAT. The equivalent noise energy for the APD readout is less than 40 keV [14]. Poor energy resolution was found in the CPI LYSO sample, but not other samples. According to the grower this was caused by intrinsic non-uniformity, which may be improved by appropriate thermal annealing. It thus is important to include in crystal specifications a requirement on the crystal's energy resolution.

Because of their fast decay time and high light output, LSO and LYSO crystals have also been used in time of flight (TOF) measurements for medical applications, such as TOF PET(positron emission tomography). Better than 500 ps FWHM was achieved for the time difference between two photons. In HEP experiments a rms time resolution of better than 150

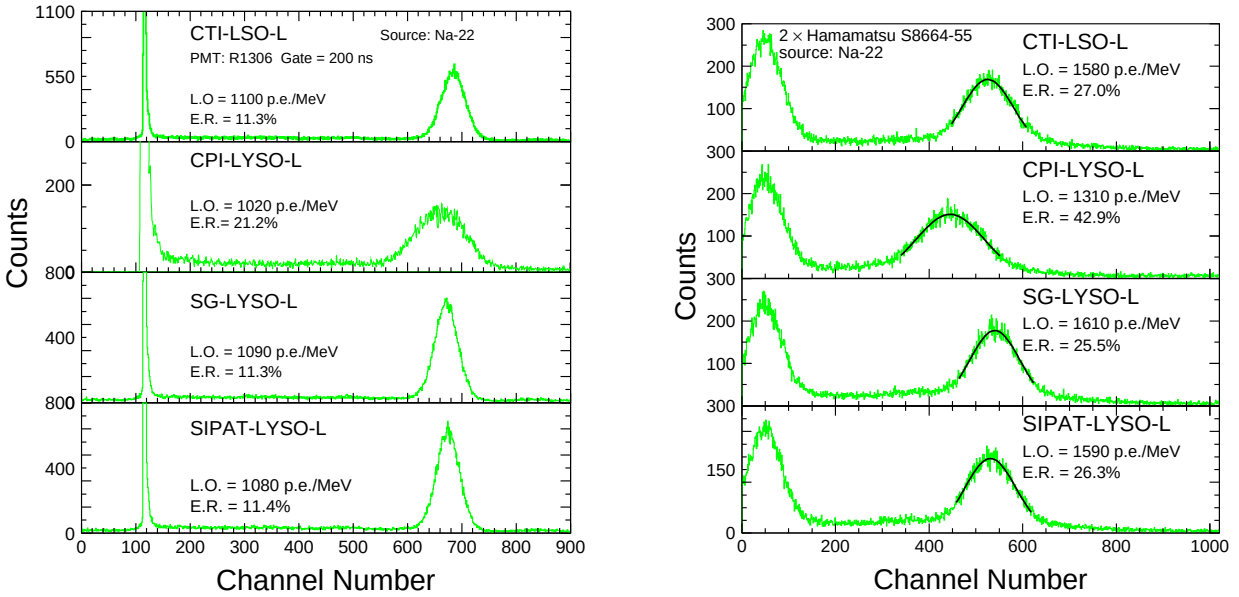

Figure 9.16: 0.511 MeV γ-ray spectra from a ^{22}Na source, measured by a Hamamatsu R1306 PMT (Left) and two Hamamatsu S8664-55 APDs (Right), with a coincidence trigger for four long LSO and LYSO samples of $2.5 \times 2.5 \times 20$ cm^3.

ps may be achieved for TOF measurements for single particles. Since the intrinsic rise time of scintillation light is about 30 ps for LSO and LYSO crystals [17], the measured time resolution for LSO and LYSO is affected mainly by the response speed of the readout device and the choice of time pick-off [16]. Doping calcium in LSO and LYSO is reported to reduce the decay time to about 20 ns [18], which would help to improve the time resolution.

Light Collection and Response Uniformity

It is well known that adequate light response uniformity along the crystal length is key for maintaining the precision offered by a total absorption crystal calorimeter at high energies [19]. The light response uniformity of a long crystal as shown in Figure 9.17 (Left) is parameterized as a linear function

$$\frac{LY}{LY_{\rm mid}} = 1 + \delta(x/x_{\rm mid} - 1), \qquad (9.6)$$

where ($LY_{\rm mid}$) represents the light output measured at the middle point of the crystal, δ represents the deviation from the flat response and x is the distance from the photo-detector. To achieve good energy resolution, the corresponding $|\delta|$ value for SuperB LYSO crystals of 18 X_0 length must be kept to less than 3% [20].

Effective light collection requires good light reflection. The glass fiber based supporting structure designed for the superB forward calorimeter is coated with a thin layer of aluminum as reflector. All measurements and simulations discussed in this section are carrired out with an aluminum coated glass fiber supporting structure cell, referred to as the RIBA Cell, around the crystal.

The light response uniformity of a long tapered LSO/LYSO crystal is affected by three factors. First, the tapered crystal geometry leads to an optical focusing effect, i.e., the response for scintillation light originating at the small end far away from the photo-detector would be higher compared to that at the large end, which is coupled to the photo-detector. This is caused by the light propagation inside the crystal, and is common for all optical objects with such geometry. Second, there is a self-absorption effect in LSO/LYSO crystals as discussed in section 9.3.1.2 since a part of the

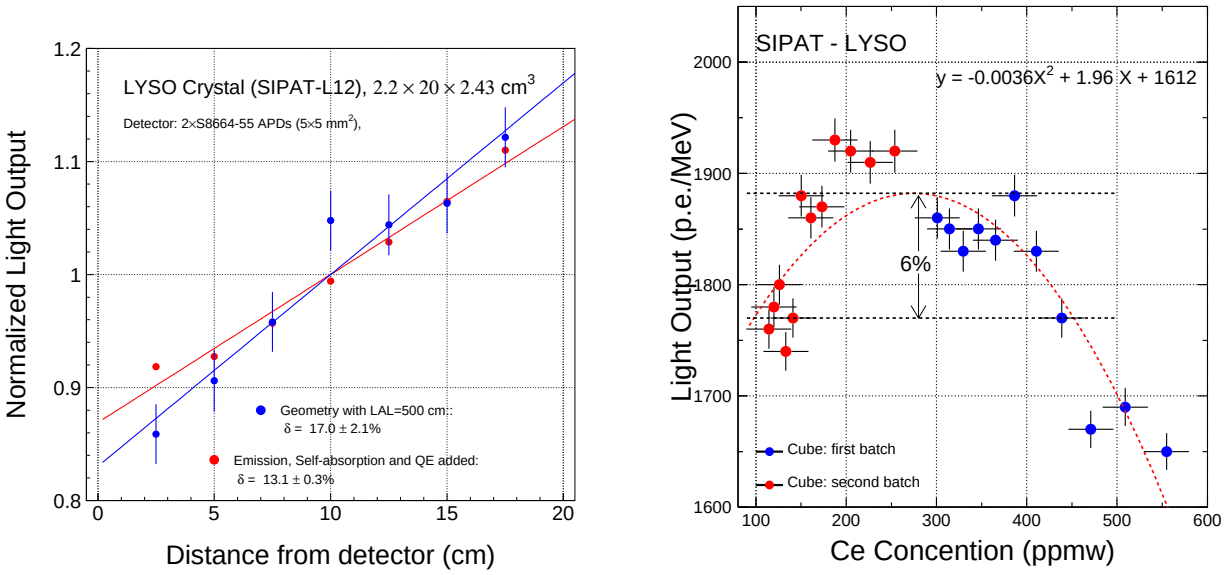

Figure 9.17: Left: Light response uniformities without (blue) and with (red) self-absorption effects, calculated by a ray-tracing program, shown for a 20 cm long crystal with tapered geometry and two Hamamatsu S8664-55 APD readout. Right: Light output measured for 17 mm LSO/LYSO crystal cubes shown as a function of the cerium concentration.

emission spectrum is self-absorbed in the crystal bulk as seen in the left plot of Figure 9.14. This effect is specific for LSO/LYSO crystals. Last, there is a non-uniform light yield along the longitudinal axis of the crystal. It is caused by the segregation process of the cerium activator in LSO/LYSO crystals during growth. Because of the small segregation coefficient (about 0.2) the cerium concentration increases from the seed end to the tail end of the crystal. Such an effect is common for all crystals doped with activator, e.g. CsI(Tl).

The left plot of Figure 9.17 shows the light response uniformities calculated using a ray-tracing program [19] for a SuperB LYSO crystal with tapered geometry and two Hamamatsu S8664-55 APD readout. The blue dots show the uniformity with only the optical focusing effect, and the red dots show the same with the self-absorption effect also included. Numerically, the optical focusing effect alone causes a δ value of 17%, which is reduced to 13% with self-absorption included. This indicates that the self-absorption effect provides a partial compensation for the optical focusing effect. The right plot of Figure 9.17 shows the light output measured for two batches of 17 mm LSO/LYSO crystal cubes (red and blue) as a function of the cerium concentrations determined by Glow Discharge Mass Spectroscopy (GDMS) analysis. It shows that the optimized cerium doping level is between 150 and 450 ppmw because of the interplay between the cerium activator density and the self absorption caused by the over-doping. Also shown in the plot is a second order polynomial fit. By adjusting the cerium doping the light yield difference along the crystal can be minimized. A difference at the level of 10% is more or less the maximum, which may provide a variation of the δ value up to 5%. Taking this into account the initial δ value of the SuperB LYSO crystals may vary between 8% to 18%.

Following the experiences of previous crystal calorimeters, such as L3 BGO and CMS PWO, a $|\delta|$ value of less than 3% may be achieved by roughening one side surface of the crystal to an appropriate roughness [21]. The left plot of Figure 9.18 shows the light response uniformities measured with two Hamamatsu S8664-55 APD readout for a tapered SuperB LYSO crys-

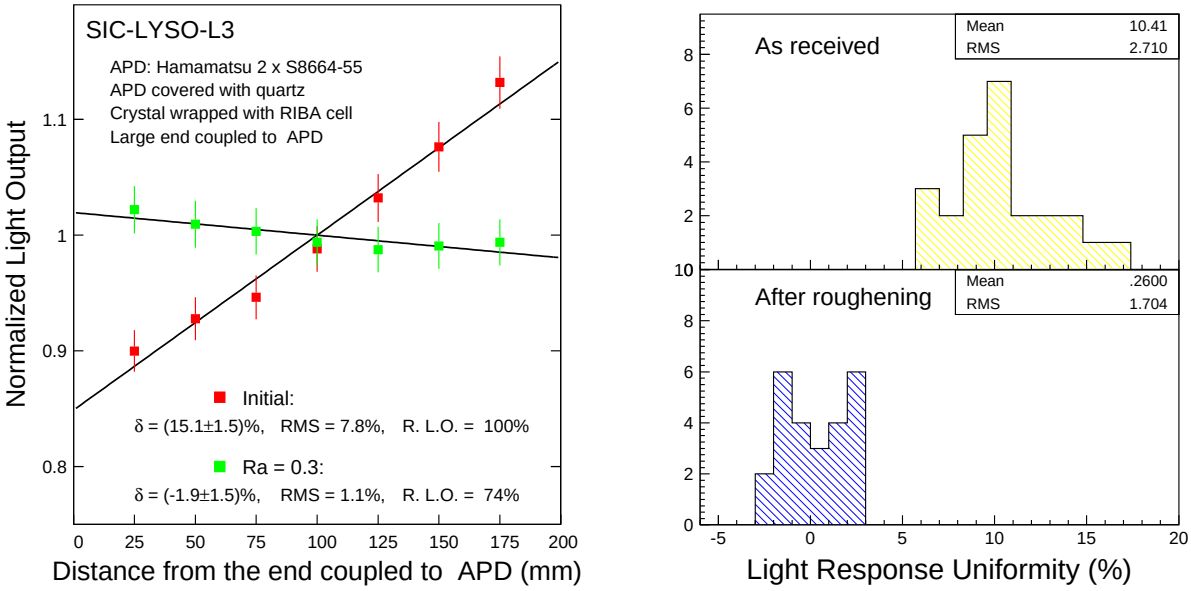

Figure 9.18: Left: Light response uniformity measured with two Hamamatsu S8664-55 APD readout for a tapered SuperB LYSO crystal SIC-L3 before (red dots) and after (green dots) uniformization by roughening the smallest side surface to Ra = 0.3. Right: The distributions of light response uniformity (δ values) are shown for 25 SuperB test beam crystals before (top) and after (bottom) uniformization by roughening the smallest side surface.

tal, SIC-L3. The δ value is reduced from 15% before (red) to -1.9% after (blue) roughening the smallest side surface to Ra = 0.3. The right plot of Figure 9.18 shows a comparison of the δ values before (top) and after (bottom) roughening for all 25 SuperB test beam crystals, showing a reduction of the average δ value from 10% to 0.26%. All 25 $|\delta|$ values after uniformization are within 3%. The reduction of light collection efficiency caused by this uniformization is about 17%. It is expected that one or two Ra values would be sufficient to uniformize mass produced LYSO crystals to achieve $|\delta|$ values of less than 3%.

9.3.1.3 Radiation Hardness

The radiation hardness of long LSO and LYSO samples has been investigated with γ-rays [22, 23] and neutrons [24]. It is found that the scintillation mechanism of this material is not damaged, while other damage can be completely eliminated by thermally annealing at 300°C and does not recover at room temperature, indicating no dose rate dependence [19]. Studies also show that it is also more radiation hard against charged hadrons [25] than other crystals.

Figure 9.19 shows the longitudinal transmittance (left) and normalized average light output (right) for four 20 cm LSO and LYSO samples from CTI, CPI, SG and SIPAT. The light output was measured by using a XP2254 PMT (top) and two S8664-55 APDs (bottom). All samples tested have a consistent radiation resistance, with degradations of the emission-weighted longitudinal transmittance (EWLT) and the light output of approximately 12% for a γ-ray dose of 1 MRad. This radiation hardness is much better than other scintillation crystals, such as BGO, CsI(Tl) and PWO.

Recently, a 28 cm (25 X_0) LYSO crystal (SIPAT-LYSO-L7) was grown at SIPAT. This LYSO sample has consistent emission, adequate light response uniformity and good radiation hardness against γ-rays up to 1 Mrad [13]. The left plot of Figure 9.20 shows the pulse height

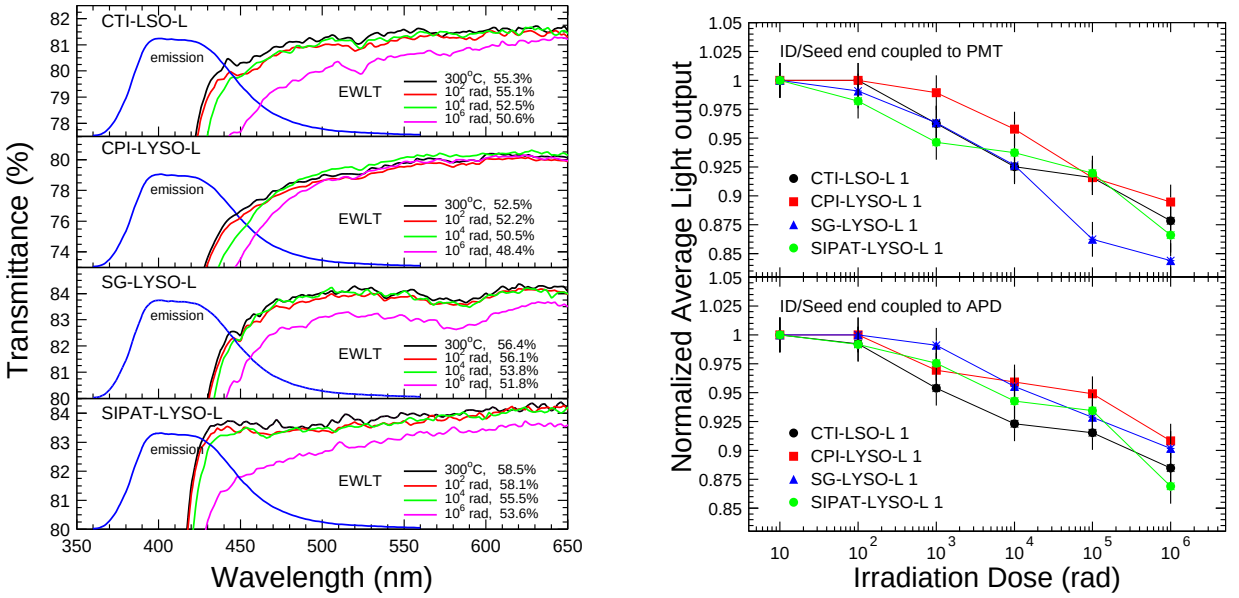

Figure 9.19: The longitudinal transmittance spectra in an expanded view (left) and the normalized light output (right) are shown as a function of the integrated dose up to 1 Mrad for four LSO and LYSO samples of $2.5 \times 2.5 \times 20$ cm^3. Also shown in the left plot is the photo-luminescence spectra (blue) in arbitrary units.

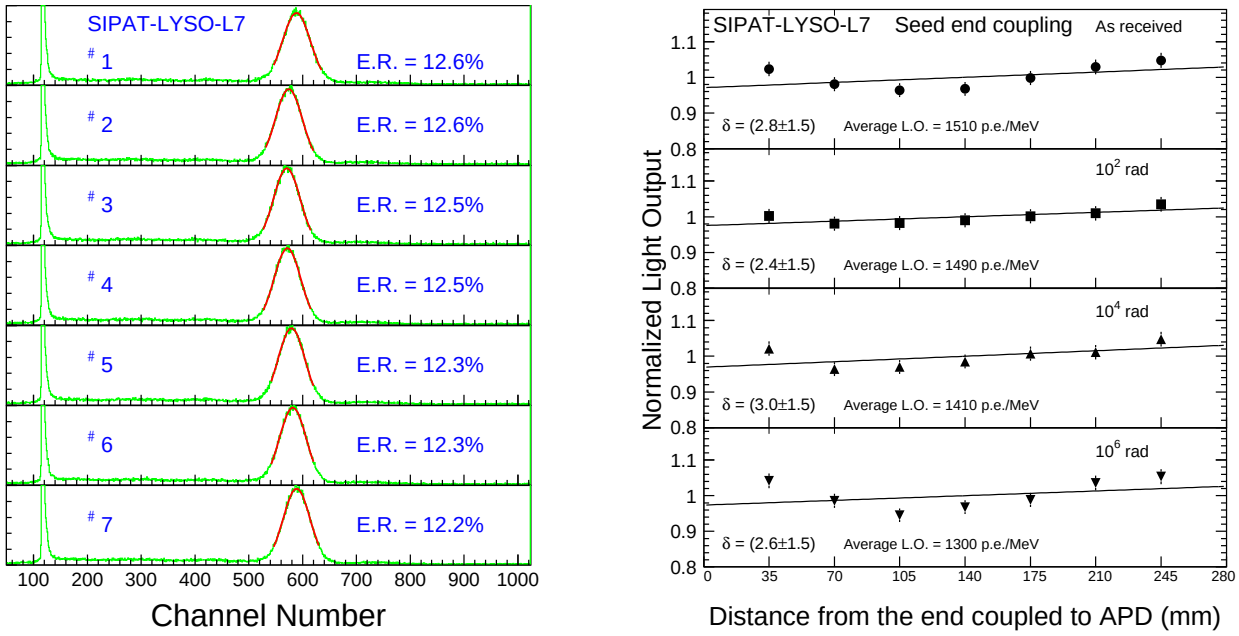

Figure 9.20: Left: The pulse height spectra of 0.511 MeV γ-ray peaks (green) and corresponding Gaussian fits (red) measured by a Hamamatsu R1306 PMT are shown at seven points evenly distributed along SIPAT-LYSO-L7. Also shown are the numerical values of the FWHM energy resolutions (E.R.). Right: Normalized light output and light response uniformity measured by two Hamamatsu S8664-1010 APDs, before and after γ-ray irradiations in several steps up to 1 Mrad are shown for SIPAT-LYSO-L7.

spectra measured by a Hamamatsu R1306 PMT at seven points evenly distributed along SIPAT-LYSO-L7. The FWHM resolutions obtained for 0.511 MeV γ-rays from the ^{22}Na source are about 12.5%. This is quite good for crystals of such length. The right plot of Figure 9.20 shows normalized light output and response uniformity measured by two Hamamatsu S8664-55 APD before and after γ-ray irradiations with an integrated dose of 10^2, 10^4 and 10^6 rad. The degradation of the light output was found to be about 13% after 1 Mrad dose. The light response uniformity of SIPAT-LYSO-L7 does not change even after 1 Mrad dose, indicating that its energy resolution may be maintained [19].

In summary, LSO and LYSO crystals are radiation hard crystal scintillators. These crystals are expected to find application in environments where severe radiation is expected.

9.3.1.4 Specifications, Production and Testing

Following our extensive R&D on LYSO crystals, the following specifications are defined for the procurement of high quality LYSO crystals from various vendors for the SuperB forward calorimeter.

- Dimension: +0.0/-0.1 mm.
- Longitudinal transmission at 420 nm: $>$ 75%.
- FWHM energy resolution: $<$ 12.5% for 0.511 MeV γ-rays measured by a Hamamatsu R1306 with DC-200 coupling at 7 points along the crystal.
- Light output will be required to be more than a defined percentage of a small crystal candle with air-gap coupling to PMT.
- Light Response uniformity ($|\delta|$): $<$ 3% measured by two Hamamatsu S8864-55 APDs.

Crystals will be produced by various vendors. The total LYSO crystal volume for the SuperB forward calorimeter is 0.24 m^3 (hybrid version with 3 CsI(Tl) rings), which is small compared to LYSO crystals grown for the medical industry. The following instruments are needed at each of the crystal vendors as well as the SuperB crystal laboratory.

- A station to measure crystal dimensions.
- A photo-spectrometer with large sample compartment to measure the longitudinal transmission along a 20 cm path.
- A PMT based pulse height spectrometer to measure light output and FWHM energy resolution with 0.511 MeV γ-rays from a ^{22}Na source.
- An APD based pulse height spectrometer to measure light response uniformity with 0.511 MeV γ-rays from a ^{22}Na source.

9.3.2 Readout and Electronics

9.3.2.1 APD Readout

The photosensors chosen for readout of the LYSO crystals of the forward endcap are an independent pair of 10×10 mm avalanche photodiodes (APDs). The APDs have several advantages over photodiodes in this application: they are a better match to the emission spectrum of LYSO, providing a quantum efficiency integrated over the spectrum of 75% (see Figure 9.21); they provide useful gain (of the order of 75) with low noise; and, as they have a thinner sensitive region, they suffer less from the nuclear counter effect.

The gain with low noise of the APDs presents two additional advantages: it can allow a reduction of the shaping and integration time constants, constants that, as shown in Sec. **??**, can be used as a handle to fight the machine background; it improves the signal-to-noise ratio for the signals used for calibration (see Sec. **??**), allowing a crystal by crystal calibration (see Sec. 9.3.3).

9.3.2.2 Electronics Block diagram

this is a test

9.3.2.3 Preamplifier

this is a second test

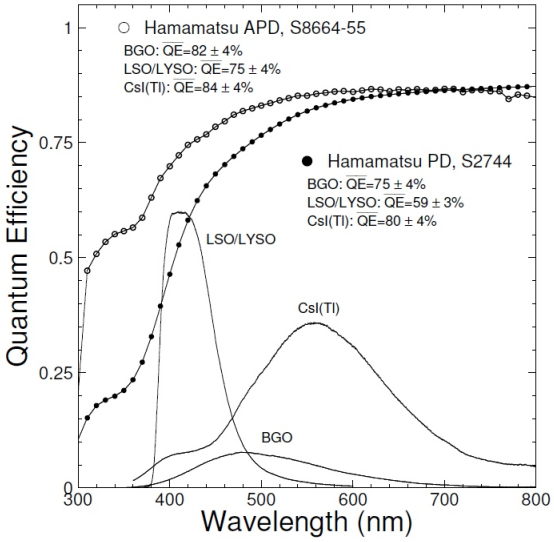

Figure 9.21: Quantum efficiency of a Hamamatsu APD and photodiode, together with the emission spectra of LYSO, BGO and CsI(Tl) crystals.

9.3.2.4 Shaper

9.3.2.5 Digitization

9.3.2.6 Requirements on mechanics

Cables, encumbrances, required cooling, ...

9.3.3 Calibrations

9.3.3.1 Initial LYSO calibration with source

A goal of the design is that the signal rate and the signal-to-noise ratio with a typical radioactive source such as ^{137}Cs be sufficient to allow individual calibration of each crystal with the readout device with which it will actually be paired. As was the case with the existing CsI(Tl) crystals, photodiode readout of large crystals does not allow the use of sources for calibration and setup. This is typically done with a reference photomultiplier, with the results then convoluted with the results of individually calibrated photosensors. Such a procedure does not, of course, fully account for the effects of surface oxidation of the crystal or glue joint losses. However, with APD readout, the response of the entire chain can be measured for the LYSO crystals.

The full setup of each crystal assembly requires each crystal/readout package to be individually adjusted to meet the uniformity requirements *in situ* and the characteristics of each object to be entered into a reference database. This involves appropriate roughening of, typically, one crystal surface to conform to a light collection uniformity specification as discussed in 9.3.1.1. The output of this setup/calibration procedure is then entered into a reference database, which serves as the initial set of calibration constants for the calorimeter system.

The fully assembled calorimeter is then calibrated with the circulated fluorinert system already used in *BABAR* (see Sec. 9.2.2.3) at appropriate intervals (one to four weeks in the case of *BABAR*). A substantial advantage of this approach is that there is an individual pedestal and gain constant for each crystal. A limitation is that the source is at a relatively low energy, although it is at a higher energy than that obtained from long-lived radioactive sources. Calibration with radiative Bhabhas can overcome this limitation, but it requires development of a complex matrix unfolding procedure, since high energy electrons deposit shower energy in many crystals, not in a single crystal as in the case of source calibration. Since LYSO is intrinsically radioactive, some of the endcap crystals will have intrinsic background, and a configurable trigger threshold will be required. A test with LYSO crystals using 6.13 MeV photons from an ^{16}O* state produced with neutrons from a ^{252}Cf source is planned.

9.3.3.2 Electronics calibration

9.3.3.3 Temperature monitoring and correction

The characteristics of APDs place fairly stringent requirements on the temperature control of the system, greater than those imposed by the temperature variation of light output of the crystals, as well as on the stability of the APD power supply voltage.

The Hamamatsu S-8664 APDs specified for the crystal readout have a temperature coefficient of gain of $\Delta G/\Delta T$ of 2.5%/°C, while the

LYSO light output varies $-0.2\%/°C$. A specification of an APD gain stability of $\pm 0.5\%$ requires knowledge of the temperature to $\pm 0.2°C$. The CERN beam test demonstrated that a measurement of the calorimeter temperature to $0.2°C$ can be easily achieved. Furthermore the energy resolution degradation due to machine background might allow to tolerate even a less stringent control.

As far as the overall structure is concerned we can keep the characteristics of *BABAR*: The entire calorimeter is surrounded by a double Faraday shield composed of two 1mm-thick aluminum walls, so that the diodes and preamplifiers are shielded from external noise. This shielding also serves as an environmental enclosure, surrounding the slightly hygroscopic CsI(Tl) crystals with a dry, temperature controlled nitrogen atmosphere. The preamplifiers (2×50 mW/crystal) and the digitizing electronics ($\sim$3 kW per end-flange) are the primary internal heat sources. The temperature was monitored by 256 thermal sensors distributed over the calorimeter. This system maintains the crystal environment at $20 \pm 0.5°C$. Dry nitrogen circulation stabilizes the relative humidity at $1 \pm 0.5\%$.

As far as gain stability is concerned, for a gain of $\sim$75, with a reverse bias voltage of $\sim$375 V, a voltage stability of better than 1 volt is required. This requirement can be met by commercially available computer-controlled high voltage supplies, such as those used for the CMS calorimeter.

9.3.4 Mechanical Structure

For cost-savings, the forward mechanicl structure from*BABAR* is reused. It is designed in order to minimize the inactive materials, as well for the barrel, and to provide hermeticity at interface with barrel itself. The design is conceptually different from that of the barrel. In fact, while the barrel remained unopened for the lifetime of *BABAR*, the endcap is capable of rapid mounting and dismounting, always keeping precision mating to barrel itself. The forward endcap is a conic section, with front and back surfaces tilted at 22.7 to the vertical, in order to match the drift chamber endplate. It is built in 2 monolithic parts able to allow an easy and quick demounting for access to inner components of detector; its total weight is approximately 4 tons (forward assembly drawing in Fig. 9.22). It is supported off the solenoid coil and precisely aligned with the calorimeter barrel; in particular it is the designed to minimize both the material and the air gap between the two parts.

9.3.4.1 Crystals

The *BABAR* forward endcap has a total of 900 CsI(Tl) crystals, made up from nine distinct radial rings (3×120, 3×100, 3×80), arranged to give approximately the same crystal dimensions everywhere; total crystals volume is 0.7 m^3. CsI(Tl) , grown in a polycrystalline form, presently populate the cells of the endcap modules. This is a soft material, not able to support load; for this reason the CFC structure support the individual crystals, avoiding load transferring to neighboring cells; CFC with 250 μm wall thickness is chosen because this presents the best compromise between strength and minimum radiation length. The design and dimensions of these crystals are described in Figure 9.23.

The CsI crystals fit loosely into their compartments; in fact they have been produced with a tolerance on crystal transverse dimensions of $\sim$225 μm. Each crystal is read out at the back with 2 large areas photodiodes (Hamamatsu S2744-08). The 2 diodes are glued onto a 1 mm polystyrene coupling plate which itself is glued onto the crystal surface. The crystals (Fig. 9.3) are wrapped with a double layer of Tyvek (150 μm each) to improve the light yield, a layer of Aluminum Foil for electrical shielding (75 μm) and a layer of Mylar (12 μm) for insulation and mechanical protection of Al foil. Furthermore there is a small aluminum box covering the photodiodes at the back of crystals, and containing the PC-board with preamplifiers.

In the hybrid scheme, we plan to replace the inner six rings of CsI(Tl) crystals with LYSO. As the Molière radius of LYSO is smaller, the replacement will be four LYSO crystals for each

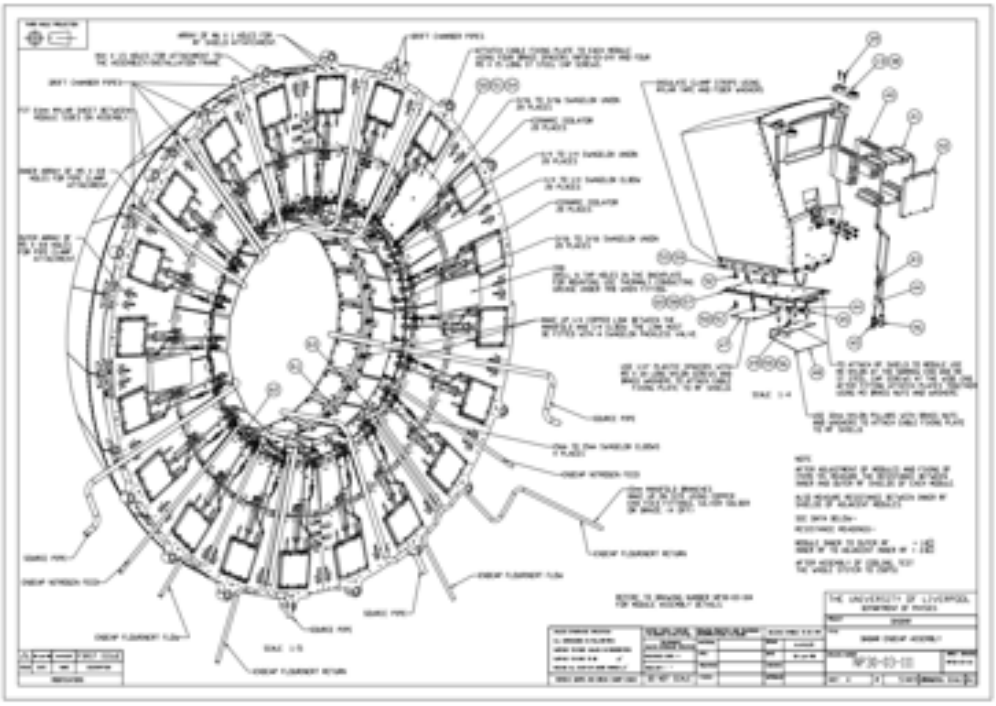

Figure 9.22: Forward assembly drawing

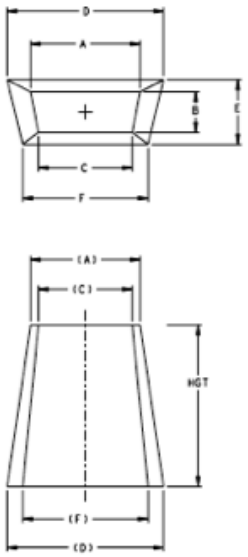

θ Row	Number Needed	Volume (cc)	A (cm)	B (cm)	C (cm)	D (cm)	E (cm)	F (cm)	Height (cm)
1	80	741.0	4.298	4.670	3.944	4.995	5.426	4.583	32.55
2	80	802.4	4.641	4.670	4.289	5.394	5.428	4.985	32.55
3	80	863.6	4.982	4.670	4.632	5.792	5.430	5.386	32.55
4	100	739.6	4.247	4.670	3.970	4.941	5.432	4.618	32.55
5	100	788.3	4.519	4.670	4.244	5.257	5.433	4.937	32.55
6	100	836.9	4.790	4.670	4.517	5.573	5.433	5.256	32.55
7	120	737.7	4.209	4.670	3.984	4.898	5.434	4.636	32.55
8	120	778.4	4.437	4.670	4.214	5.162	5.433	4.903	32.55
9	120	819.1	4.665	4.670	4.445	5.427	5.432	5.171	32.55

Figure 9.23: Definition of the sides of the crystals and their values in BaBar.

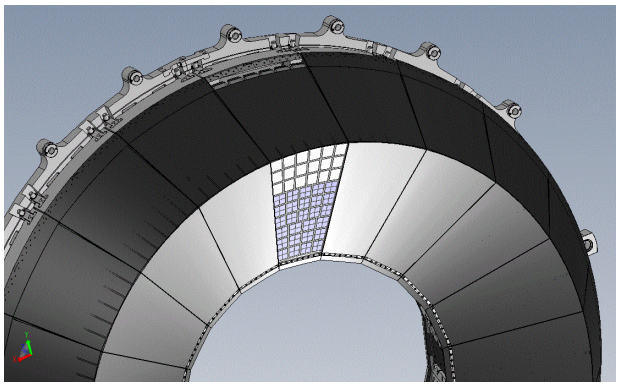

Figure 9.25: Layout of a module in the forward endcap in the hybrid plan.

CsI crystal. In this way, the same structure is used, simply inserting four LYSO crystals into each CFC cell. LYSO is a very strong crystal, so no additional support is required between them. If further cost saving in the initial implementation is required, additional rings of CsI

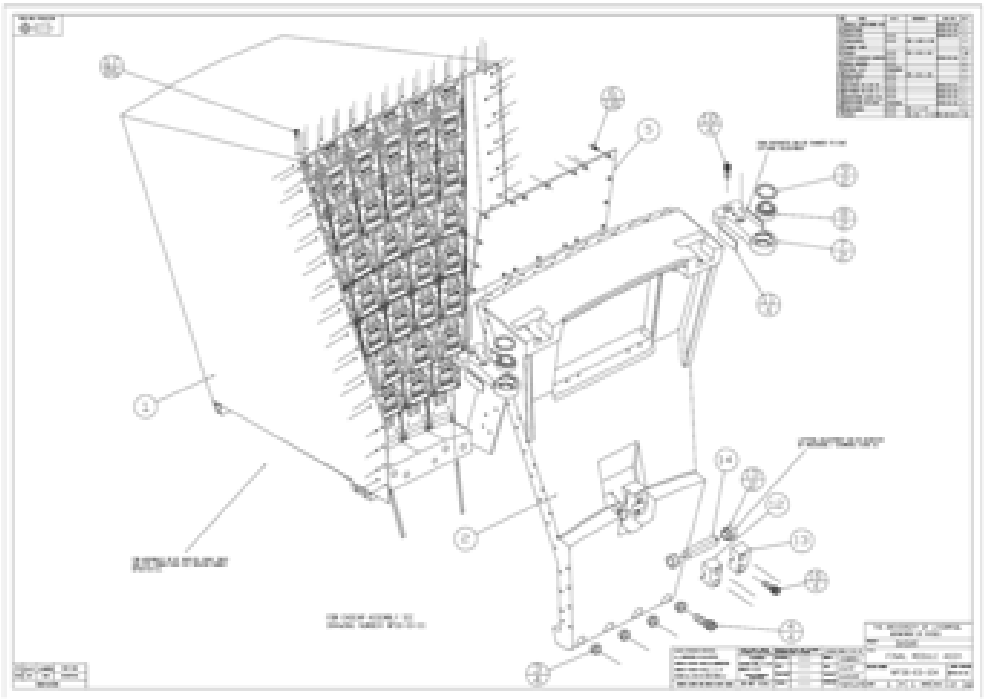

Figure 9.24: Forward module assembly drawing

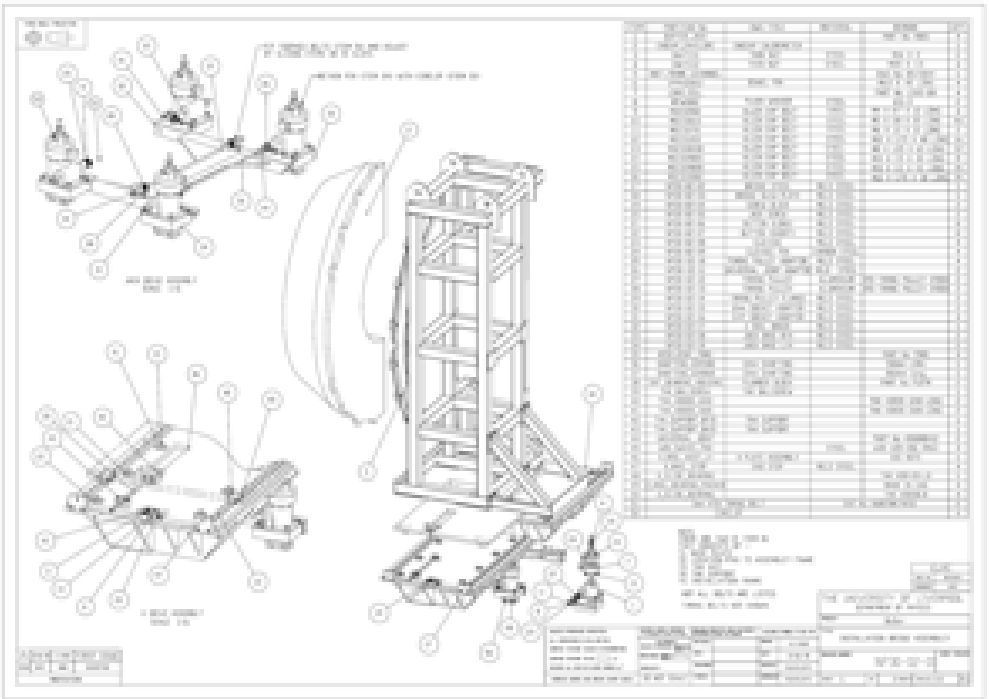

Figure 9.26: Installation Bridge drawing

may be kept from the *BABAR* endcap. A future upgrade of the detector could include replacing more rings of CsI with LYSO.

9.3.4.2 Modules

The geometry is basically projective, with the crystal axes pointing to an axial position 5 cm from the interaction point. In order to preserve optimum light collection and both spatial and energy resolution, similar-sized crystals have been used, arriving to a layout of nine rings of trapezoidal shaped crystals, grouped in 3 super-rings and arranged in 20-modules symmetry (Final Module drawing in Fig. 9.24).

As described above, we replace the six inner rings of CsI with LYSO. This is shown in Fig. 9.25.

9.3.4.3 Installation

A series of dedicated tools and instruments already exists, and a detailed procedureis under preparation, derived from *BABAR* for moving and installing the forward calorimeter. Existing tooling is being located at SLAC, as well as the documentation on the assembly and mounting of the 20 modules on the support backplate. Fig. 9.26 shows the exisitng Installation Bridge, able to move individually each one of the two monolithic endcap halves.

9.3.4.4 Refurbishment of the BaBar structure

As for the *BABAR* barrel, the andcap will be disassembled to the module level for transport. The alternative of transporting each half with modules installed carries mechanical risks, but may be investigated further. Most of the tooling for handling the endcap and modules exists at SLAC, and may be used after some refurbishing.

For the CsI(Tl) rings that are kept, each crystal and preamp will be tested and measured for signal strength, both before and after shipment. Repairs will be made as necessary. The testing in Italy may be done at a remote site at the module level, both for the CsI and the LYSO crystals. Final assembly of the endcap and installation onto the detector is best done at Tor Vergata.

The electronics for the forward calorimeter will be refurbished as for the barrel (section 9.2.4 for the CsI(Tl) rings that are kept. The LYSO readout is with APDs, with new electronics as described in 9.3.2.

9.3.4.5 Spare FWD modules survey and tests

In order to study the changes required for the LYSO crystals, two spare *BABAR* endcap structural modules have been shipped to Italy. Tests and measurements on them will be necessary to define a procedure for LYSO crystals insertion, and investigate any problems implicit inside this operation (electronics for example), and to check and validate technical information presently available; in particular regarding the CFC honeycomb region.

9.3.5 Tests on Beam

9.3.5.1 Description of apparatus

Two beam tests have been performed with a prototype LYSO matrix, one at CERN in October 2010 and one at the Beam Test Facility (BTF) in Frascati in May 2011. In both cases the prototype matrix was composed by 25 LYSO crystals of pyramidal shape with dimensions 2.3cm×2.3cm×22cm inserted in a support structure assembled by the RIBA company (Faenza, Italy) described in detail in Sec. 9.3.4. To improve light output uniformity, each crystal presents a black band of 15mm at the end of its smallest face and the area of the face not covered by the APD (or PiN) is painted with a reflective white painting. The mechanics is composed of glass fiber, covered with copper foils 35μm thick. Between one cell and the other there is a nominal thickness of 200 μm, while the external side has a thickness of 135 μm. Fig.9.27 shows a picture of the Test Beam structure with inserted one row of crystals. Of the crystals, 20 are read out with an Avalanche Photodiode (APD) in both tests while the remaining 5 are read out with PiN Diodes at CERN and with APDs at the BTF. As shown in Fig. 9.28, the readout chain is composed of: a front end board (VFE) that contains a Charge Shaper Preamplifier (CSP); Shaper Range Board which com-

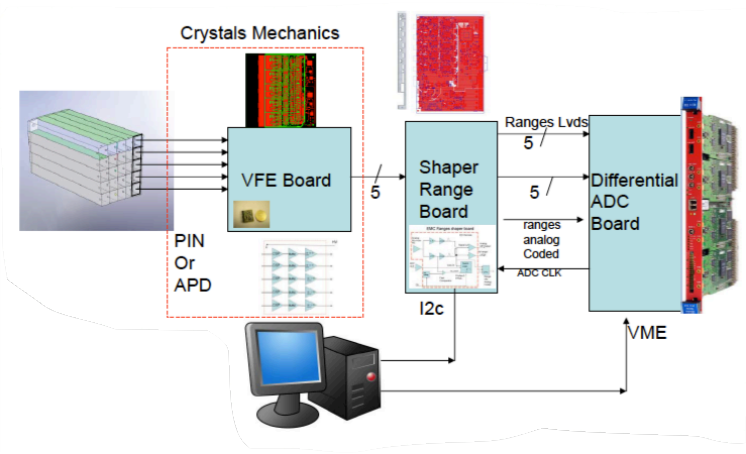

Figure 9.28: Schematic view of the electronic chain for the forward EMC.

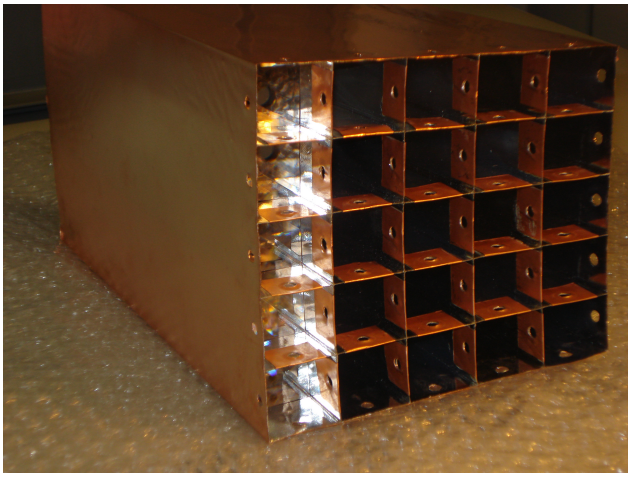

Figure 9.27: Picture of the Test Beam mechanical structure with one raw of LYSO crystals.

pletes the attenuation, already applied in the VFE board, and then divides them according to the energy. Two different ranges are foreseen in the treatment of the signals, for energies lower than 200 MeV and for energies greater than 200 MeV, although in the tests on beam the amplifications have been adjusted to use only one range; a 12 bits Caen ADC to process the signals and digitize the analogue outputs. In order to avoid saturation effects the APD's were biassed at 308V.

9.3.5.2 Description of the beams

The Beam Test at CERN has been performed at the T10 beam line in the East Area. The beam is mainly composed of electrons, muons and pions created by the scattering of protons into aluminum and tungsten target. The composition of the beam is highly dependent on the energy and for electrons it ranges from 60% at 1 GeV to 1% at 6 GeV. The maximum energy reachable at this beam line is 7 GeV with a nominal momentum spread $\Delta p/p \simeq 1\%$. The distance between the end of the beam line and the matrix is about 15 m. The event rate is of the order of 1 Hz.
Fig.9.29 shows the experimental setup used at CERN, it is composed of a Cherenkov detector for the electron-pion discrimination, two scintillators (finger counters) $2\times2\text{cm}^2$, the box containing the matrix and the VFE boards.

Figure 9.29: Schematic view of the test beam setup used at CERN.

The two scintillators of the fingers act as trigger while the information of the Cherenkov detector was both stored in order to select Minimum Ionising Particles (MIP) used for the calibration and used to prescale the triggers.

The Beam Test Facility in Frascati is part of the ΦFactory, DaΦne. It is composed of a linear accelerator LINAC, one spectrometer and two circular accelerators of electrons and positrons at 510 MeV. The LINAC is the same which supplies the test beam line at the BTF. The pulsed beam of the LINAC circulate electrons up to 800 MeV at a maximum current of 550 mA/pulsation and positrons at a maximum energy of 550 MeV with a current of 100 mA/pulsation. The typical duration of a pulsation is 10 ns, with a frequency of 50 Hz. A bending magnet select electrons of a given momentum, a line of about 12m contains quadrupoles for the uniformation of the beam and a system of slits allow to change the flux of arriving particles. The beam energy spread is 1% at 500 MeV. The setup for the beam test of the matrix at the BTF is shown in Fig.9.30. The setup

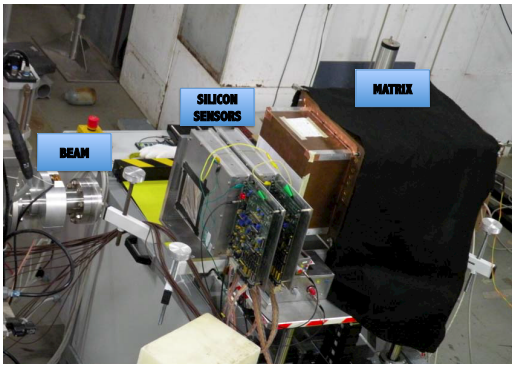

Figure 9.30: Schematic view of the test beam setup used at the BTF in Frascati.

shows the end of the electron beam line, four planes of silicon strip detector (two measurements in x and two measurements in y) and the box containing the matrix with the crystals and the VFE boards. As mentioned before, at the BTF all the crystals are equipped with APD's, and it should be mentioned that the gain of the VFE has changed with respect to CERN from 0.5 to 1, while an amplification factor has been introduced. To control the position of the beam with respect to the matrix a detector of 16 x 16 scintillating fibers of 3mm each has been used. The LINAC radiofrequency (25 Hz) was taken as trigger.

Since the beam energy spread of the CERN facility proved to be significantly larger than the specifications, based on the performances of the detector at the BTF, we will use the CERN TB data only to study the linearity at high energy, while resolution studies will be performed exclusively on the BTF data.

9.3.5.3 Description of data and calibration

For each triggered event, the output of the readout are the waveforms of the 25 channels, each constituted by 384 samples. The signal amplitude in each channel is defined as the maximum of the waveform, extracted from a gaussian fit to the sampling distribution, subtracted of a pedestal. For each crystal, the pedestal is calculated averaging the first 60 samples on a reference run. The pedestal-subtracted amplitude is considered to be the measurement of an energy deposit if it is above a threshold chosen to be three times the noise fluctuation, whose value is determined from a run taken with random triggers where no signal is present. After calibration the energy of the electron that initiated the shower, was estimated by summing all the energy deposits in all crystals ("cluster energy").

At the CERN test beam hadrons traversing the crystals horizontally were selected as Minimum Ionizing Particles (MIPs) by requiring no significant signal in the other crystals and a signal consistent with an hadron in the Cherenkov detector. Profiting from the fact that MIPs release a constant amount of energy regardless of their energy, the amplitude spectra of each crystal was fitted to extract the most likely value. After determining on the simulation the expected released energy in each crystal (Fig 9.31)

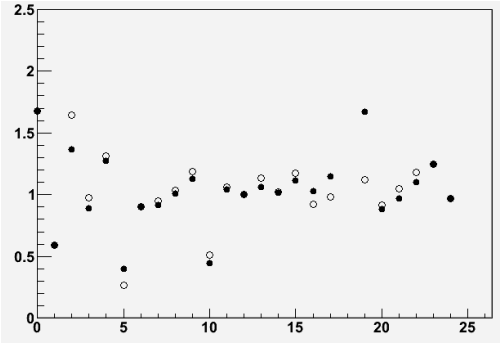

Figure 9.32: Comparison between electron and MIPs calibration at the BTF test beam as a function of the crystal number. Calibration constants are referred to crystal 12 that is therefore by definition equal to unity.

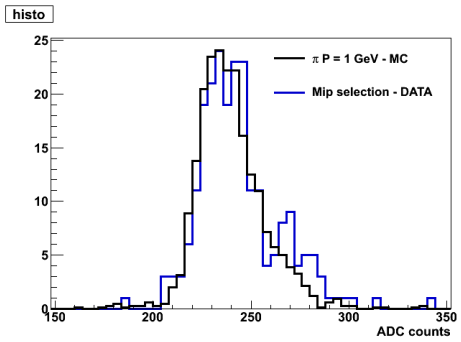

Figure 9.31: Comparison between data and MC of the energy deposited in the MIPs sample. The hypothesis that after the selection the beam is dominated by pions is made.

, the corresponding calibration constants could be extracted.

At the BTF test beam, where no hadrons were available, the relative intercalibration constants were obtained on the electron sample itself. The relative cluster energy resolution was minimized by floating a constant in front of each crystal a part from the central one. The overall energy scale was then determined from the knowledge of the beam energy. This procedure was applied on a small fraction of the runs where the electrons were approximately 500 MeV (the highest energy reached in the tests) and the corresponding constants used in all other runs. This intercalibration was also cross-checked by means of cosmic-ray data obtained with an ad-hoc trigger made of two plastic scintillator pads positioned above and below the crystal matrix. The channels where there is a significant difference are those where the electron data see very little energy because they are far from the center of the matrix. In such cases, that have little impact on the resolution studies since they contribute little to the total energy measurement, the calibration constants estimated on the MIPs are used.

9.3.5.4 Electronics noise measurements

The first information we could extract from the data are the characteristics of the electronic noise. From the signal distribution in a random trigger run at the BTF we estimated (Fig. 9.33) that a part from two channels, the noise is on average 2ADC counts. After applying the calibration, this noise corresponds to approximately 0.4MeV. To understand if there were resonant components, the noise of each crystal i was analyzed in the Fourier space, by estimating its power spectrum from waveforms acquired with a random trigger:

$$\mathrm{PS}_i(\omega_k) =< n_i(\omega_k) n_i^*(\omega_k) > . \qquad (9.7)$$

The estimated power spectrum of a representative channel is shown in Fig. 9.33, where it can be seen that the dominant source of noise is in the range 0-8 MHz, which corresponds to the frequency bandwidth of the shaper. Sources of noise occurring after the shaper give a negligible contribution, while those occurring before are filtered according to the shaper transfer function and dominate.

Also the presence of noise correlation among the crystals was estimated and found to be negligible.

9.3.5.5 Temperature corrections

A temperature dependence of several percent per degree is expected both in the light yield of the LYSO crystals and in the gain of the APDs. At the CERN test beam the position of the MIP peak as a function of the temperature measured by sensors places on the rear of the crystals has

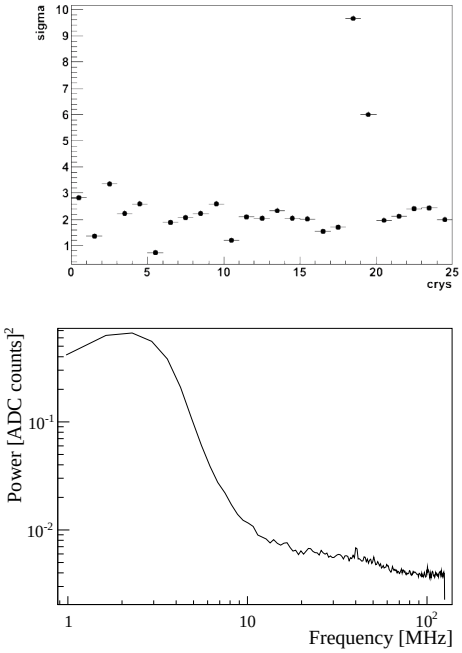

Figure 9.33: Top: Noise RMS for each channel of the BTF test beam. Bottom: power spectrum of a representative channel.

been used to extract the temperature correction (Fig. 9.34) : $E_{corr} = E_{raw}/(1 - p_0 * (T - T_0))$ where $p_0 = 2.8 \pm 0.2 \times 10^{-3}$ and $T_0 = 34$K. The same figure shows also the effect of the correction.

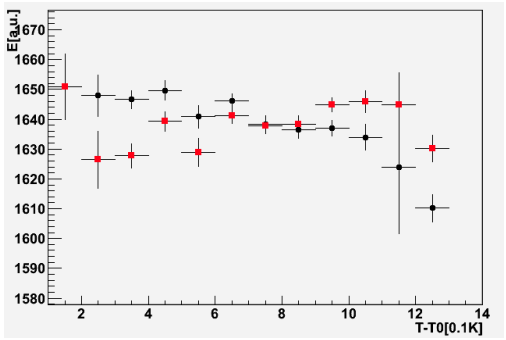

Figure 9.34: Dependence of the measured energy on the temperature before (black dots) and after (red squares) correction.

This correction proved irrelevant at the BTF test beam where the temperature was controlled to better than 0.2^{o}C

9.3.5.6 Results

In order to estimate the linearity of the response and the energy resolution, the distribution of the cluster energy is fitted for each beam configuration with a crystal ball function. The mean value of the gaussian component is considered as estimate of the energy, while the resolution is evaluated as starting from the FWHM of the whole distribution.

Fig. 9.35 shows the mean value as a function of the energy for the data collected during the CERN test beam. The linearity of the response is thus ensured.

At the BTF the beam was configured to be able to observe multiple peaks due to up to three simultaneous electrons impacting the crystal matrix. This allowed to have more than one resolution measurement for each beam energy configurations (see Fig. 9.35). In turn, this allowed to estimate the dependence of the beam spread with the energy by comparing measurements of the same amount of deposited energy, but obtained with different beam energies. The intrinsic resolution obtained by subtracting the measured beam spreads in quadrature from the average resolutions is also shown in Fig. 9.35.

Such intrinsic resolutions are then compared with the results of a full simulation of the experimental setup (Sec. 9.1.2). There is a good agreement, with a resolution smaller than 2% at 1 GeV.

9.3.6 Alternatives

9.3.6.1 Full LYSO calorimeter

The technically best solution for the forward calorimeter is to construct a new device using LYSO crystals throughout, with a thin mechanical support structure to minimize material. We have pursued extensive R&D into this option. It is not chosen as our baseling purely for cost considerations, and remains as an alternative should funding materialize. This section summarizes this alternative design.

The driving design principles are the same that were used for the *BABAR* Electromagnetic

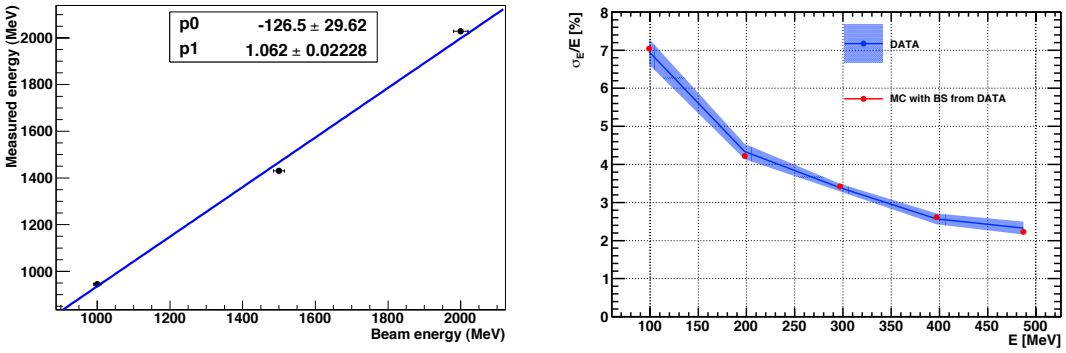

Figure 9.35: Left: Measured mean value of the energy as a function of the beam energy at the CERN test beam. Right: relative resolution as a function of the deposited energy on data and MC simulation.

Calorimeter (see Sec. 9.3.4), the biggest change being induced by the higher density of the LYSO crystals: this allows for Molière radiuses that are around a factor two smaller and also the required length of the crystals is significantly smaller. This changes both the size of the cells and the position of the center of gravity, thus altering significantly the design. A detailed report of the studies that were carried out is in Ref. [26], here we only stress the relevant points.

The proposed structure is made of four rings in theta (see Fig. 9.36) each composed of 36,42,48, and 54 modules respectively. The cells are designed in order to keep the cell front dimension.

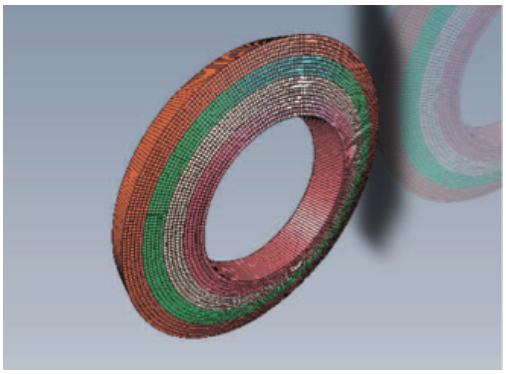

Figure 9.36: overview of the structure of the FWD EMC.

Services have not been studied in detail yet, but *BABAR* standards should be reasonably suited and also the reduced crystal size leaves further room for them.

Module design

Modules contain a 5 x 5 matrix of crystals and therefore their approximated dimensions are 110 x 110 x 230 mm^3 and the total weight of the crystals is about 25kg. The requirements on the thickness and the material of the walls constrain the module to be held in a very light container of 220g, thus making the mechanical requirements challenging.

Considering the ϕ and θ symmetries the number of crystals types that need to be produced is reduced to 20. To achieve the required energy resolution, crystal-to-crystal separation must be less than or equal to half a millimeter. The design guarantees a maximum distance between crystal faces of 0.4 mm within a module and of 0.6 mm across two modules, either in ϕ or in θ for crystal nominal dimensions. For the crystals with the smallest tolerances these values are reduced by 0.1 mm .

As described in Fig 9.37 Alveolar modules are assembled into the Shell-Support-Structure (horse collar and wedge). Alveolar front ends are driven into position by 5 tubular CFRP setpins and the front of the module is glued to the structure front plate.

To validate the submodule design, two prototypes of the alveola module have been con-

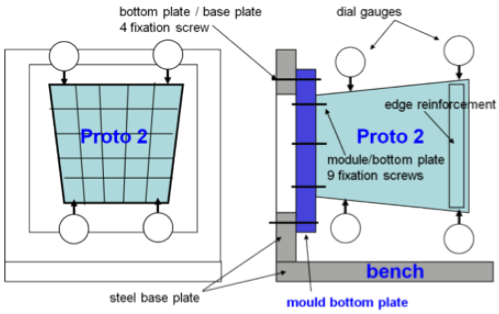

Figure 9.38: Alveolar module test setup

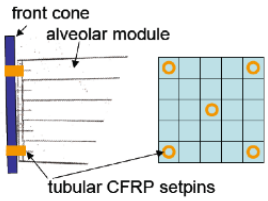

Figure 9.37: Alveola supports.

structed (see a photo in Fig. 9.27). A first prototype (Proto1) was produced to validate the cell structure concept and the production economy It was then used with its 25 crystals in a beam of particles for physics validation The Proto1 validated the whole production process and a 3D dimensional inspection performed on the internal and external walls gave evidence of the achievable dimensional tolerances. Wall thickness was measured at the cell open edge over 20mm depth on both sides of punched holes and produced the following values : a) for internal walls nominal 0,200mm 0,15 to 0,22 b) for external walls nominal 0,135mm 0,13 to 0,17

The information gathered have been used to define the production protocol.

A second prototype (Proto2) was produced in September 2011 to confirm process repeatability and to evaluate the global mechanical properties of the structure.The alveolar module is identical to that used for the physics beam test in October 2010, Proto1. The test campaign had the aim to evaluate the structure overall mechanical properties. Global deformations of the alveolar array are significant, and a loading test is essential for checking the absence of interference with the shell inside (inner and outer cone) and the absence of crystal stressing (cell bending ¡ play) in a first approximation. As shown in Fig. 9.38, the cells were loaded with dummy crystals that simulate the mass and different gravity vectors have been investigated. The mechanical tests performed on the modular structure provided basic input data to a Finite Element Analysis of the complete support structure.

Alveolar module structure finite element analysis

A detailed Finite Element Analysis was performed on the alveolar structure using material properties form data-sheet. An approximated module based on surfaces, shown in Fig. 9.39, has been used as a reference to to validate the Global Finite element model of the whole EMC. On the external wall two laminae of total thickness 0.2mm were used, together with four internal walls laminae at 0^o, 90^o,0^o, 90^o. The bottom material is isotropic of 6mm aluminium material equivalent to CFRP. 5 constraint point are putting to the centrer of 5 holes on the module bottom, (2 on the upper side 2 lower side and 1 in central position, to simulate the setpins constraints to connect the module to the mechanical forward structure), for this was used the rigid elements (rigid bar) leading the center node hole to boundary hole.

The load is the weight of crystals and each one has mass of about 1 Kg. For this purpose to simulate it, a "rigid bar" with 5 nodes was used along the centre alveolar cell, and a lumped mass 1/5 of crystal weight is positioning in each of this nodes. This nodes are then connected with some nodes near alveolar walls with rigid bar and from these latter to the alveolar walls nodes with "gap and spring" elements.

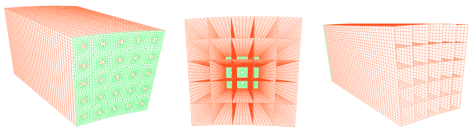

Figure 9.39: Alveolar module finite element model

The resulting stresses predicted on the structures are depicted for the 0^o case as an example in Fig. 9.40. The corresponding values for the ply stresses and for the index failure (i.e. the ratio between the predicted stress and the breakdown) are summarized in Tab. **??**.

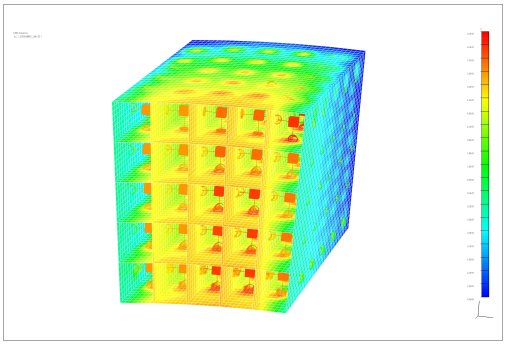

Figure 9.40: Results of the module finite element model at 0^o,

Table 9.5: Expected ply stresses and index failures.

case (^{o})/ coordinate	Ply Stress(MPa)	index failure
0/x	35	1/48
0/y	2.6	1/10
0/z	1.4	1/16
90/x	5	1/342
90/y	10	1/2.6
90/z	1.7	1/13
180/x	30	1/57
180/y	7	1/4
180/z	1.5	1/15

Support shell structure design

The shell, shown in Fig. 9.41, consists of the outer cone and front cone as one single solid body in CFRP. The inner cone, where material budget does not pose too stringent limits is a metallic shell. Back plate is the same as BaBar. The volume is defined by the line AB, AD, CD while A'B' and A'D' are construction lines resulting from technical choice.

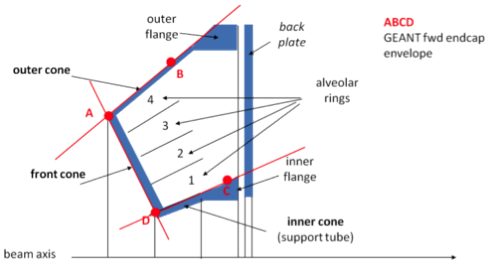

Figure 9.41: Support shell structure

The outer cone end is reinforced by a metallic ring for easy connection with the back plate. The back plate provides the EMC interface with the SuperB bearing points (position reference and transmission of loads). The alveolar array is cantilevered from the shell front cone as detailed in Fig. 9.42.

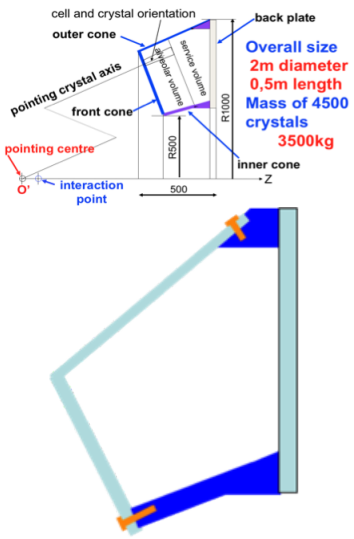

Figure 9.42: Support shell assembly

This configuration provides a logical construction and assembly sequence, in particular an easier and almost reversible access to the most delicate part of the detector, its crystals and photodiodes. There is no connection between the alveolar array and the inner and outer cone inner faces. A 1mm gap is introduced for the free elastic deformations of the alveolar array and of the shell. The front cone is connected to the inner cone by gluing secured by screws.

The outer cone is a massive CFRP (6 to 10mm) while the front cone is either a massive CFRP or a sandwich plate 20mm thick. For the production the mould is at the inner face of the outer-front cone in order to have high dimensional accuracy at the interface with the crystals modules, while a vacuum bag is at the opposite side; the parietal aluminum wedge is embedded in the structure The inner cone is a precise CNC machined massive Al 7075 piece with a thickness of 20mm.

9.3.6.2 Pure CsI

Description

Performance, tests

Mechanical changes

Electronics changes

9.3.6.3 BGO

Prior experiences with calorimeters made of BGO crystals in high energy physics come from L3 [28] and Belle [29]. In the first case BGO was used for both Barrel and Endcaps, while Belle used BGO to build the Extreme Forward Calorimeter with the purpose of improving hermeticity close to the beam line and monitor beam background. Such knowledge will be summarized here, integrated by tests that were performed to account for the particular operating conditions expected in the case of SuperB: short integration time, needed to reduce pile-up, and large radiation.

Resolution

The properties of the BGO crystals are summarized in Tab. 9.3: the mechanical properties are similar to LYSO, but with a light yield four times smaller. The scintillation time is intermediate between the LYSO and the CsI, reason for which a good performance in a high rate environment is possible.

The performances of the L3 calorimeter, read by pin-diodes were $\sigma_E/E = (1.6/\sqrt{(E)} \oplus 0.35)\%$ and $\sigma_\theta = ((6/\sqrt{(E)} \oplus 0.3) mrad)$, i.e. the statistical term of the resolution at 100MeV was 4%. Later studies with APDs [30] show that the system produces $\sim$ 420 p.e./MeV, i.e. the statistical term at 100 MeV would be 0.5%, i.e. well within the requirements.

Nonetheless, due to the requirements dictated by machine background (Sec. 9.1.1) we will not be able to operate the detector integrating over even as much as a decay time of the crystal. The degradation in resolution induced by the integration time was tested specifically for this application in the INFN-Roma1 electronics laboratory with a single $2 \times 2 \times 18$ cm^3 crystal. 660 keV photons from a radioactive source were detected with a crystal read at both ends by two EMI-9814B PMT. The waveforms of the signals provided by the PMTs were acquired by a Lecroy digital oscilloscope, having a bandwidth of 300 MHz and used with a sampling rate of 250 Ms/s. One of the two signals was used to trigger the oscilloscope. The other signal was processed with an Ortec-474 and acquired by scope. The Ortec-474 module has an integration time (RC)

that can be choosen between 20, 50, 100, 200, and 500 ns.

For each value of RC a run was recorded and for each pulse shape both the total charge, independent of the total time, and the maximum amplitude, the quantity that will eventually be used in the experiment. The resolution on the charge was found to be 9.5% consistent with 130 p.e./MeV after detection and independent of the integration time of the ORTEC. The resolution on the amplitude depends instead on the latter, as shown in Fig. 9.43 and compared with the expectations from a simple Monte Carlo simulation where only the effect of the photoelectron statistics is included [27]. This results shows that shortening the integration time the resolution worsens, but only moderately. For instance even integrating only for 20ns, compared with the 300ns scintillation time of the crystal, the contribution to resolution due to the photostatistics worsens only by 60%.

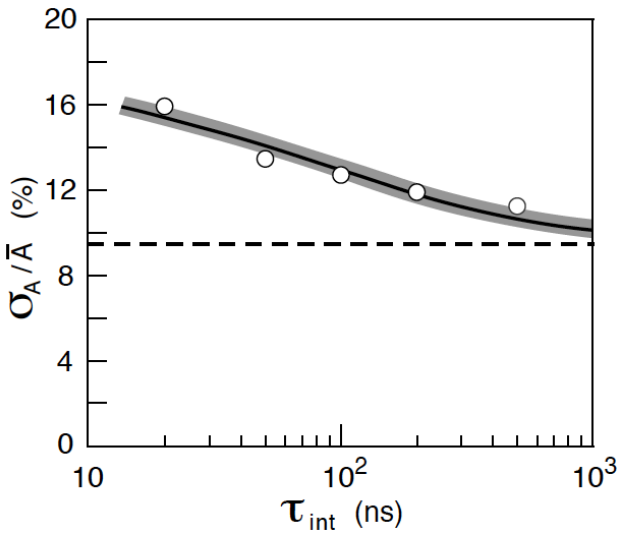

Figure 9.43: Resolution on the measurement of the total charge (dashed line) and the amplitude of the pulse shapes (dots)as a function of the integration time. The results of a Monte Carlo simulation are superimposed (shaded line).

Radiation Hardness

The BGO rad-hardness was tested up to 90Mrad [29, ?]. After a drop of about 30% in the first 20Mrad of integrated dose the crystal light yield plateaus. It will nonetheless recover up to 90% of the original light yield in approximately 10 hours and it is not documented what will happen if after this pre-irradiation the crystal receives a small dose further. For non irradiated crystals a dose of 115krad implies a light yield loss of 30% that fully recovers with a lifetime of $\sim$ 1 hour. Furthermore, these results refer to undoped, recently produced crystals, but they depend strongly on the level of doping and the manifacturer.

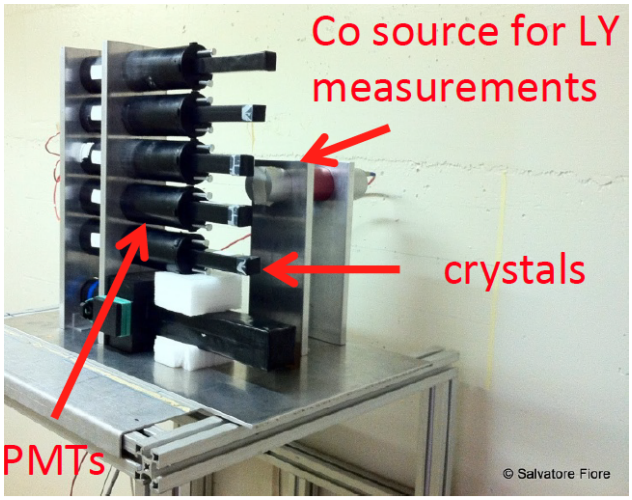

Figure 9.44: Experimental set-up for LY measurements. Crystal samples are shown while mounted on the PMTs. Crystals were coupled to the PMTs during low-dose irradiation, and data were acquired by shutting down the source for few minutes.

To customize the radiation hardness study to our case, we exposed four samples of BGO crystals to γ-rays from a high-activity ^{60}Co radioactive source. Two crystals of 2.2x2.2x18 cm^3 have been previously used in the L3 experiment at CERN, other two crystals of 2.5x2.5x20 cm^3 were recently supplied by the Shanghai Institute of Ceramics (SIC).

Irradiations and measurements took place at the Calliope Gamma Irradiation Facility at

ENEA-Casaccia center (Rome). The irradiation source is a cylindrical array of ^{60}Co source rods emitting γ-rays of 1.1 and 1.3 MeV, in an irradiation cell of 6x7x3.9 m^3 plus an attached gangway. Depending on the placement of the samples, dose rates from few rad/h up to 230 krad/h are available. The source can be moved outside or inside its shielding pool in less than two minutes.

Plastic mechanical supports for the crystals, not shielding them from the radiation, allowed us to expose the samples to different dose rates, and to couple them to EMI 9814B Photomultiplier Tubes (PMT) to perform the LY measurements using a low-activity ^{60}Co calibration source. PMTs were read out by a CAEN VME ADC.

We started our irradiation campaign by exposing the crystals to 5-10 rad/h dose rate for few hours. We were able to measure the LY once every 20 minutes of irradiation, with only two minutes delay after the source was shut down. Using this approach we measured the progressive LY reduction at different dose rates. We measured the LY recovery after 15-30 rad and 170 rad doses, and evaluated the recovery time constant for the different samples by fitting the time evolution of the LY after irradiation with the sum of two exponential functions. The results summarized in Tab. 9.6 show that the LY loss are important and that there are several components in the recovery time. The most relevant one, due to 5-10 rad/h dose rate are about four hours.

dose (rad)	rate (rad/h)	*LY drop*	τ_1 hr	τ_2 hr
15	5	25%	2.7 ± 0.4	–
170	10	67%	4.7 ± 0.2	380 (fixed)
12×10^6	23×10^4	90%	5.0 ± 2.4	381.9 ± 3.5

Table 9.6: Effect of irradiations on a BGO crystal: relative LY loss after irradiation and recovery times as measured with a fit to the time evolution with two exponential components.

We then exposed some crystals to a massive dose rate of 230 krad/h for a total dose of 12 Mrad, and then to small doses with 1.5 rad/h rate, to measure the sensitivity to small dose rates after strong delivered doses. We measured LY reductions up to 1/10 of the pre-irradiation LY value. A long-term recovery was then analyzed and exploited to measure the recovery time constant. We fit the LY recovery data with a double-exponential function, yielding a short time constant of (5.0±2.4) h and a long time constant of (381.9±3.5) h . BGO crystals from L3 experiment showed a larger damage after each irradiation, but also a faster recover capability, while crystals from SIC hardly recovered from radiation damage.

Light transmission spectra have been acquired before and after irradiations, in order to identify the nature of the LY reduction. As previously stated, the radiation-induced LY reduction could be due either to a decrease of the light transmittance, or to a damage of the scintillation mechanism itself. By comparing the LY and transmittance measurements, we observed that the main effect of the radiation damage was a reduction of the light transmission due to color-centre formation.

9.3.6.4 Comparison among options

The decision on the technology to be used for the forward calorimeter must be based on a compromise between physics performances and building costs. The options considered are the use of LYSO, pure CsI, or BGO crystals, as described in the previous subsections of this section, and the use of lead tungstate (PWO) crystals, for which the study was based on information known in literature.Such alternatives were compared with the one chosen as baseline for this study and described in the rest of the chapter, a Csi(Tl) and LYSO hybrid.

In order to compare the **physics performances** of the possible alternatives a full GEANT4 simulation was set up. It included: the correct detector geometry; the electronic noise obtained from beam- or lab- tests when available and extrapolations from them when

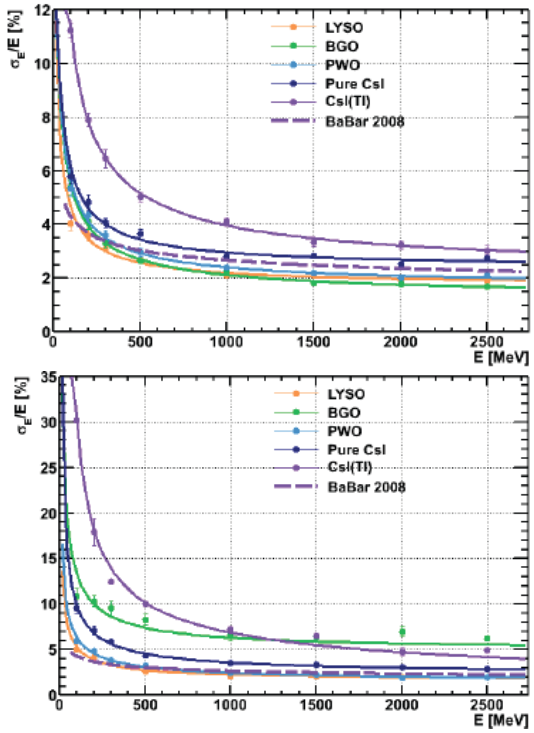

Figure 9.45: Comparison of the relative energy resolution between several options of the forward EMC. Left: nominal machine background. Right: machine background inflated by a safety factor of five. **NEED TO REDO PLOT WITH: COMPLETE HYBRID AND LATEST BACKGROUND. ALSO ADD BARREL ON TOP**

needed; signal shape obtained from detailed simulation of the expected electronic chain; signal extraction algorithm reproducing the actual electronics; clustering algorithm based on the BaBar one.

For each option and for several energies the response of the detector to monochromatic photons is fitted with a gaussian with exponential tails. The relative energy resolutions is computed as the FWHM of the fitted shape for several values of the photon energy. The comparison among the results for the different options is reported in Fig. 9.45 separately for the current estimate of the machine background and a conservative scenario where this background is increased by a safety factor five (5x-background).

The best option is clearly to use only LYSO crystals, while the option suffering for the most problems is the one with BGO. The latter is indeed very sensitive to the 5x-background most likely due to the non-optimal geometry of the simulation, which was not done ad-hoc. Also, the hybrid solution suffers from background, but all effects are comparable with the expected degradation in resolution of the barrel. All other options have comparable performances, intermediate between the full LYSO and the hybrid options.

To complete the picture, Tab. 9.7 shows a comparison of the **volume and total cost** of the scintillating crystals required for the forward endcap in different configurations. To compare options on the same basis, the costs need to include, besides the cost of the crystals, also the cost of the photodetectors, of the calibration system, and of the mounting structure.

Photo-detectors have reasonably similar costs for all options. Some saving can be achieved with the hybrid option by reusing existing channels. A more accurate calibration system is instead needed only for the options that degrade under irradiation with a short recovery time, namely BGO and PWO. Finally, the carbon fiber mechanical support needs to be redone only for the LYSO, BGO and PWO options, while in the other options the only costs are the shipping and the refurbishment of the present structure.

The table also lists three hybrid options, in which a number of the outer CsI(Tl) rings of the endcap are retained (since they are approximately at the same distance from the interaction region as are the forward barrel crystals) and the inner rings are replaced by LYSO crystals.

The two least expensive options are the hybrid and the CsI solutions. Among this the performance studies show that the hybrid option has a worse resolution. Nonetheless the properties of the CsI crystals are still under study and therefore the TDR budget was based on the more studied, albeit less performant, hybrid option.

9.4 Backward Calorimeter

The backward electromagnetic calorimeter for Super$B$ is a new device with the principal intent of improving hermeticity of the detector at modest cost. Excellent energy resolution is not a requirement, since there is significant material from the drift chamber in front of it. Thus, a high-quality crystal calorimeter is not planned for the backward region. The proposed device is based on a multi-layer lead-scintillator sampling calorimeter with longitudinal segmentation providing capability for π/e and K/π separation at low momenta. The design is derived from the analog hadron calorimeter for the ILC [32].

The active region of the backward calorimeter is located behind the drift chamber starting at $z = -1320\,\mathrm{mm}$ (see Figure 9.46) allowing room for the drift chamber front end electronics. The inner radius is 310 mm, the outer radius is 750 mm and its total thickness is less than 180 mm covering $12X_0$. It is constructed from a sandwich of 2.8 mm Pb plates alternating with 3 mm plastic scintillator strips (*e.g.*, BC-404 or BC-408). The scintillation light of each strip is collected by a wavelength-shifting fiber (WLS) coupled to a photodetector located at the outer radius. The scintillator strips come in three different geometries, right-handed logarithmic spirals, left-handed logarithmic spirals

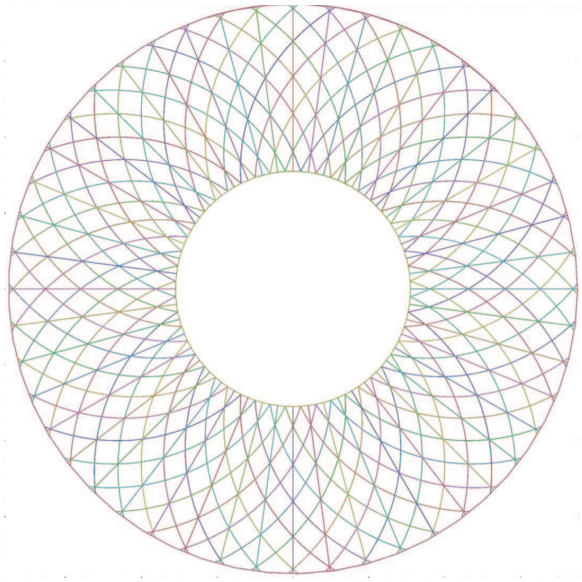

Figure 9.47: The backward EMC, showing the scintillator strip geometry for pattern recognition.

and radial wedges. This pattern alternates eight times. Each layer contains 48 strips producing a total of 1152 readout channels. The strip geometry is illustrated in Fig. 9.47

The WLS fibers, Y11 fibers from Kuraray, are embedded in grooves milled into the center of the scintillator strips. Each fiber is read out at the outer radius with a $1 \times 1\,\mathrm{mm}^2$ multi-pixel photon counter (SiPM/MPPC) [38]. A mirror is glued to each fiber at the inner radius to maximize light collection. The SPIROC (SiPM Integrated Read-Out Chip) integrated circuit (IC) [39] developed for the ILC is used to amplify and digitize the SiPM/MPPC signals, providing both TDC (100 ps) and ADC (12 bit) capability. Each ASIC contains 36 channels. Since these ASICs were developed for SiPM readout, where the intrinsic gain is much higher, an additional preamplifier is coupled to the SiPM/MPPCs. This has the advantage to place the SPIROC ASICs at a convenient place in the detector without introducing additional noise.

9.4.1 Requirements

The main goal of the backward EMC is to increase the calorimeter coverage by recording any charged or neutral particle in the backward region. This information is important in particular for analyses that utilize the recoil method with hadronic and semileptonic tags to select B meson decays with neutrinos in the final state. The backward EMC helps to increase the selection efficiency and to improve background rejection. For this task, excellent energy resolution is not necessary. It is more important to keep the costs moderate. With moderate energy resolution and good angular resolution π^0 reconstruction is anticipated. Furthermore, the backward EMC has the capability to measure time-of-flight and the energy loss via ionization of charged particle well. This information is very useful for particle identification, in particular π/e and K/π separation at low momenta.

9.4.1.1 Energy and angular resolution

Since the backward EMC prototype is still in the construction phase, presently no results on energy resolution and angular resolution exist. However, electromagnetic sampling calorimeter prototypes with plastic scintillator strips and tiles have been tested in test beams within the CALICE collaboration [40]. The energy resolution for the stochastic term is $15\%\sqrt{E[\,\mathrm{GeV}]}$ and for the constant term is around 1%. For the CALICE analog hadron calorimeter which has a non-optimized geometry for electromagnetic showers, the stochastic term was measured to be around $20\%/\sqrt{E[\,\mathrm{GeV}]}$. For low photon energies, an additional noise term of $\sim 130\,\mathrm{MeV}/E$ contributes. Thus, the backward endcap EMC is expected to have a similar performance with a stochastic term of $15 - 20\%/\sqrt{E[\,\mathrm{GeV}]}$.

The left-handed logarithmic spirals are defined by

$$x(t) = r \exp b \cdot t \cos t - r \tag{9.8}$$

$$y(t) = r \exp b \cdot t \sin t \tag{9.9}$$

$$\tag{9.10}$$

For $r = r_o/2 = 37.5$ cm and $b = 0.2$ eight left-handed spiral strips overlap with eight right-handed spiral strips defining a specific tile-shaped region. The radial strips overlap with

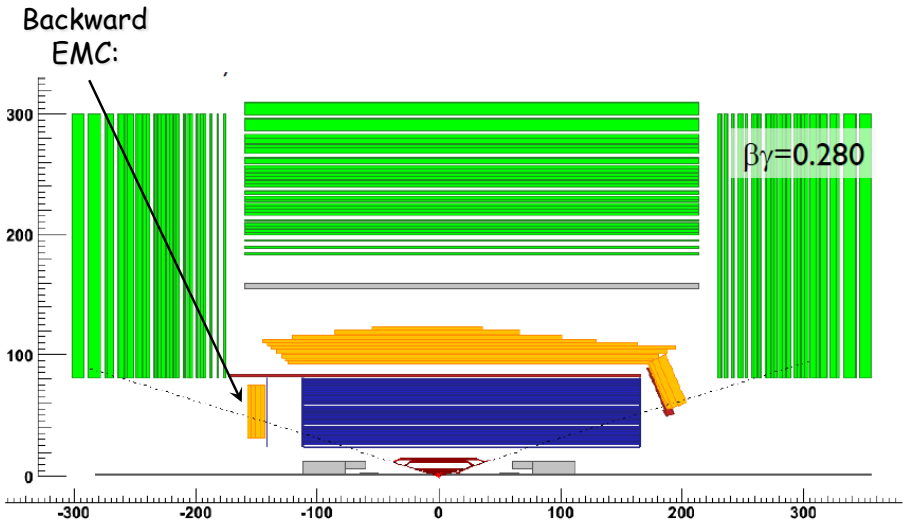

Figure 9.46: Layout of the calorimeters in the SuperB detector.

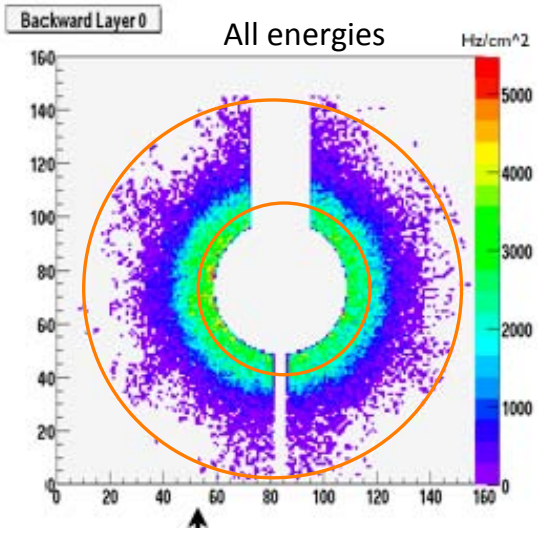

Figure 9.48: The distribution of background hits of all energies in the backward layer 0. The coverage by the backward EMC is shown by the red circles.

five left-handed (right-handed) spiral strips. In the worst case, the resolution is $\sigma_r = \sigma_\phi \simeq 29\,\text{mm}$ for a single tile in the outer region. This is improved to $\sigma_r = \sigma_\phi \simeq 12\,\text{mm}$ in the inner region. If the shower is distributed over several adjacent tiles, its position can be determined by the center-of-gravity method improving the position resolution significantly.

9.4.1.2 Background rates

Present background simulations indicate that the worst neutron rate in layer zero of the backward IFR end cap is 3.5 $\text{kHz}/\,\text{cm}^{-2}\text{s}^{-1}$. The radiation profile shown in Figure 9.48 indicates that the worst rates for all energies of 3 $\text{kHz}/\,\text{cm}^{-2}\text{s}^{-1}$ occur in the inner most region. In ten years of running this amounts to $6.1 \times 10^9\ n/\,\text{mm}^2$ in the region near the inner radius. The background rates drop significantly towards outer radius. At the location of the photodetector, the rate is reduced by more than a factor of 10. Further simulation studies are needed, since due to the high rate at the inner radius an occupation problem may be present. To deal with this issue one either subtracts a higher average background energy from each strip or divides the strips into two segments at the cost of doubling the number of photodetectors. The former solution will have an effect on the energy resolution since the background energy deposit has a wide distribution. The latter

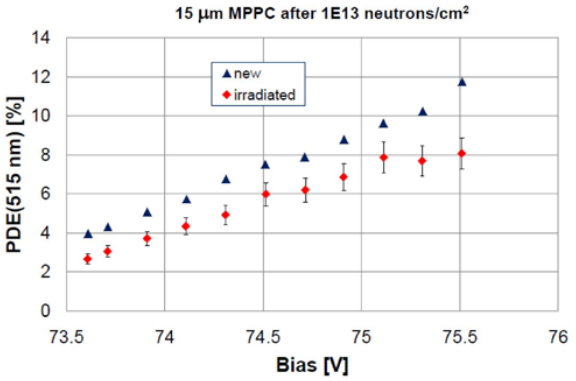

Figure 9.49: The efficiency of $15\,\mu\text{m} \times 15\,\mu\text{m}$ pixel MPPCs as a function of the bias voltage before and after irradiation with $10^{13} n/\,\text{cm}^{-2}\text{s}^{-1}$.

solution is preferable, but is about \$100k more expensive.

9.4.1.3 Radiation hardness

Irradiation of Si detectors causes the dark current to increase linearly with flux Φ:

$$\Delta I = \alpha \Phi V_{\text{eff}} G, \tag{9.11}$$

where $\alpha = 6 \times 10^{-17}$ A/ cm $V_{eff} \sim 0.004\,\text{mm}^3$, Φ is the flux, V_{eff} is the bias voltage and G is the gain. Since the initial resolution of MPPCs/SiPMs of $\sim$ 0.15 photoelectrons (pe) is much better than that of other Si detectors, radiation effects start at lower fluxes. For example, at a flux $\Phi = 10^{10}\ n/\,\text{cm}^{-2}\text{s}^{-1}$ the individual single pe signals are smeared out. The MIP peak is still visible at $\Phi \sim 10^{11}\ n/\,\text{cm}^{-2}\text{s}^{-1}$. The number of observed hot spots and the noise rate increases after irradiation of $3 \times 10^9\ n/\,\text{cm}^{-2}\text{s}^{-1}$. No significant changes are observed on the cross talk probability as well as no significant change on the saturation curves. The main effect is an increase in noise after exposure to high n dose. Hamamatsu has produced new SiPM/MPPCs with $20\,\mu\text{m} \times 20\,\mu\text{m}$ and $15\,\mu\text{m} \times 15\,\mu\text{m}$, which have lower detection efficiency than the $25\,\mu\text{m} \times 25\,\mu\text{m}$ version due to more boundaries and thus need a higher bias voltage to compensate for losses. Figure 9.49 shows the detection efficiency as a function of bias voltage for $15\,\mu\text{m} \times 15\,\mu\text{m}$ detectors before and after irradiation with $10^{13}\ n/\,\text{cm}^{-2}\text{s}^{-1}$. For the new detectors, signal/noise and the equivalent noise charge look fine after irradiation. We expect the backward endcap EMC will record $10^{11}\ n/\,\text{cm}^{-2}\text{s}^{-1}$ after 10 years operation. If the $25\,\mu\text{m} \times 25\,\mu\text{m}$ pixel SiPM/MPPC show a problem we may switch to one of the new SiPM/MPPCs with smaller pixel size.

9.4.1.4 Solid angle, transition to barrel

In the laboratory frame, the backward EMC covers a full polar angle region from 231 mrad to 473 mrad. Partial coverage extends the polar angle region from 209 mrad to 517 mrad. In the present design, there is a gap between the backward EMC and the barrel covering the region 517 mrad to 694 mrad in the laboratory frame. In the center-of mass frame, full coverage of the backward EMC is in the region 215 mrad to 442 mrad, while partial coverage exists in the region from 194 mrad to 482 mrad. If the backward EMC could move closer to the IR, the gap to the barrel calorimeter could be reduced.

9.4.2 Mechanical design

The 3 mm thick scintillator strips are cut individually from a scintillator plate. Thus, the plate size and the cutting procedure need to be carefully thought through to minimize the amount of waste. For the spiral strips the least waste and fastest production is obtained by fabricating a mould. However, this approach may be too expensive, since the total number of spiral strips is rather small. The preferred scintillator material is BC 404 from St Gobain, since it has the smallest decay time for TOF capability and its emission spectrum is reasonably matched to the Y11 absorption spectrum. The strip width is 38 mm at the inner edge increasing to 98 mm at the outer edge. The strip sides are painted with a white diffuse reflector. Front and back faces are covered with reflectors sheets (3M, Tyvec). Test bench measurements have shown that the yield along the strips varies by more than a factor of two. To restore unifor-

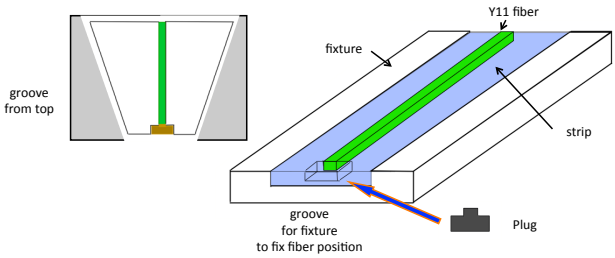

Figure 9.50: Schematic of holding the scintillator strip in a fixture for mounting the MPPC to the Y11 fiber.

mity, a pattern of black dots is printed onto the white reflector sheets.

In the center of each strip, a 1.1 mm deep groove is milled into which the 1 mm thick Y11 WLS fiber is inserted. At the outer edge of the strip, the groove is cut 0.4 mm deeper so that the active area of the SiPM/MPPC fully covers the fiber. The SiPM/MPPC is housed in a small precisely cut pocket. Especially fabricated fixtures out of Teflon or Nylon will hold a strip. The fiber groove at the outer edge is closed with a plug at the position of the photodetector. The Y11 fiber is pressed against the plug and held with a drop of glue. After removing the plug the SiPM/MPPC is inserted and is glued onto the Y11 fiber to match refractive indices. A mirror is placed at the other end of the fiber to detect the light that moves away from the photodetector. So tolerances in the length of the Y11 fiber are picked up at the mirror end. The strip layout is shown in 9.50.

To hold the strips in each layer in place 1.5 mm deep and 1 mm wide grooves are cut into the lead plates. The shape of groove matches that of the strip. A 3 mm thick and 1 m wide and 550 mm long plastic strip is inserted into the groove and is glued. This structure is strong enough to hold the scintillator strips in place. The calorimeter can be rotated by 90°. This is needed for operation with cosmic muons that yield a MIP calibration and allows for testing the calorimeter before installing it into the SuperB detector.

The entire calorimeter just weighs about 1300 Kg. An Al frame with a strong rear plate and a strong inner cylinder will hold the backward EMC in the SuperB detector. The front plate and outer cylinder needed for closure and shielding can be thin. Concerning cost and performance it is advantageous to build the backward EMC as a single unit. This requires the calorimeter to slide back on the beam pipe supported on the tunnel walls. It needs to be fixed at the tunnel and is rolled in. Since the inner radius is 31 cm, there is sufficient clearance for pumps and other beam elements. The design of this capability requires a detailed drawing of the beam pipe and the position and size of machine elements.

It is possible, however, to build the backward EMC in two halves with a vertical split. The impact of such a design is that ten strips per layer have to be cut into two segments. The inner segments of these strips have to be read out at the inner radius. This increases the number of channels by 240, requiring 240 additional SiPM/MPPCs, seven extra SPIROC boards and four extra calibration boards. This layout will deteriorate the performance near the vertical boundary. The effect needs to be studied in simulations. This adds extra costs at the order of $\sim 20\%$.

9.4.2.1 Calorimeter construction

Each completed strip with Y11 fiber and MPPC mounted is tested in the lab with a ^{106}Ru source. All important properties, such as bias voltage, gain, noise, and MIP position are recorded in a data base. Stacking will start from the rear to the front. The rear Al plate rotated by 90° is placed on the mounting table and the inner cylinder is bolted on to it. The back plate requires 48 radially milled grooves into which the plastic strips are inserted that will hold the scintillator strips. Next, all scintillator strips are mounted, the MPPCs are connected to preamplifiers and a Pb plate with right-handed logarithmic spiral grooves is placed on top completing layer 24. This procedure is repeated 24 times. Finally, another scintillator layer with radial strips and the front plate are stacked.

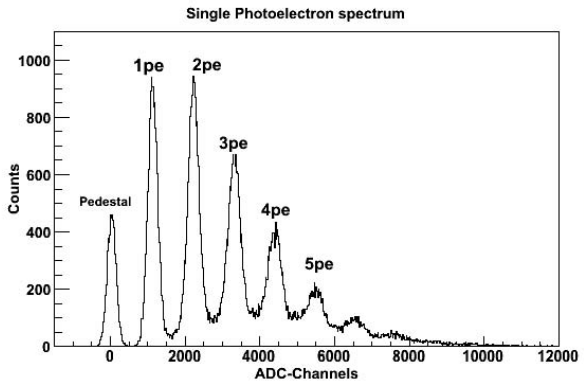

Figure 9.51: Single photoelectron spectrum measured with a Hamamatsu S10362-11-025P MPPC.

The scintillator layer 0 yields information on the shower origin.

Before the outer cylinder is bolted on, temperature sensors and clear fibers need to be installed at the outer ring that transport light from a UV LED to the strips. If each fiber illuminates 13 strips via a notch spaced equidistantly every 12 mm, a total 96 fibers are sufficient. The fibers run through small holes in the back plate from the rear to the front. Attaching four fibers per LED, 24 LEDs housed outside the rear plate are needed.

9.4.2.2 Support and services

The preferred option is to build the backward EMC as one unit. In order to avoid breaking the beam pipe when access is required to the drift chamber endplate, the backward EMC must be be able to slide back far enough. The explicit design requires a detailed design of the IR with all machine elements in place. In the detector position, the weight is supported by two brackets that are fixed at the rear endplate and on the inner wall of the IFR backward endcap. When rolling back the weight could be supported by the tunnel wall. To allow for a smooth sliding back, rolls are mounted on the inner support cylinder.

The 32 SPIROC ASICS and four calibration boards are mounted on the rear support plate of the EMC. Each SPIROC ASIC has one multiplexed USB output cable to the DAQ, a cable providing low voltage input for +5.5 V and -7.5 V, a cable for the MPPC bias voltage of 70 V, an electronic calibration input and an analog output. Since the 36 signal cables remain inside the detector, a total 192 cables have to be supplied from the outside to the SPIROC ASICs.

The four CMBs are also mounted on the rear support plate. Each CMB holds six LEDs and six PIN photodiodes and need to read out four thermocouples. Including the low voltage supplies for the CMB electronics, 80 cables are needed for the CMBs, yielding 272 cables in total.

9.4.3 SiPM/MPPC readout

The photodetectors are SiPM/MPPCs from Hamamatsu (type S10362-11-025P) with a sensitive area of 1 mm × 1 mm holding 1600 pixels with a size of 25 μm × 25 μm. These detectors are avalanche photodiodes operated in the Geiger mode with a bias voltage slightly above the breakdown corresponding to $50-70$ V providing a gain of a few 10^5. They are insensitive to magnetic fields. Each pixel typically has a quenching resistor of a few MΩ so they recover within 100 ns. The efficiency is of the order of $10-15\%$. Since the SiPM/MPPCs record single photoelectrons as shown in Fig. 9.51 for a Hamamatsu MPPC, they are auto-calibrating. SiPM/MPPCs are non-linear requiring non-linearity corrections for higher energies. As an example, Fig. 9.52 shows the response curves of 10,000 SiPMs measured at ITEP most of which were installed in the analog hadron calorimeter [32]. The dynamic range is determined by the number of pixels. Properties of several SiPM/MPPCs are listed in Table 9.8.

A concern with SiPM/MPPCs is radiation hardness. Degradation in performance is observed in studies performed for the Super$B$ IFR, beginning at integrated doses of order 10^8 1-MeV-equivalent neutrons/ cm^2 [41]. This needs to be studied further, and possibly mitigated with shielding. Another alternative is to look

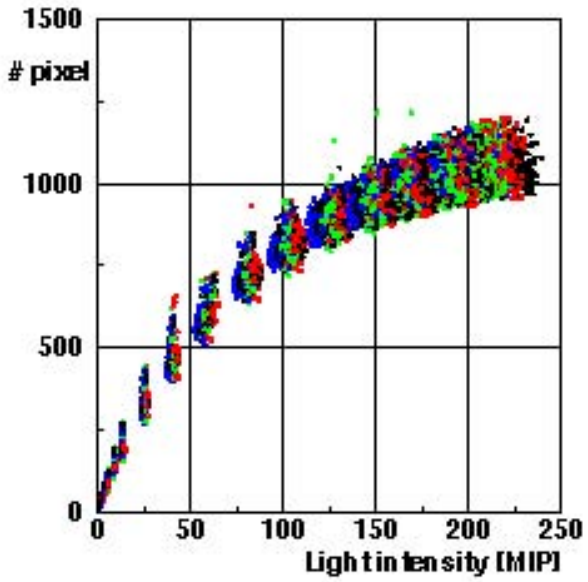

Figure 9.52: Saturation curves of 10,000 SiPMs measured in the CALICE analog hadron calorimeter.

into a different photodetector. Recently, Hamamatsu has produced SiPM/MPPCs with pixel sizes of $20\,\mu\text{m} \times 20\,\mu\text{m}$ and $15\,\mu\text{m} \times 15\,\mu\text{m}$ (see Table 9.8). A CMS study shows that the performance of these new photodetectors deteriorates only slightly after an irradiation of $10^{13} n/\,\text{cm}^{-2}\text{s}^{-1}$.

9.4.4 Electronics

The signal of the SiPM/MPPC is first amplified with a charge-sensitive preamplifier then fed into the auto-triggered, bi-gain SPIROC ASIC. The SPIROC board has 36 channels. Each channel has a variable-gain charge preamplifier, variable shaper and a 12-bit Wilkinson ADC. It allows to measure the charge Q from one photoelectron (pe) to 2000 pe and the time t with a 100 ps accurate TDC. A high-level state machine is integrated to manage all these tasks automatically and control the data transfer to the DAQ. The SPIROC ASIC was designed to supply the high voltage for the SiPM/MPPC. Using a DAC, individual high voltages within ± 5 V can be supplied to each photodetector.

The SPIROC ASIC gives Gaussian signals with no tails, shows excellent linearity and low noise. 32 ASIC readout boards are needed to read out the entire endcap. The boards are mounted in two layers behind the endcap. The first layer holds 20 boards and the second layer the remaining 12 boards. Each board connects to 36 SiPM/MPPCs via a ribbon cable that were designed for ILC at a luminosity of $\mathcal{L} = 10^{34}\ \text{cm}^{-2}\text{s}^{-1}$.

9.4.5 Calibration

An LED-based calibration system with fixed LED intensities is used to monitor the stability of strip-fiber-SiPM/MPPC system between MIP calibrations, to perform gain calibrations, determine intercalibration constants, and to measure the SiPM/MPPC response functions. This is necessary since the SiPM/MPPCs have a temperature and voltage dependence of the gain of

$$\frac{dG}{dT} \sim -1.7\%/\text{K}, \tag{9.12}$$

$$\frac{dG}{dV} \sim 2.5\%/0.1\ \text{V}. \tag{9.13}$$

The temperature and voltage dependence of measuring the charge of the scintillation signal is

$$\frac{dQ}{dT} \sim -4.5\%/\text{K} \tag{9.14}$$

$$\frac{dQ}{dV} \sim 7\%/0.1\ \text{V} \tag{9.15}$$

The calibration system is based on a new design for the analog hadron calorimeter. Light from a UV LED is coupled to clear fibers. The fibers are notched at equidistant positions. The shape of each notch changes such that it emits about the same intensity of light. For the backward EMC, 96 fibers with 13 notches each are sufficient to illuminate all strips. If four fibers are coupled to one LED, 24 LEDs are needed whose light is monitored by a PIN photodiode. A few thermocouples distributed throughout the outer edge of the EMC near MPPCs measure temperature. Both temperature and bias voltage are recorded regularly by a slow control system. After temperature and PIN

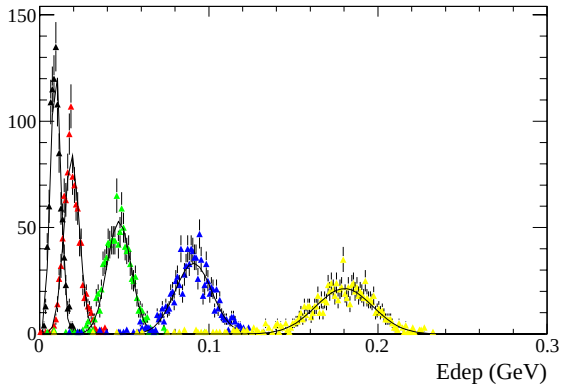

Figure 9.53: Energy depositions from mono-energetic photons (0.1 GeV, 0.2 GeV, 0.5 GeV, 1 GeV and 2 GeV) observed in the scintillators of the backward EMC.

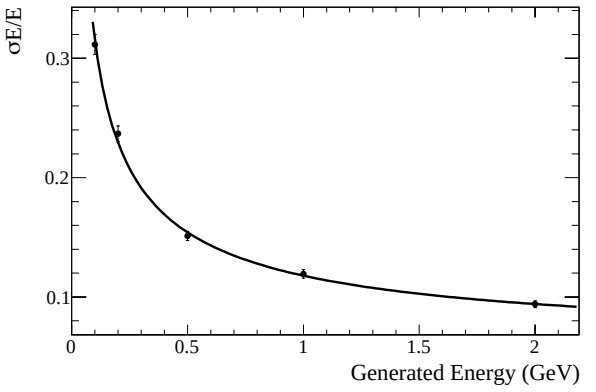

Figure 9.54: The backward EMC energy resolutions, σ_E/E, where σ_E and E are the Gaussian width and mean in Fig. 9.53, as a function of generated photon energy.

diode correction the stability of LED system is better than 1%.

The calibration boards are 40 mm × 140 mm in dimension and house one LED, one PIN diode, the electronics to read out the PIN diode, and monitor temperature and MPPC voltage. The boards are sufficiently small to be mounted at the backplate near the outer radius. They can be arranged such that the fibers can be nearly straight.

9.4.6 Backward simulation

A simple backward EMC model exists in the GEANT4 simulation that models 24 layers of scintillator and lead. Each layer is modeled by a complete disc without physical strip segmentations in r-ϕ. Support structure, fibers, electronics, and cables are presently ignored.

In the fast simulation, the model does not separate lead from scintillator. It uses instead an artificial material that approximates the overall density, radiation length, interaction length and Molière radius of the mixture of lead and plastic. The volume is divided into eight rings, each of which is divided into 60 segments. The logarithmic spirals and the lead-scintillator layers, however, are not modeled explicitly to avoid a complicated shower reconstruction and the modeling of longitudinal shower energy distribution. The energy resolution is set to $\sigma_E/E = \frac{14\%}{\sqrt{E(\,\mathrm{GeV})}} \oplus 3\%$.

9.4.7 Performance in simulations

A GEANT4 simulation is performed to study the energy resolution under the simplified conditions, ignoring the rest of the detector and shooting mono-energetic photons perpendicular to the face of the disc. All energy deposited in the scintillator is collected. No clustering algorithm is performed. Figure 9.53 shows the energy deposition for five different photons energies, 0.1, GeV 0.2 GeV, 0.5 GeV, 1 GeV, and 2 GeV. For 0.1 GeV photons, approximately 9.5% of the photon energy is deposited in the scintillator on average. This percentage drops to 9.0% for 2 GeV photons.

The energy dependence of the energy resolutions on generated energy is shown in Fig. 9.54. The distribution can be fitted with the function $\sigma_E/E = \frac{10\%}{E(\,\mathrm{GeV})^{0.485}} \oplus 6\%$.

9.4.8 Impact on physics results

Fast simulation studies have been conducted to investigate the performance gain achieved by the addition of the backward calorimeter. The

channels chosen to evaluate the impact of this detector are $B \to \tau\nu$ and $B \to K^{(*)}\nu\bar{\nu}$, since both are benchmark channels for the Super$B$ physics program and the detector hermeticity improves signal reconstruction efficiencies and background rejection.

The study of the leptonic decay $B \to \tau\nu$ is of particular interest as a test of the Standard Model (SM) and a probe for New Physics [33]. The presence of a charged Higgs boson (in *e.g.*, a Two Higgs Doublet Model) as a decay mediator could significantly modify the branching ratio with respect to the SM value, depending on the Higgs mass and couplings. A detailed analysis of this channel is therefore quite important in searches for physics beyond the SM. A complementary search for new physics can be performed using $B \to K^{(*)}\nu\bar{\nu}$ decays [34], [35]. Being mediated by a flavor-changing neutral current, these processes are prohibited at tree level in the SM and the higher order diagrams may receive contribution from a non-standard mechanism. Moreover, new sources of missing energy may replace the neutrinos in the final state.

The reconstruction of both decay modes is challenging, since the final state contains more than one neutrino and thus is only partially reconstructible. Signal events are selected using a recoil method analysis, in which the signal B-meson ($B_{\rm sig}$) is identified as the system recoiling against the other tag B meson ($B_{\rm reco}$). The tag B meson is either reconstructed fully via its hadronic decays or partially reconstructed from its semileptonic final states [36]. The rest of the event is assigned to the $B \to \tau\nu$ candidate, if it is compatible with one of the following decay modes of the tau lepton: $\mu\nu_\mu\nu_\tau$, $e\nu_e\nu_\tau$, $\pi\nu_\tau$, $\pi\pi^0\nu_\tau$, $\pi\pi^0\pi^0\nu_\tau$, $\pi\pi\pi\nu_\tau$, $\pi\pi\pi\pi^0\nu_\tau$. These final states cover about 95% of all τ decays, and have one charged particle (1-prong) or three charged particles (3-prong), with the possible addition of one or two π^0s. Since final states containing one or more π^0 cover about 40% of the tau decay modes, an increase in the EMC coverage improves substantially the efficiency of tau identification.

Candidates for the $B \to K^{(*)}\nu\bar{\nu}$ sample have to be compatible with one of the following final states: $K^{*+} \to K_S(\pi^+\pi^-)\pi^+$, $K^+\pi^0$, $K^{*0} \to K^+\pi^-$, K^+, $K_S \to \pi^+\pi^-$ (semileptonic analysis only). In the analyses with a $K^{(*)}$ in the final state, further selection criteria are applied using kinematic quantities related to the goodness of the $B_{\rm reco}$ and $K^{(*)}$ reconstruction and event shape variables that test the energy balancing in the event and the presence of missing energy due to the neutrinos in the final state. The present level of the analyses is very similar to that in Refs. [36] and [37].

Backgrounds are further rejected using, $E_{\rm extra}$, the total neutral energy in the calorimeter of particles not associated with either B-meson. Signal events peak at low values of $E_{\rm extra}$, while background events which contain additional sources of neutral showers tend to have higher values of $E_{\rm extra}$. The discriminating power of this observable obviously increases with the calorimeter coverage.

The performance of the backward EMC is assessed by comparing the signal-to-background ratio, S/B, and the statistical precision, $S/\sqrt{S+B}$, of the expected signal with and without the backward EMC used as a veto device for extra-neutral energy. For this task, the extra neutral energy reconstruction is split into two disjoint calorimeter regions: $E^{\rm extra}_{\rm brrfwd}$ covering the barrel and the forward region and $E^{\rm extra}_{\rm bwd}$ covering the backward region only. Furthermore, the effects of machine backgrounds (Sec. 14.2.2.6) superimposed on physics events are taken into account.

The results for both rare decay channels are summarized in Table 9.9. For $B \to \tau\nu$ reconstructed in hadronic tags, the improvements in $S/\sqrt{S+B}$ are shown as a range sampling over the individual τ final states. For $B \to \tau\nu$ reconstructed in semileptonic tags, the improvement in $S/\sqrt{S+B}$ is presented as an average over all τ final states. Combining $S/\sqrt{S+B}$ of both tags, the net gain is of the order of 10%. For $B \to K^*\nu\bar{\nu}$, the net gain for hadronic and semileptonic tags combined ranges between 8% and 16% depending on the final state. For $B \to K\nu\bar{\nu}$ the net gain is about 6%.

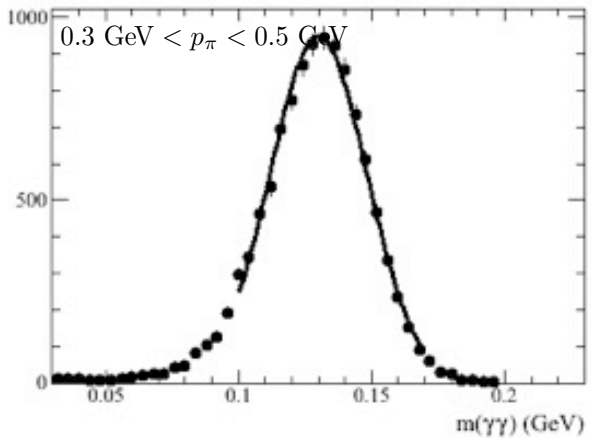

Figure 9.57: Invariant-mass resolution of $\pi^0 \to \gamma\gamma$, where one photon is detected in the backward EMC.

These improvements in turn yield improvements in the precision of measured physical observables. For example, Figure 9.55 shows the expected precision of the measured $B \to K^+\nu\bar{\nu}$ and $B \to K^*\nu\bar{\nu}$ branching fractions as a function of integrated luminosity. The yellow band represents the SM prediction [33]. The red dots with red error bars are obtained from an extrapolation of *BABAR* measurements, taking into account the improvements due to the lower boost, corresponding to a higher detector hermeticity. Dots with black error bars are obtained from the same procedure but in addition include the backward EMC. For $\mathcal{B}(B \to K^+\nu\bar{\nu})$ and $\mathcal{B}(B \to K^*\nu\bar{\nu})$ the 3σ significance for evidence without the backward EMC is reached at 5 ab^{-1} and 51 ab^{-1}, respectively. When adding the backward EMC, the 3 σ significance is already reached at 4.5 ab^{-1} and 42 ab^{-1}, respectively.

In addition to the measurement of neutral clusters, the backward EMC can be used to improve the π^0 reconstruction efficiency. If one photon is reconstructed in the backward EMC, the $\gamma\gamma$ invariant-mass resolution improves from $\sim$ 24 MeV for 200 MeV/c π^0s to $\sim$ 13 MeV for 1 GeV/c π^0s (see, e.g., Fig. 9.57).

It is worth mentioning that the inclusion of the backward EMC not only improves the background rejection, but also the B-tagging efficiency. The impact on the B reconstruction efficiency is determined by using the decays $B^- \to D^0\pi^-, D^0 \to K^-\pi^+\pi^0$. Events are separated into two groups: the first uses only photons from the barrel and forward endcap, while the second includes photons from the backward EMC with polar angle between $-0.96 < \cos\theta < -0.89$ as well. The π^0 mass window is defined as 120–145 MeV (100–180 MeV) for the first (second) group. For B candidates, D^0 s are selected by $1.830 < m_{K\pi\pi^0} < 1.880$ GeV and $-80 < \Delta E < 50$ GeV. The $m_{\rm ES}$ distribution is fitted to determine the B reconstruction efficiency. Including the backward EMC, the signal efficiency increases by nearly 4% in this particular channel (see Fig. 9.58).

9.4.9 Use for particle identification

Charged particles moving in the backward direction typically have lower momentum. Thus, ionization loss and time-of-flight measurements may provide useful information for particle identification, *e.g.* for e/π and K/π separation.

A preliminary time-of-flight study is performed with fast simulation. Single kaons or pions are generated that move towards the backward EMC. The true arrival time calculated at the first layer is smeared with a Gaussian resolution to simulate the measured time distribution. Velocity distributions are obtained for kaons and pions at a given momentum from the measured time and reconstructed track path length. Both mean and RMS values are extracted from these distributions to determine K/π separation in standard deviation units (σ) as a function of momentum for different time resolutions, in which uncertainties in the momentum measurement and path length reconstruction are included. Fig. 9.59 shows K/π separation in units of standard deviations as a function of momentum for time resolutions of 100 ps, 50 ps, 20 ps, 10 ps and perfect timing. For example for 100 ps time resolution, aK/π separation of more than three σ can be achieved for momenta up to 1 GeV/c and approximately 1.5σ up to 1.5 GeV/c.

Since each layer measures the time distribution, 24 measurements will be averaged. In ad-

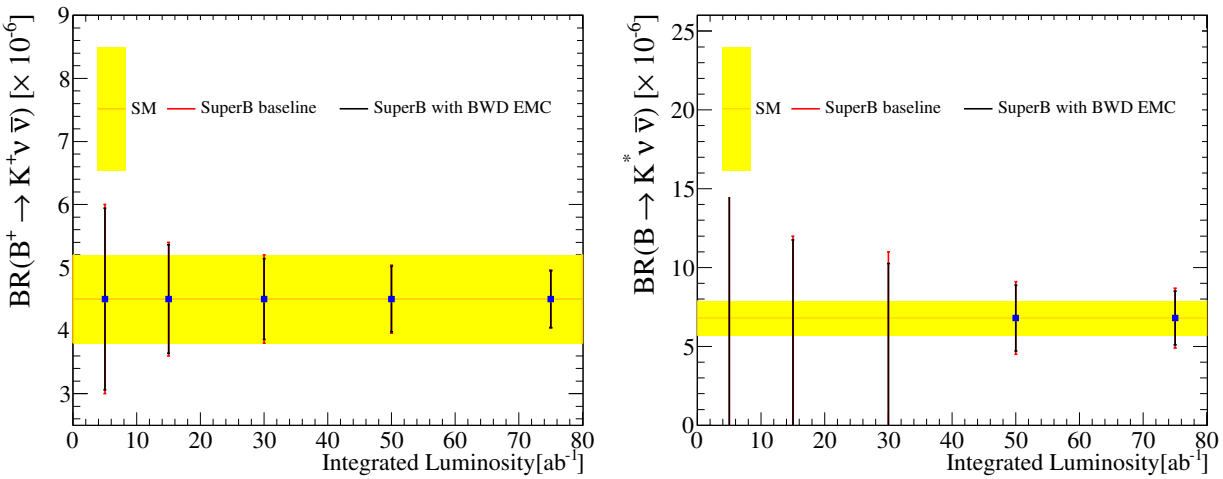

Figure 9.55: Expected precision on branching fraction measurements of (left) $\mathcal{B}(B \to K^+\nu\bar{\nu})$ and (right) $\mathcal{B}(B \to K^*\nu\bar{\nu})$ as a function of integrated luminosity. The yellow band represent the SM prediction, the black (red) error bars represent the upper limits or the branching fraction measurements with (without) the backward EMC.

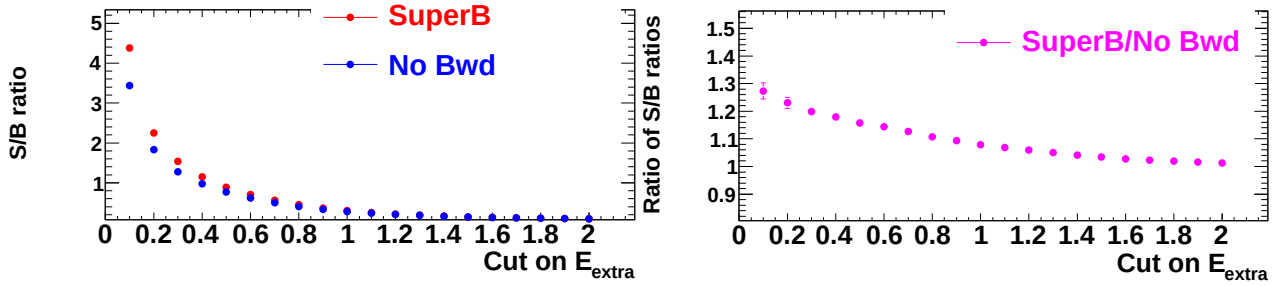

Figure 9.56: Left: Signal-to-background ratio with and without a backward EMC, as a function of the E_{extra} selection. Right: Ratio of the S/B ratio with a backward EMC to the S/B ratio without a backward calorimeter, as a function of the E_{extra} selection.

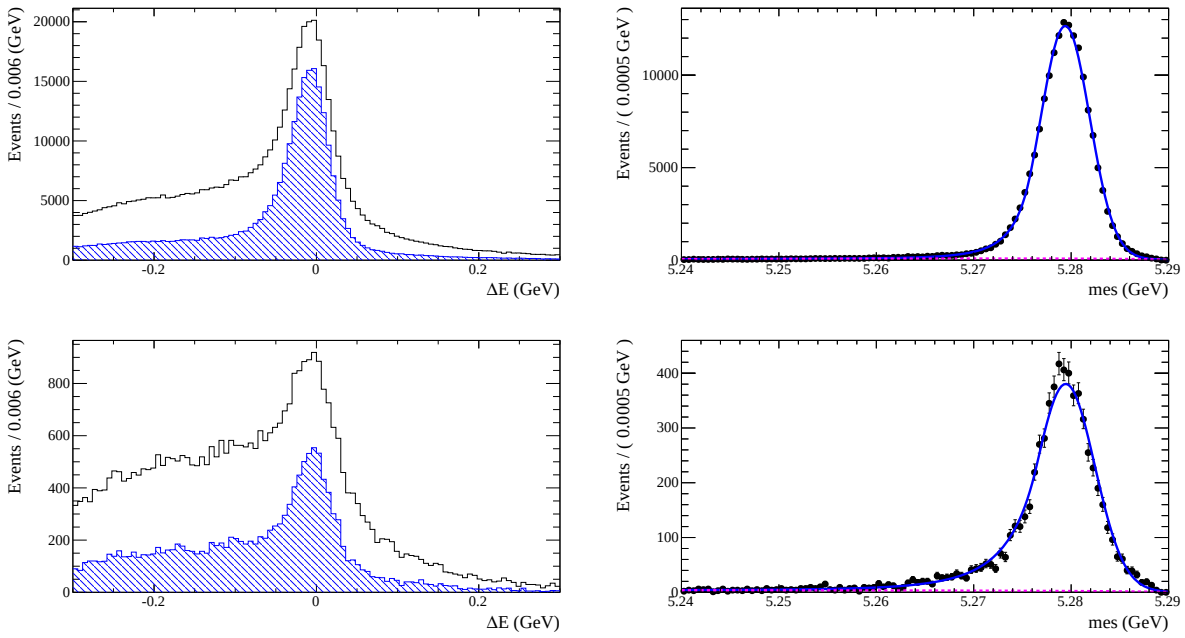

Figure 9.58: (left) ΔE and (right) $m_{\rm ES}$ distributions for the decay $B^- \to D^0\pi^-$ with $D^0 \to K^-\pi^+\pi^0$ reconstruction for (top) both γ's in barrel and forward endcap and (bottom) one γ in the backward EMC. The two histograms in each ΔE distribution are before and after a requirement on the D^0 mass.

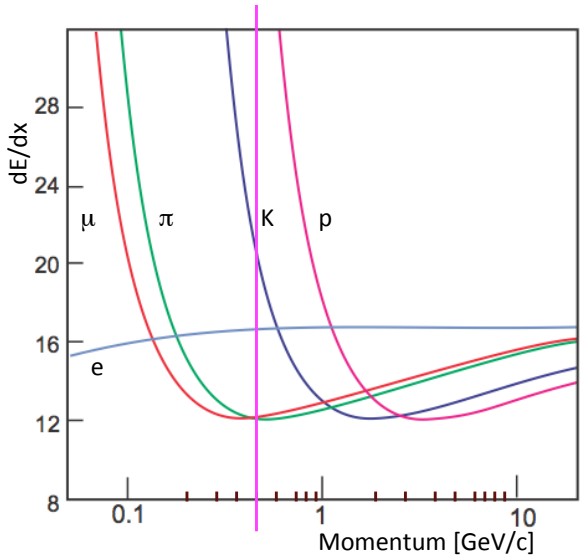

Figure 9.60: Calculated energy loss curves versus momentum for e, μ, π, K and p in one layer of the backward EMC.

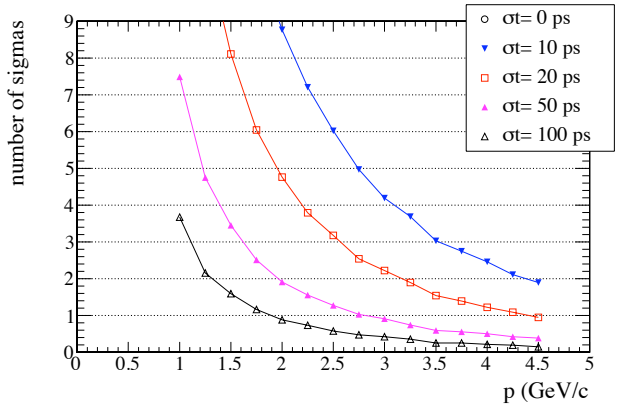

Figure 9.59: K/π separation versus measured momentum for different timing resolutions in the backward EMC. The finite separation for perfect timing is caused by uncertainties in the momentum measurement.

dition to timing, the ionization is measured in each layer. For MIP-like particles, the average energy loss per layer is $dE_{Pb} = 4.3$ MeV and $dE_{\text{scintillator}} = 0.6$ MeV. A 0.5 GeV/c π is at the ionization minimum, a 0.5 GeV/c K is below the minimum and a 0.5 GeV/c e is at the relativistic plateau. For MIP particles, the ionization loss in the 24 layers is $\Delta E = 117$ MeV. Since the energy loss below the minimum increases with decreasing momenta as $1/\beta^2$, dE/dx measurements in the endcap can be combined with the dE/dx information from the SVT and DCH. Figure 9.60 shows the ionization curves for e, μ, π, K and p as a function of momentum. A $> 3\sigma$ K/π separation is achievable for momenta up to $0.6 - 0.7$ GeV.

9.4.10 Discussion of task force conclusions

In the process of deciding how to proceed with the backward EMC, a task force was convened to evaluate its various benefits and impacts. A number of conclusions came out of this:

- The device adds to the physics program in important channels through the increased hermeticity.
- The design is technically plausible and cost-effective, however: operation of the readout in the radiation environment should be studied further; a prototype should be demonstrated in a beam test.
- The possibility of using the backward EMC for PID through time-of-flight is attractive and should be pursued with further R&D.
- The capability to install this device should be preserved, as opposed to, for example, extending the drift chamber.

9.5 Trigger

This is a reminder that we need a synopsis of the EMC trigger somewhere in the EMC chapter, although the detailed description will be in the ETD chapter. It is to be determined whether this should be in a separate section or merged with the three sub-calorimeter sections.

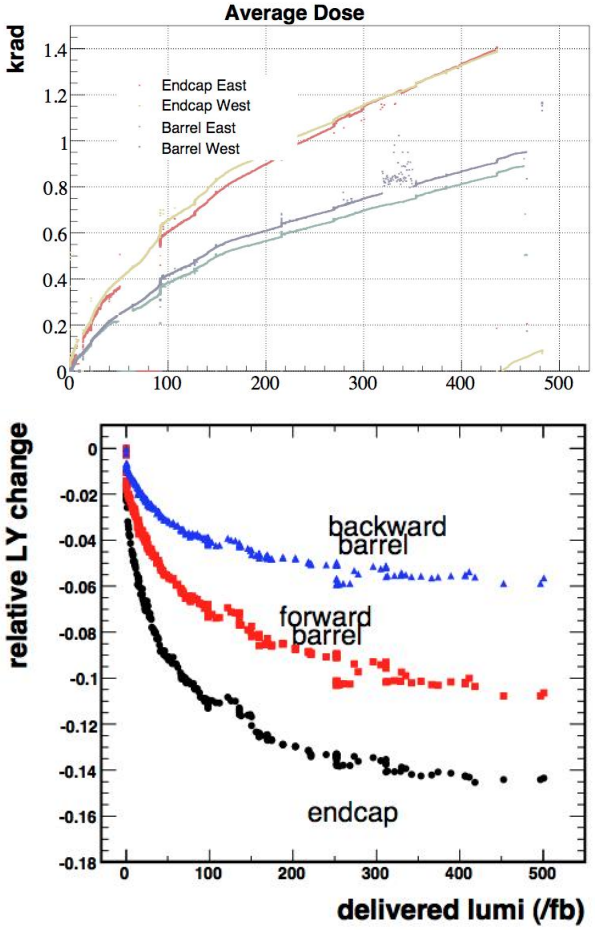

Figure 9.61: Left: Radiation dose as measured by RadFETs in the *BABAR* barrel and endcap. Right: Decrease in light output with radiation dose for the *BABAR* CsI(Tl) barrel and endcap.
These figures are placeholders; we need higher quality copies.

9.5.1 Calorimeter readout trigger

9.5.1.1 Normal mode

9.5.1.2 Calibration mode

9.5.2 Calorimeter trigger primitives

9.6 Detector protection

Personnel ES&H will be elsewhere.

9.6.1 Thermal shock

9.6.2 Mechanical shock, including earthquakes

9.6.3 Fluid spills

9.6.4 Electrical surges, outages

9.6.5 Radiation damage

Radiation exposure from Bhabha, Touschek and beam-gas scattering is monitored by a set of 56 realtime integrating dosimeters (Rad-FETs) placed in front of the barrel and 60 RadFETs in front of the endcap. The accumulated dose, measured by these RadFETs over the life of the *BABAR* detector, along with the observed loss in scintillation light output is shown in Figure[**?**], separately for the endcap, the forward, and the backward barrel of the calorimeter. The dose over the life of Super*B* is expected to be two orders of magnitude greater.

9.7 Cost & Schedule

This will appear elsewhere.

9.7.1 WBS structure

9.7.2 Gantt chart

9.7.3 Basis of estimates

9.7.4 Cost and schedule risks

Table 9.4: Photo Luminescence Weighted Quantum Efficiencies (%)

Photo Luminescence	LSO/LYSO	BGO	CsI(Tl)
Hamamatsu R1306 PMT	12.9±0.6	8.0±0.4	5.0±0.3
Hamamatsu R2059 PMT	13.6±0.7	8.0±0.4	5.0±0.3
Photonis XP2254b	7.2±0.4	4.7±0.2	3.5±0.2
Hamamatsu S2744 PD	59±4	75±4	80±4
Hamamatsu S8664 APD	75±4	82±4	84±4

Table 9.7: Comparison of crystal volume and calorimeter costs for several forward endcap configuration options.

Option	Number of new crystals	New crystal volume (cm^3)	Crystal cost/cm^3 (k$)	Crystal cost (M$)	Photo-detectors (M$)	Calibration system (M$)	Total structure (M$)	cost (M$)
LYSO full (baseline)	4500	402	25.00	10.04	0.57	-	2.27	12.88
LYSO old structure	3600	402	25.00	10.04	0.57	-	0.25	10.86
Hybrid								
3 CsI(Tl) + 6 LYSO	2160	245	25.00	6.19	0.49	-	0.25	6.93
4 CsI(Tl) + 5 LYSO	1760	198	25.00	4.95	0.40	-	0.25	5.60
5 CsI(Tl) + 4 LYSO	1360	154	25.00	3.84	0.31	-	0.25	4.40
Pure CsI	900	692	5.09	3.52	0.56	-	0.25	4.33
BGO	4500	392	9.00	3.53	0.57	1.2-3.0	2.27	7.57-9.37
$PbWO_4$	4500	306	5.00	1.53	0.57	1.2-3.0	2.27	5.57-7.37

Table 9.8: Properties of Hamamatsu MPPCs

MPPC type	# cells $1/\,\mathrm{mm}^2$	C [pF]	R_{cell} kΩ]	C_{cell} [fF]	$\tau = R_c \times C_c$ [ns]	$V_{\mathrm{break\ down}}$ [V] at T=23 C	V_{op} [V] at T=23 C	Gain [10^5]
15 μm	4489	30	1690	6.75	11.4	72.75	76.4	2.0
20 μm	2500	31	305	12.4	3.8	73.05	75	2.0
25 μm	1600	32	301	20	6.0	72.95	74.75	2.75
50 μm	400	36	141	90	12.7	69.6	70.75	7.5

Table 9.9: Relative gain in $S/\sqrt{S+B}$ by including the backward EMC in the event selection for $B \to K^{(*)}\nu\bar{\nu}$ and $B \to \tau\nu$ decay channels reconstructed in the recoil of B semileptonic and hadronic tags. The first uncertainty is statistical and the second is systematic.

channel	Semileptonic	Hadronic
$B \to \tau\nu$	$(6.1 \pm 0.1 - 0.7)\%$	$\simeq 3 - 5\%$
$B \to K^+\nu\bar{\nu}$	$(5.8 \pm 1.0 - 0.6)\%$	-
$B \to K_S\nu\bar{\nu}$	$(6.0 \pm 0.4 - 0.6)\%$	-
$B \to K^{*+}(K^+\pi^0)\nu\bar{\nu}$	$(7.0 \pm 0.2 - 0.7)\%$	$(5.9 \pm 2.5 - 0.5)\%$
$B \to K^{*+}(K_S\pi^+)\nu\bar{\nu}$		$(6.2 \pm 2.1 - 0.5)\%$
$B \to K^{*0}\nu\bar{\nu}$	$(9.1 \pm 0.4 - 0.7)\%$	$(7.3 \pm 1.8 - 0.5)\%$

Bibliography

[1] P. D. Strother, "Design and application of the reconstruction software for the BaBar calorimeter," SLAC-R-828.

[2] J. M. Bauer [BaBar EMC Group Collaboration], "The BaBar electromagnetic calorimeter: Status and performance improvements," IEEE Nucl. Sci. Symp. Conf. Rec. **2** (2006) 1038.

[3] R. Y. Zhu, Nucl. Instrum. Meth. A **413**, 297 (1998).

[4] C. Melcher and J. Schweitzer, "Cerium-doped lutetium oxyorthosilicate: a fast, efficient new scintillator," *IEEE Trans. Nucl. Sci.* **39** (1992) 502–505.

[5] D.W. Cooke, K.J. McClellan, B.L. Bennett, J.M. Roper, M.T. Whittaker and R.E. Muenchausen, "Crystal Growth and Optical Characterization of Cerium-doped $Lu_{1.8}Y_{0.2}SiO_5$," *J. Appl. Phys.* **88** (2000) 7360–7362, and T. Kimble, M Chou and B.H.T. Chai, "Scintillation Properties of LYSO Crystals," in *Proc. IEEE Nuclear Science Symposium Conference* (2002).

[6] R.H. Mao, L.Y. Zhang and R.-Y. Zhu, "Optical and Scintillation Properties of Inorganic Scintillators in High Energy Physics," *IEEE Trans. Nucl. Sci.* **NS-55** (2008) 2425–2431.

[7] W. Wisniewski, "Consideration for Calorimetry at a Super B Factory", in *Proceedings of Tenth International Conference on Calorimetry in Particle Physics*, Ed. R.-Y. Zhu, World Scientific (2002), and C. Cecchi. "A LYSO Calorimeter for a SuperB Factory ," in *Proceedings of Fourteenth International Conference on Calorimetry in Particle Physics*, Journal of Physics Series (2010).

[8] F. Happacher, "CCALT: Crystal Calorimeter at KLOE2," in *Proceedings of Fourteenth International Conference on Calorimetry in Particle Physics*, Journal of Physics Series (2010).

[9] The Mu2e Experiment, see http://mu2e.fnal.gov/.

[10] R.-Y. Zhu, Talk given at the CMS Forward Calorimetry Task Force Meeting at CERN, June 17, 2010. See http://indico.cern.ch/getFile.py/access?sessionId=0&re
materialId=0&confId=97272

[11] D.A. Ma and R.-Y. Zhu, "Light Attenuation Length of Barium Fluoride Crystals," *Nucl. Instr. and Meth.* **A333** 422-424 (1993).

[12] R.H. Mao, L.Y. Zhang and R.Y. Zhu., "Emission Spectra of LSO and LYSO crystals Excited by UV Light, X-ray and γ-ray," *IEEE Trans. Nucl. Sci.* **55** (2008) 1759–1766.

[13] Rihua Mao, Liyuan Zhang and Ren-yuan Zhu, "Quality of a 28 cm long LYSO Crystal and Progress on Optical and Scintillation Properties," Paper N38-2 in *2010 IEEE NUCLEAR SCIENCE SYMPOSIUM CONFERENCE RECORD.*

[14] J.M. Chen, L.Y. Zhang and R.-Y. Zhu, "Large Size LSO and LYSO Crystal Scintillators for Future High Energy Physics Experiments," *IEEE Trans. Nucl. Sci.* **NS-54** (2007) 718–724 and *Nucl. Instr. and Meth.* **A572** (2007) 218–224.

[15] J.M. Chen, L.Y. Zhang and R.-Y. Zhu, "Large Size LYSO Crystals for Future High Energy Physics Experiments," *IEEE Trans. Nucl. Sci.* **NS-52** (2005) 3133–3140.

[16] R.-Y. Zhu, Invited talk given at the Time Resolution Workshop at University of Chicago, April 28, 2011. See http://www.hep.caltech.edu/∼zhu/talks/ryz_110428_time_resolution.pdf

[17] S.E. Derenzo, M.J. Weber, W. W. Moses, and C. DuJardin, "Measurements of the Intrinsic Rise Times of Common Inorganic Scintillators," *IEEE Trans. Nucl. Sci.* **47** (2000) 860–864.

[18] T. Szczesniak, M. Moszynski, A. Synfeld-Kazuch, L. Swiderski, M.A.S. Koschan and C.L. Melcher, "Time resolution and decay time of LSO Crystals Co-Doped with Calcium," *IEEE Trans. Nucl. Sci.* **57** (2010) 1329–1334.

[19] Ren-yuan Zhu, "Radiation Damage in Scintillating Crystals," *Nucl. Instr. and Meth.* **A413** (1998) 297–311.

[20] *The CMS Electromagnetic Calorimeter Project*, CERN/LHCC 97-33 (1997).

[21] Rihua Mao, Liyuan Zhang and Ren-yuan Zhu, "Optimization of Light Response Uniformity for SuperB Tapered LYSO Crystals with APD Readout," Paper N29-6 in *2011 IEEE NUCLEAR SCIENCE SYMPOSIUM CONFERENCE RECORD*.

[22] J.M. Chen, R.H. Mao, L.Y. Zhang and R.Y. Zhu, "Gamma-ray induced radiation damage in large size LSO and LYSO crystal samples," *IEEE Trans. Nucl. Sci.,* **54** (2007) 1319–1326.

[23] Rihua Mao, Liyuan Zhang and Ren-yuan Zhu, "Gamma-ray induced radiation damage in PWO and LSO/LYSO crystals," *2009 IEEE NUCLEAR SCIENCE SYMPOSIUM CONFERENCE RECORD*, VOLS 1-5 (2009) 2045-2049.

[24] Rihua Mao, Liyuan Zhang and Ren-yuan Zhu, "Effects of neutron irradiations in various crystal samples of large size for future crystal calorimeter," *2009 IEEE NUCLEAR SCIENCE SYMPOSIUM CONFERENCE RECORD*, VOLS 1-5 (2009) 2041-2044.

[25] F. Nessi-Tedaldi, G. Dissertori, P. Lecomte, D. Luckey and F. Pauss, "Studies of Cerium Fluoride, LYSO and Lead Tungstate Crystals Exposed to High Hadron Fluences," Paper N32-3, 2009 IEEE NSS Conference.

[26] R. Faccini, C. Gargiulo, F. Pellegrino, V. Pettinacci, A. Zullo, "EMC Forward Mechanical Design ", SuperB Technical Note, SB-DET-2012-006

[27] V. Bocci *et al.*, "Dependence of the energy resolution of a scintillating crystal on the readout integration time," arXiv:1207.4902 [physics.ins-det]. Accepted by JINST.

[28] B. Adeva *et al.* [L3 Collaboration], "The Construction of the L3 Experiment," Nucl. Instrum. Meth. A **289**, 35 (1990).

[29] S. K. Sahu *et al.* [Belle Collaboration], "Radiation hardness of undoped BGO crystals," Nucl. Instrum. Meth. A **388**, 144 (1997).

[30] J. Chen, R. Mao, L. Zhang and Y. Ren-Zhu, "Large size LSO and LYSO crystals for future high energy physics experiments," IEEE Trans. Nucl. Sci. **54**, 718 (2007).

[31] B. Aubert *et al.* (*BABAR* Collaboration), *The BABAR Detector*, Nucl. Instrum. Methods Phys. Res., Sect. A **479**, 1 (2002) [arXiv:hep-ex/0105044].

[32] C. Adloff *et al.* [CALICE collaboration] "Construction and Commissioning of the CALICE Analog Hadron Calorimeter Prototype," JINST 5:P05004 (2010).

[33] W. -S. Hou, "Enhanced charged Higgs boson effects in $B^- \to \tau\bar{\nu}$, μ *barν* and $b \to \tau\bar{\nu} + X$," Phys. Rev. D **48** (1993) 2342-2344.

[34] W. Altmannshofer, A. J. Buras, D. M. Straub, M. Wick, "New strategies for New Physics search in $B \to K^* \nu\overline{\nu}$, $B \to K \nu\overline{\nu}$ and $B \to X_s \nu\overline{\nu}$ decays," JHEP **0904**, 022 (2009).

[35] T. Barakat, "The "$B \to K^* \nu\bar{\nu}$ rare decay in the two-Higgs doublet model", J.Phys.G G24, 1903 (1998).

[36] B. Aubert *et al.* [BABAR Collaboration], "Search for $B \to K^* \nu\bar{\nu}$," Phys.Rev. D78, 072007 (2008).

[37] P. del Amo Sanchez *et al.* [BABAR Collaboration], "Search for the Rare Decay $B \to K \nu\bar{\nu}$," Phys. Rev. D **82**, 112002 (2010).

[38] V. Andreev *et al.*, "A high granularity scintillator hadronic-calorimeter with SiPM readout for a linear collider detector", Nucl.Instrum.Meth. A540, 368 (2005); T. Takeshita, "Development of MPPC", Pramana 69, 1079 (2007).

[39] M. Bouchel *et al.*, "SPIROC (SiPM Integrated Read-Out Chip): Dedicated very front-end electronics for an ILC prototype hadronic calorimeter with SiPM read-out", JINST 6, C01098 (2011).

[40] H. Ono *et al.*, "Beam test results of a high-granularity tile/fiber electromagnetic calorimeter", Nucl.Instrum.Meth. A600, 398-407 (2009).

[41] R. Faccini, "Results from silicon photomultiplier neutron irradiation test", proceedings of 11th ICATPP Conference on Astroparticle, Particle, Space Physics, Detectors and Medical Physics Applications, Villa Olmo, Como, Italy, 2009.

10 Instrumented Flux Return

10.1 Physics Requirements and Performance Goals

Calabrese, Lesiak, Cibinetto (3, 4 pages)

The principal task of the Instrumental Flux Return (IFR) detector is the detection of muons and neutral hadrons. These goals are realized in in the large iron structure, needed as the magnet return yoke.

Muons are considered as important messengers of New Physics (NP) in the processes like $b \to s\mu^+\mu^-$, $\tau \to \mu\gamma$, $\tau^+ \to \mu^+\mu^-\mu^+$, $\tau \to \mu X$, $X = \rho, \eta^{(\prime)}, f_0 ...$, $B_s \to \mu^+\mu^-$, $D^0 \to \mu^+\mu^-$, to name but a few [**?**], [**?**]. Moreover, their detection is crucial in a substantial part of studies related to the determination of sides and angles of the unitarity triangle which are based on semileptonic decays of B mesons. Also, in these decays, the sign of the lepton charge determines the flavour of the parent heavy meson, thus providing one of the tags for the CP-asymmetry measurements.

The IFR will also act as hadronic calorimeter, thus providing the detection of neutral hadrons. Among the latter, special attention is paid to the K_L^0 mesons reconstruction, which is realized in conjunction with the information provided by the electromagnetic calorimeter. The ability to reconstruct the K_L^0s allows, in particular, to compare CP-violation effects in the decay channel $B \to J/\psi K_L^0$ with those in $B \to J/\psi K_S^0$.

10.2 Detector Overview

10.2.1 The Absorber Structure

Posocco, Benettoni (2 pages)

The SuperB Flux Return structure, used as absorber material to identify muons, will be composed by an hexagonal iron yoke constituted by a barrel and two endcaps (see fig. 10.1). Each of the two endcaps is, in turn, composed by two doors, while the barrel is composed by six sectors called sextants. All the main parts are made of welded steel plates, with a thickness in the range from 20 to 100mm. The geometry will be almost identical to the Babar IFR. The main difference will be given by the overall thickness of steel of SuperB w.r.t. Babar.
The Babar barrel counted on an overall thickness of 650 mm for the barrel and of 600mm for the endcaps, while the overall thickness of the steel in SuperB should be upgraded to a design value of 920mm, to increase the particle identification capability of the flux return.
Inside proper slots of the flux return will be lodged from 8 to 9 layers of scintillator, w.r.t. the 17 layers of detectors present in Babar. The first layer of detectors is at inner radius w.r.t. to the first steel plate and the last layer will be at outer radius, thus inside the steel only 6 or 7 slots will be needed to lodge the detector planes (see fig. 10.2).
In order to minimize the cost, the baseline design foresees the reuse of all the Babar structure, which has got 17 slots for detectors, and increase the steel thickness inserting metal plates in those of the 17 slots that are left empty. The nominal thickness of each detector plane, composed by two perpendicular layers of scintillators and a box containing them, is of the order of 25 mm, while the gap width of the Babar wedges and doors have nominal dimension between 30 and 35 mm.

The 10 or 11 gaps not used by scintillators will be filled with metal plates. To reach the 920 mm of design value there are 270 mm missing from the Babar parts in the barrel, thus the gaps should be filled with plates of 25 mm in

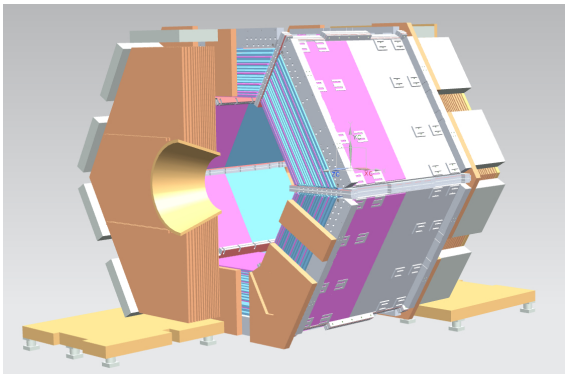

Figure 10.1: The IFR flux return structure.

the more comfortable case and 27 mm in the worst case. According to preliminary measurements, performed in the barrel gaps of Babar, 25 mm plates should fit in all the barrel, apart maybe one or two gaps of the lower sextant, where plates of 25 mm could require forced insertion. The insertion of plates of 27 mm is probably not feasible or could imply a difficult insertion of large part of the plates, with negative impact on the cost and timing of the operation. The baseline idea for the barrel foresees then the use of 25 mm thick metal plates that allow to reach 925 or 900 mm of overall metal thickness, depending on the number of detectors layer that will be defined, 8 or 9.

Figure 10.2: Front view of a sextant of the barrel.

For the doors the amount of steel can reach, by fitting the unused gaps, a thickness 50 mm smaller than the barrel, thus 850 or 875 mm of overall metal thickness. The doors geometry allows to increase their overall thickness by adding metal plates on the outer face, as it was done in the forward doors of Babar, where a plate of 100mm (4 inches) was added, on the outer face, to increase the shielding w.r.t background. This additional plate can also be reused in the SuperB, reducing the need of insertion of plates in the forward doors to 7 gaps, thus 175 mm of overall thickness of plates to be inserted in order to reach the nominal thickness of 920 mm.
In the backward door the addition of an external plate 100 mm thick is not compatible with the presence of the horsecollar as it limits the movements needed for the opening and closing of the doors, then the thickness that can be added on the outer side of the backward door must be minimized. In this case the filling of unused gaps allows to reach an overall thickness of 850 or 875mm, thus 45 or 70 mm steel plates will be added on the outer face.
In order to define the maximum thickness that can be added on the outer face of the backward door, the opening movements of the doors must be detailed and actual dimensions of the horsecollar must be measured.

The metal composing the plates to be inserted in the unused gaps should match the following criteria:

- Non magnetic material in order to avoid increasing of magnetic forces on the coil
- small interaction length
- acceptable flatness
- convenient cost

In Babar a few layers where filled with brass plates, but nowadays this choice would be very expensive due to cost of copper, strongly increasead in the last years. The choice might then be stainless steel 304L with certified low magnetic permeability. A reasonable value of permeability, low enough to avoid affecting magnetic field and increasing cost only for a few percent, is a relative magnetic permeability < 0.02. Further simulations of the IFR will be performed to determine if all plates need to

be stainless steel or the outer layers (far from the interaction region) could be magnetic, with acceptable effect on magnetic forces. The use, even partial, of standard magnetic steel (similar to the steel used for the present IFR) would reduce strongly the cost of the upgrade.
Another difference of the SuperB IFR w.r.t BaBar, will be in the connection between the barrel wedges and the outer frame (cradle and arches). As in SuperB the willing is to realize the last detector layer outside the wedges, a useful gap for detectors will be realized in between the structure and the wedges, reducing as much as possible the need of connection between the two parts. The connections will be made only at the corners of the wedges leaving available most part of outer wedges top surface to lay down scintillators. This will imply that all the involved parts (cradle, arches, outer wedges) will be modified in a workshop in order to modify the relative coupling.
The increasing of thickness also imply an increased weight of the overall structure, and on top of that, the reduction of connections between outer structure and wedges reduces the strength and stiffness of the overall steel body. Thus the overall deformation of the structure will be verified in detail to crosscheck that stresses are not critical and deformations are compatible with the overall precision needed for such experiment.
Preliminary offers for fitting the gaps of Babar with stainless steel plates 25 mm thick are around 1MEuro. The cost of shipping from US to Italy shall be added, about 0.5 MEuro, while import taxes and duty are assumed to be negligible. Modifications to cradle, arches and outer wedges are required in order to allow the outer layer of detectors, thus the overall cost of the Flux Return in case of reuse of Babar IFR should reach the order of 1.5 - 2 MEuro.

10.2.2 The Active Detector Choice

Calabrese (1 page)

The active detector choice

General layout

10.3 Backgrounds

10.3.1 Main background sources

Machine related background is one of the challenges for the Super$B$ detector and the background considerations influence several aspects of its design. The IFR detector has been simulated using Super$B$ FullSim based on GEANT4 and Bruno see Sec.[]. The results of these simulations show that the primary source of background are: radiative BhaBha events, Touschek scattering, pair production, beam-gas scattering and photons from synchroton radiation for a detailed description of the background sources see Sec.[].
Among of these background sources for the IFR detector the dominant one is due to the radiative BhaBha events as will be explained later.
All these background sources produce a high-energy primary $e^{\pm}$ or γ that strikes a beam line element within a few meters of the IP and shower secondaries that can be charged or neutral particles with energies ranging from sub-MeV to several tens of MeV. These particle hit the IFR and may affect the detector performances and speed up the photodetectors aging.

10.3.1.1 Neutron Background

In this context there is a not negligible production of neutrons via giant resonances formation [46]. The neutrons produced with this mechanism have energy of some MeV and they are moderated by the interaction with the detector material, they scatter back and forth on the nuclei both elastically and inelastically losing energy until they come into thermal equilibrium with the surrounding atoms. At this point they will diffuse through matter until they are finally captured by a nucleus. For this reason the neutron energy spectrum in the Super$B$ environment has a very wide range as shown in Fig. 10.3 where the neutrons are classified according to their kinetic energy.

Since the neutron spectrum has so different range, and the interaction with the matter

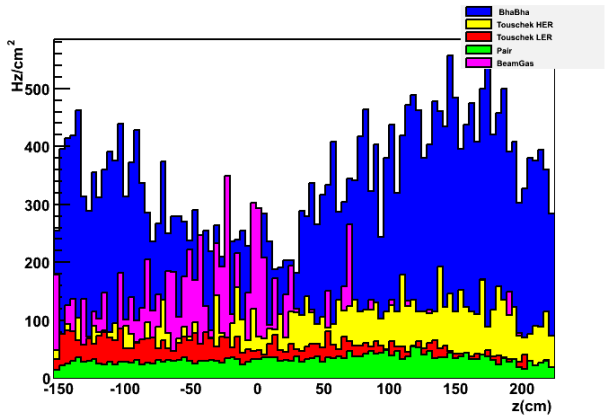

Figure 10.4: Neutron rate on IFR Barrel Layer 0 due to different background sources, the rates are normalized to 1MeV equivalent [47] .

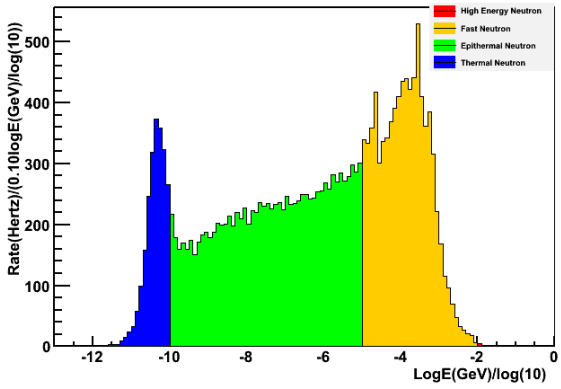

Figure 10.3: Neutron energy spectrum on IFR barrel, the neutron are classified according to their kinetic energy range as high energy neutron, fast, epithermal or thermal.

strongly depends on it, it is standard to characterize the neutron fluence from a source in terms of an equivalent mono energetic neutron fluence because the way as neutron interact has a strong dependency on its energy for additional details see. [47], [48], [49]. For this reason all the neutron rates in this section are normalized to the equivalent of a 1 MeV neutron .
The neutron background not only contribute to the radiation dose of the IFR detector but it is particularly dangerous for the SiPM, the devices used for the detector readout, since they are quite sensitive to radiation, infact if they are exposed to an integrated fluence as high as $10^{11} n_{eq}/cm^2$(n_{eq} is the equivalent number of 1 MeV neutrons on silicon) they can be severely damaged (i.e. loss of efficiency, increasing of dark current and rate [50]). In Fig. 10.4 is shown the neutron nate on the layer 0 of the Barrel due to the different background sources, the rates are normalized to 1 MeV equivalent as explained above, and they include a *safety factor* that takes into account the fact that the simulation may not reproduce perfectly the reality.

As seen in Fig. 10.4 the main background source is due to the Radiative BhaBha as discussed previously. The rate on Barrel layer 0 corresponds to a *** $neutrons/cm^2$ for a year, these rates are acceptable for a 10 year Super$B$-run and they are the results of a complex shielding system described on Section 10.3.2.

10.3.1.2 Charged Particles

The background due to charged particles is particularly interesting since it can affect directly the detector performances, since it can give fake signal in the detector and affect the track reconstruction and consequently the muon ID. In Fig. 10.5 is shown the rate for electrons and positrons coming from different background sources, as for the neutron the dominant source of the background are radiative BhaBha events. The rate shown in Fig.10.5 are for a electron energy deposited ***¿ MeV that is the nominal threshold we have chosen for the detector.

A high proton rate is observed in the IFR, these protons are produced inside the scintillator in the reaction (n,p) in which the neutron is captured by the scintillator material and a proton is emitted. The cross section for this process falls as 1/v so it is more likely to happen when the neutron has low energy, the resulting proton has a very low energy and for this reason the corresponding deposited energy is low and does not produce signal in the detector for this reason this rate can be neglected.

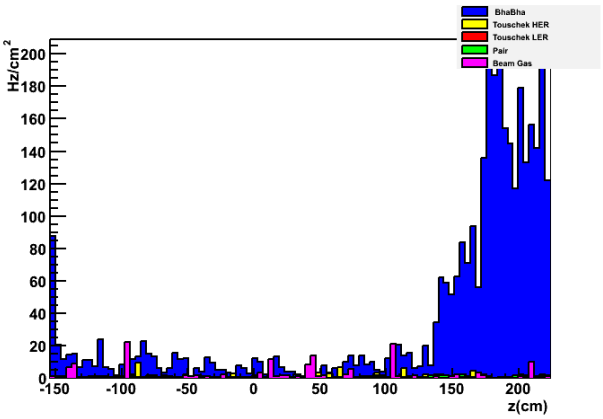

Figure 10.5: Electron rate for the IFR Barrel layer 0 due to different background sources the threshold for the deposited energy is *** MeV .

10.3.1.3 Photon background

All the background sources come from QED events for this reason we studied also the background contribution coming from the photons. The photon energy spectrum has a very broad energy range as shown in the plot of Fig. 10.6 the lines due to neutron capture on Hydrogen (2.223 MeV), due to annihilation radiation (0.512 MeV) and to the neutron capture on B^{10} (0.48 MeV) (the B^{10} is used for radiation shielding see 10.3.2) are clearly visible.

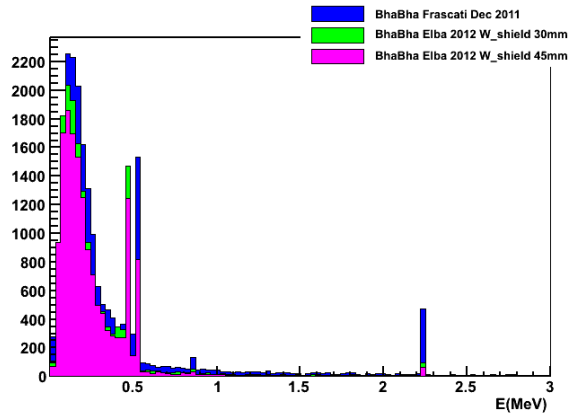

Figure 10.6: Photon energy spectrum for IFR Barrel Layer 0 .

Concerning the IFR the photon rate contribute only to the radiation dose on the scintillator and the contribution given by the high energy photons that convert is already taken into account in the rate of charged particles. The rate for photons on layer 0 of the barrel is shown in Fig. 10.7 and even if it is high it is not expect to affect the detector performance.

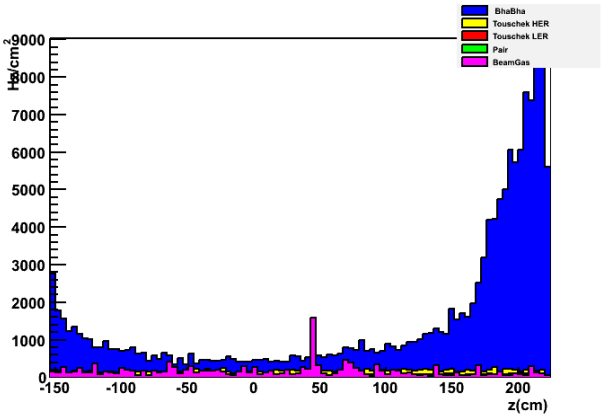

Figure 10.7: Photons Rate on IFR Barrel Layer 0 due to different background sources.

10.3.2 Background remediation

All the rates shown on the previous section are the result of a complex shielding system mainly implemented to reduce significantly the number of neutrons crossing the IFR, adding shielding material has also the effect to reduced the electron and photon rate. We implemented a shielding system to the external structure of the IFR and a inner shield to protect the IFR layer 0. The shields are made of Polyethylene ($(C_2H_4)_nH_2$), Boron Loaded (5%) since the polyethylene has a high hydrogen density which slows neutron particles down so they can be absorbed by the Boron since one of the isotope, that compose the natural Boron, the B^{10} has a very high cross section for neutron capture. This shielding design implemented in the Super$B$ Full Sim worked very well since it has reduced the neutron rate of one order of magnitude.

10.3.3 Radiation doses on the IFR detector

10.4 Identification Performances

10.4.1 Muon Detection

Muons are identified by their penetration range in the iron. Above 1.2-1.5 GeV, depending on the incident angle, muons penetrate all layers. Non penetrating muons can be identified from the measured range. More generally, pions separation is reached through a combination of range and hit pattern designed to identify the pion hadronic interaction.

In the SuperB baseline design the iron from BABAR will be reused, so many design parameters are fixed. The main important question the simulation should answer are already outlined in the *CDR*:

- total amount of iron;
- number of active layers;
- size of the scintillation bars;

The SuperB full simulation **??** based on GEANT4 is used to properly simulate the detector geometry and the interaction of the particles with the elements of the detector geometry.

The data taken using the IFR prototype have been used to validate the simulation, in particular the algorithm of digitization needed to generate actuall hits from the hits generated from GEANT4 (gHits). Look at the prototype data analysis section **??**.

In the following, the studies of the detector performances, will be based on the simulation with the prototype geometry, not of the actul detector. In the final version, all the plots and numbers, will be obtained using the SuperB full geometry.

As already outlined before, the criteria for distinguish muons from hadrons is based on the different interaction with the matter: muon track typically release just one hit in each layer, while hadrons can interact strongly in the iron, generating a hadron shower with several lower momantum particles, producing multiple hits per layer. It is also possibile that few neutrals (neutrons) are produced in the hadronic interaction, thatcan travel long distance before release an hit. In general for pion tracks the number of consecutive active layers is smaller than the muon tracks, on the same time, the average number of hits per each hitted layer is higher than the muons. The hits positions associated with a track are fitted with a second order polynomila function $y = Y(z)$ and $x = X(z)$, where z is the lingitudinal coordinate (layer position) and x and y are the two transverse coordinates given by the hitted scintillator bar. The hit residuals, summed in a $\chi^2 = \sum_{i=0}^{N_{hits}} (Hit(y_i, z_{layer}) - Hit(y_{fit}(z_{layer}), z_{layer}))^2$, are useful to identify the muons as well as the fitted parameters itself. The latter can be compared with the expected direction that comes from the inner detectors to help to suppress part of the contamination from the pion and kaon decays in fly before the first layer of the IFR.

To summarize, we used a consistent set of 10 variables related to:

1. number of hits in the x- and y-view;
2. number of active layers for the x- and y-view;
3. last layer touched, which is transalted in number of interaction length, λ_{int};
4. track continuity;
5. χ^2 of the hits to the tracks for the x- and y-view;
6. parameters of the fitted track.

Distribution of some of the useful variables, as a function of the track momentum, are reported in Fig.10.8. Simple cuts these variables, gives good pion rejection. But the experience from BaBar experiment shows that a multivariate approach gives the best performances on the muon identification even at lower energy when the

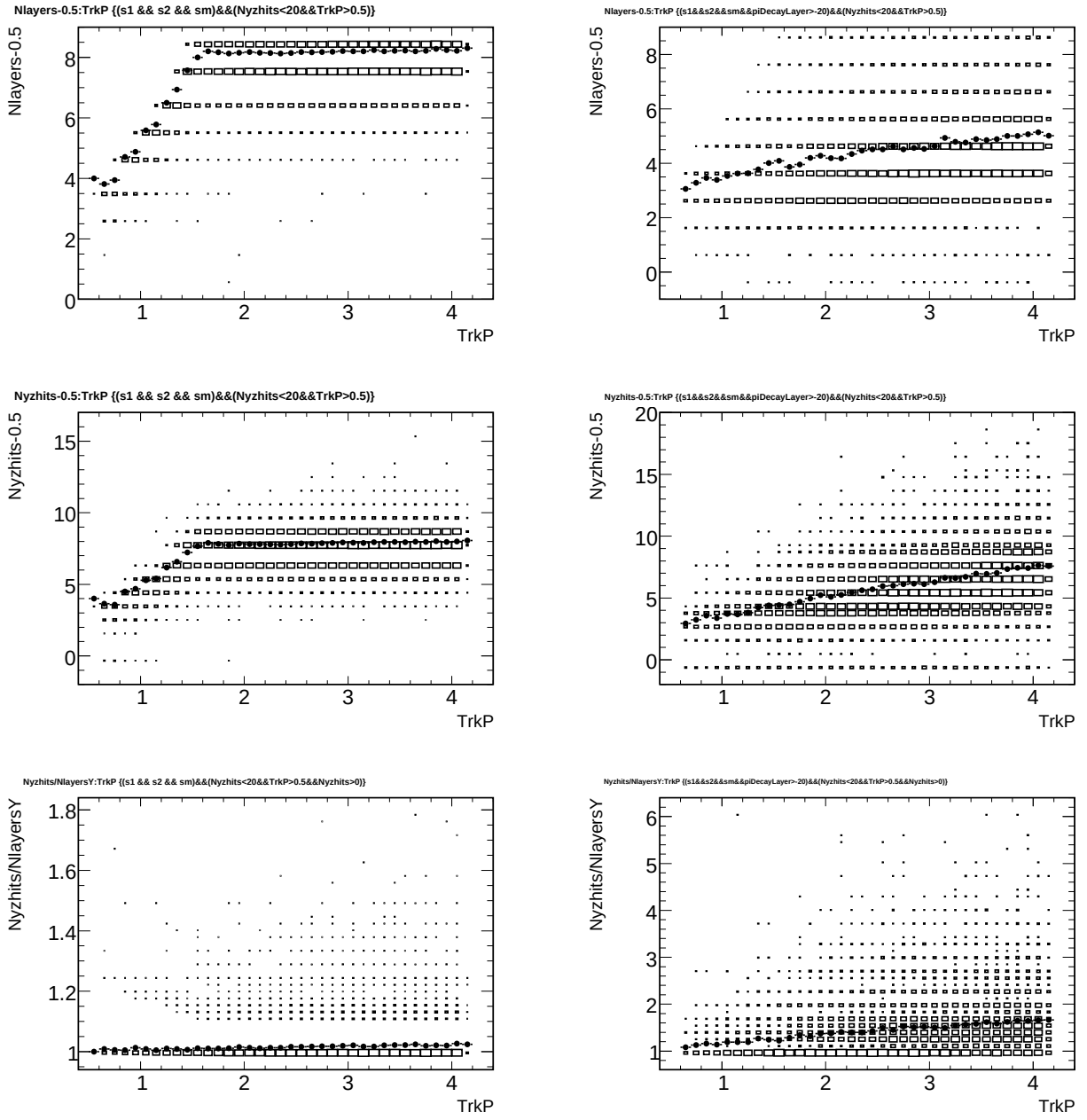

Figure 10.8: Distribution of the number of active layers, total number of hits and average number of hits per active layer, as a function of the particle momentum for μ (left) and π(right). The dots represent the profile of the distribution.

muons stop inside the IFR volume. In particular, because of the correlations between the reconstructed quantity, we used a non-linear multivariate approach like the BDT, which turned out to be very powerful and robust toward sligth changes in the inputs paramaters.

In these studies we did not use some informations that will be available with the full detector. In particular the amount of energy losses in the calorimeter which have slightly different distributions for muons and pions at low energy, can be used to reduce the pion contamination

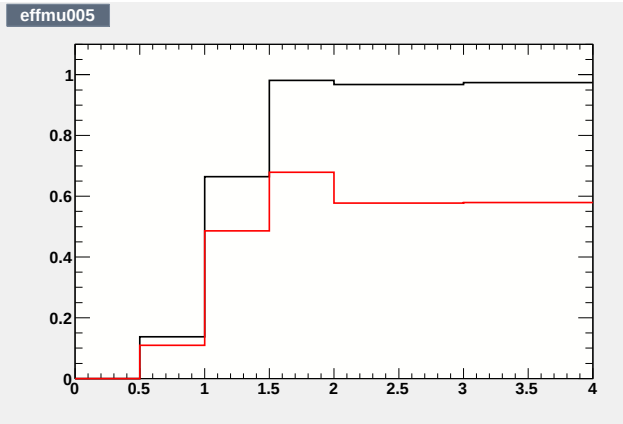

Figure 10.10: Muon efficiency as a function of the momentum, with π mis-id rate fixed in each momentum bin to be 2% (red) and 5% (black).

Table 10.1: Muon efficiency in 5 different bin of momentum between 0.5 and 4 GeV. The muon efficiency are reported with two different requirements on the pion efficiency rate.

P (GeV)	ϵ_μ, $\epsilon_\pi = 2\%$	ϵ_μ,$\epsilon_\pi = 5\%$
0.5-1.0	?	
1.0-1.5	?	
1.5-2.0	?	
2.0-3.0	?	
3.0-4.0	?	

at low momenta. An the DIRC response that also could help to give informations at lower energy. The signal efficiency - backgroun rejection curves (ROC) are reported in Fig.10.9 just as an examples, in the 1.0-1.5 GeV and 2.0-3.0 GeV range.

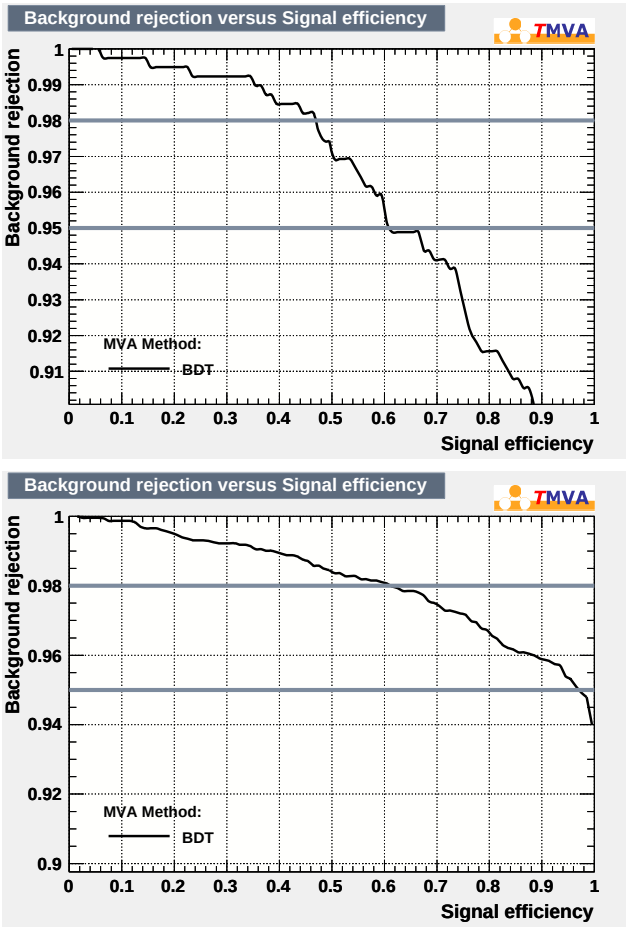

Figure 10.9: ROC curve after the BDT training for muons in the 1.0-1.5 GeV range (left) and 2.0-3.0 GeV range (right). The horizontal line at π rejection efficiency of 95% and 98% are also reported to gide the eyes.

The BDT are trained in different bins of momentum, from 0.5 to 4 GeV. The plot of the muon efficiency as a function of the momentum, with the pi-mis rate fixed at 2% and 5%, are reported in Fig.**??**.

The performances are good and as expected there is a drop in the signal efficiency below 1.5 GeV. The efficiency are reported in Tab.10.1. With the segmentation and granularity studied so far, about half of the pion contamination is due to irreducible background from the π decay in fly.

Rotondo (4 pages)

10.4.2 K_L Detection

Rotondo (3 pages)

10.5 Detector R&D

10.5.1 Module Tests and Results

Baldini, Cibinetto, Montanari (4 pages)

The Active detector technology, described in [?], is the result of an extensive R&D program, carried out in the last years and devoted to the choice of the most effective component for each detector part. In more details, the first studies were mainly dedicated to:

- Scintillators
- Fibers
- Photodetectors

10.5.1.1 Scintillators

Given the large amount of scintillator needed ($\simeq$ 20 tons), our attention was attracted since the beginning by the rather unexpensive scintillator produced at the FNAL-NICADD facility at Fermilab (**??**), where the scintillator is produced in large quantities by extrusion and a thin layer of TiO_2 is co-extruded around the active core. This production method suits particularly well our needs to produce long and thin scintillator strips with the desired shape.
We tested a few sample of scintillator strips of external dimensions: $1.0 \times 4.5 cm^2$ (already available at the FNAL -NICADD facility) and $2.0 \times 4.0 cm^2$, considering two options on the positioning of the fibers : fibers placed in an embedded hole or in surface grooves. The difference in light yield has been measured to be a$\simeq$ 10% higher for the embedded hole option. Since for long bars is very difficult to fill them with the optical glue and given the small difference in light collection, we have chosen the surface grooves as baseline option.

10.5.1.2 Fibers

Since the attenuation length of the scintillator is rather short ($\simeq$ 35cm), the light produced by the particle interaction has to be collected using Wave Length Shifting fibers, which brings it more efficiently to the photodetectors. For our application the fibers should have a good light yield to ensure a high detection efficiency for fiber lengths in the range: $\simeq 0.6 - 3\,m$. The time response was studied as well, since in the first fase of the R& D program also the Time readout option was considered.
We tested WLS fibers from Saint-Gobain (BCF92) [?] and from Kuraray (Y11-300) [?]. Both companies produce multiclad fibers with a good attenuation length ($\lambda \simeq 3.5\,m$) and trapping efficiency ($\varepsilon \simeq 5\%$) but Kuraray have a higher light yield (see fig. 10.11), while Saint-Gobain fibers have a faster response ($\simeq$ $2.7ns$ vs $\simeq$ $9ns$ for the Kuraray), which ensure a better time resolution.

——————— *to be discussed*

The most effective number of fibers was studied by measuring the light collected with cosmics through 1,2,3 fibers placed on a scintillator bar . As It can be seen on the right plot of fig. 10.11, going from 1 to 2 fibers the gain in light yield is $\simeq$ 46%*; going from 2 to 3 fibers the light yield increases by* $\simeq$ 13% *with a total gain of* $\simeq$ 65% *w.r.t. 1 fiber. So it's not worth to put more that 3 fibers in the scintillator bars. The study is still in progress, to better understand the above behaviour.*

———————————

Also the possibility of using clear fibers to bring the light signal out of the detector has been studied. As results, we have seen that $10m$ of clear fiber (Kuraray type clear-ps, $\phi = 1.5mm$) reduces, as expected from an attenuation length of $\simeq 10m$, the amount of light by a factor $\simeq$3 (fig. 10.12). This possibility is desirable since it would allow us to place the SiPMs in a region of the detector where the background radiation flux is lower. It has though many disadvantages: first, in order to have an acceptable amount of light we should use more fibers, and that would increase sensibly the costs; second, the routing of the fibers out of the detector would be very difficult, considering also that the minimum bending radius would be $\simeq 15cm$ for $1.5\,mm$ fibers; third, this solution would require a larger area SiPMs which, in turn, means higher dark noise and faster damage with radiation. Given all these considerations we decided, as baseline choice, to couple the SiPMs directly to the WLS fibres.

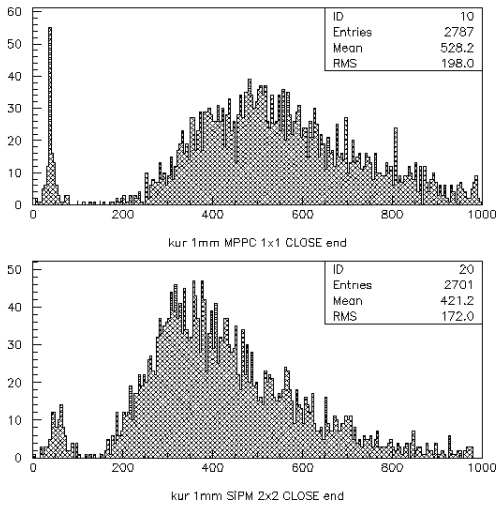

Figure 10.12: Left plot: comparison of the collected charge with cosmics from a MPPC (top) and a SiPM(bottom) in the same conditions. Right: charge collected before and after 10m of a $\phi = 1.5mm$ clear fiber.

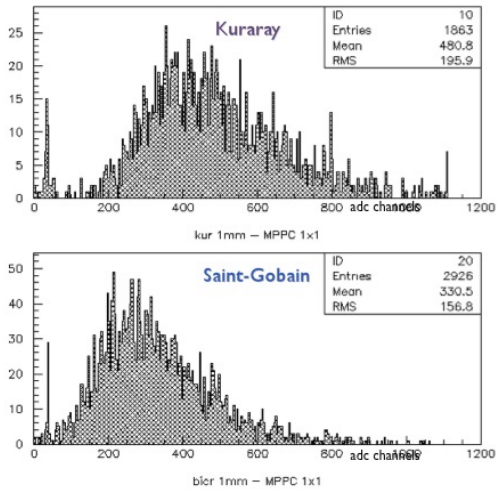

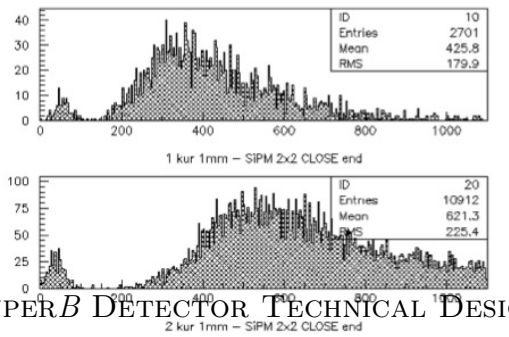

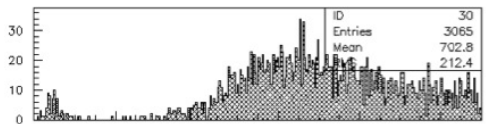

10.5.1.3 Photodetectors

Recently developed devices, called Geiger Mode APDs, suit rather well our needs to convert the light signal from WLS fibers in tight spaces and high magnetic field environment. These devices have high gain ($\simeq 10^5$), low bias voltage ($< 100V$), good Detection Efficiency ($\simeq 30\%$), fast response (risetime$< 1\,ns$), and are very small (few mm^2) and insensitive to magnetic field. They also have a few drawbacks though, like the rather high dark count rate ($few\,100\,kHz/mm^2$ at 1.5 p.e.) and rather sensitive to radiation. At present several companies produce GMAPDs. We concentrated our efforts on the devices produced by by IRST-FBK [**?**], and MPPCs from Hamamatsu [**?**].

Our first studies began with $1 \times 1mm^2$ SiPM and MPPCs but, given the low amount of light extracted out of the scintillator, with just one fiber, we soon realized that we would have needed larger devices to couple them with more fibers, while keeping the active surface (and so the noise) as low as possible. Most of our studies were then performed with ($2 \times 2\,mm^2$) FBK devices, since only $1 \times 1\,mm^2$ and $3 \times 3\,mm^2$ MPPCs (too noisy) were available at that time. The comparison between SiPMs and MPPCs showed a lower detection efficiency of the former (see fig. 10.12) but also a less critical depen-

dence, from temperature and bias voltage fluctuations, of the main parameters like gain and dark count rate. Custom devices from FBK, with a rectangular active area optimized for our needs ($1.2 \times 3.2\,mm^2$, and $1.4 \times 3.8\,mm^2$) were produced and tested for the IFR prototype.

10.5.1.4 Other related studies

Several other studies were performed related to the otimization of the detector performances. The two most relevant are the fiber surface polishing method and the aluminization of the not read-out end of the fiber.
The polishing of the fiber surface was investigated to understand which material and type of blade was optimal to obtain the best quality of the surface (and so the optimal light transmission). We compared the fiber polishing quality for natural and synthetic diamond blades, the tests showed a 10% higher light transmission for the natural diamond option.
Studies have also been performed to cover the free end of the fiber with aluminum (through a sputtering process) in order to reflect back the light, otherwise lost. The result was that the reflection coefficient, with the above technique, is of the order of 50%. We are then considering the possibility to aluminize the free end of the fibers to recover part of the light and to reduce the light yield reduction as a function of the length.

10.5.1.5 New R&D studies...

10.5.1.6 Radiation Damage Studies

SiPMs, as most of the solid state devices, are rather sensitive to radiation. In the superB environment we expect neutrons to be the main source of background, at least at the IFR level. An extensive program, started in 2009 with a first test at the ENEA- FNG (Frascati Neutron Generator) is currently ongoing to understand the effects of intense neutrons fluxes on SiPMs. Following this program, a test on low energy neutrons ($\leq \simeq keV$) has just been carried out at the GELINA (GEel LINear Accelerator) facility in Belgium, and a test with higher energies neutrons is foreseen in the next months.
The first irradiation test was carried out at the Frascati Neutron Generator facility with neutrons of 2.5 MeV [**?**]. As a result, after a dose (1MeV equivalent) of $7.3 \times 10^{10} n/cm^2$, we observed an increase in the drawn current of about a factor 30, of the dark count rate of about a factor 10 higher and a reduction of the average output signal (charge) of approximately a factor 3. While the increase in the dark current is not a major issue by itself, the increase in dark count and the reduction of the output signal might causes a significant reduction of the detection efficiency. This reduction was studied by comparing the SiPM signal from cosmics before and after the irradiation and was estimated to be, in the worst case, of the order of 15%. The

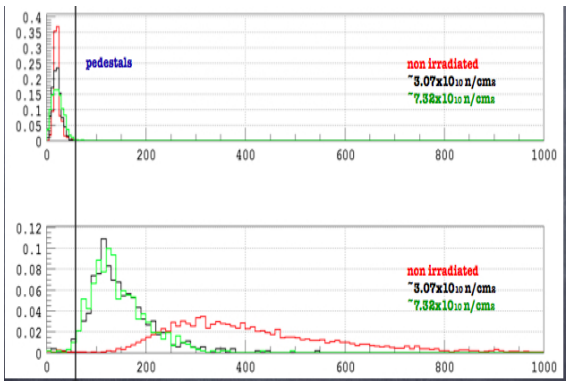

Figure 10.13: Comparison of the cosmic signal distribution before and after the irradiation, for a FBK $1mm^2$ device.

above results are anyway not conclusive. The quality of the SiPMs is fact rapidly improving with time and new tests on recently produced devices (e.g. with an initial dark count rate $\simeq$ factor 10 lower) are needed.

10.5.1.7 New Radiation Damage Studies

this might be included in the prvious paragraph.....
Since an important fraction of neutrons expected at SuperB are in the thermal energies region, a test at the GELINA facility (Geel, BE), where a neutron beam of energy up to a few tens of eV is available [**?**], has been recently carried

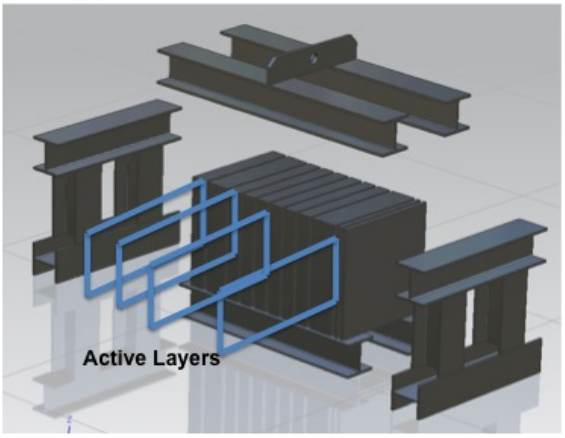

Figure 10.14: The IFR prototype.

Module #	scintillator	Fibers	Photodetectors	Module type
1	2 x 4 cm^2	Bicron, 1mm, L=4.0m	FBK 1.2x3.2 mm^2	TDC standard
2	2 x 4 cm^2	Bicron, 1mm, L=4.0m	FBK 1.2x3.2 mm^2	TDC standard
3	2 x 4 cm^2	Bicron, 1mm, L=4.0m	FBK 1.2x3.2 mm^2	TDC standard
4	2 x 4 cm^2	Bicron, 1mm, L=4.0m	FBK 1.2x3.2 mm^2	TDC standard
5	2 x 4 cm^2	Bicron, 1.2 mm, L=4.0m	FBK 1.4x3.8 mm^2	TDC special
6	2 x 4 cm^2	Bicron, 1.2 mm, L=4.0m	FBK round 1.4mm	TDC special
7	2 x 4 cm^2	Bicron, 1mm, L=4.0m	FBK 1.2x3.2 mm^2 + MPPC 2x2 mm^2	TDC special SiPM/MPPC
8	1 x 4.5 cm^2	Kuraray, 1.2mm, L_x = 110cm , L_y =160cm	FBK 1.4x3.8 mm^2	BIRO standard
9	1 x 4.5 cm^2	Kuraray, 1.2mm, L_x = 370cm , L_y =320cm	FBK 1.4x3.8 mm^2	BIRO standard
10	1 x 4.5 cm^2	Kuraray, 1.2mm, L_x = 190cm , L_y =280cm	FBK 1.4x3.8 mm^2	BIRO standard
11	1 x 4.5 cm^2	Kuraray, 1.2mm, L_x = 210cm , L_y =240cm	FBK 1.4x3.8 mm^2	BIRO standard
12	1 x 4.5 cm^2	Kuraray, 1.2mm, L_x = 210cm , L_y =240cm	FBK round 1.4mm	BIRO special

Figure 10.15: The IFR prototype.

out on a set of more that 20 SiPMs from Advansid, Hamamatsu and SenSL. Fore each device we measured the dark rate and dark current every minute and we regularly ($\simeq$ every hour) performed a I-V curve and a dark rate vs threshold scan. For a few devices we also acquired the dark noise charge spectra. A detailed analisys is ongoing, preliminary results shows that.....

effects of temperature variation.

10.5.2 Prototype Test and Results

Cibinetto

10.5.3 Design and construction of the IFR prototype

Once a baseline design was established, a full depth prototype has been built and tested on beam at the Fermilab Test Beam Facility **??**, on a muon and pion beam in the range of interest for superB.
The main goal of the beam test was to measure the detector performances: mainly the detection efficiency, the time resolution and the particle identification capability as a funcion of the beam momentum. It was also a very useful test bench to investigate and better understand the assembly strategy and, possibly, to figure out possible issues that might appear during the detector costruction fase.
Fig. 10.15 shows a schematic view of the prototype. It represent a section of $60 \times 60 cm^2$ of the IFR detector, with the full depth, and an iron structure designed to have the possibility of moving the active layers in different positions, in order to change the scintillator-iron segmentation and determine the most effective for particle identification.

A total of 12 active modules, as summarized in fig. **??** were assembled: 4 "standard" for each readout (BIRO and TDC), designed as the baseline technique, and 4 "special" to test the effect of single components (i.e. larger fibers, different photodetector etc...).

Fig. 10.16 shows the general internal structure of an active module of the prototype. The structure is rather simple: two layers of orthogonal 5cm wide scintillating bars, $\simeq 50 cm$ long with 3 fibers housed in surface grooves for each bars. For the TDC modules the scintillator bars were 2 cm thick so a single layer was present. Since the length of the fibers is different on each module, to study the detection efficiency and time resolution in different positions of the IFR detector, the fibers are collected on cylindrical supports and then coupled to the SiPM thanks to custom made plastic (plexiglas) couplers. Their length span from 45 to 370 cm for BIRO readout while are of a fixed length of $4m$ for TDC readout.
The finers are coupled
The front end electronic that provide the bias to the SiPMs, amplifies and discriminates the signals, has been custom designed and is based

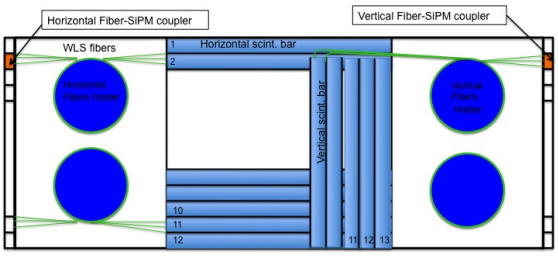

Figure 10.16: Scheme of an active module of the prototype.

on commercial amplifiers (MMIC BGA2748 , BGA 2716). Also the data acquisition and online detector control systems have been custom designed specifically for this setup.

10.5.3.1 Beam Tests

Beam Test Setup and data taking. To assess the detection and identification performances the prototype has been extensively tested with a muon and pion beam. The beam was provided by the Fermilab Test Beam Facility at FNAL [cite]; muons and pions is produced by means of a proton beam colliding on an Aluminum target. The particle momentum is selected by two dipoles and has a spread of about 5-10% at 10GeV getting worse at lower momenta. In the momentum range we explore (1-10 GeV) the beam is mainly composed by electrons and pions, with a small fraction <5% of muons. Electrons have been removed by Cherenkov signal used as veto into the trigger. Muon and pions have been selected, above 2 GeV, using another Cherenkov signal; below 2 GeV no external particle identification information was available, so such data have been used only as cross check.

Four beam tests have been performed from December 2010 to March 2012, in each test the apparatus was slightly different due to improvements and lesson learned from previous run, nevertheless the basic concept is composed by (maybe a picture can be useful):

- a slab of 16 cm of iron upstream of the apparatus to "simulate" the material in front of the IFR detector in the SuperB experiment and to get rid of most of the electrons;
- two or three scintillator detectors with PMT readout placed between the iron and the IFR prototype as trigger;
- the IFR prototype;
- another set of scintillator detectors placed after the prototype to select tracks going through the prototype.

All the PMTs and Cherenkov signals have been acquired with the prototype TDC system in order to refine trigger requests offline.

Table 10.2 shows the data samples acquired at different energies during the four beam tests among with the trigger used.

beam momentum (MeV/c)	min. bias (k evt)	muon trigger (k evt)	pion trigger (k evt)	electron veto (k evt)
1	50	-	-	386
2	60	-	-	236
3	126	134	89	155
4	101	106	76	129
5	262	87	158	25
6	230	218	230	100
8	236	375	413	125

Table 10.2: Beam test data sample.

10.5.3.2 Tests Results

The data from different data taking have been fully analyzed in order to study the detection performances and the muon identification capability of the IFR prototype that will be described in details in the following paragraphs.
In addition to that a first result is about the reliability and the operability of the apparatus: the prototype has been operated for almost forty days of beam test without causing almost any loss of useful data showing that the system design is already mature for a full scale apparatus.

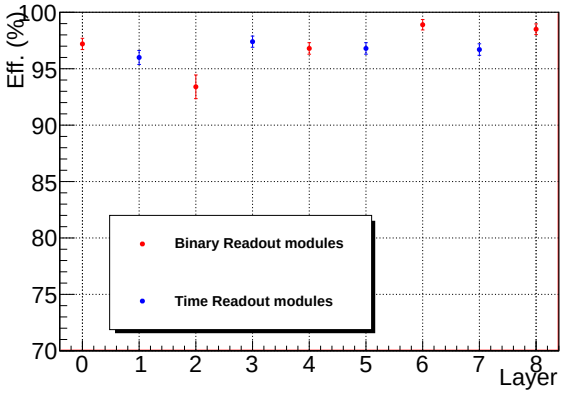

Figure 10.17: Prototype detection efficiency for each layer.

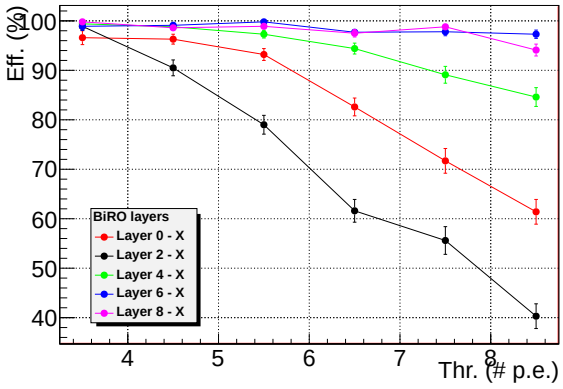

Figure 10.18: Prototype detection efficiency as function of the electronic threshold.

The count of lost channels is also very good: we had an infant mortality of just one channel over a total of 237 and after almost one and an half year of testing we end up with three missing channels mainly due to shipping and handling of the detector during the different installations.

Detection Performances. About the detection and track reconstruction performances the main purpose was to confirm the R&D results on a larger scale to assure that the system is capable not only to detect particle hits but to reconstruct three dimensional tracks passing through it. Therefor not only the detection efficiency is a parameter of a paramount importance, but also the spatial resolution; being the prototype be conceived to test the working principle of the TDC readout option too, the time resolution has been also evaluated.

The detection efficiency has been evaluated using muon events passing through the entire prototype and selected using the backward scintillators. Results are reported i Fig. 10.17 for the binary and time readout modules: the detection efficiency clearly depends on the length of the light path into the fibers that if different from module to module, but in almost any case is >95%. The only exception is for the module in layer number two which has a light path of almost 4 meters, such a long light path will not be present in the final detector design. The detection efficiency depends also on the electronic threshold, Fig. 10.18 shows that, except for the module with the long fibers (layer number two) we have room rise the threshold from the current nominal value, that is 3.5 photoelectrons, to 4.5 (maybe 5.5) with very small efficiency loss. All the results are consistent with the R&D results.

Time resolution performances shown in Fig. 10.19 are also in agreement with our R&D results; the time resolution linearly depends with the fiber length, deviations from the linear behavior are due to SiPM bias voltage overset or underset. The average time resolution is about 1.2 ns and it's enough to guarantee the spatial resolution needed to match the physics performance requirements; on the other hand there is very little space for improvements in the time resolution and moreover the risk of worsening the performances with the aging of the photodetectors.

The last consideration is about the detector occupancy; since one of the main issue of the silicon photomultiplier technology is the dark rate, the noise level has been carefully evaluated both with random trigger and special cut on the time hit. In both cases the average strip occupancy due to the readout is about 1.7%.

Muon Identification Results

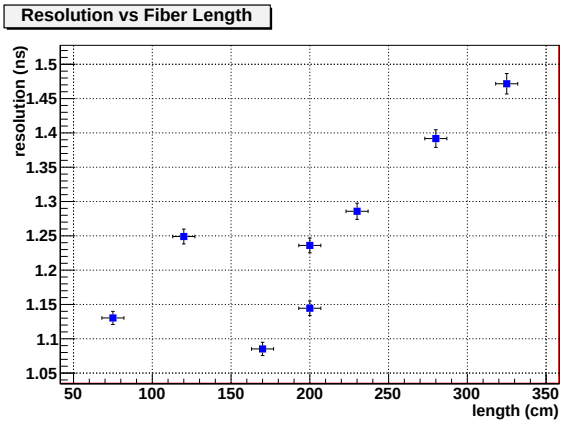

Figure 10.19: Time resolution as function of the fiber length.

10.6 Baseline Detector Design

10.6.1 System Layout

Cotta, Calabrese, Carassiti, Cibinetto (4, 5 pages)

Module concept. Before going into the details of the detector design let's summarize the main points, discussed so far, which have a substantial impact on the overall system layout.

The IFR system must have high efficiency for selecting penetrating particles such as muons, while at the same time rejecting charged hadrons (mostly pions and kaons) in a wide momentum range, from approximately 0.5 GeV to 5 GeV.

The possibility to reuse the BaBar iron offers a cheap solution for the flux return structure, on the other hand it introduces some mechanical constraints which have a significant influence on the detector design: the available space for the detection modules is limited by the dimension of the existing gaps (25mm), and the amount of absorber material is limited to $\sim$ 90 cm of iron. In addition the clarence and path for cables and other utilities is also fixed by the existing structure design.

The other major constraint is due to the machine background that can affect the system by reducing the particle identification performances and speeding up the detector aging.

The maximum rate of charged particle on the IFR detector is located in the forward endcap, close to the beam pipe and, by means of a detailed Monte Carlo simulation, it's estimated to be about xxx Hz/cm^2 decreasing rapidly with the distance from the beam axis; particle identification studies made on the same data sample show that with the current background estimation multiplied by a safety factor the muon ID performances are still acceptable for our system.

For what concern the aging of the photodetectors the main hazard comes from the high flux of neutrons originated by radiative BhaBha background. Recent neutron irradiation tests [cite Musienko] show that SiPM devices continue to work at least up to a dose of $\sim 10^{11} - 10^{12} n_{eq}/cm^2$ but with a considerable increase of dark rate and dark current and an associated efficiency loss of about 80% depending on the cell size. From Monte Carlo simulation we could estimate the neutron flux on the detector that ranges from xxx Hz/cm^2 to xxx Hz/cm^2. We use such information to identify a safe place for the SiPM.

R&D results have proven that, using 1x5 cm^2 (1x10 cm^2) strips, with three fibers for each strip, it's possible to build a detection module 2.5 m (1 m) long having a detection efficiency $> 98\%$ applying a threshold high enough to keep under control the dark count increase due to the neutron irradiation damage. Moreover, beam tests on a large scale prototype has demonstrate the muon identification capability and the reliability of the system.

The K_L^0 identification is also a requirement which has an impact on the detector design. From Mote Carlo simulation and previous experience with the BaBar experiment maintaining

the existing fine segmentation of the three internal layers is enough to retain the the capability to use the IFR

Barrel: number of active layers, channels, geometry.

Endcaps number of active layers, channels, geometry.

10.6.2 Chamber Construction and Assembly

Andreotti, Baldini, Carassiti (3 pages)

module assembly procedure

tooling for module assembly

module QC procedures

10.7 Front-End Electronics

10.7.1 Introduction

This chapter starts with a description of the basic features of the detector assemblies, since these include the very first stage of the electronic readout chain, namely the solid state photodetector with single photon resolution. This section presents then the basic characteristics of the detector assemblies and gives some basic information on their installation location within the IFR steel, because these data of the IFR construction, together with considerations on the radiation background at different location, drive the design constraints for the IFR readout electronics. The chapter describes then the details of the IFR electronics baseline design.

10.7.2 Photodetectors and PCBs

ver 0.5 sep 18 2012, Angelo Cotta Ramusino, Woijech Kucewicz

The IFR will exploit extruded plastic scintillators to detect ionizing radiation crossing the apparatus. The light from the scintillators will be collected by embedded wavelength shifting (WLS) fibers and guided to solid-state single photon detectors or silicon photomultiplier (SiPM for short). The results of the preparatory R&D activities suggest that three WLS fibers should be installed in each scintillator bar; the drawing below shows how, in principle, the plastic scintillator should be patterned to host the WLS fiber. The baseline design for the IFR detector foresees in fact that the photodetector would be applied at the end of each bar. A printed circuit board (PCB) will be designed to support the photodetector and the miniature connector to a thin coaxial cable.

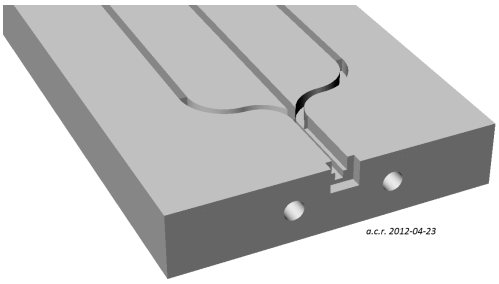

Figure 10.20: a scintillator bar machined to host three WLS fibers, the silicon photomultiplier and the carrier printed circuit board (PCB)

10.7.2.1 Photodetector PCB and optical coupling to fibers

Figures 10.21 shows details of the assembly to be installed at the end of each scintillator bar; the SiPM is first viewed (from the solder pad side) suspended in front of the machined notch where it is lodged once the PCB assembly is fastened. The WLS fibers are guided by grooves machined at the scintillator surface; the diamond-cut end of the WLS fibers are positioned flush with the SiPM notch. The SiPM dimensions should be chosen to guarantee an effiecent collection of the light from all three fibers; suitable SiPMs with an area of up to $9\,mm^2$ have been characterized during the detector R&D to evaluated their efficiency and radiation tolerance properties.

Figure 10.21 show the assembly in operation: a micro coaxial jack such as the Amphenol A-1 JB, soldered on the PCB, allows the connection of a small-diameter coaxial cable; all coaxial cables are routed out of the detector assembly enclosure and reach the front end cards to which

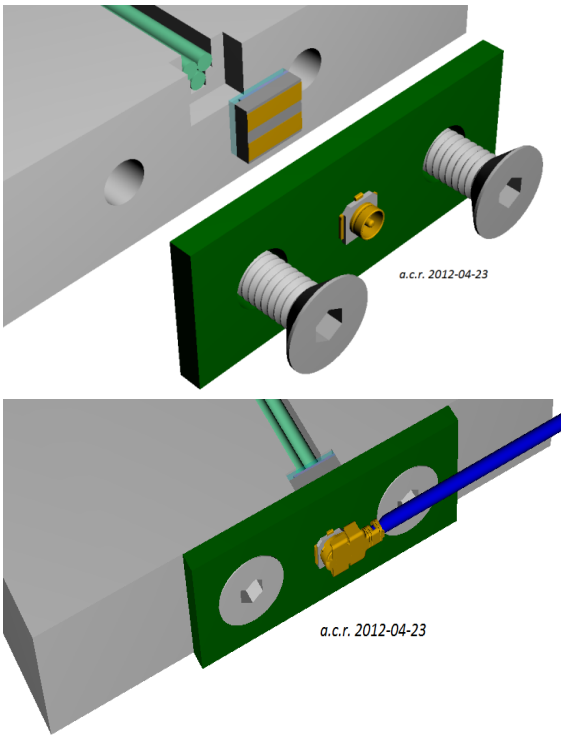

Figure 10.21: details of the three WLS fibers and the PCB for the solid state detector

they are connected via a mass-terminated high density connector as shown in Fig. 10.22.

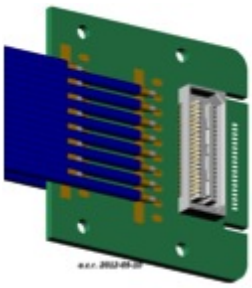

Figure 10.22: a detail of the multi coaxial connector assembly

10.7.2.2 Optical coupling to fibers

As Figure 10.21 shows, the coupling of the WLS fibers to the SiPM is defined by means of machined grooves for the fibers, of a machined notch for the SiPM and of threaded holes for the PCB mounting screws (and eventually with hole for precision positioning pins). Previous experience with the R&D prototype construction allows to estimate that the relative positions of the fiber ends and the surface of the photodetector can be controlled with a precision in the order of 100um. Optical grease or silicon pads can be used to improve the optical matching.

10.7.2.3 Photodetector location

The scintillator bars, fitted with the photo detectors, will be enclosed in light-tight sheet-aluminum boxes which will also provide mechanical rigidity to the assemblies, or modules. Each active layer of the IFR detector will actually be composed by a suitable number of modules inserted, in general, in the gap between two steel plates of the magnetic flux return.

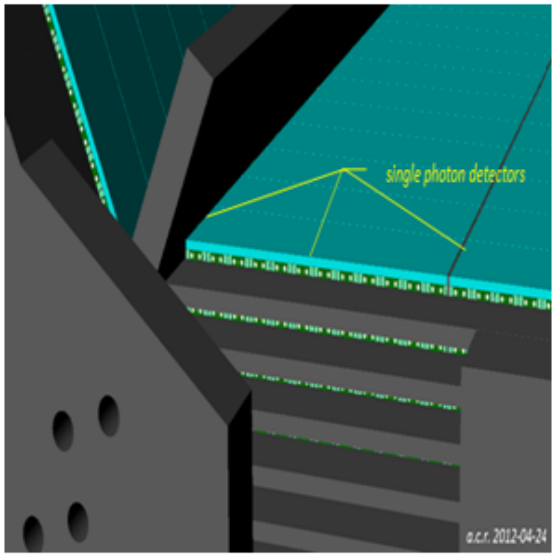

Figure 10.23: Location of the scintillator bars and SiPMs inside the IFR barrel: view of layer 0 of the IFR barrel with the modules' enclosure removed

It is to be said that once the modules are installed inside the IFR it will be impossible to perform any maintenance on the majority of them without a major overhaul of the detector; this is especially true for the barrel portion of the detector. Fig. 10.23 depicts a view of the barrel section of the IFR with a few modules of

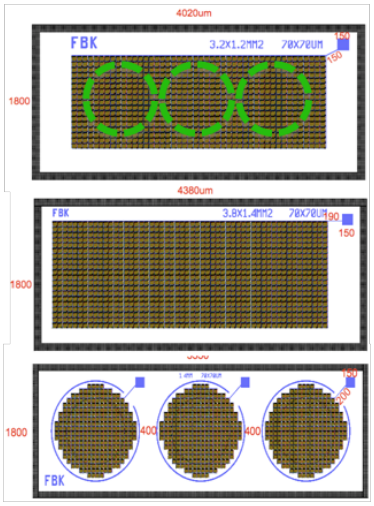

Figure 10.24: the custom SiPM manufactured by FBK for the IFR prototype

the innermost layer; the modules' envelopes are not drawn, to show the locations of the SiPMs for the barrel; a similar arrangement is foreseen for the active layers of the endcaps. The SiPMs are distributed throughout the entire surface of an active layer and they thus operate in a hostile radiation environment. The solid state photo detectors for the IFR application will thus have to be chosen on the basis of the results of irradiation tests aimed at the evaluation the radiation induced degradation of the photon detection efficiency.This assessment of the radiation tolerance of the SiPM has already been carried out for the devices available at the time the IFR prototype was assembled; more R&D and irradiation test have to be planned before the final SiPM choice is made, to characterize and possibly select devices built with the latest and most promising technologies. For the modules subject to the highest intensities of background radiation a special layout is also being investigated in which the SiPMs are relocated at more suitable positions by extending the WLS fibers length.

10.7.2.4 Photodetector choice

Different solid-state single photon detectors have been and are being evaluated for the IFR application, because the technology is rapidly evolving and it would probably be best to commit to a specific device as late as possible.

Devices tested so far by the SuperB-IFR collaboration include Silicon Photo Multiplier (SiPM) manufactured by the Fondazione Bruno Kessler (FBK), Hamamatsus' Multi-Pixel Photon Counter (MPPC) and Silicon Photomultipliers (SPM) by SensL [[8], [9], [10], [11], [12]]. The key parameters describing the performance of a single photon detector are:

- the photon detector efficiency at the WLS fiber characteristic wavelength
- the fill factor
- the optical cross-talk
- the dark count rate
- the sensitivity of breakdown voltage to temperature variations
- the gain and its sensitivity to temperature variations

The SiPM suited for the IFR application should guarantee a detection efficiency better than 95% when installed in a detector assembly and should present a dark count rate at 0.5 p.e. threshold in the range of a few 100kHz/mm^2 at room temperature and nominal bias voltage. SiPM devices satisfying these requirements and showing, after irradiation, the least perturbation of their original performances will be finally selected for the instrumentation of the IFR detector.

Another parameter which will be considered for SiPM device selection would be the availability of detector geometries which would minimize the unused surface area to minimize the ratio of dark count rate over signal rate. For the instrumentation of the IFR prototype, for instance, a special device run was commissioned to FBK and devices tailored to the IFR prototype needs were manufactured 10.24, 10.25. The IFR prototype had the majority of the channels equipped with FBK SiPMs but also had channels equipped with MMPCs and both type of silicon photomultipliers performed very

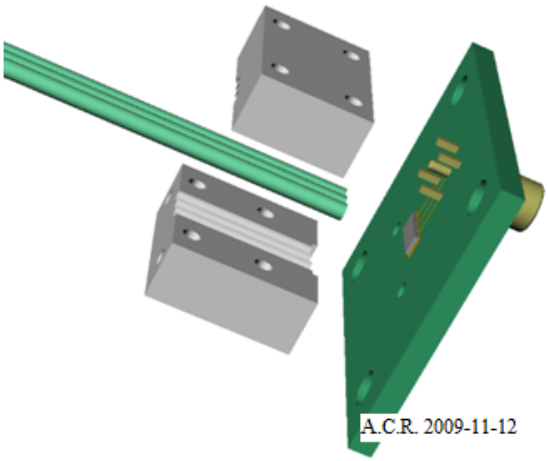

Figure 10.25: a detail of the SiPM carrier PCB with the MMCX connector

well. The final choice will have to be made after more irradiation tests aimed at evaluating the sensitivity of the key device parameters to the type and the dose of the SuperB radiation environment.

10.7.2.5 Aging and background issues

The SiPMs manufactured by FBK and the MPPC by Hamamatsu have been irradiated with neutron at the Laboratori Nazionali di Legnaro [5] and at the Frascati Neutron Generator to evaluate the effect of radiation on the devices key parameters [[6]. These tests showed that for neutron fluxes above a few 10^8 neq/cm^2 the dark current and the dark count rate begin to increase while the device gain decreases; after a few 10^10 neq/cm^2 the number of photons detected by an irradiated silicon photomultiplier instrumenting a cosmic muon detector may drop to about 80% of the initital value [6]. As a reference, the fluence of 1MeV-equivalent neutrons expected [7] at the hottest location of the IFR barrel is about 3^9 neq/cm^2 per year. The outcome of the irradiation tests results would seem to advice against installing the SiPM inside the IFR steel, where an eventual replacement would require a major overhaul of the detector and a long down time; on the other hand to position the silicon photomultipliers in accessible locations would require to carry scintillation light to them via long clear fibers spliced to the WLS fibers with increasing costs, increasing dead space and consequent loss of the photons available at the SiPM, with similar effects on the overall efficiency. Other topics to consider are that the signal processing foreseen for the "binary mode" readout of the detector is more tolerant to device performance degradation than the alternative "timing mode" readout [12] and that new silicon photomultiplier devices are being introduced which feature improved radiation tolerance. The dose received by the sensors could also be reduced by inserting multiple and shielding layers within the IFR which would thermalize the neutrons from the beam halo, capture the thermal neutrons and finally absorb the energetic photons resulting from these processes. These considerations lead the IFR collaboration to maintain the baseline design described above, while scheduling more irradiation tests to evaluate the radiation tolerance of the newest SiPMs and the effectiveness of the shielding techniques.

10.7.2.6 Temperature requirements

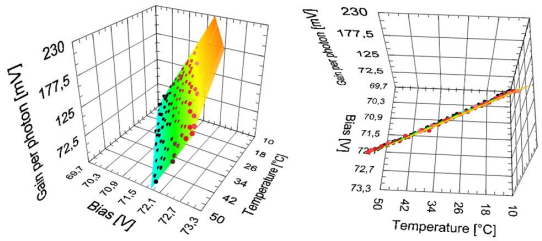

Figure 10.26: Each point on 3D graph represent a single measurement; from the whole set of points gain stabilization parameters for single SiPM are determined.

Silicon photomultipliers operating point and parameters are influenced by temperature. In the case of the IFR detector it is not foreseeable to refrigerate the devices by means of thermoelectric coolers and so we assume that the devices will operate at the temperature of the flux return steel, whose temperature was controlled, in Babar, by means of a chiller system.

Rather than control the operating temperature of the silicon photomultiplier devices, the IFR environmental control system will then periodically correct the bias point of each device to compensate for local temperature variations, a technique which was used in the latest beam tests of the IFR prototypes [13].

The results of extensive studies on the compensation of temperature induced SiPM gain variations are illustrated in the seminar "Compensation of the Temperature Fluctuations in the Silicon Photomultiplier" held in Ferrara in Feb. 2012 by Prof. Wojciech Kucewicz, at in a recent presentation at the "Instrumentation for Muon and K0L Identification at Super Flavor Factories" workshop in Krakow,Poland 6-10 September 2012 [14]. Figure 10.26 illustrates the distribution of measurements points in the (gain, bias, temperature) space, while figure 10.27 shows the effectiveness of the compensation techniques against temperature variation for two type of silicon photomultipliers.

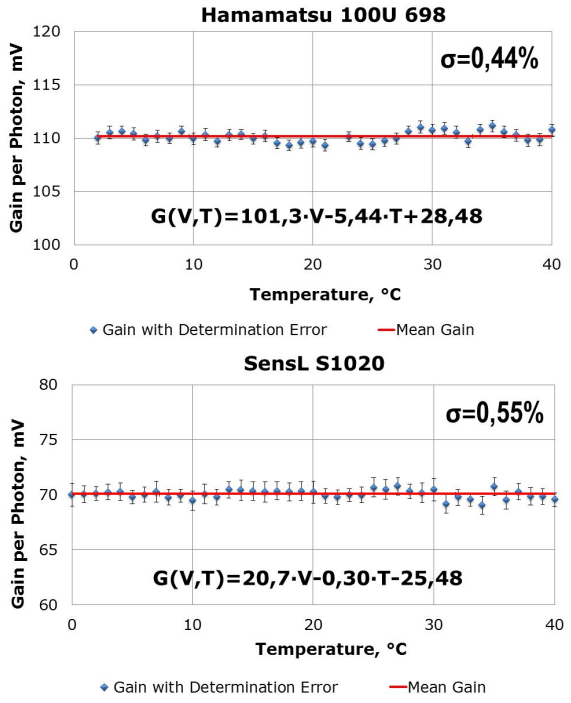

Figure 10.27: Gain stabilization results obtained at AGH Krakow for Hamamatsu (top) and sensL (bottom) SiPM devices

10.7.3 IFR readout electronics: an overview

ver 0.5 sep 18 2012, Angelo Cotta Ramusino

10.7.3.1 Introduction

This section describes first the features of the IFR detector which drive the design of the readout system. It presents then an estimation of the number of electronic channels, of the event size and the data bandwidth at the nominal Super*B* trigger rate. The design constraints determined by the expected background radiation are then reviewed, along with the results of irradiation tests on existing ASICs and off-the-shelf devices suited for the implementation of some functional blocks of the readout chain. This chapter describes, finally, the baseline IFR readout system, going from the basic requirements of a dedicated IFR front end ASIC to the proposed installation locations of the IFR electronics building blocks, to the services required in the detector hall.

10.7.3.2 Basic features of the IFR detector

LAYER WIDTH	LAYER	No. Modules per layer	LAYER ENABLE	PHI ASSUMING 50MM BARS	ZETA ASSUMING 106MM BARS
1963	1	6	1	13	17
1987	2	6	1	13	17
2050	3	6	1	13	17
2113	4	6		14	17
2176	5	6		14	17
2240	6	6		14	17
2304	7	6	1	15	17
2367	8	6		15	17
2431	9	8		12	17
2494	10	8		12	17
2569	11	8	1	12	17
2641	12	8		13	17
2712	13	8		13	17
2784	14	8	1	13	17
2879	15	8		14	17
2973	16	8	1	14	17
3068	17	8		15	17
3144	18	8	1	15	15
3296	19	8	1	16	15
NUMBER OF MODULES per sextant:		64		TOTAL PER SEXTANT	1940
TOTAL NUMBER OF MODULES	384			TOTAL CHANNELS PER BARREL	11640

Figure 10.28: estimation of the electronics channel count for the IFR barrel

ENDCAP		
top section	horizontal bars per module:	37
	vertical bars per module:	51
center section	horizontal bars per module:	36
	vertical bars per module:	64
bottom section	horizontal bars per module:	37
	vertical bars per module:	51
AVERAGE channel count per module:		92
NO_OF_MOD_PER_LAYER_EC:		3
horizontal bars per layer		110
vertical bars per layer		166
NUMBER OF LAYER PER DOOR		9
NUMBER OF DOORS IN ENDCAPS		4
TOTAL NUMBER OF MODULES IN ENDCAPS:		108
horizontal bars per door:		990
vertical bars per door:		1494
TOTAL HORIZONTAL BARS:		3960
TOTAL VERTICAL BARS:		5976
TOTAL CHANNELS IN ENDCAPS:		9936

Figure 10.29: estimation of the electronics channel count for the IFR endcaps

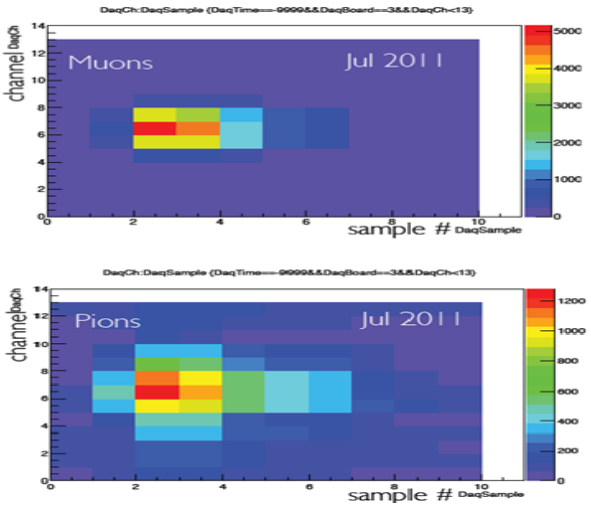

Figure 10.30: time evolution of muon and pions evaluated across the 10 samples taken for each "binary mode" event (plots from [15]). Sampling period was 12.5 ns)

The basic IFR detector element exploits an extruded plastic scintillator with WLS fibers applied in machined grooves and a SiPM installed as shown in figure 10.21. The scintillator bars, fitted with the SiPM carrier PCBs and the signal cables, will be enclosed in aluminum boxes made which will shield the assembly from the ambient light and provide it with the necessary mechanical robustness; the detector assemblies will be, in the following, referred to as "modules". The modules will be inserted, in general, in the gap between the two steel plates delimiting an "active" layer; nine active layers will be instrumented in the barrel section of the IFR and also nine will be the "active" layers in the endcaps. Figure 10.23 shows a few modules installed in the barrel section of the IFR, with the aluminum "envelopes" removed to show the scintillator orientation. The choice of tightly coupling the SiPM to the WLS fibers is driven by the need of maximizing the number of converted photoelectrons; this choice determines in turn that the coupling between the SiPMs and the first stage of the IFR signal processing chain must be done through coaxial cables and connectors.

10.7.3.3 IFR channel count estimation

The active layers of the IFR detectors are equipped with modules in which the detector bars (of different widths for the PHY and the Z views in the barrel) are assembled in two orthogonal layers. Not all gaps of the flux return steel are equipped with detectors; the"LAYER ENABLE" column in Fig. 10.28 shows the current active layer assignment and the resulting total channel count of 11640 for the IFR barrel. Figure 10.29 presents accounting details of scintillator bars in an active layer of one endcap door. The total channel count for both forward and backward endcaps amounts to 9936 for 9 equipped gaps.

10.7.3.4 Estimations of the IFR event size and data bandwidth

The IFR detector will be read out in "binary mode": the output of each SiPM device will be amplified, shaped and compared to a threshold, the binary status of each comparator's output being the variable to be recorded to reconstruct the particle tracks within the IFR detector. The downstream stages of the IFR electronics are the "digitizers" which sample the comparators' outputs at Super*B* clock rate and store the sam-

BARREL	
Maximum channel count per module:	32
Number of MOD32 processing units per module	**1**
TOTAL NUMBER OF MODULES IN BARREL	**384**
Total Number of MOD32 processing units	**384**
Sampling period = 1 / FCTS_clock (ns)	17,86
Number of samples in the trigger matching window (including framing words)	**16**
ENDCAP EVENT SIZE (kB)	**24,58**
TRIGGER RATE (kHz)	**150**
TOTAL ENDCAP BANDWIDTH (Gbps) (including 8b/10b encoding overhead)	**36,86**
Number of data links from the endcap detectors	24
Bandwidth per link (Gbps)	1,536

Figure 10.31: Estimation of the event size and data bandwidth for the IFR "Barrel" section

ENDCAP	
Average channel count per module	92
Number of MOD32 processing units per module	**3**
TOTAL NUMBER OF MODULES IN ENDCAPS	**108**
Total Number of MOD32 processing units	**324**
Sampling period = 1 / FCTS_clock (ns)	17,86
Number of samples in the trigger matching window (including framing words)	**16**
ENDCAP EVENT SIZE (kB)	**20,736**
TRIGGER RATE (kHz)	**150**
TOTAL ENDCAP BANDWIDTH (Gbps) (including 8b/10b encoding overhead)	**31,104**
Number of data links from the endcap detectors	16
Bandwidth per link (Gbps)	1,944

Figure 10.32: Estimation of the event size and data bandwidth for the IFR "Endcap" section

ples into local "on-detector" circular memories. These buffers are designed to keep the data for a time interval at least equal to the Super$B$ trigger command latency. The last stage of the "on-detector" readout system is based on Finite State Machines (FSM for short) which extract, from the local latency buffers, the data selected by the FCTS trigger command. The IFR channels will be processed by functional blocks with a modularity of 32.

Such a straightforward scheme has been successfully applied to the IFR prototype, which has been tested with cosmic muons and with the beam provided by the Muon Testing Facility of the Fermi National Accelerator Laboratory [15], [16]: the beam tests have shown that the time window for the extraction of data matched to a trigger should be about 120 ns wide (see Fig.10.30), in order to recover the entire signal from the shower initiated in the detector by an impinging hadron. The real IFR detector will be read out in the "binary mode" outlined above and the tables in Figure 13.6 report the expected IFR event size and data bandwidth at the nominal Super$B$ trigger rate. In these tables the number of samples has been set to 16 to account also for a trigger jitter in the order of 100ns. The event size and required bandwidth could be reduced by applying the data reduction scheme proposed by the ETD group: if a new trigger would select data that has already been sent in response to a previous one, the repeating data is not retransmitted and a pointer to the start of the repeating data within the previous packet would be sent instead.

10.7.3.5 Background radiation and electronics design constraints

The current knowledge on the radiation environment at Super$B$ comes from detector simulations which are constantly increasing the detail of the structures being simulated and thus the accuracy of the results. For the IFR, in particular, the simulation work ([17], [18]) analyzes the known sources of radiation background in Super$B$ and evaluates the doses in Si at the locations of the SiPMs and at the locations of the front end electronics. The largest fraction of the total dose absorbed by the IFR electronics is deposited by neutrons originating back to the radiative BhaBha and the Touschek processes. The neutron energy spectrum shown

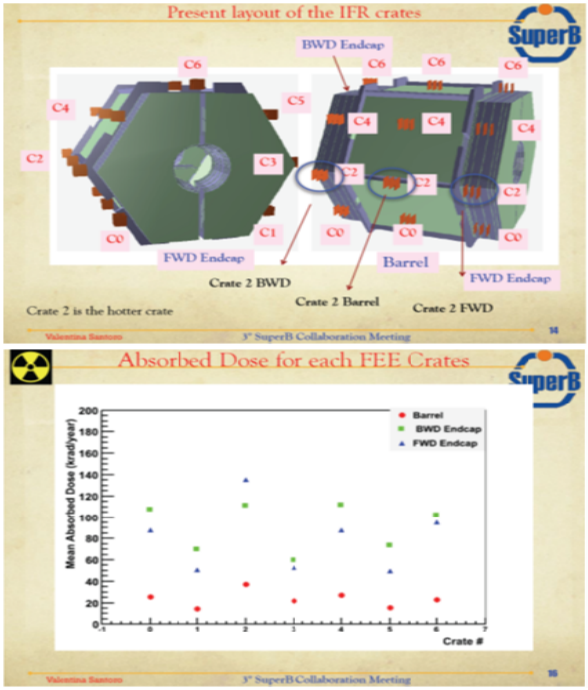

Figure 10.33: background neutrons flux: doses (krad/year) measured at some relevant locations around the detector

in figure 10.3 in the "Neutron Background" subsection of the IFR chapter is quite wide-spread and so different types of interaction processes have to be considered to assess the effects of the background neutrons on the performances of the sensors and of the IFR readout components. As a reference location for the neutron rate estimation one could take layer 0 of the IFR barrel where the neutron rate is shown in figure 10.4; the rates in this plot, which has distance in Z from the interaction point on the horizontal axis, are reported separately for the different background sources, are normalized to 1 MeV equivalent neutrons in Si and include a *safety factor* that takes into account the fact that the simulation may not reproduce perfectly the reality, as explained in the "Neutron Background" subsection. A reference rate of 500 $n_{eq}/s \times cm^2$ would result in a fluence of about $1.6 \times 10^{10} n_{eq}/cm^2$ per solar year.

Data on total dose in silicon at locations around the IFR steel where "on detector" components of the electronic readout system could be located is also provided by the IFR background simulation group: figure 10.33 gives information on the dose (in Si) absorbed at the different locations in evidence. The highest dose is found at the C2 locations of the forward endcap and it is about 140krad/year.

Electronics devices and systems which must reliably and durably operate under these radiation conditions must be designed or selected according to guidelines which have already been drawn, among others, by the LHC community. As an example one could refer to the "ATLAS Policy on Radiation Tolerant Electronics: ATLAS Radiation Tolerance Criteria" [21] to see that the neutron fluence expected for the Super*B* IFR is of the same order of magnitude simulated for the MDT muon spectrometer.

We could then, if not exploiting exactly the same technical solutions adopted there, at least follow the design guidelines established by the cited and by similar documents. A more general approach to the subject of radiation effects in silicon devices is described in [19], [20], [22], [39]. The R&D activity for the preparation of the Super*B* TDR has included the evaluation of the radiation effects on SiPM [23], [25], [26], [27], [28] and on electronic devices used to implement the basic functions of the readout system. Irradiation tests were performed at the CN facility of the INFN Laboratori Nazionali di Legnaro (LNL) on samples of:

- low power, current feedback, operational amplifiers (to be used eventually for "on detector" buffers, active summing junctions and so on)
- ACTEL proASIC3E FPGA (candidate for the implementation of digital functions of the IFR readout chain)
- the "EASIROC" ASIC developed by the Omega group of the LAL, Orsay, France [29], [30]
- the "RAPSODI" ASIC developed by W. Kucewicz and his group at the AGH University, Krakow, Poland [35]

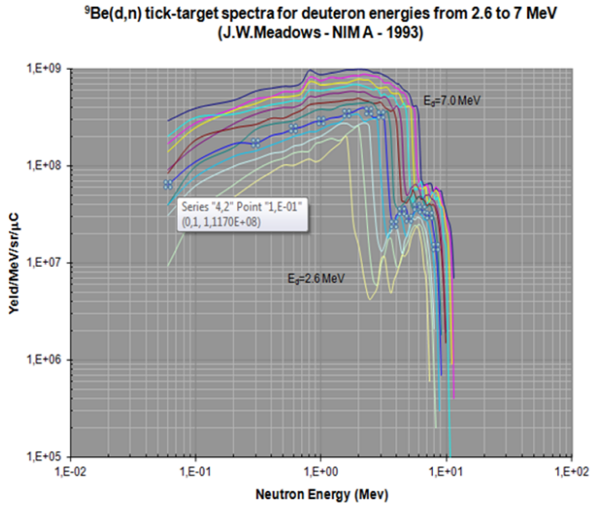

Figure 10.34: energy spectra of the neutron beam delivered by the CN line of the INFN-LNL)

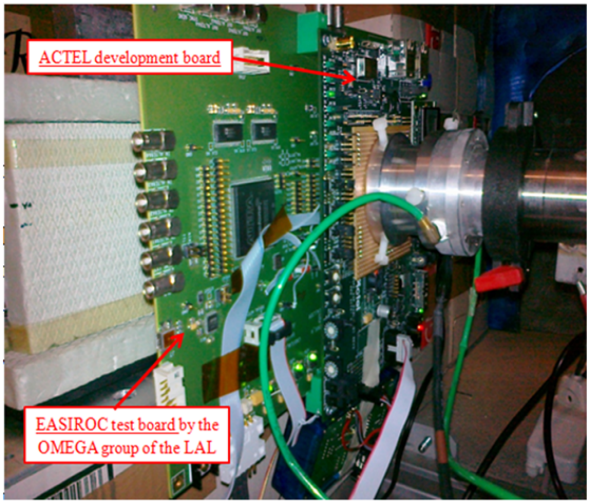

Figure 10.35: irradiation test setup at the CN facility of the INFN Laboratori Nazionali di Legnaro

total integration time (sec)	60683			
total charge (uC)	4104			
9Be(d,n) thick target yield at 0 angle (YIELD/sr/uC) (ref. 13.5.1_r15)	1,017E+09			
	ACTEL A3PE250-PQ208			EASIROC
distance from source (mm)	7			20
total fluence at the target (neutrons/cm^2)	6,118E+12			1,033E+12
total fluence at the DUT (neutrons)	**4,955E+12**			**1,694E+11**
	CONFIGURATION MEMORY BITS	SRAM BITS	FLIP FLOP	FLIP FLOP
total memory element monitored	N.A.	32768	5824	456
number of SEU detected	**0**	**752**	**26**	**0**
number of SEL detected	**0**			**0**

Figure 10.36: results of the EASIROC irradiation tests at INFN-LNL

- the "CLARO" ASIC developed by G. Pessina and his group at INFN Milano-Bicocca, Milano, Italy [42]

The CN facility of the LNL has a beam line delivering 4 MeV ^{2}H+ ions to a beryllium target; the energy spectra of the neutrons produced in the ^{9}Be(d,n)^{10}B reaction are shown in figure **??** where the 4.2 MeV curve is highlighted for convenience. Figure 10.35 shows the stack of boards carrying, in the first of the irradiation tests performed, the "EASIROC", the FPGA and the op-amps installed right in front the beampipe, and a thermally isolated SiPM box located right after, at about 4 cm from the beam pipe. Some results of this irradiation tests are presented in the table of figure 10.36 below. The OMEGA EASIROC, manufactured in the 0.35 μm SiGe technology of Austria Micro Systems, was exposed to an estimated total of 1.7×10^{11} neutrons, equivalent to a few year's exposition to the Super$B$ IFR operating conditions.

The outcome of the test showed that, as expected, while the FPGA configuration memory contents was not corrupted, the on-chip SRAM blocks and the registers in the FPGA fabric were subject to upsets. It follows that any critical part of the FPGA design should include suitable SEU protection functions. It is worth noticing that no SEU afflicted the EASIROC configuration registers, that no latch-up occurred and finally that no evidence of TID damage was found while comparing the current consumption and the analog performances before and after the irradiation test [28].The op amps to be tested had been fastened to the top of the FPGA and have thus been irradiated with a fluence of the order of 10^{12}neutrons/ cm^2 with no noticeable effect on their current consumption or DC offset.

On a later occasion, in June 2012, the "RAPSODI ASIC-2" and the "CLARO" ASICs were also irradiated at the CN facility, using similar setups as the one illustrated above. Figure 10.37 sketches the relative positions of the neutron source and the DUTs. No "Single Event Latch-up" were detected for either the CLARO

or the RAPSODI ASIC-2, which were powered at nominal operating voltage, during the irradiation. Also little effect was measured on the ASICs performances such as DACs' transfer functions, gain and comparator offset [43], [44]. As examples, figure 10.38 shows, for one of the CLARO DACs, the comparison between transfer function measurements performed before and after irradiation; figure 10.39 shows, for one of the irradiated RAPSODI chips, the comparison between linearity measurements performed before and after irradiation.

The neutron fluences delivered to the devices under test, two samples of the CLARO ASIC and two samples of the RAPSODY ASIC-2, were respectively:

- CLARO sample n.1: $1.28 \times 10^{12} n_{eq}/cm^2$;
- CLARO sample n.2: $1.32 \times 10^{12} n_{eq}/cm^2$;
- RAPSODY sample n.1: $3.3 \times 10^{13} n_{eq}/cm^2$;
- RAPSODY sample n.2: $1.32 \times 10^{12} n_{eq}/cm^2$.

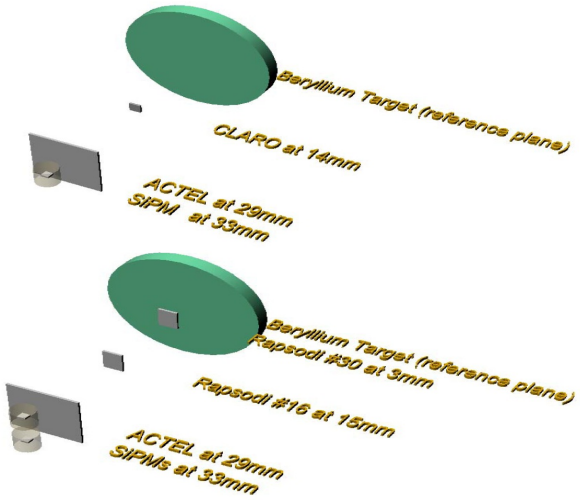

Figure 10.37: schematic representation of the CLARO and RAPSODI irradiation test setup at INFN-LNL

The results of the irradiation tests supported the decision on how to build and where to install the front end stages of the IFR readout system. As more neutron irradiation tests on SiPM are planned to assess the radiation tolerance of the latest generation devices, there will be more occasion to test, at the same time, more sample of ASICs built in the AMS 0.35 μm technology at different neutron energies and with different beam orientations w.r.t. to the device under test. The 0.35 μm CMOS technology from AMS is being tested because it represents the preferred choice for the development of a dedicated ASIC, as described in the next chapter.

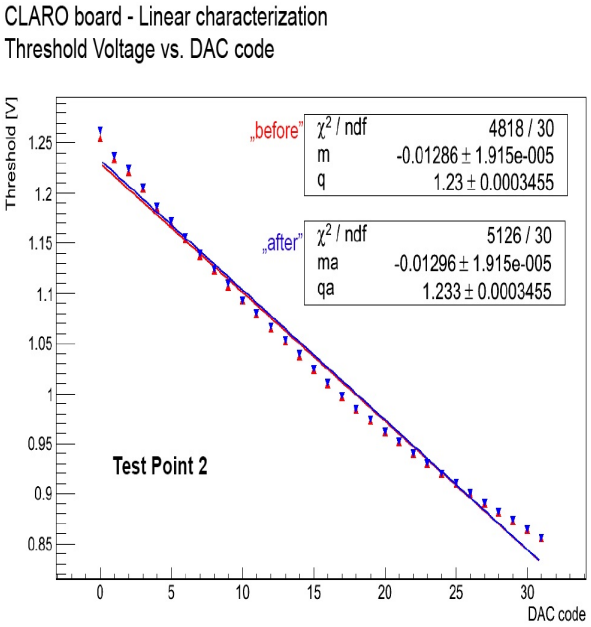

Figure 10.38: CLARO DAC test performed before and after the irradiation (Bartomiej Rachwa, AGH Krakow)

10.7.3.6 The IFR readout system

IFR readout basics: outline of the IFR prototype readout The basic principles at the bases of the IFR readout system design have been tested with the IFR prototype, which was read out in the "binary" mode described above. For the prototype readout a dedicated front end board, the "ABCD", was built from off-the-shelf components ("COTs"); Fig. 10.40 shows the "ABCD" block diagram.

The main functions which were implemented on the 32 channel "ABCD" board are:

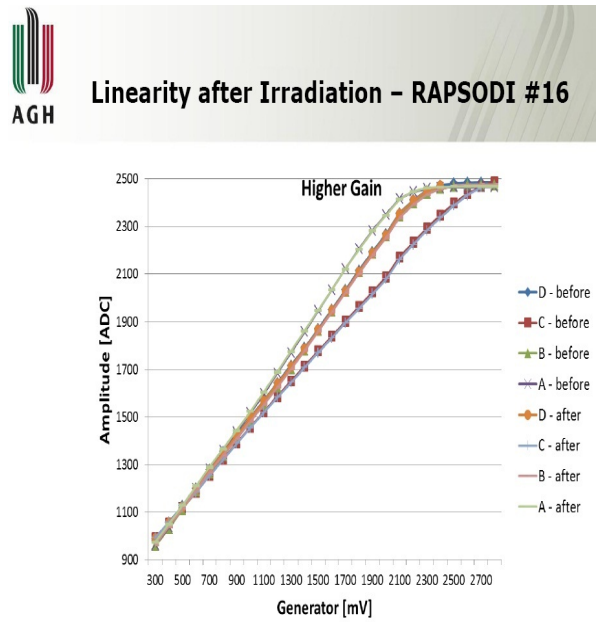

Figure 10.39: RAPSODY linearity test performed before and after the irradiation (Mateusz Baszczyk, Piotr Dorosz, AGH Krakow)

- individual "high side" regulation (with 12 bit resolution) of the SiPM bias voltage; bias voltage and SiPM signal are carried by the inner conductor of the coaxial cable, whose outer conductor is at true ground potential
- wideband (1,5GHz 3dB frequency) amplification of the SiPM signal
- discrimination of each SiPM signal to an individually programmable (with 12 bit resolution) threshold voltages; the discriminators (two per channel) used AC coupled feedback to stretch the output pulse to a width of about 20 ns
- sampling and buffering of the discriminators outputs pending the trigger signal from the experimental trigger system; an ALTERA Cyclone III FPGA was used to sample the discriminated SiPM signals and store them in an internal latency pipeline running at 80 MHz.
- trigger processing: with each trigger a set of 10 samples was extracted from the latency pipeline and transferred to an output buffer (along with suitable framing words) from where they reached the "BiRO_TLU Interface board" [32] acting as a crate-wide data-collector and interface to the DAQ PC and to the experiment's trigger logic units ("TLU")

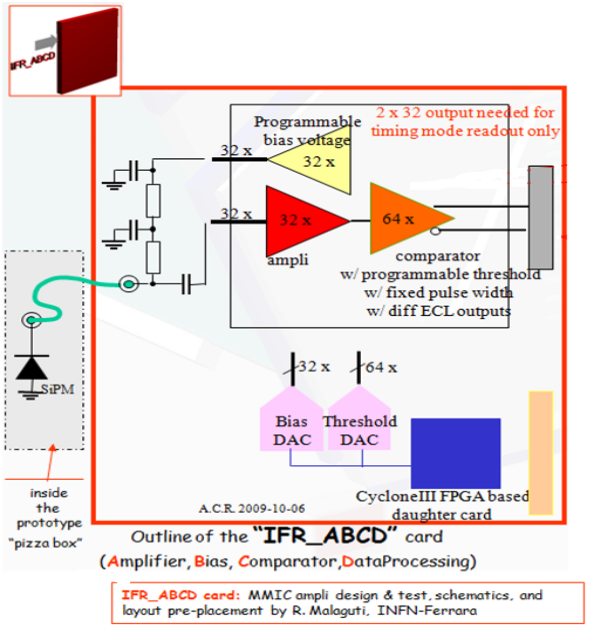

Figure 10.40: basic features of the "ABCD" card designed for the IFR prototype readout

The DAQ system developed for the IFR prototype readout also performed functions which would, in Super*B*, be performed by the Experiment Control System (ECS): ambient temperature acquisition, calculation and download to the ABCD DACs of new set points for the bias voltages (needed to stabilize the SiPM gain against variations of the operating temperature) [15]. The Fermilab beam tests of the IFR prototype have demonstrated, among other things, that connecting the SiPMs to the front end cards by means of long (4m) coaxial cables, although not optimal, was possible and resulted in a reliably operating system. This result supported the current baseline choice of locating the SiPMs near the scintillator bars and far from

the front end cards, so that these last can be installed at more convenient (better accessible) locations.

An ASIC based front end readout The COTS-based design of the "ABCD" card met goals such as short development time and flexibility (especially needed for tuning the parameters of the channels to be read out in the "timing" mode (cfr. the "white book", [33]) but it wouldn't be convenient for large volume production. A search for existing ASICs suited for "binary mode" processing of SiPM signals was started and a good candidate was found in the "*Extended Analogue Silicon pm Integrated Read Out Chip*" or "EASIROC" which had many features already suited for the IFR readout application ([29], [30]); figure 10.41 shows a block diagram extracted from the EASIROC datasheet. The EASIROC has been used, thanks to the test board and utilities provided by the LAL/OMEGA group, to test different SiPM technologies and coupling schemes [34]; figure 10.42 shows, for instance, the pulse height histograms obtained from a 1 mm^2 SensL SiPM connected to the EASIROC via:

- different lengths of coaxial cables, up to 12m (left option)
- one differential pair of a high density, double shielded, multi twisted pair cable 8m long (right option)

The features of the EASIROC which would suite the IFR readout application are:

- the integration of 8 bit DACs, one per channel, for "low side" adjustments of the SiPMs' bias voltage
- one fast (15 ns peaking time) shaper stage for each channel driving the "trigger" comparators
- the integration of a 10 bit DAC, common to all channels, for setting the threshold of the fast "trigger" comparators
- the availability of all 32 "trigger" outputs at the I/O pins (with single ended LV-TTL level) of the EASIROC
- low power consumption
- no sign of performance degradation or SEE detected during or after the irradiation tests described above

These suitable features are partially offset by others characteristics which make the EASIROC not quite usable as it is, the most important of which being the 15ns peaking time of the fast shaper: a lower value is necessary to cope with the increasing dark count rate for SiPMs operating in the Super*B* radiation environment. As the IFR collaboration has been growing in the last year to include groups experienced in VLSI design ([35], [36], [37], [38], [39], [41], [42]), the development of an ASIC implementing the front end stages of the IFR readout system has become within reach; the EASIROC and an auxiliary flash based FPGA could still be considered as building blocks for a backup solution.

The new IFR front end ASIC should implement a set of basic features:

- a preamplifier and shaper chain suited for positive and negative input signals and characterized by a dynamic range of about 100 times the single photon response signal
- a shaper peaking time not larger than 10ns to minimize the pulse pile-up effects at high input rates
- individual DACs to set, with a few mV resolution, the DC level of each input and thus the "low side" bias voltage for the DC-coupled SiPM; the current compliance of the DAC should be specified considering that the dark current of a SiPM could increase two orders of magnitude during its operational life in Super*B*
- a fast comparator design, possibly differential; some of the digital outputs should be routed to I/O pads

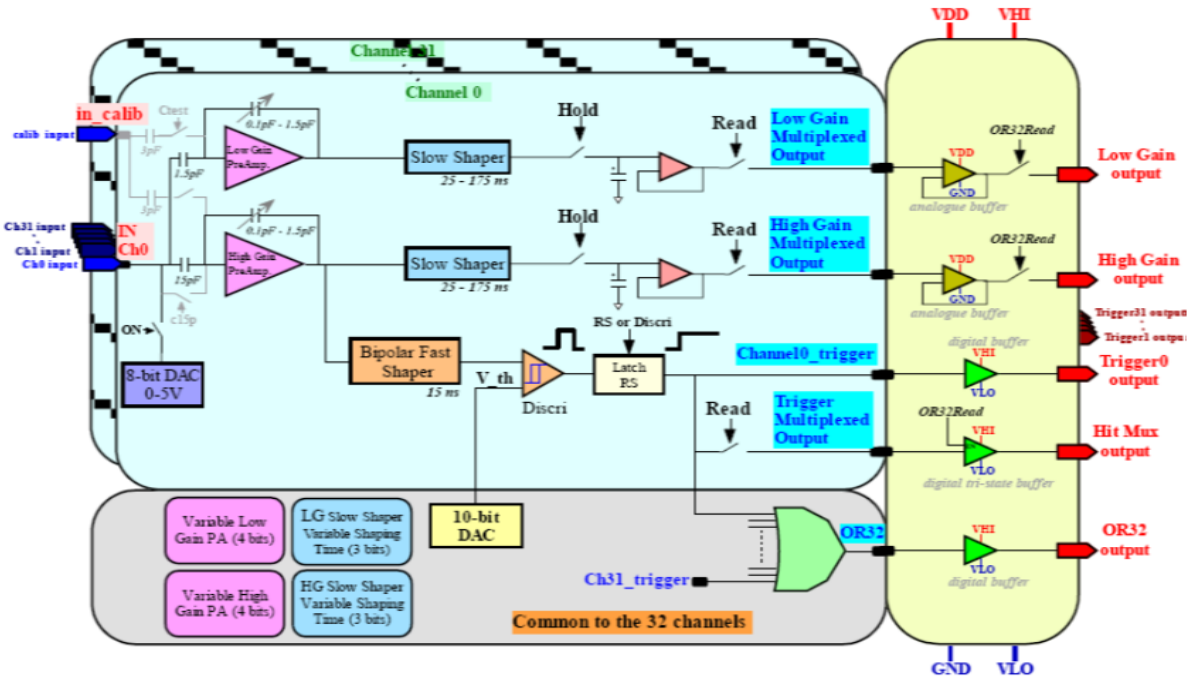

Figure 10.41: EASIROC block diagram developed by the OMEGA group of the LAL, Orsay, France

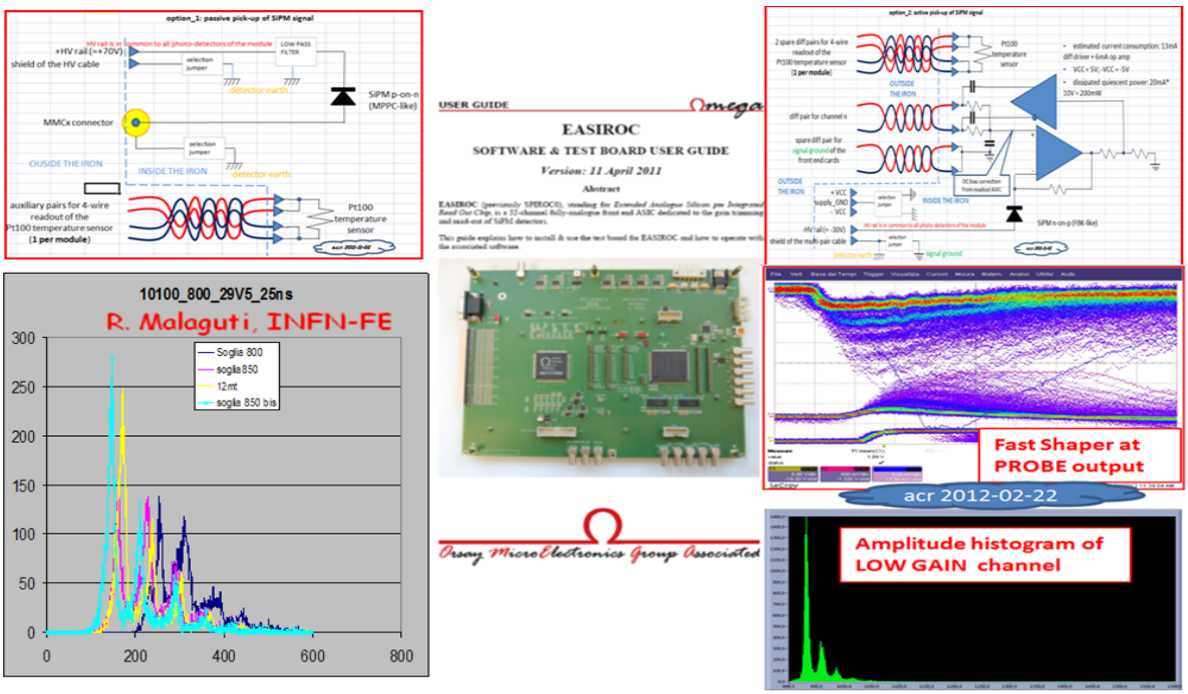

Figure 10.42: Amplitude histograms of signals processed by the EASIROC; SiPM connected with coaxial cables up to 12 m (left option) and with one differential pair of a high density cable 8 m long (right option)

- one threshold setting DAC with a resolution of at least $\frac{1}{4}$ of the single photon response signal and a linear range not larger than $\frac{1}{4}$ of the shaper linear dynamic range
- a configurable test pulse injection circuits
- a slow control interface logic: a simple serial protocol should be implemented in order to perform write and non destructive readback to/from all register controlling the ASIC's programmable features
- a clock interface unit: to avoid the need of on-chip PLLs the ASIC will receive an LVDS clock with a frequency multiple of the Super$B$ clock; the timing unit will derive from it all on-board timing signals; a suitable fast reset signal input should also be foreseen
- a trigger primitives generator: a LUT based block combining signals from a programmable set of the on-chip comparators and driving one or two trigger outputs
- SEU protection through TMR or Hamming coding for all key registers and state machines in the ASIC

and a set of application specific features such as:

- a configurable latency buffer: a dual ported memory whose width would be equal to the number of channels and whose depth would be determined by the trigger latency time interval. The constant (but configurable) offset between the write pointer and the read pointer would equal the trigger latency time expressed in terms of Super$B$ clock periods
- a trigger interface: a trigger matching logic would detect a trigger pulse from the experiment, wait for the relevant data to be extracted from the latency buffer and forward the trigger-matched data packet to the output serializer
- a set of low power serializers clocked by the input clock (which has a pace multiple of the experiment clock) needed to transfer the trigger matched data to the downstream "data collector" units. Serial output data could be 8b/10b encoded to allow the usage of AC coupled transmission links requiring DC-balancing

The features listed above are differentiated into a first set, mainly analog, and a mainly digital second set to point out that it might be convenient to implement the two lists of functions in two different ASICs, to increase the flexibility of the overall system. Figure 10.43 presents a block diagram of the new IFR readout ASIC and its connection to the SiPMs in the detector module; an IFR ASIC with a modularity of 32 channels would be able to readout all SiPMs in one module of the barrel. As shown in the inlay of figure 10.43 a ribbon-coaxial cable, mass terminated to a high density connector, could be used to carry the signals from the sensors to the IFR readout ASICs and the ancillary components on the IFR front end cards. At the right side of the IFR ASIC diagram the picture shows the input and output ports for the connections between the IFR ASIC and the downstream "data merger" cards.

Location of the front end stages of the IFR readout system The SiPMs would be installed, in the baseline design, directly on the scintillator bars and thus distributed at different locations inside the modules. The baseline design foresees, instead, the installation of the ASIC-based front end stages outside the modules, at the closest non-inaccessible locations. The reason behind this choice is that even if we were to install the front end ASICs inside the modules we would not still be able to directly connect (in order to minimize the signal/noise ratio) the SiPMs to the ASICs but, in turn, we would make it more difficult to remove the heat dissipated by the front end and we would make it impossible to access the front end cards, to replace faulty ones for instance, without disassembling large parts of the IFR system. Figure 10.44 is a detail of the IFR barrel which

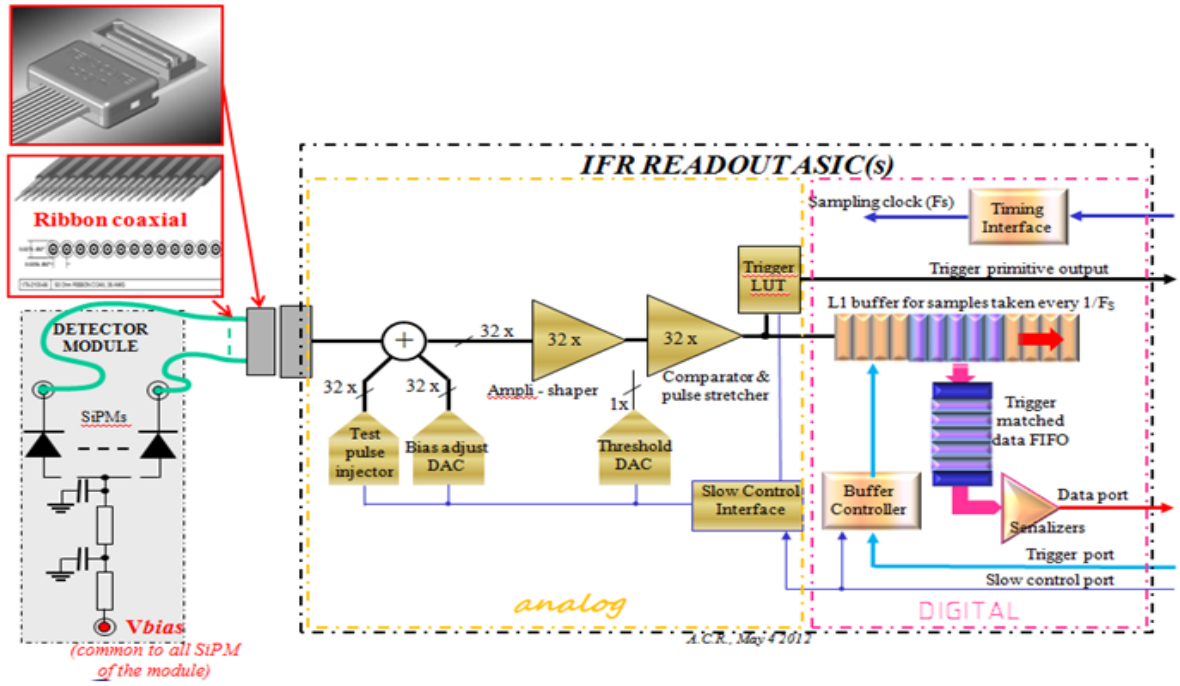

Figure 10.43: Block diagram of the IFR readout ASIC

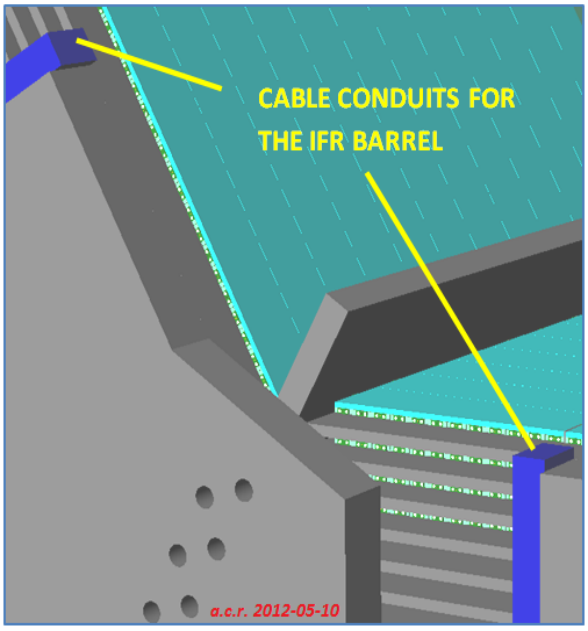

Figure 10.44: The IFR cable conduits for 2 sextants

shows the position of two of the 5" x 3" conduits through which the IFR detector signal and power cables are routed.

The printed circuit boards for the front end stages of the IFR signal processing chain could be located in these cable conduits; they would be accessible, if needed, without removing structural elements of the IFR structure. Figure 10.45 shows a section of one IFR cable conduit with a stack of 4 boards in evidence. Each IFR front end board could host 2 ASICs with 32 input channels each and since the IFR modules in the barrel are equipped with 32 SiPM at most, a stack of 3 to 4 IFR front end cards can handle all SiPMs installed in an active layer; 9 active layers are foreseen in the IFR detector. All signals to and from the 2 front end ASICs on a board are coming from the "data merger" cards downstream, physically located as close as possible to the end of the cable conduit emerging from the IFR, as illustrated in the next paragraph. The interconnection cables are shown on the right side of the figure: they are double shielded, 17 pair, Amphenol SpectraStrip part number 425-3006-034 fitted with connectors by KEL (part no. KEL 8825E-034-175D); the mating connectors on the front end and the data merger PCBs are KEL 8831E-034-170LD. Not shown in figure 10.45 are the power cables for the SiPM bias

(one common bias voltage per detector module) and for the front end card supply voltage.

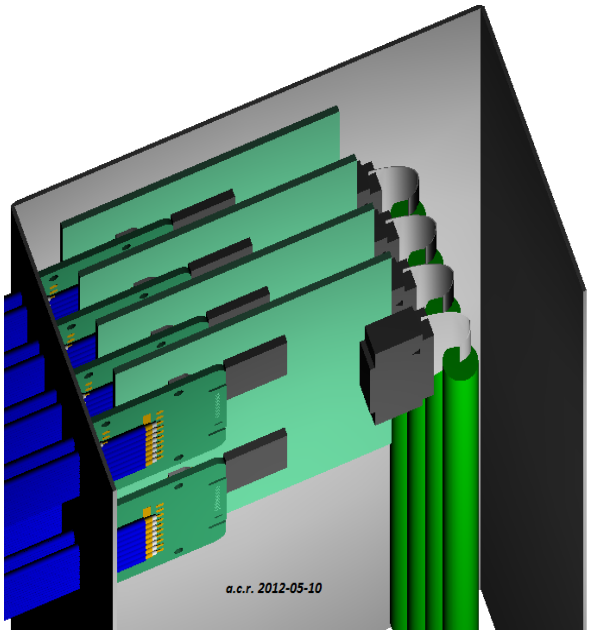

Figure 10.45: Detail of front end cards installed in the IFR cable conduit

The cable conduits have a big enough cross-section to accommodate all boards and cables needed for the 9 active layers of each barrel sextant. Not shown in the picture are also the copper pillars which are foreseen to build a thermal conduction path from the IFR front end card to the IFR steel, to which the cable conduit is fastened. If individual coaxial cables were used to carry the SiPM signals instead of ribbonized coaxial cables, then the signal cables from the module could be soldered onto a suitable interface PCB as shown in figure 10.46. The multi coaxial assembly shown in this 3D drawing features a SAMTEC QSE-20-01-F-D high density connector which mates to a QTE-020-01-F-D installed on the IFR front end PCB.

The description above concerns the instrumentation of the barrel section of the IFR detector. Figure 10.47 shows a perspective view of a pair of endcaps: the yellow callouts indicate the openings in the side lining steel through which the signal and power cables for the detector modules can be routed. The signal cables emerging from these openings are routed to the crates indicated by the red callouts. For the endcap section of the IFR, the front end cards carrying the IFR read out ASIC could be installed directly in the crate and connected to the "data merger" boards through the crate's backplane interconnections.

The IFR "data merger" crates The "data merger" crates are interfaced to the Super*B* FCTS (Fast Control and Timing System) and ECS (Experiment Control System) from which they receive and execute the commands controlling the data acquisition and the detector configuration respectively. The data merger units also collect the trigger matched data from the front end cards and merge the input streams into the output packets sent, via the high speed optical data links, to the SuperB ROM (Read-Out Modules). Figure 10.48 shows the main functions performed by the units installed in a data-merger crate:

- FCTS interface: the key element of this functional unit is the FCTS receiver module which is linked via optical fiber to the Super*B* Fast Control and Timing System (FCTS). The FCTS interface unit fans out to the IFR front end cards the timing (clock and reset) and the trigger commands decoded by the "receiver of the FCTS protocol" block
- Muon trigger module: this unit receives the trigger primitives generated by the IFR

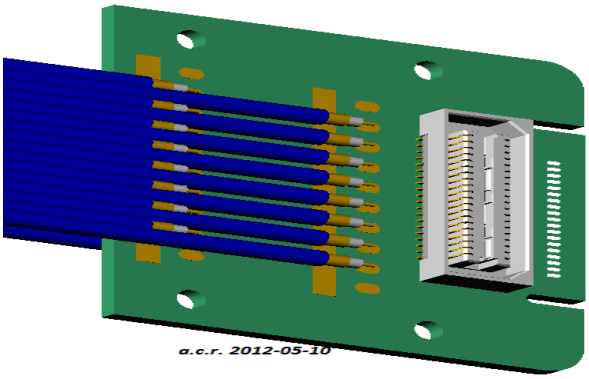

Figure 10.46: Detail of the multi coaxial connector assembly

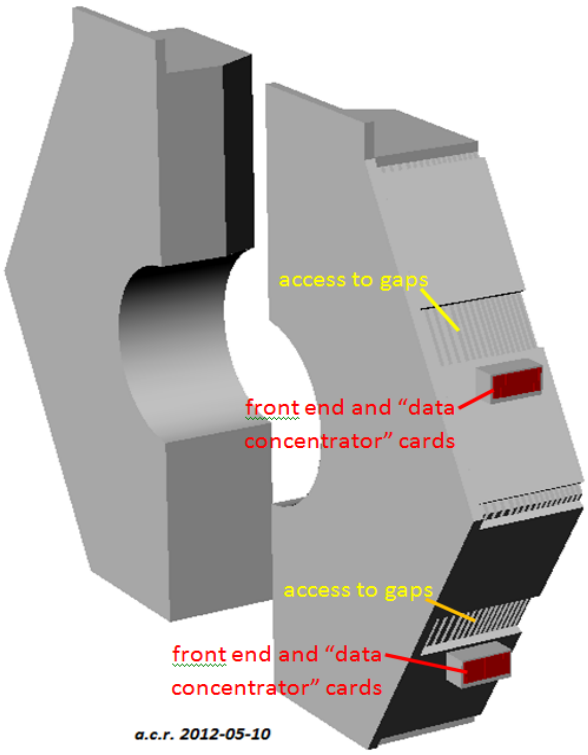

Figure 10.47: Perspective view of IFR endcaps

front end cards and combines them to generate a muon trigger for local debugging purposes

- data link: each data-merger crate is supposed, according to the baseline design, to receive and combine the serial streams of trigger matched data coming from the front end cards connected to ir and to drive a suitable number of high speed optical data links (4 for the barrel section, 2 for the endcap ones) to the Read Out Modules (ROM). A suitable modularity could be of 2 ouput data link per "data merger" board; this functional unit will exploit the common TX link driver module to reliably send data to the ROM, even in the radiation environment of the IFR

- ECS interface: the key element of this functional unit is the ECS receiver module, which is linked via optical fiber to the Super*B* Experiment Control System (ECS). The ECS unit translates commands and status information back and forth between the ECS system and the serial configuration controllers implemented in the front end ASICs

For the endcap section of the IFR the physical links between the front end and the data merger boards consist of the differential lines provided by the backplane in which the front end and the data-merger units are installed. An ATCA or Micro-TCA crate [39] provide a large number of such interconnection resources and the IFR "data merger" crates could conveniently conform to one of these TCA specifications.

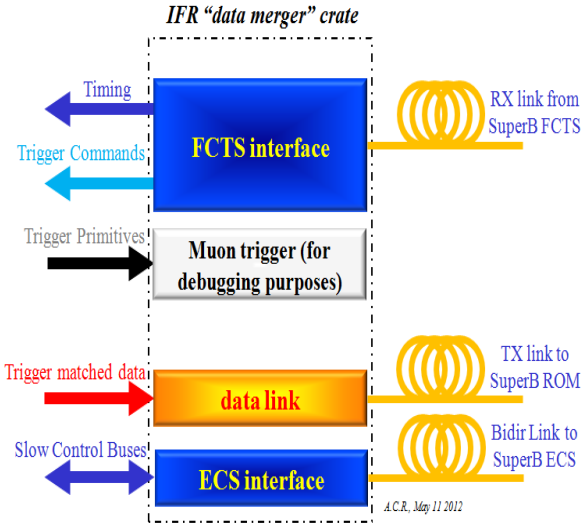

Figure 10.48: Main functions performed by the electronic units in the data-merger crate

Because of the Super*B* radiation environment it is likely that in the IFR "data merger" crates the standard xTCA IPM ("intelligent platform management") controller will be replaced by some ad-hoc interface card interfaced to the Super*B* ECS. The power supply units of the IFR data merger crate would have to be radiation tolerant or simply be installed at a larger distance from the crates; the xTCA crates integrated "power entry modules" are fit to both options. The xTCA fans will have to be tested

for operation in a radiation environment or replaced with qualified units; the convection cooling specification could be somewhat relaxed, on the other hand, since the data merger crates will most likely dissipate much less than the allowed 150W/200W per slot. Figure 10.49 shows the proposed location for one of the barrel "data merger" crates.

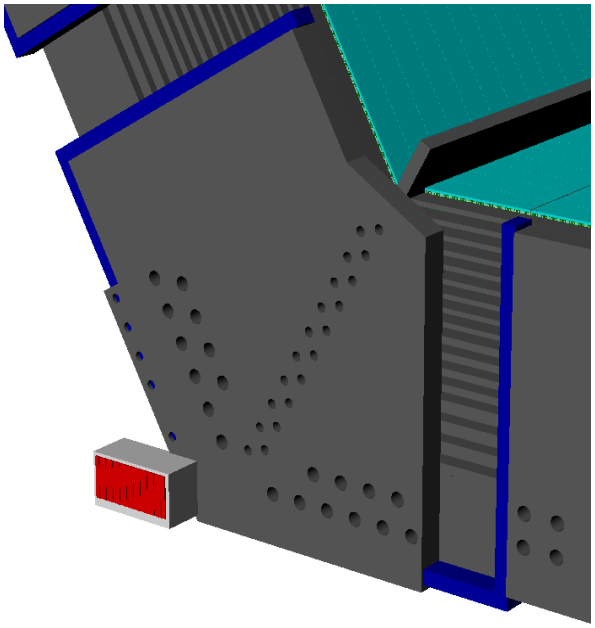

Figure 10.49: The location of one of the 6 data merger crates for the barrel

Two other such crates would be placed at 120° on the forward end of the barrel while three crates will be located in a similar arrangement at the backward end of the barrel. Each "data merger" crate serves two sextants.

Services needed for the IFR readout in the experimental hall The elements of the IFR readout system, from the detector on, need to be properly powered, monitored and cooled. This paragraph summarizes the main requirements for a readout system built according to the baseline design:

- "HV" SiPM supply: since the SiPMs are handled in groups of 32 by the front end ASICs which set the individual correction to the SiPM bias, it is preferable to bias each group of 32 SiPMs from a single "high side" supply channel. The IFR need then 384 programmable "HV" supply channel for the barrel and 324 for the endcaps, for a total of 708 "HV" independent supply voltages. An "HV" supply channel should feature: a programmable (with at least 10 bit resolution) output voltage ranging from 0 to 100V (actual range and polarity depend on the final SiPM technology chosen) and a current compliance of 25mA. The power dissipated by the SiPMs in the whole IFR under nominal operating conditions is of the order of a few tens of Watts

- "LV" front end cards supply: in the baseline design a front end card hosts two ASICs, powered at 3.3V and drawing 50mA each , and, eventually, one FPGA powered at 3.3V and drawing about 150mA. If optional ancillary opamp stages are installed, these would draw, for each group of 32 channels, a current of 350mA from both the + and - 3.3V supply rails. In summary the current consumption for a front end card would be: 600mA@+3.3V, 350mA@-3.3V, resulting in a total power consumption of about 1.6W for a 32 channel group. The IFR would then need 354 + 354 "LV" supply channels with 1A compliance and +3.3V and -3.3V output voltage respectively. Lower core voltages for the ASIC could be derived on-board by means of low-drop out regulators; the radiation tolerance of suitable LDO regulators is being characterized

- cooling: the temperature of the IFR steel should be controlled to within +/-2 degrees, as it was for BaBar; the design of the barrel cooling system should then take into account the estimated 1140W dissipated in total by the front end stages of the IFR barrel and endcap electronics.

10.8 Final assembly and installation

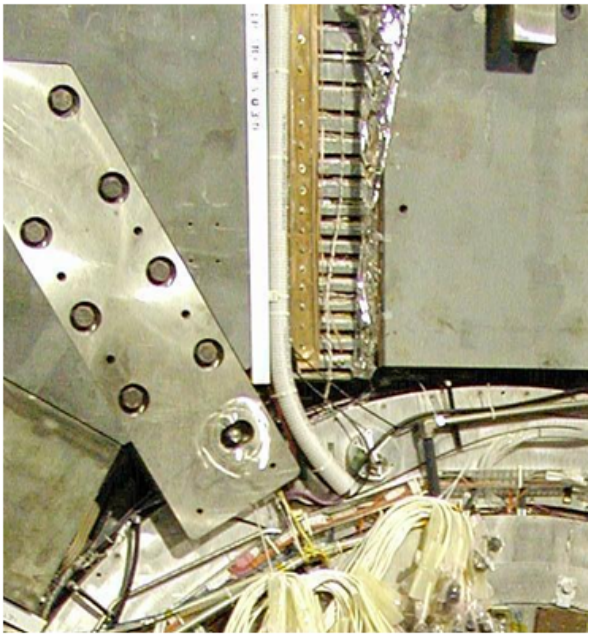

Figure 10.50: A picture from *BABAR* showing one of the elements of the cooling system for the IFR steel

Benettoni, Carassiti (1, 2 pages)

10.9 ES&H issues

10.10 Structure of the IFR group

10.11 Cost and schedule

Bibliography

[1] C. Amsler *et al.* (Particle Data Group), Phys. Lett. B **667**, 1 (2008).

[2] B. Aubert *et al.* (*BABAR* Collaboration), *The BABAR Detector*, Nucl. Instrum. Methods Phys. Res., Sect. A **479**, 1 (2002) [arXiv:hep-ex/0105044].

[3] MINOS Collaboration, *The MINOS Technical Design Report*, NuMI Note, NuMI-L-337.

[4] Bicron specs @ http://www.detectors.saint-gobain.com/fibers.aspx; Kuraray specs @ http://www.df.unife.it/u/baldini/superB/Kuraray.pdf.

[5] Flavio Dal Corso, *"Studies of SiPM @ Padova: Neutrons irradiation at LNL 9th, 13th Oct 2009"*, presented at the XI SuperB General Meeting LNF, Dec. 1st 2009

[6] M.Angelone, M.Pillon, R.Faccini, D.Pinci, W.Baldini, R.Calabrese, G.Cibinetto, A. Cotta Ramusino, R.Malaguti, M.Pozzati, *"Silicon photo-multiplier radiation hardness tests with a beam controlled neutron source"*, Nuclear Instruments and Methods in Phys. Res. A623 (2010) 921926

[7] Valentina Santoro, *"IFR Background Report"*, presented at the 3rd SuperB Collaboration Meeting, Frascati, March 21 2012

[8] Nicoleta Dinu, Pierre Barrillon, Cyril Bazin, Nicola Belcari, Maria Giuseppina Bisogni, Sylvie Bondil-Blin, Maurizio Boscardin, Vincent Chaumat, Gianmaria Collazuol, Christophe De La Taille, Alberto Del Guerra, Gabriela Llos, Sara Marcatili, Mirko Melchiorri, Claudio Piemonte, Veronique Puill, Alessandro Tarolli, Jean-Francois Vagnucci, Nicola Zorzi, *"Characterization of a prototype matrix of Silicon PhotoMultipliers"*, NUCLEAR INSTRUMENTS & METHODS IN PHYSICS RESEARCH SECTION A, vol. 610, n. 1, 2009, pp. 101-104

[9] G. Llos, N. Belcari, M. G. Bisogni, G. Collazuol, S. Marcatili, S. Moehrs, F. Morsani, C. Piemonte, A. Del Guerra, *"Energy and Timing Resolution Studies With Silicon Photomultipliers (SiPMs) and 4-Pixel SiPM Matrices for PET"*, IEEE TRANSACTIONS ON NUCLEAR SCIENCE, vol. 56, n. 3, 2009, pp. 543-548

[10] link to the *AdvanSiD* page on FBK SiPM:http://www.advansid.com/products/silicon-photomultiplier

[11] link to the *Hamamatsu* page on MPPC: http://jp.hamamatsu.com/products/sensor-ssd/4010/indexen.html

[12] link to the *sensL* page on SPM: http://sensl.com/products/silicon-photomultipliers/microsl/

[13] *"SuperB progress report"* Detector, E. Grauges et al. [SuperB collaboration], arXiv:1007.4241, 2010)

[14] Piotr Dorosz, Mateusz Baszczyk, *"Thermal Stabilization of Silicon Photomultiplier measurement system for IFR"* presented at the "Instrumentation for Muon and K0L Identification at Super Flavor Factories" workshop in Krakow, Poland 6-10 September 2012

[15] Gianluigi Cibinetto, *"Something about the prototype"*, SuperB Workshop and Kick Off Meeting, Elba, May 31 2011

[16] Gianluigi Cibinetto, *"Beam Test: data for analysis"*, I SuperB meeting, London, Sep 15 2011

[17] Valentina Santoro, *"IFR Background Report"*, III SuperB meeting, LNF-Frascati, Mar 21 2012

[18] Valentina Santoro, *"IFR Background Report"*, presented at "Instrumentation for Muon and K0L Identification at Super Flavor Factories" workshop in Krakow, Poland, Sep 7 2012

[19] Pierre Jarron, CERN 1211 Geneva 23 Switzerland, *"Radiation tolerant electronics for the LHC experiments"*, Proceedings of the 4th Workshop on Electronics for LHC Experiments, Rome, Sept 1998, p. 7

[20] Federico Faccio, CERN 1211 Geneva 23 Switzerland, *"Radiation effects in devices and technologies"*, IN2P3 school, May 2005

[21] *"ATLAS Policy on Radiation Tolerant Electronics: ATLAS Radiation Tolerance Criteria"*, http://atlas.web.cern.ch/Atlas/GROUPS/FRONTEND/WWW/RAD/RadWebPage/ATLASPolicy/Appendix_1.pdf

[22] W. Dabrowski (AGH University of Science and Technology, Krakow, Poland), *"Challenges and benefits of designing readout ASICs in advanced technologies"*, Nuclear Instruments and Methods in Physics Research A 579 (2007) pp. 821-827

[23] M.Angelone, M.Pillon, R.Faccini, D.Pinci, W.Baldini, R.Calabrese, G.Cibinetto, A.Cotta Ramusino, R.Malaguti, M.Pozzati, *"Silicon photo-multiplier radiation hardness tests with a beam controlled neutron source"*, Nuclear Instruments and Methods in Physics Research A 623 (2010) pp. 921-926

[24] G. Cibinetto, G. Tellarini, *"Preliminary results from the neutron irradiation test at Gelina"*, presented at "Instrumentation for Muon and K0L Identification at Super Flavor Factories" workshop in Krakow, Poland, Sep 7 2012

[25] Flavio Dal Corso (INFN Padova), *"Studies of SiPM @ Padova: Neutrons irradiation at LNL 9-13 Oct 2009"*, XI SuperB General Meeting , LNF, Frascati, Dec. 1 2009

[26] Enrico Feltresi (INFN Padova), *Neutron Damage on SiPMs studies at LNL*, XV SuperB General Meeting Caltech, Pasadena CA, USA, Dec. 14 2010

[27] Flavio Dal Corso (INFN Padova), *Status of SiPM; studies @ Padova*, XVI SuperB General Meeting , LNF, Frascati, Apr. 4 2011

[28] A. Cotta Ramusino (INFN Ferrara), *SuperB IFR electronics: update*, 2nd SuperB General Meeting , LNF, Frascati, Dec. 15 2011

[29] Orsay MicroElectronics Group Associated (OMEGA) (LAL, Orsay, France), *EASIROC DATASHEET Version: 5*, April 2011

[30] Orsay MicroElectronics Group Associated (OMEGA) (LAL, Orsay, France), *EASIROC SOFTWARE & TEST BOARD USER GUIDE Version: 11*, April 2011

[31] James W. Meadows, Engineering Physics Division, Argonne National Laboratory, Argonne, Illinois, USA, *The ^{9}Be(d, n) thick-target neutron spectra for deuteron energies between 2.6 and 7.0 MeV*, Nuclear Instruments and Methods in Physics Research A 324 (1993) pp. 239-246

[32] A. Cotta Ramusino (INFN Ferrara), *SuperB IFR electronics: update on prototype electronics and IFR_DAQ*, XII SuperB Workshop - LAPP Annecy, Mar. 17 2010

[33] E. Grauges et al. [SuperB collaboration], *SuperB progress report – Detector*, arXiv:1007.4241,2010

[34] A. Cotta Ramusino (INFN Ferrara), *SuperB IFR electronics: update*, 3rd SuperB meeting, LNF, Frascati, Mar. 13 2012

[35] R. Mos, J. Barszcz, M. Jastrzb, W. Kucewicz, J. Młynarczyk, E. Raus, M. Sapor, *Front-End electronics for Silicon Photomultiplier detectors*, Electrical Review 11a (2010) pp. 79-83

[36] A.Baschirotto, G.Cocciolo, M.De Matteis, A.Giachero, C.Gotti, M.Maino, G.Pessina, *A FAST AND LOW NOISE CHARGE SENSITIVE PREAMPLIFIER IN 90 nm CMOS TECHNOLOGY*, Journal of Instrumentation, Jinst, V 7 C01003 pp 1-8 2012.

[37] G. Mazza et al. (Dipartimento di Fisica - INFN Torino), *A CMOS 0.13um Silicon Pixel Detector Readout ASIC for the PANDA experiment*, 2012 JINST 7 C02015 doi:10.1088/1748-0221/7/02/C02015

[38] G. Dellacasa et al. (Dipartimento di Fisica - INFN Torino), *A 130 nm ASIC prototype for the NA62 Gigatracker readout*, Proc. of the Int. Workshop on Semiconductor Pixel Detector for Particles and Imaging (Pixel 2010), Nucl. Instr. and Meth. in Physics Research, A 650 (2011) pp. 115-119

[39] A. La Rosa et al., *Ionizing radiation effects on a 64-channel charge measurement ASIC designed in CMOS 0.35 um technology*, Nucl. Instr. and Meth. in Physics Research A 593 (2008) pp. 619-623

[40] PICMG, AdvancedTCA PCI Express PICMG 3.4 Specification, May 2003

[41] M. Baszczyk, P. Dorosz, S. Głb, W. Kucewicz, M. Sapor, *Four channels data acquisition system for silicon photomultipliers*, Elektronika 12 (2011) pp. 28-31

[42] Paolo Carniti, Andrea Giachero, Claudio Gotti, Matteo Maino, Gianluigi Pessina, *An introduction to CLARO: A fast Front-End ASIC for Photomultipliers*, 2nd SuperB Collaboration Meeting, LNF Frascati, Dec 15 2011

[43] Mateusz Baszczyk, Piotr Dorosz, *Characterization of RAPSODI ASICs after Irradiation*, presented at "Instrumentation for Muon and K0L Identification at Super Flavor Factories" workshop in Krakow, Poland, Sep 7 2012

[44] Angelo Cotta Ramusino, Bartomiej Rachwa, *CLARO and RAPSODI ASICs irradiation at the CN facility of the INFN-LNL*, presented at "Instrumentation for Muon and K0L Identification at Super Flavor Factories" workshop in Krakow, Poland, Sep 7 2012

[45] M. Andreotti *et al.*, *A Muon Detector based on Extruded Scintillators and GM-APD Readout for a Super B Factory*, Nuclear Science Symposium Conference Record, 2009. NSS '09. IEEE(2009).

[46] B.L. Berman, S.C. Fultz, Rev. Mod. Phys. (1975) 713

[47] *Standard practice for Characterizing Neutron Energy Fluence Spectra in Terms of an Equivalent Mono-energetic Neutron Fluence for Radiation Hardness Testing of Electronics"*, ASTM E 722 -93

[48] G. Lindstrom *et al.* [ROSE Collaboration], Nucl. Instrum. Meth. A **465**, 60 (2000).

[49] Nuclear Instruments and Methods in Physics Research A 426 (1999) 1?15

[50] M. Angelone *et al.*, *Silicon Photo-Multiplier radiation hardness tests with a beam controlled neutron source*, arXiv:1002.3480 [physics.ins-det].

11 Magnet and Flux Return

Fabbricatore/Wisniewski Pages ?

12 Electronics, Trigger, Data Acquisition and Online

Breton/Marconi/Luitz Pages : 7-10

12.1 Open Issues for Pisa Meeting

- Finalize agreements on clock distribution and use of mezzanines
- Review of the WBS for ETD and Online. Make sure subdetectors will update their cost and labor estimates.
- Discussion of the SEU rates and "system architecture for error handling" and recovery from loss-of-(c)lock in FEE
- Review and discussion of the power supply section
- Remaining R&D
- Discuss ETD/Online org structure (for TDR)
- Review of subdetector contributions to ELEX chapter

12.2 Architecture Overview

The Super*B* [1] Electronics, Trigger, Data acquisition and Online system (ETD) comprises the Level-1 trigger, the event data chain, and their support systems. Event data corresponding to accepted Level-1 triggers move from the Front-End Electronics (FEE) through the Read-Out Modules (ROMs), the network event builder, the High Level Trigger (HLT) to a data logging buffer where they are handed over to the offline for further processing and archival. ETD also encompasses the hardware and software components that control and monitor the detector and data acquisition systems, and perform near-real-time data quality monitoring and online calibration.

The system design takes into account the experience from running *BABAR* [2] and building the LHC experiments [3], [4], [5]. To minimize the complexity of the FEEs and the number of data links, the detector side of the system is synchronous, and the readout of all subdetectors is triggered by a fixed-latency first-level trigger. Custom hardware components (e.g. specialized data links) are only used where the requirements cannot be met by off-the-shelf commercialy available components (e.g. Ethernet). Radiation levels are significantly higher than in *BABAR*, making it mandatory to design radiation-tolerant on-detector electronics and links. Fig. 12.1 shows an overview of the trigger and the event data chain:

A first-level hardware trigger processes dedicated data streams of reduced primitives from the sub-detectors to provide trigger decisions to the Fast Control and Timing System (FCTS).

The FCTS is the central bandmaster of the system; it distributes the clock and readout commands to all elements of the architecture, and initiates the readout of the events in the detector FEE. In response to readout requests, the FEE send event fragments to the ROMs which perform a first stage internal event build and send the partially constructed events to the HLT farm where they are combined into complete events, and processed by the HLT which reduces the amount of data to be logged permanently by rejecting uninteresting events.

The trigger, data acquisition and support components of the ETD system are described

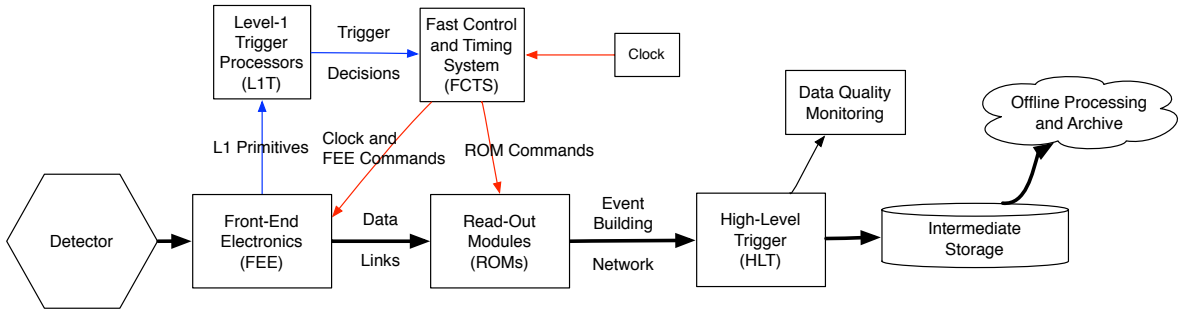

Figure 12.1: Overview of the Trigger and Data Chain

in this chapter, subdetector electronics, power supplies, grounding and shielding, and the cable plant are described in the next chapter.

12.2.1 Trigger Strategy

The *BABAR* and Belle [6] experiments both chose to use "open triggers" that preserved nearly 100% of $B\overline{B}$ events of all topologies, and a very large fraction of $\tau^+\tau^-$ and $c\bar{c}$ events. This choice enabled very broad physics programs at both experiments, albeit at the cost of a large number of events that needed to be logged and reconstructed, since it was so difficult to reliably separate the desired signals from the $q\bar{q}$ ($q = u, d, s$) continuum and from higher-mass two-photon physics at trigger level. The physics program envisioned for Super$B$ requires very high efficiencies for a wide variety of $B\overline{B}$, $\tau^+\tau^-$, and $c\bar{c}$ events, and depends on continuing the same strategy, since few classes of the relevant decays provide the kinds of clear signatures that allow the construction of specific triggers.

All levels of the trigger system are designed to permit the acquisition of prescaled samples of events that can be used to measure the trigger performance.

The trigger system consists of the following components [1]:

Level 1 (L1) Trigger: A synchronous, fully pipelined L1 trigger receives continuous data streams from the detector independently of the event readout and delivers readout decisions to the FCTS with a fixed latency. Like in *BABAR*, the Super$B$ L1 trigger operates on reduced-data streams from the drift chamber and the calorimeter.

High Level Triggers (HLT) — Level 3 (L3) and Level 4 (L4): The L3 trigger is a software filter that runs on a commodity computer farm and bases its decisions on specialized fast reconstruction of complete events. An additional "Level 4" filter may be implemented to reduce the volume of permanently recorded data if needed. Decisions by L4 would depend on a more complete event reconstruction and analysis. If the worst-case per-event performance of the L4 reconstruction algorithms does not meet the near-real-time requirements of L3, it might become necessary to decouple L4 from L3 – hence, its designation as a separate trigger stage.

12.2.2 Trigger Rate and Event Size Estimation

SL + UM

The Super$B$ L1-accept rate design standard of 150 kHz is based on an extrapolation from *BABAR* (see the Super$B$ CDR [1] for more detail). The *BABAR* Level-1 physics configuration produced a trigger of approximately 3 kHz at a luminosity of 10^{34} cm^{-2}sec^{-1}, however changes in background conditions produced large variations in this rate. The *BABAR* DAQ system performed well, with little dead time, up to approx-

[1] While at this time we do not foresee a "Level 2" trigger that acts on partial event information in the data path, the data acquisition system architecture would allow the addition of such a trigger stage at a later time, hence the nomenclature.

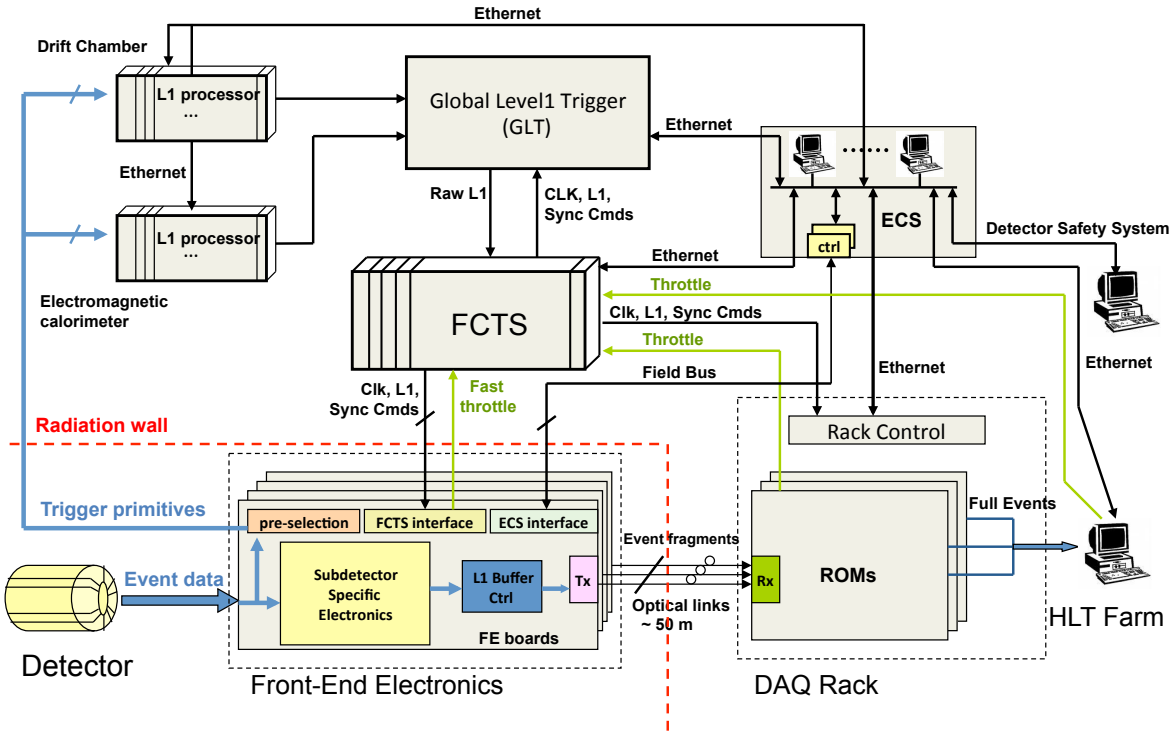

Figure 12.2: Overview of Level-1 Trigger, FCTS, FEE and ROMs.

imately 4.5 kHz. This 50% headroom was very valuable for maintaining stable and efficient operation and will be retained in Super$B$.

In *BABAR* the offline physics filter's output corresponded to a cross-section of approximately 20 nb and included a highly efficient Bhabha veto. We take this as an irreducible baseline for an open hardware trigger design; in fact this is somewhat optimistic since the offline filter used results from full event reconstruction. The accepted cross-section for Bhabhas in Super$B$ is approximately 50 nb (Note: to be checked). At the Super$B$ design luminosity of 10^{36} cm^{-2}sec^{-1} these two components add up to 70 kHz L1-accept rate without backgrounds. Scaling the beam backgrounds from *BABAR* obtain 30 kHz of background-related L1 accepts, resulting in a total of 100 kHz. Without a Bhabha veto at L1 (which is not part of the Super$B$ baseline trigger design) this is the minimum rate the readout system has to handle. By adding a *BABAR*-like reserve of 50% to both accommodate the possibility of higher backgrounds than design (e.g. during machine commissioning), and the possibility that the machine exceeds its initial design luminosity, we set the the Super$B$ design rate at 150 kHz.

The event size estimate still has uncertainties. Raw event sizes (between front-end electronics and ROMs) are understood well enough to determine the number of data links required. However, neither the algorithms for data size reduction (such as zero suppression or feature extraction) that can be safely employed in the HLT or possibly in the ROMs, nor their specific performance for event size reduction are yet known. Based on initial estimates for the SVT

and the calorimeter, we predict an event size of 500 kbyte before the HLT that can be reduced in the HLT to 200 kbyte for permanent logging.

12.2.3 Dead Time and Buffer Queue Depth Considerations

The readout system is required to handle the maximum average rate of 150 kHz, and to absorb the expected instantaneous rates, both without incurring dead time of more than 1% under normal operating conditions at design luminosity[2]. Dead time is generated and managed centrally in the FCTS based on feedback ("fast throttle") from the FEE: The FCTS drops valid L1 trigger requests when at least one FEE indicates that these would exceed its instantaneous or average rate capability. The ROMs and the event builder also provide feedback ("slow throttle") to slow down the trigger if they cannot keep up with the L1 accept rate.

The required ability to handle the maximum average rate determines the overall readout system bandwidth; the instantaneous trigger rate requirement affects the FCTS, the data extraction capabilities of the front-end-electronics, and the depth of the de-randomization buffers.

The minimum time interval between bunch crossings at design luminosity is about 2.1 ns—so short in comparison to detector data collection times that we assume "continuous beams" for the purposes of trigger and FCTS design: The inter-event time distribution is exponential and the instantaneous rate is only limited by the capability of the L1 trigger to separate events in time. Therefore, the burst handling capability of the system (i.e. the derandomization buffer size in the FEEs) is determined by the average L1 trigger rate, minimum time between L1 triggers, and the average data link occupancy between the FEEs and the ROMs. Figure 12.3 shows the result of a simple simulation of the FCTS and the FEE of a typical subdetector: The minimum buffer depth that is required to keep the event loss due to a full derandomization buffer below 1% is plotted as a function of the average data link utilization.

In Super*B*, we will target a link utilization of 90% which will require the derandomizer buffers to be able to hold a minimum of 10 events. It is very important to understand that there is no contingency in the target link utilization — all system-wide contingency is contained in the trigger rate headroom.

Additional derandomizer capacity is be required to absorb triggers generated while the fast throttle signal is propagated from the CFEE to the FCTS.

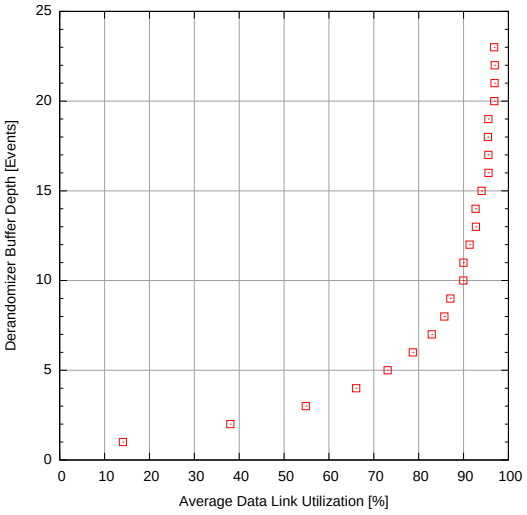

Figure 12.3: Minimum derandomizer buffer depth required to keep the event loss due to "derandomizer full" below 1% as a function of the average data link utilization.

12.3 Electronics in the SuperB Radiation Environment

DB + ?

The high luminosity of the machine and the presence of numerous massive elements close to the interaction region will generate much higher levels of radiation than in *BABAR*, where radiation effects on digital read-out electronics had

[2] The 1% dead time specification does not include events that are lost due to individual sub-detector's intrinsic dead times or the L1 trigger's limitations in separating events that are very close in time.

only been observed after the introduction of FPGAs on the end plate of the drift chamber.

In Super$B$ a large flux of charged particles and photons originating from the interaction point and the beam pipes will cross the detector, and generate large numbers of secondary neutrons as well.

Therefore a common general radiation policy has been put in place at the ETD level.

Long term radiation effects are of two types (ionizing and non-ionizing), while short term effects are linked to instantaneous ionization (Single Events). Radiation levels have been simulated, and Total Ionizing Doses (TID) range from 5 kGy down to a few Gy depending on the electronics location. The neutron fluence is required to estimate the effect of the Non-Ionizing Energy Loss (NIEL) and is still under study.

Shielding of sensitive parts of the detector like electronics is a key point of the design, which has been carefully studied. However, all electronics located on the detector have to be able to handle not only the damages linked to TID and NIEL, but also to present the smallest sensitivity to Single Event Upsets (SEUs), thanks to the intensive use of mitigation techniques like triple modular redundancy (TMR) for the latches and flip-flops and of safety codes (like parity bits) for data stored in memories. All the components used will be validated for their proven capacity to handle the integrated dose and NIEL foreseen. Power supplies are also designed specifically in order to perform safely in the radiative environment. The architecture of the system has been designed in such a way to reduce as much as possible the risk of failure, especially concerning the critical elements linked to experiment control and readout. In case of failure despite all these precautions, misfunctionning will be detected, experiment control system will be immediately warned, and a fast recovery strategy will be deployed in order to limit as much as possible the dead-time due to these radiation effects.

12.4 Trigger and Event Data Chain

The systems in the trigger and event data chain manage event selection, event filtering and end-to-end data flow from the detector to the intermediate buffer.

12.4.1 Choice of Global Clock Frequency

The Super$B$ trigger and data acquisition system requires a global clock that can be distributed to all components that operate sychronously, i.e. FCTS, the L1 trigger and the subdetector FEEs.

To allow features like selective blanking of triggers for a well-defined part of the revolution of the stored beams, it is critically important that the global clock is in well defined relation with the machine RF of 476 MHz and the revolution phase of the stored beams.

In *BABAR* the global clock was generated by dividing the RF by eight, yielding a 59.5 MHz clock that was distributed to all components of the experiment. In addition, a revolution ("fiducial") signal was fed to the FCTS, giving the system knowledge of the revolution phase of the stored beams.

For Super$B$ we will use the same parameters and distribute a 59.5 MHz clock throughout the ETD system.

Question: Would it be still possible to change this to divide by 12 instead and distribute the resulting 39 2/3 MHz clock. This would allow us to use many components and system designs that were developed and qualified for the 40MHz clock of the LHC experiments!

12.4.2 Level-1 Trigger

PB (+ SL?)

The baseline for the L1 trigger is to re-implement the *BABAR* L1 trigger with state-of-the-art technology. It will be a synchronous machine running at 59.5 MHz (or multiples of 59.5 MHz) that processes primitives produced by dedicated electronics located on the front-end boards or other dedicated boards of the respective sub-detector. The raw L1 decisions are sent to the FCTS which applies a throttle if necessary and then broadcasts them to

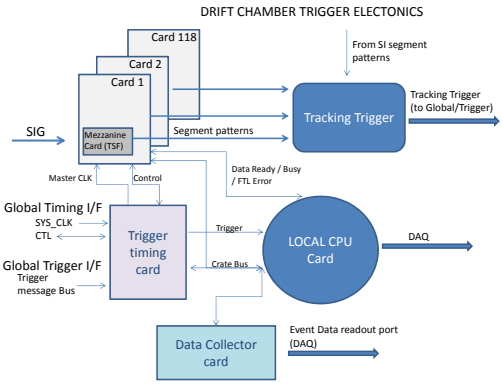

Figure 12.5: DCT Overview

the FEEs and the ROMs. The standard chosen for the crates would most likely be either ATCA for Physics (Advanced Telecommunications Computing Architecture) for the crates and the backplanes, or a fully custom architecture.

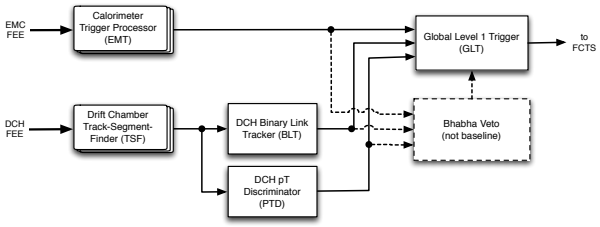

Figure 12.4: Level 1 Trigger Overview

The main elements of the L1 trigger are shown in Fig. 12.4 (see [8] for detailed descriptions of the *BABAR* trigger components):

Drift chamber trigger (DCT): The DCT consists of a track segment finder (TSF) , a binary link tracker (BLT) and a p_t discriminator (PTD). The DCT also extrapolates tracks to the IP; this allows to remove backgrounds that do not originate from the IP.

The layout of the DCT is shown in Fig. 12.5. Track finding is implemented in two stages: In the first stage, the algorithm locally searches for track segments exploiting the data available at the front-end level. The second stage links the track segments and searches for complete tracks.

Local Segment Finding: Two options are under discussion as DCH front-end (FE). In the first option time and charge are measured using FADCs and TDCs. A second option is instead based on a cluster counting technique. Granularity is 64 channels per FE in the first case and 16 channels per FE in the second. In the first case data delivered by the FE will be gathered by a single board on the FE crate and an optical link will connect the crate with the trigger crate. In the other option the DCH electronics has a modularity of 64 channels distributed on 4 contiguous radial planes. This geometry defines the super layer. Table 12.1 shows the super-layer composition for the DCH and the FE cards necessary for its data acquisition. The track segment finder is partially integrated in the DCH front-end.

The TSF will be implemented either at the crate level or at the mezzanine level; the number of optical links and TSFs will be 118 in the case of ADC/TDC-based DCH electronics or equal to the number of DCH front-end crates in the case of cluster counting. With cluster counting, data delivered by the FE will be gathered by a single board in the FE crate and sent to the trigger processor via an optical link.

Each card reads a set of super cell, and each signal will be properly stretched to accommodate at least one drift time. The TSF takes decisions at a programmable rate which can be as high as 59.5 MHz. A possible track segment is shown in Fig. 12.6.

A pattern needs 3 hits to be taken in consideration. The TSF delivers a bit stream to the following DCH stage, whose dimension depends on sampling frequency. This bit stream represents the ϕ of the segment in the super cell. These data are delivered to the trigger crate. To avoid efficiency losses a small number of contiguous channels is collected by all the neighboring cards. It is relevant in this scheme to optimize the sampling frequency as a function of track efficiency and exploited bandwidth.

Transmission links: We will use high speed serial links to deliver trigger data to the trigger

	Sl1	SL2	SL3	SL4	SL5	SL6	SL7	SL8	SL9	SL10	TOT
Planes	4	4	4	4	4	4	4	4	4	4	
Type	A	A	U	V	U	V	U	V	A	A	
n. wires	736	864	496	560	624	688	752	816	896	960	7392
n. TSF	12	14	8	9	10	11	12	13	14	15	118
n. BCD	1	1	1	1	1	1	1	1	1	1	10

Table 12.1: DCH superlayer (SL) and wire readout

crate. Therefore signal aggregation delivered by the TSF is made possible, and a single card in the trigger crate has all the data from the pertaining superlayer.

Global Tracking: A simple and efficient tracking algorithm is the Binary Link Track Finder (BLT) developed within the CLEO collaboration. This method starts from superlayer (SL) 2 and moves radially outward combining the TSFs if in the following SL one of the three contiguous TSF is active. The track length varies from the first to the last super layer. It is possible to implement a majority logic function of machine background. Track charge does not affect the algorithm and it can be implemented on programmable logic. DCT primitives are received by the DCH L1 trigger box. In this crate the optical links exploited by the DCH trigger lines are collected in such a way that each board stores the information of a single SL. A bus with a switch topology interconnects the single boards where the SL information is present with the master where all the DC TSFs are present.

Particle Counter: The BLT outputs are used to count different tracks using a multiplicity logic exploiting also isolation criteria. To define a track we can use associative memory based techniques so that in one clock cycle a pattern can be identified. The very same ASIC can in principle be used to compute the transverse momentum and the perigee parameters of the track. Track counter takes in consideration 4 SL long tracks.

Transverse Momentum: Using TSF positions and their ϕ angle it is possible to measure track multiplicity above a pre-defined threshold and their perigee parameter. The data are delivered to the GLT which on the basis of the trigger tables asserts the trigger.

Electromagnetic Calorimeter Trigger (EMT): The EMT processes the trigger output from the calorimeter to find energy clusters. From the trigger point of view the electromagnetic calorimeter in the barrel is composed of 24 (8x3) CsI (tl doped) crystal towers.

The EMT layout is shown in Fig. 12.7.

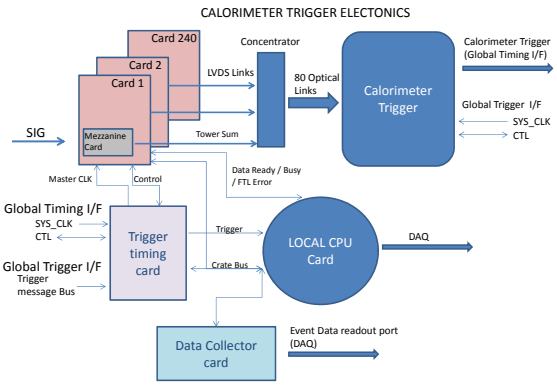

Figure 12.7: EMT Overview

The number of crystals in the barrel is 5760 this implies that the trigger box will handle 240 modules (trigger lines) in the barrel. At the moment we are thinking to divide the end-cap in 5x5 crystal tower this would imply a maximum of 60 towers. Two different strategies are under study. In the first strategy the analogic sum is computed using the information of the

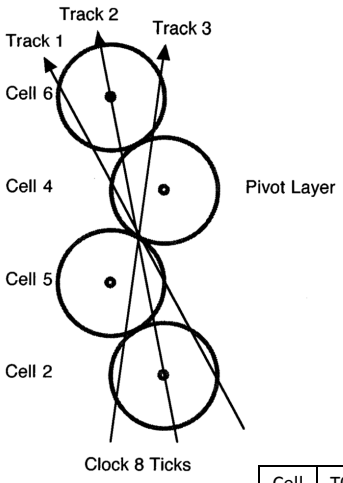

Cell	T0	1	2	3	4	T0	1	2	3	4	T0	1	2	3	4
6	0	0	0	1	2	0	1	2	3	0	0	0	0	1	2
4	0	0	0	1	2	0	0	0	1	2	0	0	1	2	3
5	0	0	0	1	2	0	0	0	1	2	0	0	1	2	3
2	0	0	0	1	2	0	1	2	3	0	0	0	0	1	2
	Track 1					Track 2					Track 3				

Cell	T0	1	2	3	4	5	6	7	8	T0	1	2	3	4	5	6	7	8	T0	1	2	3	4	5	6	7	8
6	0	0	0	0	0	1	2	3	4	0	1	2	3	4	5	6	7	0	0	0	0	0	0	1	2	3	4
4	0	0	0	0	0	1	2	3	4	0	0	0	0	0	1	2	3	4	0	0	0	1	2	3	4	5	6
5	0	0	0	0	0	1	2	3	4	0	0	0	0	0	0	1	2	3	0	0	0	1	2	3	4	5	6
2	0	0	0	0	0	1	2	3	4	0	1	2	3	4	5	6	7	0	0	0	0	0	0	1	2	3	4
	Track 1									Track 2									Track 3								

Figure 12.6: Track segment: *BABAR* vs Super*B* output bitstream. In this example we assumed to double babar samplig frequency.

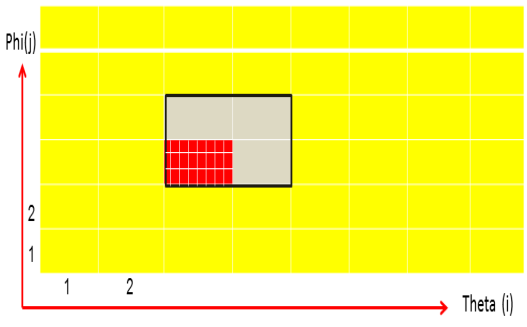

Figure 12.8: EMT trigger tower layout

same pre-amp used by the front-end. The other strategy foresees to endow each crystal with independent photon detectors (SiPm). The signal delivered by the SiPm is analogically added up at the tower level. The output can be calibrated using a look-up table and the sum can be encoded and delivered exploiting an LVDS link to an electro-optical converter shielded by radiation.

Particle Finders: Global cluster formation The energy can be released on several contiguous towers, therefore, as shown in Fig. 12.8 to assert the trigger signal we'll consider neighboring towers. Towers are scanned and their energy added if a release above a threshold of interest is exceeded in neighbouring towers.

As in Bbar, there will be 3 separate energy thresholds for clusters in the trigger: M cluster (above a low energy consistent with a minimum ionizing), G cluster (above 500-600 MeV) and cluster (electron Bhabha). The thresholds are all programmable. The Bhabha can be vetoed or pre-scaled. This algorithm will be implemented by the L1 EMT processor.

Particle Counters: Since clusters can be dynamically defined this allows to apply isolation cuts on particle definition.

L1 DCT and EMT trigger processors: A crate based on VME or ATCA technology will host L1 processors. These processors will be based on FPGA technology and have the same optical and electrical interfaces. They will differ by the firmware they run. Track finding and dynamic super-cluster definition will be implemented on the L1 processor backplane.

Global Trigger (GLT): The GLT processor combines the information from DCT and EMT (and possibly other inputs such as a Bhabha veto) and forms a final trigger decision that is sent to the FCTS. The global trigger receives the information of the detector participating to trigger definition through an optical link. The trigger can be asserted considering the information delivered by the DC and the EMC either separately or combined. This module combines the information of the detectors and compares them to pre-defined criteria. Through the use of an FPGA the trigger can be fully programmable and upgradeable.

We will study the applicability of this baseline design at Super$B$ luminosities and backgrounds, and will investigate improvements, such as adding a Bhabha veto to the L1 trigger. We will also study faster sampling of the DCH and the impact of the forward calorimeter design choice.

For the barrel EMC we will need to study how the L1 trigger time resolution can be improved and the trigger jitter can be reduced compared to BaBar. In general, improving the trigger event time precision should allow a reduction in readout window and raw event size. The L1 trigger may also be improved using larger FPGAs (e.g. by implementing tracking or clustering algorithm improvements, or by exploiting better readout granularity in the EMC).

L1 Trigger Latency: The *BABAR* L1 trigger had 12 μs latency. However, since the size, and cost, of the L1 data buffers in the sub-detectors scale directly with trigger latency, it should be substantially reduced, if possible. L1 trigger latencies of the much larger, more complex, ATLAS, CMS and LHCb experiments range between 2 and 4 μs, however these experiments only use fast detectors for triggering. Taking into consideration that the DCH adds an intrinsic dead time of about 1 μs and adding some latency reserve for future upgrades, we are currently estimating a total trigger latency of 6 μs (or less). More detailed engineering studies will be required to validate this estimate.

Monitoring the Trigger: To debug and monitor the trigger, and to provide cluster and track seed information to the higher trigger levels, trigger information supporting the trigger decisions is read out on a per-event basis through the regular readout system. In this respect, the low-level trigger acts like just another subdetector.

12.4.3 Fast Control and Timing System

DC + CB + DB + SL

The Fast Control and Timing System (FCTS) manages all elements linked to clock, trigger, and event readout, and is responsible for partitioning the detector into independent sub-systems for testing and commissioning. Fig. 12.9 shows how the FCTS is connected to the L1 trigger, FEE, ROMs and HLT.

The FCTS will be implemented in a crate where the backplane can be used to distribute all the necessary signals in point-to-point mode. This permits the delivery of very clean synchronous signals to all boards — avoiding the use of external cables. Fig. 12.10 shows the main functional blocks of the FCTS crate. The Fast Control and Timing Module (FCTM, shown in Fig. 12.11) provides the main functions of the FCTS:

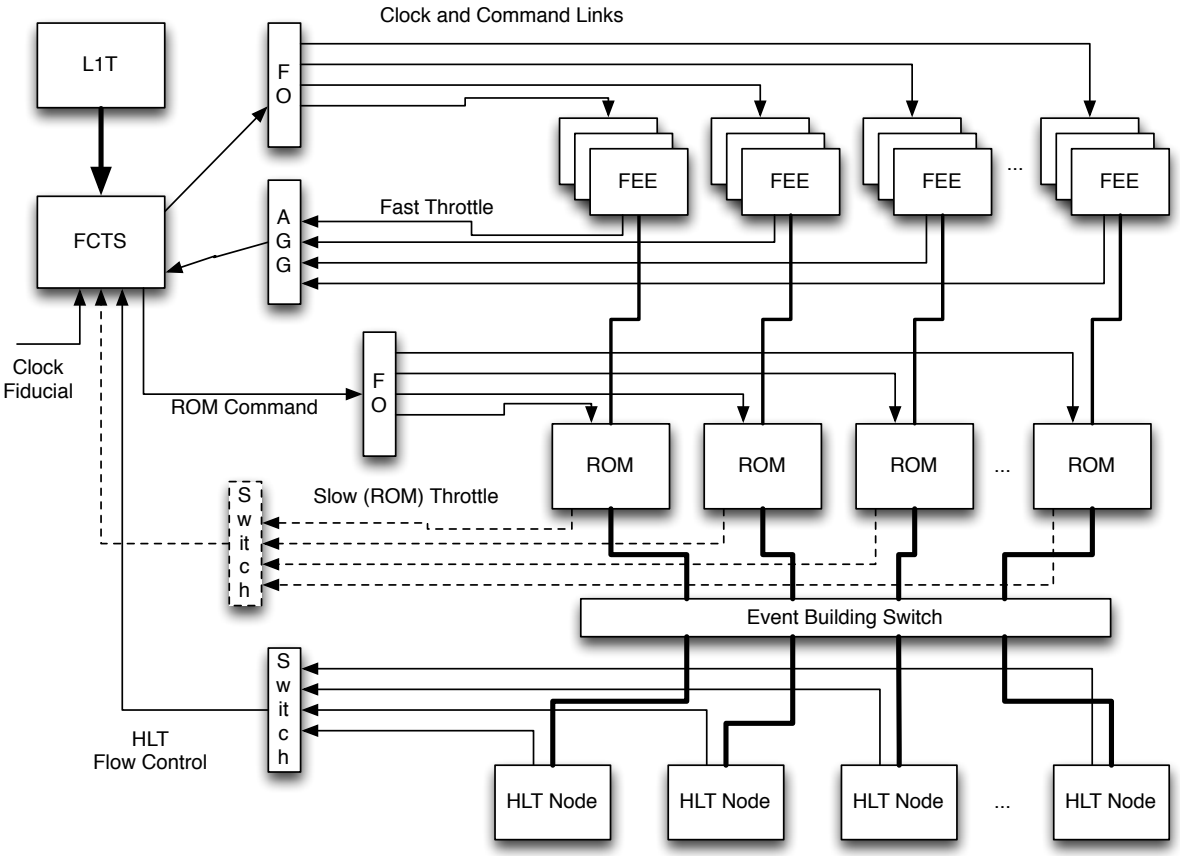

Figure 12.9: Overview of L1T/FCTS/ROM/HLT integration

Clock and Synchronization: The FCTS synchronizes the experiment with the machine and its bunch pattern, distributes the clock throughout the experiment, buffers the clock, and generates synchronous reset commands.

The baseline configuration is to distribute the clock through the FCTS command links[3]. The deserializers will extract the clock from the serialized bistream and report any loss of the clock signal or lock. Possible mechanisms to recover from such a condition are still under investigation and might include the capability of individual FEE to regain synchronization without major interruptions of the data taking.

To globally synchronize the system, all FEE must support the ability to reset all clock dividers, state machines and pipelines at system initialization and reset to ensure that divided versions of the global clock and counters are properly synchronized. This can be achived through a global reset command broadcast by the FCTS. Individual FEEs may be instructed by the ECS to resynchronize.

Trigger Handling and Throttling The FCTS receives the raw L1 trigger decisions, the fast throttle signals from the sub-detector FEE and slow throttle signals from the ROMs, generates readout commands and broadcasts them to the FEEs and the ROMs. The fast throttle is needed becauss during a spike in instantaneous rate or event size, data generated by the FEE can exceed the capacity of the data links. An FEE generates a throttle signal when the free space in the derandomizer buffer falls below a certain threshold (determined by the throttle la-

[3]Should reliability concerns arise during the final design stage, we will consider a separate, dedicated clock distribution network as a backup solution.

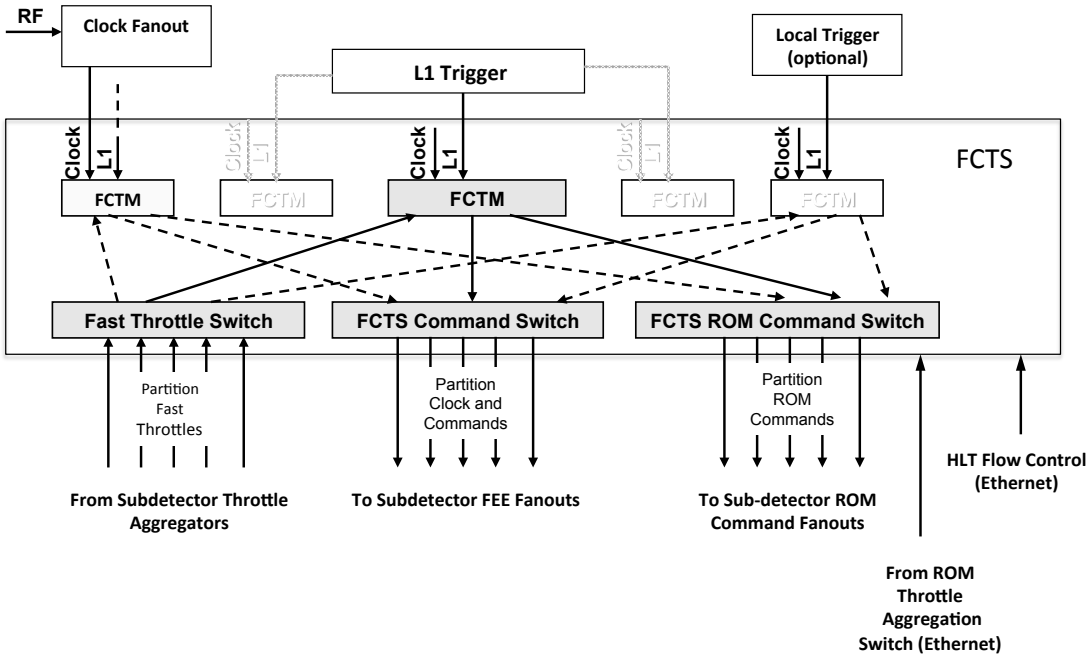

Figure 12.10: The main functional blocks in the FCTS crate

tency), Asserting a throttle signal temporarily inhibits the generation of Level-1 Accept commands in the FCTS and thus stops the readout of new events. Any L1-accepts that are already in-flight when a throttle is asserted will still need to be absorbed by the derandomizer buffer. In addition to being a rate limiting mechanism, the throttle can also be used by the FEEs as an "emergency stop" signal.

As a baseline, the fast throttle will be implemented as a 1-bit level without any framing or encoding. This minimizes the complexity of generating, aggregrating, distributing and monitoring the signals. It also allows to build a simple throttle aggregator device that can easily be standardized across all subsystems.

Every throttle line is monitored (fraction of time a throttle is signal is asserted and a counter of on/off transitions).

Detailed monitoring of the throttle-aggregation devices and detailed sub-detector specific diagnosis of the reasons for a throttle/stop can be performed through the ECS (see below).

Since there is no further local flow control mechanism on the data links, the ROMs cannot assert backpressure through the FEEs but need a separate path to slow down or stop the trigger when they are unable to offload the data through the event builder. With enough buffer space on the data link receiver cards, this throttle ("slow" throttle) does not have stringent latency requirements and can be implemented using Ethernet.

L1-accept Command Format and Distribution The commands broadcast to the FEE have a strict fixed-latency requirement and are as simple and short as possible to minimize the achievable temporal inter-command spacing during transmission and the amount of decod-

ing required in the FEE. We foresee a parity-protected 16-bit command word that in addition to the front end command code and parameters contains an event tag of at least 8 bits that allows the ROM to match the event fragment with its corresponding ROM command word. The FEEs are required to include the FEE command word with each event fragment they send to the ROMs.

The commands distributed to the ROMs are not subject to a fixed-latency requirement. In addition to a copy of the command word sent to the FEEs they contain at least an event timestamp (56 bits), the full trigger word (32 bits) and the HLT destination node (10-12 bits). Additional information such as a per-run event counter or the time since the last trickle injection pulse in the HER or LER might be included in the ROM command word as well. Since latency is variable, the ROM commands can be derandomized before transmission so that the ROM command links only need to sustain the average rate (150kHz) of ROM commands.

FEE and ROM commands are sent in the same order (parallel pipelines). Suitable ways of handling lost or corrupted FEE commands will have to be developed, however this will depend on the detailed failure modes of clock distribution and command links.

Event Management: The FCTS generates unique event identifiers, manages the assignment of events to nodes in the HLT farm and uses a per-node sliding window protocol to load-balance the HLT farm and to stop sending events to unresponsive HLT farm nodes. To do this, the FCTS manages a per-node counter of events it is still allowed to send to this node. A node's counter gets decremented with each event sent to that node. The FCTS determines the next destination node by searching for the next non-zero counter. Every HLT node asynchronously sends generic "event requests" with the number of events it is willing to take — when the FCTS receives such a request from a node it updates the corresponding counter with the value contained in the request. The ROM/HLT/FCTS protocol is described in more detail in the network event builder section below.

Super$B$ events are large enough that in an Ethernet-based event builder we will not need to batch events into multi-event-packets (MEPs), but the system does not prclude the addition of an MEP scheme. Such a scheme might be required to send overlapping events to the same HLT node or to accommodate a non-Ethernet event building network that requires transmission of data in significantly larger units.

To generate an MEP, the FCTS would simply send the same HLT destination address for subsequent events which would then be packed into the same MEP (the packing can in fact be determined by the individual ROM). Sending a ROM command with a new HLT destination will then close the current MEP and open a new one.

Handling the event distribution with the help of the FCTS minimizes the intelligence required in the ROMs.

The FCTS also keeps track of all its activity, including an accounting of triggers lost due to FEE throttling or other sources of trigger inhibits.

Calibration and Commissioning: The FCTS can trigger the generation of calibration pulses and flexibly programmable local triggers for calibration and commissioning. To support the EMC source calibration where a meaningful global trigger can not be constructed, the system will be designd support an untriggered readout of individual channels.

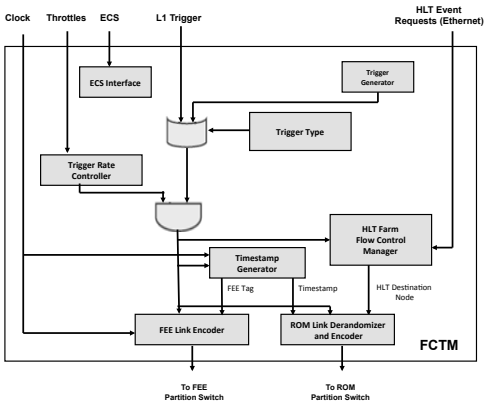

Figure 12.11: Fast Control and Timing Module

The FCTS crate includes as many FCTM boards as required to cover all partitions. One FCTM will be dedicated to the unused subsystems in order to provide them with the clock and the minimum necessary commands.

Three dedicated switches are required in order to be able to partition the system into independent sub-systems or groups of sub-systems: One switch each for FEE clock and commands, ROM commands, and fast throttle feedback from the FEEs.

12.4.4 Control and Data Links

Requirements High-speed optical links will be used for data transfer, triggering and fast control distribution. The clock recovered from the serial streams will be used to synchronize the whole experiment.

Considerations on event size, average expected trigger rate, topology, and cost of the link components, suggest to choose a per-link throughput in the 1-3 Gbit/s range.

Super$B$ policy explicitly requires the use of commercial off-the-shelf (COTS) components where available, avoiding the design of any application specific integrated circuits (ASIC).

Since the whole ETD is designed to work synchronously with a frequency-divided machine clock, the latency and the recovered clock phase of serial links deployed for trigger and fast control distribution should be fixed and predictable, at a level below 1 unit interval. This requirement does not apply to read-out links, where the latency can be variable.

Moreover, the line coding should be DC-balanced in order to allow AC-coupled transmissions where needed and in such a way not to stress, and consequently not reduce the lifetime of, optical transmitters.

Radiation Tolerance Issues Because the high-speed optical links are a key element of the ETD, their electrical and optical components must withstand the expected radiation levels.

According to preliminary simulations of the luminosity-scaling background component [cite table from Riccardo], as far as the links are concerned, the worst case TID, neutron and hadron (E¿20 MeV) fluence are respectively 7.6 Gy (Si) and $3 \cdot 10^{11} cm^{-2}$and $7.6 \cdot 10^{10} cm^{-2}$ (SAFETY FACTOR INCLUDED?)[4].

An R&D activity has been carried out in order to identify the most reliable devices in terms of radiation tolerance among those compatible with the Super$B$ requirements. This activity included the irradiation testing (with 62-MeV protons) of SERDESes, both standalone (Texas Instruments TLK2711A [10], DS92LV18 [11] and DS92LV2421 -serializer only- [12]), and embedded in SRAM-based FPGAs (Xilinx Virtex-5 [13] and Virtex-6 [14]). The DS92LV18 has also been tested with gamma rays from a ^{60}Co source. For the optical part of the link, a VCSEL-based (Avago AFBR-57R5APZ [15]) transceiver has been tested.

The links implemented with SRAM-based FPGAs have also been protected with triple modular redundancy (TMR) and configuration scrubbing mitigation techniques. The layout of the TMR-protected version has been optimized with placement-hardening algorithms and different layouts have been tested (Fig. 12.12).

Before discussing the irradiation results, it is worth remarking that the optical links are a chain of different devices (SERDES, optical transceiver, fiber) and the failure of any component impacts the whole chain. In general the

[4] We do not expect that links will be installed in the high-radiation regions that are closer to the beam than the innermost layer of the drift chamber

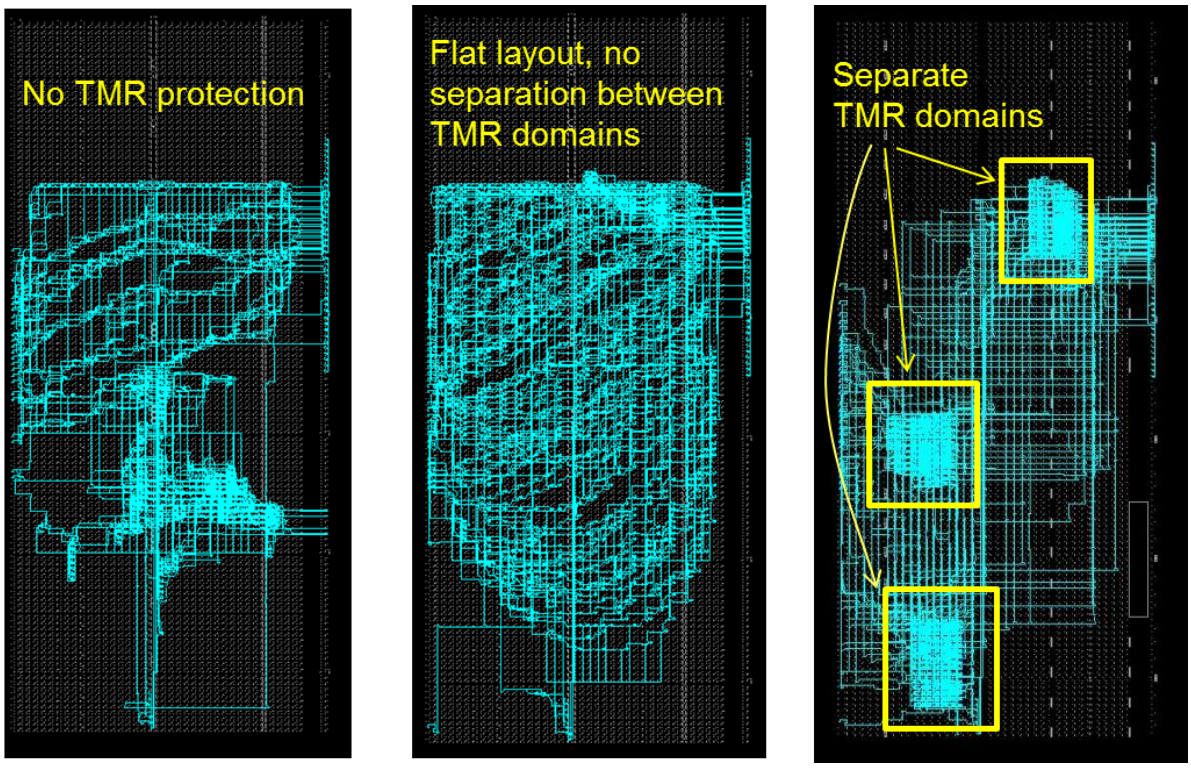

Figure 12.12: Layouts of the serial link implementation in a Xilinx FPGA V5LX50T. Left: link implementation without TMR protection. Center: TMR-protected version with flat layout. Right: TMR-protected version with separation of the TMR domains in distinct areas.

irradiation with 62-MeV protons generates both total ionizing dose and single event effects.

For the different devices the following dose effects were observed:

- **TLK2711A**: failed persistently (not recoverable by cycling power) after absorbing a dose of $\sim$ 400 Gy (Si).
- **DS92LV18**: did not fail either during testing with protons, or with gamma rays. For a total dose of 2.5 kGy(Si) the only effect observed was a moderate ($\sim$ 0.5%) variation in power dissipation.
- **DS92LV2421/22**: did not fail persistently during the testing and did not show any measurable current variation due to TID.
- **Xilinx V5 and V6 FPGAs**: did not exhibit TID-related variations of the power dissipation, however, their power consumption increased gradually during the accumulation of SEUs. Reconfiguration of the devices restored the initial power consumption.
- **Avago AFBR-57R5APZ**: failed persistently at 400 Gy (Si).

Concerning transmission errors related to single event effects, Fig. 12.13 shows the expected mean time between failures (MTBF) for each tested device, considering a reference fluence of $3 \cdot 10^{11} cm^{-2}$ 62-MeV protons per effective year (10^7 s). In the following, we use the word "failure" to refer to the following:

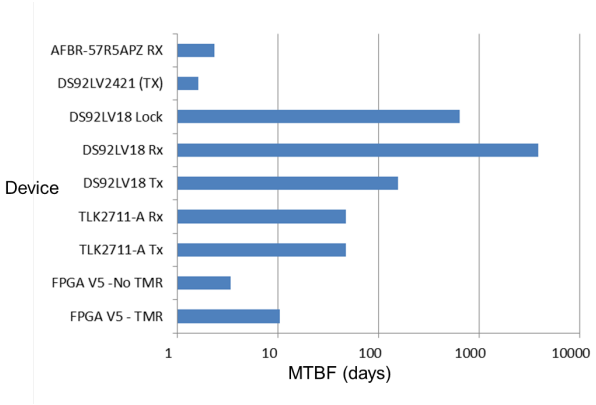

Figure 12.13: Expected failure rates at Super$B$ for a fluence of $3 \cdot 10^{11} cm^{-2}$ 62-MeV protons in one effective year (10^7s).

1. for a standalone SERDESes, to a single bit error either in the transmitter or in the receiver (for the DS92LV18 also to a loss of lock);

2. for a FPGA-embedded SERDES, a persistent failure of the link requiring the reconfiguration of the device.

The separate MTBFs for the transmitter and receiver parts of the TLK2711A and of the DS92LV18 are reported. For the DS92LV18, the rate of losses-of-lock is also shown. The Virtex-6 FPGA MTBF is not shown since it is lower than 10^{-1}days.

These results show that optical receivers are expected to be the main source of errors (we did not find any error in the transmitters during testing). For the reference fluence of $3 \cdot 10^{11} cm^{-2}$62-MeV protons, a MTBF of 2.3 days is expected for errors (either single or burst) in the optical receiver. Among the SERDESes, the most reliable are the DS92LV18 and the GTP embedded in V5 FPGAs, when protected with TMR (we do not consider the TLK2711, since it has a low tolerance to TID). Due to the line protocol of the DS92LV18, on average 10% of the incoming bit errors from the optical receiver will result in a loss-of-lock from the stream, also with the loss of the recovered clock. This means that the effective mean time between two losses of lock for the DS92LV18 will be lowered to nearly 23 days (from the value of 640 days related to the SERDES alone). On the other hand, the FPGA-based links do not lose the lock due to single or (short) bursts errors in the optical receiver and for the TMR-protected versions the failure rates are in the order of 10 days. The results in terms of MTBF suggest that link failures are unavoidable and therefore the whole ETD should be implemented as a fault-tolerant machine. This is further discussed in each ETD component subsection.

However, in the light of the present irradiation results the electrical part of the links should be based either on Virtex-5 FPGAs or on the DS92LV18. For both these devices the fixed-latency operation required by the trigger and fast control links is guaranteed. Although tested at a line rate of 2 Gbit/s, the links in V5 FPGAs can run up to 3.125 Gbit/s (limited by the embedded SERDES throughput) and the coding, including also error detection and correction (EDAC) schemes, can be completely customized by implementing the required logic in the fabric.

The DS92LV18 is limited at 1.32 Gbit/s and uses a proprietary encoding on the line, the payload can only be protected by means of external EDAC components. The line protocol of the device includes a 20-bit symbol consisting of a start bit, an 18-bit payload and a stop bit. When one of these bits is incorrect, the receiver loses the lock to the stream and the recovered clock stops toggling. Since the errors in the optical receiver are uniformly distributed on the parallel symbol, there is a 2/20=0.1 chance of hitting a start or a stop bit and losing the lock at the deserializer level.

Error Detection and Correction Two common solutions are error *correcting* codes (ECC) or the simpler error *detecting* codes (EDC). The ECC solution, for example using a Reed Solomon corrector, appears to be too intensive with regard to the computational effort of both encoding and decoding, resulting in increased hardware complexity, longer link latency and reduced reliability. The expected low error rate

will permit a simpler and faster solution in the form of a proper EDC code. This will simply flag the occurrence of the error in the transmitted block, so that the block can just be discarded. As shown below, the expected frequency of this kind of error is extremely low, thus, bit errors will not affect data quality and event reconstruction.

As far as the choice of the error detection code is concerned, both cyclic redundancy check and check-sums have been evaluated. Since CRC coding has a complexity that is comparable to a full ECC approach, it is not a viable option.

Checksums have a lower error detection ability than CRCs but have the advantage of a lower hardware complexity that meets the latency requirements and allow for a widespread use in the experiment, increasing the overall reliability. A parameter to be evaluated is the overhead in terms of ratio of the number of check-sum bits added to the useful message bits.

Let us suppose to deploy the DS92LV18 SERDES for the optical links. In this case, the 18 bits block managed as a whole by the SERDES will be buffered in groups of 3 blocks to be protected as a single 54 bit super-block. In order to achieve the best possible DC balance, the super-block will then be scrambled, checksum bits will be added and the data will be transmitted by the SERDES and the optical link. On the receiving end, the inverse process will be applied and possible errors will be flagged.

Tools have been developed in order to evaluate error detecting efficiencies of different checksums, such as *Parity*, *Modular Sum*, *One Complement Sum* and *Fletcher Sum*. The choice will be the adoption of Fletcher check-sum which provides detection of all 1 bit errors and two bits burst errors. Less frequent 2 or 3 bits errors are also detected even if not with the same 100% efficiency. Hardware complexity is limited to simple binary adders using the so called one's complement addition. Using the 54 bits block including a 6 bits check-sum, overhead is as low as 12.5%; error detection probability, evaluated by direct simulation mixed with proper analytical approach, provides the following figures for the detection efficiency: 1 bit errors 100%, 2 bits errors 98.7%, 3 bit errors 98.0%, 4 bit errors 98.1%; at the same time complete coverage is provided for burst errors encompassing 2-3-4 bits, an invaluable feature in our case foreseeing these kind of errors. The above figures, for a reference Bit Error Ratio BER=10^{-10} will deliver a probability of undetected error as low as $1.5 \cdot 10^{-19}$. This undetected error rate, in turn, for a reference 2.5 Gbit/s transmission speed, will deliver 8 years average time between undetected errors in a single link; for 1000 links this will deliver 3 days average time between undetected errors in the whole apparatus, or one over 1000 triggered events slightly degraded, which actually will be considered an acceptable degradation in the overall data quality.

Physical Implementation Serial links could be implemented on a plug-in mezzanine board. The main advantages of this approach will be :

- easier maintenance and possibility of upgrading the link performance (data rate, power, jitter) by simply replacing mezzanine cards, this guarantees protection against obsolescence of components too;
- a single design group will be in charge of characterizing performance and testing of the links;
- design parallelism, other ETD components might be designed by other groups independently in the meanwhile;
- decoupling of the link-related issues from the logic-related ones, critical link issues (latency, jitter) will be solved at the mezzanine level;
- design efficiency, the designer will focus on a 'critical but single' board, in fact a single printed circuit board (PCB) will be customized with different components to fit different needs (e.g. jitter cleaners or radhard SerDes for on detector nodes, copper and/or optical lanes where needed).

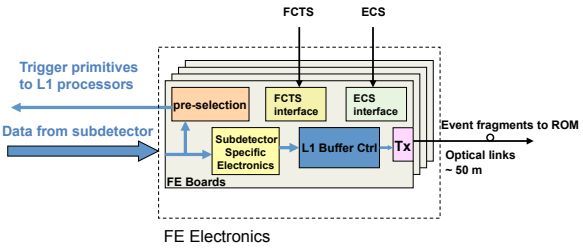

Figure 12.14: Common Front-End Electronics

The implementation of serial links, as separate systems, by means of mezzanine cards is a widespread solution. Example of this trend are the timing trigger and control (TTC) [16] system of the LHC, the S-Link [17]deployed in several CERN experiments, the SODA [18] timing distribution system adopted in the PANDA experiment. In the TTC system, the implementation on a mezzanine allowed to upgrade the receiver with a VCXO-based PLL for improved output jitter ($\sim$ 20 ps rms), compatible with the requirements of the reference clock of Gigabit/s SERDESes and other jitter sensitive devices.

Due to the limited space in the FCTS crate, the mezzanines for the FEE clock, command and throttle links will be housed in dedicated fanout crates that will also contain the logic to aggregate and monitor the throttle signals.

The ROM PCIe boards have similar space constraints, so a mezzanine solution for the data links will require the mezzanines and circuitry to convert the signals to e.g. LVDS to be housed in external crates.

Backup Solutions In order to optimize the design effort, control and data links should be based on the same components and mezzanine printed circuit boards. Should the tested devices found not be compatible with the radiation tolerance requirements of the experiment, the gigabit optical link (GOL) [19] transmitter could be considered as a backup solution for data links. The radiation-hard GBT [20] transceivers could also be considered, if available within a time scale compatible with the links realization phase.

12.4.5 Common Front-End Electronics

JM + DB

In our opinion it will be beneficial to implement the different functions required to drive the front-end electronics as independent modular elements. These elements can for example be implemented as mezzanines or as circuits directly mounted on the front-end modules. For instance, as shown in Figure 12.14, one mezzanine can be used for FCTS signals and commands decoding, and one for the ECS management.

Depending on the implementation of the FEE, it can also be useful to decode the FCTS and ECS signals on one mezzanine and to distribute them to the neighbouring boards. This would permit a great reduction in the number of links. Driving the L1 buffers may also be implemented in a dedicated common control circuitry inside a radiation-tolerant FPGA. This circuitry would handle the L1 accept commands and provide the signals necessary to control the data transfer from the latency pipeline into the derandomizer, and finally, the transmission of event fragments to the serializer, as shown in Fig. 12.15 .

The latency buffers can be implemented either in the same FPGA or directly on the carrier boards, and one such single circuit could be able to drive numerous data links in parallel, thus reducing the amount of electronics on the front-end boards.

The control circuit will also handle events that have overlapping readout windows because they were triggered very close in time. The strategy for this is that data shared between events with overlapping readout windows is only read out and transmitted once. Complete events will then be reconstituted in the ROM by duplicating the data from the overlapping region as necessary.

It is also the responsibility of the CFEE to manage the derandomizer buffer and the fast multiplexer that feeds the data link serializer.

Figure 12.14 shows a possible implementation of the L1 buffers, their control electronics and the outputs towards the optical readout links.

The control electronics may be located within a dedicated FPGA.

Another important requirement is that all (rad-tolerant) FPGAs in the FE have to be reprogrammable without dismounting a board. While this could be done through decdicated front panel connectors which might be linked to numerous FPGAs, the preferred solution is to program FPGAs through the ECS system without any manual intervention on the detector side.

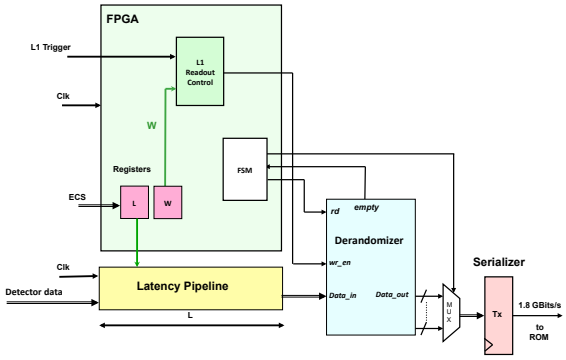

Figure 12.15: Control of latency pipeline and derandomizer in the CFEE

12.4.6 Read-Out Modules

MB + UM

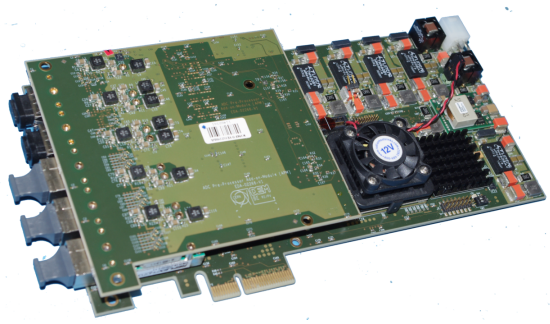

Figure 12.16: Readout Module

The Readout Modules (ROM, Fig. 12.16) are the hardware interfaces between front-end electronics and the software based event builder. ROMs map the synchronous world of FCTS-disciplined hierarchy to the asynchronous domain of the event-building computing farm. Their processing flow starts by receiving event fragments from the sub-detectors' front-end electronics and the corresponding ROM command words from the FCTS. Processing then continues with cross-checking front-end identifiers and absolute time-stamps, buffering them in de-randomizing memories, performing processing (still to be defined) on the fragment data, and eventually injecting the formatted fragment buffers into the event builder and HLT farm. Processing includes duplicating data into that have been partially transmitted because of overlapping readout windows.

Connected to the front-end electronics via optical fibers, they will be located in an easily accessible, no radiation area. The hardware design of the ROMs is identical for all sub-detectors, however, if the need arises, the pecularities of each sub-detector can be addressed by customization of the ROM firmware.

A ROM will have 10 or more optical input channels at a rate of 1 Gbit/s and at least one output channel at 10 Gbit/s. To exploit flexibility and processing power of computer technology, ROM will be manufactured as PCI Express based add-on cards for servers of the event-building farm. This solution will help keeping production costs low (when compared to a field-bus based solution) and opens a new scenario of a mixed hardware-software processing scheme for fragment data; unforeseen changes and upgrades can also be addressed with a low impact on the whole architecture. It is important to note that the space on a PCI express card is rather limited (both for connectors and mezzanines), so the strategy of using mezzanines and the mechanial design have to be reviewed carefully.

A prototype ROM has been manufactured and qualified, in order to assess the suitability of this approach. The prototype ROM is a PCI Express 2.0 based add-on card (Fig. 12.16) based on a Xilinx Virtex6-250T FPGA with 48 high speed serial transceivers. The plug-in module accommodates 3 SNAP12 optical receivers

and 2 QSP optical transceivers for a total of 44 receivers and 8 transmitters each operating at max 6.2 Gbit/s. A 8 Mbyte true dual-port ram acts as de-randomizing memory for incoming fragments, while waiting to be streamed to host server memory.

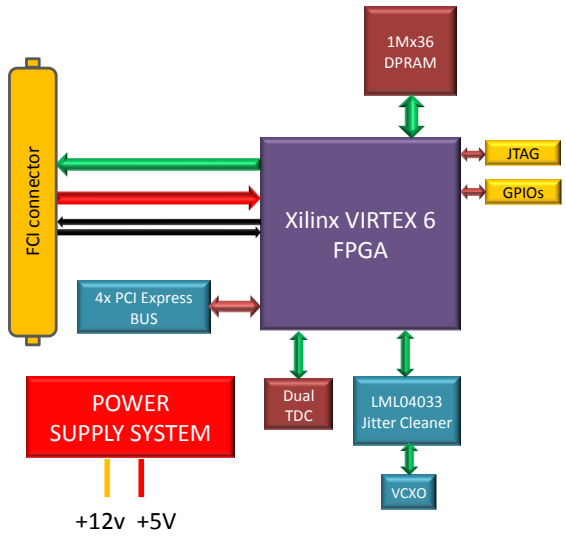

Figure 12.17: ROM block diagram – without optical adapter

The prototype ROM features a TDC and a ultra-low jitter PLL for the benefit of FPGA (Fig 12.17). A 4x PCIE 2.0 interface with an aggregate bandwidth of 20 Gbit/s per direction allows fragment data to be moved to host memory efficiently. To check worst-case power consumption, the FPGA has been configured with 38 input channels at 2.0 Gbit/s, 38 eight FIR filters for data processing, a 10 Gbit/s PCI-express interface, a scatter-gather DMA engine and a timing unit for a total of 92% occupancy of logic resources; consuming approximately 60W, no precaution has been taken for cooling when housed on a low cost 2U Dell server. By means of a custom developed Linux driver we have exercised the data transfer from the ROM dual-port RAM and the host memory; the driver addresses the custom designed scatter-gather DMA engine in the FPGA to efficiently move the fragment data from the ROM directly into user-space buffers; the driver avoids copying data from kernel address space to user address space by handling the map between Unix virtual memory pages and server physical memory regions, tunneling data from ROM dual-port RAM to user-space declared data vectors. Bandwidth tests show that fragment buffers larger than few tenths of Kbytes can be moved at a rate of approximately 950 Mbyte/s in the aforementioned configuration (4x PCIE 1.1), while almost doubling at 4x PCIE 2.0 (with a 256 bytes PCI-E payload). Test results of the prototype ROM outperform requirements in the foreseen deployment and this gives us confidence that this approach can be safely adopted.

12.4.7 Network Event Builder

SL

The ROMs receive event fragments in parallel from the sub-detector front-end-electronics, perform a first stage event-build, store the event fragments in memory buffers, and add the corresponding ROM command received from the FTCS on the dedicated ROM-command links. The resulting partially-built events are then encapsulated in UDP datagrams and sent to the HLT node determined by the destination node field in the ROM command word. Thus, all fragments of an event are sent to the same HLT node which completes the event building process by combining all fragements. Full events are passed to the HLT processes through a queue.

As described above, the FCTS determines the HLT destination node for every event using a round-robin algorithm that is tuned by a simple flow control scheme based on a per-node sliding window maintained by the FCTS. Each HLT node maintains a queue of fully built events that is filled by the event building process and drained by the HLT processes. As long as the event building process is running and the number of events in this queue stays below a high-water mark, the HLT node periodically sends requests for more events to the FCTM that is responsible for the partition. These requests are UDP packets sent over Ethernet; the aggregate rate of the requests can be limited to a fraction

of the L1-accept rate, since each request is for multiple events.

If the HLT processes on a node cannot keep up with the incoming events, the node will stop sending requests and after the FCTM has exhausted the node's window of outstanding events, no more events will be directed to the node. Only after the FCTM receives a new event request from the node, it will consider it as a valid event destination again. No events are lost, since the node will queue the outstanding events. This provides a flow-control and load balancing mechanism for the HLT farm. In case of a complete HLT node failure (or the failure of the event building process) the event loss is less or equal to the number of events last requested.

The event building process is inherently parallel and its rate can be scaled up as needed (up to the bisection bandwidth of the event building network). The baseline technology for the event builder network is standard 10 Gbit/s Ethernet. We will investigate the suitability of end-to-end flow control mechanisms (such as IEEE 802.1Qbb) at the Ethernet layer for avoiding packet loss in the event building network. We will also investigate alternative network technologies and protocols (such as RDMA or Infiniband).

With a L1 trigger rate of 150 kHz and a pre-HLT event size of 500 kbyte, the bandwidth in the network event builder is about 75 Gbyte/s, corresponding to about 750 Gbit/s with network overhead included. To avoid packet loss and to maintain stability, the event building network cannot be operated at an utilization of 100%, so we retain an additional safety factor of ~1.5. Thus, the minimum bisection bandwidth required in the event building network is 1200 Gbit/s. When implemented with 10 Gbit/s Ethernet, this means 120 "source" network interfaces on the ROMs and at least 120 "destination" interfaces on the HLT nodes. Network switches that provide the necessary bandwidth and can host at least $120 + 120 = 240$ 10 Gbit/s Ethernet ports are commercially available at the time of the writing of this document.

12.4.8 High-Level Trigger Farm

SL

The HLT farm needs to provide sufficient aggregate network bandwidth and CPU resources to handle the full Level 1 trigger rate on its input side. The Level 3 trigger algorithms should operate and log data entirely free of event time ordering constraints and be able to take full advantage of modern multi-core CPUs[5]. Extrapolating from *BABAR*, we expect 10 ms core time per event to be more than adequate to implement a software L3 filter, using specialized fast reconstruction algorithms. With such a filter, an output cross-section of 25 nb should be achievable. Using contemporary (as of Spring 2012) hardware and taking into account the CPU overhead for event building, logging and data transfer, a suitable farm could be implemented with approximately 150 nodes.

Level-4 Option To further reduce the amount of permanently stored data, an additional filter stage (L4) could be added that acts only on events accepted by the L3 filter. This L4 stage could be an equivalent (or extension) of the *BABAR* offline physics filter—rejecting events based either on partial or full event reconstruction. If the worst-case behavior of the L4 reconstruction code can be well controlled, it could be run in near real-time as part of, or directly after, the L3 stage. Otherwise, it may be necessary to use deep buffering to decouple the L4 filter from the near real-time performance requirements imposed at the L3 stage. The discussion in the Super*B* CDR [1] about risks and benefits of a L4 filter still applies.

12.4.9 Data Logging

SL + ?

The output of the HLT is logged to disk storage. We assume at least a few Tbyte of usable space per farm node, implemented either as directly attached low-cost disks in a redundant (RAID) configuration, or as a storage system connected through a network or SAN. We do not expect to aggregate data from multiple

[5] The simplest implementation would be to run multiple identical HLT threads or processes which get their input from a single queue of built events.

farm nodes into larger files. Instead, the individual files from the farm nodes will be maintained in the downstream system and the bookkeeping system and data handling procedures will have to deal with missing run contribution files. A switched Gigabit Ethernet network separate from the event builder network is used to transfer data asynchronously to archival storage and/or near-online farms for further processing. It is not yet decided where such facilities will be located, but network connectivity with adequate bandwidth and reliability will need to be provided. Enough local storage must be available to the HLT farm to allow data buffering for the expected periods of link down-time.

Assuming that the HLT accepts a cross-section of about 25 nb leads to an expected event rate of 25 kHz at a luminosity of 10^{36} $\mathrm{cm}^{-2}\mathrm{sec}^{-1}$, or a logging data rate of ~5 Gbyte/s.

While the format for the raw data has yet to be determined, many of the basic requirements are clear, such as efficient sequential writing, compact representation of the data, portability, long-term accessibility, and the freedom to tune file sizes to optimize storage system performance.

12.5 System Integration and Error Handling

AA, SC, SL, DC, UM, DB and others

Due to the radiation environment, the expected rate of SEUs and the corresponding rate of link and FEE failures cannot be neglected, as there will likely be at least a few failures per day. For this reason it is very important that detection of and recovery from these failures is reliable and fast.

Because we cannot predict all possible failure modes, the system design is based on a generic approach to recovery:

The FCTS and FEE implement mechanisms that allow individual front-ends to detect and report the loss of synchronization, and to resynchronize without the need to restart the whole system. This includes the periodic broadcasting of synchronization frames on the clock and command links, the reporting of FEE problems through the fast throttle and the ability to diagnose, reset and synchronize individual front-ends under the control of the ECS.

Other components in the system that participate in the detection of FEE problems are the ROMs, the HLT, and the data quality monitoring system.

Recovery from failures will be orchestrated by the global control system software and the ECS, this provides maximum flexibility in handling unforeseen failure modes.

12.6 Control Systems

A major lesson learned during *BABAR* operations was that achieving high operational efficiency and true "factory-mode" data taking required a high degree of automation and control system integration. The traditional approach of separate control systems for different aspects of the experiment (detector control, run control, farm and logging control) designed and implemented with completely separate tools and very limited capability to communicate with each other, greatly limited the amount of automation and automatic error detection and recovery.

In Super*B*, all routine operations will need to be orchestrated across subsystem boundaries. For example, performing a simple calibration might require high voltages to be ramped to a calibration set-point, the FEE and the FCTS to be configured for calibration, farm nodes to be allocated and configured, the calibration run to be performed, calibration data to be analyzed and after completion the system to be returned to its normal data taking configuration.

For Super*B* we therefore foresee a unified control system that can automatically perform all routine operations. The system comprises the Electronics Control System (ECS), the Detector Control System (DCS), the Farm Control System (FCS), the configuration database, sequencing engines to implement distributed state

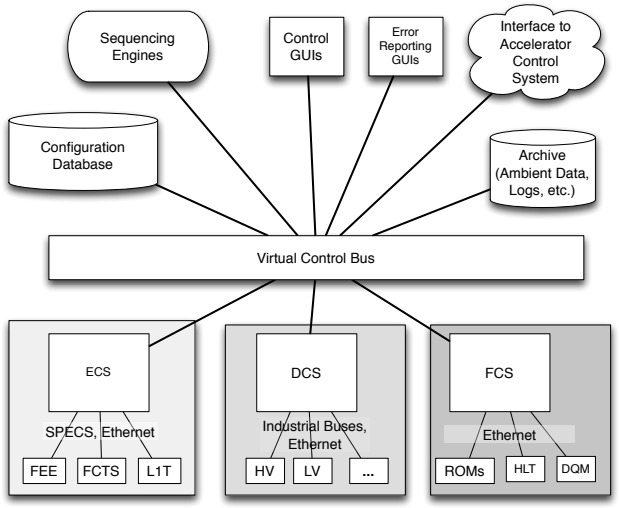

Figure 12.18: The Super*B* unified control system architecture

machines, an archiving and logging system, operator GUIs and the interface to the accelerator control system. All components are connected by a central virtual control bus ("Global Control System").

All operations are driven by the configuration database and executed under the control of one or more sequencing engine.

A large part of the system, including the central virtual control bus, will be implemented using the !CHAOS [9] control system toolkit which is currently under development for the Super*B* accelerator. !CHAOS is a state-of-the-art scalable distributed control system framework that combines high-performance data acquisition and archiving capabilities with a plugin architecture to provide low-level controller interfaces and graphical user interfaces (GUIs).

An overview of the unified control system architecture is shown in Fig 12.18; its major components are described below.

12.6.1 Electronics Control System

SL The Electronics Control System (ECS) controls and monitors the FEE, the FCTS and the Level 1 trigger. Its main responsibilities are:

Configuring the Front-ends: Many front-end parameters must be initialized before the system can work correctly. The number of parameters per channel range from a only a few to large per-channel lookup tables. The ECS may also need to read back parameters from registers in the front-end hardware to check the status or verify that the contents have not changed. For a fast detector configuration and recovery turnaround in factory mode, it is critical to not have bottlenecks either in the ECS itself, or in the ECS' access to the front-end hardware.

Calibration: Calibration runs require extended functionality of the ECS: In a typical calibration run, after loading calibration parameters, event data collected with these parameters is sent through the DAQ system and analyzed. Then the ECS loads the parameters for the next calibration cycle into the front-ends and repeats the operation.

Testing the FEE: The ECS is also used to remotely test all FEE electronics modules using dedicated software. This obviates the need for independent self-test capability for all modules.

Monitoring the Experiment: The ECS continuously monitors FEE boards, FCTS and the L1 Trigger to ensure that they function properly. This might include independent spying on event data to verify data quality, and monitoring operational parameters on the boards (such as voltages, currents, temperatures and error flags). By monitoring these parameters, the ECS also participates in protecting the experiment from a variety of hazards[6].

ECS support must be built into all electronics modules that are to be controlled by the ECS – this includes the FEE.

Programming the FPGA firmware: Where applicable, the ECS can also be used to program or update FPGA configurations. It is highly desirable to be able to perform such operations without physical access the the boards. Depending on the FPGA this may require appropriate programming voltages to be made available on the boards.

[6] An independent hardware-based detector safety system, which is part of the DCS, must protect the experiment against equiement damage in case the software-based ECS is not operating correctly.

The specific requirements that each of the sub-systems makes on ECS bandwidth and functionality must be determined (or at least estimated) as early as possible so that the ECS can be designed to incorporate them. Development of calibration, test, and monitoring routines must be considered an integral part of sub-system development, as it requires detailed knowledge about sub-system internals.

ECS Implementation: The field bus used for the ECS has to be radiation tolerant on the detector side and provide very high reliability. Such a bus has been designed for the LHCb experiment: it is called SPECS (Serial Protocol for Experiment Control System) [7]. It is a bidirectional 10 Mbit/s bus that runs over standard Ethernet Cat5+ cable and provides all possible facilities for ECS (like JTAG (Joint Test Action Group) and I2C (Inter IC)) on a small mezzanine. It could be easily adapted to the Super*B* requirements. Though SPECS was initially based on PCI boards, it is currently being translated to an Ethernet-based system, as part of an LHCb upgrade, also integrating all the functionalities for the out-of-detector elements. For the electronics located far from the detector, Ethernet will be used for ECS communication. The Super*B* ECS will be implemented using SPECS; an interface to !CHAOS will be developed.

12.6.2 Detector Control System

The Detector Control System (DCS) is responsible for ensuring detector safety, controlling the detector and detector support system, and monitoring and recording detector and environmental conditions. The DCS also provides the primary interface between the accelerator and the detector.

Efficient detector operations in factory mode require high levels of automation and automatic recovery from problems. Here, the DCS plays a key role and a tight integration with the Accelerator Control System (ACS) is hightly desirable. The DCS in conjunction with the ACS manages the accelerator-detector interlocks and beam and detector states and has access to all information from the accelerator and the detector that is needed to fully automate data taking operations.

The DCS-ACS connection is also used to provide the accelerator with beam measurements performed by the detector (such as beam spot positions or bunch-by-bunch luminosities). Operational experience from *BABAR* has shown that mutual access between machine and detector to their respective archived control system data (such as records of background levels, detector currents, trigger rates on the detector side and vacuum pressures, temperatures and stored currents on the machine side) are invaluable for improving the accelerator and detector performance.

The DCS will be implemented with !CHAOS. Due to its distributed nature and modular storage design, !CHAOS will allow us to federate the independent instances of DCS and ACS and provide a unified query interface for data archived by the respective systems.

Low-level components and interlocks responsible for detector safety (Detector Safety System, DSS) will be implemented as simple circuits or with programmable logic controllers (PLCs).

12.6.3 Farm Control System

SL

Processes on the ROMs and on the HLT farm will be started, controlled and monitored by the Farm Control System (FCS) and will be implemented using the !CHAOS framework or a traditional network inter-process communication system such as DIM.

12.7 Other Systems

12.7.1 Data Quality Monitoring System

SL

Event data quality monitoring is based on quantities calculated by the HLT, as well as quantities calculated by a more detailed analysis on a subset of the data. A distributed histogramming system collects the monitoring output histograms from all sources and makes them

available to automatic monitoring processes and operator GUIs.

12.7.2 Other Components

SL

Electronic Logbook: A web-based logbook, integrated with all major Online components, allows operators to keep an ongoing log of the experiment's status, activities and changes.

Databases: Online databases such as configuration, conditions, and ambient databases are needed to track, respectively, the intended detector configuration, calibrations, and actual state and time-series information from the DCS.

Configuration Management: The configuration management system defines all hardware and software configuration parameters, and records them in a configuration database.

Performance Monitoring: The performance monitoring system monitors all components of the Online.

Software Release Management: Strict software release management is required, as is a tracking system that records the software version (including any patches) that was running at a given time in any part of the ETD/Online system. Release management must cover FPGAs and other firmware as well as software.

Computing Infrastructure Reliability: The Online computing infrastructure (including the specialized and general-purpose networks, file, database and application servers, operator consoles, and other workstations) must be designed to provide high availability, while being self-contained (sufficiently isolated and provided with firewalls) to minimize external dependencies and downtime.

12.7.3 Software Infrastructure

GM + SL

The data acquisition and online system is basically a distributed system built with commodity hardware components. Substantial manpower will be needed to design the software components—taking a homogeneous approach in both the design and implementation phases. An Online software infrastructure framework will help organize this major undertaking. It should provide basic memory management, communication services, and the executive processes to execute the Online applications. Specific Online applications will make use of these general services to simplify the performance of their functions. Middleware designed specifically for data acquisition exists, and may provide a simple, consistent, and integrated distributed programming environment.

12.8 R&D for Electronics, Trigger and Data Acquisition and Online

All

Note: This is copied from the Whitepaper. Needs updating!

The baseline design presented in this chapter can be implemented with technology and components available at the time time of writing of this document. However, we expect that by the times when we have to freeze various aspects of the design to start construction or purchasing, components that are significantly more performant and/or cost effective will be available. In order to take advantage of these developments, we will need to develop a detailed plan on when we have to finalize the parts of our design.

Data Links: Discuss technology tracking (e.g. LHC Upgrade) here?

Event Builder and HLT Farm: The main R&D topics for the Event Builder and HLT Farm are (1) the applicability of existing tools and frameworks for constructing the event builder; (2) the HLT farm framework; and (3), event building protocols and how they map onto network hardware.

Software Infrastructure: To provide the most efficient use of resources, it is important to investigate how much of the software infrastructure, frameworks and code implementation can

be shared with Offline computing. This requires us to determine the level of reliability-engineering required in such a shared approach. We also must develop frameworks to take advantage of multi-core CPUs.

12.9 Organizational Structure of Electronics, Trigger, Data Acquisition and Online

DB + UM + SL

12.10 Conclusions

The architecture of the ETD system for Super*B* is optimized for simplicity and reliability at the lowest possible cost. It builds on substantial in-depth experience with the *BABAR* experiment, as well as more recent developments derived from building and commissioning the LHC experiments. The proposed system is simple and safe. Trigger and data readout are fully synchronous—allowing them to be easily understood and commissioned. Safety margins are specifically included in all designs to deal with uncertainties in backgrounds and radiation levels. Event readout and event building are centrally supervised by a FCTS system which continuously collects all the information necessary to optimize the trigger rate. The hardware trigger design philosophy is similar to that of *BABAR* but with better efficiency and smaller latency. The event size remains modest.

The Online design philosophy is similar—leveraging existing experience, technology, and toolkits developed by *BABAR*, the LHC experiments, and commercial off-the-shelf computing and networking components—leading to a simple and operationally efficient system to serve the needs of Super*B* factory-mode data taking.

Bibliography

[1] M. Bona *et al.*, *Super*B*: A High-Luminosity Heavy Flavour Factory. Conceptual Design Report*, arXiv:0709.0451v2 [hep-ex], INFN/AE-07/2, SLAC-R-856, LAL 07-15, also available at http://www.pi.infn.it/SuperB/CDR.

[2] B. Aubert *et al.* (*BABAR* Collaboration), *The BABAR Detector*, Nucl. Instrum. Methods Phys. Res., Sect. A **479**, 1 (2002) [arXiv:hep-ex/0105044].

[3] The ATLAS Collaboration, *ATLAS Detector and Physics Performance Technical Design Report*, http://atlas.web.cern.ch/Atlas/GROUPS/PHYSICS/TDR/access.html.

[4] The CMS Collaboration, *CMS Detector Technical Design Report*, http://cmsdoc.cern.ch/cms/cpt/tdr/.

[5] The LHCB Collaboration, *LHCB Technical Design Reports*, http://cmsdoc.cern.ch/cms/cpt/tdr/.

[6] The Belle Collaboration, *The Belle Detector*, Nucl. Instrum. Methods Phys. Res., Sect. A **479**, 117 (2002).

[7] The SPECS Web Page, https://lhcb.lal.in2p3.fr/Specs/.

[8] The *BABAR* Trigger Web Pages, http://www.slac.stanford.edu/BFROOT/www/Detector/Trigger/index.html.

[9] L. Catani *et al. Exploring a new paradigm for accelerators and large experimental apparatus control systems*, ICALECPS 2011, http://accelconf.web.cern.ch/accelconf/icalepcs2011/html/clas013.htm

[10] Texas Instruments, *1.6 to 2.7* Gbit/s *Transceiver*, September 2009, http://www.ti.com/lit/ds/symlink/tlk2711a.pdf

[11] Texas Instruments, *DS92LV18 18-Bit Bus LVDS Serializer/Deserializer - 15-66* MHz, Literature Number: SNLS156D, June 2006, http://www.ti.com/lit/ds/symlink/ds92lv18.pdf

[12] Texas Instruments, *DS92LV2421/DS92LV2422 10 to 75* MHz*, 24-bit Channel Link II Serializer and Deserializer*, January 2011, http://www.ti.com/lit/ds/snls321a/snls321a.pdf

[13] Xilinx, *Virtex-5 FPGA RocketIO GTP Transceiver User Guide*, Xilinx UG196, v1.7, 2008, http://www.xilinx.com/support/documentation/user_guides/ug196.pdf

[14] Xilinx, *Virtex-6 FPGA GTX Transceivers User Guide*, Xilinx UG366, v2.6, 2011, http://www.xilinx.com/support/documentation/user_guides/ug366.pdf

[15] Avago Technologies, *AFBR-57R5APZ Data Sheet*, 2007, http://www.avagotech.com/docs/AV02-0881EN

[16] P. Moreira, E. Murer, *TTCrx and QPLL Mezzanine Card (TTCrq)*, 2003, http://bonner-ntserver.rice.edu/cms/TTCrqSpec.pdf

[17] O. Boyle 1 , R. McLaren & Erik van der Bij, *The S-LINK Interface Specification*, 1997, http://vanderby.web.cern.ch/vanderby/s-link/spec/spec/s-link.pdf

[18] I. Konorov; H. Angerer; A. Mann; S. Paul;, *SODA: Time distribution system for the PANDA experiment*, Nuclear Science Symposium Conference Record (NSS/MIC), 2009 IEEE , vol., no., pp.1863-1865, Oct. 24 2009-Nov. 1 2009

[19] P. Moreira et al., *A radiation tolerant gigabit serializer for LHC data transmission*, in Proc. of the 7th Workshop on Electronics for LHC Experiments, Stockholm, Sweden, 10 - 14 Sep 2001, pp.145-149

[20] P. Moreira, J. Troska, *Radiation-Hard Optical Link for Experiments*, PH Faculty Meeting April 25, 2008 CERN, Geneva, Switzerland, http://ph-dep.web.cern.ch/ph-dep/NewsMeetings/FM/FM25Apr08/Troska_Moreira.pdf

13 Subdetector Electronics and Infrastructure

Breton/Marconi/Luitz

The general design approach is to standardize components across the system as much as possible, to use mezzanine boards to isolate sub-system-specific functions differing from the standard design, and to use commercially available common off-the-shelf (COTS) components where viable.

present summary table(s) of data rates, link counts, etc. here

13.1 Subsystem-specific Electronics

13.1.1 SVT Electronics

The full details of the SVT electronics has been given in chap. **??**. Here we recall the main features relevant for the data collection, trigger distribution, system programming and monitoring.

In the baseline SVT option, the detector will be equipped with double sided silicon strips (or striplets) in all layers. Custom front-end chips will be used to read the detector and transform as soon as possible the analog information of a particle traversing the detector in a digital one, characterized by position (layer, strip), energy deposit (signal time over threshold) and time. At least two different custom chips will be developed to handle separately the first layers (expecially layer 0), characterized by high occupancy and short strips (good signal/noise) and the external layers (layer 4 and layer 5) where the main concern is the length of the strips (worse signal/noise) and not the occupancy. Both front-end chips will have the same digital readout architecture and will present the same interface to the DAQ chain, although with different settings. Possible upgrades of the SVT internal layers might require to move to a pixellated detector, for which a different custom front-end chip will be designed. The digital architecture of the pixel chips, partially already develloped, will be based on the same general readout architecture so that from the point of view of trigger and DAQ system they will share the same interface.

Common characteristics of the chips will be capability to work both in data-push and data-pull mode, the presence of internal buffers to allow for a trigger latency up to 10 μs, the use of a periodic signal to time-tag the recorded hits, the serialized hit output and the chip programmability via (two) digital lines.

The full SVT data chain will therefore be able to provide and distribute all the signals, clocks, triggers, time-tagging signal to all the front-end chips in a system-wide synchronous way.

A sketch of the full data chain is given in Fig. 13.1. Starting from the detector and going to the ROM boards, the chain contains: a) the front-end chips mounted on an HDI placed immediately at the end of the sensor modules; b) wire connections to a transition card (signals in both directions and power lines); c) a transition card, placed about 50 cm from the end of the sensors, hosting the wire-to-optical conversion; d) a bidirectional optical line running above 1 Gbit/s; e) a receiver programmable board (front-end board: FEB).

Each HDI will host from 5 to 14 FE chips servicing a side of the silicon strip module (a so

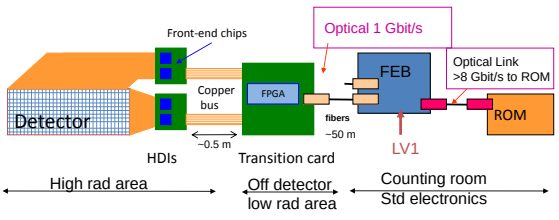

Figure 13.1: SVT Electronics

called ROS: Read-Out Section). All the chips will share the same input lines (currently: reset, clock, fastclock, trigger, time-stamp, registerIn) and at least a registerOut line. Programming of the chips can be done individually by addressing a sigle chip or via broadcast command sent to all the chips in an HDI. Hits will be serialised on a programmable number of lines (1,2,4 or 6) using the fastclock signal. Each HDI will have a maximum number of 16 output lines running at the fastclock rate.

The role of the transition card is threefold: a) it will distribute the power to the HDI, b) it will receive all the input signals for the front-end chips via the optical line connected to the programmable board and c) it will ship the data to the programmable board for data acquisition. For the inner layers (0-3) there will be a transition card for each HDI. For the outer layers (4-5) it will be possible to group the data of the two HDIs servicing the two sides of the same silicon sensor into the same transition card, reducing in this way the total number of optical links needed.

The received programmable board (FEB) will handle all the comunications with the front-end chips, the FTCS, the ECS and the upper DAQ systems. Each FEB board will be connected to a variable number of transition cards (up to 12 in the current design). Important and critical roles of this board are the clock distribution, the trigger handling and the data collection. The clock-like signals, such as an experiment clock (about 60 MHz), a fast clock (120-180 MHz) and a time-stamping clock (up to 30 MHz), have to be distributed in a system-wide synchronous manner. Special care will be taken to measure at each power-up the latencies of all the serializers and deserializers in the signal and DAQ chain so that the sent signals can be suitably adjusted in phase in order to have a system synchronous at the sensor (or front-end) level. The time-stamping clock will be used to time-tag the hits and can be different for the inner layers, where the high track rate requires short signal shaping times and short daq time windows and outer layers where the long strips and lower track rates allow for a longer shaping times (800 ns - 1 μs) and longer DAQ windows. The estimation of data volumes have been performed assuming a time-stamping of 30 ns period in the inner and outer layers. The acquisition window will be defined in a time window centered around the L1 trigger window and lasting at least 10 time-stamps (300 ns) for the inner layers and 33 time-stamps (990 ns) or more for the outer layers. The trigger request will be sent to the chips via the optical links. The most important function of the board is to collect the data coming out of the front-end chips both for monitoring and for the final daq. The data will be deserialized in the board and the redundant information will be stripped. A possible further data compression can be envisaged in order to reduce the final data volume. Finally the data will be sent-out via an optical link to a ROM module.

Data volumes. As discussed in the SVT chapter, the data rates and volumes are dominated by the background. In the design of the SVT front-end chips and DAQ chain, the latest background Bruno simulations have been considered at the nominal luminosity and a safety factor of 5 has been applied on the simulation results (design inputs). Due to the strong non-uniformity of the particle rate on the sensors, the front-end chip characteristics have been adapted to the peak hit rates, while the data volumes have been extracted from the mean rates for each layer. To evaluate the data rate a 150 kHz trigger rate with 10 μs of maximum latency and 100 ns of time jitter has been considered. An hit size of 16 bits is used as the FE chip output in the calculation that becomes 20 bits during serialization due to the 8b/10b protocol. The bandwidth needed by a layer0 ROS in a data-push configuration is of the order of 20 Gbit/s/ROS. A difficult-to-handle rate that moved us to consider a fully triggered SVT. In table 13.1 for each layer type the mean expected data load is shown.

For events accepted by the L1 trigger, the bandwidth requirement is only 1 Gbit/s and data from each ROS can be transferred on optical links to the front-end boards (FEB) and

Table 13.1: Electronic load on each layer, Readout section and optical link.

Layer	Layer type	chips/ ROS	available channels	Backgnd (MHz/cm^2)	Gbits/trig (per GROS)	FE Boards	Event Size (kB)
0	striplet u	6	768	151	0.99	4	5.3
0	striplet v	6	768	151	0.99	4	5.3
1	strip z	7	896	14.0	0.56	1	2.2
1	strip phi	7	896	16.0	0.64	1	2.6
2	strip z	7	896	9.6	0.54	1	2.2
2	strip phi	7	896	10.3	0.58	1	2.3
3	strip z	10	1280	4.2	0.50	1	2.0
3	strip phi	6	768	3.0	0.36	1	1.5
4a	strip z	5	640	0.28	0.26	1	1.4
4a	strip phi	4	512	0.43	0.38	1	2.0
4b	strip z	5	640	0.28	0.26	1	1.4
4b	strip phi	4	512	0.43	0.40	1	2.1
5a	strip z	5	640	0.15	0.17	1	1.0
5a	strip phi	4	512	0.22	0.24	1	1.5
5b	strip z	5	640	0.15	0.17	1	1.0
5b	strip phi	4	512	0.22	0.24	1	1.5

then to ROMs through the >8 Gbit/s optical readout links.

13.1.1.1 SVT Summary

In total, the SVT electronics requires 18 FEBs and 18 ROMs, 18 optical links at 10 Gbit/s, 172 links at 1 Gbit/s (radiation hard). The average SVT event size is 88 kB, 30% coming only from the layer0.

Number of Control Links	update
Number of Data Links	update
Total Event Size	88 kbyte
On-Detector Power Consumption	2.6kW check

Table 13.2: SVT summary

13.1.2 DCH Electronics

13.1.2.1 Design Goals

The Super*B* Drift Chamber (DCH) Front End Electronics (FEE) is designed to extract and process the about 8000 sense wire signals for tracking and energy loss measurements purpose and to provide informations for Global Trigger generation (trigger primitives).
Two possible scenarios have been foreseen for the dE/dx measurement. The first one is based on the measurement of the sense wires integrated charge (Standard Readout), while the second one is based on electron clusters detection (Sampled Waveforms). A description of the requirements for the two scenarios can be found in the DCH chapter.

13.1.2.2 DCH Front-end system (block diagram)

The DCH FEE chain block diagram is the same for the two options and is shown in Fig.13.2 for the Standard Readout case. The chain is split in two blocks:

- ON DETECTOR electronics: HV distribution and preamplifier boards located on the backward end-plate to preserve sense wire Signal to Noise Ratio.

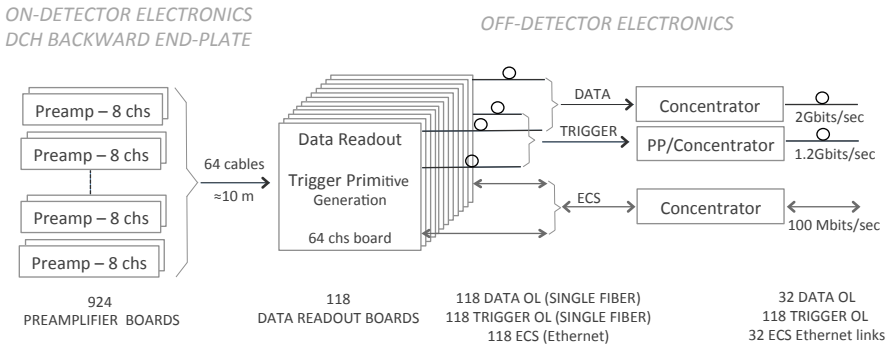

Figure 13.2: DCH front-end block diagram (Standard Readout)

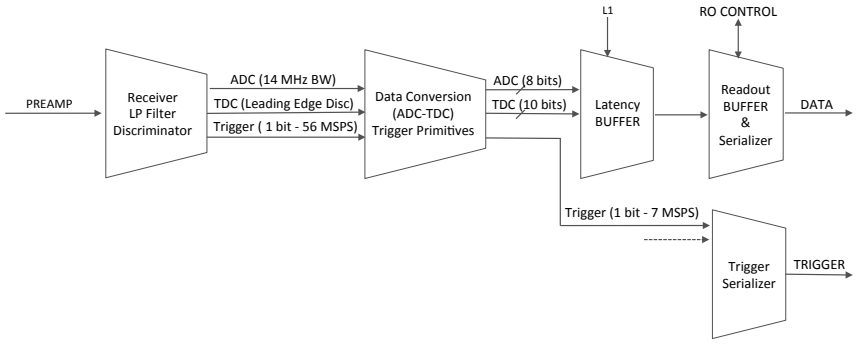

Figure 13.3: Front End Board Block Diagram (Standard Readout)

- OFF DETECTOR electronics: Data Readout and Concentrator Boards located on the top-side of the experiment.

13.1.2.3 Standard Readout - OFF DETECTOR electronics

Front End Boards - Block Diagram Front End Boards (FEB) will host up to 64 channels and will be made of three stages as shown in fig.13.3. The first one receives signals from preamplifiers and generates analog and discriminated outputs. The second stage provides digitization for charge and time measurements and includes the logic for trigger primitives generation as well. Finally, the third stage contains the Latency and Readout Buffers and the dedicated control logic. FEBs will include an ECS section as well (not shown in the block diagram) for parameters setting/sensing and FEE chain test.
Input signal connections will be implemented by means of twisted or mini-coaxial cables, while output connections will depend on the data path. DAQ chain and Trigger chain data path will use optical links while ECS will use copper links (see ETD Control System chapter).

Front-End-Boards - Receiver Section This stage amplify and split the preamplifier output signal to feed an anti-aliasing 14 MHz low-pass filter (charge measurements) and a leading edge discriminator (time measurements).

Front-End-Boards - Digitization Section The 14 MHz filter output signal is routed to an eight bits and (about) 28 MSPS FADC whose outputs feed a section of the system Latency Buffer implemented in a FPGA. Thirty-two FADC output samples (corresponding to about 1.14 μs, enough to span the full signal development) will be readout in presence of a Level 1 (L1) trigger

and, eventually, stored in a Readout Buffer.
The comparator output is routed to a FPGA where it is spit in two paths. The first one is sent to a TDC (implemented in the FPGA itself using the oversampling method) for time measurement. The second one, synchronized with the system clock and conveniently stretched to remove redundant informations, is sent to the DCH Trigger Segment Finding (TSF) modules (see ETD Trigger chapter).
The TDC outputs are routed to the second section of the Latency Buffer that, again, will be readout in presence of a L1 trigger signal.
The event data structure will not have a fixed length as L1 triggers spaced less than single event readout time will extend the time window to include the new event. Nevertheless, the board structure will be also compatible with local Feature EXtraction (FEX) implementation, i.e. the extraction of relevant information from the digitized data. In case of FEX implementation the transferred data stream would have a fixed length; an example of a possible readout data structure is shown shown in table 13.3.
In both cases the first, non zero, FADC output can be used for amplitude correction in discriminated data then minimizing input signal slewing effects.

Table 13.3: FEX based data stream (fixed length structure)

Data stream example
Digitizer Module Address (2 bytes)
Flag (1 byte)
Trigger Tag (1 byte)
Counter (1 byte)
Charge (2 bytes)
Time (2 Bytes)
1st ADC sample (different from baseline) for time walk correction (1 byte)

13.1.2.4 Sampled Waveforms - OFF DETECTOR electronics

The Cluster Counting technique for dE/dx measurement is based on the detection of electron clusters (primary ionization measurement) then high bandwidth devices and high sampling frequency digitizers (at least 1 GSPS) must be used.
Moreover, because data throughput must sustain the Super$B$ foreseen 150 kHz average trigger rate, a very fast processing is required. The constraint, at the state of art of technology, result in a huge power requirement and, as a consequence, in a low FEB modularity. Concerning tracking requirements, if we assume that full efficiency in single electron cluster detection is achieved, Cluster Counting measurement already includes information for tracking purpose (it is just required to store clusters arrival time instead of simply counting them).
Sampled Waveforms DCH FEE chain block diagram is similar to the diagram shown in fig.13.2; but, because of the lower board modularity both the number of crates and boards increase significantly (see table 13.4).

Front End Boards Front End Boards will be based on high sampling rate ($\geq$ 1 GSPS) digitizer, then a limited number of channels can be packaged in a single board, mainly because of power requirements. At present, up to 8 channels working at 1 GSPS have been packaged in a single VME 6U board. Nevertheless, in the next future, board modularity could get to 16 (or 24) with small increase in power requirements.
The circuit structure is very close to the block diagram shown in 13.3. Differences arise in digitizing section as no TDC is required for time measurements and also trigger primitives are generated from FADC outputs.
A sensitive issue concerns the FEX. Because of the large amount of data per channel (about 1 thousand of bytes) we can not transfer raw data to the DAQ then FEX must be implemented in the FEB itself. Thus when an L1 accept is raised all the event samples must be examined to identify clusters. The time required to implement the procedure is still compatible with the average trigger rate foreseen at the nominal Super$B$ luminosity ($\sim$ 150 kHz), but it could be a limit if the luminosity increases.
Another issue concerns the radiation background, as high performances RAM based FPGA must be used in the design.

Table 13.4: Number of links (Data, ECS, Trig), FEBs and crates for 64 channels Standard Readout (SR) and 16 channels Sampled Waveforms (SW) board modularity

	Mod	Data	ECS	Trig	Boards	Crates
SR	64	32	32	118	118	8
SW	16	32	32	118	462	29

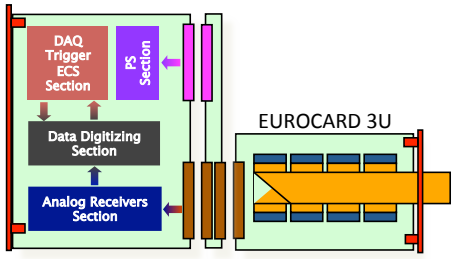

Figure 13.4: VFEB - FEB connections (FEB board - Custom Backplane - Interconnection Board

13.1.2.5 Front End Crates

Each Front End Crate will host up to 16 FEB, a Power Supply board for VFEB, Data Concentrators and, eventually, Trigger Patch Panel o Trigger Concentrator. Custom backplanes will be designed to:

- distribute power and common signals to the FEBs
- allow the use of Interconnection Boards to collect low modularity VFEB cables (fig 13.4)
- route some of the trigger signals to the neighbors boards (see ETD Trigger chapter) and (eventually) to distribute common signals to the boards

13.1.2.6 Number of crates and links

Table 13.4 shows the estimation of the number of links, boards and crates required for both DAQ and Trigger FEE chains (each crate is supposed to host up to 16 FEB). As shown in the table the number of Trigger OL do not change despite the different FEB number for Standard Readout or Sampled Waveforms scenarios. This is because the Sampled Waveform option foresees a Concentrator board also for the trigger chain to compensate for FEBs low modulerity. The board will collect Trigger OL coming from several FEBs and will deliver a single OL to the TFS modules.
The estimation has been done assuming:

- 150 kHz L1 trigger rate, 7392 sense wires (subdivided in 10 super-layers)
- 10% chamber occupancy in 1 μs time window
- 48 bytes per channel data transfer
- single link bandwidth is 2 Gbits/sec for DAQ data path and 1.2 Gbits/sec for Trigger data path

13.1.2.7 ECS

Each FEB will host a mezzanine board to manage ECS communication. Besides the control of the board, ECS mezzanine should provide the capability of data readout for debugging purpose. Detail can be found in the ETD ECS chapter.

13.1.2.8 Cabling

Because the large number of channels involved, DCH cable layout must be carefully designed. The main requirement concerns the possibility of replacing, in case of failure, a VFEB without disconnecting too many cables. Thus, signal and HV cables should be routed through the chamber outermost layer to minimize cables overlap. Table 13.5 shows the foreseen number of cables and a rough estimation of cable sizes.

13.1.2.9 Power Requirements

A very preliminary power requirement estimation is shown in table 13.6. The estimation for ON-DETECTOR electronics is based on preamplifier simulation and prototype test, while estimation for OFF-DETECTOR electronics come from the state of art of digitizing board available. Local (VFEB) voltage regulation is supposed to be implemented by means of linear low-drop hard-rad regulator.

Table 13.5: Estimation of the number and dimension of DCH cables (7392 sense wires - VFEB modularity = 8 channels)

	LVPS	HV	Signal (coax)	Signal (twisted)
Quantity	118	32	7392	924
N of cores	16	25	1	16
Cond. area (mm^2)	0.5	0.07		
Overall diam. (mm)	12	12	1.8	6.5

Table 13.6: Power requirement estimation for bot Standard Readout (SR) and Sampled Waveform (SW)

	Channel	Board	Overall
SR VFEB	30 mW		250 W
SW VFEB	150 mW		1.2 kW
SR FEB		40 W	5 kW
SW FEB		40 W	19 kW
SR & CC Data Conc.		30 W	240 W
SW Trig Conc.		30 W	870 W

13.1.2.10 DCH Summary

Number of Control Links	32
Number of Data Links	32
Total Event Size	update
On-Detector Power Consumption	0.25-1.2kW

Table 13.7: DCH summary

13.1.3 PID Electronics

The electronics will equip the 18,432 channels of the 12 sectors of the FDIRC. The electronics chain is based on a high resolution/ high count rate TDC, a time associated charge measurement over 12 bits and an event data packing sending event data frames to the data acquisition system (DAQ). The target performance of the overall electronics chain is a time precision of 200ps rms. This chain has to deal with a count rate per channel up to 500 KHz, a trigger rate up to 150 KHz and a minimum spacing between triggers of about 50 ns.

The estimated radiation level is expected to be about 100 rads per year. The use of radiation tolerant components or off-the-shelf radiation-qualified components is mandatory. However, the expected energy of the particles may make the latch-up effect almost impossible. Thus, the design has to take into account only Single Event Upsets. We selected the ACTEL family FPGA components for their non-volatile flash technology configuration memories, which are well adapted to radiation environment.

The baseline design assumes a 16-channel TDC ASIC with steps of 200 ps and a overall precision of 100 ps rms, embedding an analog pipeline in order to provide an amplitude measurement associated with the hit time. Thanks to a 12-bit ADC, the charge measurement will be used for electronics calibration, monitoring and survey purposes. The front-end (FE) board FPGA synchronizes the process, associates the time and charge information and finally packs them into a data frame which is sent via the backplane to the FBLOCK control board (FBC). The FBC is in charge of distributing signals coming from the FCTS and ECS, packing the data received from the FE boards to an n-event frame including control bits and transferring it to the DAQ.

13.1.3.1 The Front-end Crate

The board input will fit the topological distribution of the PMTs on the FBLOCK. The PMTs are arranged as a matrix of 6 in vertical direction by 8 in horizontal direction. Each column of 6 PMTs will fit to one FE board. One vertical backplane (PMT Backplane) will interface between the 4 connectors of each PMT base to one connector of FE board. The PMT Backplane is also in charge of distributing the High Voltage, thus avoiding HV cables to pass over the electronics. The FB crate will use as much as possible the elements of a commercial crate, in order to avoid the design of too many specific elements like board guides.

13.1.3.2 The Communication Backplane

The communication backplane distributes the ECS and FCTS signals from the FBC to the 8 FE boards thanks to point to point LVDS links. It connects each FE board to the FBC for data transfer.

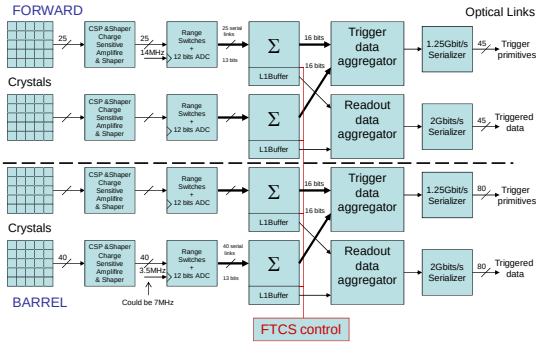

Figure 13.5: EMC Electronics

13.1.3.3 The PMT Backplane

The PMT backplane is an assembly of 8 motherboards, each corresponding to a column of 6 PMTs.

13.1.3.4 Cooling and Power Supply

The cooling system must be designed in order to maintain the electronics located inside at a constant temperature close to the optimum of 30 degrees. The air inside the volume must be extracted while the dry, clean temperature controlled air will be flowing inside. Each FB crate will have its own fan tray like in a commercial crate. 4000 m3/h can be considered as the baseline value for the whole detector. The crate and boards will be cooled by a water based cooler system.

13.1.3.5 The Front-end Board

One FE board is constituted of 6 channel-processing blocks thus handling a total of 96 channels. The channel-processing block is based on one SCATS chip, one ADC, one ACTEL FPGA and the associated glue logics. The FPGA receives event data from the TDC and the converted associated charge from the ADC. The 16-bit data bus coming out of the TDC is de-serialized and split into 16 data bus corresponding to the 16 channels. A dedicated mechanism inside the FPGA permits to insert the events at their proper position, with respect to the hit time, in the event buffer. At this level, the design perfectly fits with the common proposal for the latency buffer and derandomizer (CFEE). Event data is stored in the event buffer where it is kept until either been thrown away if it is too old, or sent to the derandomizer located in the master FPGA upon the reception of the L1 trigger.

The master FPGA receives event data from the 6 channel processing blocks, packs it in a frame with parity bits for data checking and transmits it in a serial differential LVDS format to the FBC via the communication backplane.

13.1.3.6 The Crate Controller Board (FBC)

The master FPGA receives event data from the 6 channel processing blocks, packs it in a frame with parity bits for data checking and transmits it in a serial differential LVDS format to the FBC via the communication backplane.

13.1.3.7 PID Summary

There is thus one link per sector, leading to a total of 12 readout links for the whole FDIRC. Each link has a mean occupancy of 15%, thus far below the limit fixed to 90% by ETD official rules.There is thus one link per sector, leading to a total of 12 readout links for the whole FDIRC. Each link has a mean occupancy of 15%, thus far below the limit fixed to 90% by ETD official rules.

Number of Control Links	12
Number of Data Links	12
Total Event Size	5 kbyte
On-Detector Power Consumption	15kW

Table 13.8: PID summary

13.1.4 EMC Electronics

This is still the version from the Whitepaper!!!

Two options have been considered for the EMC system design—a *BABAR*-like push architecture where all calorimeter data are sent over synchronous optical 1 Gbit/s links to L1 latency buffers residing in the trigger system, or a "triggered" pull architecture where the trigger system receives only sums of crystals (via synchronous 1 Gbit/s links), and only events ac-

cepted by the trigger are sent to the ROMs through standard 2 Gbit/s optical links.

The triggered option, shown in Fig. 13.5, requires a much smaller number of links and has been chosen as the baseline implementation. The reasons for this choice and the implications are discussed in more detail below.

To support the activated liquid-source calibration, where no central trigger can be provided, both the barrel and the end-cap readout systems need to support a free running "self-triggered" mode where only samples with an actual pulse are sent to the ROM. Pulse detection may require digital signal processing to suppress noisy channels.

Forward Calorimeter The 4500 crystals are read out with PIN or APD photodiodes. A charge preamplifier translates the charge into voltage and the shaper uses a 100 ns shaping time to provide a pulse with a FWHM of 240 ns.

The shaped signal is amplified with two gains ($\times 1$ and $\times 64$). At the end of the analog chain, an auto-range circuit decides which gain will be digitized by a 12 bit pipeline ADC running at 14 MHz. The 12 bits of the ADC plus one bit for the range thus cover the full scale from 10 MeV to 10 GeV with a resolution better than 1%. A gain is set during calibration using a programmable gain amplifier in order to optimize the scale used during calibration with a neutron-activated liquid-source system providing gamma photons around 6 MeV.

Following the *BABAR* detector design, a push architecture with a full granularity readout scheme was first explored. In this approach, the information from 4 channels is grouped, using copper serial links, reaching an aggregate rate of 0.832 Gbit/s per link to use up most of the synchronous optical link's 1 Gbit/s bandwidth. A total of 1125 links are required. The main advantage of this architecture is the flexibility of the trigger algorithm that can be implemented off-detector using state of the art FPGAs without constraining their radiation resistance. The main drawback is the large cost due to the huge number of links.

The number of links can be reduced by summing channels together on the detector side, and only sending the sums to the trigger. The natural granularity of the forward detector is a module which is composed of 25 crystals. In this case, data coming from 25 crystals is summed together, forming a word of 16 bits. Then the sums coming from 4 modules are aggregated together to produce a payload of 0.896 Gbit/s. In this case, the number of synchronous links toward the trigger is only 45. The same number of links would be sufficient to send the full detector data with a 500 ns trigger window. This architecture limits the trigger granularity, and implies more complex electronics on the detector side, but reduces the number of links by a large factor (from 1125 down to 90). However, it cannot be excluded that a faster chipset will appear on the market which could significantly reduce this implied benefit.

Barrel Calorimeter The EMC barrel reuses the 5760 crystals and PIN diodes from *BABAR*, with, however, the shaping time reduced from 1 μs to 500 ns and the sampling rate doubled from 3.5 MHz to 7MHz. The same considerations about serial links discussed above for the forward EMC apply to the barrel EMC. If full granularity data were pushed synchronously to the trigger, about 520 optical links would be necessary.

The number of synchronous trigger links can be drastically reduced by performing sums of 4×3 cells on the detector side, so that 6 such energy sums could be continuously transmitted through a single optical serial link. This permits a reduction in the number of trigger links so as to match the topology of the calorimeter electronics boxes, which are split into 40 ϕ sectors on both sides of the detector. Therefore, the total number of links would be 80 both for the trigger and the data readout toward the ROMs, including a substantial safety margin (> 1.5).

13.1.4.1 EMC Summary

13.1.5 IFR Electronics

ver 0.5 sep 18 2012, Angelo Cotta Ramusino

The full description of the IFR readout electronics, going from the design constraints determined by the IFR detector's features to the detailes of the adopted baseline design is given in the subdetector chapter. The present subchapter is meant to highlight those features of the IFR electronics description which are most related to the Super$B$'s common ETD and ECS infrastructures. The active layers of the IFR are equipped with modules in which the detector elements (of different widths for the PHY and the Z views in the barrel) are assembled in two orthogonal layers. The overall IFR electronics channel count amounts to 11604 for the barrel section and 9540 for the endcaps, assuming that, for both sections, the IFR is instrumented with 9 active layers.

BARREL	
Maximum channel count per module:	32
Number of MOD32 processing units per module	**1**
TOTAL NUMBER OF MODULES IN BARREL	**384**
Total Number of MOD32 processing units	**384**
Sampling period = 1 / FCTS_clock (ns)	17,86
Number of samples in the trigger matching window (including framing words)	**16**
ENDCAP EVENT SIZE (kB)	**24,58**
TRIGGER RATE (kHz)	**150**
TOTAL ENDCAP BANDWIDTH (Gbps) (including 8b/10b encoding overhead)	**36,86**
Number of data links from the endcap detectors	24
Bandwidth per link (Gbps)	1,536

Figure 13.6: Estimation of the event size and data bandwidth for the IFR "Barrel" section

The IFR detector will be read out in "binary mode": the output of each SiPM device will be amplified, shaped and compared to a threshold, the binary status of each comparator's output being the variable to be recorded to reconstruct the particle tracks within the IFR detector. The downstream stages of the IFR electronics are the "digitizers" which sample the comparators' outputs at Super$B$ clock rate and store the samples into local "on-detector" circular memories. These buffers are designed to keep the data for a time interval at least equal to the Super$B$ trigger command latency. The last stage of the "on-detector" readout system is based on Finite State Machines (FSM for short) which extract, from the local latency buffers, the data selected by the FCTS trigger command.

ENDCAP	
Average channel count per module	92
Number of MOD32 processing units per module	**3**
TOTAL NUMBER OF MODULES IN ENDCAPS	**108**
Total Number of MOD32 processing units	**324**
Sampling period = 1 / FCTS_clock (ns)	17,86
Number of samples in the trigger matching window (including framing words)	**16**
ENDCAP EVENT SIZE (kB)	**20,736**
TRIGGER RATE (kHz)	**150**
TOTAL ENDCAP BANDWIDTH (Gbps) (including 8b/10b encoding overhead)	**31,104**
Number of data links from the endcap detectors	16
Bandwidth per link (Gbps)	1,944

Figure 13.7: Estimation of the event size and data bandwidth for the IFR "Endcap" section

In the baseline version of the IFR electronics design the digitizer blocks introduced above have 32 input channels. The "trigger matched" data output by each digitizer in response to a received trigger pulse is sent, via serial links on copper, to the "data merger" units. These units assemble the trigger matched data from a number of front end digitizers into event data packets of suitable size and forward them to the ROMs via the Super$B$ fast data links. The application of the binary readout scheme to the IFR prototype detector developed in the R&D

phase has allowed the determination of parameters, such as the sampling frequency and the number of samples, which are relevant to the performance of IFR readout system.

Tables in figures 13.6 and 13.7 show the estimated event size and data bandwidth required for the IFR readout at the nominal SuperB trigger rate of 150kHz. The figures presented in the tables take into account a trigger jitter of 100ns. The event size and required bandwidth could be reduced by applying the data reduction scheme proposed by the ETD group: if a new trigger would select data that has already been sent in response to a previous one, the repeating data is not retransmitted and a pointer to the start of the repeating data within the previous packet would be sent instead.

LAYER WIDTH	LAYER	No. Modules per layer	LAYER ENABLE	PHI ASSUMING 50MM BARS	ZETA ASSUMING 106MM BARS
1963	1	6	1	13	17
1987	2	6	1	13	17
2050	3	6	1	13	17
2113	4	6		14	17
2176	5	6		14	17
2240	6	6		14	17
2304	7	6	1	15	17
2367	8	6		15	17
2431	9	8		12	17
2494	10	8		12	17
2569	11	8	1	12	17
2641	12	8		13	17
2712	13	8		13	17
2784	14	8	1	13	17
2879	15	8		14	17
2973	16	8	1	14	17
3068	17	8		15	17
3144	18	8	1	15	15
3296	19	8	1	16	15
NUMBER OF MODULES per sextant:		64		TOTAL PER SEXTANT	1940
TOTAL NUMBER OF MODULES	384			TOTAL CHANNELS PER BARREL	11640

Figure 13.8: Block diagram of the IFR readout ASIC

The IFR scintillation detectors, each equipped with a single-photon counting device (silicon photomultiplier or SiPM for short), are grouped in modules which are inserted in selected gaps of the flux return steel or around it. The signals from all SiPMs of a module are carried by thin coaxial cables which exit the module's aluminum enclosure and are mass-terminated to a high density connector on a carrier PCB (printed circuit board). The average length of the coaxial assemblies connecting the sources (SiPMs) to the first amplification stages is in the order of a few meters because it is convenient to locate the ASICs' carrying boards where they would be accessible for any maintenance eventually needed.

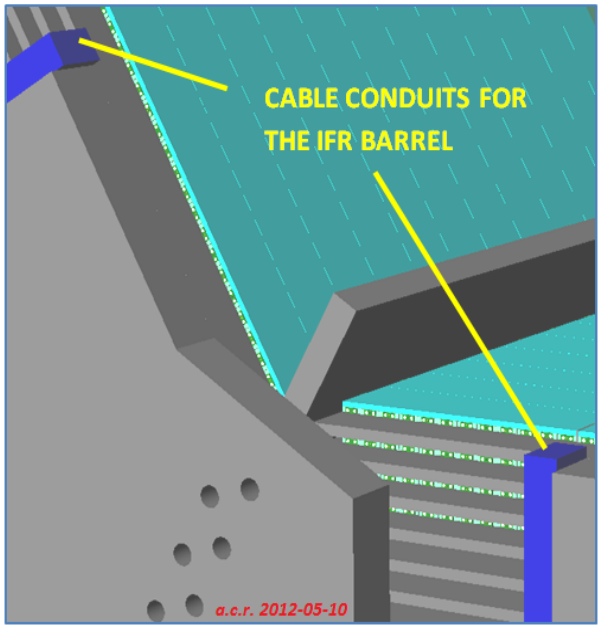

Figure 13.9: The IFR cable conduits for 2 sextants

While a readout system based on "COTS" ("Components Off The Shelf") was designed and successfully exploited for the readout of the IFR prototype, the front end stages of the electronic readout chain for the Super*B* IFR detector, for the reasons illustrated in the IFR subdetector chapter, will be implemented in an ASIC, whose block diagram is shown in figure 13.8.

Fig. 13.9 shows the situation for the IFR barrel: in this representation the metal enclosures of the modules are not shown; the closest convenient locations for the ASICs carrying boards are indicated by the yellow callouts.The front end cards are installed inside the 3" x 5" cable conduits as suggested in figure 13.10. While

the figure only shows the double shielded, multi differential-pair cables (green jacket) needed to route the front end cards' output serial lines to the data merger units, the cable conduits are also meant to host cables for the distribution of the SiPM bias voltages (one bias voltage common to all SiPMs of a module), of the fast (FCS) and slow (ECS) commands and, finally, of the supply voltages for the front end cards.

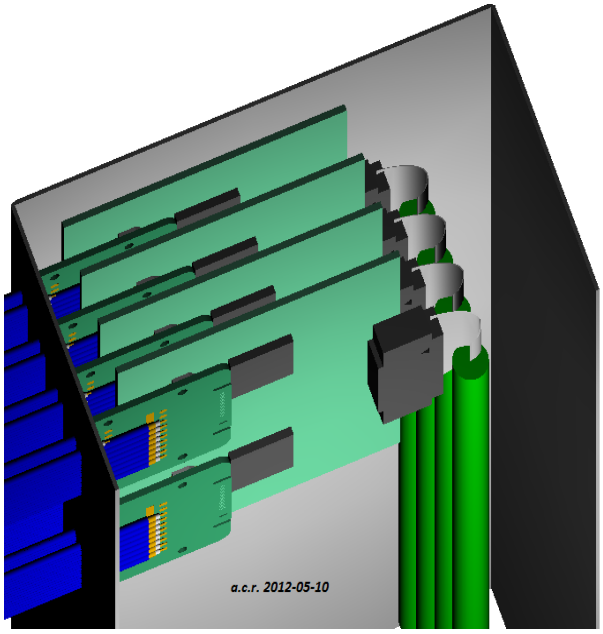

Figure 13.10: Detail of front end cards installed in the IFR cable conduit

Figure 13.11 shows the perspective view of the two doors of an endcap: the yellow callouts indicate the openings in the side-lining steel through which the data, control and power cables for the detector modules will be routed. The signals emerging from these openings are routed to the crates indicated by the red callouts. For the endcap section of the IFR, the front end cards carrying the IFR read out ASICs could be installed directly in the crate and connected to the data merger cards through the crate's backplane interconnections.

The "data merger" crates are interfaced to the Super*B* FCTS (Fast Control and Timing System) and ECS (Experiment Control System) from which they receive and execute the commands controlling the data acquisition and the detector configuration respectively. The data merger units also collect the trigger matched data from the front end cards and merge the input streams into the output packets sent, via the high speed optical data links, to the SuperB ROM (ReadOut Modules).

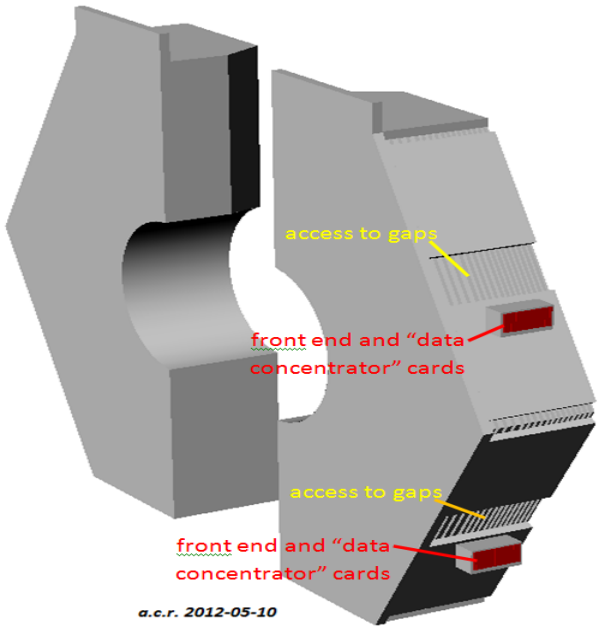

Figure 13.11: Perspective view of IFR endcaps

The IFR barrel will be equipped with a total of 6 "data merger" crates while 8 are foreseen for the endcaps. Further details on partitioning, location and construction of the data merger crates are given in the IFR subdetector chapter, which also provides a description of the services needed by the IFR readout in the experimental hall: - SiPM supply voltages: 384 (barrel) + 324 (endcaps) = 708 "HV" channels with: maximum output voltage 100V, 10 bit resolution, maximum output current 25mA. The power dissipated by the SiPMs in the whole IFR under nominal operating conditions is of the order of a few tens of Watts - front end cards supply voltages: 354 + 354 "LV" supply channels with: +3.3V or -3.3V output voltage respectively, maximum output current 1A, IR drop compensation The power dissipated by

the front end stages for each 32 SiPM group is around 1.6W and thus the power dissipated by the front end stages is about 620W for the barrel and 520W for the endcap - cooling: the temperature of the IFR steel should be controlled to within a few degrees, as it was for BaBar; the design of the barrel cooling system should then take into account the estimated 1140W dissipated in total by the front end stages of the IFR barrel and endcap electronics.

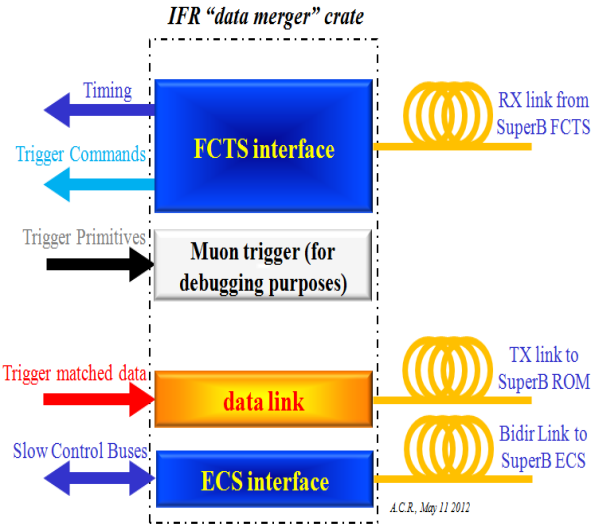

Figure 13.12: Main functions performed by the electronic units in the "data merger" crate

13.1.5.1 IFR Summary

Number of Control Links	20
Number of Data Links	40
Total Event Size	45 kbyte
On-Detector Power Consumption	1.2kW

Table 13.10: PID summary

13.2 Electronics Infrastructure

13.2.1 Power supplies, grounding and cabling

Gianluigi Pessina

13.2.1.1 Power Supply to the Front-end:

The voltage supply system is normally composed by a cascade of AC/DC, DC/DC and linear regulators. Depending on the power dissipation and noise requirements some of the above elements can be avoided. The supply system of an accelerator-based experiment has known additional constraints to be satisfied. The large particle fluence and the presence of a strong magnetic field can have an impact on the aging and behavior of the electronic equipment. The first constraint is addressed only by adopting radiation hardened (rad-hard) technology and using suitable layout recipes for the monolithic circuits. This is common to all the devices that sit in the detector area. Magnetic field has generally less impact except for AC/DC and DC/DC converters that need to use inductances and/or transformers, having ferromagnetic cores.

Power Supply outside the detector area: In the following we will describe our solution, able to face the above constraints. The strategy we would adopt is to minimize the number of regulators in the detector area. The distance between the regulators and the front-end can be a few tens of meters. The energy the cable is able to store in its inductive component can be large and attention must be adopted to protect the connected electronic equipment in case of accidental short circuit to ground. Fig. 13.13 shows an example of the recovery from a short circuit of $50\,m$ cable with $4\,mm^2$ section. The short circuit current was limited to $20\,A$. A N-MOS, IPP50CN10NG, with $50\,m\Omega$ ON resistance simulated the short circuit and it breaks down above about $100\,V$ when in open state, that explains the reason of the clipping. The measurement has been taken in the worst condition of no applied load. It is clear from this that an accidental short circuit is very critical in producing possibly destructive damaging.

We have found that most of the cables with 3 or 4 poles and cross-section between $1.5\,mm^2$

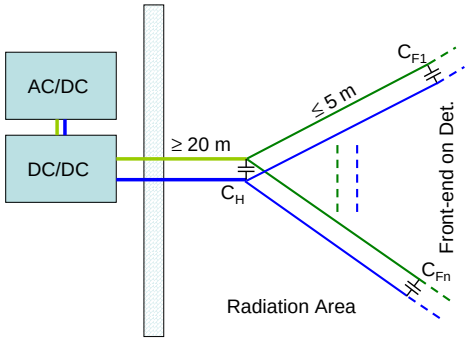

Figure 13.14: Possible layout for a sub-detector for what concerns voltage supply.

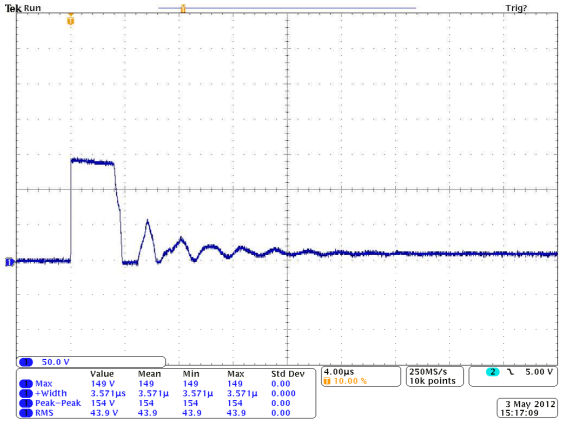

Figure 13.13: Signal at the end of a 50 m cable after a short circuit. The clipping at 150 V is due to the breakdown of the MOS switch used.

and $4\,mm^2$ have an inductance per unit length, L_M, of the order of $0.7\,\mu H/m$, from DC to few hundred of KHz. Calling I_{short} the maximum delivering current available from the power supply and l the cable length, then:

$$E_{nergy} = \frac{1}{2} L_M l I_{short}^2 \qquad (13.1)$$

is the available energy driven to the load in case of accidental short circuit. To limit the voltage at a safe level our straightforward solution is to add in parallel to the load a capacitance able to store such released energy. This can be done if we satisfy that:

$$\frac{1}{2} C_{lim} V_{over}^2 = \frac{1}{2} L_M l I_{short}^2 \qquad (13.2)$$

where V_{over} is the maximum voltage that must not be exceeded and C_{lim} is the capacitance whose value must be chosen to satisfy the eq. with the given voltage V_{over}. As an instance, with $50\,m$ of cable length, $I_{short} = 20\,A$ and $C_{lim} = 160\,\mu F$ the maximum over voltage excursion would be less than $9.5\,V$.

Adopting the introduced technique a hub with a distribution to several shorter cables can be implemented as shown in Fig. 13.14. A large value capacitance, C_H, is at the end of the cable that connects the DC/DC regulators from the outside to the inside of the detector area. In our example we continue with considering $50\,m$ of cable length and $C_H = 160\,\mu F$. From this point several shorter cables, or stubs, connect the various parts of the detector or sub-detector front-end. To save space, the sections of these last cables can be smaller since they have each to manage a smaller current. At the end of each of these stubs, $5\,m$ in our present example, a smaller value capacitance, C_{Fx}, $(33\,\mu F)$ is connected. In case of short at the end of a stub all the current flows into it. But as soon as the short is opened capacitance C_H absorbs the energy of the longer cable, while the energy of the shorted stub is managed by the corresponding capacitance C_{Fx}. Fig. 13.15 shows that the signal at the end of the $50\,m$ cable has an over voltage of only about 10 %. The maximum current was $20\,A$ and it can be seen that the baseline before the short is released is about $2\,V$, the dropout generated by the $20\,A$ current across about $0.1\,\Omega$ given by the sum of the stub (as a reference a section of $1\,mm^2$ has an impedance of about $16\,\Omega/Km$) and the ON resistance of the N-MOS. Fig. 13.16 shows the over voltage present at the stub end where the short is generated and released; again the over voltage is contained within about 10 %. As it can be appreciated, the baseline that precedes the release of the short is about $1\,V$, namely $20\,A$ developed across the about $50\,m\Omega$ ON resistance of the N-MOS. In the test setup of the laboratory we implemented 2 stubs and Fig. 13.17 is the signal at the stub end where the short circuit was

not present. Again the over voltage is respecting the safety conditions. The principle applies well also if a low regulated voltage is considered and Fig. 13.18 is an example of release from a short of more than $25\,A$ on a $5\,m$ cable ($2.5\,mm^2$ of cross-section) loaded with $160\,\mu F$ capacitance.

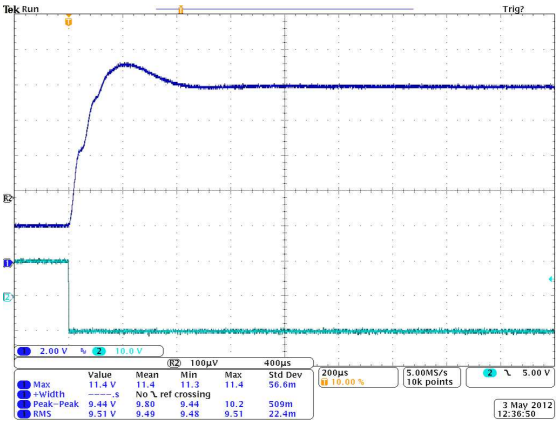

Figure 13.15: Signal at the end of a $50\,m$ cable (blue line) after that a short circuit is generated at one end of a stub. The $50\,m$ cable is loaded with a $160\,\mu F$ capacitor and the short current is $20\,A$; the supply voltage is $10\,V$. Every stub is loaded with $33\,\mu F$. The green line is the voltage driver at the gate of the switched N-MOS.

The suppression capacitance must show a very small series resistance and inductance. Capacitors with plastic dielectric such as Metalized Polypropylene Film satisfy this condition. As an example the $160\,\mu F$ we have adopted for the test has only $2.2\,m\Omega$ of series resistance, but, being big in volume, it shows a series inductance of a few tens of nH. To compensate for this last effect a smaller value (and volume) capacitance ($1\,\mu F$) is put in parallel, able to account for the fast part of the rising signal. Metalized Polypropylene Film capacitances have a range of values limited to a few hundreds of μF. As a consequence, a limited value of current per cable, $10\,A$ to $20\,A$, results in a good compromise. Many commercial regulators, also in the form of the so called bricks and half-bricks layouts, are available on the shelf at low cost. This strategy is particularly usefully for minimizing the dropout along the cable and it is of particular concern when a low voltage is needed.

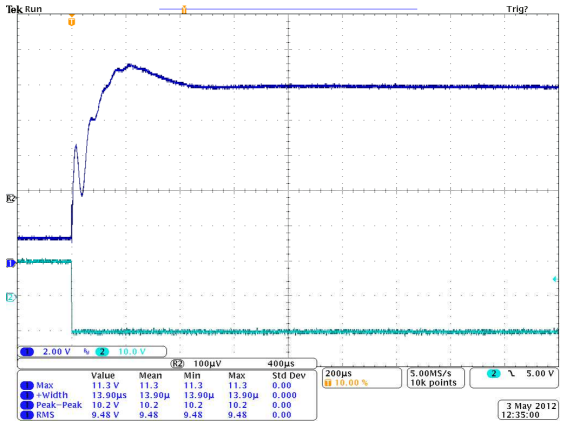

Figure 13.16: Signal at the end of a stub of Fig. 13.14 after a short circuit (blue line). Two stubs were present in the test setup. C_H is $160\,\mu F$, the C_{Fx} are $33\,\mu F$ and the short current is $20\,A$; the supply voltage is $10\,V$. The green line is the voltage driver at the gate of the switched N-MOS.

We cannot forget that an over-voltage can happen due to a possible malfunctioning of the regulator. To reject rapidly and with good precision this effect a stack of fast diodes is a good choice. For instance with a voltage supply of $10\,V$ the series connection of about 20 diodes allows to maintain the safe operating condition provided that they are in contact with a heat sink in case the problem persists for a while. The location of the stack of diodes can be close to the regulator and space occupation would not constitute a problem.

Noise cabling and shielding: The combination of the inductance component of the wires and the suppression capacitance has a twofold utility as it behaves also as a low pass filter. Fig. 13.19 shows the noise at the end of the $50\,m$ cable plus $2 \times 5\,m$ stubs when $160\,\mu F$ plus $2 \times 33\,\mu F$ capacitances load the combination. The applied supply voltage was $10\,V$ and the load $3.3\,\Omega$. In

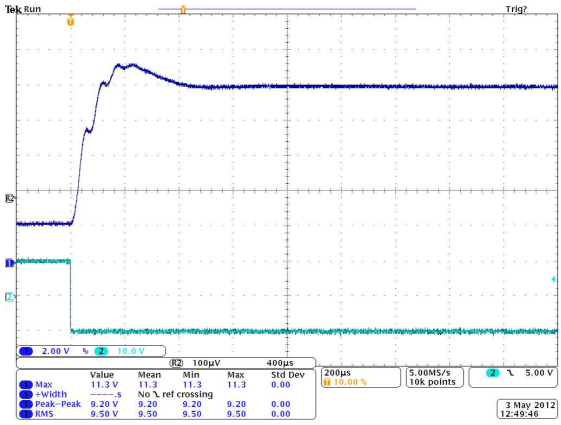

Figure 13.17: Signal at the end of a stub of Fig. 13.14 after a short circuit (blue line) happened at another stub. Two stubs were present in the test setup. C_H is 160 μF, the C_{Fx} are 33 μF and the short current is 20 A; the supply voltage is 10 V. The green line is the voltage driver at the gate of the switched N-MOS.

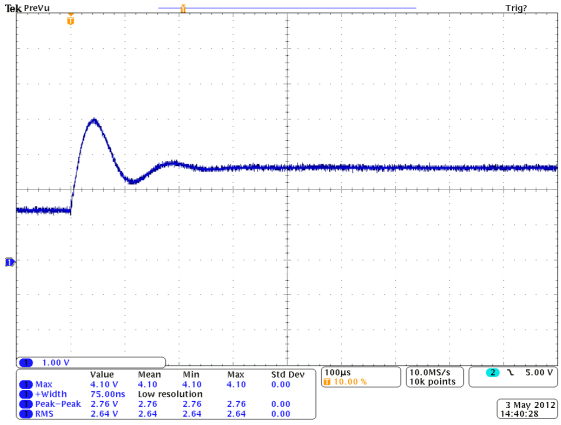

Figure 13.18: Short circuit release on a 5 m cable with 2.5 mm^2 cross-section.

this case a standard commercial regulator has been used. Very low noise DC/DC regulators have been designed [30] and Fig. 13.20 shows the noise performance under the same conditions. Even better performances can be obtained by cascading the DC/DC to a linear regulator of very good quality [31].

Low noise results are obtained if care is considered on the type of cables adopted. In all the measurements described so far cables used were all armored. This precaution allows to shield the supply voltage from outside disturbances but also to avoid to create disturbances to the outside world. We intend to adopt this kind of layout solution for the final experimental setup. In addition, where needed, we intend to add a double shield by inserting the cables inside a tubular copper mesh.

The connection scheme of Fig. 13.14 is, in a natural way, suitable to route ground. Let's suppose that the ground of every detector or sub-detector to which the cables are routed have their ground isolated. Then, we can route a tinned copper wire (or a copper bar) very close to the power supply cables so as to suppress area sensitive to EMI interferences. Such a routing scheme allows a 'star' connection with only one ground contact node (we remember that AC/DC and DC/DC regulators are floating), that is the standard requirement.

Shielding is considered for whose region were the electric or magnetic field can affect the performances. The shields can be considered for the whole sub-detector or individually on a channel by channel basis. This is particularly true with the effect of magnetic field on those detectors that extend on a large volume, such as photomultiplier tubes (PMTs). Past experience showed that in these cases a local shield implemented with mu-metal around every PMT is essential.

Power Supply in the detector area: We are considering the opportunity to use both DC/DC and linear regulators inside the detector area. Inductances and transformers cannot be based on a ferromagnetic coil. As a consequence they are limited in range of values and the switching speed of the DC/DC must be very large. This is the case for the monolithic DC/DC regulator we are considering [32], developed in 0.35 μm CMOS technology based on rad-hard layout and components, and having a switching frequency of the modulator of a few MHz, which allows the use of a coil-free inductance. Based on the same technology a linear regulator is also available [33].

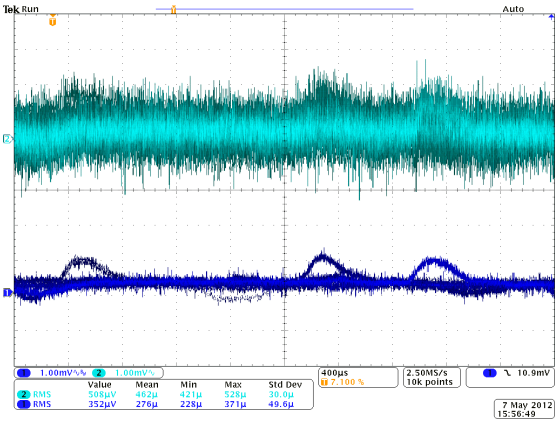

Figure 13.19: Noise after 50 m cable loaded with $160 + 2 \times 33\,\mu F$ capacitance at $10\,V$ and with $3.3\,\Omega$ load. Upper noise is with the full 350 MHz bandwidth of the oscilloscope, Lower noise has the scope bandwidth limited to 20 MHz.

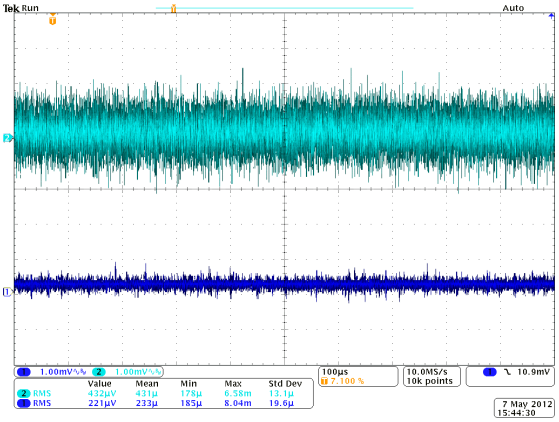

Figure 13.20: Very low noise DC/DC regulator [30]. Measurements condition and setup as for Fig. 13.19

13.2.1.2 High Voltage Power Supply to the Detectors:

High voltage power supplies suffer of similar problems as AC/DC and DC/DC regulators. As a consequence these regulators must be located outside the detector, sub-detector area (we do not know about any commercial rad-hard high voltage regulator). The energy released to the load in case of accidental short circuit would be not an issue thanks to the fact the, normally, such regulators have their driving current limited to a few hundred of μA. As an instance, if we load the line with a $1\,nF$ high voltage capacitor and considering $1\,A$ the short circuit current we expect an over-voltage of about $0.2\,V$. Finally, commercial over-voltage protectors based on gas discharge tubes are very efficient and fast.

13.2.2 Grounding and Shielding

This section has been incorporated in the Power Supply section

13.2.3 Cable Plant

This section has been incorporated in the Power Supply section

Bibliography

[1] A. Sharma, F. Sauli, Nucl. Instr. and Meth. A 350 (1994) 470.

[2] C. Avanzini et Al. Nuclear Instruments and Methods in Physics Research A449 (2000). 237-247.

[3] P.R.Burchat and John Hiser Studies of helium gas mixtures in drift chambers SLAC-PUB-5626 SCIPP 91/25 September 1991.

[4] Gianluigi Cibinetto, *Something about the prototype*, SuperB Workshop and Kick Off Meeting, Elba, May 31 2011

[5] Gianluigi Cibinetto, *Beam Test: data for analysis*, I SuperB meeting, London, Sep 15 2011

[6] Valentina Santoro, *IFR Background Report*, III SuperB meeting, LNF-Frascati, Mar 21 2012

[7] Pierre Jarron, CERN 1211 Geneva 23 Switzerland, *Radiation tolerant electronics for the LHC experiments*, Proceedings of the 4th Workshop on Electronics for LHC Experiments, Rome, Sept 1998, p. 7

[8] Federico Faccio, CERN 1211 Geneva 23 Switzerland, *Radiation effects in devices and technologies*, IN2P3 school, May 2005

[9] *ATLAS Policy on Radiation Tolerant Electronics: ATLAS Radiation Tolerance Criteria*, http://atlas.web.cern.ch/Atlas/GROUPS/FRONTEND/WWW/RAD/RadWebPage/ATLASPolicy/Appendix_1.pdf

[10] W. Dabrowski (AGH University of Science and Technology, Krakow, Poland), *Challenges and benefits of designing readout ASICs in advanced technologies*, Nuclear Instruments and Methods in Physics Research A 579 (2007) pp. 821-827

[11] M.Angelone, M.Pillon, R.Faccini, D.Pinci, W.Baldini, R.Calabrese, G.Cibinetto, A.Cotta Ramusino, R.Malaguti, M.Pozzati, *Silicon photo-multiplier radiation hardness tests with a beam controlled neutron source*, Nuclear Instruments and Methods in Physics Research A 623 (2010) pp. 921-926

[12] Flavio Dal Corso (INFN Padova), *Studies of SiPM @ Padova: Neutrons irradiation at LNL 9-13 Oct 2009*, XI SuperB General Meeting , LNF, Frascati, Dec. 1 2009

[13] Enrico Feltresi (INFN Padova), *Neutron Damage on SiPMs studies at LNL*, XV SuperB General Meeting Caltech, Pasadena CA, USA, Dec. 14 2010

[14] Flavio Dal Corso (INFN Padova), *Status of SiPM; studies @ Padova*, XVI SuperB General Meeting , LNF, Frascati, Apr. 4 2011

[15] A. Cotta Ramusino (INFN Ferrara), *SuperB IFR electronics: update*, 2nd SuperB General Meeting , LNF, Frascati, Dec. 15 2011

[16] Orsay MicroElectronics Group Associated (OMEGA) (LAL, Orsay, France), *EASIROC DATASHEET Version: 5*, April 2011

[17] Orsay MicroElectronics Group Associated (OMEGA) (LAL, Orsay, France), *EASIROC SOFTWARE & TEST BOARD USER GUIDE Version: 11*, April 2011

[18] James W. Meadows, Engineering Physics Division, Argonne National Laboratory, Argonne, Illinois, USA, *The $^{9}Be(d, n)$ thick-target neutron spectra for deuteron energies between 2.6 and 7.0 MeV*, Nuclear Instruments and Methods in Physics Research A 324 (1993) pp. 239-246

[19] A. Cotta Ramusino (INFN Ferrara), *SuperB IFR electronics: update on prototype electronics and IFR_DAQ*, XII SuperB Workshop - LAPP Annecy, Mar. 17 2010

[20] E. Grauges et al. [SuperB collaboration], *SuperB progress report – Detector*, arXiv:1007.4241,2010

[21] A. Cotta Ramusino (INFN Ferrara), *SuperB IFR electronics: update*, 3rd SuperB meeting, LNF, Frascati, Mar. 13 2012

[22] R. Mos, J. Barszcz, M. Jastrzb, W. Kucewicz, J. Młynarczyk, E. Raus, M. Sapor, *Front-End electronics for Silicon Photomultiplier detectors*, Electrical Review 11a (2010) pp. 79-83

[23] A.Baschirotto, G.Cocciolo, M.De Matteis, A.Giachero, C.Gotti, M.Maino, G.Pessina, *A FAST AND LOW NOISE CHARGE SENSITIVE PREAMPLIFIER IN 90 nm CMOS TECHNOLOGY*, Journal of Instrumentation, Jinst, V 7 C01003 pp 1-8 2012.

[24] G. Mazza et al. (Dipartimento di Fisica - INFN Torino), *A CMOS 0.13um Silicon Pixel Detector Readout ASIC for the PANDA experiment*, 2012 JINST 7 C02015 doi:10.1088/1748-0221/7/02/C02015

[25] G. Dellacasa et al. (Dipartimento di Fisica - INFN Torino), *A 130 nm ASIC prototype for the NA62 Gigatracker readout*, Proc. of the Int. Workshop on Semiconductor Pixel Detector for Particles and Imaging (Pixel 2010), Nucl. Instr. and Meth. in Physics Research, A 650 (2011) pp. 115-119

[26] A. La Rosa et al., *Ionizing radiation effects on a 64-channel charge measurement ASIC designed in CMOS 0.35 um technology*, Nucl. Instr. and Meth. in Physics Research A 593 (2008) pp. 619-623

[27] PICMG, AdvancedTCA PCI Express PICMG 3.4 Specification, May 2003

[28] M. Baszczyk, P. Dorosz, S. Głb, W. Kucewicz, M. Sapor, *Four channels data acquisition system for silicon photomultipliers*, Elektronika 12 (2011) pp. 28-31

[29] Paolo Carniti, Andrea Giachero, Claudio Gotti, Matteo Maino, Gianluigi Pessina, *An introduction to CLARO: A fast Front-End ASIC for Photomultipliers*, 2nd SuperB Collaboration Meeting, LNF Frascati, Dec 15 2011

[30] C. Arnaboldi, A. Bau, A. Giachero, C. Gotti, M. Maino, A. Passerini, and G.Pessina, *A Very Low Noise AC/DC Power Supply System For Large Arrays Of Cryogenic Detectors*, 2011 IEEE Nuclear Science Symposium Conference Record, pp. 791-793, February 2012.

[31] G. Pessina Rev. Sci. Instr. **70**, 3473, 1999.

[32] S. Michelis, B. Allongue, G. Blanchot, F. Faccio, C. Fuentes, S. Orlandi, S. Saggini, S. Cengarle, F. Ongaro, J. of Instrumentation, JINST, 7, C01072, 2012.

[33] F. Faccio, P. Moreira, A. Marchioro, S. Velitchko, *A radiation-tolerant LDO voltage regulator for HEP applications* , Conference proceeding of the TWEPP-2005, Valencia (Spain).

14 Software and Computing

Bianchi Pages ?

14.1 Computing Overview F.Bianchi 2 pages

The Super$B$ detector will produce in excess of 500 PB of raw data in 5 years of data taking. The event reconstruction step and the Monte Carlo production will results in 300 additional PB of data. Predictable progress in computing technology will provide performance increase that will help to cope with those data volumes. In addition, effective exploitation of computing resources on the Grid, that has become well established in the LHC era, will enable Super$B$ to access a huge pool of world wide distributed resources.

Crucial issues will be the capacity to efficiently exploit the modern CPU architecture and to efficiently and reliably access huge amount of data physically located in different sites.

The Super$B$ computing effort has been devoted so far to the development and the support of the simulation software tools and the computing production infrastructure needed for carrying out the detector studies and to the design of the computing model of the experiment.

The existing software tools are presented in the first part of this section. To illustrate the scale of the computing problem and how the Super$B$ computing group foresees to handle it, the seconf part of this section contains an overview of the current baseline computing model with an estimate of the Super$B$ computing requirements and a presentation of a possible computing infrastructure. The dedicated R&D program to investigate possible technical solutions is also described.

14.2 Tools to support detector studies F.Bianchi 1 pages

So far, a significant effort of the computing group has been devoted to the development and the support of the simulation software tools and the computing production infrastructure needed for carrying out the detector design and performance evaluation studies.

Quite sophisticated and extended detector and physics studies can now be performed thanks to:

- the development of a detailed Geant4-based Monte Carlo simulation (Bruno) and of a much faster parametric fast simulation (FastSim) which can directly leverage the existing *BABAR* analysis code base;
- the implementation of a production system for managing very large productions that can parasitically exploit the computing resources available on the European and US Grids.

In addition a collaboration like Super$B$ facing the task of preparing design documents and developing software code needs to be supported by a set of suitable computing tools in carrying out its day-by-day coordinated activities.

A description of the tools made available and their capabilities is presented in the following.

14.2.1 Full Simulation A. Di Simone - E. Paoloni - A. Perez 4 pages

The availability of reliable tools for full simulation is crucial in the present phase of the design of both the accelerator and the detector.
First of all, the background rate at the subdetectors needs to be carefully assessed for each proposed accelerator design. Secondly, for a

given background scenario, the designs of the sub-detectors themselves must be optimized to obtain optimal performance. Moreover, full simulation software can be used to improve the results of the fast simulation in some particular cases, as discussed in the following.

14.2.1.1 Bruno: the SuperB full simulation software

The choice was made to re-write from scratch the core simulation software, aiming at having more freedom to better profit from both the Babar legacy and the experience gained in the development of the full simulation softwares for the LHC experiments. Geant4 as the underlying technology was therefore the natural choice, as well as C++ as the programming language.
After some years of implementation, the SuperB full simulation software is, in its present status, usable (and, indeed, used) to assist in the design of the accelerator and detector. Basic functionality is in place, and more is being added following user requests. We will give in the following a short overview of the main characteristics, emphasizing areas where future development is planned.

14.2.1.2 Geometry description

The need to re-use as much as possible the existing geometrical description of the Babar full simulation, called for some interchange, application-independent format to convey the information concerning the geometry and materials of the sub-detectors. Given the present phase of the SuperB experiment, a human-readable format was to be preferred, in order to allow easy changes to the geometry details to reflect different design alternatives.
Amongst the formats currently used in High Energy Physics applications, the Geometry Description Markup Language (GDML) was chosen for the following reasons:

- its XML-based structure allows for relatively easy human inspection and editing, while still providing (by construction) a certain level of robustness.
- it provides some level of modularization, by allowing to split the global geometry into smaller files.
- its specification is an independent project, not linked to any specific application
- Geant4 provides native interfaces to read and write GDML files. This allowed, for example, to export the Babar original geometry, modify it as necessary, and read it back into Bruno.
- ROOT can process GDML geometry as well, allowing for example to easily visualize some simulation result together with the underlying detector geometry using ROOT embedded geometry viewer

The present implementation relies on GDML as the only source of geometry information. The file structure reflects the natural division in sub-detectors, with one global file defining only sub-detector envelopes, each filled in turn (using a different file) with all needed details. Space allocation is thus centrally managed at the level of the top file, while sub-detector communities have the freedom of experimenting different layouts without interfering one with the other.
The consistency of the geometry (volume overlaps, volume overshootings) is periodically checked by means of the default Geant4 tools.
The choice of GDML also brings in some limitations, of course, an example being the limited support for loops and volume parameterization. In the longer term, with the progressive stabilization of the detector layout, it is not to be excluded that the GDML-based approach will be dropped in favor of some custom solution, thus gaining in flexibility while loosing the no-more-crucial easiness of inspection.

14.2.1.3 Simulation input: Event generators

Bruno can be interfaced to an event generator in two ways: either by direct embedding of the generator code or by using an intermediate exchange format.
In the latter case, the event generator is run as a different process and its results are saved in

a file, which is then used to seed the full simulation job. Bruno presently supports two interchange formats: a plain ASCII file and a purely ROOT-based one, using persistified instances of the TParticle class.

14.2.1.4 Simulation output: Hits and MonteCarlo Truth

Hits from the different sub-detectors are created by specific SensitiveDetectors. The transient representation is managed through instances of custom implementations of the G4VHit interface which are translated into instances of ROOT-based classes for persistification. Presently, all sub-detectors are producing hits, which are then saved in the output (ROOT) file for further processing and analysis.
In addition to hits, which represent the simulated event as seen from the detector, another important type of simulation information is the MonteCarlo Truth (MCTruth), intended as a summary of the event as seen by the simulation engine itself, i.e. with full detail. The same ROOT-native class (TParticle) is used in this case for both the transient and persistent representation.
Examples of MCTruth information presently handled by Bruno include:

- full snapshots of the simulation status at different scoring volumes. All particles crossing a given scoring volume are be saved to file, allowing easy estimation of particle flux. Predefined scoring volumes include all sub-detector boundaries, and the list is extensible/modifiable at runtime without need to recompile.
- detailed list of secondaries produced within a given volume. The secondaries can be filtered based on the particle type or energy
- full particle trajectories, i.e. the list of steps the particle is doing while propagating through the detector. Due to its very high level of detail, this information would be of little use without advanced filtering. The present implementation allows, for example, to save the trajectories only for particles of selected type/energy, being produced in a given volume, under the condition that the particle leaves the volume it was created in. This is specially tailored for studying the effect of shielding components.

14.2.1.5 Simulation optimization

In order to properly optimize the simulation results, several parameters need to be adjusted.
The most important one is probably the physics list to be used. Presently, a conservative choice was made with QGSP_BERT_HP, which is known from other experiments to provide a good description of both electromagnetic and hadronic physics (including low-energy neutron interactions), at the cost of a reduced computing performance. Tests with different physics lists are foreseen in the near future.
On top of the default physics lists, the user can choose to apply some SuperB-specific tunings, such as simulation of optical photons or different models of multiple Coulomb Scattering.
One more crucial aspect is the choice of the production threshold for different particles in different parts of the detector, since this has impact on both computing and physics performance. Present policy is to use the default Geant4 production cut (0.7mm) unless specific studies from sub-detectors provide motivation for different settings. Such studies are already ongoing, and results will be reflected in the default configuration.

14.2.1.6 Staged simulation

In particular in the design phase, a very frequent use-case will be the one in which a detector modified its layout and wants to use full simulation to better evaluate the effect of the change. This would result in the production of an appropriate number of events. In the scenario in which all sub-detectors are working in parallel on their own implementations, this may result in sub-optimal use of computing resources. One way to ease this situation is the use of staged simulation.
The basic idea is that if the layout of a detector

changes, there is no need to re-simulate all the interactions taking place *before* that detector: simulation must be redone only for that detector (and the ones downstream). For example, if the IFR wants to test a new layout, all existing simulated events can be re-used up to the electromagnetic calorimeter, and only the very last step needs to be redone.
The infrastructure for this kind of application is already implemented and validated, and it uses features already described above, namely:

- all simulated events save snapshots of the simulation status at sub-detector boundaries. This information is saved in the output ROOT file.
- the resulting TParticles can be read back by Bruno as if they were the output from an event generator, thus seeding the new simulation process

In the concrete IFR example, one only needs to use the existing simulated events as input to the new simulation, instructing Bruno to consider the snapshot at the exit of the electromagnetic calorimeter as a seed.

14.2.1.7 Interplay with fast simulation

As already mentioned in the introduction, full simulation can also be used to help the fast simulation programs in certain particular contexts. The design of the interaction region in particular has a deep influence on the background rates are seen from the detector. Simulating such a complex geometry with the required level of details would be beyond the purpose of the fast simulation. On the other hand, full simulation is not fast enough to generate the high statistics needed for signal events.
SuperB implements presently a hybrid approach to this problem:

- Bruno is used to simulate background events up to (including) the interaction region
- a snapshot of the simulation status is saved, along the lines of what already discussed above
- in order to gain time, the full simulation of the event can optionally be aborted once the relevant information has been saved

The result of this procedure is a set of *background frames*, which can be read back in the fast simulation program whose role would be, at this point, to propagate those particle though the simplified detector geometry and overlay the resulting hits to the ones coming from signal events.
This approach allows to combine the two simulations and effectively use each one only for the tasks it performs better.
Another aspect where the interplay between fast and full simulation is needed is the evaluation of the neutron background. The idea is to make Bruno handle all particle interactions within the interaction region, as explained above, *plus* all neutron interactions afterwards. Neutrons are tracked in full simulation until they decay, and the decay products saved in the output file, as part of the background frame. Fast simulation can then include these interactions the overlaying procedure.
All these functionalities are presently implemented, and have been used in the recent productions.

14.2.1.8 Long term evolution of the full simulation software

Even if already capable of providing adequate functionality for the design phase of the experiment, the present software will need to be constantly updated and improved to be ready to cope with the needs of the data taking period.
First of all, one will need a working digitization framework, including digit persistency, in order to perform the needed studies on readout electronics. Being digitization in general less demanding in terms of CPU, it will be implemented as a separate step from the full simulation, to be possibly run in a different job, starting from the persistified hits.
A particular attention will be devoted for performance issues. This should be intended as a twofold problem indeed:

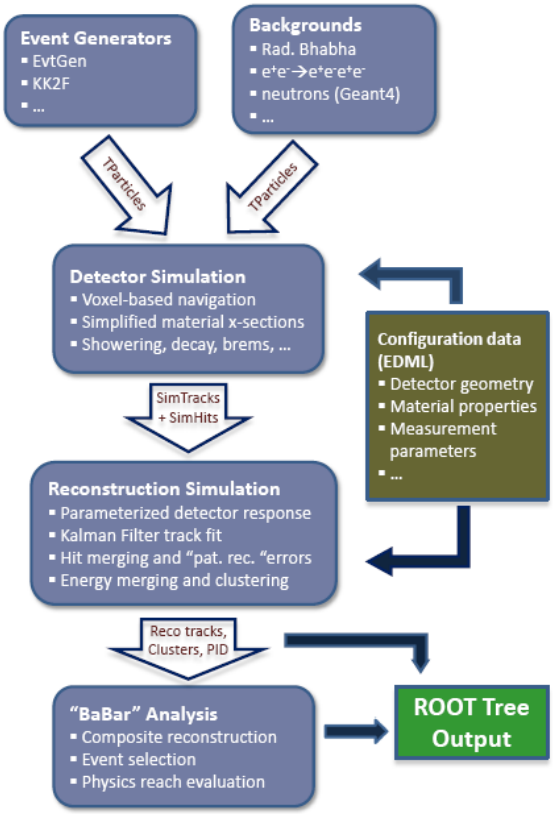

Figure 14.1: Simulation diagram of FastSim.

- **physics performance** must be improved, both through a finer tuning of Bruno's internal parameters and by following closely the evolution of the Geant4 code itself, in order to better profit from improved modelization of the underlying physics processes

- obtaining optimal **computing performance** is also of paramount importance, in particular in contexts of highly distributed and/or parallelized computing. The present implementation is already capable of running on distributed computing resources, while it still lacks all possibility of intra-event parallelism. This is mainly due to limitations of the stock Geant4 toolkit itself, which will hopefully be overcome in a timescale compatible with the lifespan of the SuperB experiment. In such case, Bruno will most likely need to be heavily restructured to better profit from the new parallelization features. Similar considerations hold for what concerns the optimal exploitation of the new (yet already widespread) computing architectures, such as multi/many core CPUs and GPUs.

14.2.2 Fast Simulation M. Rama 4 pages

FastSim relies on simplified models of the detector geometry, materials, response, and reconstruction to achieve an event generation rate a few orders of magnitude faster than is possible with a Geant4-based[1] detailed simulation, but with sufficient detail to allow realistic physics analyses. In order to produce more reliable results, FastSim incorporates in some measure the effects of expected machine and detector backgrounds. It is easily configurable, allowing different detector options to be selected at runtime, and is compatible with the BaBar analysis framework, allowing sophisticated analyses to be performed with minimal software development.

A diagram summarizing the structure of FastSim is reported in Fig. 14.1. The simulation proceeds through four main steps: particles generation, detector configuration and response, particles reconstruction and analysis of the event.

14.2.2.1 Event generation

Since FastSim is compatible with the BaBar analysis framework, we can exploit the same event generation tools used by BaBar. On-peak events ($e^+e^- \to \Upsilon(4S) \to B\bar{B}$), with the subsequent decays of the B and $\bar{B}$ mesons, are generated through the EvtGen package [2]. EvtGen also has an interface to JETSET for the generation of continuum $e^+e^- \to q\bar{q}$ events ($q = u, d, s, c$), and for the generic hadronic decays that are not explicitly defined in EvtGen. The Super$B$ machine design includes the ability to operate with a $70-80\%$ longitudinally polarized electron beam, which is especially relevant for tau physics studies. Events $e^+e^- \to \tau^+\tau^-$ with polarized electron beam are generated using the KK generator and Tauola[3]. Machine backgrounds are superimposed to the physics event at this stage.

14.2.2.2 Detector description

FastSim models Super$B$ as a collection of *detector elements* that represent medium-scale pieces of the detector. The overall detector geometry is assumed to be cylindrical about the solenoid $\vec{B}$ axis (z axis), which simplifies the particle navigation. Individual detector elements are described as sections of two-dimensional surfaces such as cylinders, cones, disks and planes, where the effect of physical thickness is modeled parametrically. Thus a barrel layer of Si sensors is modeled as a single cylindrical element. Intrinsically thick elements, such as the electromagnetic (EM) calorimeter crystals, are modeled by layering several elements and summing their effects. Gaps and overlaps between the real detector pieces within an element are modeled statistically.

The density, radiation length, interaction length, and other physical properties of common materials are described in a simple database. Composite materials are modeled as admixtures of simpler materials. A detector element may be assigned to be composed of any material, or none.

Sensitive components are modeled by optionally adding a *measurement type* to an element. Measurement types describing Si strip and pixel sensors, drift wire planes, absorption and sampling calorimeters, Cherenkov light radiators, scintillators, and TOF are available. Specific instances of measurement types with different properties (resolutions) can co-exist. Any measurement type instance can be assigned to any detector element, or set of elements. Measurement types also define the time-sensitive window, which is used in the background modeling.

The geometry and properties of the detector elements and their associated measurement types are defined through a set of XML files using the EDML (Experimental Data Markup Language) schema, invented for Super$B$.

14.2.2.3 Interaction of particles with matter

FastSim models particle interactions using parametric functions. Coulomb scattering and ionization energy loss are modeled using the standard parameterization in terms of radiation length and particle momentum and velocity. Molière and Landau tails are modeled. Bremsstrahlung and pair production are modeled using simplified cross-sections. Discrete hadronic interactions are modeled using simplified cross-sections extracted from a study of Geant4 output. Electromagnetic showering is modeled using an exponentially-damped power law longitudinal profile (a simplified version of the gamma distribution in [4][5]) and a double Gaussian transverse profile[6], which includes the logarithmic energy dependence and electron-photon differences of shower-max. Hadronic showering is modeled with a simple exponentially-damped longitudinal profile[7] tuned using Geant4 output.

Unstable particles are allowed to decay during their traversal of the detector. Decay rates and modes are simulated using the BaBar EvtGen code and parameters.

14.2.2.4 Detector response

All measurement types for the detector technologies relevant to Super$B$ are implemented. Tracking measurements are described in terms of the single-hit and two-hit resolution, and the efficiency. Si strip and pixel detectors are modeled as two independent orthogonal projections, with the efficiency being uncorrelated (correlated) for strips (pixels) respectively. Wire chamber planes are defined as a single projection with the measurement direction oriented at an angle, allowing stereo and axial layers. Ionization measurements (dE/dx) used in particle identification (PID) are modeled using a Bethe-Bloch parameterization.

Cherenkov rings are simulated using a lookup table to define the number of photons generated based on the properties of the charged particle when it hits the radiator.*[MR: At present there's a simplified version. Fix]* Timing detectors are modeled based on their intrinsic resolution.

In the EM calorimeter the energy deposits are distributed across a grid representing the crystal or pad segmentation taking into account profile fluctuations and crystals energy resolution. In the muon detector (IFR) the hadronic shower

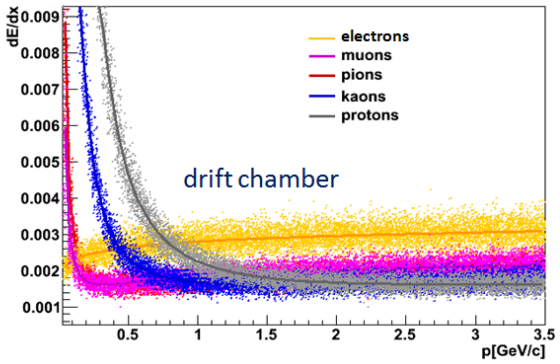

Figure 14.2: Measured dE/dx in the drift chamber as a function of the track momentum.

profile produced by charged pions or the ionization energy loss by muons are used to determine the 2-dim hits distribution over the scintillator planes, taking into account the intrinsic spatial resolution. The detector response for charged pions and K_L is also simulated.

14.2.2.5 Reconstruction

A full reconstruction based on pattern-recognition is beyond the scope of FastSim. On the other hand, a simple smearing of particle properties is insensitive to important effects like backgrounds. As a compromise, FastSim reconstructs high-level detector objects (tracks and clusters) from simulated low-level detector objects (hits and energy deposits), using the simulation truth to associate detector objects. Pattern recognition errors are introduced by perturbing the truth-based association, using models based on observed BaBar pattern recognition algorithm performance.

In tracking, hits from different particles within the two-hit resolution of a device are merged, the resolution degraded, and the resultant merged hit is assigned randomly to one particle. Hits overlapping within a region of 'potential pattern recognition confusion' are statistically mis-assigned based on their proximity. The final set of hits associated to a given charged particle are then passed to the BaBar Kalman filter track fitting algorithm to obtain reconstructed track parameters at the origin and the outer detector. Outlier hits are pruned during the fitting, based on their contribution to the fit χ^2.

Ionization measurements from the charged particle hits associated to a track are combined using a truncated-mean algorithm, separately for the SVT and DCH hits. The truncated mean and its estimated error are later used in PID algorithms. Fig. 14.2 shows the reconstructed dE/dx in the drift chamber as a function of the particle momentum for different particle types. The measured Cherenkov angle from the DIRC is smeared according to its intrinsic resolution and the Kalman filter track fit covariance at the radiator.*[MR: At present there's a simplified version. Fix]*

In the EM calorimeter, overlapping signals from different particles are summed across the grid. A simple cluster-finding based on a local maxima search is run on the grid of calorimeter response. The energies deposited in the cluster cells are used to define the reconstructed cluster parameters (cluster energy and position). A simple track-cluster matching based on proximity of the cluster position to a reconstructed track is used to distinguish charged and neutral clusters.

In the IFR hits are clustered, and clusters are fitted with a straight line ($\vec{B}$ is zero outside the coil). A number of quantities useful to distinguish pions and muons are computed, such as the number of interaction lengths crossed by the particle. The distribution of this quantity for charged pions crossing the BaBar IFR is shown in Fig. 14.3. The fast simulation agrees reasonably well with the BaBar detailed simulation.

FastSim has its own event display. Fig. 14.4 shows a reconstructed $e^+e^- \to \Upsilon(4S) \to B\bar{B}$ event with the B mesons decaying to hadrons. The subsystems have cylindrical symmetry. Both charged particles and photons (straight segments) are visible. The green spots are reconstructed clusters in the EM calorimeter.

14.2.2.6 Machine backgrounds

The main contributions to machine background at Super$B$ are radiative Bhabhas, pairs production ($e^+e^- \to e^+e^-e^+e^-$), Touschek back-

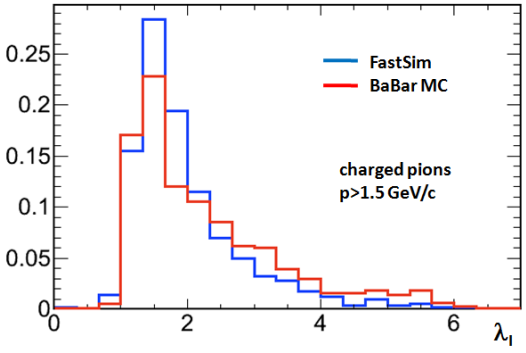

Figure 14.3: Number of interaction lengths for $\pi^{\pm}$ crossing the BaBar IFR.

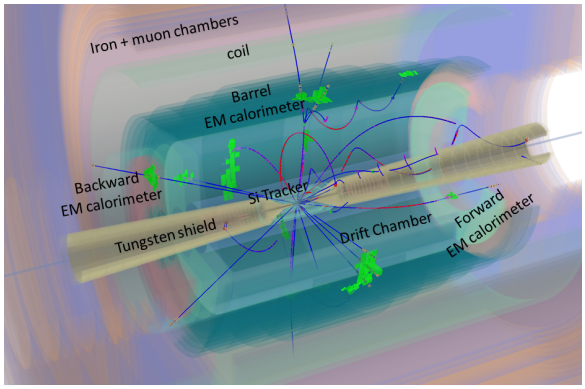

Figure 14.4: Reconstructed $e^+e^- \to \Upsilon(4S) \to B\bar{B}$ event with $B \to$ hadrons represented using the FastSim event display.

ground and beam-gas interactions. Background events are generated in dedicated full simulation (based on Geant4) runs, and then superimposed to the FastSim physics event. Geant4 is needed to model the effect of background showers in the elements of the interaction region, as a detailed description of these elements and the processes involved are beyond the scope of FastSim. Background events are stored as lists of the generated particles (*TParticles* [8]), which are then filtered to save only those which enter the sensitive detector volume.

Background events from all sources are overlaid on top of each generated physics event during FastSim simulation. The time origin of each background event is assigned randomly across a global window of 0.5 μs (the physics event time origin is defined to be zero). Background events are sampled according to a Poisson distribution whose mean is the rate of the background process times the global time window. Particles from background events are simulated exactly as those from the physics event, except that the response they generate in a sensitive element is modulated by their different time origin. In general, background particle interactions outside the time-sensitive window of a measurement type do not generate any signal, while those inside the time-sensitive window generate nominal signals. Background particle EM calorimeter response is modeled based on waveform analysis, resulting in exponentially-decaying signals before the time-sensitive window, and nominal signals inside. The hit-merging, pattern recognition confusion and cluster merging described earlier are also applied to background particle signals, so that fake rates and resolution degradation can be estimated from the FastSim output. A mapping between reconstructed objects and particles is kept, allowing analysts to distinguish background effects from other effects.

Background effects on electronics (hit pileup) and sensors (saturation or radiation damage) are also crucial for Super$B$, but are best studied using the full simulation and other tools. Their impact on the measurement performance can be implemented parametrically at the detector response or reconstruction level.

14.2.2.7 Analysis tools

FastSim has been designed to be compatible with the BaBar analysis framework, so that existing BaBar analysis tools such as vertexing and combinatorics engines can be run in FastSim with small modifications. PID selectors are also available. They provide lists of identified particles (pions, kaons, electrons, etc.) selected by combining the PID information measured in the relevant subsystems and are key ingredients in most of the Super$B$ physics analyses.

User packages have been developed to support the reconstruction and analysis of specific decay modes. For instance, packages are available for the selection of tau decays in $\tau^+\tau^-$ events or the reconstruction of semi-inclusive

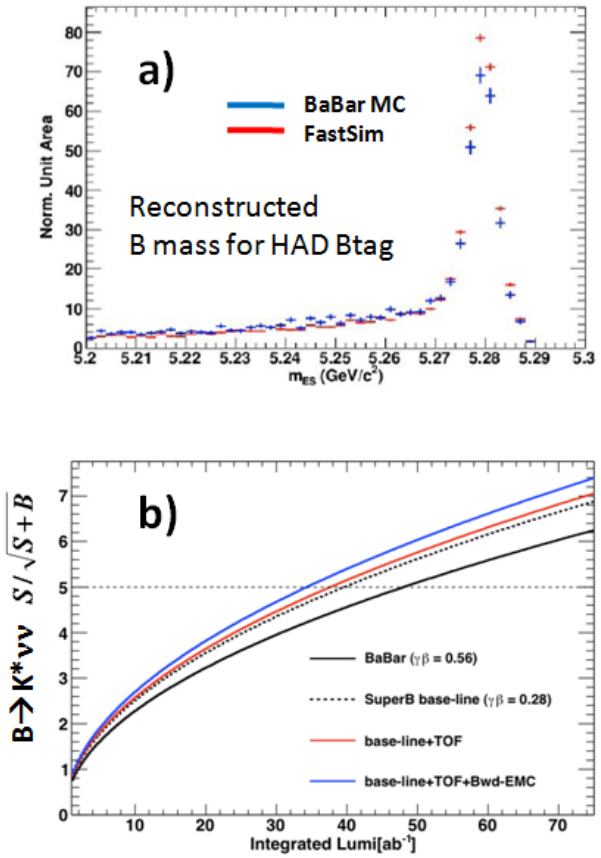

Figure 14.5: Top: Mass of the reconstructed B decays selected into hadronic final states. Bottom: $B \to K^*\nu\bar{\nu}$ measurement precision as a function of the integrated luminosity in four different detector configurations.

hadronic and semileptonic B decays for the *recoil* analysis of rare B decays.

The standard tool used in BaBar to store analysis information into a ROOT tuple has been adapted to work in FastSim, allowing even complex analyses to be run in FastSim approximately as in BaBar.

Typical per event processing times on a dual quad core Intel(R) Xeon(R) CPU E5520 @ 2.27GHz architecture are 1 ms for particle generation, 10 ms for propagation of particles through the detector, 100 ms for reconstruction, between 100 and 1000 ms for composites selection depending on the event complexity.

14.2.2.8 Simulation validation and detector studies

Many aspects of FastSim have been validated either by simulating the BaBar detector and comparing the output with the full simulation or real data of the BaBar experiment, or by comparing the output of the Super$B$ full simulation. In general the outcome of these comparisons is quite satisfactory. The tracking simulation works particularly well, despite the lack of a real pattern recognition.

FastSim is being used extensively to optimize the Super$B$ design by studying the performance of different detector layouts. Since the complete simulation and reconstruction chain is available, including the tools to perform a complete physics analysis of the simulated events, it is possible to compare two or more detector configurations directly in terms of the physics reach in some benchmark channels. For example, the analysis of the rare decay $B \to K^*\nu\bar{\nu}$ has been performed in the BaBar configuration and in three Super$B$ detector layouts with or without a forward TOF and backward EM calorimeter. To suppress the background to an acceptable level it is necessary to reconstruct one B meson in a large number of hadronic and semileptonic decay channels (tag B) and then search the signal in the remaining part of the event. The top plot of Fig. 14.5 shows the reconstructed mass of the tag B mesons selected in hadronic decays, with FastSim superimposed to the BaBar full simulation. The bottom plot shows the final result: how $S/\sqrt{S+B}$ (S=signal, B=background) scales as a function of the integrated luminosity and detector layouts.

14.2.3 Distributed computing tools G. Donvito - A. Fella - E. Luppi - S. Pardi L. Tomassetti 10 pages

To extract statistically significant results from the data analysis, a huge number of Monte Carlo simulated events is needed. Such a production is way beyond the capacity of a single computing farm so it was decided to design, even to support the detector TDR studies, a distributed model capable of fully exploiting the existing HEP world wide Grid computing in-

frastructure [13][12][16]. So far, the main effort of the computing group has been devoted to the development and the support of the simulation software tools, the computing production and analysis infrastructure needed for carrying out the usual HEP experiment research activity. An intense R&D program is on course; it covers both data and workload management subjects permitting to converge on the final Computing Model Definition foreseen in one year from this document publication time. Data access and Data storage system studies besides DIRAC framework evaluation work have been discussed in details in this chapter.

14.2.3.1 Distributed resources

The total computing resources needed for one year of data taking at nominal luminosity are of the same order as the corresponding figures, estimated in the spring of 2010, by the Atlas [27] and CMS [28] experiments for the 2011 running period. Therefore a computing model capable of exploiting the existing HEP worldwide distributed computing infrastructure is needed. The distributed computing infrastructure includes several sites residing allover the countries participating in SuperB collaboration, in specific in Europe and North America are collected the majority of resources. Each site implements a Grid flavor depending on its own affiliation and geographical position, EGI [13] and OSG [12] Grid flavour have been enabled at present time. Trying to quantify the type and the size of distributed resources enabled for SuperB Virtual Organization (VO) we can refer to LHC Tier classification: thirty sites of which four Tier1s and sixteen Tier2s sites.

The estimation of network, CPU and disk space resources consumption have been reported here to demonstrate at a glance, the amount of involved computing infrastructure:

- 5Gbyte/s of network bandwidth as experiment output
- 1000 PB amount of data collected after 5 year of experiment life
- 50-60000 CPU Cores needed for all the activities for the first year of data taking

The LHC Computing Grid (LCG) architecture [16] was adopted to provide the minimum set of services and applications upon which the SuperB distributed systems have been built. The Grid services involved in production and analysis systems work-flows resulted to be widely adopted and long-term supported by Grid initiatives, moreover a particular attention has been given in identifying the multi-flavor Grid projects compliant ones. A briefly description follows:

- Job brokering service: the Workload Manager System in addition to the job brokering specific tasks, manages jobs across different Grid infrastructures (OSG, EGI, NorduGrid [**?**], WestGrid [**?**], etc), performs job routing, bulk submission, retry policy, job dependency structure, other
- Authentication and accounting system: Virtual Organization Membership System (VOMS) [20] manages users authorization in accessing Grid resources at Virtual Organization (VO) level, providing support for group membership and roles.
- File meta-data catalog: the LCG File Catalog (LFC) [22] is a catalog containing logical to physical file mappings. In the LFC, a given file is represented by a Grid Unique Identifier (GUID).
- Data handling: LCG-Utils [17] permits to perform data handling tasks in a fully LFC/SRMV2 compliant solution.
- Job management system: GANGA [25] is an easy-to-use front-end for job definition and submission management implemented in Python. It provides interfaces for different back-ends (LSF, gLite, Condor, etc.) and includes a light job monitor system with a user-friendly interface.

- Storage resource manager layer: SRM [23] provides data management capabilities in a Grid environment to share, access and transfer data among heterogeneous and geographically distributed data centres. StoRM [24], dCache [26], DPM [30], Lustre [32] and Hadoop [31] are some implementations in use by the remote sites involved in the production distributed system deployment at present time.

14.2.3.2 Distributed systems design: a bird's-eye view

The Fig. 14.6 shows the SuperB tool suites and the related information systems involved in distributed resource computation. The MC production and data analysis systems rely on bookkeeping database to retrieve metadata information related to the Fast and Full simulation, dataset structures and data placement on Grid resources.

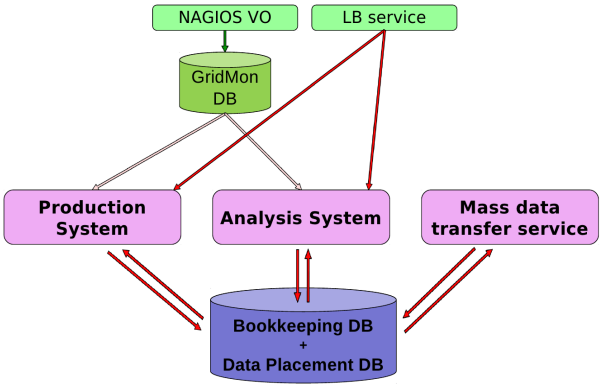

Figure 14.6: Distributed systems bird's-eye view

Mass data transfer system is intended to be an application layer on top of gLite File Transfer Service (FTS); related work is in progress to permit a fruitful integration with SuperB specific information systems. Green boxes represent the services involved in Grid resource monitoring; the above mentioned systems refer to GridMon DB and to Logging and Bookkeeping gLite service to take decisions about resource exploitation and management. In particular the Nagios-per-VO system, specifically setup for SuperB VO only, performs SuperB use cases related tests allover distributed resources and reports a digest status result in GridMonDB.

14.2.3.3 The production system

The SuperB experiment needs large samples of MonteCarlo simulated events in order to assist in several detector study items and estimate the analysis results and performances. As we already discussed in "Distributed resources" section, the accomplishment of such a requirement can be achieved with the effective exploitation of distributed resources. A Production framework has been developed and improved during the last three years, it is capable to solve the problem permitting job and file management in Grid environment, tight integration with a bookkeeping backend and specific control in operation tasks via web portal.

The key concepts at the base of job workflow design are "standard" and "stable": from the point of view of Grid services, job submission path is determined by a direct routing to selected site CE via WMS service, submission method is limited to bulk. The inclusion of WMS service into the job workflow permits to exploit Grid flavor interoperability features. The job JDL file do not include data handling management neither customization in terms of JobType, moreover the design do not include the output sandbox withdraw at job completion. Data handling system relies on SRMV2 standard protocol implemented at LCG-Util layer permits a transparent interaction with heterogeneous site SE storage management systems. Authentication and file catalogue are respectively managed by VOMS and LFC services. All the cited EGI Grid services have been included in LHC experiment computing models and largely used in several VO distributed system design. Furthermore such a set of services have a consolidated set of functionality and have been identified as long term projects in EGI roadmap definition.

The job workflow shown in 14.7 is synthesized in the following three steps:

- Pre-submission operations: the distributed system design includes the possibility of

jobs to have access to input data, of the order of O(10GB) in size. Input job data are expected to be the strictly necessary information permitting job simulation specificity.

- Job preparation and submission: the job script definition and database session initialization are performed via production tools layer at central site. The resulting script should be launched from UI by a VOMS authorized user. An automatic portal submission is now available, it is based on MyProxy service [21]. Job bulk submission is performed by Ganga system properly configured to be able to interact with LCG environment.

- Job running time: WMS service routes the job to the requested CE and takes care of Grid flavor interoperability. The job starts on remote site worker node with a general environment test check, subsequently performs the transfer of input files from local SE, launches the simulation executable and finally transfers to the designed site SE the generated output and log files. During the entire life cycle the job communicates its own status updates to the bookkeeping database via RESTful protocol. Input and output file transfers are performed by LCG-Utilities commands permitting run time file registration to the catalogue service, LFC.

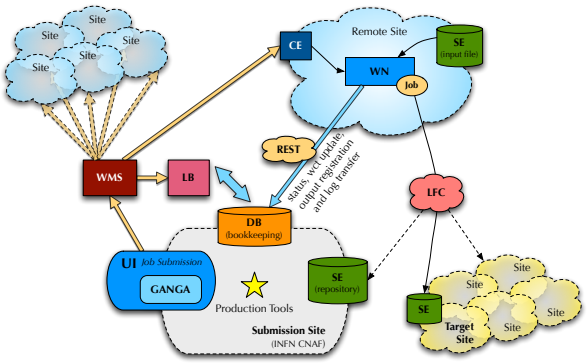

Figure 14.7: Simulation production work-flow

Job submission management is delegated to Ganga system. Various studies and configuration tests have been performed with the aim of customize Ganga functionality to be able to work as a simple and efficient submission engine. The lines of intervention can be summarized in: unused sub services deactivation, setup bulk as unique submission method, Grid submission information collection. GANGA developer team expressed interests in this use case and an active collaboration on the specific subject started. A GANGA specific script has been developed to permit run time customization and site specific JDL file generation. The results of the use of GANGA system in this particular role have been optimal in terms of submission reliability and robustness: a negligible failure rate in submission operations has been registered in a multi submitter environment.

An automated submission procedure and rich monitor features are of the utmost importance in order to speed up the production manager workflow completion, to keep data and metadata consistent, and to provide an easy-to-use interface for non-expert users. As a matter of fact, the major hurdle in accessing the Grid infrastructure for non-expert users is given by its intrinsic complexity and their lack of expertise. To accomplish this task, a Web-based user interface has been developed, which takes care of the bookkeeping database interactions, the job script preparation according to the user's input, and the job management; it also provides monitor functionality and procedures to query the stored metadata. The various Grid monitor projects nowadays in place can be fully used side by side with the system embedded monitor features. The Web-interface has been developed in PHP server-side scripting-language and makes use of Javascript for AJAX functionality. Obviously, it is strictly bounded to the bookkeeping database in order to allow the job definition (job initialization phase) and monitoring. It includes FastSim and FullSim specialized main sessions each of them is divided in a submission and a monitor related subsections. Their content, which mainly consists of web forms, is dynamically generated from the bookkeeping database

schema and state in order to include the job-type specific fields.

The Web-interface provides rich monitoring features by means of querying the bookkeeping database and interacting with Logging and Bookkeeping gLite service. The user can retrieve the list of jobs as a function of their unique identifier (or range of them), their specific parameters, the execution site, status, and so forth. The monitor provides, for each job, the list of output files if any and a direct access to the corresponding log files. Reports on output file size, execution time, site loading, job spreading over workflow requirements, and the list of the last finished jobs (successfully or with failures) are also provided.

A basic authentication and authorization layer, based on a LDAP directory service permits the differentiation of users and grants the access to the corresponding sections of the Web-Interface. In the present implementation, the job-initialization interface provides a set of automatically-generated nested scripts. Portal automatically executes the script wich subsequently launches a GANGA session taking care of job submissions. x509 proxy authentication has been introduced in submission step permitting the fully compliant Grid security standards for resource access.

14.2.3.4 The data analysis system prototype

Providing a user-friendly solution to workload management in a distributed resource system is one of the key goal of a HEP community as SuperB experiment. Physicists involved in Monte Carlo simulation productions and in data analysis should be able to perform job management and basic data transfer operations limiting as possible training costs and maximizing flexibility in resource exploitation.

The SuperB computing group adopted Ganga as the interface layer of such distributed analysis infrastructure. A SuperB-specific Ganga-plugin has been developed to accomplish experiment-specific requirements as information system interface, use cases implementation, dataset management and job wrapper interactions.

The main components of the SuperB data-analysis prototype suite are the job wrapper, the bookkeeping and data-placement database and the Ganga plugin software layer. Interactions among these three entities build up the user analysis capabilities of a typical mid-sized HEP community. This very simple structure is an interesting peculiarity of our implementation. Job wrapper permits the management of stage-in, user application execution, monitoring and stage out phases. Its interaction with Ganga plugin layer regards monitor purpose only. Bookkeeping and data-placement databases are the metadata backend providing Ganga plugin with all the information about target submission distributed resources, dataset structure and placement and output metadata, permitting basic data movement features. Through Ganga interaction the user can manage personal datasets performing creation, deletion and status updates; in addiction, it makes possible to define jobs input data, permitting the system to automatically create job input data structures. The main Ganga plugin components as Application, Backend, InputDataset, Splitter and Merger have been inherited and extended to accomplish SuperB requirements. Collaboration with Ganga developer team has been tight and profitable; after specific code review sessions and plugin test-setup, the SuperB layer has been included into official Ganga release.

The SuperB analysis prototype is reported here as a step by step workflow description. See Figure 14.8:

- Working on User Interface (UI): user creates his/her own working directory including the application and all it's necessary for analysis or personal production purpose. Executable script must comply with a few environment constraints on input and output file placement on remote worker node.
- Job preparation from Ganga interface: user launches Ganga from UI. He/She can select the input dataset, declare the events to be processed per job, create the output dataset, define work directory and ex-

ecutable path and finally submit the jobs. Ganga system will take care of user working directory transfer to job running location.

- Job run-time and stage-in procedure: SuperB job wrapper prepares user software package, checks the environment, transfers requested input files to the conventional area on worker node and launches the user application.
- Job stage out phase: at job completion, the output files residing into the conventional area will be transferred and registered in GRID to output site. The list of logical file names (LFN) job output files is transferred to UI via outputsandbox together with the job log-out file.
- Job Monitoring and output retrieval: Ganga interface permits the user to check jobs status, manage jobs (kill, resubmit, copy, etc.) and check logging job information.
- Data movement: SuperB Ganga plugin includes a set of specific methods permitting the user to perform data transfer of its own datasets.

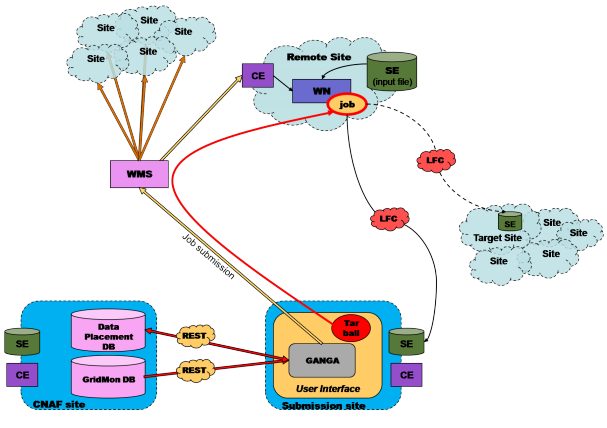

Figure 14.8: Analysis job work-flow from user submission to stage-out completion.

At present time the data-analysis suite implements two use cases. The first one concerns the data analysis and reduction. It is used to analyze both the official and personal Montecarlo simulation production datasets and to perform the generic analysis of sub-product dataset. The second one regards the personal Monte Carlo simulation production.

14.2.3.5 The bookkeepieng and data placement database

Both the distributed production and data analysis systems require a way to identify interesting data files and to locate the storage holding them among distributed resources. Moreover the prompt availability of information on the execution status of jobs and their specific meaning and parameters is crucial to the users in order to plan their activities and summarize the results. To make this possible, the developed framework needs a data bookkeeping system to store the semantic information associated to data files and keep track of the relation between executed jobs and their parameters and outputs.

This same bookkeeping database is extensively used by the production job management system itself in order to schedule subsequent submissions and bring completion level of requests and site availability information up to date. The bookkeeping database was modeled according to the general requirements of a typical simulation production application; At present time, its design adheres to the relational model and the current implementation makes use of PostgreSQL rDBMS in a centralized way.

The database connections from/to processes running in a Wide Area Network scenario has been managed via a web service technology, in particular a RESTfull layer in front of database has been developed. Long range DB accesses between jobs running on remote sites and the information system is authenticated by VOMS proxy certificate and the communication channel is encrypted on https protocol. As discussed in the previous sections, the bookkeeping database needs to interact either with the production portal or the job in execution on the WNs. Depending on the sender/receiver, these communications are therefore managed by a direct connection to PostgreSQL or via

a RESTful interface. The latter case is required from remote sites because typically only outbound communication over http/https is allowed. Strong authentication, by means of X509 proxy certificates over https, is used to grant jobs access to the database. It is important to stress that such a specific DB access pattern by production and analysis systems is crucial and permits to distinguish it from others portal-like solutions available to the HEP community.

The feasibility of including and integrating a different information system schema-free and/or document oriented, for instance is under study. This may help in extending the covered use case by making easier the inclusion of new attributes and structures and going towards a distributed solution which can exploit a incremental replication with bi-directional conflict detection and management.

14.2.4 Collaborative tools M. Corvo - A. Gianoli - S. Longo - R. Stroili 2 pages

14.2.4.1 Overview

This section briefly describes the computing tools and their organization setup to study the Detector performances and requirements for the SuperB experiment.

14.2.4.2 Authorization

The need to manage the relatively large number of people that are involved, or could be involved in the future, in the collaboration, both from the point of view of authentication and authorization impose the use of some kind of database. As several services (code repository, internal WEB pages, wiki, etc.) require an autentication/authorization system, the choice is gone to a directory service based on the LDAP application protocol, as LDAP can be interfaced to several such systems, allowing users to have a unique access password. This service also allows us to organize people and groups of people in a logical and hierarchical manner, providing other application with both authentication information and authorization (people belonging to particular groups). The LDAP server runs on a virtual machine as a single master server and a backup is performed regularly. Other LDAP server can be installed and they can be arranged as a multimaster structure or as a more traditional master-slave structure.

14.2.4.3 Portal System

Web is employed both to present the collaboration, its work and results and also as a collaboration space where SuperB members can share content, knowledge and so on. At first SuperB has employed two separate CMS, one dedicated to an outreach site for the general public, and another employed as a collaboration web site.
Considering the proliferation of collaborative tools, we have decided to move web services to a portal system in the aim to facilitate tools usage, aggregating as much services as possible in a single place.
The Collaboration Portal is a *Liferay* based portal system [41], associated to a Single-Sign-On authentication system (*Jasig CAS* [39]) allowing members to log-in to the portal and then use external services from portal pages, without having to sing-in to each tool indipendently. The portal system is currently used both as an outreach website and a collaboration site, having section accessible depending on each user role inside the collaboration.
At present all the collaboration tools are accessible inside the portal (not all with SSO technology). The portal is also used as a container for several utility (SuperB event calendar, Members PhoneBook, etc) and applications. In particular, through the development of custom portlets, the portal is employed as an interface to database data. At present the Administrative DataBase, containing information on members, affiliations, roles, etc, is accessible through a dedicated *organization* site (Management site, used by H.R. managers). Subscription of new members and speackers management are other tasks performed via portal applications.

14.2.4.4 Document repository

After evaluation of several tools, a complete document management system for SuperB was implemented using the *Alfresco* platform [38]: an enterprise class suite of programs dedicated

to content management.
The repository is fully integrated with the collaboration portal and the authentication/SSO system and is accessible both via web interfaces or WebDAV. Some of the most interesting feature available to members are:

- Document level security gained through users and groups management. Private spaces available for each user and management group
- Data dictionary extend to host SuperB specific documents (internal notes, presentations, pubblications and reports)
- Documents are fully indexed (metadata and content) and cetegorized. The repository can be browsed or searched by category or keywords
- Auditing and Versioning of every document

Each "directory" inside the repositry is called *smartspace* since it does not only act as a container but allows also to define actions that are automatically performed on documents. This feature allows the definition of content rules like document movement, modification or transformation into other formats; the same feature is also employed in the definition of document workflows, for document requiring some type of approval steps.
Beside the document repository, two web application are available for "everyday" user access. The first one is *Alfresco Document Explorer* that allows a user to interact with the repository with an interface similar to *Windows Explorer* or *Konqueror*. With this application - integrated with the SuperB authentication system - a user can access it's home and the document shared by other members (presentations, seminars, etc.) and can performs operations on space/content as he do on directory/files on his desktop.
Alongside with *Alfresco Document Explorer*, we have also setup *Alfresco Share*, a web application particularly dedicated to project collaboration. With this tool it's possible to access to the document repository as *Alfresco Document Explorer*, moreover it's possible for members working on the same project to define a dedicated space (project site) where they can share documents and other informations. Project sites may contain several type of contents: from regular documents to blog and wiki pages, forums, calendar and so on. *Alfresco Share* may also be profitably used to assign jobs to colleagues, as an example to assign revision tasks on documents to other participants to the same project.

14.2.4.5 Documentation

The document repository site nothwithstanding, the collaboration has realized from the beginning the need for a tool that allows:

- an easy way to create web pages to be used as internal documentation
- to create meaningful topic associations between different pages by making link creation an easy task, and showing wheter an intended target page exists or not
- to quickly modify already existing pages, keeping track of what changed recently

This kind of requirements leads us to considering the use of a Wiki. A wiki website in fact allows for the easy creation and editing of any number of web pages using just a browser and a WYSIWYG text editor or a simplified markup language.
Since several opensource wikis exist, we did a little testing to see if they can provide additional benefits like: integration with directory service, handling formulas written in TeX, handling different kind of pictures/plots. The final choice was the mediawiki software because when the system was set up a couple of years ago it was the best suited to match the different requirements. The system is generally used by several subdetector groups.

14.2.4.6 Code repository

SuperB code is managed via a *Version Control System* (VCS from now on). In particular SuperB is currently using *Subversion* [43] as its VCS to manage the FastSim and FullSim code,

as several component projects and documentation. The collaboration is as well evaluating other systems like Git [44]. Currently the code is organized in different repositories. Generally a single repository collects the code of some specific detector subsystems, like e.g. SVT or IFR, or code for specific activities, like e.g. R&D on the Framework or the Storage system. Inside each repository the code is organized in *packages*, a package being a collection of coherent classes and modules. Each package is organized in subdirecories, Fig. 14.9:

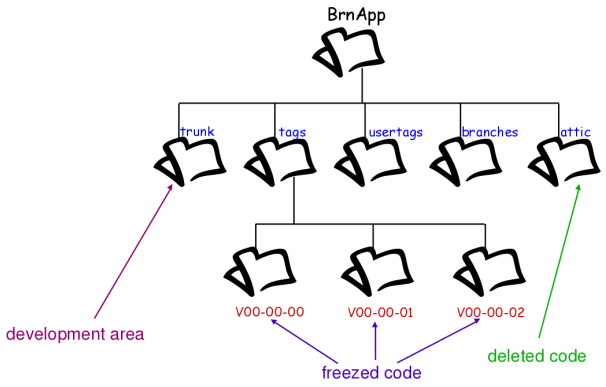

Figure 14.9: Repository structure

- *trunk*: the actual development path
- *tags*: to keep official freezes versions of the code
- *usertags*: to keep user freezes versions of the code
- *branches*: to branch code development
- *attic*: to keep track of removed code

Subversion does not have an intrinsic freezing mechanism, like CVS [45], in order to freeze the code a special *pre-hook* module has been developed such that, once created, a given tag cannot be modified any longer.

Every repository has a corresponding Trac [46] page associated, with several services associated, such as:

- code navigation via web browser
- a ticketing system
- a wiki for the documentation
- a blog
- a discussion forum
- a timeline tracking

Both accesses to Subversion repositories and to the corresponding Trac sites are mediated by the LDAP server.

14.2.4.7 Code packaging and distribution

The software release system is based on the *RPM* [47] packaging system: both FastSim and FullSim are defined as different software products, for each of them, even if they share some of the software packages, an independent release and distribution strategy could be defined.
The RPM packaging system has been chosen as it provides an easy way to install/unisnstall and update software; it also provides a mechanism to declare explicit dependencies from other RPM packages. Also external packages as ROOT, Geant4 and others are packaged and distributed in RPM format.
In order to be independent from other experiment or system requirements it was decided to put *sb* in the package name as to put the release number of the package, so that, configuring the installation directory with the release number in the path, it's possible to have installed at the same time, without conflicts, several releases of the same package.
Overall this packaging system provides an efficient and reliable system that has one significant issue still to be fixed: package installation must be done as administrator.
The code distribution is done setting up a *yum* [48] server: yum is an automatic updater and package installer/remover for rpm systems. It automatically computes dependencies and figures out what things should occur to install packages.

14.3 Computing model outline F. Bianchi - A. Fella - C. Grandi - S. Luitz - E. Luppi - S. Pardi - L. Tomassetti 6 pages

The computing models of the *BABAR* and Belle experiments have proven to be quite successful in handling the data volume generated by a flavor factory in the $\mathcal{L} = 10^{34}\,\mathrm{cm}^{-2}\mathrm{s}^{-1}$ luminosity regime. A super flavor factory at a luminosity of $\mathcal{L} = 10^{36}\,\mathrm{cm}^{-2}\mathrm{s}^{-1}$ will produce much larger data volumes, but predictable progress in the computing industry will provide much of the performance increase needed to cope with them. In addition, effective exploitation of computing resources on the Grid, that has become well established in the LHC era, will enable Super$B$ to access a much larger set of resources than were available to *BABAR*.

Crucial issues will be the capacty to efficiently exploit the modern CPU architecture and to efficiently and reliably access huge amount of data physically located in different sites, nevertheless a computing model similar to the *BABAR* one can work also for Super$B$.

To illustrate the scale of the computing problem and how the Super$B$ computing group envisage to attack it, the first part of this section contains an overview of the current *BABAR*-inspired computing baseline model with an estimate of the extrapolated Super$B$ computing requirements and a presentation of a possible computing infrastructure. A dedicated R&D program to investigate possible technical solutions has started and is describend in the second part of the section.

14.3.1 Data processing

The data processing strategy for Super$B$ is envisaged to be similar to the one employed in *BABAR* and can be summarized as follows.

The "raw data" coming from the detector are permanently stored, and reconstructed in a two step process:

- a "prompt calibration" pass performed on a subset of the events to determine various calibration constants.
- a full "event reconstruction" pass on all the events that uses the constants derived in the previous step.

Reconstructed data are also permanently stored and data quality is monitored at each step of the process.

A comparable amount of Monte Carlo simulated data is also produced in parallel and processed in the same way.

In addition to the physics triggers, the data acquisition also records random triggers that are used to create "background frames". Monte Carlo simulated data, incorporating the calibration constants and the background frames on a run-by-run basis, are prepared.

Reconstructed data, both from the detector and from the simulation, are stored in two different formats:

- the Mini, that contains reconstructed tracks and energy clusters in the calorimeters as well as detector information. It is a relatively compact format, through noise suppression and efficient packing of data.
- the Micro, that contains only information essential for physics analysis.

Detector and simulated data are made available for physics analysis in a convenient form through the process of "skimming". This involves the production of selected subsets of the data, the "skims", designed for different areas of analysis. Skims are very convenient for physics analysis, but they increase the storage requirement because the same events can be present in more than one skim.

From time to time, as improvements in constants, reconstruction code, or simulation are implemented, the data may be "reprocessed" or new simulated data generated. If a set of new skims become available, an additional skim cycle can be run on all the reconstructed events.

14.3.2 Resource estimate F.Bianchi - S. Luitz 4 pages

Computing resource estimates for Super$B$ are based on the extensive experience with *BABAR* computing. As described above, the baseline Super$B$ computing model is very similar to the *BABAR* one. This allows us to estimate the Super$B$ computing resource needs by extrapolating from the well-understood *BABAR* computing parameters. Table 14.1 shows the basic parameters of the *BABAR* and Super$B$ computing models.

Compared to *BABAR*, the Super$B$ raw data size increases by about a factor of 6, mostly due to detectors with higher granularity and sampling rates and the very likely need to permanently store raw EMC waveforms to allow to recover detector performance during reconstruction. After reconstruction, the event sizes in Mini and Micro are expected to be about twice the corresponding sizes in *BABAR*.

We expect the CPU needs to increase by a factor of 4 for reconstruction and simulation production and by a factor of 3 for all other activities. The factor of 3 is a guess based on an assumption that skimming and analysis will require more CPU compared to *BABAR* to handle increased combinatorics and for advanced algorithms to handle the larger backgrounds. The factor of 4 reflects the additional penalty caused by the need to handle the relatively large raw events.

For storage, we anticipate two copies of the raw data stored at different geographical locations.

Table 14.2 shows the computing resource estimate for the first 5 years of Super$B$ data taking. The data set and storage sizes include replication factors, contingency, on-disk fractions and support storage. The data aquisition system should cope with the foreseen luminosity and recorded cross section. The first processing of raw data should happen at the same rate of the data aquisition, possibly within a 48 hours latency and the generation of the corresponding simulated data set within a month. As a consequence the CPU required for these activities scales with the peak luminosity. Instead the CPU required to reprocess the data collected in the previous years scales with the integrated luminosity.

14.3.3 Computing Infrastructure F.Bianchi - S. Luitz - S. Pardi 4 pages

Super$B$ will exploit distributed computing resources using Grid or eventually Claud technologies. At this early stage in the experiment life, the Super$B$ virtual organisation is already enabled on over 26 sites and actively accessing the available hardware.

At data taking time we foresee to acceess pledged resources in computing centers located in Tier0/1/2 in Italy and in the other partecipating contries.

In Italy there is already the CNAF computing center in Bologna and 4 new centers are under construction in Bari, Catania, Cosenza, and Napoli funded by the PON ReCaS. As a consequence, only minimal computing resources are needed at the experiment site for data acquisition and for the calibration pass of the raw data processing that can provide useful feed back on detector status. Raw data will be sent to CNAF and to another center for permanent storage on tape, and to the ReCaS centers for the full reconstruction step. Disk buffers will be needed at the Cabibbo Lab to cope with network failures and at the ReCaS sites to host the raw data for the first processing and, after the first year of data taking, for the reprocessing of the data collected in the previous years. In this schema, Cabibbo Lab, CNAF and the ReCaS centers will have the functionalities of a distributed Tier0.

In the other partecipating contries there are already Tier1/2 primarely used by the LCH experiments. Pledged resources for Super$B$ are expected to become available and to fulfill of the order of 50% of the Super$B$ computing needs.

Monte Carlo production will be performed at all classes of Tier sites, while skimming will be done only at Tier0 and Tier1.

Multiple copies of real and Monte Carlo events in Mini and Micro format together with the collections of skimmedy events will be stored

Parameter	*BABAR*	Super*B*		Factor
Raw event size	35	200	kbyte	~ 6
Raw data size	875	5250	Tbyte/ ab^{-1}	~ 6
Mini/Micro event size	42	84	Tbyte/ ab^{-1}	2
CPU for Reconstruction	88.4	354	kHS06/ ab^{-1}	4
CPU for Simulation Production	280	1120	kHS06/ ab^{-1}	4
CPU for Skimming (Data)	40.8	122	kHS06/ ab^{-1}	3
CPU for Skimming (MC)	40	120	kHS06/ ab^{-1}	3
CPU for Physics Analysis (Data)	4.8	14.4	kHS06/ ab^{-1}	3
CPU for Physics Analysis (MC)	5.2	15.6	kHS06/ ab^{-1}	3
Number of raw data copies		2		
Number of Mini copies		1		
Number of Micro copies		4		
Skim expansion factor		5		
Fraction of Mini on disk		100% $\rightarrow$ 10% (Year 5+)		
Reprocessing cycle / year		1		

Table 14.1: Basic Super*B* computing resource estimate parameters

on disk at Tier1 an Tier2 for physics analysis. The possibility of using also the Tier0 for physics analysis is under study. To estimate the amount of data replication required to cope with the analysis load and sites and networking failures is difficult at this stage, we have used a conservative factor 4 in the estimate of storage requirements.

The network bandwidth required for data transfer is estimated to be 100 Gb/s. The GARR-X network in Italy and similar networks in other countries will provide that bandwidth.

14.4 R & D program M. Corvo - G. Donvito - A. Fella - F. Giacomini - S. Longo - S. Pardi 8 pages

14.4.1 R& D on parallelization

Parallelism is one of the most promising programming paradigms to improve the performances of the analysis tools for future particle physics experiments. Since different parallelism strategies and techniques exist, understanding how to combine present technologies to support the SuperB use case on next generation hardware is a challenge we must address.

R& D on parallelization has been going on for some time, basically in three directions: i) identify which parts of the simulation and/or analysis code is worth to parallelize; ii) understand how to use Intel .MIC. architecture for HEP applications, and the performance we can achieve for different tasks; iii) understand how to use the nVidia .GPU. architecture for HEP applications, and the performances we can achieve for different tasks.

The first item has been carried out mainly in Padova. It has so far shown the need to have a framework that is aware of the parallel hardware at a site. Although the other two items have shown promising results for some algorithms, the work done has also shown that the hardware and the programming tools are not yet mature. Intel MIC hardware is not yet on the market and only available to us in a beta test state at CNAF. It can only be used with a proprietary Intel compiler which needs opti-

	Year	1	2	3	4	5	
Luminosity	Peak	**0.25**	**0.7**	**1.0**	**1.0**	**1.0**	10^{36} cm^{-2}sec^{-1}
	per Year	3.75	10.51	15.01	15.01	15.01	ab^{-1}
	integrated	3.75	14.26	29.26	44.27	59.28	ab^{-1}
Data Sets	Raw Data	39.4	149.7	307.3	464.9	622.4	Pbyte
	Mini	1.2	4.5	9.2	14.0	18.7	Pbyte
	Micro	2.8	10.6	21.8	33.0	44.1	Pbyte
	User	0.4	1.3	2.8	4.2	5.6	Pbyte
Storage	Disk	9.4	31.4	51.3	68.5	77.1	Pbyte
	Tape	43.7	168.0	348.2	530.7	713.1	Pbyte
CPU	Reconstruction	0.09	0.34	0.69	1.04	1.40	MHS06
	Simulation	0.28	1.06	2.18	3.30	4.42	MHS06
	Skimming	0.06	0.26	0.59	0.95	1.32	MHS06
	Analysis	0.11	0.43	0.88	1.33	1.78	MHS06
	Total	**0.54**	**2.09**	**4.34**	**6.63**	**8.91**	MHS06

Table 14.2: Computing resource estimate for the first 5 years of Super$B$ data taking.

mization. nVidia hardware is more mature, but the combination of hardware and software availble in Napoli and at CNAF, still shows enormous latencies in memory handling and in data transfers from and to the GPU board. Despite these deficiencies, efforts on all three items lneed to be continued in the Super$B$ collaboration, as parallelization will allow a significant reduction of CPU cost and speed-up in data analysis.

14.4.2 GPU R& D

GPUs are many-core architectures with SIMT (Single Instruction Multiple Thread) parallelism. They allow for interesting scenarios, but at the same time require extensive studies and major changtes to the existing code and implementation paradigms. Several groups in the HEP community are working on exploiting GPUs for many use cases.

The GPU-related activities of the Super$B$ collaboration started in 2011 and are ongoing. They are mainly related to offline analysis software and the main goals are:

- Assess the effectiveness of using the GPU as co-processor for specific computing-intensive Super$B$ analysis tasks;
- Evaluate the cost-to-benefits ratio of porting legacy sequential code to GPU, and;
- Create a prototype to be integrated in the current Super$B$ code development.

The primary focus of the Super$B$ effort is on framework parallelization, including reconstruction analysis, and fit parallelization for user analysis.

INFN Napoli has started a first phase of inspection and profiling of the existing physics reconstruction algorithms that are part of the Super$B$ fast simulation. The focus is on the Super$B$ Physics software that provides the basic tools for composition of particle hypotheses, fitting of four-momenta, and track vertexing. These high-level reconstruction procedures are performed in during central productions when the complete data is filtered and processed into overlapping subsets optimized for particular analyses (skimming). This process is combinatorial in nature and computationally expensive, but has the potential of great gains from parallelization.

A second R&D activity, conducted by a team of UC (University of California) and OSC (Ohio

Num of modules	127
Graph Depth	10
Min Rank	1
Max Rank	54
Avg Rank	12

Figure 14.10: Tree data

Supercomputer Center), aims at the parallelization of maximum likelihood fits of complex physics models, evaluating the probability density functions on the GPU, while the MINUIT algorithm is run on the CPU as usual. The first tests of fitting on simple, simulated datasets already showed encouraging results with speed-up factors up to several hundreds with respect to running on a single CPU.

14.4.3 Framework R & D

The SuperB collaboration is investigating the advantages of new CPU architectures (multi and many cores) also to understand how to exploit their capability of task parallelization in the framework for simulation and analysis software.

This R & D task is spread in several areas as described below.

Measurements on Legacy Software The first step in the design of a parallel Framework Prototype for SuperB consisted in taking measurements on some typical software code. To perform this task we have employed the SuperB Fast Simulation (FastSim in the following), a software developed to study both the detector optimization and the physics in a super flavor factory like SuperB.

FastSim software consists of several hundreds of modules each specialized in tasks like event generation, track reconstruction, filtering and so on, glued together by the BaBar framework, which enables users to define their analysis setup. By the use of configuration files, a user can instruct the BaBar Framework to create lists of modules, set their parameters and then define the execution sequence of the analysis. For our measurements we have employed a typical use-case, with a full analysis path: from event generation to the detector simulation and finally the track reconstruction/ events selection.

At first we had focused our attention on the knowledge of the parallelism at the modules level, to understand how the execution pattern can be moved to a parallel environment.

We have studied the dependencies of each FastSim module, to define the requirement for their execution, from which we have built the dependencies graph. The result of this analysis was quite interesting: as expected, we have found a strongly interconnected tree with several nodes that can run in parallel. Tab. 14.10 shows a summary of the results found for a typical simulation example: the tree has only 10 levels, with an average rank - defined as the number of nodes at the same depth - equal to 12, so our use case is intrinsically parallel.

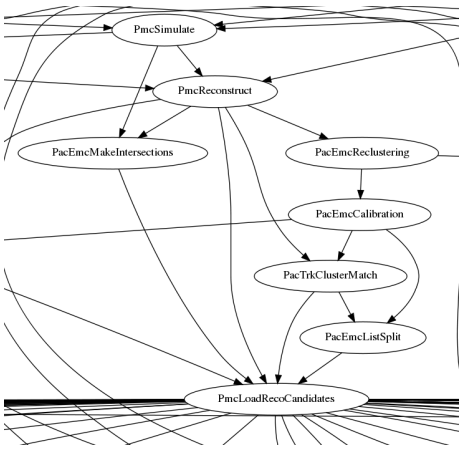

Figure 14.11: Dependent nodes

Even if the graph, with 127 nodes on 10 levels, is too complex to be shown in this paper, some examples can be usefull to understand the structure found. Fig. 14.11 shows a snapshot of the dependencies graph, where several *dependent* nodes are present: each node on a level requires something produced in a previous level of the tree to start the execution. Alongside to this type of subgraph we have found other subtrees made by nodes without inter-dependencies as in Fig. 14.12. Close the the completion of the

analysis process it's also possible to find *reduction* subtrees: sets of indipendent nodes converging in a single node in the next tree level.

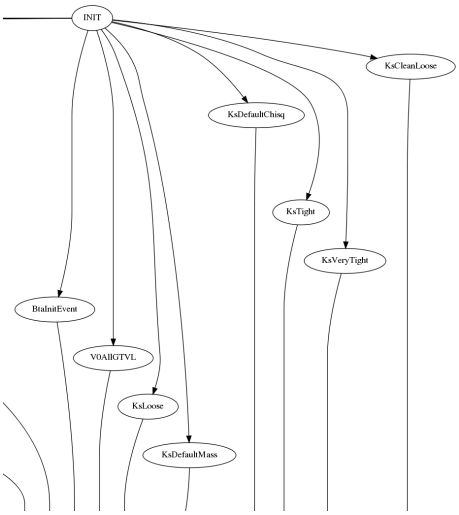

Figure 14.12: Independent nodes

Having understood the dependencies among modules, we have moved to the measurements of the performances that a parallel environment can produces. We have developed a scheduling algorithm able to produces execution sequences of modules based on their dependencies, than we have developed a simulation to calculate the computing time of a parallel execution of FastSim, possibly with constrains on the number of available cores.

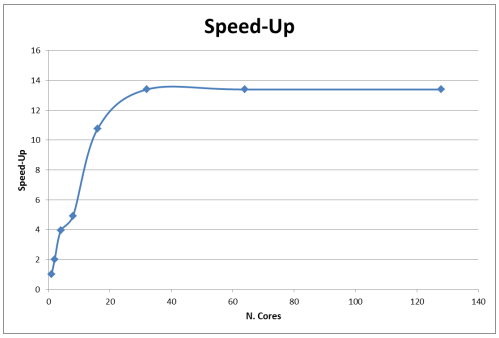

Figure 14.13: Speed-Up vs Available cores

With this software we have calculated an expected speed-up as a function of the available cores in a system [Fig. 14.13]: the use case considered in our analysis exposes a good linear speed-up until 16 nodes, then it starts to flatten (from 32 to 128 cores the speed-up remains around 13.4). The last step was studying the thread distribution over time as a function of the available cores [Fig. 14.14] that exposes a good resources utilization.

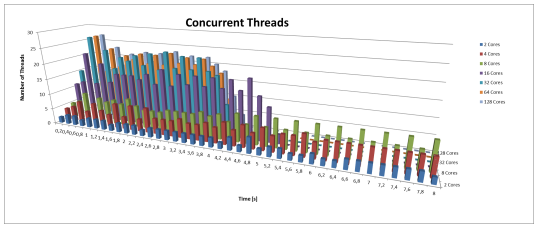

Figure 14.14: Threads time distribution

The use case employed in this analysis, rappresentative of a typical flavor factory computing job, has proved to be a good candidate for parallelization at the module level, even if the case exposes some limits on the maximum number of cores usable.

Framework Architecture Modules operate on data which are generally incapsulated inside a so called *event*. Modules communicate among them through messages while putting the results of their computation inside the *event*. When a module generates a new physics object it is called a *producer*. In general, to produce something, a module needs some input, possibly taken from the *event*, which is processed by its algorithms whose ouput is registered back inside the *event*. This scenario suggests a common feature of all modules, that is the existence of *required* input and *provided* output.

Having identified each module by the data it requires or produces, it's possible to define an execution schedule based on dependencies. This approach leads naturally to the definition of execution graphs, where each node represents a module and each arch a data product. In this structure the path form the root to each node is the sequence of products which are required to start the execution of that module.

We have investigated several system libraries for thread management to understand which product most closely matches our requirements. At present we are employing *Intel Thread Building Block* [49] for the characteristics briefly described in the following.

Intel TBB has a native support for graphs [Fig. 14.15], allowing a near 1 to 1 mapping of the tree we produce from module dependencies. *Intel TBB* manages graphs with a message passing like protocol: this approach easilly fits the requires/provides node design where, in particular, we can also employ directly the *event* as the passing message. This final choice not only simplify the management of node scheduling but also allow us to design a framework able to parallelize the analysis also at the event level. Indeed performing the same analysis on several events should only require to inject the corresponding event object in the root node of the tree. Finally, even if this aspect does not relate exactly with the subject of this paper, *Intel TBB* allows us also to parallelize algorithms inside each module.

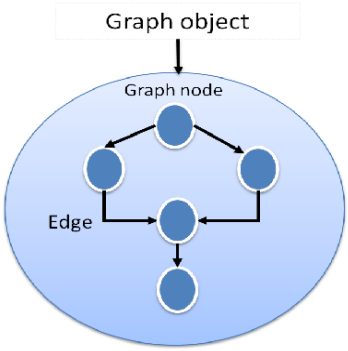

Figure 14.15: Intel TBB Graph

Prototype We are developing a framework prototype based on *Intel TBB* as a proof of concept for the SuperB offline analysis. Scheduling is done using TBB `flow::graph` built according to the provide/require schema previously exposed.

Currently we are also working on the migration of analysis modules from the legacy serial environment to our prototype, focusing mainly on the parallelization at the module level (parallelization inside algorithms will be one of the next steps). At the same time we are even working on aspects of the framework not necessarily related to parallel software, like analysis configuration and so on, with the aim to produce a prototype that can be used as a complete test bed.

Work is still in progress, we plan to have preliminary measures of how our prototype performs in multi-core environments in the near future.

14.4.4 DIRAC framework evaluation

DIRAC [10] (Distributed Infrastructure with Remote Agent Control) was initially developed as a Monte Carlo production tool using pilot jobs for for LHCb experiment, afterwards also data management functionalities have been added and it became the default data and workload management system for such an experiment. DIRAC aims to provide a complete Distributed Computing environment capable to supply all features needed to satisfy requirements of a small-medium size VO, in particular DIRAC provides a complete Grid solution for both workload and data management tasks on a distributed resource scenario.

The DIRAC framework can be profitably used to manage all the SuperB needs in terms of Grid service management and typical HEP use cases:

- Complete Data and Workload management
  - Simulation, Reconstruction, general re-processing, end user data analysis use cases
  - Data storage, replication, movement, catalogue, integrity check
  - Software distribution
  - Monitoring and statistics
- Single point to control and manage entire system
- Native use of pilot job model
- Two supported file catalogs:

  - LHC File Catalog (LFC)
  - DIRAC File Catalog (DFC)

- Easily extensible via Agents and Services (highly customizable)
- Compliant with EGI and OSG Grid flavours
- Cloud integration via VMDIRAC module
- Ganga system integration via DIRAC API

14.4.4.1 Pilot jobs model

DIRAC introduced the now widely used concept of Pilot Agents. Pilot jobs are nothing more than empty resource reservation containers submitted to the available computing resources with the aim of executing the most appropriate pending payload in DIRAC central job queue. Pilot and payload scheduling and submission are managed by the DIRAC Workload Management System (WMS). This job management model permits to increase the process efficiency and the control of computational resources. It is widely adopted by all the major HEP community including the four LHC experiments. There are several advantages in this approach with respect to a more classical payload push scheduling mechanism:

- Pilots allow to perform a preliminary basic sanity check of the running environment. In case of problems they can be reported to the DIRAC WMS for further actions. Such problems can not affect the specific user payload application in fact it has not still assigned to the related pilot.
- Pilots allow an effective implementation of the pull scheduling paradigm. Once they are safely running in the computing resource, they contact central WMS servers for a late binding of the resource to the payload.
- Pilots allow to create an overlay network that masks the central DIRAC WMS components from the heterogeneity of the underlying resources.
- Pilot jobs can work in filling mode: in a single CPU time slot, a pilot can run several payload jobs.

Every DIRAC pilot job performs an in situ DIRAC installation including a full download of the most recent version of configuration files. In this fresh installation and after checking the working conditions (exact location where execution is taking place, available disk space, memory, cpu, available Grid environment, running platform, ...) a DIRAC Job Agent is executed. This Job Agent is responsible for placing the payload request to the central DIRAC WMS server and for the later execution of the received payload.

14.4.4.2 Dirac data management

DFC have been tested in order to understand the features that DIRAC framework provides to users in the field of data management. Dirac File Catalogue provides a set of advanced functionality with respect to the LFC for what concern the file metadata administration. All the SuperB Storage Elements (SE) have been configured in DFC. Each of the storage element configured in Dirac is mapped to its geographical location, the Grid site and the Grid flavor. The DFC provides simple interfaces that allow the end user to add a file to the catalogue at a given SE, replicate files on different SE and retrieve file's replica status. DFC gives also the possibility to use an interactive command line interface in order to browse the file catalogue content and to exploit all the available features. DFC automatically stores a complete and detailed set of metadata information per file. The user can access such an information using SQL-like queries. Moreover, DFC introduces the concept of file ancestor that permit to create and manage a dependency file graph.

Data placement and mass data transfer system are very important subjects for HEP communities. DIRAC offers an advanced software layer upon the low level File Transfer System

provided by Grid initiatives. DIRAC framework have been successfully tested in transferring data to/from all the activated FTS SuperB channels. Managing FTS transfers via DIRAC offers some interesting features:

- automatic catalogue updated at FTS transfer execution
- automatic proxy and myproxy server functionalty management
- simplified FTS configuration management, e.g.: user set target and source SE using their name, not their url
- source file passed using its Logical File Name (LFN)

Thanks to the characteristics mentioned above, the DIRAC mass data transfer management resulted particularly easy with respect to the other available HEP solutions.

14.4.4.3 DIRAC API

The DIRAC API is written in Python, the software is organized in a structured and organic class tree. Using the API classes it is easy to write small scripts or complex services integrated in the general DIRAC infrustructure. While it may be exploited directly by the users, the DIRAC API also serves as backend for the Ganga system.

14.4.4.4 User Management

DIRAC user management permits a fine grain permission configuration based on groups; every group can be mapped via VOMS attributes. Permissions and job priorities can be configured for groups and users, allowing VO manager to easily manage jobs priority.

14.4.4.5 Tested Use Cases

Two realistic use cases have been successfully tested: distributed analysis and Montecarlo production. Job input data have been registered in DFC and replicated on several sites SE. At job's execution time, input data have been copied from nearest Storage Element to the job worker node and the user application starts its execution. Job stage out phase includes the output transfer to the target SE.

In case of failure in saving output to target site, DIRAC automatically saves data on a fallback set of Storage Elements, choosing the nearest Storage Element to Computing Element where job have been executed. DIRAC also tries to resubmit failed jobs up to a maximum configurable number of trials, reducing total failures.

14.4.4.6 SuperBDIRAC module

Porting of simulation production functionalities provided by the prototype production system called WebUI is under development. SuperB specific features will take place in a new DIRAC module named SuperBDIRAC. Integration between DIRAC and the SuperB bookkeeping database (SBK5) is in development phase. SQLAlchemy tool suite has been chosen to implement DIRAC-SBK5 integration. DIRAC webportal will be extended to include all the activities currently offered by WebUI to perform Montecarlo productions. Severus is the name of the job wrapper code permitting the execution of Montecarlo production and analysis jobs. The most recent Severus version was successfully tested via DIRAC.

14.4.4.7 Building up a DIRAC Infrastructure for SuperB

The DIRAC Infrastructure for SuperB can be easily built and setup thanks to its modular and distributed architecture.

Since DIRAC offers a very large set of functionalities and services, a minimal infrastructure can be initially deployed.
The minimal set of functionalities included in a DIRAC installation are the DIRAC framework, the configuration service, the data and workload management services, accounting functionalities, the bookkeeping service, log and sandbox storage and the web interface. While DIRAC components can be deployed on several servers, a single well equipped machine can be configured as head node to run all previously cited functionalities. The head node needs at least 10 GB of RAM to avoid bottlenecks due to MySQL DB istances, morever a 64bit multi-core CPU is

recommended. At least 100GB of disk space should be available on head node for Log Storage and spare Sandbox Storage space.

During first phase of DIRAC infrastructure setup, all necessary servers can be installed in the same site. The future infrastructure improvement plan includes the distribution of services on diverse sites:

- file catalog server can be added in Tier-1 sites
- additional Sandbox Servers can be installed in order to decrease CPU load on head node
- additional WorkloadManagement servers can be installed in order to increase head node performance
- configuration service can be installed in Tier-1 sites to distribute the network connection load

The DIRAC configuration permits concurrent schemas setup.

14.4.4.8 Future Works

Future works will be focused on completing DIRAC evaluation, testing advanced features and implementing SuperB specific use cases. A detailed task list follows:

- DFC-LFC integration study to share metadata and replicas info among file catalogues
- Mass data transfer full features test
- Data integrity check and recovery features test
- DIRAC infrastructure setup for a representative SuperB Montecarlo production
- SuperBDIRAC module development

14.4.5 Data management and distributed storage R&D

One of the key drivers for Super$B$ computing R&D activities is the study of data management in a distributed resource environment. Since Super$B$ is [at least a few years away], it is important that we investigate the next generation of tools in this field. The main interests are Wide Area Network (WAN) data access, mass data transfer and file catalogues.

14.4.5.1 WAN data access

In this section we will discuss the state of the art in the data management field. For WAN data access our current focus is on the use of HTTP or xrooted as the underlying data transport protocols, and the optimization of remote data access through mechanisms such as prefetch and caching.

During the next 2-5 years we expect to be able to exploit remote data access solutions in order to simplify the management of a typical Super$B$ computing center, and to increase the flexibility of data movement and placement.

This approach is supported by the trends in the computing models of other HEP experiments. The LHC experiments are very interested in dynamic and remote data access to augment the data placement models already in place. the Alice [29] experiment has been fully working with this paradigm for the last two years; CMS and ATLAS have recently implemented such solutions for specific use cases (Reference needed).

Neither the current grid-based data management solutions in EGI (ref!) and OSG (ref!), nor the SRM protocol provide a solid infrastructure for direct remote WAN data access; their model still relies on a data driven computing paradigm.

The ALICE data access strategy uses the xrootd/ROOT suite, which natively provides name spaces and data brokering.

The following use cases will greatly benefit from the adoption of a reliable direct WAN data access design:

- Interactive usage of SuperB data, such as event display and single event browsing
- Analysis code development and debugging
- Opportunistic analysis tasks executed on resources not dedicated to Super$B$, for example non-Super$B$ grid computing centers or dynamically allocated cloud resources.

- Job execution on small sites in where the experiment does not have an allocation of storage resources (Tier-3-like)
- Improved reliability and availability, especially when recovering from temporary or partial storage failure at Super$B$ sites

Suitable network protocols for remote data access will have to provide at least the following functionalities:

- Support of a minimal Posix-like API (open, read, seek, close)
- Ability to work through routers and firewalls
- Caching and pre-fetching mechanisms to improve performance over high-latency networks ("latency-hiding")
- Native (really?) support by ROOT [8] framework

At present time at least two protocols are viable candidates that could fulfill these requirements: xrootd [**?**] and HTTP.

Xrootd was developed and is being used primarily within the HEP environment, and provides a high level of functionality useful in HEP. In contrast, HTTP is the dominating protocol on the Internet, is very mature, and is collecting huge interest also outside the HEP environment for use as large-scale data distribution and access protocol.

14.4.5.2 Data access library

Like all the other HEP experiments, Super$B$ is developing its own software framework. As part of this framework, it will be important to implement a library and APIs to standardize and facilitate end user access to data, hiding the complexity of the underlying hardware and software storage implementations, and network contexts.

The development of this general file/data access library is in progress, and it will implement the following features:

- Intelligent pre-fetching and buffering, using the time spent in processing events to read the data from remote storage
- Mapping of logical file names to different (and multiple?) storage URIs.
- Enabling the support of storage protocols not already supported by ROOT
- Read-ahead and caching mechanisms in order to match the performance requirements of different network, application, and storage solution

W

14.4.5.3 File Transfer Service evolution

In addition to direct remote data access, Super$B$ will also need mechanisms for pre-determined data placement. Many other HEP experiments use experiment-developed framworks to move data between sites, that rely on FTS (File Transfer Service, developed within the gLite middleware) as an underlying transport. Currently, FTS can only be used if sites provide an SRM interface for managing the files and a gridftp server to transfer the data. As soon as new protocols like xrootd and HTTP are widely used, it will be important to have an FTS implementation that support these protocols. Within the EMI (European Middleware Initiative) project, there are developments to improve the FTS service, and to add these new protocols.

14.4.5.4 Dynamic file catalogue technology

One of most important components of a distributed data and computing architecture is the File Catalogue. Today, each HEP experiment has its own implementation of this. Super$B$ should consider reusing one of the already available file catalogue solutions, choosing the one that best fits the needs of the experiment. Since HTTP does not provide multi-site brokering functionality, its use will require the file catalogue to manage and provide lists of replicas in HTTP. The next-generation LFC (LCG File Catalogue, ref needed) will provide this functionality. As soon as it is released, we will start tests to confirm that it will fulfill the Super$B$ requirements.

14.4.5.5 Storage system evaluation

Moving and accessing the large volumes of Super$B$ data puts significant requirements on the performance of the underlying storage systems and necessitates dedicated storage system R&D. This is particularly important in order to provide adequate guidance to the site admin community that has to manage the experiment's data.

Data Storage During the last few years the evolution of storage and file system technologies provided significant new features in the areas of clustering and distributed data management. Today we have a multitude of available file system solutions, ranging from open-source file systems to commercial products. The large body of experience in the HEP community will facilitate the selection of working solutions that accommodate the most relevant requirements of Super$B$ computing. The sites that are already running production systems for Super$B$ and other experiments constitute large testbeds for specific file systems like GPFS and Lustre. Their experiences provide the starting point for our evaluation campaign.

The expected use of many-core CPUs has a major impact on storage system capabilities; technology is moving towards a computational model built upon clusters of nodes with large amounts of computing power provided by many-core CPUs as well as GPUs. Such configurations place much higher demands on the I/O subsystem and networks and can easily introduce bottlenecks and scalability problems between CPU nodes and storage systems. The availability of cost-effective multi-10 Gbit/s networks in the near future will also affect how we distribute the access to our data.

These new developments could invalidate the current cluster and site configurations and open up new ways of data distribution and analysis techniques. The Super$B$ storage R&D program is expected to yield feedback on the best use of these new technologies to support the requirements of the experiment.

The Distributed Storage R&D group is in the process of testing several file systems. This activity has two main goals:

- Provide input to the SuperB computing centres on the storage technologies that could be used to serve the storage requirements of the experiment.
- Identify storage technologies that are suitable for building one ore more "virtual computing centres" from loosely coupled federations of geographically distributed data centres and that can provide complete failover solutions for Super$B$ data processing.

The main storage technologies currently under test are: GlusterFS [33], HADOOP-FS, NFSv4.1 [34] and EOS/xrootd [35]. The tests primarily focus on:

- Fail-over characteristics;
- Performance in data analysis and simulation production use cases, and;
- Scalability.

14.5 Summary F.Bianchi 1 pages

Bibliography

[1] http://geant4.web.cern.ch/geant4/.

[2] http://robbep.home.cern.ch/robbep/EvtGen/GuideEvtGen.pdf.

[3] S. Jadach, B. F. L. Ward, and Z. Was, Comput. Phys. Commun. **130**, 260 (2000), arXiv:hep-ph/9912214.

[4] E. Longo and I. Sestili, Nucl. Instr. Meth. **128**, 283 (1975).

[5] K. Nakamura et al. (Particle Data Group), J. Phys. **G37**, 075021 (2010), chapter 27.

[6] G. Grindhammer *et al.*, in Proceedings of the Workshop on Calorimetry for the Supercollider, Tuscaloosa, AL, March 1317, 1989, edited by R. Donaldson and M. G. D. Gilchriese (World Scientific, Teaneck, NJ, 1989), p. 151.

[7] R. K. Bock *et al.*, Nucl. Instr. Meth. **186** (1981) 533. D. Acosta *et al.*, CERN-PPE/91-223, 29 November 1990.

[8] http://root.cern.ch.

[9] http://xrootd.slac.stanford.edu.

[10] http://diracgrid.org/.

[11] http://www.eu-egee.org.

[12] http://www.opensciencegrid.org.

[13] http://www.egi.eu.

[14] http://www.nordugrid.org.

[15] http://www.westgrid.ca.

[16] The LCG TDR Editorial Board, *LHC Computing Grid, Technical Design Report* LCG-TDR-001, CERN-LHCC-2005-024 (2005).

[17] http://lcg.web.cern.ch/LCG.

[18] http://glite.web.cern.ch/glite.

[19] http://glite.web.cern.ch/glite.

[20] http://hep-project-grid-scg.web.cern.ch/hep-project-grid-scg/voms.html.

[21] J. Basney, M. Humphrey and V.Welch, *The MyProxy online credential repository* published online in Wiley InterScience. DOI:10.1002/spe.688.

[22] https://twiki.cern.ch/twiki/bin/view/LCG/LfcAdminGuide.

[23] http://sdm.lbl.gov/srm-wg/doc/SRM.v2.2.html.

[24] A Corso *et al.*, *StoRM, an SRM Implementation for LHC Analysis Farms*, in Computing in High Energy Physics (CHEP 2006), Mumbai, India, Feb. 13–17.

[25] http://ganga.web.cern.ch/ganga.

[26] P. Fuhrmann and V. Glzow, *dCache, Storage System for the Future*. New York: Lecture Notes in Computer Science (Springer, 2006), Vol. 4128, pp. 1106—1113.

[27] The ATLAS Collaboration, ATLAS Detector and Physics Performance Technical Design Report, http://atlas.web.cern.ch/Atlas/GROUPS/PHYSICS/TDR/a

[28] The CMS Collaboration, CMS Detector Tech- nical Design Report, http://cmsdoc.cern.ch/cms/cpt/tdr/.

[29] K. Aamodt et al. (ALICE collaboration), The ALICE experiment at the CERN LHC, Journal of Instrumentation 3, S08002 (2008).

[30] https://twiki.cern.ch/twiki/pub/LCG/DataManagementUsefulPresentations/chep07_poster_DPM.ppt.

[31] http://hadoop.apache.org/

[32] http://www.lustre.org

[33] http://www.gluster.org

[34] http://www.pnfs.com

[35] http://eos.cern.ch/

[36] M. Flechl and L. Field, Grid interoperability: Joining grid information systems, J. Phys. Conf. Ser., vol. 119, p. 062030, 2008.

[37] Fielding R.T., *Architectural Styles and the Design of Network-based Software Architectures* , PhD. Thesis, University of California Irvine, 2000.

[38] http://www.alfresco.com/.

[39] http://www.jasig.org/cas.

[40] http://www.joomla.org/.

[41] http://www.liferay.com/.

[42] http://www.mediawiki.org/wiki/MediaWiki.

[43] http://subversion.apache.org/.

[44] http://git-scm.com/.

[45] http://www.nongnu.org/cvs/.

[46] http://trac.edgewall.org/.

[47] http://www.rpm.org/.

[48] http://yum.baseurl.org/.

[49] http://threadingbuildingblocks.org/.

[50] http://proj-clhep.web.cern.ch/proj-clhep/.

[51] http://cernlib.web.cern.ch/cernlib/.

[52] http://xerces.apache.org/xerces-c/.

15 Facilities, Mechanical Integration and Assembly

Wisniewski/Raffaelli

15.1 Introduction

The *BABAR* detector was built to a design optimized for operations at a high luminosity asymmetric B meson factory. The detector performed well during the almost nine years of colliding beams operation, at luminosities three times the PEP-II accelerator design. There are substantial cost and schedule benefits that result from reuse of detector components from the *BABAR* detector in the Super$B$ detector in instances where the component performance has not been significantly compromised during the last decade of use. These benefits arise from two sources: one from having a completed detector component which, though it may require limited performance enhancements, will function well at the Super$B$ Factory; and the other from requiring reduced interface engineering, installation planning and tooling manufacture (most of the assembly/disassembly tooling can be reused). The latter reduces risk to the overall success of the mechanical integration of the project. Though reuse is very attractive, risks are also introduced. Can the detector be disassembled, transported, and reassembled without compromise? Will components arrive in time to meet the project needs?

The reuse of elements of the PID, EMC and IFR system, and associated support structures have been described in previous chapters. In this section, issues related to the magnet coil and cryostat, and the IFR steel and support structure are discussed as well as the integration and assembly of the Super$B$ detector, which begins with the disassembly of *BABAR*, and includes shipping components to Italy for reassembly there.

15.1.1 Magnet and Instrumented Flux Return

The *BABAR* superconducting coil, its cryostat and cryo-interface box, and the helium compressor and liquefier plant will be reused in whole or in part. The magnet coil, cryostat and cryo-interface box will be used in all scenarios. Use of on-detector pumps and similar components may not be cost effective due to electrical incompatibility. An initial review of local refrigeration facilities at the proposed Frascati Super$B$ site suggests that there may not be sufficient capacity in that system to cool both the detector magnet and the final focus superconducting magnets. The existing *BABAR* helium liquefier plant, which is halfway through its forty year service life, has sufficient capacity. The final decision about reuse of these external service components will take into account electrical compatibility, schedule and cost.

The initial *BABAR* design contained too little steel for quality μ identification at high momentum. Additional brass absorber was added during the lifetime of the experiment to compensate The flux return steel is organized into five structures: the barrel portion, and two sets of two end doors. Each of these is, in turn, composed of multiple structures. The substructures were sized to match the 50 ton load limit of the crane in the *BABAR* hall.

Each of the end doors is composed of eighteen steel plates organized into two modules joined together on a thick steel platform. This platform rests on four columns with jacks and Hilman rollers. A counterweight is also located on the platform. There are nine steel layers of 20 mm thickness, four of 30 mm thickness, four

of 50 mm thickness, and one of 100 mm thickness. During 2002, five layers of brass absorber were installed in the forward end door slots in order to increase the number of interaction lengths seen by μ candidate tracks. In the baseline, these doors will be retained, including the five 25 mm layers of brass installed in 2002, as well as the outer steel modules which can house two additional layers of detectors. Additional layers of brass or steel will be added, following the specification of the baseline design in the instrumented flux return section. A cost-benefit analysis will be performed to choose between brass and steel. The aperture of the forward plug must be opened to accommodate the accelerator beam pipe. Compensating modifications to the backward plug are likely to be necessary. These modifications to the steel may affect the central field uniformity and the centering forces on the solenoid coil, and so must be carefully re-engineered.

The barrel structure consists of six cradles. These are each composed of eighteen layers of steel. The inner sixteen layers have the same thicknesses as the corresponding end door plates. The two outermost layers are each 100 mm thick. The eighteen layers are organized into two parts; the inner sixteen layers are welded into a single unit along with the two side plates, and the outer two layers are welded together and then bolted into the cradle. The six cradles are in turn suspended from the double I-beam belt that supports the detector. During the 2004/2006 barrel LST upgrade, layers of 22 mm brass were installed, replacing six layers of detectors in the cradles. In the Super*B* baseline, these brass layers will be retained, as well as all the additional flux return steel attached to the barrel in the gap between the end doors and barrel. As in the end doors, additional layers of absorber will be placed in gaps occupied in *BABAR* by LSTs. In order to provide more uniform coverage at the largest radius for the μ identification system, modifications to the sextant steel support mechanism are likely to be needed. Finite element analyses are in progress to confirm that deflections of the steel structure due to this alternative support mechanism do not reduce inter-plate gaps needed for the tracking detectors.

15.2 Component Extraction

Extraction of components for reuse requires the disassembly of the *BABAR* detector. This process began after the completion of *BABAR* operations in April 2008. The first stage of the project was to establish a minimal maintenance state, including stand alone environmental monitoring, that preserves the assets that have reuse value. The transition was complete in August. In order to disassemble the detector into its component systems, it must be moved off the accelerator beam line where it is pinned between the massive supports of accelerator beamline elements into the more open space in the IR2 Hall. This required removal of the concrete radiation shield wall, severing of the cable and services connections to the electronics house which contained the off detector electronics, and roll-back of the electronics house 14 m. Electronics, cables and infrastructure that were located at the periphery of the detector were removed. Beamline elements close to the detector were removed to allow access to the central core of the detector by July 2009, allowing removal of the support tube, which contained the PEP-II accelerator final beamline elements as well as the silicon vertex detector, the following month.

The core disassembly sequence was optimized after the Conceptual Design Report. Completion of disassembly of the detector now requires fewer steps, less time, and poses fewer risks, with the end doors being disassembled while the detector is on beamline. As of mid-May 2010, three of the four end doors have been broken down into component parts, and the EMC forward endcap and the drift chamber have been removed, with the final end door breakdown to be completed within a month.

This work has been accomplished as a low priority project with a small crew of engineers and technicians. Though the disassembly project is behind schedule, due to laboratory priori-

ties, the earned value compared to actual costs indicates that the level of effort estimated to perform the disassembly is very accurate. The same methodology used to determine the level of effort needed for the *BABAR* disassembly has been applied in estimating the needs for Super*B* assembly.

The components from *BABAR* that are expected to be reused in Super*B* are expected to be available for transport to Italy in mid-2011. This should present no challenge to the Super*B* project schedule. The remaining steps in the *BABAR* disassembly, which represents more than half of the effort, are outlined below. Tooling that was used in the initial installation of the detector at IR2 is in the process of being refurbished and additional tooling is being fabricated for the disassembly effort. All of this tooling is available for use on Super*B*.

After rolling off the beamline, the next phase of detector disassembly consists of extraction of the DIRC and its support system from the core of the detector. The SOB camera is first removed and will not be reused. In order to minimize the possibility of damage to the DIRC bar boxes and their fused silica bar content, disassembly proceeds with removal of the bar boxes one by one from the bar box support structure inside the DIRC. The twelve bar boxes will be stored in an environmentally controlled container to await shipment to Italy. The DIRC structure is then removed from the barrel.

The barrel EMC is then removed from the barrel steel. The solenoid is removed from the barrel steel. A temporary structure is assembled inside the barrel hexagon to support the upper cradles during disassembly. The upper half of the support belt is removed. Because of the load limitations of the IR2 crane, the six cradles must be disassembled in situ. The outer sections of the top cradles are removed, followed by the inner part of each of the three cradles. The temporary support structure is removed. The inner part of the lower cradles is removed, followed by the outer portions. The balance of the structural belt is disassembled.

15.3 Component Transport

The magnet steel components will be crated for transport to limit damage to mating surfaces and edges. Most, if not all, of these components can be shipped by sea.

The *BABAR* solenoid was shipped via special air transport from Italy to SLAC. It is expected that this component can be returned to Italy in the same fashion. The original transport frame needs some refurbishment. Drawings exist for parts fabrication so that only a small engineering effort is needed here.

The DIRC and barrel calorimeter present transportation challenges. In both cases transport without full disassembly is preferred. In the case of the DIRC, the central support tube will be separated from the strong support tube and transported as an assembly, assuming that engineering studies indicate that this is possible. The transport cradle for the central support tube has had no design effort yet. The bar boxes have a storage container which provides a dry environment. Whether this can be used for air transport, or a newly designed and fabricated container is required, remains to be determined. Disassembly of the bar boxes exposes the precious bars to damage; it is not considered a viable option.

In the case of the EMC, there are two environmental constraints on shipment of the device or its components. The glue joint that attached the photodiode readout package to the back face of the crystal has been tested, in mock-up, to be stable against temperature swings of $\pm 5^{\circ}$C. During the assembly of the endcap calorimeter, due to a failure of an air conditioning unit, the joints on one module were exposed to double this temperature swing. Several glue joints parted. The introduction of a clean air gap causes a light yield drop of about 25%. In order to avoid this reduction in performance, temperature swings during transport must be kept small. Since the crystals are mildly hygroscopic, it is best that they be transported in a dry environment to avoid changes in the surface reflectivity, and consequent modification in the

longitudinal response of the crystal. Individual *BABAR* endcap modules constructed in the UK were successfully shipped to the USA in specially constructed containers that kept the temperature swings and humidity acceptably small.

Disassembly of the barrel calorimeter for shipment presents a substantial challenge. Both the disassembly and assembly sites need to be temperature and humidity controlled. The disassembly process requires removal of the outer and inner cylindrical covers, removal of cables that connect the crystals with the electronics crates at the ends of the cylinder, splitting of the cylinder into its two component parts and removal of the 280 modules for shipment. Though much of the tooling is still in hand, the environmentally conditioned buildings used in calorimeter construction at SLAC no longer exist, though alternative facilities could be outfitted. The cooling and drying units used in the module storage/calorimeter assembly building continue to be available.

The clear preference is to ship the barrel calorimeter as a single unit by air. With tooling support stand and environmental conditioning equipment, the load is likely to exceed 30 tons. It is anticipated that such a load could be transported in the same way as the superconducting coil and its cryostat, but verification is needed. Detailed engineering studies, which model accelerations and vibrations involved with flight that might cause the crystal containing carbon fiber modules to strike against one another, are needed to determine if the calorimeter can be safely transported. It may be that a module restraint mechanism will need to be engineered and fabricated. A transport frame must be designed and its performance modeled. Engineering studies have begun.

15.4 Detector Assembly

Assembly of the Super*B* detector is the inverse of the disassembly of the *BABAR* detector. Ease of assembly will be influenced by the facilities which are available. In the case of *BABAR*, the use of the IR2 hall, which was "too small", led to engineering compromises in the design of the detector. Assembly was made more complicated by the weight restrictions posed by the 50 ton crane. Upgrades were made more difficult because of limitations in movement imposed by the size of the hall.

The preferred dimensions for the area around the Super*B* detector when it is located in the accelerator housing are 16.2 m transverse to the beamline, 20.0 m along the beamline, 11.0 m from the floor to the bottom of the crane hook, 15.0 m from floor to ceiling, and 3.7 m from the floor to the beamline. The increased floor to beamline height relative to *BABAR*-PEP-II , will require redesign effort for the underpinnings of the detector cradle. However, this will permit improved access for installation of cable and piping services for the detector, as well as make possible additional IFR absorption material for improved μ detector performance below the beamline. In order to facilitate detector assembly, the preferred capacity for the two hook bridge crane is 100/25 tons.

16 The SuperB Collaboration and Project Management

During the pre-approval phase of the project, the Super$B$ detector was organized as a "Proto-collaboration", with a structure modeled on that of the *BABAR* detector. Leadership was centered in the 'Proto-technical" Board which included technical leadership for all subsystems (SVT, DCH, PID, EMC,IFR); the general detectors systems (electronics, DAQ, computing, and simulation), and the machine detector interface (MDI). The "Proto-technical" Board was led by Detector Co-leaders and the Proto-Technical Coordinator who provided executive direction and decision making for the collaboration with the guidance of the Board. Subsystem status and progress were reviewed by the Board at regularly scheduled meetings. Major overall decisions about the detector were also reviewed by the Board, aided in the more challenging cases by recommendations provided by ad-hoc review committees and a geometry working group appointed by the leadership.

Following formal project approval in Dec. 2010, the Super$B$ detector "Proto-Collaboration" began the transition to the Super$B$ detector Collaboration. The inaugural Collaboration forming meeting was held in Elba in May-June 2011. Initial steps were defined to begin to organize the experimental collaboration, while allowing time for new groups to become involved from the worldwide community. The basic model was suggested by the long history of successful experimental collaborations in particle physics with particular reference to the successful experience of the *BABAR* detector. Given the success of the Super$B$ Proto-collaboration to date and its ability to deal with most executive and technical functions, this structure was retained during the interim period until the new executive and technical structures could be defined by the Collaboration and new leadership appointed. This bootstrapping process began by establishing a Proto-council composed of the PIs of the collaborating institutions to provide input to the process, approve default membership and interim leadership, and provide monitoring of the working committees. This Proto-council then approved the appointment of a Governance committee to develop the bylaws of the collaboration, and a continuation of the Proto-speakers bureau to select speakers for conferences to the bridging period.

The Governance committee, in consultation with collaboration membership, Proto-collaboration leadership, and the Laboratory project leadership (now the Cabbibo Laboratory), drafted a Governance document for the collaboration. This document [1] was unanimously approved at the March 2012 meeting of Super$B$ and the Proto-council became the Council of the Collaboration. Following the procedures described in the Governance document, The Council chair was selected and a Council committee is now being appointed to select the leadership of the collaboration. The Council also appointed an Executive Board to deal with issues that go beyond those managed by the Proto-technical board. Given the fact that the collaboration will evolve substantially in the coming months, the initial terms for this Executive Board were set to one year.

In this chapter, we summarize the collaboration organization as detailed in the Governance document. Fig ?? shows a schematic outline of the present organization.

16.1 Collaboration Membership

The Super$B$ Detector Collaboration is the organization of scientists belonging to academic or research Institutions worldwide whose goal is the exploitation of the physics potential of the Super$B$ electron-positron asymmetric collider. Institutions who participate in the Collaboration are expected to make significant contributions to the construction and operation of the Super$B$ detector, including its computing systems, both hardware and/or software. Participating Institutions are entitled to be represented in the Collaboration Council, and, to preserve their membership, they must actively participate in the Super$B$ program and comply with the obligations that are defined by the Collaboration in terms of financial and service contributions. Ph.D. physicists, engineers, and Ph.D. thesis students who belong to a participating Institution can become members of the Collaboration if they intend to devote a substantial fraction of their research time to the Super$B$ program over a period of several years. Participation of an individual in Super$B$ is at the discretion of the Institution to which he or she is accredited. Members of the Collaboration are eligible to be included in the author list.

16.2 The SuperB Collaboration Council

The Collaboration Council, representing the full membership of the Collaboration, is the principal governing body of the Collaboration. Institutions with two or more Collaboration members who are Ph.D. physicists will be directly represented on the Collaboration Council. Members of the Collaboration from Institutions with fewer than two Ph.D. physicists may affiliate with another Institution for the purpose of representation, while larger institutions will be given additional representation. The Council has an elected Chair and Vice-Chair. Council decisions are to be agreed by consensus wherever possible. Should a situation arise where consensus cannot be reached, a time scale shall be set for the decision to be reached at a later date and the matter will then be decided at a subsequent meeting of the Council, by a vote if necessary.

The Council selects and may remove the executive leadership of the collaboration, particularly the Spokesperson and the Executive Board via specific defined procedures of the Governance document. The Spokesperson is the scientific leader of the Collaboration, responsible for financial, scientific, technical, and organizational decisions pertaining to the Collaboration. The Spokesperson is assisted by a Management Team. The Executive Board is responsible for advising the Spokesperson on all scientific, financial, and organizational matters pertaining to the Collaboration. The details of the management structure, including the roles and responsibilities of individual managers, the roles and responsibilities of additional groups such as the Technical Board, the Management Team, the Publication Board, and Physics Analysis Groups will be established in a management plan, proposed by the Spokesperson, endorsed by the Executive Board and ratified by the Council.

The Collaboration Council will concern itself with issues related to the overall framework of the Collaboration. It will ratify the Collaboration by-laws and the organizational structure, insofar as it is specified in the Collaboration Constitution, and vote on proposed amendments, which may be introduced by any Council representative or by the Spokesperson.

The Chairperson, in consultation with the Collaboration, possibly through the appointment of a search committee, will select candidates for ratification by Council for the several boards and committees that are to be established by the Council.

The Collaboration Council will appoint a Membership Committee, which will make recommendations to the Council regarding membership issues, including the admission of new Institutions. Ratification of such recommendations requires a two-thirds majority vote of the Council.

The Collaboration Council will be responsible for developing a publications policy and for appointing a Publications Board to approve papers for publication. The Board will be responsible for maintaining a list of eligible authors for both instrumental and physics papers. The Collaboration Council will also be responsible for appointing a Speakers Bureau to organize Collaboration presentations at conferences and workshops as appropriate and to determine who will represent the Collaboration at such meetings.

16.3 The SuperB Spokesperson

The Collaboration will be led by a single Spokesperson, who is the scientific leader of the Collaboration, responsible for financial, scientific, technical, and organizational decisions pertaining to the Collaboration. The Spokesperson also serves, ex-officio, as Chair of the Executive Board and as an ex-officio member of the international body of agencies organized by the Cabibbo-Lab to support the Super*B* detector experiment Collaboration through the construction and operation phases (indicated in the following as IFC, International Finance Committee).

The Spokesperson, with the endorsement of the Executive Board, proposes a Management Plan to the Council for ratification, and a Management Team that will assist him/her in the execution of the Super*B* program. The Spokesperson is expected to devote all his/her research time to the position, and must be willing and able to take up residence at Cabibbo-Lab when detector commissioning begins.

During the construction phase, the initial term for the Super*B* Spokesperson is 3 year long, renewable, which will allow long-range planning and will provide continuity. Renewal for additional terms will be discussed and endorsed by the Council at least 9 months before the end date. The construction phase, and the Spokesperson term, will end on the September 1 that follows the first year in which the experiment has accumulated at least three months of beam. During the data taking phase, the Spokesperson will serve a single 2 year term, non-renewable, beginning September 1 of the relevant year, during which time he/she must be resident at the laboratory. At the end of his/her term, the retiring spokesperson serves for a year in the management team by mutual agreement with the incoming spokesperson.

16.4 The SuperB Executive Board

The Executive Board advises the Spokesperson on all scientific, financial, and organizational matters of the Collaboration. It consists of members distinguished by their scientific judgment, technical expertise, commitment to the experiment, and ability to speak knowledgeably and effectively for the regions they represent.The Spokesperson will chair the Executive Board. The Executive Board will meet at least eight times per year. The Board will also meet at least once each year with ex-officio members not present to review the performance of the management team. By a two-thirds majority vote of the entire Executive Board, the Board may recommend to the Collaboration Council that the Spokesperson be removed.

The number of members reflects the national composition of the collaboration. Initially, the Board will consist of one representative each from Canada, France, Russia, Poland, U.S., and the U.K. and six representatives from Italy. In addition, the Spokesperson, the Spokesperson-Elect, and the Chairperson of the Collaboration Council will be nonvoting ex-officio members of the Executive Board. The Cabibbo-Lab Directorate will appoint a senior scientist who is also a member of the Super*B* Detector Collaboration to sit on the Executive Board as an ex-officio member. From time to time, the Board will review its regional composition, in consultation with the Cabibbo-Lab management, and will propose changes to the Collaboration Council that it mayl approve with a qualified majority.

Membership on the Collaboration Council does not preclude membership on the Executive

Board. However, members of the Management Team may not serve simultaneously as members of the Executive Board. The normal term of office for the Executive Board will be three years, renewable, with one-third of the members being replaced or renewed each year.

16.5 The SuperB Management Team and Management Plan

The overall execution of the Super$B$ program is the responsibility of a Management Team led by the Spokesperson. The Management Team consists of: the Spokesperson, the Physics Analysis Coordinator, the Technical Coordinator, the Computing Coordinator, and the Spokesperson-elect when that office is filled. The Spokesperson may decide to designate at most two additional members to the management team, such as a Deputy Spokesperson, Financial Coordinator, and/or a Senior Advisor.

The Technical Coordinator is in charge of detector operations and hardware development. He/she is responsible for the common project construction and the technical integration of all Super$B$ components. He/she provides oversight for the implementation of Super$B$ engineering standards and procedures and the subsystem construction, commissioning and operations. He/she is assisted by managers responsible for the sub-systems. The Physics Analysis Coordinator is in charge of coordinating the analysis infrastructure and planning for physics analyses leading to publication. He/she is assisted by physics-topic group conveners . The Computing Coordinator is in charge of planning for and coordinating the software and computing activities and resources necessary for data acquisition and analysis.

The precise details of the management structure may evolve with time, including the roles and responsibilities of individual members of the Management Team and of additional groups such as the Technical Board, and Physics Analysis Groups will be established in a Management Plan, proposed by Spokesperson, approved by the Executive Board by a majority vote and ratified by the Council with a majority vote. In particular, the roles of the Technical Board and its members will be at the heart of collaboration activities during the fabrication and commissioning phases of the experiment, but will become less central as time passes. The Technical Coordinator will be nominated with the agreement of the Cabibbo-Lab Management.

16.6 International Finance Review Committee

An International Finance Review Committee instituted by the Cabibbo Laboratory will monitor the financial aspects of the experiment as detailed in the management plan and agreed between the Cabibbo Laboratory, the collaboration, and the International Funding Agencies. This will be described in Memoranda of Understanding between the participating institutional partners and Cabibbo Laboratory.

16.7 Interaction with the Cabibbo-Lab

The Spokesperson will plan regular meetings with Cabibbo-Lab management. He/she will report to the International Cabibbo-Lab Scientific Committee on different aspects of the experiment in order to converge on the detector design, review the construction, installation and commissioning. He/she will also propose for endorsement to the Cabibbo-Lab and International Finance Committee the annual construction, maintenance and operation budgets of the detector.

16.8 Communications

Collaboration meetings are held four times per year, typically March, May/June, September, and December. At least one meeting per year

is expected to be held outside Italy. Routine operations require extensive and consistent use of modern multi-site interaction and communication tools and methods. These methods are widely understood and practiced within the community. (????More here)

16.9 Construction Responsibilities

The design of the Super*B* detector described in this report began with the excellent *BABAR* detector. It then went through an extended process of optimization of the design of individual systems and the detector as a whole against the required physics performance, the interests and technical capabilities of the collaborating institutions, and financial constraints. In cases where there were conflicting requirements or competing technologies, task forces were employed to evaluate alternatives and recommend the appropriate choice. These include task forces for the forward PID, the backward EMC, and the forward EMC. All design decisions have been informed by a long term simulation task force (the Geometry Working Group), and background simulation effort.

Specific responsibilities for design and construction of the various detector subsystems have yet to be fully specified, and will be discussed more completely in a later document. We expect that they will be assigned through the traditional process of matching interests, capabilities, and resources. Final responsibilities will be detailed in Memoranda of Understanding. The collaboration expects to finance certain items through a common fund. Details remain under discussion.

??????????????????

Bibliography

[1] M. Morandin *et al.* (Super$B$ Governance Committee),"SuperB Detector Collaboration Constitution", Where is this? (2012).

17 Cost and Schedule

FF+BR+All

The Super$B$ detector cost and schedule estimates, presented in this chapter, rely heavily on experience with the *BABAR* detector at PEP-II . The reuse and refurbishing of existing components has been assumed whenever technically possible and financially advantageous. Though these Super$B$ estimates are based on a bottoms-up evaluation using a detailed work breakdown schedule, it should be emphasized that the detector design is still incomplete, with numerous technical decisions remaining to be made, and limited detailed engineering to date, so that that cost and schedule can not yet be evaluated at the detailed level expected in a technical design report.

The costing model used here is similar to that already used for the Super$B$ CDR. The components are estimated in two different general categories; (1) "LABOR" and, (2) M&S (Materials and Services). M&S cost estimates are given in 2010 Euros and include 20% of Value Added Tax (VAT). The "LABOR" estimates comprise two sub categories which are kept and costed separately as they have differing cost profiles;(1) EDIA (Engineering, Design, Inspection, and Administration) and (2) Labor (general labor and technicians). Estimates in both categories are presented in manpower work units (Man-Months) and not monetized, as a monetary conversion can only be attempted after institutional responsibilities have been identified and the project timescale is known. The total project cost estimate can be calculated, once the responsibilities are identified, by summing the monetary value of these three categories.

Given the long term nature of this multinational project, there are several challenging general issues in arriving at appropriate costs including (1) fluctuating currency exchange rates, and (2) escalation. M&S costs and factory quotes that have been directly obtained in Euros can be directly quoted. M&S estimates in US Dollars are translated from Dollars to Euros using the exchange rate as of Jun 1, 2010 (0.8198 Euros/US$). For costs in Euros that were obtained in earlier years, the yearly escalation is rather small. For simplicity, we use a cost escalation rate of 2% per year which is consistent with the long term HICP (Harmonized Index of Consumer Prices) from the European Central Bank. Costs given in 2007 Euros are escalated by the net escalation rate (1.061) for three years to arrive at the 2010 cost estimates given here [1].

For all items whose cost basis is *BABAR*, we accept the procedure outlined in the Super$B$ CDR which arrived at the costs given there in 2007 Euros. This procedure escalated the corresponding cost (including manpower) from the PEP-II and *BABAR* projects from 1995 to 2007 using the NASA technical inflation index [2] and then converted from US Dollars to Euros using the average conversion rate over the 1999—2006 period [3]. The overall escalation factor in the CDR from 1995 Dollars to 2007 Euros is thus $1.21 = 1.295 \times 0.9354$.

Similarly, the replacement values ("Rep.Val.") of the reused components, *i.e.*, how much money would be required to build them from scratch, as presented in separate columns of the cost tables, have been obtained by escalating the corresponding *BABAR* project cost (including manpower) from 1995 to 2007. Though it is tempting to sum the two numbers to obtain an estimate of the cost of the project if it were to be built from scratch, this procedure yields somewhat misleading results because of the different treatment of the manpower (rolled up in the replacement value; separated for the new cost estimate) and because of the double counting when the refurbishing costs are added to the initial values.

Contingency is not included in the tables. Given the level of detail of the engineering and the cost estimates, a contingency of about 35% would be appropriate.

17.1 Detector Costs

The costs, detailed in Table 17.1, are presented for the detector subsystem at WBS level 3/4.

Table 17.1: Super$B$ detector budget.

WBS	Item	EDIA mm	Labor mm	M&S kEuro	Rep.Val. kEuro
1	**Super$B$ detector**	**4037**	**2422**	**52953**	**48922**
1.0	**Interaction region**	**21**	**12**	**860**	**0**
1.0.1	**Be Beampipe**	**10**	**4**	**260**	**0**
1.0.1.1	Vertex chamber design	4	0	0	**0**
1.0.1.2	Finalize Physics Req.mnts	1	0	0	**0**
1.0.1.3	Fab method	1	0	0	**0**
1.0.1.4	Design Review	1	0	0	0
1.0.1.5	Chamber detailing	2	0	0	0
1.0.1.6	Support procurement	2	0	5	0
1.0.1.7	Procure Beampipe Assembly	0	0	243	0
1.0.1.8	Procure Vx chamber Misc parts	0	0	12	0
1.0.1.9	Assemble Vx chamber, test, clean	0	2	0	0
1.0.2	**Tungsten Shield**	**9**	**6**	**540**	**0**
1.0.2.1	Shield optimization	3	0	0	0
1.0.2.2	Shield detailing and integration	3	0	0	0
1.0.2.3	Shield procurement	1	0	540	0
1.0.2.4	Shield assembly and installation	2	6	0	0
1.0.3	**Radiation monitors**	**2**	**2**	**60**	**0**
1.1	**Tracker (SVT + Strip + MAPS)**	**408**	**442**	**6444**	**0**
1.1.1	**SVT**	**222**	**309**	**4326**	**0**
1.1.1.1	Mechanical	48	129	399	0
1.1.1.2	Cooling	8	10	155	0
1.1.1.3	Silicon Wafers and Fanout	24	120	2642	0
1.1.1.4	On-detector electronics	72	42	1013	0
1.1.1.5	Detector monitoring	4	4	92	0
1.1.1.6	Detector assembly	6	4	0	0
1.1.1.7	System Engineering	60	0	24	0
1.1.2	**L0 Striplet option**	**36**	**55**	**542**	**0**
1.1.2.1	Mechanical	12	30	60	0
1.1.2.2	Cooling	3	3	48	0
1.1.2.3	Silicon Wafers and Fanout	16	18	327	0
1.1.2.4	On-detector electronics	5	4	108	0
1.1.3	**L0 MAPS option**	**150**	**78**	**1576**	**0**
1.1.3.1	Mechanical	18	48	90	0
1.1.3.2	Cooling	6	6	96	0
1.1.3.3	MAPS Modules Components	126	24	1390	0
1.1.4	**L0 Hybrid Pixel option**	**156**	**84**	**1684**	**0**
1.1.4.1	*Mechanical*	*18*	*48*	*90*	*0*
1.1.4.2	*Cooling*	*6*	*6*	*96*	*0*
1.1.4.3	*Hybrid Pixel Modules Components*	*132*	*30*	*1498*	*0*
1.2	**DCH**	**165**	**139**	**3421**	**0**
1.2.1	System engineering	24	0	60	0
1.2.2	Endplates	16	6	660	0
1.2.3	Inner cylinder	8	2	200	0
1.2.4	Outer cylinder	6	2	120	0
1.2.5	Wire	4	6	308	0
1.2.6	Feedthroughs	9	10	439	0

Continued on next page

Table 17.1 – continued from previous page

WBS	Item	EDIA mm	Labor mm	M&S kEuro	Rep.Val. kEuro
1.2.7	Endplate systems	8	0	385	0
1.2.8	Assembly & Stringing	74	96	960	0
1.2.9	Gas System	10	8	240	0
1.2.A	Test	6	9	48	0
1.3	**PID**	**116**	**236**	**5820**	**7138**
1.3.1	**DIRC Barrel (Focusing DIRC)**	**116**	**236**	**5820**	**7138**
1.3.1.1	Radiator Support Structure	4	4	10	2516
1.3.1.2	Radiator box/FBLOCK assembly	14	40	2819	4515
1.3.1.3	New Camera mechanical boxes	14	28	305	0
1.3.1.4	Photodetector assembly	18	32	2607	0
1.3.1.5	Calibration System	2	4	59	0
1.3.1.6	Mechanical Utilities	4	8	20	107
1.3.1.7	System Integration	60	120	0	0
1.4	**EMC**	**219**	**360**	**12147**	**31574**
1.4.1	**Barrel EMC**	**20**	**5**	**205**	**31574**
1.4.1.1	Crystal Procurement	0	0	0	21742
1.4.1.2	Light Sensors & Readout	0	0	0	2654
1.4.1.3	Crystal Support Modules	0	0	0	2875
1.4.1.4	Barrel Structure	0	0	0	3419
1.4.1.5	Calibration Systems	0	0	0	650
1.4.1.6	Project Management	0	0	0	233
1.4.1.7	Barrel Transport	20	5	205	0
1.4.2	**Forward EMC**	171	312	11565	0
1.4.2.1	Crystal Procurement	25	102	9403	0
1.4.2.2	Light Sensors \& Readout	47	70	992	0
1.4.2.3	Crystal Support Modules	26	64	450	0
1.4.2.4	Endcap Structure	26	52	444	0
1.4.2.5	Calibration Systems	24	24	156	0
1.4.2.6	Project Management	24	0	120	0
1.4.3	**Backward EMC**	28	43	377	0
1.4.3.1	Scintillator	2	10	121	0
1.4.3.2	Radiator	1	4	22	0
1.4.3.3	Fibers	4	8	18	0
1.4.3.4	Photodetectors	2	5	46	0
1.4.3.5	Mechanical support	17	15	146	0
1.4.3.6	Project Management	2	2	24	0
1.5	**IFR**	**37**	**184**	**1374**	**0**
1.5.1	Scintillators	0	0	266	0
1.5.2	WLS fibers	0	0	362	0
1.5.3	Photodetectors and PCBs	1	2	685	0
1.5.4	Mechanics (Production and QC)	16	62	60	0
1.5.5	Module Installation	20	120	0	0
1.6	**Magnet**	**93**	**59**	**3767**	**10210**
1.6.0	System Management	36	0	0	612
1.6.1	Superconducting solenoid	0	0	0	2421
1.6.2	Mag. Power/Protection	0	0	0	181
1.6.3	Cryogenics	34	36	1753	0
1.6.4	Cryo monitor/Control	17	11	214	0

Continued on next page

Table 17.1 – continued from previous page

WBS	Item	EDIA mm	Labor mm	M&S kEuro	Rep.Val. kEuro
1.6.5	Flux return	6	12	1800	6481
1.6.6	Installation/test equipment	0	0	0	515
1.7	**Electronics**	**994**	**342**	**9234**	**0**
1.7.1	SVT	11	21	561	0
1.7.2	DCH	74	76	1668	0
1.7.3	PID Barrel (32k channels)	136	18	612	0
1.7.4	EMC	110	164	2726	0
1.7.5	IFR	38	51	1487	0
1.7.6	Infrastructure	4	12	314	0
1.7.7	Systems Engineering	12	0	0	0
1.7.8	Hardware Trigger	97	0	678	0
1.7.9	ETD (without Trigger)	512	0	1188	0
1.8	**Online System**	**912**	**24**	**2074**	**0**
1.8.1	Event Flow	282	0	1676	0
1.8.2	Run Control / Slow Controls / ECS	270	0	53	0
1.8.3	Infrastructure	48	12	246	0
1.8.4	Software Triggers	216	0	0	0
1.8.5	Coordination and Commissioning	72	12	0	0
1.8.6	Online System R&D	24	0	98	0
1.9	**Installation and integration**	**353**	**624**	**7596**	**0**
1.9.1	Disassembly	95	161	612	0
1.9.2	Assembly	222	463	3984	0
1.9.3	Structural analysis	36	0	0	0
1.9.4	Transportation	0	0	3000	0
1.A	**Project Management**	**720**	**0**	**216**	**0**
1.A.1	Project engineering	300	0	120	0
1.A.2	Budget, Schedule and Procurement	300	0	48	0
1.A.3	ES & H	120	0	48	0

The Super*B* detector is not completely defined: some components, such as the forward PID, have overall integration and performance implications that need to be carefully studied before deciding to install them; for some other components, such as the SVT Layer0, promising new technologies require additional R&D before they can be definitively used in a full scale detector. The cost estimates list the different technologies separately, but the rolled-up value includes the baseline detector choice that is considered most likely to be used. Technologies that are not included in the rolled-up value are shown in italics.

17.2 Basis of Estimate

Vertex Detector and Tracker: System cost is estimated based on experience with the *BABAR* detector and vendor quotes. A detailed estimate is provided for the cost of the main detector (layers 1 to 5). The costs associated with Layer0 are analyzed separately. The costing model assumes that a striplet detector will be installed initially – followed by a second generation upgrade to a pixel detector, which could either be either a MAPs or hybrid pixel device. Substantial R&D on these new technologies is needed in either case before such a detector can be built. The total SVT cost is obtained by summing the baseline detector cost (with striplets for Layer0) to the MAPS Layer0 cost.

Drift Chamber: The DCH costing model is based on a straightforward extrapolation of the actual costs of the existing *BABAR* chamber to 2010, since, as discussed in Sec. 7 the main design elements are comparable, and many related components, such as the length of wire, number of feedthroughs, duration of wire stringing, etc., can be reliably estimated. Although the cell layout is still being finalized, the total cell count will likely be about 25% larger The endplates will be fabricated from carbon fiber composites instead of aluminum. Though this will require a somewhat longer period of R&D and engineering design, it is unlikely to result in significantly larger production costs for the final endplates. The DCH electronics on Table 17.1 assumes standard readout as discussed in Sec. 13.1.2. A *cluster counting* readout option is under R&D, but is not yet sufficiently advanced that costs can be provided.

Particle Identification: Barrel PID costs and replacement values are derived from *BABAR* costs as extrapolated to 2010, with updated quotes from vendors. The main new component of the barrel FDIRC is its new camera. For each module, the optical portion consists of the focusing block (FBLOCK), an addition to the wedge (the New Wedge) and possibly a Micro-Wedge. We have contacted about twelve optics companies and received four preliminary bids. We use the average bid in the present budget. We hope to continue to refine the values through further R&D. The photon detector cost estimate is based on the Hamamatsu bid for 600 H-8500 MaPMTs. No budget estimate is included at this time for a forward endcap PID. Though several options are being studied, their performance and cost are yet to be well understood, and the overall performance gains and losses of including a forward PID in the detector are as yet unsettled. However, as a general principle, given the limited solid angle covered by such a device, the cost of a forward PID detector must be a modest fraction of the barrel.

Electromagnetic Calorimeter: There are four components to the calorimeter cost: (1) the barrel calorimeter from *BABAR*; (2) the forward calorimeter; (3) the replacement of the front-end preamps in the barrel; and (4) the backward calorimeter. As described in the calorimeter section, there are a number of uncertainties remaining in the design. The present cost estimate is for our baseline design.

The reuse value of the barrel calorimeter is based on the actual cost of the barrel escalated for inflation from the time of construction to the current year. Manpower estimates for the barrel construction were obtained by using the costs for EDIA and Labor, knowledge of the mix of engineers and technicians who contributed to

the design and fabrication of individual components, and knowledge of their salaries. Manpower and costs for engineering and tooling required for the removal and transport of the barrel EMC from SLAC are engineering estimates.

The main cost driver for the forward endcap is the cost of LYSO crystals. This is estimated based on guideline quotes from vendors. The next largest element is the APD photodetectors, with a cost based on a quote from the vendor. The estimate for the crystal support modules is based on costs for the beam test prototype. Estimates for the remaining smaller items are based on estimator experience and judgment.

The cost estimate for replacing the preamplifiers in the barrel calorimeter is based on the endcap preamplifier cost as well as the cost of dealing with the mechanical issues.

For the backward endcap, the scintillator, lead, wavelength-shifting fiber, and readout MPPC costs, as well as some other minor materials, are all based on vendor quotes. Other items are based on experience and estimator judgment.

Instrumented Flux Return: The IFR cost is based on quotations received for the prototype construction appropriately scaled to the real detector dimensions. While the active part of the detector is quite inexpensive the total cost is driven by the electronics and the photodetectors. The current baseline design allows the reuse of the *BABAR* iron structure with some modification that needs to be taken into account. Manpower and cost for engineering and module installation is based on the *BABAR* experience.

Electronics, Trigger, DAQ and Online: The cost for the Electronics and Trigger subsystems is estimated with a combination of scaling from the *BABAR* experience and from direct estimates. For items expected to be similar to those used in *BABAR* (such as infrastructure, high and low voltage or the L1 trigger) costs are scaled from *BABAR*. The same methodology is used to estimate EDIA and Labor costs for the Online system. However, some modifications based on "lessons learned" are applied. In particular, we are including costs for development work that, in our opinion, should have been centralized across sub-detectors in *BABAR* (but wasn't) and work that should have been done upfront but was only done or completed as part of *BABAR* Online system upgrades.

The readout systems for which the higher data rates require redesigned electronics are estimated from the number of different components and printed circuit boards, and their associated chip and board counts. This methodology is also used for the possible new detectors (forward EMC, backward EMC, forward PID) and for the elements of the overall system architecture that are very different from *BABAR*.

The hardware cost estimates for the Online computing system (including the HLT farm) are, very conservatively, based on the current prices of hardware necessary to build the system, with the assumption that Moore's Law will result in future systems with the same unit costs but higher performance. This is justified by our observation that for COTS components, constraints from system design, topology and networking are more likely to set minimum requirements for the *number* of devices than for the per-device performance.

Transportation, installation, and commissioning: Installation and commissioning estimates, including disassembling and reassembling *BABAR*, are based on the *BABAR* experience, and engineering estimates use a detailed schedule of activities and corresponding manpower requirements. The transportation costs have been estimated from costs associated with disassembling and transporting *BABAR* components for dispersal, if they were not to be reused.

17.3 Schedule

The detector construction schedule is shown in Fig. 17.1. The construction starts with design finalization and a technical design report, after which the fabrication of the detector subsystems can proceed in parallel. At the same time the *BABAR* detector is disassembled, transported to

the new site, and reassembled. The detector subsystems will be installed in sequence. An extended detector commissioning period, including a cosmic ray run, will follow to ensure proper operation and calibration of the detector. The total construction and commissioning time is estimated to be a little over five years.

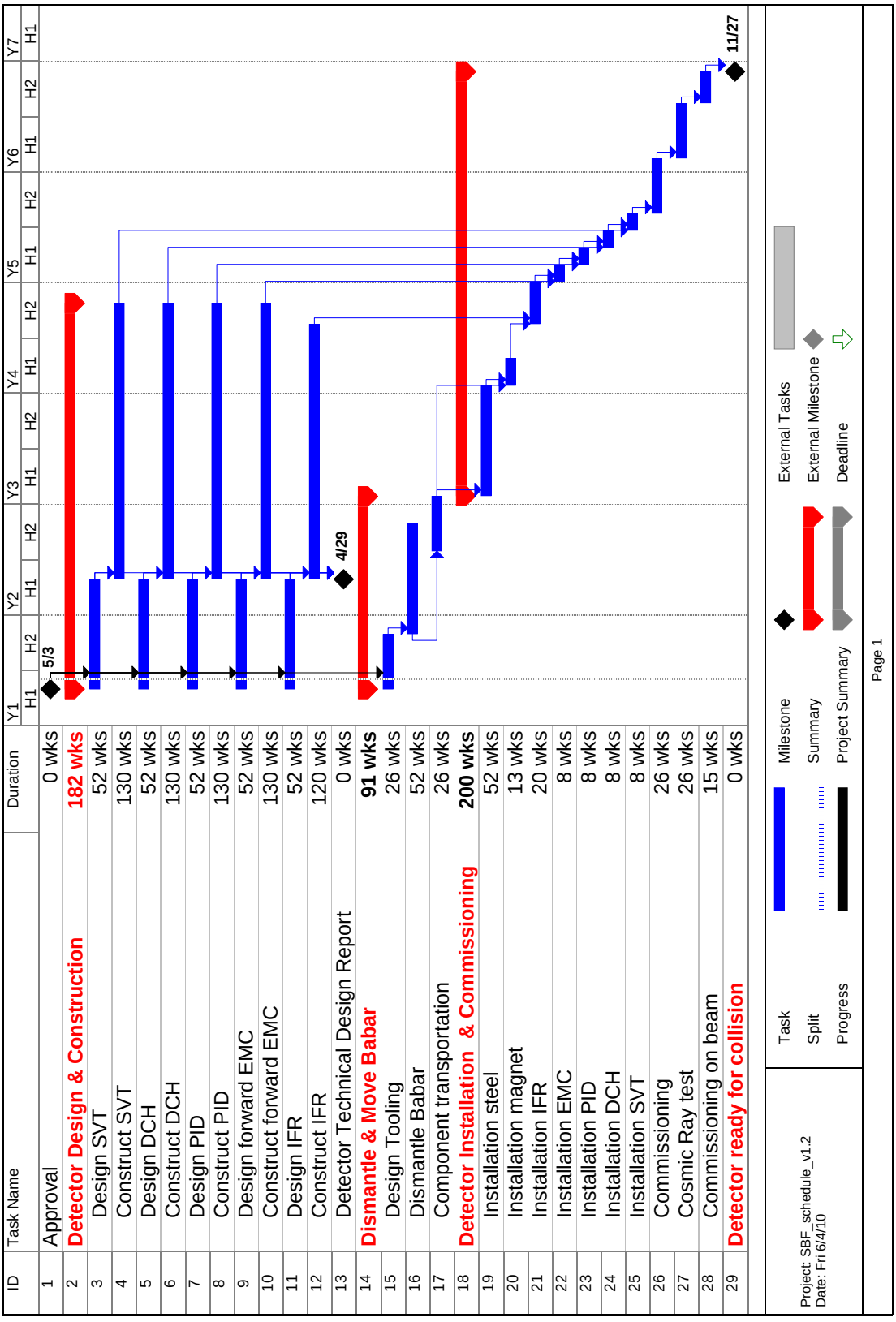

Figure 17.1: Schedule for the construction of the Super$B$ detector.

Bibliography

[1] Euro Inflation Rates, http://www.ecb.int/stats/prices/hicp/html/index.en.html.

[2] NASA Inflation Calculator, http://cost.jsc.nasa.gov/inflation/nasa/inflateNASA.html.

[3] Federal Reserve Foreign Exchange Rates, http://www.federalreserve.gov/releases/g5a/.